Universität Hamburg
DER FORSCHUNG | DER LEHRE | DER BILDUNG

Two Particle Consistent Ladder Dynamical Vertex Approximation

Dissertation
zur Erlangung des Doktorgrades an der
Fakultät für Mathematik, Informatik und Naturwissenschaften
Fachbereich Physik Universität Hamburg

Vorgelegt von
Julian Stobbe

Hamburg, 2024

Gutachter der Dissertation:	Prof. Dr. Georg Rohringer Prof. Dr. Alexander Lichtenstein
Zusammensetzung der Prüfungskommission:	Prof. Dr. Georg Rohringer Prof. Dr. Alexander Lichtenstein Prof. Dr. Michael Potthoff Prof. Dr. Michael Thorwart Prof. Dr. Michael A. Rübhausen
Vorsitzende/r der Prüfungskommission:	Prof. Dr. Michael Potthoff
Datum der Disputation:	22.5.2025
Vorsitzender des Fach-Promotionsausschusses Physik:	Prof. Dr. Wolfgang J. Parak
Leiter des Fachbereichs Physik:	Prof. Dr. Markus Drescher
Dekan der Fakultät MIN:	Prof. Dr.-Ing. Norbert Ritter

Eidesstattliche Versicherung

Hiermit versichere ich an Eides statt, die vorliegende Dissertationsschrift selbst verfasst und keine anderen als die angegebenen Hilfsmittel und Quellen benutzt zu haben.

Sofern im Zuge der Erstellung der vorliegenden Dissertationsschrift generative Künstliche Intelligenz (gKI) basierte elektronische Hilfsmittel verwendet wurden, versichere ich, dass meine eigene Leistung im Vordergrund stand und dass eine vollständige Dokumentation aller verwendeten Hilfsmittel gemäß der Guten wissenschaftlichen Praxis vorliegt. Ich trage die Verantwortung für eventuell durch die gKI generierte fehlerhafte oder verzerrte Inhalte, fehlerhafte Referenzen, Verstöße gegen das Datenschutz- und Urheberrecht oder Plagiate.

24-02-2025 

Datum Unterschrift der Doktorandin / des Doktoranden

Zusammenfassung Viele wichtige elektronische Eigenschaften in der Festkörperphysik, wie magnetische Ordnung und Hochtemperatursupraleitung, entstehen durch starke elektronische Korrelationen. Seit den späten 1990er Jahren hat die Beschreibung stark korrelierter Systeme im Rahmen des Hubbard-Modells, dank der Einführung der dynamical mean-field theory (DMFT), enorme Fortschritte gemacht. Die Art dieser Näherung limitiert die Beschreibung der Korrelationen jedoch auf die rein lokale Ebene. Obwohl viele Fortschritte vorgeschlagen wurden, um diese Einschränkung zu überwinden, hat sich bisher kein klar überlegener Ansatz durchgesetzt. In dieser Arbeit diskutiere ich jüngste Verbesserungen an einem dieser Ansätze, der sogenannten Ladder Dynamical Vertex Approximation (lDΓA).
lDΓA gehört zur Familie der Feynmanschen diagrammatischen Erweiterungen von DMFT und nutzt den Parquet-Formalismus, um verbesserte Propagatoren zu konstruieren, die Nichtlokalität durch höhere Korrelationsfunktionen mittels der Schwinger-Dyson-Bewegungsgleichung einführen. Es ist jedoch allgemein bekannt, dass Theorien dieser Art inhärent nicht in der Lage sind, sowohl thermodynamische als auch Zwei-Teilchen-Konsistenz gleichzeitig zu erfüllen. In dieser Arbeit argumentieren wir für eine Behandlung dieses Nachteils auf einem effektiven Nivau, indem wir eine effektive Reskalierung der Korrelationslänge in der thermodynamischen Suszeptibilität einführen, die aus der Zwei-Teilchen-Konsistenz abgeleitet wird. Die resultierenden Vorhersagen zeigen, dass die Prognosegenauigkeit im Vergleich zu früheren Ansätzen dieser Klasse von Näherungen für das Hubbard-Modell mit abstoßender Wechselwirkung, in zwei und drei räumlichen Dimensionen verbessert wird.
Um ein klares Bild von der Funktionsweise, den Vorteilen und den potenziellen Einschränkungen dieses Ansatzes zu vermitteln, diskutiere ich zunächst die notwendigen technischen Details des Formalismus der Greenschen Funktionen und deren Anwendung zur Bestimmung magnetischer Eigenschaften des Hubbard-Modells. Anschließend werden Erhaltungssätze und die Zwei-Teilchen-Konsistenz zuerst allgemein und dann im Detail für die vorgeschlagene Verbesserung von lDΓA erörtert. Um diese Methode in den Kontext aktueller diagrammatischer Erweiterungen von DMFT einzuordnen, werden kurz einige eng verwandte Methoden beschrieben, bevor Vorhersagen für das abstoßende Hubbard-Modell in drei Dimensionen bei Halbbesetzung sowie für das zweidimensionale Hubbard-Modell mit Parametern präsentiert werden, die bekannte Supraleiter auf Basis von Cupraten nahe der Fermi-Oberfläche modellieren.
Abschließend wird eine detaillierte Diskussion der numerischen Details der Methode gegeben. Dies umfasst einen sehr allgemeinen Ansatz zur verbesserten Summation von Greenschen Funktionen sowie spezifische Details zu den Herausforderungen der lDΓA Methode.

Abstract Many important electronic properties in solid-state physics, such as magnetic ordering and high-temperature superconductivity, arise from strong electronic correlations. Since the late 1990s, the description of strongly correlated systems using the Hubbard model has experienced tremendous advances with the introduction of dynamical mean-field theory (DMFT). However, the nature of this approximation limits the description of correlations to the purely local level. While many advancements to alleviate this limitation have been proposed, a clearly superior approach among them has yet to be established. In this thesis, I discuss recent improvements to one of these approaches, the ladder dynamical vertex approximation (lDΓA).

lDΓA belongs to the family of Feynman diagrammatic extensions to DMFT, utilizing the parquet formalism to construct improved propagators that introduce nonlocality from higher-order correlation functions via the Schwinger-Dyson equation of motion. It is, however, known on general grounds that these types of theories are inherently unable to simultaneously satisfy both thermodynamic and two-particle consistency. Here, we argue for an effective treatment of this deficiency by introducing an effective correlation length rescaling in the thermodynamical response function, derived from two-particle consistency. The resulting predictions are demonstrated to improve the predictive power over previous approaches in this class of approximation on the repulsive Hubbard model in two and three spatial dimensions.

In order to present a clear picture of the workings, advantages, and potential limitations of this approach, I will first discuss the necessary technical details of Green's function formalism and the application thereof to obtain magnetic properties of the Hubbard model. Subsequently, conservation laws and two-particle consistency are discussed, first in general and then in detail for the proposed improvement to lDΓA . To provide additional context, abbreviated descriptions of some closely related methods are also provided before presenting predictions for the repulsive Hubbard model in three dimensions at half-filling and for the two-dimensional Hubbard model with parameters that are known to closely model cuprate superconductors close to the Fermi surface.

Finally, a detailed discussion of numerical details for the method is given. This includes a very general approach for the improved summation of Green's functions and specific details for challenges of lDΓA .

Contents

1 Introduction

In the pursuit of describing physical systems with a macroscopic number of particles, one must inevitably simplify the microscopic details of the theory. What may seem like a concession at first glance can be seen as an opportunity to investigate a system's driving physical mechanism systematically. In fact, many macroscopic effects are more suitably described by effective models, which explicitly consider the collective behavior of the particles. For example, what looks like a cloud of randomly moving water molecules on one scale can possibly be well described as a wave on another. A generalization of this principle, in the sense that we cannot construct qualitative descriptions of all phenomena from microscopic principles but discover new physics emerging, has been most incisively put into the phrase "more is different" by P. W. Anderson [10]. However, the scale on which new physics emerges will not be the same for different phenomena. Therefore, one task in theoretical solid-state physics can be formulated as identifying and describing the correct scale and corresponding driving mechanism for physical phenomena. Additional complications may arise if competing scales contribute to the descriptions. This is, for example, the case in cuprate high-temperature superconductors and heavy-fermion systems in which strong electronic interactions give rise to various low-energy states around the Fermi level.

The goal of this thesis is to systematically derive and investigate a method for the description of strongly correlated electron systems, including collective phenomena, in particular long-range charge and spin fluctuations. Strong correlations imply that a description of electrons by means of a single particle in an effective potential is not possible because the influence of this single electron on the constituents of the potential is nonnegligible. Long-range fluctuations mean that particles far apart can influence each other, i.e. the correlations between spatially distant electrons become important. This is, however, neither a prerequisite nor a consequence of strong correlations because a spontaneous transition in an effective medium description may well describe these long-range effects.

Both of these conditions are present in electronic systems where the valence electrons occupy narrow orbitals, typically partially filled d or f shells (leading to strong correlations in these orbitals), and the system itself has a low spatial dimension or is in the vicinity of a second-order phase transition. We will investigate two systems that meet both of these conditions. (i) The three-dimensional Hubbard model at half-filling, where strong correlations are extremely important, manifests in the Mott insulating phase, and long-range fluctuations emerge close to the antiferromagnetic phase transition. (ii) Cuprate high-temperature superconductors, where the quasi-two-dimensional nature of the copper-oxygen planes induces long-range spin fluctuations, while the superconducting state and the pseudogap phenomena can be, in large part, attributed to strong correlation effects between electrons.

There have been numerous attempts to describe these kinds of systems, none of which have been able to capture all aspects of the observed phenomena.

A well-established pathway for obtaining numerical results for the electronic structure of a solid-state system is ab initio calculations, using density functional theory (DFT) [103], which employ a one-to-one mapping between the interacting electron system and an effective one-particle system [140], described by a density functional. In practice, this mapping cannot be made exact because of the forced choice of an approximation to the exchange-correlation potential. It was established very early on that the DFT formalism is not suited to describe certain effects in semiconductors, leading to a gap of the exchange-correlation potential [191, 229, 87], such as the strong correlation effects we want to investigate. Among the many proposed improvements that aim to solve this issue is the mapping states close to the Fermi surface to a low-energy model that can be treated with a higher degree of microscopic detail. In this thesis, we will investigate a newly extended method for the solution of such a low-energy model. It is based on a diagrammatic extension of the dynamical mean-field theory (DMFT) [172]. DMFT is able to capture strong correlations but fails to incorporate long-range fluctuations. Diagrammatic extensions of DMFT are able to reintroduce these effects again. Our approach aims to improve on earlier attempts in this direction by incorporating consistency relations that arise either from the Pauli principle or conservation laws as a consequence of Ward-Takahashi identities [286, 258]. Our construction introduces an effective renormalization of correlation functions obtained from a diagrammatic perturbation theory around the non-perturbative DMFT starting point that preserves some of the thermodynamic consequences of these identities without the explicit construction of a conserving set of diagrams.

In addition to the detailed discussion of this method, this thesis also aims to provide a link to the existing literature for the numerous mathematical and physical concepts involved and an in-depth discussion of numerical details.

Structure In **chapter** 2, we recall the most important points of the Green's function formalism relevant to this thesis. Here, the most important concepts from the literature are reiterated, and a

coherent notation is established. Besides an introduction to Green's functions for many-particle systems, an emphasis is placed on susceptibilities and 4-point correlators, which are important for the methods discussed later in the thesis.
In **chapter** 3, we give an introduction to the Hubbard model, which serves as the low-energy model. This chapter aims specifically at the most important aspects of magnetic ordering and strong electronic correlations on the two-particle level.
In **chapter** 4, we discuss aspects of thermodynamical and two-particle consistency. This chapter builds the foundation for the newly introduced extension to the ladder dynamical vertex approximation. We derive Ward identities for the Hubbard model and describe the effective renormalization scheme for susceptibilities that we employ to restore consistency relations in the parquet-based approaches. These are based on finding two effective parameters (called λ_m and λ_d) that renormalize the physical susceptibilities according to consistency relations between thermodynamical quantities on the one- and two-particle levels. Furthermore, we also discuss the Luttinger-Ward function as a basis for thermodynamical consistency in this chapter.
In **chapter** 5, we present the ladder dynamical vertex approximation (lDΓA), the recent developments towards the achievement of an effectively two-particle consistent description, and the dynamical mean-field theory as its foundation. In addition, closely related methods are also presented here to provide a context for the lDΓA method.
In **chapter** 6, we address the numerical challenges and their solutions, which we encountered during the development of the new lDΓA scheme. We also discuss aspects that are not critical but closely related in the hope that the proposed solutions will help future extensions of this work. There are also two less closely related numerical projects discussed here. A general series acceleration technique and a machine learning model that was designed to learn features of the Luttinger Ward functional.
In **chapter** 7, we demonstrate the improved predictive power of the effective inclusion of consistencies through the λ parameters over the non-two-particle consistent variants by discussing two systems that exhibit strong electronic correlations in conjunction with long-range fluctuations. For one, we discuss already published results on the three-dimensional Hubbard model at half-filling, close to the antiferromagnetic phase transition. Here, we find substantial improvements in the quantitative description of the model, in particular with respect to a previous, non-self-consistent, lDΓA description in the weak to intermediate coupling regime. Finally, we discuss preliminary results on the two-dimensional Hubbard model with parameters that are known to represent cuprate superconductors sufficiently close for a qualitative description. Here, we neglect certain aspects, like the charge-transfer character that requires a multi-band Hubbard model, but nevertheless see a significantly improved qualitative description. Specifically, the influence of non-local charge fluctuations on the emergence of the superconducting dome even matches quantitative values from the literature.

2 Green's functions

This chapter serves as a reference for calculations done throughout the thesis and as a bridge to textbooks. Readers familiar with Green's functions or the usual notation in publications such as in Chapter 7 may want to skip it.
However, since Green's functions and the functional integral formalism are not standard knowledge for all students in solid-state theory, this chapter aims to connect the notation in later chapters to the appropriate textbooks and give a very brief introduction to the most important topics.
We introduce Green's functions in the imaginary time and frequency domain, then discuss susceptibilities in some more detail, as they will be central to our methods. Subsequently, we motivate the core quantities of the functional integral formalism and finally give a detailed introduction to the two-particle Green's function. The last section connects the discussions here with notations and derivations in the thesis of Georg Rohringer [205]. This reference specifically should be seen as complementary, and many important points from it will not be repeated here.

2.1 Definitions and Identities

This section summarizes basic identities and well-known results from textbooks. It serves as a reference for the rest of this thesis and is a bridge to the literature for readers who are not familiar with the notation in this thesis.

2.1.1 Notation

The following gives a brief summary of common notions throughout this thesis.
Indices for frequencies and momenta will be placed as superscripts and subscripts respectively. With ω for bosonic and ν for fermionic frequencies. We will typically omit Matsubara indices when the context permits it to shorten the notation:

$$f^{\nu}_{\mathbf{k}} \coloneqq f(i\nu_n, \mathbf{k}) \tag{2.1}$$

The following abbreviations for integrals over imaginary times, summations over the first Brillouin zone, and Matsubara frequencies will be used to shorten the notation:

$$\int \mathrm{d}\tau f(\tau) \coloneqq \int_0^\beta \mathrm{d}\tau f(\tau) \tag{2.2}$$

$$\sum_{\mathbf{k}} f_{\mathbf{k}} \coloneqq \frac{1}{V_{\mathrm{BZ}}} \int_{1.\mathrm{BZ}} \mathrm{d}\mathbf{k} f(\mathbf{k}) \tag{2.3}$$

$$\sum_{\nu} f^{\nu} \coloneqq \frac{1}{\beta} \sum_{n=-\infty}^{\infty} f(i\nu_n) \tag{2.4}$$

The appropriate normalizations for integrals and sums are always implied when they are trivial.
Occasionally, the following combined notation for indices is used when many free indices (for example, in 2-particle Green's functions) have to be summed over. A bar over an index means summation and/or integration:

$$(1) = (\nu_1, \mathbf{k}_1, \sigma_1) \tag{2.5}$$

$$f(1;2)g(2;3) \coloneqq f_{\sigma_1,\sigma_2,\alpha_1\alpha_2}(\tau_1,\tau_2) g_{\sigma_2,\sigma_3,\alpha_2\alpha_3}(\tau_2,\tau_3) \tag{2.6}$$

$$f(1;\bar{2})g(\bar{2};3) \coloneqq \int \mathrm{d}\mathbf{k}_2 \sum_{n',\sigma_2} f^{\nu_1\nu_2}_{\sigma_1\sigma_2,\mathbf{k}_1\mathbf{k}_2} g^{\nu_2\nu_3}_{\sigma_2\sigma_3,\mathbf{k}_2\mathbf{k}_3} \tag{2.7}$$

Usually, however, a more explicit notation is preferred. We will repeatedly need a small regularization parameter to avoid singularities. We will denote this by η and implicitly assume a limit that can only be carried out if it exists, for example:

$$n_\sigma = \mathrm{Tr}\left[G^{\nu}_{\sigma,\mathbf{k}} e^{-i\nu_n(-\eta)}\right] = \sum_{\nu\mathbf{k}} G^{\nu}_{\sigma,\mathbf{k}} e^{-i\nu_n(-\eta)} \coloneqq \lim_{\eta\to 0} \sum_{\nu} G^{\nu}_{\sigma,\mathbf{k}} e^{-i\nu_n(-\eta)} \tag{2.8}$$

In the previous shorthand notation, this is indicated by a + superscript: $f(1^+)$.

2.1.2 Fock basis and coherent states

A commonly used basis for Hilbert spaces for many-particle systems is the Fock basis. It is defined by the occupation numbers n_i for each state $|i\rangle$.

$$|\psi\rangle = |n_1, \ldots, n_i, \ldots\rangle \tag{2.9}$$

The creation and annihilation operators on these states i are defined as follows:

$$\hat{c}_i^\dagger |\ldots, n_i, \ldots\rangle = (1 - n_i) |\ldots, n_i + 1, \ldots\rangle \tag{2.10a}$$

$$\hat{c}_i |\ldots, n_i, \ldots\rangle = \hat{n}_i |\ldots, n_i - 1, \ldots\rangle \tag{2.10b}$$

$$\hat{b}_i^\dagger |\ldots, n_i, \ldots\rangle = \sqrt{1 + n_i} |\ldots, n_i + 1, \ldots\rangle \tag{2.10c}$$

$$\hat{b}_i |\ldots, n_i, \ldots\rangle = \sqrt{n_i} |\ldots, n_i - 1, \ldots\rangle \tag{2.10d}$$

The eigenstates of the annihilation operators are called coherent states:

$$\hat{a}_i |\phi\rangle = \phi |\phi\rangle \tag{2.10e}$$

$$\hat{a}_i^\dagger |\phi\rangle = \zeta \partial_i |\phi\rangle \tag{2.10f}$$

We adopt the notation from [111, Chapter 1], fermionic operators are written with the letter $\hat{c}$, bosonic ones with $\hat{b}$ and $\hat{a}$ as a placeholder for both. The construction from the vacuum state also yields the unity operator and matrix element of operators needed, for example, for the construction of path integrals:

$$|\phi\rangle = e^{\zeta \sum_i \phi_i \hat{a}_i^\dagger} |0\rangle \tag{2.11}$$

$$\mathbb{1} = \int \mathrm{d}\mu_\varsigma e^{-\sum_i \bar{\phi}_i \phi_i} |\phi\rangle \langle\phi| \tag{2.12}$$

The necessary details for the measure and Grassmann algebra for fermions can also be found in [111, Chapter 1].
Starting from Chapter 4, we will discuss consistency relations that can be expressed in terms of continuity equations. There are two possibilities to formulate these, both of which will be employed. The first makes use of the operator formalism, and the second uses functional integrals. We will introduce the former here and then give a brief introduction to the latter in Sec. 2.6.
To obtain continuity equations, the time dependence of operators is expressed using the Heisenberg equation of motion.

Definition 2.1.2.1 (Time evolution and Heisenberg equation of motion)
The general time evolution operator is defined as:

$$\hat{U}(t,t') = \mathcal{T} e^{-i\int_{t'}^{t} \mathrm{d}s \hat{H}(s)} \tag{2.13}$$

In this thesis, we only consider time-independent Hamiltonians and will therefore use the accordingly simplified version without the time ordering operator (defined below) $\mathcal{T}$:

$$\hat{U}(t) = e^{-it\hat{H}} \tag{2.14}$$

The time evolution for time-dependent operators is then given according to the Heisenberg equation of motion. Here, we also assume no explicit time dependence in the Hamiltonian.

$$\frac{\mathrm{d}}{\mathrm{d}t}\hat{O}(t) = i[\hat{H}, \hat{O}(t)] \tag{2.15}$$

$$\frac{\mathrm{d}}{\mathrm{d}\tau}\hat{O}(\tau) = -[\hat{H}, \hat{O}(\tau)] = [\hat{O}(\tau), \hat{H}] \tag{2.16}$$

To emphasize the notation used here, we quickly go through a proof of the equivalence between Eq. (2.15) and the Schrödinger equation. The definition Eq. (2.14) is clearly a formal solution of the time-dependent Schrödinger equation. We also recall that the operators $O_\mathrm{H}(t)$ in the Heisenberg picture are time-dependent (and the wave functions are time-independent) and relate to a time-independent operator in the Schrödinger picture O_S.

$$O_\mathrm{H}(t) = U^\dagger(t) O_\mathrm{S} U(t), \qquad \frac{\mathrm{d}U(t)}{\mathrm{d}t} = -iHU(t), \qquad \frac{\mathrm{d}U^\dagger(t)}{\mathrm{d}t} = iU^\dagger(t)H \tag{2.17}$$

We can, therefore, evaluate the time derivative of an operator in the Heisenberg picture:

$$\begin{aligned}\frac{\mathrm{d}O_\mathrm{H}(t)}{\mathrm{d}t} &= \frac{\mathrm{d}U^\dagger}{\mathrm{d}t} O_\mathrm{S} U + U^\dagger \frac{\partial O_\mathrm{S}}{\partial t} U + U^\dagger O_\mathrm{S} \frac{\mathrm{d}U}{\mathrm{d}t} \\ &= iU^\dagger H O_\mathrm{S} U + 0 + U^\dagger O_\mathrm{S}(-iHU) = iU^\dagger H U U^\dagger O_\mathrm{S} U + -iU^\dagger O_\mathrm{S} U U^\dagger H U \\ &= i\,[H, O_\mathrm{S}(t)]\end{aligned}$$

The subscripts, indicating the Heisenberg and Schrödinger picture, are omitted in all other places since the operator and state character are evident from the context.

Commutator Relations We recall the usual commutator relations for the density and fermionic creation/annihilation operators. These are, of course, well-known but are restated here since they will be used repeatedly in calculations throughout the thesis.

$$[AB, C] = A[B, C] + [A, C]B \tag{2.18}$$

$$[A, BC] = B[A, C] + [A, B]C \tag{2.19}$$

$$[A, BC] = \{A, B\}C - B\{A, C\} \tag{2.20}$$

The fermionic commutation relations then read:

$$\{\hat{c}_i^\dagger, \hat{c}_{\,j}\} = \delta_{ij}, \qquad \{\hat{c}_{\,i}, \hat{c}_{\,j}\} = \{\hat{c}_i^\dagger, \hat{c}_j^\dagger\} = 0 \tag{2.21}$$

$$\begin{aligned}[\hat{n}_{i\sigma}, \hat{c}_{j\sigma'}^\dagger] &= \hat{c}_{i\sigma}^\dagger \{\hat{c}_{\,i\sigma}, \hat{c}_{j\sigma}^\dagger\} - \{\hat{c}_{i\sigma}^\dagger, \hat{c}_{j\sigma}^\dagger\} \hat{c}_{\,i\sigma} = \quad \hat{c}_{i\sigma}^\dagger \delta_{ij} \delta_{\sigma\sigma'} \\ [\hat{n}_{i\sigma}, \hat{c}_{\,j\sigma'}] &= \hat{c}_{i\sigma}^\dagger \{\hat{c}_{\,i\sigma}, \hat{c}_{\,j\sigma}\} - \{\hat{c}_{i\sigma}^\dagger, \hat{c}_{\,j\sigma}\} \hat{c}_{\,i\sigma} = -\hat{c}_{\,i\sigma} \delta_{ij} \delta_{\sigma\sigma'}\end{aligned} \tag{2.22}$$

Expectation Values The ground state and the thermal expectation values are defined with the ground state $|\Psi_0\rangle$ and the grand canonical ensemble.

Definition 2.1.2.2 (Expectation Values)
The ground state and thermal expectation values of an operator O are defined as:

$$\langle \hat{O} \rangle_{T=0} = \langle \Psi_0 | \hat{O} | \Psi_0 \rangle \tag{2.23}$$

$$\langle \hat{O} \rangle_{T>0} = \frac{1}{Z} \operatorname{Tr}\left(\hat{O} e^{-\beta((\hat{H}-\mu\hat{N}))} \right), \qquad Z = \operatorname{Tr}\left(e^{-\beta(\hat{H}-\mu\hat{N})} \right) \tag{2.24}$$

This work almost exclusively discusses finite temperature results. We will, therefore, omit the subscript $T > 0$ in most cases.

We will be working with operators in the second quantization form, specifically Green's functions. These intrinsically respect fermionic and bosonic statistics[1], which is encapsulated by constructing the operator in terms of creation and annihilation operators for occupied states with all permutations included. A shorthand notation for this is the time-ordering operator.

Definition 2.1.2.3 (Time Ordering)
The time ordering operator T_ζ — for bosonic/fermionic, $\zeta \pm 1$ statistics — is defined as the time-ordered product over all permutations.

$$\mathcal{T}_\zeta \left[\hat{O}_1(t_1) \dots \hat{O}_n(t_n) \right] = \sum_{\sigma \in S_n} \zeta^{\mathrm{P}(\sigma)} \prod_{i=1}^{n-1} \Theta(t_{\sigma(i)} - t_{\sigma(i+1)}) \prod_{j=1}^{n} \hat{O}_{\sigma(j)}(t_{\sigma(j)}) \tag{2.25}$$

Where S_n is the symmetric group over $\{1, \dots, n\}$, $\mathrm{P}(\sigma) = \begin{cases} 1 & \text{if } \sigma \text{ even} \\ 0 & \text{otherwise} \end{cases}$.
$\zeta = \pm 1$ for bosonic/fermionic operators is typically omitted when it is clear from the context that we use fermionic operators.
The analogous definition for imaginary time operators is implied here.

For example, Def. 2.1.2.3 expands as follows for just two fermionic annihilation operators:

$$T_{-1}[\hat{a}_1(t_1)\hat{a}_2(t_2)] = \theta(t_1 - t_2)\hat{a}_1(t_1)\hat{a}_2(t_2) - \theta(t_2 - t_1)\hat{a}_2(t_2)\hat{a}_1(t_1).$$

General n-particle operators can be written in terms of creation and annihilation operators for arbitrary states α as follows:

$$\hat{V} = \bigotimes_{ij} \langle \alpha_i | V | \alpha'_j \rangle \prod_{ij} \hat{a}^\dagger_{\alpha_i} \hat{a}_{\alpha_j} \tag{2.26}$$

Following the notation from [111, Chapter1] one can shorten the notation occasionally, by defining (anti-) symmetrized overlaps:

$$\{\alpha\beta|\hat{v}|\alpha'\beta'\} = \zeta\{\alpha\beta|\hat{v}|\beta'\alpha'\} \tag{2.27}$$

2.2 Green's functions

Our tool of choice to describe and analyze properties of strongly correlated electron systems will be the Green's function formalism. They not only allow the calculation of physical observables but also formulate approximations incorporating many-body interactions. Furthermore, they can be intuitively understood as propagation operators. Parts of this section have been adapted from Chapter 3 of my Master's thesis [246].

2.2.1 Motivation

Mathematics has established a solid foundation for (what in our case amounts to a special case of) Green's functions under the name of Fredholm theory. Here, the Green's function takes the role of a fundamental solution of a partial differential equation. The following paragraph aims to give a brief introduction of Green's functions from the perspective of differential equations in order to motivate their subsequent formal definition.
For a linear differential operator L and $f, g : \mathbb{R} \to \mathbb{R}$ (see [33, Chapter 8]):

$$Lf(x) = g(x), \tag{2.28}$$

[1] By this, we mean the minus sign a fermionic wave function picks up under the exchange of two particles. This is the well-known but deceptively hard-to-fathom spin-statistics theorem [60]

the fundamental solution G is given as:

$$LG(x,x') = \delta(x'-x) \tag{2.29}$$

The full solution $f(x)$ for the boundary value problem can be constructed via a convolution with G. This can be seen by integrating Eq. (2.28) on both sides and using the linearity of L.

$$f(x) = \int \mathrm{d}x' g(x') G(x,x') f_0(x) \tag{2.30}$$

Eq. (2.30) implies that knowledge of the Green's function and the homogeneous solution provides us with full information about the solution to the boundary value problem. The formal integral type is known as the inhomogeneous Fredholm equation, for which an extensive amount of literature is available. Of particular interest are the resolvent operator formalism[2] and its value in defining mathematically rigorous perturbation series for linear operators, such as L. As an introduction, we will motivate a solution of the single-particle Schrödinger equation in terms of Green's functions. The argument follows part (I) of [184]. We define our differential operator by rearranging the Schrödinger equation with a Hamilton operator of a free particle. For this brief motivation, we consider only one spatial dimension.

$$i\frac{\partial}{\partial t}\psi(x,t) = \hat{H}\psi(x,t)$$

It is useful to emphasize the operator character with a hat since Green's function can take on two different roles. Next, we reorder the Schrödinger equation to bring it in line with our previous definition.

$$\hat{L} = i\frac{\partial}{\partial t} + \frac{1}{2m}\nabla^2$$

$$\hat{L}\psi_n(x,t) = V(x,t)\psi_n(x,t) \tag{2.31}$$

$$\hat{L}\hat{G}(x,t;x',t') = \delta(x-x')\delta(t-t') \tag{2.32}$$

This introduces the notation for the physical Green's function with x', t' being the initial and x, t the outgoing positions and times. For this example, we ignore the complications that arise from the fact that the wave function $\psi(x,t)$ appears on the right *and* the right side[3]. Using the definition of the time evolution operator Eq. (2.14), we expand the wave function of Eq. (2.31):

$$\begin{aligned}\Theta(t-t')\psi(x,t) &= \langle x|\,\Theta(t-t')\hat{U}(t,t')\,|\psi(t')\rangle \\ &= i\int \langle x|\,-i\Theta(t-t')\hat{U}(t,t')\,|x'\rangle \left\langle x'\,\middle|\,\psi(t')\right\rangle \mathrm{d}x' \\ &= \int G^{\mathrm{R}}(x,t;x',t')\psi(x',t')\mathrm{d}x'\end{aligned} \tag{2.33}$$

With Eq. (2.33) defining the retarded Green's function, the Heaviside function enforces causality in the retarded propagator. The factor of $-i$ has been introduced to ensure consistency with the upcoming definition of the many-particle Green's function. Furthermore, we observe from Eq. (2.30) and Eq. (2.31) that the Green's function can be used to introduce a potential into the solution for a free system. This will become especially important when approximations around small interactions are made since perturbations are naturally suited to be formulated with Green's functions, for example in Sec. 2.4.

The advanced Green's function, while not causal, is also often useful and defined with the opposite time ordering. For example, one may describe the propagation of electron holes with this time ordering. We can easily verify that Eq. (2.32) is fulfilled and that the Green's function can be formally written as:

$$\left(i\frac{\partial}{\partial t} - \hat{H}\right)\hat{G}(x,t;x',t') = \delta(x-x')\delta(t-t')$$

$$\hat{G}(x,t;x',t') \text{ “=” } \left[i\frac{\partial}{\partial t} - \hat{H}\right]^{-1}$$

The quotation marks are necessary since only the homogeneous solution is captured and the Green's function is only the resolvent *kernel*, i.e. we need Eq. (2.33) as well.

As is often the case, we may rewrite the differential equation as an algebraic one by utilizing Fourier transforms. This will be done in Sec. 2.3 after extending the definition of the single-particle Green's function to many-particle systems and finite temperatures. However, before moving on, let us restate the formal definitions obtained in this section.

Definition 2.2.1.1 (Real time single particle Green's function)
We define the Green's function as the retarded (measuring the response of a system after a pertur-

[2] A particularly formal approach is presented in [126] (for example chapter 5) and [138].
[3] This eigenvalue problem has been investigated with Fredholm theory, and the resulting formal solution will appear in the section on the spectral representation of Green's functions, see [36, 126].

bation) or advanced propagation amplitude between two positions and times.

$$G^{\mathrm{R}}(x,t;x',t') = -i\Theta(t-t')\langle x|\, e^{-iH(t-t')}\,|x'\rangle \tag{2.34}$$

$$G^{\mathrm{A}}(x,t;x',t') = -i\Theta(t'-t)\langle x|\, e^{-iH(t-t')}\,|x'\rangle \tag{2.35}$$

Alternatively, we can understand the Green's function as a resolvent kernel to the Hamiltonian operator:

$$\left(i\frac{\partial}{\partial t} - \hat{H}\right)\hat{G}(x,t;x',t') = \delta(x-x')\delta(t-t') \tag{2.36}$$

We denote the resolvent operator character by explicit inclusion of the hat symbol.

The definition in Eq. (2.34) emphasizes the role of the Green's function as propagation of a state from one position x' and time t' to a different position and state x and t. The Heaviside function forces the retarded Green's function to be 0 if the initial time lies before the final one, enforcing causality. These are the main features we want to retain for a generalized definition of Green's functions that are better suited to formulate collective excitations in many-particle systems. From this definition, it is also immediately clear that systems without explicit time-dependent potentials lead to a Green's function only dependent on the difference in times $t-t'$. The same is true for positions $\vec{r}$ and $\vec{r}'$ in systems with translational invariance. Both symmetries are present in our version of the Hubbard model, and we will, therefore, often write Green's function with only a single time and position argument. The advanced Green's function is especially useful as a tool in the context of spectral functions Sec. 2.3 and, therefore, included in the definitions here.

2.2.2 Many-Body Green's Function

Having motivated the concept of Green's functions in the previous section, we now immediately jump to the most general definition for many-body Green's functions and then work our way back and discuss all necessary properties.

Definition 2.2.2.1 (Many particle Green's function)
The general n-point correlator time-ordered in the real and imaginary time domain for states α_i, real/imaginary times t_i/τ_i and bosonic/fermionic statistics $\zeta = \pm 1$

$$G^{\mathrm{R/A}}_{\alpha_1\alpha_2}(t;t') = -i\Theta(t \mp t')\left\langle[\hat{c}_{\alpha_1}(t), \hat{c}^\dagger_{\alpha_2}(t')]_{-\zeta}\right\rangle \tag{2.37}$$

$$G_{\alpha_1,\dots\alpha'_n}(t_1,\dots,t_n;t'_1,\dots,t'_n) = (-i)^n\left\langle T_\zeta\left[\hat{a}_{\alpha_1}(t_1)\cdots\hat{a}_{\alpha_n}(t_n)\hat{a}^\dagger_{\alpha'_n}(t'_n)\cdots\hat{a}^\dagger_{\alpha'_1}(t'_1)\right]\right\rangle \tag{2.38}$$

$$G_{\alpha_1,\dots\alpha'_n}(\tau_1,\dots,\tau_n;\tau'_1,\dots,\tau'_n) = \left\langle T_\zeta\left[\hat{a}_{\alpha_1}(\tau_1)\cdots\hat{a}_{\alpha_n}(\tau_n)\hat{a}^\dagger_{\alpha'_n}(\tau'_n)\cdots\hat{a}^\dagger_{\alpha'_1}(\tau'_1)\right]\right\rangle \tag{2.39}$$

$$G^{\nu_1,\dots\nu_n\nu'_1\dots\nu'_n}_{\alpha_1,\dots\alpha_n\alpha'_1\dots\alpha'_n} = \mathcal{F}G_{\alpha_1,\dots\alpha'_n}(\tau_1,\dots,\tau_n;\tau'_1,\dots,\tau'_n) \tag{2.40}$$

This specifically impacts the spin index convention in Sec. 2.7.2.1.
We are exclusively concerned with fermionic Green's functions and, therefore, define $T = T_{\zeta=-1}$.
For the frequency representation, we routinely use frequency and spin index conventions to shorten the notation. These are discussed in Sec. 2.7.2 and Sec. 2.7.1. Furthermore, we omit the subscript for Matsubara indices (see Sec. 2.2.5 below).
⚠ *The index conventions and ordering of operators are inconsistent in the Literature. Here, we follow [111], which is different from [205].*

The extension to the previous concept of Green's function arises naturally from the change of perspective introduced by the second quantization. Eq. (2.37) extends our previous definition in Eq. (2.33) by also considering the propagation of holes through the introduction of the commutator. Note that we now have three definitions of Green's functions: retarded, advanced, and time-ordered. However, they contain the same information (compare Eq. (2.41) and definitions). As an additional insight, the relationship between the retarded and advanced Green's function is also investigated in the calculation preceding Eq. (2.69).
To illustrate the role of the commutator in the definition of the retarded and advanced Green's function, we verify that it selects the appropriate time ordering in the single-particle case:

$$\begin{aligned} G_{\alpha_1\alpha'_1}(t;t') &\overset{2.38}{=} -i\left\langle T_\zeta\left[\hat{a}_{\alpha_1}(t)\hat{a}^\dagger_{\alpha'_1}(t')\right]\right\rangle \\ &\overset{2.37}{=} -i\Theta(t-t')\frac{1}{Z}\left\langle\hat{a}_{\alpha_1}(t)\hat{a}^\dagger_\beta(t')\right\rangle + \zeta i\Theta(t'-t)\frac{1}{Z}\left\langle\hat{a}^\dagger_{\alpha'_1}(t')\hat{a}_{\alpha_1}(t)\right\rangle \end{aligned} \tag{2.41}$$

2.2.3 Symmetries

All Hamiltonians in this thesis are invariant under the following three transformations [205, p. 33-44]:

$\hat{S}_i$: We only consider the paramagnetic case of the Hubbard model (i.e. no external magnetic field). This implies symmetry under a global rotation of the spins (the Hamiltonian is $SU(2)$ symmetric) and from that conservation of the total spin. For single-particle Green's functions we will, therefore, omit the redundant spin index.

$\hat{T}_t$: Systems at equilibrium, without spin-orbit coupling or inside an external magnetic field, usually experience time-reversal symmetry. This manifests in a time-independent Hamiltonian ($\hat{H}(t) \equiv \hat{H}$), which allows us to write the time evolution operator Eq. (2.14) in a simplified form:

$$\hat{U}(t) = e^{-i\hat{H}t} \tag{2.42}$$

Furthermore, the time dependence of the Green's function can be rewritten in terms of differences, removing one time/frequency dependency.

$$G(\tau_1, \tau_2) = G(\tau_1 - \tau_2, 0) \to G(\tau) \tag{2.43}$$

For the single-particle case, a short proof is given, preceding Eq. (I8.1) in Sec. 1. For the general n-particle case, we then only need $2n-1$ time arguments; a proof is given in [205, Chapter 2.2.2.1].

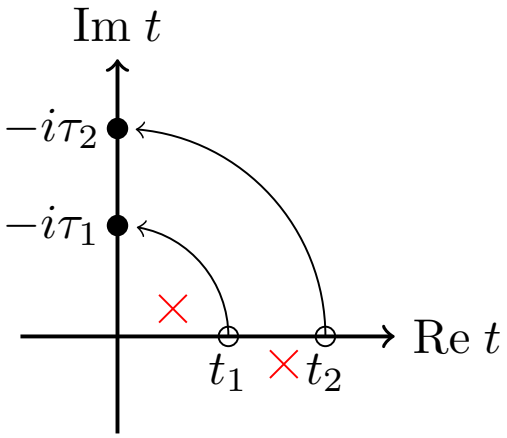

Figure 2.1: Illustration for the mapping of points from the real to the imaginary time axis, under the Wick rotation. The red crosses mark examples of poles that need to be considered when transforming integration paths under this transformation.

$\hat{T}_{\mathbf{R}}$: Invariance under translation by a lattice vector $\mathbf{R}$ analogously yields a reduction of the spatial/$\mathbf{k}$-dependence by one. Similar to the time-reversal symmetry, space inversion symmetry would then imply one less momentum index.

Symmetry considerations play a vital role in this thesis in the form of implied conservation laws through Ward identities, see Sec. 4.2. There is one much more direct way in which they have been exploited: Numerical values of functions related by simple operations (e.g. $f(x,y) = f^*(y,x)$ are completely symmetric functions ($g(x,y) = g(y,x)$) need to be computed only once per equivalent point in the sample set. Specifically, the symmetries listed in table 2.1 and table 2.2 from [205] have been used to reduce the amount of computation needed. We will discuss an algorithm that has been developed for this thesis in order to make use of this minimal representation in Sec. 6.4.

2.2.4 Imaginary Time and Finite Temperature

First, we want to motivate the introduction of imaginary times in Eq. (2.39).
We will work in the grand canonical ensemble. To shorten the notation, the additional term, which fixes the density, is absorbed into the definition of the Hamiltonian:

$$\hat{H} \coloneqq \hat{H} - \mu\hat{N} \tag{2.44}$$

This term can sometimes lead to additional contributions and will be expanded in calculations if needed. A very important concept in finite-temperature calculations is the Wick rotation. Since we are only concerned with a $0+1$ dimensional field theory, some conceptual obstacles present in the mapping between Euclidean and Minkowski space can be circumvented. The functions we are considering are meromorphic, giving us the opportunity to view this rotation as an analytic continuation. By extending the Green's functions from real to complex functions $G_{\alpha_1\alpha_2}(t) \to G_{\alpha_1\alpha_2}(z)$, we can write

$$z = t - i\tau \tag{2.45}$$

$$f(\tau) \coloneqq f(0 - i\tau) \tag{2.46}$$

The continuation from real to imaginary times leads to a natural formulation of finite temperatures, as one could speculate by the similarity of the Fokker-Planck and Schrödinger equation under variable transformation[4]. The conceptual advantage becomes clear with the observation that the time

[4] In some setups, the transition may also help transform oscillatory integrals into exponentially decaying ones. In general quantum field theories, similar methods transform the integral measure of the associated path integral into

evolution operator for a time-independent Hamiltonian takes the role of the Boltzmann factor in the thermal Green's function. Furthermore, the imaginary-time formalism takes the periodicity (see property (1) Sec. 1) into account naturally. This motivates the identification of an imaginary time since perturbation in the Boltzmann factor, and the interaction term can then be treated with a single imaginary time evolution operator:

$$Z = U(\beta, 0) = e^{-\hat{H}\beta} \tag{2.47}$$

2.2.5 Matsubara frequencies

The β (anti-) periodicity of the imaginary time Green's function (property (5), Eq. (I8.5)) leads to a Fourier expansion with discrete coefficients.

$$\int_{-\infty}^{\infty} f(\nu) \to \frac{1}{\beta} \sum_{n=-\infty}^{\infty} f(i\nu_n) \tag{2.48}$$

These are called Matsubara frequencies and are denoted by ν_n (ω_m) for fermionic (bosonic) statistics throughout this thesis. We will give a very abbreviated overview of this formalism here, mostly to precisely define the notation, which is not consistent throughout the literature.

Definition 2.2.5.1 (Fourier transformations for imaginary times)
We define Matsubara frequencies for bosons and fermions as follows

$$\nu_n = \frac{(2n+1)\pi}{\beta} \tag{2.49}$$

$$\omega_n = \frac{2n\pi}{\beta} \tag{2.50}$$

Furthermore, we abbreviate the notation of the Fourier transforms of imaginary times and frequencies due to their frequent repetition in calculations:

$$\int \mathrm{d}\tau f(\tau) := \int_0^\beta \mathrm{d}\tau f(\tau) \tag{2.51}$$

$$\sum_\nu f^\nu := \frac{1}{\beta} \sum_{n=-\infty}^{\infty} f(i\nu_n) \tag{2.52}$$

The (inverse) Fourier transformations are given as follows.

$$G^\nu_{\alpha\alpha'} := G^{i\nu_n}_{\alpha\alpha'} = \frac{1}{2} \int_{-\beta}^{\beta} \mathrm{d}\tau e^{i\nu_n\tau} G_{\alpha\alpha'}(\tau) = \int_0^\beta \mathrm{d}\tau e^{i\nu_n\tau} G_{\alpha\alpha'}(\tau) \tag{2.53}$$

$$G_{\alpha\alpha'}(\tau) = \sum_\nu e^{-i\nu_n\tau} G^\nu_{\alpha\alpha'} \tag{2.54}$$

⚠ *The symbols for fermionic and bosonic frequencies are not consistent throughout the literature! In many references, ω instead refers to the fermionic frequencies.*

The Fourier transform of the general n-particle imaginary time Green's function is then (for a detailed discussion on the domain and symmetries, see [205, Sec. 2.2.1.1]):

$$G^{\nu_1,\ldots,\nu'_n}_{i_1,\ldots,i'_n} = \int e^{-i(\nu_1\tau_1+\cdots-\nu'_1\tau'_1)} \{\mathrm{d}\tau_i\} G_{i_1,\ldots,i'_n}(\tau_1;\ldots;\tau'_n) \tag{2.55}$$

$$G_{i_1,\ldots,i'_n}(\tau_1;\ldots;\tau'_n) = \sum_{\{\nu_i\}} e^{i(\nu_1\tau_1+\cdots-\nu'_1\tau'_1)} G^{\nu_1,\ldots,\nu'_n}_{i_1,\ldots,i'_n} \tag{2.56}$$

The relationship between Heisenberg and Schrödinger picture of the operators for time-independent Hamilton operators becomes:

$$\hat{O}_\mathrm{H}(\tau) = e^{\tau\hat{H}} \hat{O}_\mathrm{S} e^{-\tau\hat{H}} \tag{2.57}$$

We will drop the subscript for Heisenberg and Schrödinger picture, as before.
As an important implication of the imaginary time formalism, the time evolution operator is no longer unitary. We will make repeated use of the following properties:

$$e^{i\nu_n\beta} = -1, \qquad e^{i\omega_m\beta} = 1, \qquad \sum_n \frac{1}{i\nu_n} = \frac{1}{2} \tag{2.58}$$

the Wiener measure [81, Chapter 3]. The Fokker-Planck equation describes diffusion processes, i.e. the time evolution of densities under Brownian motion or stock price evolution in financial mathematics [247]. The integrated form of this stochastic differential equation, using the Feynman-Kac formula, leads to a stochastic Îto integral, directly linked to path integrals [138].

2.3 Spectral Representation

Our next goal is to give a short introduction to the Green's function formalism in frequency space. In the process, we will isolate the spectral function as the central quantity containing all information for the different finite- and zero-temperature representations of the single-particle Green's function. This quantity is also central to this formalism because it is experimentally accessible. We will, therefore, also give a short overview of experimental techniques that have been developed to probe electronic systems.

⚠ in the following, we will often use E_n as the eigenstate of the grand-canonical Hamiltonian, Eq. (2.44), to shorten the notation. The energy eigenstates, therefore, have an additional term and should be understood as

$$E_n \coloneqq \tilde{E}_n - \mu N, \quad \text{with } \hat{H}\,|n\rangle = \tilde{E}_n\,|n\rangle \tag{2.59}$$

We first compute the Lehmann representation of a general correlator, serving as a building block for the subsequent spectral representation.

$$\begin{aligned}
\chi^{\mathrm{C}}_{\hat{O}_1\hat{O}_2}(t,t') \coloneqq \langle \hat{O}_1(t)\hat{O}_2(t')\rangle &= \mathrm{Tr}\Big[e^{-\beta\hat{H}}e^{i\hat{H}t}\hat{O}_1 e^{-i\hat{H}t}e^{-\hat{H}t'}\hat{O}_2 e^{-i\hat{H}t'}\Big] \\
&= \sum_{nm} e^{-\beta E_n}\,\langle n|\,e^{i\hat{H}t}\hat{O}_1 e^{-i\hat{H}t}\,|m\rangle\,\langle m|\,e^{i\hat{H}t'}\hat{O}_2 e^{-i\hat{H}t'}\,|n\rangle \\
&= \sum_{nm} e^{-\beta E_n}e^{iE_nt}\,\langle n|\,\hat{O}_1\,|m\rangle\,e^{-iE_m(t-t')}\,\langle m|\,\hat{O}_2\,|n\rangle\,e^{-iE_nt'} \\
&= \sum_{nm} e^{-\beta E_n}e^{i(E_n-E_m)(t-t')}\,\langle n|\,\hat{O}_1\,|m\rangle\,\langle m|\,\hat{O}_2\,|n\rangle
\end{aligned} \tag{2.60}$$

Equivalently in imaginary time using Eq. (2.57), we obtain:

$$\langle \hat{O}_1(\tau)\hat{O}_2(\tau')\rangle = \sum_{nm} e^{-\beta E_n}e^{(E_n-E_m)(\tau-\tau')}\,\langle n|\,\hat{O}_1\,|m\rangle\,\langle m|\,\hat{O}_2\,|n\rangle \tag{2.61}$$

These are extremely useful identities for many solid-state theory calculations (whenever the Hamiltonian is time-independent and the time evolution operator in the first line can be written in this simple form), but especially in the context of this thesis. The value lies in the decomposition of the expectation value for the time-dependent operators into expectation values of static correlators and a phase factor. We now use this to obtain the so-called spectral or Lehmann representation for the Green's function. Other applications in this thesis are the explicit calculation of observables in the atomic limit Sec. 3.3.1 and the implementation of an exact diagonalization solver for the Dynamical Mean Field Theory (DMFT) method Sec. 6.6.

The Lehmann representation of the real- and imaginary time single-particle Green's functions given by

$$\begin{aligned}
G^{\mathrm{R/A}}_{\alpha\alpha'}(t,t') &= -i\Theta(t\pm t')\langle T\hat{c}_{\,\alpha}(t)\hat{c}^\dagger_{\alpha'}(t')\rangle \\
&= -i\Theta(t\pm t')\frac{1}{Z}e^{-\beta E_n}\sum_{nm}\big[e^{i(E_n-E_m)(t-t')}\,\langle n|\,\hat{c}_{\,\alpha}\,|m\rangle\,\langle m|\,\hat{c}^\dagger_{\alpha'}\,|n\rangle \\
&\qquad + e^{i(E_n-E_m)(t'-t)}\,\langle n|\,\hat{c}^\dagger_{\alpha'}\,|m\rangle\,\langle m|\,\hat{c}_{\,\alpha}\,|n\rangle\big]
\end{aligned} \tag{2.62}$$

Analogously for the imaginary time Green's function using Eq. (2.61):

$$G_{\alpha\alpha'}(\tau) = \frac{1}{Z}e^{-\beta E_n}\sum_{nm}\big[e^{(E_n-E_m)\tau}\,\langle n|\,\hat{c}_{\,\alpha}\,|m\rangle\,\langle m|\,\hat{c}^\dagger_{\alpha'}\,|n\rangle - e^{-(E_n-E_m)\tau}\,\langle n|\,\hat{c}^\dagger_{\alpha'}\,|m\rangle\,\langle m|\,\hat{c}_{\,\alpha}\,|n\rangle\big] \tag{2.63}$$

The two terms suggest that this procedure becomes much more cumbersome for higher-order correlators, whith the 4-point correlator already has 3! = 6 possible permutations of time arguments in addition to 4 state summations from the insertion of unit operators. Next, we will discuss the real and imaginary frequency versions of this representation.

Real frequencies

We will shorten the following derivation by assuming a time independence of the Hamiltonian.

Following from Eq. (2.33), we can omit one argument since $G(x,t-t';x') = G(x,t;x't')$ (see Eq. (I8.1) for the proof in imaginary time). We start with the original definition of the single-particle Green's function, Eq. (2.36), but now already for generalized states instead of the special case of a position basis (in that case, the overlaps become wave functions $\langle\alpha\,|\,n\rangle \to \psi_n(x)$). Here, our goal is to isolate the real part from the imaginary part before considering the full spectral representation. In the following, we use the integral representation of the Heaviside function

$$\Theta\left(\pm(t-t')\right) = \frac{i}{2\pi}\int \mathrm{d}\nu \frac{e^{\mp i\nu(t-t')}}{\nu \pm i\eta}, \tag{2.64}$$

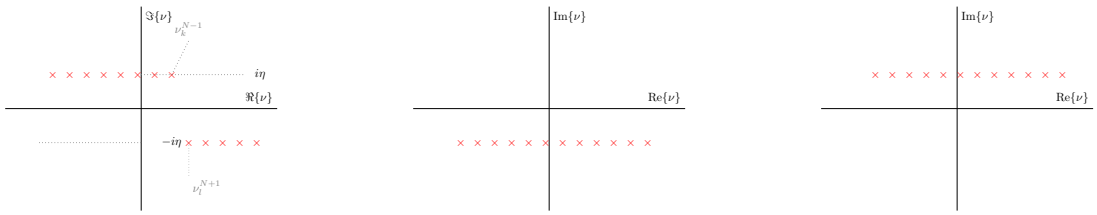

Figure 2.2: Singularities of Green's function with energies relative to the chemical potential. Red Crosses mark poles of the time-ordered, retarded, and advanced Green's functions [246].

and Eq. (2.60), to write the Fourier transform of the Lehmann representation as:

$$\begin{aligned}
\mathcal{F}\left[G^{\mathrm{R/A}}_{\alpha\alpha'}(t)\right](\nu) &= \int_{-\infty}^{\infty} e^{i\nu s}(-i\Theta(\pm s)) \sum_{n,m} \langle\alpha\,|\,n\rangle\langle n|\, e^{-i\hat{H}s}\,|m\rangle\langle m\,|\,\alpha'\rangle \,\mathrm{d}s \\
&= -i\int_0^{\infty} e^{i\nu s} \sum_{nm} \delta_{mn}\langle\alpha\,|\,n\rangle\, e^{-iE_n s}\langle m\,|\,\alpha'\rangle \,\mathrm{d}(\pm s) \\
&= -i\sum_n \langle\alpha\,|\,n\rangle \int_0^{\infty} e^{i\nu s} e^{-iE_n s}\mathrm{d}(\pm s)\langle n\,|\,\alpha'\rangle \\
&= -i\sum_n \langle\alpha\,|\,n\rangle \int_0^{\infty} e^{i(\nu-E_n)s}\mathrm{d}(\pm s)\langle n\,|\,\alpha'\rangle \qquad (2.65) \\
&= \sum_n \langle\alpha\,|\,n\rangle \frac{e^{i(\nu\pm i\eta-E_n)s}}{i(\nu\pm i\eta-E_n)}\Big|_0^{\infty}\langle n\,|\,\alpha'\rangle \qquad (2.66) \\
&= \langle\alpha|\left[(\nu\pm i\eta)\mathbb{1}-\hat{H}\right]^{-1}|\alpha'\rangle \\
\Rightarrow \hat{G}^{\mathrm{R/A},\nu}_{\alpha\alpha'} &= \left[(\nu\pm i\eta)\mathbb{1}-\hat{H}\right]^{-1} \qquad (2.67)
\end{aligned}$$

Here, a small shift η is usually introduced to avoid mathematical complications of dealing with the δ distribution, which would otherwise arise from the Fourier transformation of a plane wave. A more comprehensive derivation is given in [298, p. 23].
In the next step, we isolate the real and imaginary parts of the Green's function, where the difference between both one-sided limits recovers the Lorentzian representation of the delta distribution. First, we use the Green's function in the eigenbasis Eq. (2.65), after evaluating the integral.

$$G^{\mathrm{R/A},\nu}_{\alpha\alpha'} = \sum_n \frac{\langle\alpha\,|\,n\rangle\langle n\,|\,\alpha'\rangle}{\nu\pm i\eta-E_n} \qquad (2.68)$$

Next, we use the following identity linking the Dirac delta distribution to the limit of the Cauchy-Lorentz distribution.

$$\lim_{\eta\to0}\int_{-\infty}^{\infty} f(x)\frac{\eta}{x^2+\eta^2}\mathrm{d}x \overset{\eta u=x}{=} \lim_{\eta\to0}\int_{-\infty}^{\infty} f(\eta u)\frac{1}{u^2+1}\mathrm{d}u = \lim_{\eta\to0} f(\eta u)\pi = \pi f(0)$$

With $f(x)$ a test function ($f\in C^{\infty}$ and compact support).
We can now calculate the limit of $\eta\to0$ of the retarded and advanced Green's functions:

$$\begin{aligned}
\lim_{\eta\searrow0} G^{\mathrm{R/A},\nu}_{\alpha\alpha'} &= \sum_n \langle\alpha\,|\,n\rangle\langle n\,|\,\alpha'\rangle \lim_{\eta\searrow0}\left[\frac{(\nu\mp i\eta)-E_n}{(\nu-E_n)^2+\eta^2}\right] \\
&= \sum_n \langle\alpha\,|\,n\rangle\langle n\,|\,\alpha'\rangle \lim_{\eta\searrow0}\frac{\nu-E_n}{(\nu-E_n)^2+\eta^2} + i\sum_n \langle\alpha\,|\,n\rangle\langle n\,|\,\alpha'\rangle \lim_{\eta\searrow0}\frac{\mp\eta}{(\nu-E_n)^2+\eta^2} \\
&= \sum_n \frac{\langle\alpha\,|\,n\rangle\langle n\,|\,\alpha'\rangle}{\nu-E_n} + \mp\pi i\sum_n \langle\alpha\,|\,n\rangle\langle n\,|\,\alpha'\rangle\,\delta(\nu-E_n) \qquad (2.69)
\end{aligned}$$

This means the retarded and advanced Green's functions have poles at the eigenvalues of the Hamiltonian, which also define the difference between them. In fact, the difference between both has a straightforward physical meaning, as it encodes the generalization of the density of states to interacting systems, called the spectral function.

Important 2.3.0.1 (Spectral Representation In Real Frequencies)

Following from Eq. (2.68)*, the Green's function then reads in the Lehmann representation:*

$$G^{\mathrm{R/A},\nu}_{\alpha\alpha'} = \frac{1}{Z}\sum_{nm}(e^{-\beta E_n}+\zeta e^{-\beta E_m})\frac{\langle m|\,\hat{c}_{\alpha}\,|n\rangle\langle n|\,\hat{c}^{\dagger}_{\alpha'}\,|m\rangle}{\nu+E_n-E_m\pm i\eta} \qquad (2.70)$$

$$\&$$

$$\Rightarrow G^{\mathrm{R},\nu}_{\alpha\alpha'} - G^{\mathrm{A},\nu}_{\alpha\alpha'} = -i(e^{\beta\nu}+\zeta)A^{\nu}_{\alpha\alpha'} = -2n^{\nu}_{\zeta}\,\mathrm{Im}\,G^{\mathrm{R},\nu}_{\alpha\alpha'} \tag{2.71}$$

With the usual Fermi/Bose distribution

$$n^{\nu}_{\zeta} = \left[e^{\beta\nu}+\zeta\right]^{-1} \tag{2.72}$$

We make two observations here: (i) From the results above, it follows that the (advanced) retarded Green's functions have singularities in the (upper) lower half of the complex plane. These positions correspond to the energy states of the many-particle system. In Fig. 2.2 the poles are illustrated for causal, retarded and advanced Green's function. (ii) From Eq. (2.103) and Eq. (2.104), we observe that the spectral function exactly captures that excitation spectrum of the many-particle system. This provides insight into the role of the spectral function as a measure of available states (determined by the overlap term between the energy states m and n), which have particle numbers differing by one. In fact, in Sec. 2.4.3, we will discuss that the spectral function is best viewed as the generalization of the density of states to interacting many-particle systems.

2.3.1 Observables from Green's Functions

One important property of Green's functions is the ability to obtain observables from them. For single particle operators we can write [70, Chapter 7]:

$$\left\langle \widehat{O}^{(1)}(t)\right\rangle = i\zeta \sum_{\alpha_1\alpha_2} \langle\alpha_1|\,\widehat{O}\,|\alpha_2\rangle\, G_{\alpha_1\alpha_2}(t;t') \tag{2.73}$$

$$= \zeta \sum_{\alpha\alpha_2} \langle\alpha|\,\widehat{O}\,|\alpha_2\rangle\, G_{\alpha_1\alpha_2}(\tau;\tau') \tag{2.74}$$

Specifically for this thesis, we will obtain the density, kinetic, and potential energies from the interacting Green's function.

Density Sums over Green's functions have to be carried out carefully by considering convergence factors. As an example, we show the sum over one-particle Green's functions to obtain the electron density. This is specifically important in our context since we aim to restore the consistency of this quantity throughout the method discussed later. A derivation of an improved numerical sum formula for the density, is given in Sec. 6.3.6.
Instead of computing the total electron density from the density operator via

$$\hat{n}_i = \hat{n}_{i\uparrow} + \hat{n}_{i\downarrow}, \tag{2.75}$$

we can obtain this quantity in terms of the single-particle Green's function. From the definition of the imaginary time Green's function in Eq. (2.39) (here $\sum_\sigma G_\sigma(\tau) = \Theta(\tau)\langle \hat{c}_{\ \sigma}(\tau)\hat{c}^\dagger_\sigma\rangle - \Theta(-\tau)\langle\hat{c}^\dagger_\sigma \hat{c}_{\ \sigma}(\tau)\rangle$), the Fourier transform in Eq. (2.53) and the definition of the density $n = \sum_\sigma\langle\hat{c}^\dagger_\sigma\hat{c}_{\ \sigma}\rangle$ we obtain the following:

$$\lim_{\eta\searrow 0} G(\tau+\eta) = 1 - \frac{n}{2} = \sum_n e^{-i\nu_n\eta}G^{\nu} \tag{2.76}$$

$$\lim_{\eta\searrow 0} G(\tau-\eta) = \frac{n}{2} = \sum_n e^{-i\nu_n\eta}G^{\nu} \tag{2.77}$$

$$\Rightarrow \frac{n}{2} = \lim_{\eta\searrow 0}\sum_n e^{i\nu_n\eta}G^{\nu} \tag{2.78}$$

Throughout this thesis, the last definition will be implicitly assumed whenever the precise limit is not given.
The argument above is given without momentum dependence. Non-local Green's function pick up an additional integration over $\mathbf{k}$-space:

$$n = 2\lim_{\eta\searrow 0}\sum_{\mathbf{k},n} e^{i\nu_n\eta}G^{\nu}_{\mathbf{k}} \tag{2.79}$$

Energies The kinetic and potential energies can be obtained from Eq. (2.74) (for a derivation see [70, Chapter 7]):

$$E_{\mathrm{kin}} = \mathrm{Tr}\left[\epsilon_{\mathbf{k}}G^{\nu}_{\mathbf{k}}\right] \tag{2.80}$$

$$E_{\mathrm{pot}} = \frac{1}{2}\lim_{\eta\searrow 0}\sum_{\mathbf{k}}\left[-\partial_\tau - \epsilon_{\mathbf{k}} + \mu\right]\mathrm{Tr}\,G_{\mathbf{k}}(\tau) = \mathrm{Tr}\left[\Sigma^{\nu}_{\mathbf{k}}G^{\nu}_{\mathbf{k}}\right] \tag{2.81}$$

2.4 Susceptibilities and Linear Response

In this section, we discuss the application of the Green's function formalism to the responses of the system. We focus on the effective single particle responses; generalization to the 4 point correlator functions is deferred to Sec. 2.7.3. First, we give a brief reminder of linear response theory, as found in most textbooks, in order to motivate susceptibilities as response functions. subsequently

2.4.1 Linear Response

A typical method to study physical systems is to apply some external perturbation and subsequently observe its response. Here, we will discuss the simplest approach to model the response, namely, by limiting ourselves to linear order.
Let us start by imagining a system described by a Hamiltonian $\hat{H}_0$ in equilibrium that is disturbed by an external time- and space-dependent perturbation $f(\mathbf{r},t)$. Examples of such disturbances are a magnetic field applied to the system, single high-energy photons, or neutrons. The system will react in different ways, depending on the energy scale and the type of disturbance. This is described on a microscopic level by different operators coupling to the perturbation. These observables can then be used to probe the system behavior under certain effects and, thereby, gain insight into the driving dynamics. Examples of observables could be magnetization, spectral function, and spin susceptibility. We give a brief overview of some experimental techniques and their relation to the Green's function formalism in Sec. 2.4.4.In an experiment, we will measure the expectation value of this observable:

$$\langle \hat{A}(\mathbf{r},t)\rangle \tag{2.82}$$

With a coupling of the perturbation to the observable given as an external Hamiltonian:

$$\hat{H}_{\text{ext}} = \int \mathrm{d}\mathbf{r}\hat{O}(\mathbf{r},t)f(\mathbf{r},t) \tag{2.83}$$

The perturbation stemming from a magnetic field, for example, would look like this (see also Sec. 2.4.6 for further examples and the definition of the spin operator $\hat{\boldsymbol{S}}_i$):

$$\hat{H}_{\text{ext}} = -\mu_{\text{B}} \sum_i \hat{\boldsymbol{S}}_i \cdot \hat{\boldsymbol{B}}(t), \tag{2.84}$$

Where the integration over the position space collapsed into a sum over positions of spins. The full Hamiltonian is now given as the sum of the Hamiltonian for the equilibrium system and the perturbation.

$$\hat{H}_{\text{P}} = \hat{H}_0 + \hat{H}_{\text{ext}} \tag{2.85}$$

We continue by considering weak perturbations of the system, which allow us to take only the leading (i.e. linear) Taylor term of the response into account. The usual time evolution from Eq. (2.14) is then given by:

$$\hat{U}_{\text{ext}}(t,t_0) = \mathcal{T} e^{-i\int_{t_0}^{t}\mathrm{d}s H_{\text{ext}}(s)} = 1 - i\int_{t_0}^{t}\mathrm{d}s H_{\text{ext}}(s) + \mathcal{O}(f^2(\mathbf{r},t)) \tag{2.86}$$

The system was unperturbed initially, i.e. $t_0 \to -\infty$, lets us assume $\lim_{t_0\to-\infty}\hat{H}_{\text{P}}(t) = \hat{H}$. Using this ansatz and that the time evolution of the full (perturbed) system is a product of the equilibrium and external system, $\hat{U}_{\text{P}}(t,t_0) = \hat{U}(t,t_0)\hat{U}_{\text{ext}}(t,t_0)$, yields for the total time evolution operator:

$$\hat{U}_{\text{P}}(t) = \hat{U}(t) - i\int_{-\infty}^{t}\mathrm{d}s\hat{U}(t,s)\hat{H}_{\text{ext}}(s)\hat{U}(s) \tag{2.87}$$

With this result, containing the linear approximation, we are able to evaluate the observable Eq. (2.82) under some state ψ:

$$\langle \hat{A}(\mathbf{r},t)\rangle = \langle\psi(t)|\,\hat{A}(\mathbf{r},t)\,|\psi(t)\rangle = \langle\psi|\,\hat{A}(\mathbf{r},t)\,|\psi\rangle + i\int_{-\infty}^{t}\mathrm{d}s\,\langle\psi|\,[\hat{H}_{\text{ext}}(s),\hat{A}(\mathbf{r},t)]\,|\psi\rangle \tag{2.88}$$

We can then write the deviation of the observable $\hat{A}$ from its equilibrium value due to the perturbation in terms of response functions χ:

$$\Leftrightarrow \delta\langle \hat{A}(\mathbf{r},t)\rangle = \langle \hat{A}(\mathbf{r},t)\rangle_{\text{P}} - \langle \hat{A}(\mathbf{r},t)\rangle_0 = i\int_{-\infty}^{t}\mathrm{d}s\,\langle\psi|\,[\hat{H}_{\text{ext}}(s),\hat{A}(\mathbf{r},t)]\,|\psi\rangle \tag{2.89}$$

$$= i\int\mathrm{d}\mathbf{r}\int_{-\infty}^{t}\mathrm{d}s\,\langle\psi|\,[\hat{O}(\mathbf{r},s),\hat{A}(\mathbf{r},t)]\,|\psi\rangle\, f(\mathbf{r},t) \tag{2.90}$$

$$=: -i\int\mathrm{d}\mathbf{r}\int_{-\infty}^{\infty}\mathrm{d}s\chi^{\text{R}}_{\hat{O}\hat{A}}(\mathbf{r},s;\mathbf{r}',t)f(\mathbf{r}',t) \tag{2.91}$$

The last line defines the retarded linear response susceptibility $\chi^{\text{R}}_{\hat{O}\hat{A}}(\mathbf{r},s;\mathbf{r}',t)$ of an observable $\hat{A}(\mathbf{r},t)$ stemming from an external perturbation $f(\mathbf{r},t)$ that couples to $\hat{O}$ (see also Def. 2.4.2.1). This is the well-known Kubo formula for time-dependent perturbations [149].
In general, we can then write the time-dependent expectation value of an observable $\hat{A}$ to a perturbation

$\hat{O}$ in linear response as:

$$\langle A\rangle_t = \langle A\rangle + \int_{-\infty}^{\infty} \mathrm{d}s \chi^{\mathrm{R}}_{\hat{O}\hat{A}}(\mathbf{r}, s; \mathbf{r}', t) f(\mathbf{r}', t) \tag{2.92}$$

2.4.2 General Correlation Functions

In general, we consider correlation functions as the difference between their connected and unconnected parts.

$$\begin{aligned} C_{\hat{O}_1\ldots\hat{O}_n}(\tau_1,\ldots\tau_n)\langle T_\zeta \hat{O}_1(\tau_1)\ldots\hat{O}_n(\tau_n)\rangle = C^{\mathrm{C}}_{\hat{O}_1\ldots\hat{O}_n}(\tau_1,\ldots\tau_n)\langle T_\zeta \hat{O}_1(\tau_1)\ldots\hat{O}_n(\tau_n)\rangle \\ - C^{0}_{\hat{O}_1\ldots\hat{O}_n}(\tau_1,\ldots\tau_n)\langle T_\zeta \hat{O}_1(\tau_1)\ldots\hat{O}_n(\tau_n)\rangle \end{aligned} \tag{2.93}$$

Here, we defined two commonly encountered quantities, the connected susceptibilities and unconnected susceptibilities. The latter are typically called bare susceptibilities.

$$\chi^{\mathrm{C}}_{\hat{O}_1\hat{O}_2}(t,t') \coloneqq \langle \hat{O}_1(t)\hat{O}_2(t')\rangle \tag{2.94}$$

$$\chi^{0}_{\hat{O}_1\hat{O}_2}(t,t') \coloneqq \langle \hat{O}_1(t)\rangle\langle \hat{O}_2(t')\rangle \tag{2.95}$$

The meaning of the full susceptibility can be motivated in the statistical analog of the quantum mechanical correlator, which is also discussed around Sec. 2.6.2. From this identification, we understand that the two-operator correlator with a single time argument is equivalent to the covariance or, more generally, joint cumulant [5]:

$$\begin{aligned} \chi_{\hat{O}_1\hat{O}_2}(t) &= \langle \big(\hat{O}_1(t) - \langle\hat{O}_1(t)\rangle\big)\big(\hat{O}_2 - \langle\hat{O}_2\rangle\big)\rangle \\ &= \langle \hat{O}_1(t)\hat{O}_2\rangle - \langle\hat{O}_1(t)\rangle\langle\hat{O}_2\rangle - \langle\hat{O}_1(t)\rangle\langle\hat{O}_2\rangle + \langle\hat{O}_1(t)\rangle\langle\hat{O}_2\rangle \\ &= \langle \hat{O}_1(t)\hat{O}_2\rangle - \langle\hat{O}_1(t)\rangle\langle\hat{O}_2\rangle \\ &= \chi^{\mathrm{C}}_{\hat{O}_1\hat{O}_2}(t) - \chi^{0}_{\hat{O}_1\hat{O}_2}(t) \end{aligned} \tag{2.96}$$

This quantity should be zero for uncorrelated observables. In this case, the connected susceptibilities decouple into the unconnected ones, and one can, therefore, understand this to be the proper definition. Comparing with the definition of the real-time Green's function in Eq. (2.37), we clearly see the relationship to Green's functions and may also add the definition of the retarded susceptibility and the equivalent to the spectral function here.

Important 2.4.2.1 (Susceptibility)
We define the retarded susceptibility χ^{R} as follows:

$$\widetilde{\chi}_{\hat{O}_1\hat{O}_2}(\mathbf{r},t;\mathbf{r}',t') = \frac{1}{2}\langle[\hat{O}_1(\mathbf{r},t),\hat{O}_2(\mathbf{r}',t')]\rangle \tag{2.97}$$

$$\chi^{\mathrm{R}}_{\hat{O}_1\hat{O}_2}(\mathbf{r},t;\mathbf{r}',t') = i\Theta(t-t')\widetilde{\chi}_{\hat{O}_1\hat{O}_2}(\mathbf{r},t;\mathbf{r}',t') \tag{2.98}$$

$$\chi_{\alpha_1\ldots\alpha_4}(\tau_1\ldots\tau_4) = G^{(2)}_{\alpha_1\ldots\alpha_4}(\tau_1\ldots\tau_4) - G^{(1)}_{\alpha_1\alpha_2}(\tau_1,\tau_2)G^{(1)}_{\alpha_3\alpha_4}(\tau_3,\tau_4) \tag{2.99}$$

Furthermore, the susceptibility $\widetilde{\chi}$ takes on a role similar to the spectral function for Green's functions.

$$\widetilde{\chi}^{\omega} = \frac{1}{2i}\left(\chi^{\mathrm{R},\omega} - \chi^{\mathrm{A},\omega}\right) \tag{2.100}$$

Eq. (2.116) *demonstrates its role as a measure of dissipation in the system.*

Lehmann Representation The Lehmann representation in Matsubara space can be obtained analogously to the Green's function; see also Sec. 2:

$$\chi^{\omega}_{\hat{O}_1\hat{O}_2,\mathbf{q}} = \frac{1}{Z}\sum_{nm}\frac{e^{-\beta(E_n-E_m)}}{E_m - E_n - i\omega_m}\langle n|\hat{O}_1(\mathbf{q})|m\rangle\langle m|\hat{O}_2(-\mathbf{q})|n\rangle \tag{2.101}$$

This representation can be used to obtain numerical values with the Exact Diagonalization (ED) method.

2.4.3 Spectral functions

The two main textbook quantities for the description of non-interacting electron systems are the band structure $\epsilon_{n,\mathbf{k}}$ and the Density Of States (DOS). Bloch's theorem justifies the former and is typically

[5] Note, that this definition corresponds to correlation functions (or autocorrelation functions if $\hat{O}_1(t) = \hat{O}_2(t)$) if one reinterprets the operator as a stochastic process in time t.

justified in systems with Fermi liquid behavior (see Sec. 2.5, where quasiparticles with renormalized electron masses and velocities take the role of bare electrons). The latter has a more well-defined generalization for interacting systems called spectral function. Similar to the DOS, the spectral function measures excitations in the energy spectrum and can be measured by photoemission spectroscopy (the best known of which is probably Angle-resolved photoemission spectroscopy (ARPES). We discuss further experimental setups below).

Important 2.4.3.1 (Spectral Functions)
Following Eq. (2.69) *and [70, p295], we define the spectral function as the difference between the imaginary part of the advanced and retarded Green's function*

$$A^{\nu}_{\mathbf{k}} = \mathrm{Im}[G^{\mathrm{A},\nu}_{\mathbf{k}} - G^{\mathrm{R},\nu}_{\mathbf{k}}] = -2\tanh^{\zeta}\left(\frac{1}{2}\beta\nu\right)\mathrm{Im}[G^{\nu}_{\mathbf{k}}] \tag{2.102}$$

This identifies the spectral function as the central object, connecting the retarded, advanced, and causal Green's functions.
Following our discussion of the spectral representation of the real-time Green's function, we also have the spectral representation of the Green's function

$$A^{\nu}_{\alpha\alpha'} = \frac{1}{Z}\sum_{nm} e^{-\beta E_n}\left(e^{\beta E} - \zeta\right)\langle m|\,\hat{c}_{\alpha}\,|n\rangle\langle n|\,\hat{c}^{\dagger}_{\alpha'}\,|m\rangle\,\delta(\nu - (E_n - E_m)) \tag{2.103}$$

Furthermore, the spectral function also connects real and imaginary frequencies:

$$G^{\mathrm{R/A},\nu}_{\mathbf{k}} = \frac{1}{2\pi}\int \frac{A^{\nu'}_{\mathbf{k}}}{\nu - \nu' \pm i\eta}\mathrm{d}\nu' \tag{2.104}$$

$$G^{\nu_n}_{\mathbf{k}} = \frac{1}{2\pi}\int_{-\infty}^{\infty} \frac{A^{\nu'}_{\mathbf{k}}}{i\nu_n - \nu'}\mathrm{d}\nu' \tag{2.105}$$

The spectral function fulfills properties of a probability distribution and is therefore positive and normalized [162]:

$$A^{\nu}_{\mathbf{k}} \geq 0 \tag{2.106}$$

$$\sum_{\omega\mathbf{k}} A^{\nu}_{\mathbf{k}} = 1 \tag{2.107}$$

The spectral function is of great special importance to Green's function formalism because it is directly measurable in experiments, which we will discuss next.

2.4.4 Experimental Techniques

This thesis is focused on method development for a theoretical model far removed from real materials calculations. However, no theoretical setup can claim validity without connection to experiments. In fact, the thermodynamical consistency discussed in Sec. 4 specifically aims to improve two of these measurable quantities. Specifically, we have the following observables linked to experiments [180, Sec. 4.3]: The spectral function, which is, for example, measurable by ARPES or Scanning Tunneling

Name	Observable	Technique
Spectral Function	$A^{\nu}_{\mathbf{k}}$	ARPES, STS, ERS
Magnetic Susceptibility	$\chi^{\omega}_{\mathrm{m},\mathbf{q}}$	NMR, INS
Charge Susceptibility	$\chi^{\omega}_{\mathrm{d},\mathbf{q}}$	IR, EELS

Table 2.1: Experimental techniques, adapted from [180, Sec. 4.3].

Spectroscopy (STS), is able to probe the available states of the system around the Fermi surface. In STS, by measuring tunneling through a metallic tip close to the surface [180, Sec. 4.3.2] and [190, Chapter 14]

$$\int \rho(\omega)\left(n^{\omega}_{\mathrm{F}} - n^{\omega - V_{\mathrm{bias}}}_{\mathrm{F}}\right)\mathrm{d}\omega \tag{2.108}$$

with a bias voltage V_{bias}. In ARPES, the photoelectric effect is used to directly probe the available states in Eq. (2.103).
Electronic Raman Scattering (ERS) is also used for probing systems with vastly differing energy scales of gaps as a function of $\mathbf{k}$, such as in the pseudogap region of cuprates [260]. While, from the theory side, ARPES certainly seems to be the more prominent experimental technique, it is inherently understood as a single-particle method, while ERS is not [57]. In Sec. 3, we try to argue on the example of the atomic limit that this poses a problem when trying to determine the strong correlation effects

of a system. However, careful investigation seems to indicate that ARPES is indeed applicable for the measurement of the bulk spectral function in cuprates [297].
To obtain magnetic susceptibilities, inelastic neutron (X-Ray) scattering (INS)/(RIXS) and Nuclear Magnetic Resonance (NMR) are regularly used techniques [180, Sec. 4.3.3-4.3.4]. The former, again, probes the available states directly, as given in the Lehmann representation. This is possible because neutrons carry a spin but no charge and, therefore, interact with bulk magnetic moments. NMR probes magnetic moments by aligning them in an external field (typically a strong constant bias and a weak perturbation) and measuring radiation emitted when excited states return to their ground state when the magnetic field switches off.
Especially for cuprates, the (dynamic, i.e. ω and $\mathbf{q}$ dependent) charge susceptibility is of importance because charge density waves play an important role in understanding the phase diagram around the superconducting dome Sec. 7.2. Direct measurement techniques of the dynamical charge susceptibility seem to be far less established than for optical conductivity in the $\mathbf{q} \to 0$ measurement through Infrared Reflectivity (IR) measurements. In order to directly measure the momentum-resolved charge susceptibility, more recently, a technique to directly probe the momentum-resolved absorption spectrum of electrons (M-EELS) has been proposed [276].

2.4.5 Positivity of the Susceptibility

Because the physical susceptibility plays a central role in the Sec. 5.4 method, we derive the positivity property here. However, comprehensive derivations are left for the literature, for example [266, Chapter 10] and [61, Chapter 3.4].

We will make repeated use of the strict positivity of the physical susceptibility. In fact, this was the driving motivation for the development of improved Matsubara summation formulas in Sec. 6.1. Numerically unstable or poorly approximated quantities can violate this property and lead to severe qualitative discrepancies in the lDΓA method that relies on a renormalization of this quantity.
Due to its importance for this thesis, the argument is presented here but can also be found here in expanded form [266, Chapter 10.6]. The power dissipation of the external perturbation from Eq. (2.83) is given by the work done per unit of time. We use the Kubo formula to evaluate the expression:

$$\frac{\mathrm{d}W}{\mathrm{d}t} = \frac{\mathrm{d}\hat{H}_{\mathrm{ext}}(t)}{\mathrm{d}t} \tag{2.109}$$

$$= \int \mathrm{d}\mathbf{r} \left(i\hat{H}\hat{O}(\mathbf{r}) e^{-i\hat{H}t} f(\mathbf{r},t) - i e^{i\hat{H}t} \hat{O}(\mathbf{r}) \hat{H} f(\mathbf{r},t) + e^{i\hat{H}t} \hat{O}(\mathbf{r}) \hat{H} e^{-i\hat{H}t} \frac{\mathrm{d}f(\mathbf{r},t)}{\mathrm{d}t} \right) \tag{2.110}$$

$$= -[\langle H_0 \rangle + \langle \hat{H}_{\mathrm{ext}} \rangle] \frac{\mathrm{d}f(\mathbf{r},t)}{\mathrm{d}t} \tag{2.111}$$

Computing the total energy $\overline{W} = \int_{T/2}^{T/2} \mathrm{d}t W(t)$, which must be positive, we obtain after Fourier transformation using Eq. (2.92) (here we also use a general basis as in Sec. 2.4.2.1 instead of real space):

$$-\int \frac{\mathrm{d}\omega}{2\pi} f_i^{-\omega} \chi^{\mathrm{R},\omega}_{\hat{O}_1\hat{O}_2}(i\omega) f_j^{\omega} > 0 \tag{2.112}$$

The same expression, except for a global minus sign, can be obtained under exchange of variables $\omega \to -\omega$ and $i \to j$. Adding both expressions together still leaves us with a positive value. Finally, we use the spectral representation from Eq. (2.70) and obtain

$$0 < \overline{W} = -\frac{1}{2} \int \frac{\mathrm{d}\omega'}{\pi} f_i^{-\omega} \left[\frac{\widetilde{\chi}^{\omega}_{\hat{O}_1\hat{O}_2}}{\omega' - (\omega + i\eta)} - \frac{\widetilde{\chi}^{\omega}_{\hat{O}_2\hat{O}_1}}{\omega' - (-\omega + i\eta)} \right] (i\omega) f_j^{\omega} \tag{2.113}$$

$$\Leftrightarrow \overline{W} = \int \frac{\mathrm{d}\omega}{2\pi} \left(f_i^{\omega}\right)^* \omega \widetilde{\chi}^{\omega}_{\hat{O}_1\hat{O}_2} f_j^{\omega} \tag{2.114}$$

$$\Rightarrow 0 < \overline{W} = \omega \left(f_i^{\omega}\right)^* \widetilde{\chi}^{\omega}_{\hat{O}_1\hat{O}_2} f_j^{\omega} \tag{2.115}$$

$$\Rightarrow 0 < \overline{W} = \omega \widetilde{\chi}^{\omega}_{\hat{O}_1\hat{O}_1} \tag{2.116}$$

The last two lines follow since the frequency dependence of the external field is arbitrary.
We will use this property of the analog of the spectral function of the retarded susceptibility, for example, in Sec. 5.2.1.
Even more important is the strict positivity for magnetic and charge susceptibility (see below). From the spectral representation in Matsubara frequencies, Eq. (2.101), we get for hermitian operators $\hat{O}_1$ and $\hat{O}_2$:

$$\chi^{\omega}_{\hat{O}_1\hat{O}_2,\mathbf{q}} = [\chi^{\omega}_{\hat{O}_1\hat{O}_2,-\mathbf{q}}]^* \tag{2.117}$$

$$\Rightarrow \chi^{\omega}_{\hat{O}_1\hat{O}_2} = \mathrm{Re}\, \chi^{\omega}_{\hat{O}_1\hat{O}_2} \tag{2.118}$$

The usual fraction expansion trick (multiply $\hat{O}_1$ by $(E_n - E_m + i\omega_m)\hat{O}_2$ and the analog for $\hat{O}_2$ to make

the denominator real values) gives the very important property:

$$\mathrm{Re}\,\chi^{\omega}_{\hat{O}_1\hat{O}_2,\mathbf{q}} \overset{|m|\to\infty}{\sim} \frac{1}{(i\omega_m)^2} \tag{2.119}$$

In fact, for the most important susceptibilities we will encounter, the charge and spin susceptibilities (see next section), the coefficient of this tail is the kinetic energy. Both identities hold for real and imaginary frequency-valued susceptibilities.

2.4.6 Important Definitions for Susceptibilities

Having introduced the susceptibilities from a linear response point of view, we will now introduce the common variants of these response functions used in this thesis. As motivated above, the two operator susceptibilities $\chi_{\hat{O}_1\hat{O}_2}$ describe responses of one observable $\hat{O}_1$, while $\hat{O}_2$ changes. Or, more generally, the generalized covariance of two operators. Consequently, the equal operator susceptibility $\chi_{\hat{O}}(\tau) = \chi_{\hat{O}\hat{O}}(\tau)$ is a generalization of the autocorrelation function, which is a measure for spin fluctuations in the system. We first define the pseudospin operators:

$$\hat{S}_j = \frac{1}{2}\sum_{\sigma\sigma'} \hat{c}^\dagger_\sigma \sigma_j^{\sigma\sigma'} \hat{c}_{\sigma'} \tag{2.120}$$

$$\sigma_j = \begin{pmatrix} \delta_{j3} & \delta_{j1} - i\delta_{j2} \\ \delta_{j_1} + i\delta_{j2} & -\delta_{j3} \end{pmatrix} \tag{2.121}$$

$$\Rightarrow \hat{S}_x = \frac{1}{2}\left(\hat{c}^\dagger_\uparrow \hat{c}_\downarrow + \hat{c}^\dagger_\downarrow \hat{c}_\uparrow\right), \qquad \hat{S}_y = -\frac{i}{2}\left(\hat{c}^\dagger_\uparrow \hat{c}_\downarrow - \hat{c}^\dagger_\downarrow \hat{c}_\uparrow\right), \qquad \hat{S}_z = \frac{1}{2}\left(\hat{c}^\dagger_\uparrow \hat{c}_\uparrow - \hat{c}^\dagger_\downarrow \hat{c}_\downarrow\right) \tag{2.122}$$

SU(2) symmetry implies that $[\hat{H}, \hat{S}_{p,i}] = 0$, see [205, Sec. 2.2.2.6], with:

$$\hat{S}_{\mathrm{p},X} = \frac{1}{2}\left(\hat{c}^\dagger_\uparrow \hat{c}^\dagger_\downarrow + \hat{c}_\downarrow \hat{c}_\uparrow\right), \qquad \hat{S}_{\mathrm{p},Y} = -\frac{i}{2}\left(\hat{c}^\dagger_\uparrow \hat{c}^\dagger_\downarrow - \hat{c}_\downarrow \hat{c}_\uparrow\right), \qquad \hat{S}_{\mathrm{p},Z} = \frac{1}{2}\left(\hat{c}^\dagger_\uparrow \hat{c}_\uparrow + \hat{c}^\dagger_\downarrow \hat{c}_\downarrow - 1\right) \tag{2.123}$$

These can then be used to define the spin and charge susceptibilities. We call the response of the system, which is defined through the spin operators Eq. (2.121), magnetic response, χ_m:

$$\chi^{\omega}_{\mathrm{m}} = \chi^{\omega}_{\hat{S}_j} \tag{2.124}$$

More generally, we define the magnetic and density response in terms of the spin indices of the generalized susceptibility, here already written with the shorthand spin index notation from Sec. 2.7.2.1.

Important 2.4.6.1 (Magnetic and Density Susceptibilities)
Later we will often use the charge and spin channels instead of actual spin combinations. These are conveniently defined in matrix notation as follows:

$$\overline{\chi} = \begin{pmatrix} \chi_{\uparrow\uparrow} & \chi_{\uparrow\downarrow} \\ \chi_{\downarrow\uparrow} & \chi_{\downarrow\downarrow} \end{pmatrix}, \qquad B_\mathrm{d} = \begin{pmatrix} 1 \\ 1 \end{pmatrix}, \qquad B_\mathrm{m} = \begin{pmatrix} 1 \\ -1 \end{pmatrix} \tag{2.125}$$

$$\chi_\mathrm{d} = B_\mathrm{d}^T \overline{\chi} B_\mathrm{d} \tag{2.126}$$

$$\chi_\mathrm{m} = B_\mathrm{m}^T \overline{\chi} B_\mathrm{m} \tag{2.127}$$

⚠ *The terms charge and density, as well as the terms spin and magnetic channel, are used interchangeably. This holds for many references given in this thesis and even codes in Sec. 6.*

A comprehensive introduction to this notation and symmetry properties can be found in [180, Chapter 4] or [205, Sec. 2.2.2.6].
The relationship between the static susceptibilities ($\lim_{\mathbf{q}\to 0}\lim_{\omega\ to 0}\chi^{\omega}_{\mathbf{q}}$) and observables of the system is also important for this thesis. These are the magnetization and compressiblity of the system, see also Sec. 4.4.2.

$$-\chi^{\omega=0}_{\mathrm{m},\mathbf{q}=\mathbf{0}} = -\sigma \frac{\mathrm{d}\langle m\rangle}{\mathrm{d}h}\Big|_{h=0} \tag{2.128}$$

$$\chi^{\omega=0}_{\mathrm{d},\mathbf{q}=\mathbf{0}} = \kappa \tag{2.129}$$

2.5 Fermi Liquid and Quasi Particles

This section introduces the concept of quasiparticles from the perspective of Fermi liquid theory. Although not applicable in the arguably most interesting parts of the phase diagram for the Hubbard

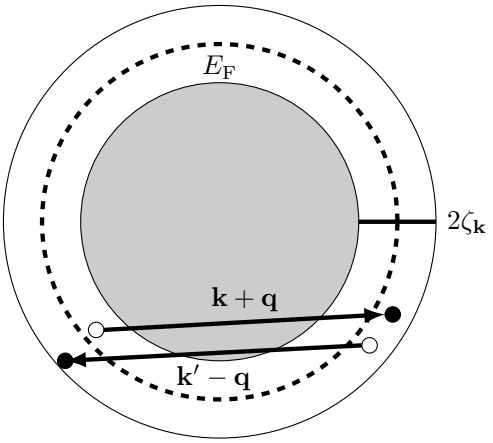

(a) Two-particle scatting around the noninteracting surface, adapted from [39, Figure 14.1]. The Fermi surface is shifted by the quasiparticle energy $\xi_{\mathbf{k}}$ (here drawn without $\mathbf{k}$ dependence) through scattering processes.

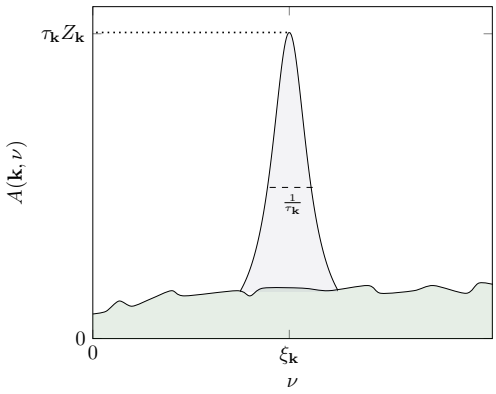

(b) Illustration of spectral function, adapted from [39, Figure 14.2]. The peak of the spectral function is interpreted as the excitation of a quasiparticle with energy $\xi_{\mathbf{k}}$ with lifetime $\tau_{\mathbf{k}}$. $Z_{\mathbf{k}}$ gives the spectral weight, with $1 - Z_{\mathbf{k}}$ being the background, to fulfill the condition $\int \mathrm{d}\nu A_\nu = 1$.

model, the strong coupling regime, the breakdown of Fermi-liquid behavior is in itself a useful tool for the analysis of the Mott phase because precisely this fact indicates the onset of a non-perturbative phase transition[6]. Especially the phase diagram of the cuprate high T_C superconductors shows signs of Fermi liquid breakdown in the critically doped regime [273]. We will give a very broad overview of the conditions that govern the applicability of Fermi-liquid theory and the concept of quasiparticles and parameter renormalizations.

The Fermi-liquid theory describes metallic systems based on the assumption that the ground state of an interacting system is adiabatically connected to the noninteracting one, known as the Gell-Mann-Low theorem [78]. The core insight of Landau was that small excitations can be described as deformations of the Fermi surface, and the newly obtained Fermi surface can be characterized as containing quasiparticles (for example, electrons with renormalized mass) with similar properties as the real particles of the noninteracting system [153, 156, 155]. The physical picture is that interactions excite electrons from the previously noninteracting system above the Fermi surface, keeping the quantum numbers such as spin and charge conserved. This excitation leads to a change in the density distribution functions $\delta n_\sigma(\mathbf{k}) = n_\sigma(\mathbf{k}) - n^0_\sigma(\mathbf{k})$. In Fig. 2.3a, an illustration of this two-particle scattering is depicted, leading to a deformation of the Fermi surface, proportional to the lifetime of the quasiparticle. The important conditions here are that the quasiparticle excitation energy is much larger than a fluctuation introducing it and the lifetime is sufficiently long. We can see this through the consideration of a perturbed Hamiltonian, acting on a noninteracting system, over a short time period (we need the time-dependent version of Eq. (2.14) here) [39, Chapter 14]:

$$\hat{H}_\xi = \hat{H}_0 + \hat{H}_{\mathrm{int}} e^{-\xi t} \tag{2.130}$$

Bringing in the adiabatic connection

$$\lim_{t\to\infty} \left\langle \psi_{\mathbf{k}\sigma}(t) \,\middle|\, \psi'_{\mathbf{k}\sigma}(t) \right\rangle = \left\langle \psi_{\mathbf{k}\sigma} \,\middle|\, \psi'_{\mathbf{k}\sigma} \right\rangle, \tag{2.131}$$

We can deduce two conditions: (i) the quasiparticle excitation energy must be small on the scale of the rate of change of the system; (ii) the lifetime of the excitation must be large, compared to the inverse excitation energy:

$$\frac{\tau_{\mathbf{k}}}{\hbar} \gg \frac{1}{\xi_{\mathbf{k}}} \gg \beta \tag{2.132}$$

Before moving on, we want to give a very brief glimpse into the mechanism by which the Fermi-liquid theory accomplishes the computation of renormalized quantities, such as masses, for the quasiparticles[7]. For this purpose, the ground state can be assumed to be a Fermi gas with density $n^0_\sigma(\mathbf{k}) = \Theta(\mathbf{k} - \mathbf{k}_F)$. Then, an energy functional of the electron density is minimized to find the quasiparticle energies and states:

$$E[n_\sigma(\mathbf{k})] = E_0 + \sum_{\mathbf{k},\sigma} \epsilon_\sigma(\mathbf{k}) \delta n_\sigma(\mathbf{k}) + \frac{1}{2} \sum_{\mathbf{k},\sigma,\mathbf{k}'\sigma'} \varphi_{\sigma,\sigma'}(\mathbf{k},\mathbf{k}') \delta n_\sigma(\mathbf{k}) \delta n_{\sigma'}(\mathbf{k}') \tag{2.133}$$

[6] It is also known, that in the case of the two-dimensional Hubbard model, which we will be concerned with in7.2, the Fermi-liquid description is valid away from half-filling [25].

[7] This is meant as an illustration and uses a semi-classical formulation. It does, however, emphasize the assumption that quasiparticles can only be well-defined when their excitation is close to the Fermi-surface and well described in an effective mean-field [1, Chapter 1.2.2] and for further discussions in the context of Green's functions [1, Chapter 4].

Here we make the two Fermi-liquid assumptions explicit by including the variation of densities (i.e. mean-field excitations) into account. The function φ is a mean-field-like interaction function, coupling density fluctuations to each other. This functional yields the properties of the quasiparticles via the functional derivative. For example, the quasiparticle energy can be obtained in this way:

$$\epsilon^*_{\mathbf{k}} = \left(\frac{\delta E}{\delta n_\sigma(\mathbf{k})}\right)\Bigg|_{n_\sigma(\mathbf{k})=n^{(0)}_\sigma(\mathbf{k})} = \epsilon_\sigma(\mathbf{k}) + \sum_{\mathbf{k}'\sigma'} \varphi_{\sigma,\sigma'}(\mathbf{k},\mathbf{k}')\delta n_{\sigma'}(\mathbf{k}') \tag{2.134}$$

Instead of applying this to various interactions and observables (see, for example [39, Chapter 14] for a discussion), we instead move directly to a description of this principle in terms of Green's functions. Here, the density variation is microscopically introduced by excitations of single electrons above the Fermi surface. To this end, we use Eq. (2.102) (i.e. the spectral function as the difference between the retarded and advanced Green's function) and Eq. (2.60), giving us the interpretation of $A^\nu_{\mathbf{k}}$ as a collection of excitations. We now study the excitation of one additional mode, appearing as a pole at $\xi_{\mathbf{k}} - i\gamma_{\mathbf{k}}$ with residue $Z_{\mathbf{k}}$ in the spectral representation. Carefully considering the integration path (originally [199], see also [70, Fig. 7.2]) to avoid the pole and applying the residue theorem, one is left with the following:

$$A_{\mathbf{k}}(t) = Z_{\mathbf{k}} e^{-it(\xi_{\mathbf{k}}+i\gamma_{\mathbf{k}})} + \int_{-i\infty}^{0} \frac{\mathrm{d}\nu}{2\pi} e^{-i\nu t}\left[G^{\mathrm{A},\nu}_{\mathbf{k}} - G^{\mathrm{R},\nu}_{\mathbf{k}}\right] \tag{2.135}$$

The remaining integral can be approximated if the real part of the pole is much larger than the imaginary one, which means (in accordance with our illustration in Fig. 2.3b), that the quasiparticle weight $Z_{\mathbf{k}}$ is much larger than the background noise [1, Eq. 7.35 ff] and [199]:

$$A_{\mathbf{k}}(t) \approx Z_{\mathbf{k}} e^{-it(\xi_{\mathbf{k}}+i\gamma_{\mathbf{k}})} \qquad \text{if } \gamma_{\mathbf{k}} \ll \xi_{\mathbf{k}} \tag{2.136}$$

This already gives an intuition of the quantities in the quasiparticle excitation: γ^{-1}, the inverse distance to the real axis, governs the lifetime, $Z_{\mathbf{k}}$ gives the weight and $\xi_{\mathbf{k}}$ acts as an energy. We can make this argument a bit more convincing for a many-body system by involving the self-energy. To do so, we consider the definition of the spectral function (Sec. 2.4.3) and retarded Green's function in this limit. Following the idea of small excitations, we expand the Green's function around wave vectors close to $\mathbf{k}_{\mathrm{F}}$, where [39, Chapter 14.4]:

$$\xi_{0,\mathbf{k}} \approx \epsilon_{\mathbf{k}} - \mu \approx -\operatorname{Re}\Sigma^0_{\mathbf{k}_{\mathrm{F}}} \tag{2.137}$$

This leads us to the expression of the retarded Green's function [1, Eq. 21.28]:

$$G^{\mathrm{R},\nu}_{\mathbf{k}} = \left[\nu - \epsilon_{\mathbf{k}} + \mu - \Sigma^{\mathrm{R},\nu}_{\mathbf{k}}\right]^{-1} = \left[\nu - \left(\xi_{0,\mathbf{k}} - \operatorname{Re}\Sigma^{\mathrm{R},\nu}_{\mathbf{k}}\right) - i\operatorname{Im}\Sigma^{\mathrm{R},\nu}_{\mathbf{k}}\right]^{-1} \tag{2.138}$$

One can then Taylor expand around small energy deviations around the Fermi surface to obtain:

$$\approx \left[\nu - (\nu-0)\partial_\nu \operatorname{Re}\Sigma^{\mathrm{R},\nu}_{\mathbf{k}_{\mathrm{F}}}\Big|_{\nu=0} - (\mathbf{k}-\mathbf{k}_{\mathrm{f}})\nabla_{\mathbf{k}}(\xi_{0,\mathbf{k}} + \operatorname{Re}\Sigma^{\mathrm{R},\nu}_{\mathbf{k}})\Big|_{\mathbf{k}=\mathbf{k}_{\mathrm{F}}} - i\operatorname{Im}\Sigma^{\mathrm{R},\nu}_{\mathbf{k}_{\mathrm{F}}}\right]^{-1} = Z_{\mathbf{k}}\left[\nu - \xi_{\mathbf{k}} + i\frac{1}{\tau^\nu_{\mathbf{k}}}\right]^{-1} \tag{2.139}$$

where we defined the quasiparticle lifetime $\tau_{\mathbf{k}}$, energy $\xi_{\mathbf{k}}$ and spectral weight $Z_{\mathbf{k}}$:

$$\tau^\nu_{\mathbf{k}} = -2\frac{Z_{\mathbf{k}}}{\gamma_{\mathbf{k}}} \approx -\left[Z_{\mathbf{k}}\operatorname{Im}\Sigma^{\mathrm{R},\nu}_{\mathbf{k}}\right]^{-1}, \qquad \xi_{\mathbf{k}} = (\mathbf{k}-\mathbf{k}_{\mathrm{f}})Z_{\mathbf{k}}\nabla_{\mathbf{k}}\left(\xi_{0,\mathbf{k}} + \operatorname{Re}\Sigma^{\nu=0}_{\mathbf{k}}\right)\Big|_{\mathbf{k}=\mathbf{k}_{\mathrm{F}}}, \qquad Z^{-1}_{\mathbf{k}} = 1 - \partial_\nu \operatorname{Re}\Sigma^{\mathrm{R},\nu}_{\mathbf{k}}\Big|_{\nu=0} \tag{2.140}$$

Finally, we can also express the renormalized mass using $\xi_{\mathbf{k}} \approx \frac{(\mathbf{k}-\mathbf{k}_{\mathrm{F}})\mathbf{k}_{\mathrm{F}}}{m^*}$ [39, Chapter 14]:

$$\frac{m}{m^*} = Z_{\mathbf{k}}\left[1 + \frac{m}{\mathbf{k}_{\mathrm{F}}}\nabla_{\mathbf{k}} \operatorname{Re}\Sigma^{\nu=0}_{\mathbf{k}}\Big|_{\mathbf{k}=\mathbf{k}_{\mathrm{F}}}\right] \tag{2.141}$$

The spectral function is the central quantity connecting the Green's function formalism to experiments. In the Fermi liquid picture, it furthermore provides an intuitive understanding of the excitation spectrum for collective modes in the electronic system. We know that the Green's function for free fermions without spin has exactly two poles, resulting in the corresponding spectral function having only two delta peaks. From Eq. (2.135) we can also follow a δ like shape for infinite quasiparticle lifetimes $\gamma_{\mathbf{k}} = \tau^{-1}_{\mathbf{k}}$. Therefore, the following heuristic expression for the spectral function in the form of a Lorentzian seems appropriate[8]:

$$A^\nu_{\mathbf{k}} = \frac{1}{\pi}\frac{-\operatorname{Im}\Sigma^{\mathrm{R},\nu}_{\mathbf{k}}}{\left(\nu - \epsilon_{\mathbf{k}} + \mu - \operatorname{Re}\Sigma^{\mathrm{R},\nu}_{\mathbf{k}}\right)^2 + \left(\Sigma^{\mathrm{R},\nu}_{\mathbf{k}}\right)^2} \tag{2.142}$$

This corresponds to the form of Fig. 2.3b, where the δ-like peak is broadened by the inverse of the lifetime. The corresponding spectral function will have a sharp peak at $\xi_{\mathbf{k}}$ with height proportional to $Z_{\mathbf{k}}/\gamma_{\mathbf{k}}$ and width proportional to $\gamma_{\mathbf{k}}$. The incoherent background takes up the remaining spectral

[8] Using Eq. (2.136), it follows that $G^{\mathrm{R}}(t) \propto i\Theta(t)e^{-it\xi_{\mathbf{k}}}e^{-t/\tau_{\mathbf{k}}}$. Fourier transform gives the familiar Lorentzian shape

weight $1 - Z_{\mathbf{k}}$.
Restating the necessary condition for a Fermi-liquid:

$$\lim_{\substack{\nu\to 0\\ \mathbf{k}\to\mathbf{k}_F}} \operatorname{Im}\Sigma^{\nu}_{\mathbf{k}} = 0, \tag{2.143}$$

we can use this concept as a tool to investigate the onset of Mott physics, where the condition is violated and the spectral density at the Fermi surface is suppressed. This encapsulates strong correlation physics in which the adiabatic connection to a metal-like state is disrupted. $Z_{\mathbf{k}}$ can, for example, be measured by Compton scattering as it is proportional to the distribution function at the Fermi level.

2.6 Diagrammatic Perturbation Theory and Functional Integrals

Many concepts and methods in this thesis are much more conveniently formulated in the functional integral formalism. They are also very convenient, in conjunction with functional methods, for the construction of conserving theories such as Two-Particle Self-Consistent Approach (TPSC), using the Luttinger-Ward functional in Sec. 4.3.
Since this formalism is not too common in solid-state theory, we will motivate it from two perspectives. The Feynman path integral point of view briefly connects our notation to that of [111], where an excellent introduction can be found. We will then also briefly connect the notion of generation functionals to the analog concept from probability theory before introducing the necessary quantities for the rest of this thesis.
Some of the following texts are taken from my master's thesis [246].

2.6.1 Feynman Path Integral

Although not strictly necessary, a very good motivation for the functional integral formalism used in this thesis is Feynman path integrals. Here, we give a very brief introduction, jumping directly ahead into the definition of coherent state (i.e. a formulation in creation and annihilation operators instead of a spatial basis) path integrals, following the notation from [111, chapter 2]. These integrals naturally arise from the decomposition of the time evolution operator Eq. (2.14) where the Hamiltonian is expressed in terms of the creation and annihilation operators Eq. (2.10), i.e.

$$U(\tau_{\mathrm{f}} - \tau_{\mathrm{i}}) = e^{-(\tau_{\mathrm{f}}-\tau_{\mathrm{i}})\hat{H}(\{\hat{a}^{\dagger}_{\alpha_i},\hat{a}_{\alpha_i}\})} \tag{2.144}$$

To construct the path integral for many-particle states, the propagation is subdivided into N slices, using insertions of the unity operator of coherent state eigenstates Eq. (2.12) at imaginary time intervals $\epsilon = \frac{\tau_{\mathrm{f}}-\tau_{\mathrm{i}}}{N}$. The number of slices N is then taken to the limit ∞, where we assume the existence of the appropriate integral measure. The k-the insertion of the component α for a coherent state (see Sec. 2.1.2) is written as $\phi_{\alpha,i}$ [9].

$$U(\phi_{\mathrm{f}},\tau_{\mathrm{f}};\phi_{\mathrm{i}},\tau_i) = \langle x_f|\, e^{-\hat{H}(\tau_{\mathrm{f}}-\tau_{\mathrm{i}})}\,|x_i\rangle \tag{2.145}$$

$$= \lim_{N\to\infty}\int\prod_{k=1}^{N-1}\prod_{\alpha} \mathrm{d}\mu(\overline{\phi}_{\alpha,k},\phi_{\alpha,k}) e^{-\sum_{k=1}^{N-1}\sum_{\alpha}\overline{\phi}_{\alpha,k}\phi_{\alpha,k}} \times e^{-\sum_{k=1}^{N}\left(\sum_{\alpha}\overline{\phi}_{\alpha,k}\phi_{\alpha,k-1}+\epsilon H(\phi^{\star}_{\alpha,k}\phi_{\alpha,k-1})\right)} \tag{2.146}$$

We can transition to a smooth trajectory, following the arguments preceding [111, Eq. 2.61], using $\lim_{\epsilon\to 0}\frac{\phi_{\alpha,k}-\phi_{\alpha,k-1}}{\epsilon} = \partial_\tau\phi_\alpha(\tau)$, and $H(\overline{\phi}_{\alpha,k},\phi_{\alpha,k-1}) = H(\overline{\phi}_\alpha(\tau),\phi_\alpha(\tau))$, to arrive at the coherent path integral formulation used in our setting:

$$U(\phi_{\mathrm{f}},\tau_{\mathrm{f}};\phi_{\mathrm{i}},\tau_{\mathrm{i}}) = \int_{\phi_\alpha(\tau_i)}^{\overline{\phi}_\alpha(\tau_f)}\mathcal{D}\left[\overline{\phi}_\alpha(\tau),\phi_\alpha(\tau)\right] \times\exp\left[-\sum_\alpha\overline{\phi}_\alpha(\tau_f)\phi_\alpha(\tau_f)-\int_{\tau_i}^{\tau_f}\mathrm{d}\tau\underbrace{\left(\sum_\alpha\overline{\phi}_\alpha(\tau)\partial_\tau\phi_\alpha(\tau)+H(\overline{\phi}_\alpha(\tau),\phi_\alpha(\tau))\right)}_{\mathcal{L}(\overline{\phi}_\alpha(\tau)\phi_\alpha(\tau))}\right] \tag{2.147}$$

$$= \int_{\phi_\alpha(\tau_i)}^{\overline{\phi}_\alpha(\tau_f)}\mathcal{D}\left[\overline{\phi}(\tau),\phi\ (\tau)\right] e^{-\sum_\alpha\overline{\phi}_\alpha(\tau_f),\phi_\alpha(\tau_f)} e^{-S[\overline{\phi}_\alpha(\tau),\phi_\alpha(\tau)]} \tag{2.148}$$

With the Lagrangian density $\mathcal{L}$ and the action S.
The way in which different evaluations of the action contribute to overall propagation is illustrated in Fig. 2.4. The factor $1/\hbar$ illustrates that only the stationary action contributes to the classical temperature limit.
As before (Eq. (2.47)), we can write the partition function, using the trace over the time evolution

[9] Note, that we skip the normal ordering argument which can be found leading up to [111, Eq. 2.60]

operator. Here, the boundary value term involving τ_f in Eq. (2.148) vanishes:

$$Z = \int_{\phi_{\alpha(0)}=\zeta\overline{\phi}_{\alpha(\beta)}} \mathcal{D}\left[\overline{\phi}(\tau),\phi\,(\tau)\right] e^{\int_0^\beta \mathrm{d}\tau\left(\Sigma_\alpha \overline{\phi}_\alpha(\tau)(\partial_\tau-\mu)\phi_\alpha(\tau)+H(\overline{\phi}_\alpha(\tau),\phi_\alpha(\tau))\right)} \tag{2.149}$$

Note, that the $-\mu$ term obtained from the grand canonical ensemble in Eq. (2.44) has also been included here. Furthermore, the trace leads to the (anti-) periodic boundary condition for (fermionic) bosonic statistics.

The usefulness of this formulation in our setting stems from the fact that we can apply functional generalizations of derivatives as formal operations. This either shortens derivations compared to the operator formalism or makes certain reasoning even possible in the first place. For example, the Φ derivability in Sec. 4.3.

This paragraph only serves as a very broad motivation for the functional integrals, and details are left to the literature. Our notation specifically follows [70] and [111].

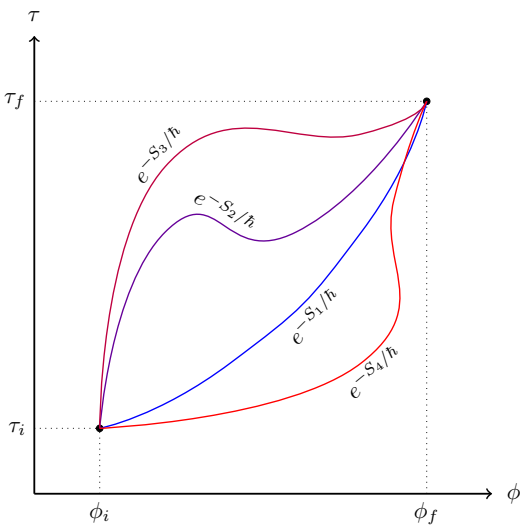

Figure 2.4: Cartoon of paths through the configuration space. The weight of $1/\hbar$ is supposed to illustrate that in the classical limit only the stationary action contributes.

2.6.2 Generating Functionals

Connection to Thermodynamics

The previously introduced path integral formalism lends itself well to further generalization. When coupling the fields to external source fields $\langle\overline{\phi}, J\rangle$ and $\langle\phi, \bar{J}\rangle$, we obtain the so-called generating functionals. These resemble generalized generating functions of probability distributions in that functional derivatives generate all possible correlation functions, whereas derivatives of characteristic functions generate moments and cumulants of the distribution. We can make use of this analogy to illustrate the thermodynamic role of the quantities and derive some computational rules in a simpler form along the way[10].

Following the argument in [118, 233], we first remember that the characteristic function of a probability distribution is defined as its Fourier transform of and the moment-generating function is its extension to complex numbers (we assume existence for this short illustration):

$$\phi_X(t) = \mathbb{E}[e^{itX}], \qquad M_X(t) = \phi_X(-it) \tag{2.150}$$

with moments defined as:

$$\mu_n = \mathbb{E}[X^n] = \frac{\partial^n}{\partial t^n} M_X(t)\Big|_{t=0} = i^{-n}\frac{\partial^n}{\partial t^n}\phi_X(t)\Big|_{t=0} \tag{2.151}$$

The cumulants are then defined as the derivatives of the cumulant-generating function.

$$K_X(t) = \ln \mathbb{E}[e^{tX}] = \ln M_X(t), \qquad \kappa_n = \frac{\partial^n}{\partial t^n} K_X(t)\Big|_{t=0} \tag{2.152}$$

While indirectly defined through the logarithm of the moment-generating function, cumulants turn out to be the more intuitive objects. The first 4 are (up to a normalization of a lower order cumulant) the mean, variance, skewness, and kurtosis of a distribution. The thermodynamic interpretation can be obtained by considering the probability of a classical particle in an energy state E_i. Then, the classical partition function $Z[\beta]$, and the associated moment-generating function are defined as follows:

$$p(E_i) = \frac{e^{-\beta E_i}}{Z[\beta]}, \qquad Z[\beta] = \sum_i e^{-\beta E_i} \tag{2.153}$$

$$\Rightarrow M_E(t) = \sum_i p_i e^{tE_i} = \frac{Z[\beta - t]}{Z[\beta]} \tag{2.154}$$

$$\Rightarrow K_E(t) = \ln(Z[\beta - t]) - \ln(Z[\beta]) \tag{2.155}$$

[10] This analogy is purely meant as an illustration of the core objects in the functional integral formalism. The value here is to emphasize the role of the functionals in analogy to thermodynamic quantities. However, there is an actual connection via the Martin–Siggia–Rose formalism, connecting stochastic differential equations to path integrals out of equilibrium [34]. A detailed argument for the role of moments and cumulants in many body theory and thermodynamics can be found in [148] for complex valued functions. Generalizations for operators [27] and applications to DMFT have also been studied [41].

With a probability p_i of an energy state E_i. We have deliberately introduced a functional-looking notation for the partition function Z here already, to make the connection to the functionals in the next section clear.

The particular use of cumulants (in our case) and the associated functional $W[J]$ below is the systematic generation of connected "groups" (Feynman diagrams), while moments are made up of these connected building blocks. For Feynman diagrams, this is known as the linked-cluster theorem (connecting Eq. (2.164) and Eq. (2.165)), see Sec. 2.6.2. We can sketch this here (similarly to the replica trick used in the diagrammatic case) by assuming the existence of a Taylor expansion for the cumulant generating function:

$$\begin{aligned} M_X(t) = e^{K_X(t)} &= \exp\left[\sum_{n=1}^{\infty} \frac{t^n}{n!}\kappa_n\right] = \prod_{n=1}^{\infty} \exp\left[\frac{t^n}{n!}\kappa_n\right] \\ &= \prod_{n=1}^{\infty}\sum_{p_n=0}^{\infty} \exp\left[\frac{t^{n\cdot p_n}}{(n!)^{p_n}}\frac{\kappa_n^{p_n}}{p_n!}\right] \end{aligned} \tag{2.156}$$

When obtaining the m-th moment, all powers smaller and larger than n will vanish, according to Eq. (2.151). We can therefore rearrange in terms of powers of t, transforming the product of sums into a sum over all groups with $m = \sum_{p_n} n$:

$$\Rightarrow \kappa_m = \sum_{[p_n]} \prod_n \left[\frac{m!\kappa_n^{p_n}}{p_n!(n!)^{p_n}}\right] = \sum_{[p_n]} \prod_n \left[\binom{m}{\underbrace{n,\ldots,n}_{p_n}} \frac{1}{p_n!}\kappa_n^{p_n}\right] \tag{2.157}$$

This means the m-th moment can be understood as composed of all possible groupings of m cumulants into groups of n. Similarly, but without proof, we will use the composition of general Green's functions from connected ones, as generated by the functional analogs. The second line can be interpreted as copies of the system Z^n, using Eq. (2.154). A derivation starting with the thermodynamical partition function followed by a functional generalization is given in the lecture notes of A. M. Tremblay [266, Chapter 80], where a number of pitfalls and subtleties when dealing with functional derivatives are also discussed. Readers unfamiliar with practical calculations will find all the necessary mathematical details for this chapter in [111] and applications to our specific context with many helpful remarks in [266].

Both Eq. (2.154) and Eq. (2.155) will be generalized to functionals in Eq. (2.164) and Eq. (2.165). The last generating functional is that of the effective action, obtained through functional Legendre transformation of Eq. (2.165). A statistical analog of Γ does exist in the form of rate functions (a concept from the theory of large deviations). The connection to statistical physics does not seem clear enough to justify a further discussion in this context. Instead, we will now give a very brief introduction to generating functionals, by reminding the reader of the most important concepts.

Definitions and Basic Properties

For the construction of generating functionals, we introduce source fields $\overline{J}$ and J coupling to creation and annihilation fields. In our case of fermionic operators, these are Grassmann fields. These serve as a tool to allow the functionals to *generate* desired quantities. In our case, the source fields will be set to zero after the functional derivative acts on the functional. We start with the generating functional of Green's functions Z:

$$Z\left[\overline{J}, J\right] = \int \mathcal{D}\left[\overline{\phi}, \phi\right] e^{-S\left[\overline{\phi},\phi\right]} \times e^{-\sum_\alpha \int_0^\beta \mathrm{d}\tau\left[\overline{J}_\alpha(\tau)\phi_\alpha\ (\tau)+\overline{\phi}_\alpha(\tau)J_\alpha(\tau)\right]} = \left\langle e^{-\left\langle\overline{J},\phi\right\rangle-\left\langle\overline{\phi},J\right\rangle}\right\rangle \tag{2.158}$$

With the generalized inner product

$$\left\langle\overline{J},\phi\right\rangle = \sum_\gamma \int \mathrm{d}\tau' \overline{J}_\gamma(\tau')\phi\ \gamma(\tau') \tag{2.159}$$

Here we also used the action S, as the integral of the Lagrangian density $\mathcal{L}$:

$$S[\overline{J}(\tau), J(\tau)] = \sum_\alpha \int_0^\beta \mathrm{d}\tau \mathcal{L}[\overline{J}_\alpha, J_\alpha] = \int \mathrm{d}\tau \left[\sum_\alpha \overline{J}_\alpha(\tau)(\partial_\tau - \mu)J_\alpha(\tau) + H[\overline{J}_\alpha(\tau), J_\alpha(\tau)]\right] \tag{2.160}$$

For example, the actions for the Hubbard and Anderson impurity model (Sec. 3.2 and Sec. 3.7) are:

Important 2.6.2.1 (Action For Hubbard and Anderson Impurity Model)
The actions for Hubbard and Anderson impurity model can be computed from Eq. (3.12) *and* Eq. (3.99)*:*

$$S_{\text{Hubbard}} = \int \mathrm{d}\tau \sum_{ij\sigma} \left(\overline{\phi}_{i\sigma}(\tau)\left[\delta_{ij}(\partial_\tau - \mu) - t_{ij}\right]\phi_{i\sigma}(\tau) + U\delta_{ij}\overline{\phi}_{i\uparrow}(\tau)\phi_{i\uparrow}(\tau)\overline{\phi}_{i\downarrow}(\tau)\phi_{i\downarrow}(\tau)\right) \tag{2.161}$$

$$S_{\mathrm{AIM}} = \sum_{\sigma} \int \mathrm{d}\tau \mathrm{d}\tau' \overline{\phi}_{\sigma}(\tau) \mathcal{G}^{-1}_{i\sigma}(\tau - \tau') \phi_{\sigma}(\tau') + U \int \mathrm{d}\tau \overline{\phi}_{\uparrow}(\tau) \phi_{\uparrow}(\tau) \overline{\phi}_{\downarrow}(\tau) \phi_{\downarrow}(\tau) \tag{2.162}$$

with

$$\mathcal{G}^{-1}_{i\sigma}(\tau - \tau') = \delta(\tau - \tau')(\partial_{\tau} - \mu) + |V_i|^2 (\Theta(\tau - \tau') - n_{\mathrm{F}}(\epsilon_i)) \tag{2.163}$$

For this thesis, we will use three different functionals, corresponding to generalizations of momentum, cumulant, and rate generating functionals, according to the considerations in the previous paragraph.

$$G[\overline{J}, J\,] = \frac{1}{Z[0,0]} Z\left[\overline{J}, J\,\right] \tag{2.164}$$

$$W[\overline{J}, J\,] = \ln\left(G[\overline{J}, J\,]\right) \tag{2.165}$$

$$\Gamma\left[\overline{\phi}, \phi\right] = \sup_{J, \overline{J}} \left\{ -W[\overline{J}, J\,] - \langle \overline{\phi} J\,\rangle - \langle \phi\, \overline{J} \rangle \right\} \tag{2.166}$$

In reference to statistical physics, we understand Z and W as generalizations of the partition function and grand-canonical potential, specifically motivated by the analogy with generating functions from probability theory in the previous section.
In Eq. (2.166), we have used the functional generalization of a Legendre transformation. The details of which are left to the literature, for example [274].
$G[\overline{J}, J\,]$ and $W[\overline{J}, J\,]$ generate full and connected Green's functions, while $\Gamma\left[\overline{\phi}, \phi\right]$ is the generating functional for irreducible diagrams, called effective action. Especially the effective action and the role of irreducible diagrams will be discussed below in Sec. 2.6.3. ⚠Note that we do not specify which types of irreducible diagrams are generated by Γ. This depends on the type of source field. We will elaborate on this in Sec. 2.6.3.
One can express expectation values of the fields $\phi_{\alpha} = \langle 0 | \hat{\phi}_{\alpha} | 0 \rangle$ and $\overline{\phi}$ as functional derivatives. This is done similarly to the moment trick for the n-th moment of Gaussian integrals, where one writes the moment as partial derivatives of some auxiliary variable (source field), setting it to 0 afterward.

$$\phi_{\alpha} e^{-\langle J, c \rangle} \leftrightarrow \left(\frac{\delta}{\delta J_{\alpha}} \right) \tag{2.167}$$

We can readily verify this for the single-particle Green's function:

$$G^{(1)}_{\alpha_1 \alpha_1'}(\tau_1; \tau_1') = \left\langle T_{\zeta} \left[\hat{c}_{\alpha_1}(\tau_1) \hat{c}^{\dagger}_{\alpha_1'}(\tau_1') \right] \right\rangle = \zeta \frac{\delta^2 G[\overline{J}, J]}{\delta \overline{J}_{\alpha_1}(\tau_1) \delta J_{\alpha_1'}(\tau_1')} \bigg|_{J = \overline{J} = 0} \tag{2.168}$$

This method is central to diagrammatic perturbation theory as the above and similar generating functionals can be used in conjunction with Wick's theorem to systematically generate Feynman diagrams. Similarly, derivatives of the functional $W[\overline{J}, J]$ with respect to the sources yield the (complex conjugate) fields, which gives this functional its name of *effective potential*:

$$\frac{\delta}{\delta \overline{J}_{\alpha}} W[\overline{J}, J] = \langle \hat{a}_{\alpha} \rangle_{\overline{J}, J} = \phi_{\alpha} \tag{2.169}$$

$$\frac{\delta}{\delta J_{\alpha}} W[\overline{J}, J] = -\zeta \langle \hat{a}^{\dagger}_{\alpha} \rangle_{\overline{J}, J} = \overline{\phi}_{\alpha} \tag{2.170}$$

Explicit differentiation and comparison with the cumulant generating function from the last paragraph motivates that this functional generates all *connected* Green's functions[11].

Definition 2.6.2.2 (Green's functions as functional derivatives)
We can generate (connected) Green's functions in this way:

$$G^{(n)}_{\alpha_1 \ldots \alpha_n \alpha_1' \alpha_n'}(\tau_1, \ldots, \tau_n; \tau_1', \ldots, \tau_n') = \frac{1}{\zeta^n} \frac{\delta^{2n} G[\overline{J}, J]}{\delta \overline{J}_{\alpha_1}(\tau_1) \cdots \overline{J}_{\alpha_n}(\tau_n) J_{\alpha_n'}(\tau_n') \cdots J_{\alpha_1'}(\tau_1')} \bigg|_{J = \overline{J} = 0} \tag{2.171}$$

$$G^{\mathrm{c},(n)}_{\alpha_1 \ldots \alpha_n \alpha_1' \alpha_n'}(\tau_1, \ldots, \tau_n; \tau_1', \ldots, \tau_n') = \zeta^n \frac{\delta^{2n} W[\overline{J}, J]}{\delta \overline{J}_{\alpha_1}(\tau_1) \cdots \overline{J}_{\alpha_n}(\tau_n) J_{\alpha_n'}(\tau_n') \cdots J_{\alpha_1'}(\tau_1')} \bigg|_{J = \overline{J} = 0} \tag{2.172}$$

For now, we focus on the most important details of the functional integral formalism that is required

[11] Note, that the will only consider fermionic non-symmtry breaking Green's functions in this thesis and, therefore, derivatives only occur in pairs of J and $\overline{J}$.

for this thesis. ⚠When comparing to [266] one should be careful to not confuse source fields (for us J, in that reference ϕ) and Grassmann fields. We follow the notation of [111].

Important 2.6.2.3 (Functional Integral Identities)
The following identities will be used for calculations later. A generalization of the Gaussian integral identities for fermionic (and for completeness also bosonic) fields:

$$\int \mathcal{D}[\overline{\phi},\phi] \exp\Big(-\sum_{\alpha\beta}\overline{\phi}_\alpha M_{\alpha\beta}\phi_\beta + \overline{J}_\alpha\phi_\alpha + \overline{\phi}_\alpha J_\alpha\Big) = [N_\zeta \det(M)]^{-\zeta}\, e^{\sum_{\alpha\beta}\overline{J}_\alpha\left[M^{-1}\right]_{\alpha\beta}J_\beta} \tag{2.173}$$

$$N_\zeta = \begin{cases} 1, & \zeta = -1 \\ 2\pi i, & \zeta = 1 \end{cases} \tag{2.174}$$

The expectation value of an observable $\hat{O}$:

$$\langle\hat{O}\rangle = \frac{1}{Z}\int \mathcal{D}[\overline{\phi},\phi]\,\hat{O}e^{-S[\overline{\phi},\phi]} \tag{2.175}$$

We will now connect the functional integral formalism with Feynman diagrams by considering small perturbations. The goal is to introduce the notation for this thesis; details are again left to the literature.

Small Perturbations

Green's functions play an important role in the development of perturbative expansions, which can be seen from the following argument.
Let $\hat{H} = \hat{H}_0 + \gamma\hat{V}$ such that $\hat{H}_0|\epsilon_k\rangle = \epsilon_k|\epsilon_k\rangle$ is exactly solvable and V a small perturbation. We write the usual Dyson series in imaginary time as

$$U_{\text{int}}(\tau) = \mathcal{T}\exp\left[-\int_0^\tau \mathrm{d}\tau' V(\tau')\right] \tag{2.176}$$

$$\frac{Z}{Z_0} = \frac{\mathrm{Tr}\left[e^{-\beta(H_0-\mu N)}U_{\text{int}}(\beta)\right]}{\mathrm{Tr}\left[e^{-\beta H_0-\mu N}\right]} \equiv \langle U_{\text{int}}(\beta)\rangle_0 \tag{2.177}$$

Explicit expansion yields:

$$= \sum_{n=0}^{\infty}\frac{(-1)^n}{n!}\int_0^\beta \mathrm{d}\tau_1\ldots\mathrm{d}\tau_n\left\langle T V(\hat{a}^\dagger_{\alpha_1}(\tau_1),\cdots\hat{a}_{\alpha_k}(\tau_1))\cdots V(\hat{a}^\dagger_{\alpha_1}(\tau_n)\cdots\hat{a}_{\alpha_k}(\tau_n))\cdots\right\rangle_0, \tag{2.178}$$

with the partition function of the non-interacting system:

$$Z_0 = \int \mathcal{D}[\overline{\phi},\phi]\exp\left[-\sum_\alpha\int \mathrm{d}\tau\overline{\phi}_\alpha(\tau)\underbrace{(\partial_\tau-\mu)}_{G^{-1}_{0,\alpha}(\tau)}\phi_\alpha(\tau)\right] \tag{2.179}$$

This leads to an expanded form of the interacting Green's function in terms of the perturbation:

$$\Rightarrow G^{(n)}_{\alpha_1\ldots\alpha'_n}(\tau_1\ldots\tau'_n) = \frac{\left\langle T_\zeta\left[U_{\text{int}}(\beta)\hat{a}_{\alpha_1}(\tau_1)\ldots\hat{a}^\dagger_{\alpha'_1}(\tau'_1)\right]\right\rangle_0}{\langle U_{\text{int}}(\beta)\rangle_0} \tag{2.180}$$

The notation $\langle\cdot\rangle_0$ stands for the average with respect to a zero potential Hamiltonian H_0 with partition function Z_0.

Wick's Theorem

A tool for the evaluation of expectation values under the non-interacting Hamiltonian (such as in Eq. (2.180)) is Wick's theorem. A pair of creation and annihilation operators is called a contraction and can be visualized using brackets in the following way:

$$\begin{aligned}\left\langle a^?_{\alpha_1}(\tau_1)a^?_{\alpha_2}(\tau_2)\cdots a^?_{\alpha_n}(\tau_n)\right\rangle_0 = \sum_{\pi\in K}\prod_{i=1}^n\zeta^{\text{sgn}(\pi)}\left\langle\hat{a}_{\alpha_{\pi(1)}}(\tau_{\pi(1)})\hat{a}^\dagger_{\alpha_{\pi(2)}}(\tau_{\pi(2)})\right\rangle_0 \\ \cdots\left\langle\hat{a}_{\alpha_{\pi(n-1)}}(\tau_{\pi(n-1)})\hat{a}^\dagger_{\alpha_{\pi(n)}}(\tau_{\pi(n)})\right\rangle_0\end{aligned} \tag{2.181}$$

With $K \in S_n$ (S_n is the symmetric group) such that no permutations with two creation/annihilation operators occur. The minus sign for fermions can be obtained by counting the number of times lines

cross each other. For example:

$$\left\langle \overbrace{a_{\alpha_1}(\tau_1)\overbrace{a_{\alpha_2}(\tau_2)a^\dagger_{\alpha_3}(\tau_3)}a^\dagger_{\alpha_4}(\tau_4)}\right\rangle_0 = \zeta\delta_{\alpha_1\alpha_3}G_{0,\alpha_1\alpha_3}(\tau_1-\tau_3)\delta_{\alpha_1\alpha_4}G_{0,\alpha_1\alpha_4}(\tau_1-\tau_4) + \delta_{\alpha_2\alpha_3}G_{0,\alpha_2\alpha_3}(\tau_2-\tau_3)\delta_{\alpha_2\alpha_4}G_{0,\alpha_2\alpha_4}(\tau_2-\tau_4)$$

Feynman Diagrams

We will simplify the notation for many of the following calculations by using Feynman diagrams. Creation (field) operators for a state α at time τ are represented by an outgoing arrow that originates at a point labeled τ. Annihilation operators are defined in the same way but with an incoming arrow. Equal times are connected at a single point, called a vertex. This means that the propagation of a state α_2 to α_1 from time τ_2 to τ_1 is written as follows:

$$\alpha_2\tau_2 \longrightarrow \alpha_1\tau_1 \quad = G_{\alpha_1\alpha_2}(\tau_1;\tau_2) \tag{2.182}$$

An instantaneous two-particle interaction with a potential $\hat{v}$ at time τ is written in second quantization form as:

$$\hat{V}(\hat{a}^\dagger(\tau),\hat{a}(\tau)) = \sum_{\alpha\beta\gamma\delta}\{\alpha\beta|\hat{v}|\alpha'\beta'\}\hat{a}^\dagger\alpha(\tau)\hat{a}^\dagger_\beta(\tau)\hat{a}_{\ \beta'}(\tau)\hat{a}_{\ \alpha'}(\tau) \tag{2.183}$$

This is graphically represented as follows:

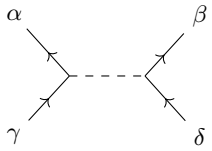

$$= \langle\alpha\beta|\, v\,|\gamma\delta\rangle \tag{2.184}$$

The rules governing these diagrams are too lengthy to define in this context. The notation and example below directly connect to [111, Chapter 2.3] and [61, Chapter 1.5].
In order to remind the reader of the most important properties and for reference in a later chapter, we will, however, give the diagrammatic construction for the 2-particle interaction from Eq. (2.180). Using Eq. (2.178) we obtain the two first-order diagrams:

$$\begin{aligned}
\hat{V}(\hat{a}\ (\tau),\hat{a}^\dagger(\tau)) &= \frac{1}{2}\sum_{\alpha\beta\gamma\delta}\langle\alpha\beta|\,\hat{v}\,|\gamma\delta\rangle\,\hat{a}_{\ \gamma}(\tau)\hat{a}_{\ \delta}(\tau)\hat{a}^\dagger_\alpha(\tau)\hat{a}^\dagger_\beta(\tau)\\
\left[\frac{Z}{Z_0}\right]_{n=1} &= -\frac{1}{2}\int_0^\beta \mathrm{d}\tau\sum_{\alpha\beta\gamma\delta}\langle\alpha\beta|\,\hat{v}\,|\gamma\delta\rangle\left\langle\hat{a}^\dagger_\alpha(\tau)\hat{a}^\dagger_\beta(\tau)\hat{a}_\gamma(\tau)\hat{a}_\delta(\tau)\right\rangle_0\\
&= -\frac{1}{2}\int_0^\beta \mathrm{d}\tau\sum_{\alpha\beta}\left[\left(\langle\alpha\beta|\,\hat{v}\,|\alpha\beta\rangle + \zeta\,\langle\alpha\beta|\,\hat{v}\,|\beta\alpha\rangle\right)\underbrace{G_{0,\alpha}(0)}_{=n_\alpha}G_{0,\beta}(0)\right] \qquad (2.185)
\end{aligned}$$

$$= -\frac{1}{2}$$ 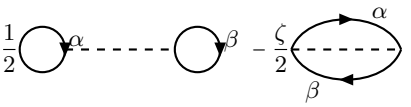

(2.186)

These are also often referred to as the Hartree and Fock diagrams. Taking only these two diagrams into account is equivalent to neglecting fluctuations of quadratic and higher order. An example of this is given in the context of the Stoner mean-field Hamiltonian for the Hubbard model in Eq. (3.70)[12].

2.6.3 Irreducible Diagrams

As mentioned before, irreducible diagrams are central objects in the construction of the diagrammatic extensions to DMFT, which are discussed in this thesis. We begin with the definition of irreducibility.

Definition 2.6.3.1
n particle irreducibility Diagrams that decompose into two disconnected diagrams of a lower order by cutting n lines are called n particle irreducible (nPI). For example, the diagram 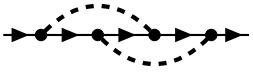 *is One particle irreducible (1PI), while* 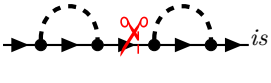 *is not. Ex-*

[12] The link here is that we can insert the mean-field Hamiltonian into the free energy functional and find the stationary value via $\frac{\delta^2}{\delta n_\alpha \delta n_\beta}W_{\mathrm{MF}} = \ldots = \hat{V}n_\alpha - \hat{V}n_\beta$.

amples for Two particle, two-particle irreducible (2PI) diagrams are given in the context of the parquet decomposition in Eq. (2.244).

There exists an analog to the generating functional for Green's functions for 1PI diagrams. This is the effective action Γ (introduced in Eq. (2.166)). As the Legendre transform of $W[J]$, functional derivatives with respect to the (Grassmann) fields ϕ generate the source:

$$\frac{\delta\Gamma[\overline{\phi},\phi]}{\delta\phi_\alpha} = -\zeta\overline{J}_\alpha \tag{2.187}$$

The $2\times n$-th derivative, with the appropriate boundary conditions, yields the n-particle 1PI vertex[13]

$$\Gamma^{(n)}_{\alpha_1\dots\alpha_n\alpha'_1\alpha'_n}(\tau_1,\dots,\tau_n;\tau'_1,\dots,\tau'_n) = \frac{1}{\zeta^n}\frac{\delta^{2n}\Gamma[\overline{J},J]}{\delta\overline{J}_{\alpha_1}(\tau_1)\cdots\overline{J}_{\alpha_n}(\tau_n)J_{\alpha'_n}(\tau'_n)\cdots J_{\alpha'_1}(\tau'_1)}\bigg|_{J=\overline{J}=0} \tag{2.188}$$

Let us first tackle the concept of one-particle irreducibility by summarizing the three most important points (for this thesis) of [111, Chapter 2.4], before considering the implications and construction of full Green's functions (in the form of the Dyson and Bethe-Salpeter equation). We will demonstrate that the effective action acts as the functional inverse of the connected Green's functions, that it can be used to generate the full Green's function via tree diagrams, and finally, use it to construct the Dyson equation.
We may also use this opportunity to introduce a more compact notation, where we indicate a set of corresponding indices with just that index, i.e. $(\tau_1,\alpha_1)\to 1$; a bar implies summation/integration over all corresponding indices (see also Sec. 2.1.1, as before further details are found in [111, Chapter 2]). First, we derive an auxiliary chain rule for an arbitrary functional F:

$$\frac{\delta F}{\delta\phi(1)} = \frac{\delta F}{\delta\overline{J}(\overline{2})}\frac{\delta\overline{J}(\overline{2})}{\delta\phi(1)} + \frac{\delta F}{\delta J(\overline{2})}\frac{\delta J(\overline{2})}{\delta\phi(1)} = -\zeta\frac{\delta F}{\delta\overline{J}(\overline{2})}\frac{\delta^2\Gamma}{\delta\phi(1)\delta\phi(\overline{2})} - \frac{\delta F}{\delta J(\overline{2})}\frac{\delta^2\Gamma}{\delta\phi(1)\overline{\phi}(\overline{2})}$$

Then, we expand the unity in terms of a field derivative and use Eq. (2.169) to expand these fields in terms of derivatives with respect to the sources. In the second line, we insert the identity from above to eliminate the outer derivative:

$$\delta(31) = \frac{\delta\overline{\phi}(3)}{\delta\phi(1)} = \frac{\delta}{\delta\phi(1)}\left[-\zeta\frac{\delta W}{\delta J(3)}\right] \tag{2.189}$$

$$= \frac{\delta^2 W}{\delta\overline{J}(2)\delta J(3)}\frac{\delta^2\Gamma}{\delta\phi(1)\delta\phi(2)} + \frac{\delta^2 W}{\delta J(2)\delta J(3)}\frac{\delta^2\Gamma}{\delta\phi(1)\delta\overline{\phi}(2)} \tag{2.190}$$

Three similar equations are obtained for the other index combinations. We consider only equal numbers of creation and annihilation operators and, therefore arrive at the following:

$$\delta(13) = G^{\mathrm{c}}(1,\overline{2})\Gamma_{\overline{\phi}\phi}(\overline{2},3) = \Gamma_{\phi\overline{\phi}}(1,\overline{2})G^{\mathrm{c}}(\overline{2},3) \tag{2.191}$$

$$\Leftrightarrow \delta(13) = \tag{2.192}$$

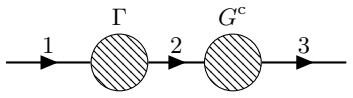

$$\Rightarrow \quad \Gamma^{(1)}(1,2) = G^{\mathrm{c},-1}(1,2) \tag{2.193}$$

This yields an important identity: the connected one-particle Green's function is the inverse operator to the two-point vertex function.

Definition 2.6.3.2 (self-energy and Dyson Equation)
The self-energy is the difference between 1 particle irreducible (1PI) diagrams of interacting and non-interacting systems.

$$\Sigma(1;2) = \Gamma(1;2) - \Gamma_0(1;2) \tag{2.194}$$

Γ_0 *denotes the inverse of the connected, non-interacting Green's function, according to* Eq. (2.193) *With* Eq. (2.193)*, this is equivalent to the Dyson equation:*

$$G^{-1} = G_0^{-1} + \Sigma \tag{2.195}$$

And without suppressed indices in Matsubara space and a scalar dispersion relation, a notation we

[13] Note, this functional does *not* generate 2PI diagrams! To achieve this, one introduces bilinear source fields that couple to two fields, resulting in the Luttinger-Ward functional Sec. 4.3. For details and derivations see [69, Chapter 6].

will use throughout this thesis, we have:

$$G^{\nu}_{\mathbf{k}} = \frac{1}{i\nu_n - \epsilon_{\mathbf{k}} + \mu - \Sigma^{\nu}_{\mathbf{k}}} \tag{2.196}$$

The class of fully irreducible diagrams, with the self-energy being the most prominent one, plays a central role in this thesis as they encapsulate correlation effects, as we will discuss in more detail in Sec. 3.3. Rearranging Eq. (2.195) and using the formal equivalence of the limit for a geometric series, one can immediately see its role in the difference between the propagation of a free and fully interacting particle:

$$G = \left[G_0^{-1} - \Sigma\right]^{-1} \tag{2.197}$$

$$= G_0 - G_0\Sigma G = G_0 - G_0\Sigma G_0 + G_0\Sigma G_0\Sigma G_0 \pm \cdots \tag{2.198}$$

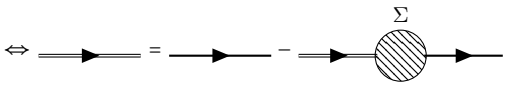

(2.199)

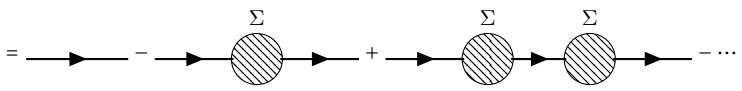

(2.200)

Here, we have also introduced a double line for the full propagator that includes all self-energy contributions. From the last expression, the role of self-energy as an effective one-body potential (since it is the only term that changes in comparison to G_0) becomes clear. When it is clear from the context, we will, however, use a single line even for the dressed propagator.
We have also seen previously in Sec. 2.5 that the pole structure of the Green's function is related to the features of the quasiparticle spectrum and, furthermore, quantities such as the effective mass or density of states are directly calculated as derivatives of the self-energy.
In Sec. 3.3 and Sec. 3.4, we will make use of this approach to investigate the leading order of physical processes in the Hubbard model at the limit of strong and weak interaction strength. Importantly, this diagrammatic approach will help us to understand the DMFT method when introducing Anderson Impurity Model (AIM) as the infinite coordination number limit of the Hubbard model in Sec. 3.6. The central theme for this thesis is to make approximations to the 1 and 2-particle 1 and 2-particle irreducible vertices and then construct the full Green's functions. The assumption here is that truncations or approximations in this set of diagrams have a less severe impact or are, in a sense, more tractable than direct approximations to the Green's functions themselves. One possible motivation here follows from Eq. (2.200): Whichever approximation is taken for the self-energy, we can still hope to retain some sort of propagation through the infinite convolution with the free propagator. At least in the single-particle case, this is additionally a numerically very inexpensive operation due to the geometric series limit.

Hartree-Fock

It is certainly worthwhile to look at the lowest-order approximation for the self-energy in this context to illustrate this reasoning with a concrete example. The leading order diagrams of the self-energy are:

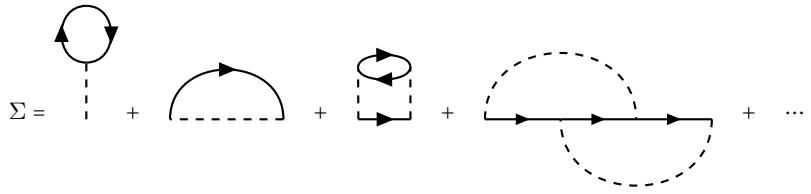

(2.201)

The simplest possible approximation takes only the first two diagrams (those with just one interaction) into account; this is the well-known Hartree-Fock method. We do not assume an instantaneous interaction for now; otherwise, both diagrams would be the same (since the dashed lines contract).

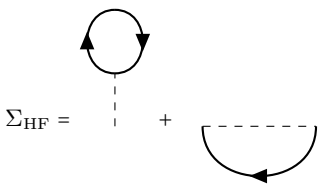

(2.202)

Algebraically, these diagrams are given as follows:

$$= -\sum_{\mathbf{k}'\nu'\sigma'} \langle \mathbf{k}\mathbf{k}' | v | \mathbf{k}\mathbf{k}' \rangle G^{\nu'}_{0,\mathbf{k}'\sigma'} e^{i\nu'_n \eta}$$
$$= v(0) n_{\mathrm{HF}}(\mathbf{k}) \tag{2.203}$$

$$= \zeta \sum_{\nu'\sigma'} \langle \mathbf{k}\mathbf{k}' | v | \mathbf{k}'\mathbf{k} \rangle \delta_{\sigma,\sigma'} G^{\nu'}_{0,\sigma',\mathbf{k}'} e^{i\nu'_n \eta}$$
$$= \zeta v(\mathbf{k} - \mathbf{k}') n_{\mathrm{HF}}(\mathbf{k}) \tag{2.204}$$

$$\Rightarrow \Sigma^{\nu}_{\mathrm{HF},\mathbf{k}} = \frac{1}{V} \left(v(0) + \zeta v(\mathbf{k} - \mathbf{k}') \right) n_{\mathrm{HF}}(\mathbf{k}) \tag{2.205}$$

The Hartree and Fock contributions are given in Eq. (2.203) and Eq. (2.204). We also set:

$$\sum_{\nu} G^{\nu}_{\mathrm{HF},\mathbf{k}} e^{i\nu_n \eta} = -\zeta n_{\mathrm{HF}}(\mathbf{k}) \tag{2.206}$$

This is a self-consistency equation since the distribution function $n_{\mathrm{HF}}(\mathbf{k})$ is a function of the self-energy that again determines the electron distribution. Self-consistency conditions are a core ingredient in mean-field theories, for which the Hartree-Fock is our first example; see also Sec. 3.4.2. We will also discuss the two-particle version of the Hartree-Fock approximation, Random Phase Approximation (RPA), in more detail later Sec. 5.2.1.

Bilinear Source fields

The choice of the source fields J is arbitrary and has been motivated by the desired quantities that we wanted to compute, namely the (connected) Green's functions and the 1PI vertices. However, we will also need 2PI vertices for this thesis, specifically in the context of the Luttinger-Ward functional in Sec. 4.3. It turns out that the corresponding generating functional can be constructed by considering bilinear sources of the form [111, p 119]:

$$Z[\eta, \overline{\eta}, \eta^*] = \exp\left[\int \mathrm{d}\tau \sum_{\alpha\beta} \eta_{\alpha_\beta} \overline{\phi}_\alpha \overline{\phi}_\beta + \overline{\eta}_{\alpha_\beta} \overline{\phi}_\alpha \phi_\beta + \eta^*_{\alpha_\beta} \phi_\alpha \phi_\beta \right] \tag{2.207}$$

The resulting effective action Γ generates all amputated 2PI diagrams. Specifically in the fermionic, non-symmetry breaking case where only the second term above contributes, we can obtain a version of Γ as a functional of Green's functions, which is closely related to the Luttinger-Ward functional see Sec. 4.3. Note that the previous identities of the effective action Γ can be derived for bilinear sources as well [111, Problem 2.12].

2.7 Two-Particle Green's Functions

Since the primary focus of this thesis is the inclusion of 2-particle correlations in the DMFT — and, more importantly, many technical details of the implementation rely on specific properties of this quantity — we will collect the definitions and discuss a number of important properties in this chapter. Furthermore, we will discuss the notation and generalizations of the decomposition into irreducible and reducible diagrams that will later be used for the DΓA method 5.3.

2.7.1 frequency index convention

Energy conservation allows us to use only 3 frequencies[14]. We will adopt the commonly used particle-hole and particle-particle notation, which describes corresponding scatterings with some energy transfer ω.

Definition 2.7.1.1 (Frequency Index Convention)
The frequency representation of 2-particle quantities with translational invariance has three independent times. We commonly use two conventions for writing the Fourier transform. The

[14] For a generalization of the proof from Eq. (I8.1) to the n-particle case see [205, Sec. 2.2.2.1]

*particle-hole convention (*ph*) and particle-particle (*pp*) convention. Let f be an arbitrary 2 point correlator of a system in equilibrium.*

$$f^{\nu\nu'\omega}_{\mathrm{ph},\alpha_1\ldots\alpha_4} = \int \mathrm{d}\tau_1\tau_2\tau_3 e^{i(\omega+\nu)\tau_1} e^{i\nu' 0} e^{-i\nu\tau_1'} e^{-i(\omega+\nu')\tau_2'} f_{\mathrm{ph},\alpha_1\ldots\alpha_2'}(\tau_1, 0; \tau_1', \tau_2') \tag{2.208}$$

In terms of Feynman diagrams, we can write a general four-frequency object $f^{(2)}$ (using translational invariance, only three are independent) on the two-particle level as follows:

$f^{(2),\nu\nu'\omega}_{\mathrm{ph},\alpha_1\ldots\alpha_2'} :=$ 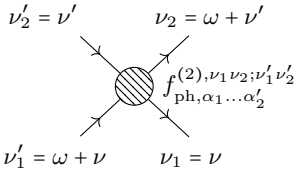

(2.209)

(2.210)

$f^{(2),\nu\nu'\omega}_{\mathrm{pp},\alpha_1\ldots\alpha_2'} :=$ 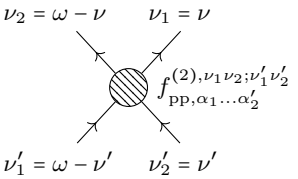

(2.211)

The external legs are not one-particle Green's functions in this case; they are just in the illustration to mark the free indices of the two-particle object.
⚠ *The frequency numbering does not match the one in [205] (especially page 58) due to the different definition of the operator ordering in Sec. 2.2.2.1.*

The reason for this redefinition of the frequencies is the better physical interpretability, made possible by the reduction to three frequency indices. (i) The particle-hole channel can be viewed (letting the time axis in the diagram go from bottom to top) as one incoming electron with energy $\nu + \omega$ and one incoming hole with energy $-\nu'$. After the generalized scattering, governed by the function f, the energies of particle and hole are changed from $\nu \to \nu'$, but the difference ω remains. (ii) This frequency index convention yields – after summation over the two fermionic frequencies and momenta ν, ν' and $\mathbf{k}$,$\mathbf{k}'$ – exactly the equal time, bosonic frequency operator, that we have introduced in Sec. 2.4, thus justifying the name "generalized" susceptibility.

2.7.2 Spin Index Conventions

The many symmetries (usually 4, 5 with particle-hole symmetry, see [205, Chapter 2]) in the two-particle quantities throughout this thesis are reflected in the number of independent spin and frequency indices. Furthermore, certain combinations carry specific physical meanings and/or have become customary in the literature. We will be very explicit in the definition of these conventions here, as they can be confusing or misleading in the literature, where no coherent notation has emerged yet. In two-particle quantities (i.e. 4 spin indices) only 6 of the total $2^4 = 16$ remain [205, Sec. 2.2.2.2]. One can, therefore, shorten the notation as follows.

Definition 2.7.2.1 (Spin Index Convention)
For general two-particle quantities f, we will only use 2 of the formally 4 needed spin indices, including a bar notation, to obtain the remaining combinations:

$$f_{\sigma\sigma'} := f_{\sigma\sigma'\sigma\sigma'} \tag{2.212}$$
$$f_{\overline{\sigma\sigma'}} := f_{\sigma'\sigma'\sigma\sigma} \tag{2.213}$$

Furthermore, for many physically measurable quantities, we want to use the physically easier to interpret conventions:

$$f_{\mathrm{d}} = f_{\mathrm{ph},\uparrow\uparrow} + f_{\mathrm{ph},\uparrow\downarrow} \tag{2.214}$$
$$f_{\mathrm{m}} = f_{\mathrm{ph},\uparrow\uparrow} - f_{\mathrm{ph},\uparrow\downarrow} \tag{2.215}$$
$$f_{\mathrm{s}} = f_{\mathrm{pp},\uparrow\uparrow} - f_{\mathrm{pp},\overline{\uparrow\downarrow}} \tag{2.216}$$
$$f_{\mathrm{t}} = f_{\mathrm{pp},\uparrow\uparrow} + f_{\mathrm{pp},\overline{\uparrow\downarrow}} \tag{2.217}$$

We use a subscript $r \in \{\mathrm{d}, \mathrm{m}\}$ or $r \in \{\mathrm{s}, \mathrm{t}\}$ to denote the channel. The context and further subscript of pp *or of* ph *(⚠ the* ph *subscript is suppressed in most cases since it is the more common one) allow us to identify the definition of r in the context.*

Note, that for $\sigma = \sigma'$ above, Eq. (2.212) and Eq. (2.213) coincide. The total number of possible combinations, therefore, matches the 6 independent combinations after applying the symmetries. Furthermore, the crossing symmetry [205, Table 2.1], relates Eq. (2.212) and Eq. (2.213). For this reason, we will rarely make use of Eq. (2.213) and, consistent with some of the literature, omit the "ph" subscript when the context allows it.
The transformation from the $\sigma\sigma'$ to magnetic and density channel notation can more formally be defined using the projection operators from Eq. (2.125):

$$P_\mathrm{d} = B_\mathrm{d} \otimes B_\mathrm{d}^T = \begin{pmatrix} 1 & 1 \\ 1 & 1 \end{pmatrix} P_\mathrm{m} = B_\mathrm{m} \otimes B_\mathrm{m}^T = \begin{pmatrix} 1 & -1 \\ -1 & 1 \end{pmatrix} \tag{2.218}$$

One can then subsequently define magnetic and density susceptibility as:

$$\chi_\mathrm{m} = -P_\mathrm{m}^T \chi P_\mathrm{m} \tag{2.219}$$
$$\chi_\mathrm{d} = -P_\mathrm{d}^T \chi P_\mathrm{d} \tag{2.220}$$

With $\overline{chi}$ from Eq. (2.125). It is possible to generalize this to the case with fewer symmetries and more contributing channels, see [180, Chapter 4].
Using crossing and SU(2) symmetry, we can also find two more identities for the singlet and triplet channels [205, Eq. 2.167]:

$$\Gamma_\mathrm{s}^{\nu\nu'\omega} = \Gamma_{\mathrm{pp},\uparrow\downarrow}^{\nu\nu'\omega} - \Gamma_{\mathrm{pp},\overline{\uparrow\downarrow}}^{\nu\nu'\omega} \overset{\text{crossing}}{=} \Gamma_{\mathrm{pp},\uparrow\downarrow}^{\nu\nu'\omega} + \Gamma_{\mathrm{pp},\uparrow\downarrow}^{\nu(\omega-\nu')\omega} \overset{\mathrm{SU}(2)}{=} 2\Gamma_{\mathrm{pp},\uparrow\downarrow}^{\nu\nu'\omega} - \Gamma_{\mathrm{pp},\uparrow\uparrow}^{\nu\nu'\omega} \tag{2.221}$$
$$\Gamma_\mathrm{t}^{\nu\nu'\omega} = \Gamma_{\mathrm{pp},\uparrow\downarrow}^{\nu\nu'\omega} + \Gamma_{\mathrm{pp},\overline{\uparrow\downarrow}}^{\nu\nu'\omega} \overset{\text{crossing}}{=} \Gamma_{\mathrm{pp},\uparrow\downarrow}^{\nu\nu'\omega} - \Gamma_{\mathrm{pp},\uparrow\downarrow}^{\nu(\omega-\nu')\omega} \overset{\mathrm{SU}(2)}{=} \Gamma_{\mathrm{pp},\uparrow\uparrow}^{\nu\nu'\omega} \tag{2.222}$$

Mapping between pp and ph Notation

Using the symmetry relations from [205, Table 2.1] we find two viable mapping between pp and ph channels.

$$\omega_\mathrm{pp} = \omega_\mathrm{ph} - \nu_\mathrm{ph} - \nu'_\mathrm{ph}, \qquad \mathbf{q}_\mathrm{pp} = \mathbf{q}_\mathrm{ph} - \mathbf{k}_\mathrm{ph} - \mathbf{k}'_\mathrm{ph} \tag{2.223}$$
$$\nu_\mathrm{pp} = \nu_\mathrm{ph}, \quad \nu'_\mathrm{pp} = \nu'_\mathrm{ph}, \qquad \mathbf{k}_\mathrm{pp} = \mathbf{k}_\mathrm{ph}, \quad \mathbf{k}'_\mathrm{pp} = \mathbf{k}'_\mathrm{ph} \tag{2.224}$$

Or

$$\omega_\mathrm{pp} = \nu_\mathrm{ph} - \nu'_\mathrm{ph}, \qquad \mathbf{q}_\mathrm{pp} = \mathbf{k}_\mathrm{ph} - \mathbf{k}'_\mathrm{ph} \tag{2.225}$$
$$\nu_\mathrm{pp} = \nu'_\mathrm{ph}, \quad \nu'_\mathrm{pp} = -\nu_\mathrm{ph}, \qquad \mathbf{k}_\mathrm{pp} = \mathbf{k}'_\mathrm{ph}, \quad \mathbf{k}'_\mathrm{pp} = -\mathbf{k}_\mathrm{ph} \tag{2.226}$$

These mappings are used, for example, for the determination of the superconducting phase transition, discussed in Sec. 4 and Sec. 7.2.

2.7.3 Generalized Susceptibilities

For the description of our methods in Sec. 5.4 a slightly different convention for the two-particle correlator is useful. Here, we only consider connected scattering processes; i.e. this correlator becomes zero for a vanishing interaction. Due to their relationship with physical response functions (see Def. 2.7.3.2), these correlators are called generalized susceptibilities.

Definition 2.7.3.1 (Susceptibilities)
We define the bare susceptibility or bubble term χ_0 and full susceptibility χ as:

$$\chi_{0,\sigma_1\sigma_2\sigma_3\sigma_4}(\tau_1, \tau_2; \tau'_1, \tau'_2) = G^{(1)}_{\sigma_1\sigma_2}(\tau_1; \tau'_1) G^{(2)}_{\sigma_3\sigma_4}(\tau_2; \tau'_2) \tag{2.227}$$
$$\chi_{\sigma_1\sigma_2\sigma_3\sigma_4}(\tau_1, \tau_2; \tau'_1, \tau'_2) = G^{(2)}_{\sigma_1\sigma_2\sigma_3\sigma_4}(\tau_1, \tau_2; \tau'_1, \tau'_2) - \chi_{0,\sigma_1\sigma_2\sigma_3\sigma_4}(\tau_1, \tau_2; \tau'_1, \tau'_2) \tag{2.228}$$

As usual, we can also understand the generalized susceptibility in terms of diagrams as a scattering process. The full vertex $F^{\nu\nu'\omega}_{\sigma\sigma',\mathbf{kkq}}$ describes a scatting process of two particles at equilibrium, containing all diagrams. In Sec. 2.8.1 we discuss how to partition these into classes, in order to facilitate approximations. Then the susceptibility is given as the difference between the connected and unconnected (bare) parts:

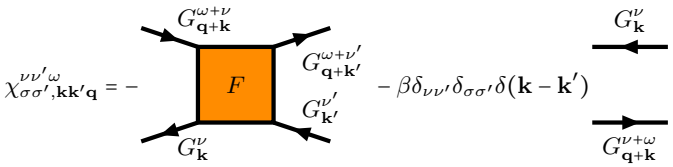

(2.229)

We will often use a channel-dependent interaction U_r, the reason is the leading-order diagrammatic contribution in this channel.

$$U_\mathrm{m} = -U + \mathcal{O}(U^2), \qquad U_\mathrm{d} = U + \mathcal{O}(U^2) \tag{2.230}$$

Definition 2.7.3.2 (Physical and Generalized Susceptibilities)
The bare bubble, or unconnected susceptibility, is defined in Fourier space, according to Eq. (2.7.3).

$$\chi^{\nu\nu'\omega}_{0,\mathrm{ph/pp},\mathbf{kq}} = -\beta\delta_{\nu\nu'}G^{\omega\pm\nu}_{\mathbf{q}\pm\mathbf{k}}G^{\nu}_{\mathbf{k}} \tag{2.231}$$

We commonly use partially summed versions of the bare susceptibility:

$$\chi^{\nu\nu'\omega}_{0,\mathrm{ph/pp},\mathbf{q}} = \sum_{\mathbf{k}}\chi^{\nu\nu'\omega}_{0,\mathrm{ph/pp},\mathbf{kq}}, \qquad \chi^{\nu\omega}_{0,\mathrm{ph/pp},\mathbf{q}} = -\sum_{\nu'}\chi^{\nu\nu'\omega}_{0,\mathrm{ph/pp},\mathbf{q}} \tag{2.232}$$

For quantities without momentum dependence, as encountered for DMFT in Sec. 5.1 and later, the sum is not present.

$$\chi^{\nu\nu'\omega}_{\sigma\sigma',\mathbf{kk'q}} = -\beta G^{\nu}_{\mathbf{k}}G^{\nu}_{\mathbf{k+q}}\delta_{\nu\nu'}\delta_{\sigma\sigma'} - G^{\nu}_{\mathbf{k}}G^{\nu+\omega}_{\mathbf{k+q}}F^{\nu\nu'\omega}_{\sigma\sigma',\mathbf{kk'q}}G^{\nu'}_{\mathbf{k'}}G^{\nu'}_{\mathbf{k'+q}} \tag{2.233}$$

The physical response functions can be obtained from the generalized ones by summation over the fermionic frequencies and momenta.

$$\chi^{\omega}_{r,\sigma\sigma',\mathbf{q}} = \sum_{\substack{\nu\nu'\\\mathbf{kk'}}}\chi^{\nu\nu'\omega}_{\sigma\sigma',\mathbf{kk'q}} \tag{2.234}$$

2.7.4 Schwinger-Dyson Equations of Motion

There is a general notion that connects higher-order Green's functions to lower-order ones. On an operator level, this is typically encountered when taking the time derivative of an operator, following the application of the Heisenberg equation of motion Eq. (2.16). The formal connection is given by the Schwinger-Dyson equation of motion (SDE) and can also be obtained using the functional integral formalism.
Consider a general functional F that respects the usual boundary conditions:

$$\int \mathcal{D}[\phi]\,\frac{\delta F[\phi]}{\delta\phi_\alpha} = \prod_\alpha \int \mathrm{d}\phi_\alpha \frac{\partial F[\phi]}{\partial\phi_\alpha} = 0 \tag{2.235}$$

We can use this to obtain the SDE by expansion of the expectation value for this functional, from Eq. (2.175):

$$0 \overset{\text{Eq. (2.235)}}{=} \int \mathcal{D}[\phi]\,\frac{\delta}{\delta\phi_\alpha}\left[F[\phi]e^{-S\left[\overline{\phi},\phi\right]}e^{-\langle\overline{J},\phi\rangle-\langle\overline{\phi},J\rangle}\right] \tag{2.236}$$

$$= \int \mathcal{D}[\phi]\left[\frac{\delta F[\phi]}{\delta\phi_\alpha} - F[\phi]\left(\frac{\delta S\left[\overline{\phi},\phi\right]}{\delta\phi_\alpha} + \overline{J}\right)\right]e^{-S\left[\overline{\phi},\phi\right]}e^{-\langle\overline{J},\phi\rangle-\langle\overline{\phi},J\rangle} = -\left\langle F[\phi]\left(\frac{\delta S\left[\overline{\phi},\phi\right]}{\delta\phi_\alpha} + \overline{J}\right)\right\rangle \tag{2.237}$$

Since this must hold for an arbitrary functional F, we deduce:

$$-\left\langle\frac{\delta S\left[\overline{\phi},\phi\right]}{\delta\phi_\alpha}\right\rangle = \overline{J}_\alpha, \qquad -\left\langle\frac{\delta S\left[\overline{\phi},\phi\right]}{\delta\overline{\phi}_\alpha}\right\rangle = J_\alpha \tag{2.238}$$

We then carry out the $\overline{J}$ and J derivatives according to Eq. (2.171) and obtain the SDE, relating n particle Green's functions to $n+1$ and $n+2$ ones. This is the same hierarchy obtained through imaginary time derivatives of the Green's function, as done in Sec. 3.3.1. For details on this calculation (e.g. chain rule for Grassman variables), see [61, Chapter 1.6.1]. We use an interaction appropriate for

our setting: $V_{\alpha_1,\dots\alpha_4}(\tau_1-\tau_1')$ and with

$$\frac{\delta S\left[\overline{\phi},\phi\right]}{\delta\overline{\phi}_{\alpha_1}} = \sum_{\alpha_1'}\int \mathrm{d}\tau_1' G^{-1}_{0,\alpha_1\alpha_1'}(\tau_1;\tau_1')\phi_{\alpha_1'}(\tau_1') + \frac{1}{3!}\sum_{\alpha_2\alpha_1'\alpha_2'}\int \mathrm{d}\tau_1' V_{\alpha_1\alpha_1'\alpha_2'\alpha_3'}(\tau_1-\tau_1')\overline{\phi}_{\alpha_2}(\tau_2)\overline{\phi}_{\alpha_1'}(\tau_1')\phi_{\alpha_2'}(\tau_1'), \tag{2.239}$$

we obtain the SDE for the two-particle Green's function:

$$G_0^{-1}(1;\bar{3})G(\bar{3};2) + \sum_{\alpha_3'\alpha_4'\alpha_2'}\int \mathrm{d}\tau_1' V_{\alpha_1\alpha_1'\alpha_2'\alpha_3'}(\tau_1-\tau_1')G_{\alpha_1'\alpha_2'\alpha_3'\alpha_2}(\tau_1,\tau_1';\tau_1'+\eta,\tau_2) = \delta(1-2) \tag{2.240}$$

This is the specific version of the SDE, connecting one and two-particle Green's functions, see also Eq. (5.54). We can furthermore obtain the expression for the single-particle potential energy, Eq. (2.81), from this expression. Comparison with the Dyson equation (i.e. "$G_0^{-1}G - \mathbb{1} = \Sigma G$") yields

$$\Sigma(1;\bar{3})G(\bar{3};2) = -\sum_{\alpha_3'\alpha_4'\alpha_2'}\int \mathrm{d}\tau_1' V_{\alpha_1\alpha_1'\alpha_2'\alpha_3'}(\tau_1-\tau_1')G_{\alpha_1'\alpha_2'\alpha_3'\alpha_2}(\tau_1,\tau_1'-\eta;\tau_1'+\eta,\tau_2) \tag{2.241}$$

Note, that we obtain the Galitskii Migdal formula [75] for the potential energy for $\tau_2 \to \tau_1 + \eta$:

$$\Sigma(\bar{1};\bar{3})G(\bar{3},\overline{1+\eta}) = \sum_{\alpha_1\alpha_3'\alpha_4'\alpha_2'}\int \mathrm{d}\tau_1'\int \mathrm{d}\tau_1 V_{\alpha_1\alpha_1'\alpha_2'\alpha_3'}(\tau_1-\tau_1')G_{\alpha_1'\alpha_2'\alpha_3'\alpha_2}(\tau_1,\tau_1';\tau_1',\tau_1+\eta) = 2\langle V\rangle \tag{2.242}$$

After Fourier transformation to Matsubara space we obtain the familiar form for the Hubbard model, we will use later in Sec. 5.4:

$$\sum_{\omega\mathbf{k}}\Sigma^{\nu_\mathbf{k}}G^{\nu}_{\mathbf{k}}e^{-i\nu_n(-\eta)} = U\langle\hat{n}_\uparrow\hat{n}_\downarrow\rangle \tag{2.243}$$

2.8 Parquet Decomposition and Bethe-Salpeter Equation

2.8.1 Parquet Decomposition

The decomposition of a full Green's function into a subset of uniquely defined diagrams and a set of rules to construct the original one is not unique to 1PI diagrams as a subset. In this section, we discuss the parquet decomposition that will be used as a basis for the DΓA method (see Sec. 5.3), following [97]. This decomposition of the full vertex F will be discussed in Sec. 5.4 (see Eq. (5.57)). Here, we will introduce the generalization of the Dyson equation, the Bethe-Salpeter Equation (BSE), that connects the connected and full Green's functions.
Contrary to the single-particle case, for 2-particle Green's functions, there is more than one possible way to cut internal lines. This necessitates an additional step before the description of the equations between the connected and the full set of diagrams. Here, we use the parquet decomposition, which segments the class of all two-particle diagrams into 4 disjoint sets[15].

Important 2.8.1.1
The full vertex F decomposes into four classes: fully irreducible diagrams Λ and diagrams Φ_r that are reducible in exactly one channel r:

$$F = \Lambda + \Phi_{\mathrm{ph}} + \Phi_{\overline{\mathrm{ph}}} + \Phi_{\mathrm{pp}} \tag{2.244}$$

It will frequently be useful to write formulas in terms of diagrams that are irreducible *in the channel r.*

$$r \in \{\mathrm{ph}, \overline{\mathrm{ph}}, \mathrm{pp}\} \tag{2.245}$$

They can be written in two ways (i) all diagrams without the reducible ones:

$$\Gamma_r = F - \Phi_r \tag{2.246}$$

(ii) all irreducible ones together with the ones that are reducible in exactly one channel $r' \neq r$:

$$\Gamma_r = \Lambda + \sum_{r'\neq r}\Phi_{r'} \tag{2.247}$$

The three possible combinations, corresponding to different scattering processes, are illustrated here,

[15] This is not a unique decomposition, as the single-boson-exchange decomposition demonstrates [145]. We will make use of this decomposition in the context of lDΓA, in a form similar to [125] and formally derived for the 1PI method [205].

reproduced from [97, Fig. 5]

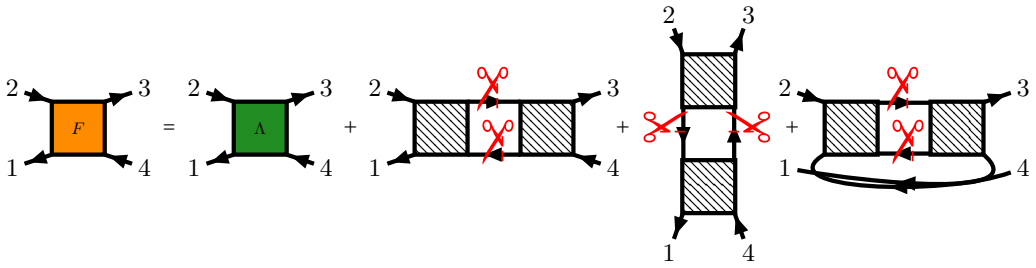

(2.248)

The red scissors mark the 2-particle reducibility in the diagrams, while the blobs consist of irreducible diagrams in the corresponding channel, such that each possible 2-particle diagram falls into one of the four categories above. Γ consists of 2PI diagrams, i.e. diagrams that cannot be made unconnected by cutting two propagator lines. The leading-order diagrams for the fully irreducible 2-particle vertex are the bare interaction U and the envelope diagram (compare also the self-energy for the one-particle analog in Eq. (2.186)):

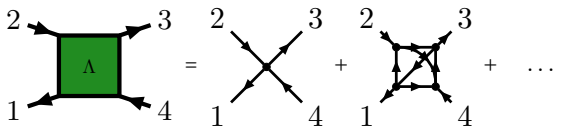

(2.249)

2.8.2 Bethe-Salpeter Equation

With this generalized notion of reducibility, we can now define the construction method to obtain the full vertex F from the irreducible vertices, similar to the Dyson equation. This section only gives a very general idea (specifically, we will omit the exact frequency notation). Details can be found in [205, Appendix B].
The full vertex can be trivially decomposed into the sum of the sets of diagrams that are reducible and irreducible in any channel r:

$$F = \Gamma_r + \Phi_r \Leftrightarrow \Phi_r = F - \Gamma_r \tag{2.250}$$

The insight now is that the reducible diagrams Φ_r can be constructed from irreducible ones through a similar construction illustrated in Eq. (2.249). Using Eq. (2.250), we can express the full vertex through the irreducible vertex in each channel.

Important 2.8.2.1 (Bethe-Salpeter Equation)
The Bethe-Salpeter equation relates the full vertex F to the two-particle vertex containing only two-particle irreducible diagrams (we abbreviate this by 2PI) in the channel r:

$$F = \Gamma_r + \Phi_r \tag{2.251}$$
$$\Phi_r = F \star (G \star G)_r \star \Gamma_r \tag{2.252}$$

The star marks a convolution over the appropriate internal indices corresponding to the channel.

In terms of diagrams, the BSE in the particle-hole channel is given as follows:

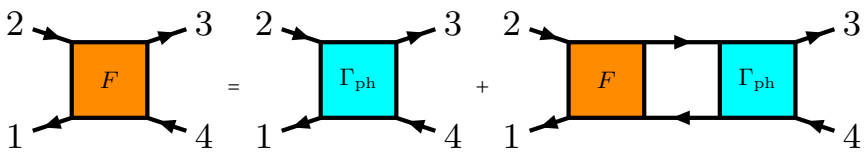

(2.253)

These depend on the channel and can, with illustrations, be found in [205, Fig $B.1$]. We will frequently use the BSE in the context of the DΓA method in Sec. 5.3 to obtain the reducible vertices in the density and magnetic channel from F and vice versa, introducing nonlocal corrections in the process.
Note that the full vertex F appears on the left- and right-hand sides. Luckily, the equations are in our setting linear in Matsubara space and can be solved through matrix inversion[16]. For the density and

[16] One might consider solving the matrix equation directly, as matrix inversions are known to be numerically unstable. However, the structure (specifically the third index) of this equation does not allow for such an improvement.

magnetic channel, the solution for Γ is readily obtained by matrix inversion from Eq. (2.251):

$$\Gamma^{nu\nu'\omega}_{\mathrm{d/m}} = \sum_{\nu_1} F^{\nu\nu_1\omega}_{\mathrm{d/m}} \left[M^{-1}\right]^{\nu_1\nu'\omega}, \qquad M^{\nu\nu'\omega} = \mathbb{1} + \frac{1}{\beta} G^{\nu} G^{\nu+\omega} F^{\nu\nu'\omega}_{\mathrm{d/m}} \tag{2.254}$$

Some more details for the actual computation of this quantity are given in Sec. 6.3 and Sec. 6.5. For the physical susceptibilities, one can also rewrite the BSE in the following way to obtain the irreducible vertex from the generalized susceptibility [207, Appendix. B]:

$$\Gamma^{\nu\nu'\omega}_{r} = \beta^2 \left[\left(\chi^{\omega}_{r}\right)^{-1} - \beta \left(\chi^{\nu\nu'\omega}_{0}\right)^{-1} \right]_{\nu\nu'\omega} \tag{2.255}$$

From Eq. (2.258) we can observe, that the irreducible vertex $\Gamma^{\nu\nu'\omega}$ may diverge when the generalized susceptibility has eigenvalues crossing 0 [205, p. 129] associated with corresponding critical eigenvalues of $\Gamma^{\nu\nu'\omega}_{r}$. These can be understood as precursors of the Mott transition [204, 215, 220, 89]. This is, however, not the focus of this thesis, instead, we investigate the divergencies of the generalized (or more precisely physical) susceptibility, which indicates second-order phase transitions.
The transformation of the spin indices to the density and magnetic channels can be done by using the projectors from Eq. (2.219). A full derivation including proper definition of all indices can be found in [205, Appendix B].

Important 2.8.2.2 (BSE for Full and Irreducible Vertex)
In terms of the full vertex F, the BSE is given by:

$$F^{\nu\nu'\omega}_{r} = \Gamma^{\nu\nu'\omega}_{r} + \sum_{\nu_1} \Gamma^{\nu\nu_1\omega}_{r} G^{\nu_1} G^{\omega+\nu_1} F^{\nu_1\nu'\omega}_{r} \tag{2.256}$$

In terms of the irreducible vertex and generalized susceptibility is reads:

$$\chi^{\nu\nu'\omega}_{r} = \chi^{\nu\nu'\omega}_{0} - \sum_{\nu_1\nu_2} \chi^{\nu\nu_1\omega}_{0} \Gamma^{\nu_1\nu_2\omega}_{r} \chi^{\nu_2\nu'\omega}_{r} \tag{2.257}$$

$$= \left[\mathbb{1} - \chi^{\nu\nu'\omega}_{0} \Gamma^{\nu\nu'\omega}_{r}\right]^{-1} \chi^{\nu\nu'\omega}_{0} \tag{2.258}$$

One can also obtain the BSE through a generating functional approach by derivatives of the effective potential, according to Eq. (2.193). We omit all unnecessary indices for this illustration. Details can be found in [266, Chapter 56]:

$$\chi_{\sigma\sigma'} = \frac{\delta\Gamma[G_\sigma]}{\delta G_{\sigma'}} = G_\sigma G_\sigma \delta_{\sigma\sigma'} - G_\sigma \left[\frac{\delta\Sigma_\sigma}{\delta G_{\overline{\sigma}}} \frac{\delta G_{\overline{\sigma}}}{\delta J_{\sigma'}}\right] G_\sigma \tag{2.259}$$

This form will be used in the discussion of conserving approximations, specifically Sec. 5.2.1. With $\frac{\delta\Sigma_\sigma}{\delta G_{\overline{\sigma}}} = \Gamma$ and $\frac{\delta G_{\overline{\sigma}}}{\delta J_{\sigma'}} = \chi$ and reintroduction of all indices (we still combine momentum and frequency indices here), one obtains the Bethe-Salpeter equation for the generalized susceptibilities given in Eq. (2.257).

2.8.3 Parquet Equations

The set of equations we will construct can be obtained by first considering the decomposition of irreducible diagrams in exactly one channel r from Eq. (2.247). We insert Eq. (2.251) into Eq. (2.247) and solve for Φ_r yielding the following set of three (Eq. (2.245)) equations:

$$\Phi_r = F - \Gamma_r = F \star G \star G \star \Lambda + \sum_{r' \neq r} F \star G \star G \star \Phi_{r'} \tag{2.260}$$

Together with Eq. (2.247) and Eq. (2.244) this can be written in the diagrammatic form of Eq. (2.253) [97, Fig. 7]:

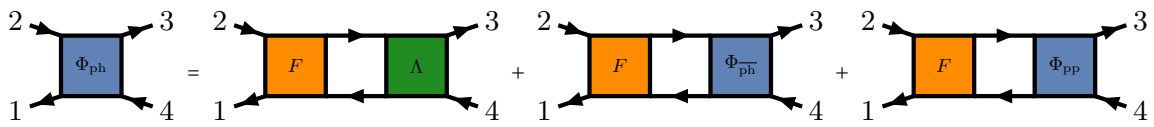

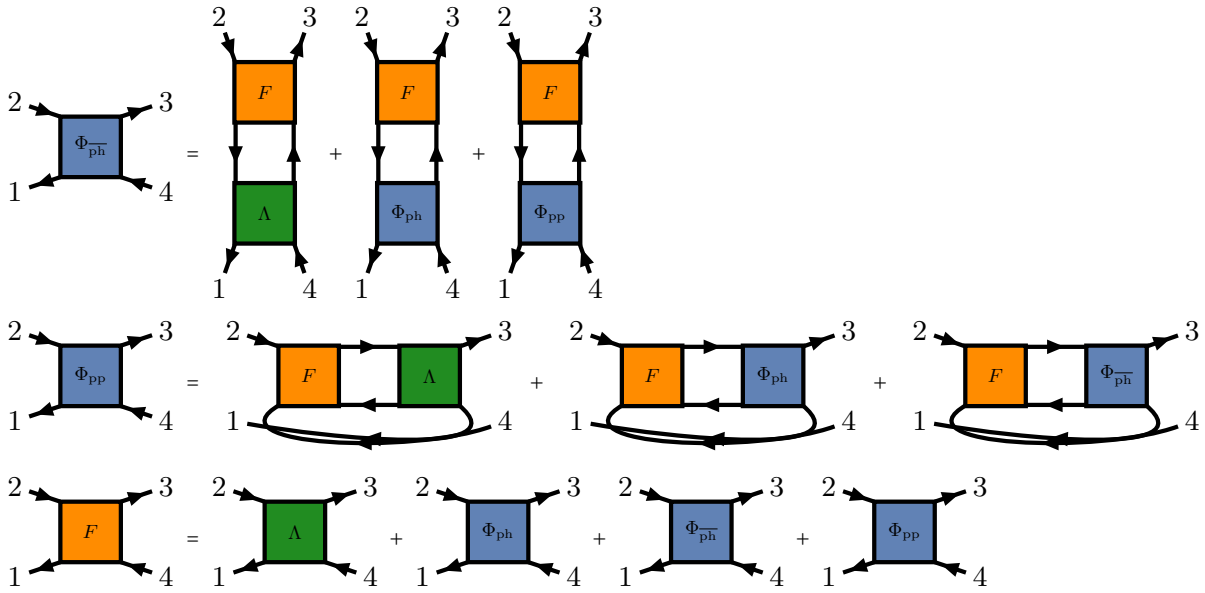
2
3
1
4
$\Phi_{\overline{\text{ph}}}$
=
F
Λ
+
Φ_{ph}
Φ_{pp}
Φ_{pp}
Φ_{ph}
$\Phi_{\overline{\text{ph}}}$

3 Hubbard Model

In this chapter, a general introduction to the Hubbard model and its magnetic phases is given. Many of the topics discussed in this section can also be found in textbooks or lecture scripts and are presented here for the purpose of giving a collection of concepts and methods that are instrumental in our investigation of the antiferromagnetic phase diagram of the Hubbard model in a three-dimensional lattice at half-filling in Sec. 7.1 and in the further development of the newly developed method investigated on the two-dimensional Hubbard model for arbitrary filling and the application to the phase diagram of cuprates in Sec. 7.2.
Readers familiar with the Hubbard model, mean-field theories, and the effects of correlation in this setting may want to skip this chapter.

3.1 Introduction

In this chapter, we want to motivate the Hubbard model as an abstraction for correlations between electrons in low-energy lattice modes. This will neglect many degrees of freedom, such as the spatial positions of electrons or the movement of nuclei. However, this model has proven tremendously successful in describing magnetic ordering, the Mott insulating phase, and superconductivity. Its application to many problems in solid-state theory is ubiquitous because it has long been believed to capture the essence of superconductivity [11] A review of the current state of research and numerical methods can be found in [13] and [198]
We will now motivate the Hubbard model by walking through the necessary approximations, starting with the general non-relativistic[1] Hamiltonian for the interactions of N_e electrons with positions denoted with lower case $\mathbf{r}$: and N_n nuclei with positions denoted with upper case $\mathbf{R}$:

$$\hat{H} = \underbrace{-\sum_i^{N_e} \frac{\hbar^2}{2m_i} \nabla_{\mathbf{r}_i}^2}_{\hat{T}_e} \underbrace{-\sum_m^{N_n} \frac{\hbar^2}{2M_m} \nabla_{\mathbf{R}_m}^2}_{\hat{T}_n} + \underbrace{\frac{1}{2} \sum_{i \neq j} \hat{V}_{e-e}(\mathbf{r}_i, \mathbf{r}_j)}_{\hat{V}_{e-e}} + \underbrace{\frac{1}{2} \sum_{m \neq n} \hat{V}_{n-n}(\mathbf{R}_m, \mathbf{R}_n)}_{\hat{V}_{n-n}} + \underbrace{\sum_i^{N_e} \sum_m^{N_n} \hat{V}_{e-n}(\mathbf{r}_i, \mathbf{R}_m)}_{\hat{V}_{e-n}} \quad (3.1)$$

The 5 terms describe the movement of electrons and nuclei, interactions among electrons, interactions among nuclei, and finally, interactions between electrons and nuclei. This model not only incorporates different energy scales, since nuclei move much more slowly than electrons but also results in a system of 10^{23} coupled differential equations for macroscopic systems. The first problem can be tackled by separating electronic and atomic movements. The observation that the ratio of electrons and nuclei is $\frac{m_e}{M_n} \sim 1/2000$ justifies this assumption. Therefore, it is justified to separate the wave function into a product and solve the electronic system with static positions for the ions.

$$\psi_{\text{total}}\left(\{\mathbf{r}_i\}; \{\mathbf{R}_k\}\right) = \psi_e\left(\{\mathbf{r}_i\}; \{\mathbf{R}_k\}\right) \times \psi_{\text{ion}}\left(\{\mathbf{R}_k\}\right) \quad (3.2)$$

This is known as the Born-Oppenheimer approximation [35], leading to a Hamiltonian for the electrons in which the lattice vectors $\mathbf{R}_i$ only appear as static parameters (and vice versa).
Although there are important applications of the degree of freedom of the lattice, we will exclusively discuss the electronic structure in this thesis[2]. Our general Hamiltonian from Eq. (3.1) will therefore be reduced to three terms:

$$\hat{H} = -\sum_i^{N_e} \frac{\hat{p}_i^2}{2m_i} + \frac{1}{2} \sum_{i \neq j} \hat{V}_{e-e}(\mathbf{r}_i, \mathbf{r}_j) + \sum_i^{N_e} \sum_m^{N_n} \hat{V}_{e-n}(\mathbf{r}_i, \mathbf{R}_m) \quad (3.3)$$

The second simplification, downfolding, is much less straightforward, leading to many Hubbard-related models. Let us assume that we have access to electronic wave functions from an ab initio method, most commonly Density Functional Theory (DFT) [140]. In that case, we denote the Kohn-Sham orbital for a state α (combined spin and orbital) by $\psi_\alpha(\mathbf{k})$. Correlation effects are assumed only to play a significant role at low energies and partially filled narrow orbitals (d and f). As a reason, we can imagine that the small spatial extent of these orbitals plays a role in the lack of electron-electron screening. However, screening is necessary to justify mean-field-like approaches that neglect explicit correlations, as we will discuss in Sec. 3.4. Therefore, one needs to find a model for the lowest energy bands (a process called downfolding, which is in itself subject to ongoing research [15]), calculate corrections to the band structure, and then map the corrections back to the original band structure. Additionally, to obtain a lattice model, we also need to determine a local basis for these wave functions. Both requirements, reducing to the correct bands and orbitals and the localization, can be fulfilled by maximally-localized Wannier functions [139, 165]. Here, a transformation U_{mn} is determined, mapping the occupied bands (this restricts the sum over α below) that belong to the correlated orbitals to this Wannier basis:

$$|\phi_\beta(\mathbf{r})\rangle = \frac{1}{\mathcal{N}} \int_{\text{BZ}} \mathrm{d}\mathbf{k} e^{-i\mathbf{k}\cdot\mathbf{R}} \sum_\alpha M_{\alpha\beta}(\mathbf{k}) |\psi_\alpha(\mathbf{k})\rangle \quad (3.4)$$

under the localization restriction (i.e. minimal variance),

$$\min\{\langle\phi_\beta(\mathbf{r})| \mathbf{r}^2 |\phi_\beta(\mathbf{r})\rangle - \langle\phi_\beta(\mathbf{r})| \mathbf{r} |\phi_\beta(\mathbf{r})\rangle\} \quad (3.5)$$

We can now transform the Hamiltonian in Eq. (3.3) (this time already in $\mathbf{k}$ space) using the transformation matrix, with $\mathbf{r}_i$ and $\mathbf{r}_j$ marking positions of atoms in the unit cell and the site indices i, j, k, l split off from the multi-indices for general quantum-states $\alpha, \beta, \gamma, \delta$. The "localized" tight-binding Hamiltonian in real space (the real space basis is chosen to emphasize the locality of the basis) is then

[1] This is already the first simplification. Relativistic effects play a role in the electronic states of heavy ions, where spin-orbit coupling becomes significant. These systems will, however, not be investigated in this thesis.
[2] Note that even for superconductivity in cuprates, which we will discuss, the phonon coupling can usually not be neglected[86]. However, including these effects in our newly developed methods is left as the subject of future research. One well-known extension incorporating photonic (i.e. lattice) effects is known as the Hubbard-Holstein model.

written as follows:

$$H_{\alpha\beta}(\mathbf{r}_i - \mathbf{r}_j) = \frac{1}{\mathcal{N}} \int \mathrm{d}\mathbf{k} e^{-i\mathbf{k}(\mathbf{r}_i - \mathbf{r}_j)} \sum_{\gamma\delta} M^{\dagger}_{\alpha\gamma} H_{\gamma\delta}(\mathbf{k}) M_{\delta\beta} \tag{3.6}$$

$$\Rightarrow \hat{H} = \sum_{\substack{\alpha\beta \\ ij \\ \sigma}} t_{ij}^{\alpha\beta} \hat{c}^{\dagger}_{\alpha i\sigma} \hat{c}_{\ \beta j\sigma} + \frac{1}{2} \sum_{\substack{\alpha\beta\gamma\delta \\ ijkl \\ \sigma\sigma'}} U^{ijkl}_{\alpha\beta\gamma\delta} \hat{c}^{\dagger}_{\alpha i\sigma} \hat{c}^{\dagger}_{\beta j\sigma'} \hat{c}_{\ \gamma k\sigma} \hat{c}_{\ \delta l\sigma'} \tag{3.7}$$

With the hopping amplitude t and the effective Coulomb interaction $U_{\cdots}$; between sites i, j, spins σ, σ' and states (orbitals, bands) α, β:

$$t_{ij}^{\alpha\beta} = \int \mathrm{d}^3\mathbf{r} \, \langle \phi_{\alpha i}(\mathbf{r}) | \hat{T}_e + \hat{V}_{e-n} | \phi_{\beta j}(\mathbf{r}) \rangle \tag{3.8}$$

$$U_{ijkl}^{\alpha\beta\gamma\delta} = \int \mathrm{d}^3\mathbf{r}\mathrm{d}^3\mathbf{r}' \, \langle \phi_{\alpha i}(\mathbf{r}) \, \phi_{\beta j}(\mathbf{r}') | \hat{V}_{e-e}(\mathbf{r}, \mathbf{r}') | \phi_{\gamma k}(\mathbf{r}') \, \phi_{\delta l}(\mathbf{r}) \rangle \tag{3.9}$$

The Hamiltonian has been written in terms of creation and annihilation operators (see Sec. 2.1). If the downfolding and restriction to localized (d and f) orbitals is done carefully (and the system allows it because the delocalized bands are sufficiently separated in energy), the spatial integration with few basis functions will not destroy much information, and the obtained model can be assumed to be a good approximation for the low-energy states. However, this Hamiltonian is still too general for our purpose, and we typically make further approximations based on the locality of the interactions. First, we will drop the band index, as we will only consider single-band systems in this thesis. This approximation is generally not permissible. However, for high-temperature superconductors, which are candidate materials for the methods in this thesis, two well-known material classes exhibit a sufficiently well-behaved band structure. Cuprates, while having three bands contributing to the low energy states through the charge transfer character [93], have only one Fermi crossing; therefore, they are often qualitatively described in a single-band model, which we will discuss, including a brief introduction to the literature about the validity of the single-band approximation, in Sec. 7.2. Nickalates may also be treated this way [134, 45], although the applicability of this approximation is still disputed [124, 45]. We first tackle various simplifications for the Coulomb interaction. Here, one has to consider the leading orders of interaction in the system carefully. For example, the consideration of d orbitals (which do exhibit sizable correlation effects due to their narrow shape) in transition-metal oxides and iron-based superconductors usually leads to considerable contribution of t_{2g} orbitals, with one of the driving mechanisms being the Hund's coupling [79]. The resulting simplification reads [123]:

$$\begin{aligned} \hat{H} = &\sum_{\substack{\alpha\beta \\ ij \\ \sigma}} t_{ij}^{\alpha\beta} \hat{c}^{\dagger}_{\alpha i\sigma} \hat{c}_{\ \beta j\sigma} + U \sum_{\alpha} \hat{n}_{\alpha\uparrow} \hat{n}_{\alpha\downarrow} + U' \sum_{\alpha \neq \beta} \hat{n}_{\alpha\uparrow} \hat{n}_{\beta\downarrow} \\ &+ (U' - J) \sum_{\alpha<\beta,\sigma} \hat{n}_{\alpha\sigma} \hat{n}_{\beta\sigma} - J \sum_{\alpha\neq\beta} \hat{c}^{\dagger}_{\alpha\uparrow} \hat{c}_{\ \alpha\downarrow} \hat{c}^{\dagger}_{\beta\uparrow} \hat{c}_{\ \beta\downarrow} + J \sum_{\alpha\neq\beta} \hat{c}^{\dagger}_{\alpha\uparrow} \hat{c}^{\dagger}_{\alpha\uparrow} \hat{c}_{\ \beta\downarrow} \hat{c}_{\ \beta\downarrow} \end{aligned} \tag{3.10}$$

With $\hat{n}_{\alpha\sigma} = \hat{c}^{\dagger}_{\alpha\sigma} \hat{c}_{\ \alpha\sigma}$ being the density operator for spin σ in orbital α.
Compared with Eq. (3.9), we observe that only some elements for the 8 rank tensor $U_{ijkl}^{\alpha\beta\gamma\delta}$ survive, and all have associated distinct physical processes. The U and U' terms correspond to Coulomb repulsion of electrons with a different spin, occupying the same orbital, with $U \neq 0$ only for density-density interactions[3], but still inter-band effects in the form of the interaction U' and Hund's first rule with $U' - J$.

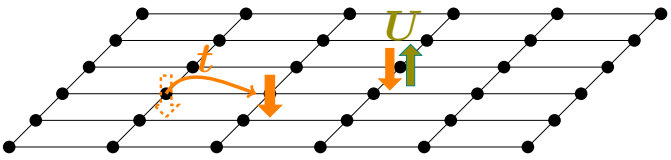

Figure 3.1: Illustration of simple Hubbard Model for a 2D lattice with hopping t and Coulomb density-density interaction U

This thesis will be concerned with a simpler model and neglect Hund's coupling. However, future extensions of this model introduce the direction of multi-band, and Hund's coupling inclusion could be valuable since the alternatives for treating strong non-local correlations in compounds such as iron-based superconductors are sparse [2]. Our last two approximations are the cutoff for distances of the hopping and a further restriction on the interaction term. The hopping is assumed to connect only neighboring atoms, at most 3 sites apart. We will usually write t, t', and t'' for nearest, next-nearest, and next-next-nearest neighbor hopping. All other hoppings, as well as hoppings between orbitals and bands, are neglected.

$$t_{ij} = -\frac{1}{\mathcal{N}} \sum_{\alpha\beta} \delta_{\alpha,\beta} e^{i\mathbf{k}(R_i - R_j)} \epsilon_{\alpha}(\mathbf{k}) \tag{3.11}$$

[3] This gets rid of 2 indices, we also let $U_{ij}^{\alpha\beta} \to U^{\alpha\beta}$

Note that the simplification in the amount of hopping terms taken into account will have little to no impact on the computational performance of the calculations for the correlated system. Finally, we assume that the electron interaction only occurs when they occupy the same site. From that, we get the Hubbard Hamiltonian used throughout this thesis:

$$\hat{H} = -\sum_{ij\sigma} t_{ij}\hat{c}^{\dagger}_{i\sigma}\hat{c}_{j\sigma} + U\sum_{i}\hat{n}_{i\uparrow}\hat{n}_{i\downarrow} - \mu\sum_{i\sigma}\hat{n}_{i\sigma} \tag{3.12}$$

When only nearest neighbor hoppings are considered, we write $\langle ij\rangle$ in the summation index. In this thesis, we are exclusively interested in the repulsive Hubbard model, i.e. $U > 0$.
Figure 3.1 illustrates the Hubbard model on a 2D lattice. Despite its simplicity with only 2 (assuming for the moment $t' = t'' = 0$) parameters, this model can capture important correlation effects, such as the Mott-insulator transition, and it is believed to be an excellent candidate to encapsulate effects leading to high-temperature super-conductivity [119, 13]. Furthermore, the details of physics arising from this model are still the subject of ongoing research in many numerical fields [198].
One may develop an intuitive understanding of the complex physics of this model by observing the competition between the kinetic and potential energy terms. Specifically, the potential energy term in the simple density-density interaction version of the Hubbard model in Eq. (3.12) can furthermore be fully described in terms of charge and spin fluctuations (we use the definitions for charge and spin operator in Eq. (2.75) and Eq. (2.122)):

$$U\hat{n}_{i\downarrow}\hat{n}_{i\uparrow} = \frac{U}{4}\left(\hat{n}_{i\downarrow} + \hat{n}_{i\uparrow}\right)^2 - \frac{U}{4}\left(\hat{n}_{i\downarrow} - \hat{n}_{i\uparrow}\right)^2 = \frac{U}{4}\hat{n}_i\hat{n}_i - \frac{U}{4}\hat{S}^z_i\hat{S}^z_i \tag{3.13}$$

This fact will play a role in Sec. 5.2.1 and Sec. 5.4, when we discuss a renormalization of these quantities.
Our goal for the following sections is to gain a qualitative understanding of the driving physical mechanisms in limiting cases of the parameter space that allows projection into subspaces with fewer physical processes. Later, in Sec. 7.1, we discuss an improvement of the quantitative description over most state-of-the-art methods for the special case of half-filling, 3 spatial dimensions, and a single band. In Sec. 7.2, we will also discuss a method that could overcome the first two limitations.
To better understand the physics of the Hubbard model, we will now discuss different coupling regimes.

3.2 Hubbard Physics and Magnetic Ordering

In the following, we will discuss general properties of the Hubbard Hamiltonian on a qualitative level.
Let us first consider the possible electronic states of the single-band Hubbard model: Each lattice point can have one of four different states, beginning occupied by 2 ($|\uparrow\downarrow\rangle$), 1 ($|\downarrow\rangle$ or $|\uparrow\rangle$) or 0 ($|0\rangle$) electrons. It is clear that the double-occupied state is energetically less favorable the larger U/t becomes. At the same time, double occupations and empty sites will generally serve as a pathway for lowering the kinetic energy term. To make this more systematic, we will discuss the leading-order contributions to limiting cases of the Hubbard Hamiltonian. Using a scaling in the units of $1/t$, the Hubbard model has, apart from the temperature[4], three notable degrees of freedom: (i) interaction strength U/t, (ii) electron density n, and (iii) lattice coordination number. The first two depend on the lattice type considered, while the last one is (almost) lattice-independent. We will first discuss the implications of the first two limits and spend some more time discussing (iii), as it is crucial for DMFT Sec. 5.1. Note that the effect of frustration plays a very important role, as it effectively destroys antiferromagnetic ordering. We will omit this discussion for this section; however, some aspects are discussed in Sec. 7.2. The effects of the lattice on the driving physics of the model are, of course, crucial, typically driven by frustration and topological effects [157, 293]. For the following considerations, we will, however, assume nearest-

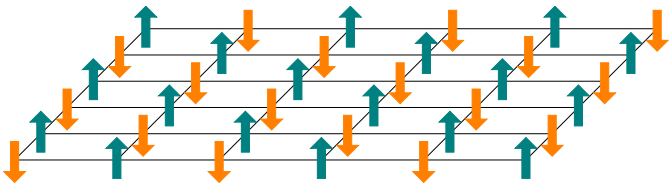

Figure 3.2: Illustration of Mott insulating state on a 2 dimensional Hubbard Model with an antiferromagnetic order. Note that this picture does not aim to depict an actual ground state, as the spins are drawn with classical arrows – furthermore, vacuum fluctuations will also contribute to a real quantum-mechanical ground state (such as virtual exchange processes). Lastly, the Mott insulating state does not necessarily imply antiferromagnetic ordering, for example, on frustrated lattices.

[4] For this section, we assume reasonably small T/t and discuss temperature dependence only in passing. For more than two spatial dimensions, finite-temperature phase transitions do occur, but we defer the discussion of the temperature-dependent phase diagram for now.

neighbor hopping and a bipartite lattice[5]in order to gain a general understanding of the model. Furthermore, the half-filling case ($n = 1$) will be central to our discussion, as it is unique in exhibiting Mott insulating behavior for strong coupling [179]. The Mott phase transition is characterized by a half-filled band with a Fermi level crossing (that is, a metal according to the band structure) becoming insulating as the interaction U increases above a critical U_c. In the Mott insulating phase, every site is occupied by exactly one electron and the energy bands are separated by the Mott gap. No conduction can occur because the electron hopping is suppressed by a prohibitively large repulsive effective Coulomb interaction U. Figure 3.2 gives an illustration of one example of this state on a bipartite lattice. However, the insulating state is a singular point on the density axis, and charge fluctuations start to emerge for any finite doping. What remains outside of the (fully) Mott insulating state, depicted in Fig. 3.2, for finite doping is often the antiferromagnetic ordering[6]. At weak coupling, this state reduces the potential energy that arises from $U\sum_i \langle \hat{n}_{i\uparrow}\hat{n}_{i\downarrow}\rangle$. However, the picture is much less clear than it might seem at first glance. The competition of itinerant magnetism in the weak coupling and local moments in the strong coupling regime, together with the dilution of charge carriers, makes the understanding of the driving mechanisms in the intermediate regimes astoundingly complicated. The next two sections aim to introduce the limiting cases of strong and weak coupling, their governing physics, and some common approaches to solving systems in this limit. Chapters 7 will make use of the groundwork from this chapter and discuss the temperature dependence of antiferromagnetic ordering as well as the driving mechanisms in the stabilization of the phase in the intermediate regimes and moderate temperatures away from the limits discussed here.
Note that we only need to consider one direction of doping for the Hubbard model on bipartite lattices since it is symmetric around half-filling (we still assume $t' = t'' = 0$), as demonstrated by the particle-hole transformation.

$$\hat{c}'^{\dagger}_{i\sigma} = (-1)^i \hat{c}^{\dagger}_{i\sigma} \Rightarrow \hat{c}'^{\dagger}_{i\sigma}\hat{c}'_{j\sigma} = \overbrace{(-1)^{i+j}}^{=0} \hat{c}^{\dagger}_{i\sigma}\hat{c}_{j\sigma}, \qquad \hat{c}'^{\dagger}_{i\sigma}\hat{c}'_{i\sigma} = 1 - \hat{c}^{\dagger}_{i\sigma}\hat{c}_{i\sigma} \Rightarrow \mu \to \mu + \frac{U}{4} \tag{3.14}$$

We will use this fact and discuss doping without specification of the dopant for the discussion of limiting behavior in the remainder of this section.

3.3 Strong Coupling Limit

In this section, we investigate the physics of the Hubbard model for strong coupling $U/t \gg 1$. To this end, we will first discuss the limiting case for $U/t \to \infty$, called the atomic limit, followed by the exact solution for a 2-site model (Hubbard dimer). This will serve as motivation for the consideration of dominating processes in the strong coupling regime outside the atomic limit, culminating in the definition of the $t-J$ model, Sec. 3.3.3, and its limit, the Heisenberg model.

3.3.1 Hubbard Bands and Atomic Limit

The $U/t \to \infty$ limit is, arguably, not a very compelling one, given that many interesting phenomena emerge precisely from the competition between electron hopping and interaction. However, it provides us with an entry point for understanding the general impact of the Hubbard U in a situation where not only charge fluctuations but also Heisenberg-like dipole coupling is neglected. Namely, the understanding of Hubbard bands and the implication of the self-energy for correlated systems will be the subject of this section. Additionally, we will give an abbreviated overview of the derivation for the one-particle Green's function for an atomic limit Hubbard lattice, providing (together with the weak-coupling limit in Sec. 3.4) a further introduction to the Green's function formalism.

Exact Diagonalization

We begin completely disregarding the hopping term in the Hubbard Hamiltonian. Letting $U_{ijkl} \equiv U$ and $U/t \to \infty$, the Hubbard model becomes diagonalizable[7],

$$\hat{H}_{\mathrm{AL}} = U\sum_i \hat{n}_{i\uparrow}\hat{n}_{i\downarrow} - \mu\sum_{i\sigma}\hat{n}_{i\sigma} \tag{3.15}$$

This Hamiltonian factorizes and we can consider the following 4 possible states at each site i independent of the site:

$$\hat{H}_i|0\rangle = 0|0\rangle, \qquad \hat{H}_i|\uparrow\rangle = -\mu|\uparrow\rangle, \qquad \hat{H}_i|\downarrow\rangle = -\mu|\downarrow\rangle, \qquad \hat{H}_i|\uparrow\downarrow\rangle = (U-2\mu)|\uparrow\downarrow\rangle \tag{3.16}$$

[5] Viewing the lattice a graph $\mathcal{G}(V,E)$ with atoms as vertices V and hopping directions $\hat{c}^{\dagger}_i\hat{c}_j$ as edges E, the edges can be segmented into two disjoint sets V_1, V_2 and fulfill the condition $\forall(e_1,e_2)\in E : (e_1 \in V_1 \wedge e_2 \in V_2)\vee(e_2 \in V_1 \wedge e_1 \in V_2)$.

[6] This only holds in our very constrained parameter space! The Mott insulating state does not directly imply antiferromagnetism; the Mott insulating phase suppresses charge fluctuations, and different magnetic ordering can be obtained, for example, on frustrated lattices.

[7] The challenge in the intermediate coupling region stems exactly from the fact that the Hamiltonian can not be simultaneously diagonalized in the hopping term which is diagonal in the localized Wannier basis for the Coulomb interaction.

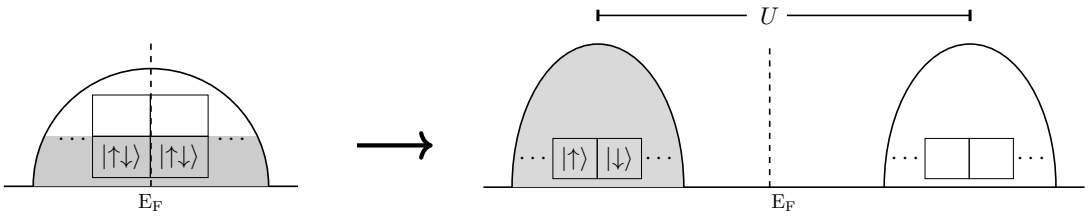

Figure 3.3: Illustration of formation of Hubbard bands from the perspective of photoemission spectroscopy, as computed through the spectral function. The left side shows a half-filled band with double-occupied states. The right side illustrates the band structure after the application of a strong Hubbard interaction. It now consists of 2 bands, one of which is completely filled, while the other (containing the double occupation states) is separated by an energy of U. The illustration was adapted from [167], where also the case of a doped system is shown.

$$\Rightarrow H_i = \mathrm{diag}\{0, -\mu, -\mu, U - 2\mu\} \tag{3.17}$$

Inserting the Hamiltonian in this basis into the Lehmann representation yields the partition function and the Green's function[8].

$$Z_i = \mathrm{Tr}\, e^{-\beta H_i} = 1 + 2e^{+\beta\mu} + e^{-\beta(U-2\mu)} \tag{3.18}$$

$$G^{\mathrm{AL}}_{ij,\sigma}(\tau) = -\delta_{ij}\frac{1}{Z}\,\mathrm{Tr}\left[e^{-(\beta-\tau)\hat{H}}\hat{c}_{\ i\sigma}e^{-\tau\hat{H}}\hat{c}^{\dagger}_{i\sigma}\right] = -\delta_{ij}\frac{1}{Z}\left[e^{\mu\tau} + e^{(\mu-U)\tau+\beta\mu}\right] \tag{3.19}$$

We can drop the spin index, as the Green's function does not depend on it for the SU(2) symmetric case. We perform a Fourier transformation to the Matsubara space and obtain:

$$G^{\nu}_{ij,\mathrm{AL}} = \delta_{ij}\int \mathrm{d}\tau e^{i\nu_n\tau}G_{ij}(\tau) = \frac{1}{Z}\left(\frac{1+e^{\beta\mu}}{i\nu_n+\mu} + \frac{e^{\beta\mu}+e^{-\beta(U-2\mu)}}{i\nu_n+\mu-U}\right)$$

In this limit, however, we can obtain a closed-form expression for the retarded Green's function and, subsequently, the spectral function.

$$G^{\mathrm{R},\nu}_{\mathrm{AL}} = \frac{1+e^{\beta\mu}}{Z}\frac{1}{\nu+\mu+i\eta} + \frac{e^{\beta\mu}+e^{-\beta(U-2\mu)}}{Z}\frac{1}{\nu+\mu-U+i\eta} \tag{3.20}$$

$$A^{\nu}_{\mathrm{AL}} = \frac{1+e^{\beta\mu}}{Z}\delta(\nu+\mu) + \frac{e^{\beta\mu}+e^{-\beta(U-2\mu)}}{Z}\delta(\nu+\mu-U) \tag{3.21}$$

The spectral function A^{ν}_{AL} consists of two δ peaks with an electron-density filling prefactor (see also the calculation preceding Eq. (3.20) for a justification). This particular form can be understood in the context of Fig. 3.3, where the Hubbard interaction splits a single band into two Hubbard bands separated by an energy U. It describes two possible excitations separated by an energy difference of U. A noteworthy remark is that the spectral function is precisely the same as in the non-interacting limit, with separated bands located at energy levels $-U/2$ and $U/2$ (see Sec. 3.4). However, the distinction in the physical situations between these two scenarios is reflected in the difference of the self-energies. For simplicity, we consider the half-filling case and assume a constant energy level $\epsilon_{\mathbf{k}} \equiv U$ for the non-interacting system, in accordance with our 2-band picture from above:

$$\begin{aligned}
\Sigma^{\nu}_{\mathrm{AL}} &= [G^{\nu}_{\mathrm{AL}}]^{-1} - [G^{\nu}_{U\to 0}]^{-1} \\
&= 2\left[\delta(\mathbf{k}-\mathbf{K})\left(\frac{1}{i\nu_n+\frac{U}{2}} + \frac{}{i\nu_n-\frac{U}{2}}\right)\right]^{-1} - \left[\frac{1}{i\nu_n+\frac{U}{2}+U}\right]^{-1} \\
&= \left[\frac{1}{i\nu_n-\frac{U^2}{4i\nu_n}}\right]^{-1} - i\nu_n + \frac{U}{2} + \epsilon(\mathbf{k}) = \left[i\nu_n - \frac{U^2}{4i\nu_n}\right] - \left[i\nu_n + \frac{U}{2} - U\right] \\
&= \frac{U}{2} - \frac{U^2}{4i\nu_n}
\end{aligned}$$

[8] This is also the way exact diagonalization methods solve the Hubbard model on finite lattice sizes. For example, the annihilation operators in this basis are: $c_\uparrow \doteq \begin{pmatrix} 0 & 1 & 0 & 0 \\ 0 & 0 & 0 & 0 \\ 0 & 0 & 0 & 1 \\ 0 & 0 & 0 & 0 \end{pmatrix}, c_\downarrow \doteq \begin{pmatrix} 0 & 0 & 1 & 0 \\ 0 & 0 & 0 & 1 \\ 0 & 0 & 0 & 0 \\ 0 & 0 & 0 & 0 \end{pmatrix}$. One then has to sum over the trace with 4 summands, of which one 2 survive in our case: $\langle\downarrow| e^{-\beta\hat{H}}\hat{c}_{\ \uparrow}(\tau)\hat{c}^{\dagger}_{\uparrow}|\downarrow\rangle = e^{\beta\mu}\langle\downarrow| e^{\hat{H}\tau}\hat{c}_{\ \uparrow}e^{-\hat{H}\tau}|\uparrow\downarrow\rangle = e^{\beta\mu}\langle\downarrow| e^{\hat{H}\tau}\hat{c}_{\ \uparrow}e^{-(U-2\mu)\tau}|\uparrow\downarrow\rangle = e^{\beta\mu}\langle\downarrow| e^{-\mu\tau}e^{-(U-2\mu)\tau}|\downarrow\rangle = e^{(\mu-U)\tau+\beta\mu}$ and $\langle 0| e^{-\beta\hat{H}}\hat{c}_{\ \uparrow}(\tau)\hat{c}^{\dagger}_{\uparrow}|0\rangle = \langle 0| e^{0}\hat{c}_{\ \uparrow}e^{-\hat{H}\tau}|\uparrow\rangle = e^{\mu\tau}$. Evaluation of the $\sigma = \downarrow$ Green's function yields the same result. For more details, see also Sec. 6.6.

As we will see in Sec. 3.3.3, this is not enough to explain important processes of the Hubbard Model and will therefore give quantitatively wrong results, as evident by the quantitative shortcomings of iterated perturbation theory [122], see also [246, Chapter 6]. The formal derivation for this result can be found in [66].

Correlations and self-energy

The distinction between noninteracting and atomic limits through the differences of the self-energies is somewhat unsatisfying because we need to impose the vanishing self-energy as additional knowledge for the $U = 0$ Green's function. Only then do we obtain the difference to the atomic limit Green's function, according to the Dyson equation Eq. (2.195). Moreover, while the self-energy does contain strong coupling interactions, namely Mott physics, the spectral function (as measured from experiments) cannot distinguish between two bands originating from a band insulator and a Mott insulator directly [9]. But by virtue of our argument in Sec. 2.4.3, the spectral function contains all information for the construction of the single-particle Green's function. Therefore, an argument can be made that strong correlations are inherently a two-particle property and can only be treated on an effective (or better, projected) level when considering one-particle quantities exclusively. Here, the effect of correlations can be obtained by the difference between the full two-particle Green's function and the product of single-particle ones. Similarly to the way the interacting and non-interacting Green's functions are connected via the self-energy, the factorization of $G^{(2)}$ into a product of single-particle Green's functions $G^{(1)}$ is prevented by correlation effects with the irreducible vertex $\Gamma^{\nu\nu'\omega}$ as the two-particle counterpart to the self-energy.

Two particle correlator and consistency

The two-particle Green's function and the fully irreducible vertex can also be obtained explicitly [205, Sec. 3.2] and [263]. The more complex structure and possible divergences do not lend themselves to a high-level discussion. However, we may use the technique from Sec. 4.4 and obtain a 2-particle correlator through the equation of motion. We use Eq. (2.16) to evaluate the time derivative, following (in our much simpler case because $U/t \to \infty$) [66, 65]:

$$\begin{aligned}
\frac{\partial \hat{c}_{\,i\sigma}}{\partial \tau} &= \left[\hat{c}_{\,i\sigma}, \hat{H}_{\,\mathrm{AL}}\right] = U \sum_j \left[\hat{c}_{\,i\sigma}, \hat{n}_{\,j\uparrow}\hat{n}_{\,j\downarrow}\right] - \mu \sum_{j\sigma'} \left[\hat{c}_{\,i\sigma}, \hat{n}_{\,j\sigma'}\right] \\
&\overset{\text{Eq. (2.19)}}{=} U \sum_{j\sigma} \left(\hat{n}_{\,j\uparrow}\left[\hat{c}_{\,i\sigma}, \hat{n}_{\,j\downarrow}\right] + \left[\hat{c}_{\,i\sigma}, \hat{n}_{\,j\uparrow}\right]\hat{n}_{\,j\downarrow}\right) - \mu \sum_{j\sigma'} \hat{c}_{\,i\sigma}\delta_{ij}\delta_{\sigma'\sigma} \\
&\overset{\text{Eq. (2.22)}}{=} U \sum_{j\sigma} \left(\hat{n}_{\,j\uparrow}\hat{c}_{\,i\sigma}\delta_{ij}\delta_{\sigma\downarrow} + \hat{c}_{\,i\sigma}\delta_{ij}\delta_{\sigma\uparrow}\hat{n}_{\,j\downarrow}\right) - \mu\hat{c}_{\,i\sigma} \\
&= U\hat{n}_{\,i\uparrow}\hat{c}_{\,i\downarrow} + U\hat{c}_{\,i\uparrow}\hat{n}_{\,i\downarrow} - \mu\hat{c}_{\,i\sigma} = U \sum_{\sigma'} \hat{c}_{\,i\sigma'}\hat{n}_{\,i\bar{\sigma}'} - \mu\hat{c}_{\,i\sigma}
\end{aligned} \tag{3.22}$$

$$\frac{\partial \hat{c}^\dagger_{i\sigma}}{\partial \tau} = -U \sum_{\sigma'} \hat{c}^\dagger_{i\sigma'}\hat{n}_{\,i\bar{\sigma}'} + \mu\hat{c}^\dagger_{i\sigma} \tag{3.23}$$

Inserting Eq. (3.23) in the definition of the Green's function Eq. (2.39), using the chain rule and $\partial_\tau \Theta(\tau) = \delta(\tau)$ yields:

$$\begin{aligned}
\Rightarrow \frac{\partial G^{(1)}_{i\sigma,\mathrm{AL}}(\tau)}{\partial \tau} &= \frac{\partial}{\partial \tau}\left[\Theta(\tau)\left\langle \hat{c}_{\,i\sigma'}(\tau)\hat{c}^\dagger_{i\sigma}\right\rangle + \Theta(-\tau)\left\langle \hat{c}^\dagger_{i\sigma}\hat{c}_{\,i\sigma'}(\tau)\right\rangle\right] \\
&= \delta(\tau) + \left\langle T\left(U \sum_{\sigma'} \hat{c}_{\,i\sigma'}(\tau)\hat{n}_{\,i\bar{\sigma}'}(\tau) - \mu\hat{c}_{\,i\sigma}(\tau)\right)\hat{c}^\dagger_{i\sigma}\right\rangle \\
&= \delta(\tau) + U\left\langle T\hat{c}_{\,i\sigma}(\tau)\hat{n}_{\,i\bar{\sigma}}(\tau)\hat{c}^\dagger_{i\sigma}\right\rangle - \mu G^{(1)}_{i\sigma,\mathrm{AL}}(\tau) \qquad (3.24) \\
&= \delta(\tau) + UG^{(2)}_{i\sigma,\mathrm{AL}}(\tau) - \mu G^{(1)}_{i\sigma,\mathrm{AL}}(\tau) \qquad (3.25)
\end{aligned}$$

We have dropped the j index due to the locality of the Hamiltonian (avoiding the δ_{ij} prefactors) and introduced the superscripts (1) and (2) to emphasize the coupling of lower to higher-order Green's functions[10]. This was, of course, expected after our considerations in the Green's functions chapter. However, in this special case, the hierarchy does not continue. This is a special case. because the density operator commutes with the Hamiltonian ($[\hat{H}_{\mathrm{AL}}, \hat{n}_{i\sigma}] = ...[\hat{n}_{j\sigma'}, \hat{n}_{i\sigma}] = 0 \Rightarrow \partial n/\partial\tau = 0$). We

[9] There are, however, numerous ways to approach the distinction between band and Mott insulators experimentally. One can, for example, make use of the fact that Mott bands exhibit particle-hole (local) excitations instead of band excitations (nonlocal). It is also possible to use other signatures of Mott physics (some of which we discuss in this chapter), such as doping-dependent spectral weight transfer between the charge-transfer band and the Mott gap [106]. See also Sec. 2.4.4 for a very brief overview.

[10] Note that we did not obtain the full two-particle Green's function here. The imaginary time arguments are contained to just one instead of three. One time argument is lost because we assumed symmetries in the one-particle Green's function and *then* derived the equation of motion instead of working with the unconstrained version.

furthermore need $\hat{n}_{i\sigma}\hat{n}_{i\sigma} = \hat{n}_{i\sigma}$ and can then evaluate the imaginary time derivative of the higher-order Green's function:

$$\begin{aligned}\frac{\partial G^{(2)}_{i\sigma,\mathrm{AL}}(\tau)}{\partial\tau} &= \delta(\tau)\langle\hat{n}_{i\bar{\sigma}}\rangle + U\left\langle T\left(U\sum_{\sigma'}\hat{c}_{\ i\sigma'}(\tau)\hat{n}_{\ i\bar{\sigma}'}(\tau) - \mu\hat{c}_{\ i\sigma}(\tau)\right)\hat{n}_{\ i\bar{\sigma}'}(\tau)\hat{c}^{\dagger}_{i\sigma}\right\rangle \\ &= \delta(\tau)\langle\hat{n}_{i\bar{\sigma}}\rangle + UG^{(2)}_{i\sigma,\mathrm{AL}}(\tau) - \mu G^{(2)}_{i\sigma,\mathrm{AL}}(\tau) \end{aligned} \tag{3.26}$$

After using the imaginary time formalism for the derivation of the consistency equations, we now switch back to Matsubara space solve Eq. (3.26), using use $\mathcal{F}[\delta(\tau)] = 1$ and $\mathcal{F}\left[\frac{\partial f(\tau)}{\partial\tau}\right] = i\nu_n f(i\nu_n)$:

$$G^{\nu,(2)}_{i\sigma,\mathrm{AL}} = \frac{\langle\hat{n}_{i\bar{\sigma}}\rangle}{i\nu_n + \mu - U} \tag{3.27}$$

$$\Rightarrow G^{\nu,(1)}_{i\sigma,\mathrm{AL}} = \frac{1-\langle\hat{n}_{i\bar{\sigma}}\rangle}{i\nu_n + \mu} + \frac{\langle\hat{n}_{i\bar{\sigma}}\rangle}{i\nu_n + \mu - U} \tag{3.28}$$

For one, this recovers the one-particle Green's previously obtained from the Lehmann representation in Eq. (3.20) with $\langle\hat{n}_{i\bar{\sigma}}\rangle = \frac{e^{\beta\mu}+e^{-\beta(U-2\mu)}}{Z}$. More importantly, it demonstrates the following:

Important 3.3.1.1 (Conclusions from the Atomic Limit)
(1) Correlation effects can be obtained naturally from the consideration of the higher-order Green's functions.
(2) The electron density contributes at the lowest order to the Green's functions at the one- and two-particle levels.

Observation (1) follows by considering we did not have to make an assumption about the existence of a free Green's function and the self-energy to arrive at Eq. (3.28). The single-particle Green's functions of the atomic and free limit can be mapped to each other by choosing a suitable dispersion relation $\epsilon_{\mathbf{k}} = \pm U/2$, as can be seen by comparison to the derivation in the limit of no interaction $U = 0$ below (see computation preceding Eq. (3.58)). This suggests that the lack of correlation effects in the $U = 0$ limit is specifically contained in the premature truncation of the correlator hierarchy and, therefore, a feature of the two-particle correlator.
Observation (2) might seem trivial at this point, but the lDΓA violates specifically the consistency of the electron densities when computed on the one- and two-particle levels. We will later introduce approximations in the equation of motion connecting both levels. That leads to a violation of the conservation of the particle number. The implication from this observation is that consequently the lowest-order tail contributions in the self-energy are then also no longer consistent. In Chapter 4, this will be discussed in more detail.

3.3.2 Hubbard Dimer

Prior to relaxing the $U/t \to \infty$ limit and permitting certain fluctuations, it is useful to develop an understanding of the underlying physics by considering the simplest version of the Hubbard model, one with only two sites. This Hubbard dimer is a minimal model example of a system in which to study Mott physics. It will prove useful because of its closed-form solution, which provides a first example of the interactions that are involved beyond the purely localized atomic limit. We summarize only some points that are conducive to the arguments in this chapter. A detailed derivation can be found, for example, in [188, Chapter 7] and [62]. Therefore, we also fix the number of electrons to that of the lattice sites.
The Hubbard dimer already has $4^2 = 16$ possible states without further restrictions. However, because we do not allow for fluctuations in particle number and the uniform interaction $U_{ijlk} = U$ does not allow for spin-flip terms, we can focus on a smaller sector of the Hilbert space. This is done by considering the two operators associated with these operations. They need to commute with the Hamiltonian if they leave the system invariant, and we can thus find a common block-diagonal form and diagonalize individual blocks (each of which has a pair of these two quantum numbers associated) independently. Here, we will consider the sector with total spin 0 and particle number 2 (i.e. half-filling) as an example. The basis for this block consists of the states $|\uparrow\downarrow,0\rangle, |\uparrow,\downarrow\rangle$ and $|\downarrow,\uparrow\rangle |\cdot,\uparrow\downarrow\rangle$, leading to the following Hamiltonian:

$$\begin{pmatrix} U & -t & -t & 0 \\ -t & 0 & 0 & -t \\ -t & 0 & 0 & -t \\ 0 & -t & -t & U \end{pmatrix} = V\,\mathrm{diag}\begin{pmatrix} E_- \\ 0 \\ U \\ E_+ \end{pmatrix} V^{-1} \tag{3.29}$$

With Eigenvectors for $U: \frac{1}{\sqrt{2}}(|0,\uparrow\downarrow\rangle - |\uparrow\downarrow,0\rangle)$ and $0: \frac{1}{\sqrt{2}}(|\downarrow,\uparrow\rangle - |\uparrow,\downarrow\rangle)$. $E_\pm$ is defined below.
We can make two observations here: (1) The separation between the energy levels of U (apart from a

constant energy shift because we did not include a chemical potential $\mu = U/2$ term) is an indication of the Mott gap already discussed above. (2) Taylor expansion around $U/t \to \infty$ results in the following asymptotic behavior beyond the zero-order Mott energy gap of U:

$$E_\pm = \frac{U}{2} \pm \frac{\sqrt{U^2 + 16t^2}}{2} = \frac{U}{2} \pm \left(\frac{U}{2} + \frac{4t^2}{U} + \mathcal{O}(t^4) \right) = \begin{cases} U + J \\ -J \end{cases} \tag{3.30}$$

This is the antiferromagnetic exchange coupling that governs the costs of spin flips between sites. Note that this exchange coupling appeared even though we did not include explicit non-local spin flip terms in the Coulomb interaction above (we set $U_{ijlk} = U$). We will see this term reemerging when approaching the limit $U/t \to \infty$ from the perspective of the projected subspace in Sec. 3.3.3, where this energy scale is determined by neighboring spins (anti-) aligning. In Fig. 3.4, the lowest and highest eigenvalues of the Hubbard dimer and the asymptotic behavior are shown in first order. We observe that the Heisenberg limit (see next section) is reached at $U/t \approx 3.5$. This qualitative behavior turns out to be transferable to more general situations. For example, the lDΓA results show convergence to this limit for the 3 dimensional cubic lattice in Sec. 7.1.

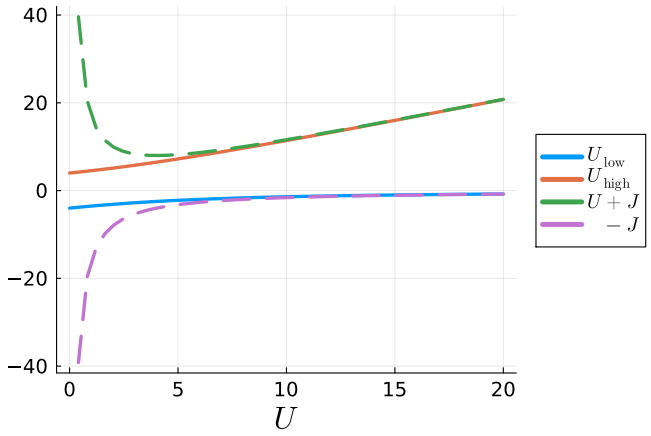

Figure 3.4: Hubbard dimer energies $\frac{U}{2} \pm \frac{\sqrt{U^2+16t^2}}{2}$ and their asymptotic behavior $J = \frac{4t^2}{U}$ and $U + J$.

An additional advantage of this model and our approach to the solution is the demonstration of the ED method. This is a commonly used numerical scheme to solve model systems. The Fock basis can, for example, be encoded with bitstrings of 1 and 0; the Hamiltonian is then constructed from inputs for a predefined model. Analogously to the approach by hand, the Hamiltonian is block diagonalized, using good quantum numbers of the system (in this example, N and S). Afterward, each block is diagonalized, using linear algebra routines (this could also mean only computing the largest or smallest by employing a Krylov subspace method, such as the Lanczos algorithm [152]). The exact diagonalization method has been heavily employed during my thesis for DMFT calculations and other projects Sec. 6.7. Although mostly replaced by continuous time quantum Monte Carlo (CTQMC) for state-of-the-art materials calculations, ED outperforms CTQMC when it comes to predictability and numerical performance at high to intermediate temperatures, which can outweigh the benefits of (theoretically) exact results of CTQMC. The code used to generate the ED results in this paragraph is available at [121]. For a more detailed discussion of the algorithm, see also Sec. 6.8.3.

Finally, we also want to discuss the Green's function in this limit. Using the Lehmann representation, we first find $\alpha = \alpha' = i, \sigma$. We notice that the sectors for different particle numbers are now connected, unlike in the atomic limit. Intuitively, this makes sense since the Green's function measures the impact of particle excitations. The derivation is a straightforward extension of the approach above, now with all sectors; see [62, Appendix A] for the derivation. We will follow the argument from that source, as it illustrates one more important concept for this thesis: the impact of correlations on the self-energy; here, specifically, the momentum dependence. This will be discussed in depth on a quantitative level for the 3-dimensional and 2-dimensional Hubbard model in Sec. 7.1 and Sec. 7.2 respectively. Finally, this also provides an introduction to the quantities used to describe the infinite coordination number limit in Sec. 3.6. The local Green's function (i.e. G_{ii}, not containing G_{ij} terms as given in [62, Eq. 9]; see also Sec. 3.6.

$$G_{ii} = \frac{w_+}{i\nu_n - E_- - t + \mu} + \frac{w_-}{i\nu_n - E_+ - t + \mu} + \frac{w_-}{i\nu_n - E_- + t + \mu} + \frac{w_+}{i\nu_n - E_+ + t + \mu} \tag{3.31}$$

with

$$w_\pm = \frac{1}{4} \pm \frac{t}{\sqrt{U^2 - 16t^2}} \tag{3.32}$$

The Fourier transform of the Hubbard dimer consists of two terms, one at the nodal ($k = \pi$) and anti-nodel ($k = 0$) points.

$$\Rightarrow G_k^\nu = \frac{1}{2}\frac{1}{i\nu_n + \mu + t - \Sigma_0^\nu} + \frac{1}{2}\frac{1}{i\nu_n + \mu + t - \Sigma_\pi^\nu} \tag{3.33}$$

$$\Sigma_k^\nu = \frac{U}{2} + \frac{U^2}{4}\frac{1}{i\nu_n + \mu - \frac{U}{2} - 3te^{ik}} \tag{3.34}$$

$$\Rightarrow \Delta\Sigma = \Sigma_\pi^\nu - \Sigma_0^\nu = \frac{U^2}{2}\frac{3t}{(3t)^2 - \left(i\nu_n + \mu - \frac{U}{2}\right)^2} \tag{3.35}$$

The last line demonstrates that a momentum differentiation appears depending on the filling, with a minimal difference of zero at half-filling. The DMFT method (which we will discuss in Sec. 3.6 and Sec. 5.1) neglects specifically this momentum dependence by scaling $t \propto 1/\sqrt{d}$ with $d \to \infty$. This obviously also leads to $\Delta\Sigma = 0$ in our toy example. However, specifically, the momentum differentiation of the Fermi surface is relevant to the pseudogap phase, one of the most interesting phenomena in the context of cuprate superconductors; see Sec. 7.2. The real part of the momentum dependence of the self-energy is directly linked to that of the Fermi surface through:

$$\lim_{\nu\to 0} \mathrm{Re}\,\Sigma^{\mathrm{R},\nu}_{\mathbf{k}_\mathrm{F}} = \mu - \epsilon_{\mathbf{k}_\mathrm{F}}, \tag{3.36}$$

It is desirable to develop methods that can capture the physics of this kind. A key aspect of the method developed during this thesis is the introduction of momentum dependence on top of the local[11] DMFT results.

This concludes our investigation of the Hubbard model in the effectively exactly solvable strong-coupling cases. Using the knowledge of the dominant energy contributions in the atomic limit and dimer case, we will now finish the considerations of the strong coupling regime by considering a mapping to the dominant subspace of the full Hilbert space.

3.3.3 t-J and Heisenberg model

Our goal for the last section of the investigation in the strong coupling regime is the generalization of the concept of spin-exchange interactions by presenting an abbreviated version of the derivation for the t–J model. Furthermore, we will be able to relax the condition of (almost) complete localization in this case. We do this in preparation for the thorough quantitative studies that involve considerably more numerics of the Hubbard model in 3 and 2 dimensions in Sec. 7.1 and Sec. 7.2 respectively.

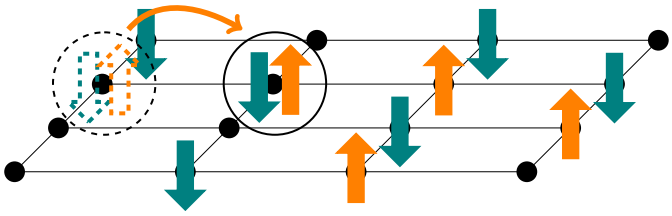

Figure 3.5: Illustration of a coupled pair propagating, giving an alternative picture to the allowed processes in the projected subspace of the $t-J$ model.

$t-J$ Model

We start by considering the Hubbard model at strong coupling, near half-filling, and putting no restrictions on the type of lattice, except for short-range hoppings. This does allow for frustration effects, for example, in triangular lattices.

We will now systematically derive how, on frustrated lattices or doped systems, double occupancies are unavoidable, but their formation still is on a different energy scale than the propagation of electrons or already doubly occupied electron/hole pairs. There are several approaches to exploit this energy separation in order to obtain a simplified description of the system. On bipartite lattices close to half-filling, the Hilbert space "almost" factories, i.e. a hopping between Hubbard bands discussed in Sec. 3.3.1 is strongly suppressed, but still possible. First, we relax the strong approximation of Sec. 3.3.1 and allow a kinetic energy term to act, still keeping the $U/t \gg 1$ limit and the accompanying energy separation of double-occupied states. We could completely truncate the Hilbert space, as was done in the derivation of the Hubbard model itself. However, leaving a small perturbative connection between two energetically very different sectors of the Hilbert space simplifies the model while still keeping some amount of coupling between the subspaces. This was first used by Schrieffer and Wolff in relating the AIM (see Sec. 3.7) to the Kondo model [224]. The central idea is to decouple the Hilbert space segments in the first order of a perturbative expansion. We will abbreviate some ideas of this projection of Hubbard to the $t-J$ model, following the review by Józef Spałek, who first derived the $t-J$ model [236]. Our goal is to partition the Hilbert space into two segments that are only "weakly" connected. The weak interaction between the subspaces can be quantified in terms of a perturbative expansion of an operator $\hat{S}$, which connects the two partitions of the Hilbert space only in second order

[11] We will quantify this in Sec. 3.6. Specifically, it allows to capture the non-perturbative physics of the Mott transition.

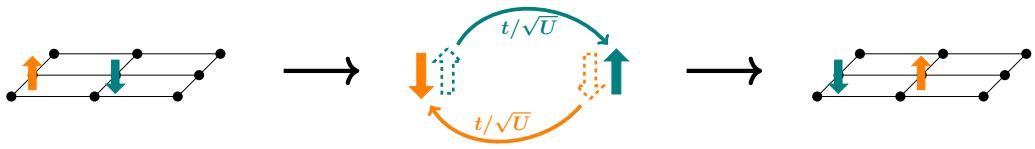

Figure 3.6: Illustration of the virtual hopping in the superexchange mechanism, with amplitude $J = \frac{t^2}{U}$. The process can be understood as suppressed by $1/U$ due to the virtual double occupancy during the exchange of the spins.

in the following way:

$$\hat{H}' = e^{\lambda \hat{S}} \hat{H} e^{-\lambda \hat{S}} = \hat{H} + \lambda[\hat{S}, \hat{H}] + \frac{\lambda^2}{2!}[\hat{S}, [\hat{S}, \hat{H}]] + \cdots \tag{3.37}$$

$$H_1 + \lambda[\hat{S}, \hat{H}_0] \stackrel{!}{=} 0 \tag{3.38}$$

In the strong coupling limit, we perturb around small $t/U = \lambda$. According to our initial goal, we want to separate the Hilbert space with double occupancies and will therefore rewrite the original Hubbard Hamiltonian, using operators for the creation and annihilation of double-occupied sites, a *doublon* state[12].

$$\hat{d}^\dagger = \hat{c}^\dagger_{i\sigma}(1 - \hat{n}_{i\bar{\sigma}}), \qquad \hat{d}_{\,i\sigma} = \hat{c}_{\,i\sigma}(1 - \hat{n}_{i\bar{\sigma}}), \qquad \nu_{i\sigma} = \hat{d}^\dagger_{i\sigma}\hat{d}_{\,i\sigma}, \tag{3.39}$$

In the context of this operator, we may interpret $\hat{d}^\dagger$ as the propagation of a bound state of two electrons. An illustration of such a pair propagating through the lattice is given in Fig. 3.5.

$$\hat{H} = \underbrace{-\sum_{\langle ij\rangle\sigma} t_{ij}\left(\hat{c}^\dagger_{i\sigma}\hat{c}_{\,j\sigma} + \hat{d}^\dagger_{i\sigma}\hat{d}_{\,j\sigma}\right) + U\sum_i \hat{n}_{i\uparrow}\hat{n}_{i\downarrow}}_{H_0} + \underbrace{\sum_{\langle ij\rangle\sigma}\left(\hat{d}^\dagger_{i\sigma}\hat{c}_{\,j\sigma} + \hat{c}^\dagger_{i\sigma}\hat{d}_{\,j\sigma}\right)}_{H_1} \tag{3.40}$$

Following [43], we now insert this Hamiltonian into the perturbative expansion Eq. (3.37) and use the Schrieffer-Wolff condition Eq. (3.38):

$$\Rightarrow \hat{H}' = \hat{H}_0 + \underbrace{\hat{H}_1 + t[\hat{S}, H_0]}_{=0} + t[\hat{S}, H_1] + \frac{t^2}{2!}[\hat{S}, [\hat{S}, \hat{H}_0]] + \frac{t^2}{2!}[\hat{S}, [\hat{S}, \hat{H}_1]] + \ldots \tag{3.41}$$

An important observation has to be noted here: Instead of the naïve approach that would treat the double occupancies themselves as a perturbative effect, this form treats the *formation* and *destruction* of double occupancies as perturbations, but already formed spin-up spin-down pairs still propagate. The condition Eq. (3.38) is met by the following ansatz ($[\hat{H}_1, \hat{d}^\dagger_{i\sigma}] = U\hat{d}^\dagger_{i\sigma}$):

$$\hat{S} = \sum_{\langle ij\rangle\sigma} t_{ij}\left(\hat{d}^\dagger_{i\sigma}\hat{c}_{\,j\sigma} - \hat{c}^\dagger_{i\sigma}\hat{d}_{\,j\sigma}.\right) \tag{3.42}$$

Lengthy calculation of the commutator $[\hat{S}, \hat{H}_1]$ (neglecting all terms involving creation of annihilation of doublons, i.e. uneven numbers of $\hat{d}^{(\dagger)}$ operators) due to the suppression of charge fluctuation in this subspace, leads to the following Hamiltonian [6, 101]:

$$H_{t-J,0} = -\sum_{\langle ij\rangle\sigma} t_{ij}\hat{d}^\dagger_{i\sigma}\hat{d}_{\,j\sigma} + \sum_{\langle ijk\rangle}\frac{t_{ij}t_{jk}}{U}\left(\hat{d}^\dagger_{i\uparrow}\hat{d}^\dagger_{j\downarrow} - \hat{d}^\dagger_{i\downarrow}\hat{d}^\dagger_{j\uparrow}\right)\left(\hat{d}_{\,j\uparrow}\hat{d}_{\,k\downarrow} - \hat{d}_{\,j\downarrow}\hat{d}_{\,k\uparrow}\right) \tag{3.43}$$

This is the full $t-J$ Hamiltonian. The first term propagates electrons but does not allow the creation or destruction of doubly occupied states. These are captured through virtual processes in the second term. An example of such a coupling is shown in Fig. 3.6.
For our purpose of approaching the driving mechanisms of increasingly strong coupling, there are still terms remaining that can be neglected. First, we will disregard the three-site hopping term, as it scales with t^2, and rewrite Eq. (3.43) with fermionic operators. Furthermore, we assume uniform hopping $t_{ij} \equiv t$:

$$H_{t-J} = -t\sum_{\langle ij\rangle\sigma}\hat{c}^\dagger_{i\sigma}\hat{c}_{\,j\sigma} + J\sum_{\langle ij\rangle}\left(\mathbf{S}_i\cdot\mathbf{S}_j - \frac{\hat{n}_i\hat{n}_j}{4}\right) \tag{3.44}$$

[12] We will leave out the $-\mu\sum_\sigma \hat{n}_\sigma$ term, implying half-filling. In fact, a solution including this term is rather complicated and is still the subject of current research [159]. The resulting segmentation of the Hilbert space includes additional processes beyond superexchange and three site hopping mechanisms, allowing additional doublon-holon interactions.

with the usual spin operator in terms of the vector of Pauli matrices $\boldsymbol{\sigma}$ (see Sec. 2.4.6):

$$\hat{\mathbf{S}}_i = \frac{1}{2}\begin{pmatrix}\hat{c}_{i\uparrow}\\ \hat{c}_{i\downarrow}\end{pmatrix}^\dagger \boldsymbol{\sigma}_{\sigma\sigma'}\begin{pmatrix}\hat{c}_{i\uparrow}\\ \hat{c}_{i\downarrow}\end{pmatrix} \tag{3.45}$$

Here we have also explicitly written the antiferromagnetic exchange coupling $J = \frac{4t^2}{U}$. This model still describes many important aspects of the Hubbard Hamiltonian for strong interactions while being defined over a simpler Hilbert space.

Heisenberg Model

Our final consideration is again concerned with the limit in which charge fluctuations are completely frozen, this time from the perspective of the Hilbert subspace consideration above. In Sec. 7.1 we will use this limit as confirmation that the strong-coupling physics is indeed recovered by our non-local correction approach. Neglecting all charge fluctuations in Eq. (3.44), but allowing for anisotropic exchange interactions $J \to J_{ij}$, we arrive at the Heisenberg model:

$$H_{\mathrm{H}} = -\frac{1}{2}\sum_{ij} J_{ij}\mathbf{S}_i \cdot \mathbf{S}_j \tag{3.46}$$

Where $J_{ij} = J_{ji}$ and the factor $\frac{1}{2}$ account for double counting. From the fact that the Heisenberg model is obtained as the strong coupling limit of the Hubbard model, we can (again) deduce that the Hubbard model will prefer antiferromagnetic ordering with no charge fluctuations at strong coupling when permitted by the lattice. This limit will be used in Sec. 7.1 in order to verify correct critical behavior in the strong coupling limit. However simple, this model still contains rich physics encapsulated by spin dynamics that stem from magnetic ordering, such as frustrated magnetism and spin liquids, that do not require charge carrier mobility.

3.4 Weak Coupling

In this section, we discuss the opposite limiting case from the previous one. The Hamiltonian now becomes (almost) diagonal in the momentum instead of the position basis, and we can employ a new set of approximation methods. Mean-field approaches are particularly useful and will, therefore, be discussed in some detail. Later in this chapter, we will expand this and introduce the DMFT method as a very successful approach to describe local correlations in the Hubbard model.
We start with the obvious fact that the Hubbard model approaches the solution of the bare dispersion in the limit $U = 0$, where we recover the tight-binding solution of the noninteracting free Fermi gas (we only consider more than one spatial dimension). However, even at arbitrarily small distances from this limit, nontrivial physics starts to reemerge. For example, the limits $\lim_{\searrow 0} U/t$ and $\lim_{\nearrow 0} U/t$ are not adiabatically connected [198]. Nevertheless, being concerned with the repulsive Hubbard model exclusively, it is reasonable to assume that physics close to the non-interacting case can be attributed to nesting effects of the Fermi surface (which could be deformed in the context of Fermi liquid theory, Sec. 2.5).
Let us first look at the Green's function in the noninteracting case and then move on to some results in the vicinity thereof, turning to an overview of weak coupling schemes.
Because the Hubbard Hamiltonian is diagonalizable without the Coulomb interaction, we can directly switch to the momentum basis for the creation and annihilation operators [13]:

$$U = 0 \Rightarrow \hat{H}_{U=0} = -\sum_{ij\sigma} t_{ij}\hat{c}^\dagger_{i\sigma}\hat{c}_{j\sigma} - \mu\sum_{i\sigma}\hat{n}_{i\sigma} = -\sum_{ij\sigma}(t_{ij}+\mu\delta_{ij})\,\hat{c}^\dagger_{i\sigma}\hat{c}_{j\sigma} \tag{3.47}$$

$$\hat{H}_{U=0} = (\epsilon_{\mathbf{k}\sigma} - \mu)\, n_{\mathbf{k}\sigma} \tag{3.48}$$

$$G_{\mathbf{k}\sigma}(\tau) = \langle e^{-\beta\hat{H}}\hat{c}_{\mathbf{k}\sigma}(\tau)\hat{c}^\dagger_{\mathbf{k}\sigma}\rangle = \begin{cases}\frac{1}{Z}\operatorname{Tr} e^{-\beta\hat{H}}\hat{c}_{\mathbf{k}\sigma}(\tau)\hat{c}^\dagger_{\mathbf{k}\sigma}, & 0<\tau<\beta\\ -\frac{1}{Z}\operatorname{Tr} e^{-\beta\hat{H}}\hat{c}^\dagger_{\mathbf{k}\sigma}\hat{c}_{\mathbf{k}\sigma}(\tau), & 0>\tau>-\beta\end{cases} \tag{3.49}$$

$$= \begin{cases}\frac{1}{Z}\operatorname{Tr} e^{-\beta\hat{H}}(1-\hat{c}^\dagger_{\mathbf{k}\sigma}\hat{c}_{\mathbf{k}\sigma}(\tau)), & 0<\tau<\beta\\ -\frac{1}{Z}\operatorname{Tr} e^{-\beta\hat{H}}\hat{c}^\dagger_{\mathbf{k}\sigma}\hat{c}_{\mathbf{k}\sigma}(\tau), & 0>\tau>-\beta\end{cases} = \begin{cases}e^{-\beta\epsilon_{\mathbf{k}}\tau}(1-n_{\mathrm{F}}(\epsilon_{\mathbf{k}})), & 0<\tau<\beta\\ -e^{-\beta\epsilon_{\mathbf{k}}}n_{\mathrm{F}}(\epsilon_{\mathbf{k}}), & 0>\tau>-\beta\end{cases} \tag{3.50}$$

With the Fermi distribution $n_{\mathrm{F}}(\epsilon_{\mathbf{k}}) = \frac{1}{e^{\beta\epsilon_{\mathbf{k}}}+1}$. We therefore obtain the free Green's function in imaginary time and frequency space as:

$$G_{\mathbf{k}}(\tau) = e^{-\beta\epsilon_{\mathbf{k}}}\left(\Theta(\tau)(1-n_{\mathrm{F}}(\epsilon_{\mathbf{k}})) + n_{\mathrm{F}}(\epsilon_{\mathbf{k}})\Theta(-\tau)\right) = e^{-\beta\epsilon_{\mathbf{k}}}\left(n_{\mathrm{F}}(\epsilon_{\mathbf{k}}) - \Theta(\tau)\right) \tag{3.51}$$

$$G^{i\nu_n}_{\mathbf{k}} = \frac{1}{i\nu_n + \mu - \epsilon_{\mathbf{k}}} \tag{3.52}$$

[13] as mentioned before, the kinetic part of Hamiltonian is diagonal in the momentum basis, while the interaction part is diagonal in the position basis, making both parts not simultaneously diagonalizable

The analytic continuation to the real frequency Green's function yields (using the Sokhotski–Plemelj theorem and the Cauchy principal value):

$$G^{\nu}_{\mathbf{k}} = \frac{1}{\nu + \mu - \epsilon_{\mathbf{k}} \pm i\eta} = \mathcal{P}\frac{1}{\nu + \mu - \epsilon_{\mathbf{k}}} \pm i\pi\delta(\nu + \mu - \epsilon_{\mathbf{k}}) \tag{3.53}$$

From this, we follow with the definition of the spectral function in Eq. (2.102):

Important 3.4.0.1 (DOS as Limit of the Spectral Function)
From Eq. (3.53)*, we obtain the spectral function in the non-interacting limit:*

$$A^{\nu}_{\mathbf{k}} = 2\pi\delta(\nu + \mu - \epsilon_{\mathbf{k}}) \tag{3.54}$$

$$\Rightarrow A^{\nu} = \int \mathrm{d}\mathbf{k}\delta(\nu + \mu - \epsilon_{\mathbf{k}}) = D(E) \tag{3.55}$$

This demonstrates that the $\mathbf{k}$*-integrated spectral function becomes the DOS in the noninteracting limit (the normalization factors of* π *have been absorbed into the integral).*

As in the previous section, we can also employ the equation-of-motion approach here. We are specifically interested in how the two-particle Green's function looks in the noninteracting limit after we discovered in Sec. 3.3.1 that it encapsulates the correlation physics. As before, we calculate the derivative of the Green's function by employing the Heisenberg equation of motion first for the creation and annihilation operators:

$$\begin{aligned}
\frac{\partial \hat{c}_{l\sigma}}{\partial\tau} &= [\hat{c}_{l\sigma}, \hat{H}_{U=0}] = \sum_{ij,\sigma'} t_{ij}[\hat{c}_{i\sigma}, \hat{c}_{j\sigma'}\hat{c}^{\dagger}_{j\sigma'}] - \mu\sum_{j\sigma'}[\hat{c}_{l\sigma}, \hat{n}_{j\sigma'}] \\
&\overset{\text{Eq. (2.20)}}{=} \sum_{ij,\sigma'} t_{ij}\left(\{\hat{c}_{l\sigma}, \hat{c}_{j\sigma'}\}\hat{c}^{\dagger}_{j\sigma'} - \hat{c}_{j\sigma'}\{\hat{c}_{l\sigma}, \hat{c}^{\dagger}_{j\sigma'}\}\right) - \mu\sum_{j\sigma'}[\hat{c}_{l\sigma}, \hat{n}_{j\sigma'}] \\
&= -\sum_{ij,\sigma'} t_{ij}\hat{c}_{j\sigma'}\delta_{lj}\delta_{\sigma\sigma'} - \mu\hat{c}_{l\sigma} \\
&= -\sum_{i} t_{il}\hat{c}_{i\sigma} - \mu\hat{c}_{l\sigma}
\end{aligned} \tag{3.56}$$

This result allows us to calculate the derivative of the Green's functions:

$$\begin{aligned}
\Rightarrow \frac{\partial G^{(1)}_{ij,\sigma,U=0}(\tau)}{\partial\tau} &= \delta(\tau)\delta_{ij} - \left\langle T\sum_{j}\left(t_{ij}\hat{c}_{i\sigma}(\tau) - \mu\delta_{ij}\hat{c}_{i\sigma}(\tau)\right)\hat{c}^{\dagger}_{j\sigma}\right\rangle \\
&= \delta(\tau)\delta_{ij} - \sum_{ij} t_{ij}\left\langle T\hat{c}_{i\sigma}(\tau)\hat{c}^{\dagger}_{j\sigma}\right\rangle - \left\langle T\mu\delta_{ij}\hat{c}_{i\sigma}(\tau)\hat{c}^{\dagger}_{j\sigma}\right\rangle
\end{aligned} \tag{3.57}$$

Analogous to the previous calculation after Eq. (3.26), we Fourier transform and solve to obtain the equation of motion and finally an explicit expression for the single-particle Green's function:

$$i\nu_n G^{\nu,(1)}_{\mathbf{k}\sigma,U=0} = \mathbb{1} + \mu G^{\nu,(1)}_{\mathbf{k}\sigma,U=0} - \epsilon_{\mathbf{k}} G^{\nu,(1)}_{\mathbf{k}\sigma,U=0} \tag{3.58}$$

$$\Rightarrow G^{\nu,(1)}_{\mathbf{k}\sigma,U=0} = \frac{1}{i\nu_n + \mu - \epsilon_{\mathbf{k}}} \tag{3.59}$$

Again, this reproduces the Green's function obtained through our diagonalization approach. But compared to the case of the atomic limit in Sec. 3.3.1, the hierarchy of higher-order correlators ends. This time it does not even yield a 2-particle Green's function. As discussed in the previous section, correlation effects are not captured explicitly on the single-particle level, whereas the two-particle level incorporates them natively.

3.4.1 Nesting and Slater Ferromagnetism

In the simple cubic lattice with lattice constant a at half-filling, the Fermi surface can be connected by a constant vector $\mathbf{Q} = (\pi/a, \pi/a, \dots)$, with

$$\epsilon_{\mathbf{k}+\mathbf{Q}} = \epsilon_{\mathbf{k}} \tag{3.60}$$

This property is illustrated for 2 dimensions in Fig. 3.7 The response function without interactions (see also Sec. 5.2.1) is given by the bare susceptibility.

$$\chi^{\omega}_{0,\mathbf{q}} = -\beta\sum_{\mathbf{k}} G^{\nu+\omega}_{0,\mathbf{k}+\mathbf{q}} G^{\nu}_{0,\mathbf{k}} = \sum_{\mathbf{k}} \frac{n_{\mathrm{F}}(\epsilon_{\mathbf{k}}) - n_{\mathrm{F}}(\epsilon_{\mathbf{k}+\mathbf{q}})}{i\omega_m + \epsilon_{\mathbf{k}+\mathbf{q}} - \epsilon_{\mathbf{k}}} \tag{3.61}$$

$$\overset{\text{Eq. (3.60)}}{=} \int_{-B}^{B} \frac{D_d(\epsilon)}{\epsilon}\tanh\left(\frac{\beta\epsilon}{2}\right)\mathrm{d}\epsilon \tag{3.62}$$

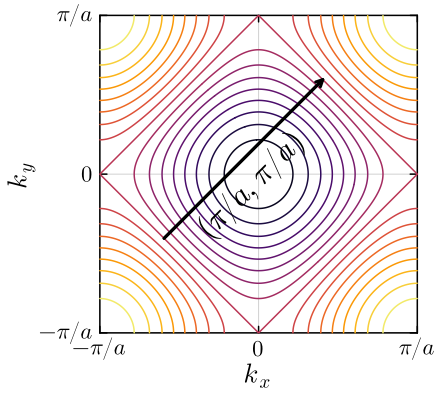

Figure 3.7: Illustration of the Fermi surface of the two-dimensional square lattice (unit ϵ_F/t). In blue, the nesting vector $(\pi/a, \pi/a)$ connecting two parts of the Fermi surface is shown.

With $D_d(\epsilon)$ being the d-dimensional density of states with a bandwidth B. This function will have a finite value for most dimensions, as shown in Fig. 3.9, and we obtain a logarithmically divergent susceptibility for low temperatures $\chi_{0,\mathbf{Q}} \sim 2D(0)\ln(\beta E_0)$ (with $E_0 \sim B$). The two-dimensional density of states in Fig. 3.9 has a van-Hove singularity at $\epsilon = 0$. This leads to a quadratic enhancement of the susceptibility at the ordering vector $\mathbf{Q} = (\pi/a, \pi/a)$ over $\mathbf{q} = 0$, indicating antiferromagnetic ordering [61, Sec. 6.2.1]. This tendency towards antiferromagnetic ordering through an instability of the susceptibility introduced by a nesting vector is known as Slater antiferromagnetism. This Hartree-Fock approach, therefore, predicts antiferromagnetic ordering at all interaction strengths, with a Néel temperature at weak interactions $U \ll t$ is then given by [61, Sec. 6.4]:

$$T_N \sim E_0 e^{-\frac{1}{UD(0)}} \qquad (d > 2) \tag{3.63}$$

$$T_N \sim t e^{-2\pi\frac{t}{U}} \qquad (d = 2) \tag{3.64}$$

In two dimensions, this is an obvious violation of the Mermin-Wagner theorem Sec. 4.5.2. However, the qualitative result of an onset local moment ordering in this temperature range will remain true. Methods beyond the mean-field treatment of this Hartree-Fock approach, that take additional correlations into account, will then lower the Néel temperature. We discuss this in more depth for the 3 dimensional case in Sec. 7.1.

3.4.2 Mean Field Treatment: Stoner Criterion and Pauli Susceptibility

This section serves two purposes: (i) we will discuss a simple (and analytically solvable) mean-field theory; (ii) it gives us the opportunity to discuss susceptibilities for the evaluation of dynamic properties of a system. We have already encountered the simplest versions of this in the case of the Hubbard dimer in Sec. 3.3.2, where the momentum was restricted to 0 or π.
A weakly interacting system can be well described through the following mean-field idea: Consider a single electron in a static potential from the ionic lattice. This single-particle problem can be easily solved and yields a potential for other electrons. Now, this potential can be "copied" to all other electrons in the system, and the new total potential energy is a superposition of all these copies of the single-particle potential. This gives rise to a new single-particle problem, which can be solved, yielding a new potential that can be copied to the other electrons and so on. If this process has a fixed point, i.e. there is a self-consistent solution, we call this the mean-field solution. We will explore two variants of this idea in this chapter: the traditional mean-field method here will lead us to results in the weak-coupling regime, where the itinerant magnetic order arises from delocalization of the electrons (i.e. Slater determinants), and later we will discuss DMFT in Sec. 5.1, which expands around a complementary limit of complete localization.

Stoner Mean-Field Model

In the following, we will consider the Hubbard model in a mean-field decoupling approach, yielding the same results as with a Slater variation Ansatz (therefore, we will also call this Slater mechanism in Sec. 7.1). The result will be a ferromagnetic ordering because of the way we employ the mean-field decoupling scheme here. The aim is to introduce mean-field methods in a concrete example. The concrete ordering vector is secondary, and we will discuss how to obtain antiferromagnetic ordering at the end of the section.
For the following, it is more convenient to work with the Hubbard interaction term in momentum representation. Fourier transformation and conservation of momentum yield (we absorb the normalization

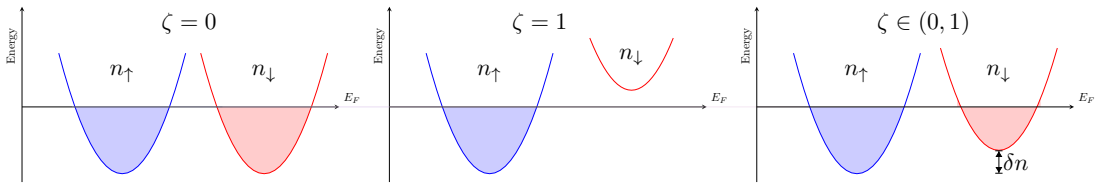

Figure 3.8: Illustration for ferromagnetic differentiation of up and down densities, as obtained by the Stoner model. the DOS for the three different regions of $\zeta = \frac{n_\uparrow - n_\downarrow}{n_\uparrow + n_\downarrow}$ from Eq. (3.76) are shown. δn marks the difference in occupation numbers.

constants into the sum, as usual):

$$\hat{H} = -\sum_{\mathbf{k}\sigma} \epsilon_{\mathbf{k}} \hat{c}^\dagger_{\mathbf{k}\sigma} \hat{c}_{\mathbf{k}\sigma} + \frac{U}{2} \sum_{\substack{\mathbf{k}\mathbf{k}'\mathbf{q} \\ \sigma\sigma'}} \hat{c}^\dagger_{\mathbf{k}+\mathbf{q},\sigma} \hat{c}^\dagger_{\mathbf{k}'-\mathbf{q},\sigma'} \hat{c}_{\mathbf{k}',\sigma'} \hat{c}_{\mathbf{k},\sigma} \tag{3.65}$$

This index convention also provides an intuitive interpretation of the Coulomb interaction in momentum space: two electrons with momentum $\mathbf{k}$ and $\mathbf{k}'$ exchange momentum $\mathbf{q}$ in a collision with amplitude U. We now apply the mean-field decoupling, i.e. we neglect fluctuations $\delta\hat{X}$ of second order around the mean-field $\langle\hat{X}\rangle$ (the normal expected value from the previous chapter), giving an abbreviated derivation of the argument found in many textbooks, for example, in [39].

$$\hat{X} = \langle\hat{X}\rangle + \left(\hat{X} - \langle\hat{X}\rangle\right) = \langle\hat{X}\rangle + \delta\hat{X} \tag{3.66}$$

$$\begin{aligned} \Rightarrow \hat{X}\hat{Y} &= \hat{X}\langle\hat{Y}\rangle + \delta\hat{X}\langle\hat{Y}\rangle + \delta\hat{Y}\langle\hat{X}\rangle + \delta\hat{X}\delta Y = \hat{X}\langle\hat{Y}\rangle + \left(\hat{X} - \langle\hat{X}\rangle\right)\langle\hat{Y}\rangle + \left(\hat{Y} - \langle\hat{Y}\rangle\right)\langle\hat{X}\rangle + \delta\hat{X}\delta Y \\ &\approx \hat{X}\langle\hat{Y}\rangle + \langle\hat{X}\rangle\hat{Y} - \langle\hat{Y}\rangle\langle\hat{X}\rangle \end{aligned} \tag{3.67}$$

Furthermore, we make the mean-field assumption that the interaction is only acting for $\mathbf{k} = \mathbf{k}'$

$$\langle\hat{c}^\dagger_{\mathbf{k}\sigma}\hat{c}_{\mathbf{k}'\sigma}\rangle = \delta_{\mathbf{k}\mathbf{k}'} n_{\mathbf{k}\sigma} \tag{3.68}$$

Applying this to the Hubbard Hamiltonian we obtain the mean-field version of the Hamiltonian, using $\hat{c}^\dagger_{\mathbf{k},\sigma}\hat{c}^\dagger_{\mathbf{k},\sigma} = \hat{c}_{\mathbf{k},\sigma}\hat{c}_{\mathbf{k},\sigma} = 0$ and the usual commutator relations Eq. (2.21) (we follow [39, Chapter 4]):

$$\begin{aligned} \hat{H}_{\mathrm{MF}} &= -\sum_{\mathbf{k}\sigma} \epsilon_{\mathbf{k}} \hat{c}^\dagger_{\mathbf{k}\sigma}\hat{c}_{\mathbf{k}\sigma} + \frac{U}{2} \sum_{\substack{\mathbf{k}\mathbf{k}',\mathbf{q} \\ \sigma\sigma'}} \hat{c}^\dagger_{\mathbf{k}+\mathbf{q},\sigma}\hat{c}^\dagger_{\mathbf{k}'-\mathbf{q},\sigma'}\hat{c}_{\mathbf{k}',\sigma'}\hat{c}_{\mathbf{k},\sigma} \\ &\approx \hat{H}_{\mathrm{kin}} + \frac{U}{2} \sum_{\substack{\mathbf{k}\mathbf{k}'\mathbf{q} \\ \sigma\sigma'}} \Big[\langle\hat{c}^\dagger_{\mathbf{k}+\mathbf{q},\sigma}\hat{c}_{\mathbf{k},\sigma}\rangle \hat{c}^\dagger_{\mathbf{k}'-\mathbf{q},\sigma'}\hat{c}_{\mathbf{k}',\sigma'} + \hat{c}^\dagger_{\mathbf{k}+\mathbf{q},\sigma}\hat{c}_{\mathbf{k},\sigma}\langle\hat{c}^\dagger_{\mathbf{k}'-\mathbf{q},\sigma'}\hat{c}_{\mathbf{k}',\sigma'}\rangle - \langle\hat{c}^\dagger_{\mathbf{k}+\mathbf{q},\sigma}\hat{c}_{\mathbf{k},\sigma}\rangle\langle\hat{c}^\dagger_{\mathbf{k}'-\mathbf{q},\sigma'}\hat{c}_{\mathbf{k}',\sigma'}\rangle \\ &\qquad - \langle\hat{c}^\dagger_{\mathbf{k}+\mathbf{q},\sigma}\hat{c}_{\mathbf{k}',\sigma'}\rangle\hat{c}^\dagger_{\mathbf{k}'-\mathbf{q},\sigma'}\hat{c}_{\mathbf{k},\sigma} - \hat{c}^\dagger_{\mathbf{k}+\mathbf{q},\sigma}\hat{c}_{\mathbf{k}',\sigma'}\langle\hat{c}^\dagger_{\mathbf{k}'-\mathbf{q},\sigma'}\hat{c}_{\mathbf{k},\sigma}\rangle + \langle\hat{c}^\dagger_{\mathbf{k}+\mathbf{q},\sigma}\hat{c}_{\mathbf{k}',\sigma'}\rangle\langle\hat{c}^\dagger_{\mathbf{k}'-\mathbf{q},\sigma'}\hat{c}_{\mathbf{k},\sigma}\rangle \Big] \\ &\overset{\text{Eq. (3.68)}}{=} \hat{H}_{\mathrm{kin}} + \frac{U}{2} \sum_{\substack{\mathbf{k}\mathbf{k}'\mathbf{q} \\ \sigma\sigma'}} \Big[\delta_{\mathbf{q}0} n_{\mathbf{k}\sigma} \left(\hat{c}^\dagger_{\mathbf{k}',\sigma'}\hat{c}_{\mathbf{k}',\sigma'} + \hat{c}^\dagger_{\mathbf{k},\sigma}\hat{c}_{\mathbf{k},\sigma} - n_{\mathbf{k}'\sigma'} \right) \\ &\qquad - \delta_{\mathbf{k}',\mathbf{k}+\mathbf{q}} n_{\mathbf{k}\sigma} (\hat{c}^\dagger_{\mathbf{k}'-\mathbf{q},\sigma'}\hat{c}_{\mathbf{k},\sigma} + \hat{c}^\dagger_{\mathbf{k}+\mathbf{q},\sigma}\hat{c}_{\mathbf{k}',\sigma'} - \delta_{\sigma\sigma'} n_{\mathbf{k}\sigma'}) \Big] \end{aligned}$$

We can now also decouple sums over momenta $\mathbf{k}$ and $\mathbf{k}'$, since these only appear in the mean-field parameters and operators separately. with

$$n_\sigma = \sum_{\mathbf{k}} n_{\mathbf{k}\sigma} = \sum_{\mathbf{k}} \langle\hat{c}^\dagger_{\mathbf{k}\sigma}\hat{c}_{\mathbf{k}\sigma}\rangle_{\mathrm{Mf}}, \tag{3.69}$$

This allows us to define:

$$\hat{H}_{\mathrm{MF}} = -\sum_{\mathbf{k}\sigma} \hat{c}^\dagger_{\mathbf{k},\sigma}\hat{c}_{\mathbf{k},\sigma}\epsilon^{\mathrm{MF}}_{\mathbf{k}\sigma} - U\sum_{\sigma\sigma'} n_\sigma n_{\sigma'} + U\sum_\sigma n_\sigma^2 \tag{3.70}$$

With the mean-field dispersion

$$\epsilon^{\mathrm{MF}}_{\mathbf{k}\sigma} = \epsilon_{\mathbf{k}} + U\sum_{\sigma'} n_{\overline{\sigma}} \tag{3.71}$$

Using the assumption of a free electron gas at zero temperature (i.e. the Fermi function is a Heaviside function), we can determine the mean field parameters, i.e. fillings for spin up and down. This is a self-consistency equation, as is usual with mean-field theories (see also Sec. 5.1):

$$n_\sigma \overset{!}{=} \sum_{\mathbf{k}} D(\epsilon^{\mathrm{MF}}_{\mathbf{k}\sigma}) = \sum_{\mathbf{k}} n_{\mathrm{F}}(\epsilon^{\mathrm{MF}}_{\mathbf{k}\sigma}) \tag{3.72}$$

$$= \int \frac{\mathrm{d}\mathbf{k}}{(2\pi)^3} \Theta\left(\mu - \frac{\mathbf{k}^2}{2m_\mathrm{e}} - U n_{\overline{\sigma}}\right) \tag{3.73}$$

$$\Rightarrow \mu = \frac{(6\pi n_\sigma)^{2/3}}{2m_\mathrm{e}} + U n_{\overline{\sigma}} \tag{3.74}$$

These two equations (for $\sigma = \uparrow$ and $\sigma = \downarrow$) can be solved (e.g. [39, Eq. 4.47]):

$$\zeta = \frac{n_\uparrow - n_\downarrow}{n_\uparrow + n_\downarrow}, \qquad \gamma = \frac{2m_\mathrm{e} U (n_\uparrow + n_\downarrow)^{1/3}}{(3\pi^2)^{2/3}} \tag{3.75}$$

$$\gamma\zeta = (1+\zeta)^{2/3} - (1-\zeta)^{2/3} \tag{3.76}$$

Allowing for three qualitatively different solutions: $\zeta = 0$, $\zeta = 1$ and $\zeta \in (0,1)$. The solutions correspond to a normal state (no difference in the occupation of up and down electrons), a strong ferromagnet, and a weak ferromagnet.
In Fig. 3.8 the three solutions are illustrated. We can observe from the ranges of $\gamma \propto U$ that the mean-field treatment predicts a wrong solution (ferromagnetic instead of antiferromagnetic) at strong coupling. ⚠This is an effect of the way we decoupled the operators in the interaction term of Eq. (3.65)! Since we chose to couple the mean field with an ordering vector of $\mathbf{q} = 0$, the effective background field made it advantageous for a spin to align with this field, thus amplifying the self-consistent solution of all spins aligning and strengthening this field. However, had we chosen $\langle \hat{c}^\dagger_{\mathbf{k}} \hat{c}_{\mathbf{k}+\mathbf{q}} \rangle$ for $\mathbf{q} = (\pi, \pi, \pi)$, antiferromagnetic ordering would have been preferable.
This emphasizes a weakness of mean-field theories: One has to understand the dominant physics of the system before applying a mean-field decoupling scheme because the predictions of the resulting model qualitatively depend on that choice. This deficiency can also be remedied by investigating the ordering with a different scheme first. The RPA susceptibility $\chi^{\omega=0}_{0,\mathbf{q}}$, discussed in Sec. 5.2.1, will show an instability at $\mathbf{q} = \mathbf{0}$ in the dilute limit $n \ll 1$ and an antiferromagnetic ($\mathbf{q} = \mathbf{\Pi}$) ordering, due to the nesting property from the last section, around half-filling.

3.5 Summary

In this section, we have given a brief overview of the energy scales and magnetic properties of the Hubbard model on bipartite lattices (specifically, this neglects the effects of frustration, leading to substantial changes in the magnetic ordering because of the suppression of antiferromagnetism) in more than one spatial dimension and in the limit of strong and weak coupling. Here, we only focused on broad observations to develop a general picture of applicable conceptualizations, leaving detailed discussion to the next chapter. At half-filling, we observed an opening of an energy gap from weak to strong coupling, proportional to the Hubbard U, called the Mott gap. Away from half-filling, charge fluctuations, previously suppressed by the Mott phase, start to reemerge. Here, we have discussed magnetic ordering. In the strong coupling regime, the Heisenberg exchange coupling emerged as the defining feature for the onset of this limit, leaving us with the interpretation of a local moment-driven magnetization. In the intermediate to strong coupling, we also found that the virtual superexchange mechanism, through the derivation of the $t-J$ model, is an important constituent of the governing physics.
The weak coupling regime was treated as a Fermi liquid, and we used the opportunity to introduce the concept of mean-field theories (with the example of the Stoner model) and description of second-order phase transitions in terms of susceptibilities. The description through Fermi-liquid theory has already been discussed in Sec. 2.5.
Until now, the discussion served purely to set the stage for our detailed discussion of the Hubbard model for three- and two dimensions in Sec. 7, leaving a comprehensive overview of the current results on the Hubbard model to the literature, for example [13, 198].
The next section still discusses a limit of the Hubbard model but already marks the transition to the methods chapter, as it will become important only in the context of DMFT.

3.6 Infinite Coordination Number

This section discusses the extremely important (for this thesis) limiting case of infinite coordination number. We will discuss here how the Hubbard model can be mapped to the Anderson impurirty model (see next section) in this case. Subsequently, in Sec. 5.1, we will discuss the DMFT method as an approximate solution for the Hubbard model before moving on to the corrections necessary to remedy the infinite coordination number approximation in 2 and 3 spatial dimensions.
As repeatedly done in the chapter for Green's functions, we will follow a probabilistic approach to motivate the limit of infinite coordination number first. We will then substatiate our findings by considering the Feynman diagrams in the infinite coordination number limit.

3.6.1 Example: Weiss Mean Field for the Ising Model

Ising Mean-Field Following the pedagogical approach from [189, Chapter 1], we first discuss a classical mean-field model in infinite dimensions before applying the approach to the Hubbard model. This approach was pioneered by Pierre Weiss in order to understand ferromagnetism and, for this reason, the associated mean-field quantities still often have his name associated [287].
Consider the Ising model (the classical limit of the aforementioned Heisenberg model):

$$H = -J \sum_{\langle i,j \rangle} s_i s_j - h \sum_i s_i \tag{3.77}$$

With classical spins, i.e $s_i \in \{+1, -1\}$. Following the mean-field idea, we investigate a single spin in an effective field:

$$H_i = -s_i \left[\sum_{j=1}^{z} J s_j + h \right] = -s_i \left[zJm + h \right] - \left[J \sum_{j=1}^{z} (s_j - m) \right] \tag{3.78}$$

Now we neglect fluctuations and introduce the mean-field in Eq. (3.80) below:

$$H_i \approx -s_i \left[zJm + h \right] \tag{3.79}$$

The self-consistency equation is obtained by computing the average spin:

$$m = \langle s_i \rangle = \frac{\mathrm{Tr}\left[s_i \exp\{\beta s_i (zJm + h)\} \right]}{\mathrm{Tr}\left[\exp\{\beta s_i (zJm + h)\} \right]} = \tanh\left(\beta z J m + \beta h\right) \tag{3.80}$$

This leads to the ordinary (non-linear) equation that can be solved numerically.

$$H_i = \tanh\left(\beta z J m + \beta h\right) \tag{3.81}$$

We can see in Eq. (3.78) that the approximation becomes exact if we define a renormalized $J \to \frac{J^\star}{z}$ and let $z \to \infty$, so the number of neighbors (coordination number) also approaches infinity.

$$\lim_{z \to \infty} \sum_{j=1}^{z} \frac{J^\star}{z} s_j = J^\star \langle m \rangle \tag{3.82}$$

There are two points to make about this example: (i) the mean-field idea was applied in the local moment regime (contrasting our considerations in the weak-coupling section). This idea of considering a local moment in an effective bath, stemming from an infinite coordination number, will carry over to the DMFT idea. (ii) The classical field coupling is scaled by $1/D$. This is an often repeated distinction between classical and quantum mechanical mean-field theories. However, since the hopping amplitude appears squared in the exchange coupling $J = t^2/U$, as obtained through the full quantum mechanical argument in Eq. (3.30), we may already expect a $1/\sqrt{D}$ scaling of t when we go from classical complete localization back to the full Hubbard model that also includes a hopping term.

3.6.2 Hubbard Model

Scaling Behavior of the Hopping Term

Let us take the hypercubic lattice on the Hubbard model with isotropic hopping between nearest neighbors (i.e. $t_{ij} \equiv t$) as an example. The dispersion relation in d dimensions is given as

$$\epsilon_{\mathbf{k}} = -2t \sum_{i=1}^{d} \cos(\mathbf{k}_i) \tag{3.83}$$

Following the original argument by W. Metzner and D. Vollhardt [172], we can understand the hopping amplitudes in infinite dimensions by viewing the hopping as a random process, described by a random variable

$$\mathbf{k}_i \sim \mathcal{U}(-\pi, \pi) \tag{3.84}$$

$$X_i = \sqrt{2} \cos(\mathbf{k}_i) \tag{3.85}$$

The mutual independence of the scattering processes in the infinite coordination number limit is motivated by the fact that the scatterings become randomized by umklapp processes [173, 171]. It is straightforward to show[14] that X_i is distributed as follows:

$$f_X(x) = \frac{1}{\pi} \frac{1}{\sqrt{2 - x^2}}, \qquad x \in [-\sqrt{2}, \sqrt{2}] \tag{3.86}$$

[14] Using the usual transformation of variables with $P(Y \le y) = P(\sqrt{(}2)\cos(Y) \le y) = \arccos\left(-y/\sqrt{2}\right)/\pi$ and $f_Y(y) = \frac{\mathrm{d}}{\mathrm{d}y} \arccos\left(-y/\sqrt{2}\right)/\pi = \left(2 - y^2\right)^{-1/2}$

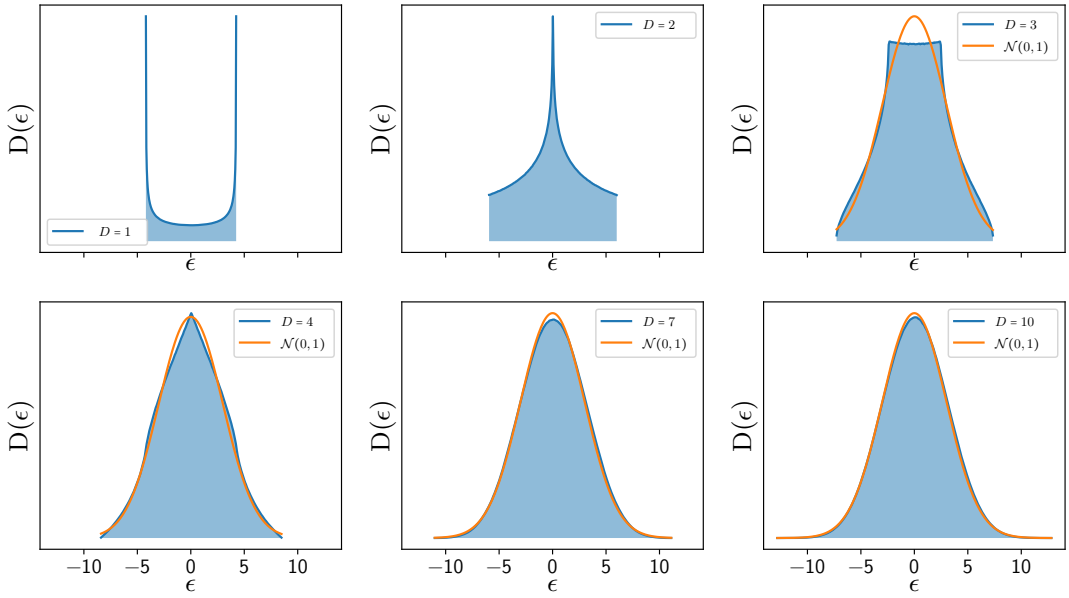

Figure 3.9: DOS for different dimensions on a hypercubic lattice with dispersion $\epsilon_0(k) = -2t^\star \sum_d^D \cos(k_d a)$. A Gaussian distribution is shown in orange, illustrating the convergence of the DOS towards this limit. The bandwidth becomes infinite for $D \to \infty$. Image adapted from [246], originally reproduced from [64].

$$\Rightarrow \mathbb{E}[X_i] = \int_{-\sqrt{2}}^{\sqrt{2}} \mathrm{d}x \frac{1}{\pi} \frac{x}{\sqrt{2-x^2}} = -\frac{\sqrt{2-x^2}}{\pi}\Big|_{-\sqrt{2}}^{\sqrt{2}} = 0 \tag{3.87}$$

$$\mathbb{V}\mathrm{ar}[X_i] = \int_{-\sqrt{2}}^{\sqrt{2}} \mathrm{d}x \frac{1}{\pi} \frac{x^2}{\sqrt{2-x^2}} - \mathbb{E}^2[X_i] = \frac{1}{\pi}\left(\arcsin\left(x/\sqrt{2}\right) - \frac{x}{2}\sqrt{2-x^2}\right)\Big|_{-\sqrt{2}}^{\sqrt{2}} = 1 \tag{3.88}$$

This calculation explains the factor of $\sqrt{2}$, it is used to fix the variance, which turns out to be the bandwidth for our infinite dimensional system, to one[15] The full dispersion relation is then the sum over these hoppings of different momenta $\mathbf{k}_i$. By virtue of the central limit theorem, this sum is (in infinite dimensions exactly) normal distributed. A reminder of the CLT in the Lindeberg-Lévy version: Let X_i be a sequence of independent, identically distributed random variables with finite first two moments μ, σ^2, then the sum $\bar{X}_i = \sum_{i=1}^d X_i/\sqrt{d}$ is normal distributed with:

$$\left(\bar{X}_i - \mu\right) \sim \mathcal{N}(0, \sigma^2) \tag{3.89}$$

For our choice of X_i we have $\mu = 0$ and $\sigma^2 = 1$

$$\epsilon_{\mathbf{k}} = \lim_{d\to\infty} \frac{1}{d} \sum_{i=1}^{d} X_i \tag{3.90}$$

$$\text{CLT} \Rightarrow \epsilon_{\mathbf{k}} \sim \mathcal{N}(0,1) \tag{3.91}$$

$$\Rightarrow D(E) = \sum_{\mathbf{k}} \delta(E - \epsilon_{\mathbf{k}}) = \frac{1}{\sqrt{2\pi}} e^{E^2/2} \tag{3.92}$$

This means for a scaling of the hopping amplitude by

$$t_{ij}^* = \frac{t_{ij}}{\sqrt{d}}, \tag{3.93}$$

we obtain a normal distribution for the infinite coordination number density of states, which has a bandwidth of 1. The convergence in this limit is shown in Fig. 3.9. Note that the DOS in one and two dimensions exhibits van Hove singularities, making it deviate drastically from the limiting distribution. Although interactions smooth out these divergences, the DMFT approach (which we are working toward with this limit) is known to exhibit limitations in this kind of lattice types [300]. This has been pointed out early on by E-Müller-Hartmann, and can easily be argued by considering the characteristic function [181, Eq. 8].

[15] Fixing the second moment as we did here, for the infinite bandwidth, which can be very helpful when comparing different lattice types. Therefore, an appropriate scaling of the hopping has been adopted throughout this thesis.

Lastly, we should point out the form of the scaling $1/\sqrt{d}$. This factor leaves the density states finite (higher or lower powers would lead to infinite or zero bandwidth), thereby preserving competition between kinetic and potential energy terms in the limiting mean-field Hamiltonian.

Diagrammatic Contributions

Next, we will discuss the implications on the Feynman diagrams of the Hubbard model under this limit. For that, we consider the kinetic energy part of the Hubbard model and scale the hopping amplitude according to the proper scaling argument $\frac{1}{\sqrt{z}}$

$$E_{\mathrm{kin},\sigma} = \sum_{\langle ij\rangle} t^* \langle \hat{c}^\dagger_{i\sigma} \hat{c}_{\ j\sigma} \rangle = \sum_{\langle ij\rangle} t^* \int \mathrm{d}\nu G^\nu_{ij,\sigma} e^{+i\nu\eta} \tag{3.94}$$

The potential energy term $U\sum_i \hat{n}_{i\uparrow}\hat{n}_{i\downarrow}$ does not scale with the connectivity because it already is local.

$$G_{0,ij}(\tau) \overset{d\to\infty}{\propto} \mathcal{O}\left(t^{|i-j|}\right) = \mathcal{O}\left(d^{\frac{|\mathbf{r}_i-\mathbf{r}_j|}{2}}\right) \propto \mathcal{O}\left(\frac{1}{\sqrt{z}}\right) + \delta_{ij}\mathcal{O}(1) \tag{3.95}$$

Here we used the rescaled hopping from Eq. (3.93). This scaling also leads to a collapse of diagrams for infinite dimensions (tables for the collapse of the first three orders in the self-energy are computed here [172]). As one might guess from this argument, the collapse of the propagators results in a purely local self-energy [181]:

$$\lim_{d\to\infty} \Sigma^\nu(\mathbf{r}_i, \mathbf{r}_j) = \delta_{ij}\Sigma^\nu(\mathbf{r}_i, \mathbf{r}_i) \tag{3.96}$$

From this follows by Fourier transformation a momentum independent self-energy in the infinite-dimensional limit

$$\lim_{d\to\infty} \Sigma^\nu_{\mathbf{k}} = \Sigma^\nu \tag{3.97}$$

It is important to note that the particles are not localized but only the transition between fixed lattice points i and j becomes negligible (as it should, since there are now infinitely many neighbors). The remaining class of skeleton diagrams are exactly equivalent to those of the AIM. These are diagrams without any self-energy insertions, i.e. no subgraph is 1PI. The following diagram is an example of a non-skeleton diagram, due to the insertion of a 1PI diagram on one of the propagators:

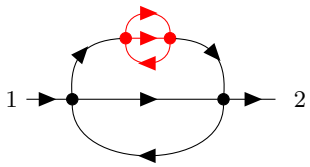

(3.98)

We will now discuss this model, specifically comparing it to the Hubbard model, before moving on to the methods chapter. There, we will discuss the DMFT method, which uses the correspondence between the Hubbard and Anderson impurity model at the limit of infinite coordination number to construct a mean-field solution for the former.

3.7 Anderson Impurity Model

The Anderson impurity model is defined as a non-interacting bath with a single correlated site. It was introduced by P. Anderson in order to describe the effects of localized states on magnetism [9] but is today also often employed as a local reference system when constructing non-local solutions for the Hubbard model. It is related to the Hubbard model with $U_{ij} \to \delta_{i0}U$ and $t_{ij} = \delta_{i0}\left(V_i\hat{c}^\dagger_{i0}\hat{c}_{\ 0i} + V_i^*\hat{c}_{\ i0}\hat{c}^\dagger_{0i}\right)$. Furthermore, the chemical potential for each bath site is given by ϵ_i

$$\hat{H}_{\mathrm{AIM}} = \sum_{\sigma,ij\neq 0} t_{ij}\hat{c}^\dagger_{j\sigma}\hat{c}_{\ i\sigma} + \sum_i \left(V_i\hat{c}^\dagger_{i\sigma}\hat{d}_{\ \sigma} + V_i^*\hat{d}^\dagger_{\ \sigma}\hat{c}_{i\sigma}\right) + U\hat{n}_\uparrow\hat{n}_\downarrow - \mu\sum_\sigma \hat{n}_\sigma \tag{3.99}$$

$$= \hat{H}_0 + \hat{H}_\Delta + \hat{H}_{\mathrm{U}} \tag{3.100}$$

$\hat{d}^\dagger$ and $\hat{d}$ are the creation and annihilation operators for the impurity. The density operator only acts on the impurity $\hat{n}_\sigma = \hat{d}^\dagger_\sigma\hat{d}_{\ \sigma}$. Due to the single-site problem, we could also use the Fourier representation of $\hat{H}_0 = \sum_{\mathbf{k}\sigma}\epsilon_{\mathbf{k}}\hat{c}^\dagger_{\mathbf{k}\sigma}\hat{c}_{\ \mathbf{k}\sigma}$ and $\hat{H}_\Delta = \sum_{\mathbf{k}\sigma}\left(V_{\mathbf{k}}\hat{c}^\dagger_{\mathbf{k}\sigma}\hat{d}_{\ \sigma} + V^*_{\mathbf{k}}\hat{d}^\dagger_{\ \sigma}\hat{c}^\dagger_{\mathbf{k}\sigma}\right)$.

The parameters ϵ_l and V_l are called Anderson parameters in this thesis, specifically in Sec. 6.6 where we present one of the methods of solving this model by explicitly constructing the Hamiltonian in a basis with finitely many parameters $l < \infty$. The more modern (but also numerically more expensive and sometimes less reliable) CTQMC method, which gives unbiased results for the infinite bath site model, has been discussed in detail in my master's thesis [246]. The possibility of constructing the Hamiltonian explicitly already gives an indication of the usefulness of this model, due to the greatly reduced number

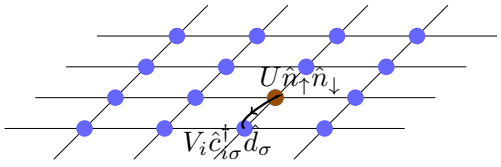

(a) Illustration of a two-dimensional square lattice, with embedded impurity. The impurity couples with a hybridization amplitude V_l to neighboring, non-interacting bath sites l. No hopping between bath sites occurs, thereby transforming this lattice into to one shown in Fig. 3.10b.

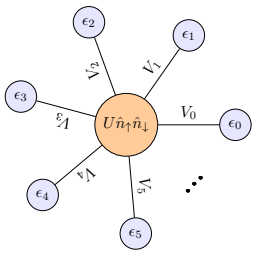

(b) Illustration of the Anderson impurity model as a star geometry, mapped from (for example) from the lattice in Fig. 3.10a, often used by impurity solvers for DMFT.

of Hilbert space dimensions compared to the full Hubbard model. This is useful for this thesis for two reasons: (i) The AIM can (in the sense of the skeleton expansion of the self-energy) be viewed as the infinite spatial dimension limit of the Hubbard model, giving rise to the DMFT, discussed in the last section and Sec. 5.1. (ii) It is an exactly solvable model, which still contains important physics, such as the Kondo effect. We will use this to construct exact pairs of Green's functions and self-energies in our attempt to learn some structure of the Luttinger-Ward Functional (LWf) in Sec. 6.7.

3.7.1 Limiting Cases

We can obtain the Green's functions in the non-interacting and atomic limit, analogously to our derivation in the Hubbard model (here, we just abbreviate the calculation presented in [205, p. 2.2.7.1]).

Interaction Limit: By letting $U \to 0$, the Hilbert space again becomes diagonalizable:

$$\partial_\tau \hat{c}_{i\sigma}(\tau) = -\epsilon_i \hat{c}_{i\sigma}(\tau) - V_i \hat{d}_\sigma(\tau) \tag{3.101}$$

$$\partial_\tau \hat{d}_{i\sigma}(\tau) = -\sum_i V_i \hat{c}_{i\sigma}(\tau) + \mu \hat{c}_{i\sigma} \tag{3.102}$$

Analogously to the derivation in the Hubbard model, we find for the Green's function:

$$\Rightarrow \partial_\tau G_{0,ij} = -\epsilon_i G_{0,ij} - V_i G_{\Delta,i} - \delta(\tau)\delta_{ij} \tag{3.103}$$

$$\partial_\tau G_{\Delta,i} = -\sum_i V_i G_{0,ij} + \mu G_{\Delta,i} \tag{3.104}$$

$$\partial_\tau G_{\mathrm{Imp}} = -\sum_i V_i G_{\Delta,i} + \mu G_{\mathrm{Imp}} - \delta(\tau) \tag{3.105}$$

Here, we defined the commonly used names for the impurity, bath, and hybridization Green's functions. This set of equations can be solved, thereby defining the impurity Green's function and hybridization function Δ^ν, the self-energy of the hybridization Green's function:

$$G_{\mathrm{Imp}} = \left[i\nu_n + \mu - \Delta^\nu\right]^{-1} \tag{3.106}$$

$$\Delta^\nu = \sum_l \frac{|V_l|^2}{i\nu_n - \epsilon_l} \tag{3.107}$$

The spectral function can be obtained from the analytical continuation (using the Sokhotski–Plemelj theorem) of the hybridization function, according to Sec. 2.4.3.1:

$$A^\nu = 2\,\mathrm{Im}\,G^{\mathrm{R},\nu} = \frac{1}{\pi}\frac{\mathrm{Im}\,\Delta^\nu}{(i\nu_n)^2 + (\mathrm{Im}\,\Delta^\nu)^2} \tag{3.108}$$

We observe that an increase in the imaginary part of the hybridization broadens a quasi-particle peak, according to Eq. (2.142).
The atomic limit becomes trivial in the case of the AIM, since the Hilbert space is not only diagonalizable, as in the Hubbard model, but additionally consists of a single site. This directly reproduces the result from Eq. (3.28), without the site index. Accordingly, we can again observe a Hubbard band splitting of $\pm U/2$ in the spectral function.

With Interaction For the AIM, the explicit calculation of the time derivative above can also be done using an interaction term.

$$\partial_\tau \hat{c}_{i\sigma}(\tau) = -\epsilon_i \hat{c}_{i\sigma}(\tau) - V_i \hat{d}_{i\sigma}(\tau) \tag{3.109}$$

$$\partial_\tau \hat{d}_{i\sigma}(\tau) = -\sum_i V_i \hat{c}_{i\sigma}(\tau) + \mu \hat{c}_{i\sigma} + \left[\hat{H}_U, \hat{d}_\sigma(\tau)\right] \tag{3.110}$$

$$= -\sum_i V_i \hat{c}_{i\sigma}(\tau) + \mu \hat{c}_{i\sigma} + -U\hat{n}_{\bar{\sigma}}(\tau)\hat{d}_\sigma(\tau) \tag{3.111}$$

This, again, leads to a set of coupled equations of motion. However, this time, they are not explicitly solvable. The AIM is particularly useful in describing Kondo physics, i.e. spin-flip scattering of electrons on impurities in a conduction band. One of the defining attributes of this is a screening of the impurity, resulting in a constant, non-zero limit of the scattering rate when the temperature approaches zero. For us, the physics described by the AIM is less important for the description of our system (because it only serves as a surrogate for the Hubbard model solution within DMFT) but from a numerical point of view. Within the ED approach that we use to obtain DMFT solutions for the two-particle Green's function (see Sec. 6.6), one has to consider the Kondo screening as a limiting effect for numerical precision at low temperatures. As the screening becomes more important, the number of bath sites, e.g. Fig. 3.10b needs to be increased, exponentially enlarging the Hilbert space and thereby limiting the approach to a relatively high-temperature range when compared to CTQMC.

4 Conserving Approximations and Two-Particle Consistency

This chapter is concerned with the foundation of conservation laws on the thermodynamic and microscopic levels. Thermodynamic consistency will be discussed in the form of the Luttinger-Ward functional and its role in the construction of conserving theories. We then derive Ward–Takahashi identities as another consequence of symmetries. Subsequently, a mechanism for restoring consistencies between single and two-particle levels on an effective level is introduced. We thereby investigate the concept of two-particle and thermodynamic consistency. Some details and derivations are provided here to illustrate important concepts; for the understanding of the lDΓA *method, it is, however, sufficient to note a number of identities.*
We furthermore review some properties of thermodynamics and phase transitions that are important to understand the role of the λ-corrections.

4.1 Thermodynamics and Phase Transition

We will now investigate the generating functionals introduced in Sec. 2.6.2 in the thermodynamic setting. Specifically, the Luttinger-Ward functional is of interest, as it forms the basis for approximations that satisfy thermodynamic consistency and conservation laws. Theories that fulfill these conservation laws consequently also satisfy continuity equations and may, therefore, be assumed to have better explanatory power for questions regarding transport observables. We also sketch why this consistency is, in a sense, orthogonal to the two-particle consistency discussed in Sec. 5.3. Fulfillment of the Pauli principle, the Mermin-Wagner theorem (Sec. 4.5.2), and consistency between observables when calculated from the one- and two-particle levels must be considered separately.
Our goal for this chapter is to develop an understanding of what a conserving theory is, how they are constructed.
Subsequently, we will discuss consistency conditions for the one- and two-particle levels. This means agreement of the values for the observables when calculated from two- or one-particle operators. We also put an emphasis on the difference between thermodynamical and many-particle consistencies. In fact, it has been convincingly argued that for all parquet-based approaches, only exact theories fulfill both [234, 113] and [227, Chapter 6].

4.2 Ward Identities

4.2.1 Motivation

It is a well-known fact that continuous global symmetries lead to locally conserved charge densities and the associated Noether current via Noether's theorem [183]. Here, we want to investigate their consequences in the Hubbard model, specifically by virtue of Ward-Takahashi identities [286, 258]. We will give a brief introduction and then derive the Ward identities required for the construction of our effectively conserving method in Chapter 4.5.1.
As a reminder of the relationship between symmetries and conservation laws in classical theories, we reiterate the most important steps for the proof of Noether's theorem (abbreviating the take-home message from [61, Chapter 2.3]): A continuous, global ($\epsilon(x) \equiv \epsilon$) transformation $F[x, \psi(x)]$ of a classical field $\psi_j(x)$ with components j

$$\psi_j(x) \to \psi_j(x) + i\epsilon F_j(x), \tag{4.1}$$

that leaves the Lagrangian density unchanged, implies a conserved Noether current $j = (j_0, \mathbf{j})$:

$$\partial_t j_0(x) + \nabla \mathbf{j}(x) = 0 \tag{4.2}$$

$$Q = -\int j_0(x), \qquad \frac{\mathrm{d}Q}{\mathrm{d}t} = 0 \tag{4.3}$$

We will encounter conservation laws in the form of such a continuity equation below in Sec. 4.4.
Ward identities lift Noether's theorem to quantized field theories. Here, a local transformation of a quantized field $\phi'_j(x) \to \phi_j(x) + i\epsilon(x)F_j(x)$[1] that leaves the functional action S_{int} invariant (we do not need to assume the existence of a Lagrangian density) leads to the following change in the total action (compare Sec. 2.1.1 for the notation):

$$S = S_0 + S_{\mathrm{int}} + S_J = -\frac{1}{2}\phi(\overline{1})G_0^{-1}(\overline{1},\overline{2})\phi(\overline{2}) + S_{\mathrm{int}} \tag{4.4}$$

$$\Rightarrow \delta S = \delta S_0 + \delta S_J = \delta\epsilon(\mathbf{r}_1\tau_1)F(\overline{1})G_0^{-1}(\overline{1},\overline{2})\phi(\overline{2}) + \delta S_J \tag{4.5}$$

We have also taken the coupling to the external generator fields J from Eq. (2.158) into S_J.
Since the transformation leaves the partition function unchanged, the expectation values must remain the same:

$$\langle \phi'(1), \dots \phi'(n)\rangle_S = \langle \phi(1), \dots \phi(n)\rangle_S \tag{4.6}$$

We follow that the functional must be stationary:

$$\delta S = \int \mathcal{D}[\phi]\, e^{-S-S_J}\left[\sum_{\alpha_1\alpha_2} F(1)G^{-1}_{0,\alpha_1\alpha'_1}(1,\overline{2})\phi(\overline{2})\phi(\overline{2}) + J(\overline{1})F(\overline{1})\right] = 0 \tag{4.7}$$

Expanding the free Green's function and pulling the derivatives outside of the expectation values gives a more familiar-looking form of this generalized continuity equation when compared to Eq. (4.2) and Sec. 4.4.

$$i\partial_\tau\langle j_0\rangle + \nabla\cdot\langle \mathbf{j}\rangle = -i\sum_k J_{\alpha_k}(\tau,\mathbf{r})\langle F_{\alpha_k}(\tau,\mathbf{r})\rangle \tag{4.8}$$

[1] This is a transformation in the position and (imaginary) time domain $x_1 = (\mathbf{r}_1, \tau_1)$, leaving state indices α, such as the spin, unchanged. The combined indices are still defined as $1 = (\alpha_1, \mathbf{r}_1, \tau_1)$ and sums over just the states α are then written explicitly as $\sum_{\alpha_1} f(1)$

Concrete Ward identities for the n-point correlator are then obtained through n functional derivatives, setting the source $J = 0$ afterwards:

$$\begin{aligned}\langle\phi_{j_n}(x_n)\dots\phi_{j_1}(x_1)F_{\alpha_1}(1)\phi(\overline{n})\phi(\overline{2})\rangle G^{-1}_{0,\alpha_1\alpha_2}(1,\overline{2})\\ = -\sum_k \delta(x-x_k)\langle\phi_{j_n}(x_n)\phi_{j_{n+1}}(x_{n+1})\dots F_{j_k}(x_k)\phi_{j_{n-1}}(x_{n-1})\dots\phi_{j_1}(x_1)\rangle\end{aligned} \tag{4.9}$$

This discussion motivates the role of the effective action $\Gamma[\phi]$ in the formulation of Ward identities since it naturally incorporates the source-coupling term in Eq. (4.7). It is possible to derive the Ward identities, discussed in the following, using the functional formalism above [61, Chapter 2.3]. Here, also, the relationship between local ($\epsilon(x)$) and global ($\epsilon(x) \equiv \epsilon$) transformations and the emergence of Goldstone bosons from global transformations is discussed. We are, however, not focused on spontaneous symmetry breaking and will instead choose the much more concrete operator formalism. This will also provide more immediate results for the case of the Hubbard Hamiltonian.

4.3 Luttinger Ward Functional and Conserving Approximations

We will now give a brief summary of some of the points made first by (i) G. Baym and P. Kadanoff [23, 22] for the investigation of macroscopic conservation laws and a method to construct approximate theories that fulfill these; (ii) J. Luttinger and J. Ward [162], specifically linking the core quantity to a generalization of the grand canonical potential and (iii) M. Potthoff for the non-perturbative construction of the functional.
The Luttinger-Ward functional $\Phi[G]$ is closely related to the effective action, in this context. We have already discussed some aspects of this functional around Eq. (2.165). This is the case because Φ turns out to be the sum over all closed, dressed 2PI skeleton diagrams [194]. Comparing with the definition of the effective action functional in Sec. 2.6.3 we can therefore define it as the difference between interacting and non-interacting 2PI effective action [69, Sec. 6.4.5]:

$$\Phi[G] = \Gamma[G] - \Gamma_0[G] = \Gamma[G] - \mathrm{Tr}\ln(-G) - \mathrm{Tr}\left((G_0^{-1} - G^{-1})G\right) \tag{4.10}$$

The usefulness stems from the relation to the grand canonical potential, as well as the ability to generate irreducible functions from derivatives with respect to the full Green's function.

$$\Omega = \mathrm{Tr}\ln(G) - \mathrm{Tr}(\Sigma G) + \Phi[G] \tag{4.11}$$

This functional is stationary for the exact self-energy of the system:

$$\frac{\delta\Phi[G]}{\delta\Sigma} = \frac{\delta\Phi[G]}{\delta G}\frac{\delta G}{\delta\Sigma} = 0 \quad \Leftrightarrow \frac{\delta\Omega}{\delta\Sigma} = 0 \tag{4.12}$$

This then implies fulfillment of thermodynamic consistencies in theories based on approximations of this functional, as will be discussed in Sec. 4.3. There are two important properties of the Luttinger-Ward functional (specifically in the context of DMFT) [194]:

$$\Phi[G] = 0, \text{ if } U = 0 \tag{4.13}$$

$$\Phi[G] \quad \text{universal} \tag{4.14}$$

The second property means that Φ is the same for two Hubbard systems with identical U regardless of the hopping parameter t. This is central to the application in DMFT. Importantly, the non-perturbative construction demonstrates that the LWf exists, even when a perturbative construction is not possible. The leading order diagrams are given as follows [194]:

$\Phi =$ 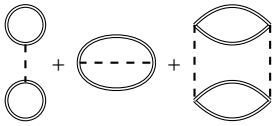 $+ \dots$ (4.15)

Since functional derivatives can be graphically represented by cutting one closed line, it can be understood by comparison with Eq. (2.201) that the functional derivative generates the self-energy. This also yields property Eq. (4.13) of the LWf; when the interaction vanishes, only diagrams of zeroth order are left [195].
There are two subtleties to consider: (i) the existence of the LWf is deduced from a "vanishing curl" condition [22]:

$$\frac{\delta\Sigma(1;1')}{\delta G(2';2)} = \frac{\delta\Sigma(2;2')}{\delta G(1';1)} \tag{4.16}$$

The curl condition is equivalent to the property that the functional derivative with respect to the Green's function yields the self-energy [266, Chapter 72.1]:

$$\frac{\delta\Phi[G]}{\delta G(2';1')} = \Sigma(1';2') \tag{4.17}$$

(ii) the mapping $G[G_0]$ must exist and be unique, which has been demonstrated not always to be the case [88]. Although this could pose a significant issue due to a potential breakdown of a well-defined parquet decomposition, we ignore this pitfall in this thesis.
Our application for the Luttinger-Ward functional will be to discuss conserving approximations, specifically DMFT and RPA. Furthermore, we will discuss an attempt to learn certain features of the LWf through a machine learning approach in Sec. 6.7.

4.3.1 Conserving Approximations

As mentioned in the previous section, the LWf is closely related to the grand canonical potential. It acts as a functional generalization of a thermodynamic potential, extending the definition from static to dynamic quantities, thus representing the full state of a system. Consequently, theories obtained through approximations of this functional are conserving in a thermodynamical sense [22] and by making approximations to the LWf, one can develop theories that retain this conserving nature. These theories are called Φ-derivable and are supplemented by the set of equations discussed above (just as a thermodynamic potential is complemented by equations of state involving the natural variables):

$$\frac{\delta\Phi[G]}{\delta G(1;1')} = \Sigma(1';1), \qquad \frac{\delta\Sigma(1';1)}{\delta G(2;2')} = \Gamma(1',1;2',2) \tag{4.18}$$

Note that we cannot disregard the second argument in the self-energy, even for equilibrium calculations. Furthermore, the 2-particle 2-particle irreducible vertex Γ appears, but not the 2-particle Green's function itself. Φ-derivability makes no statement about how to obtain those or quantities generated from it. This will be discussed in detail in Sec. 4.5.
A detailed discussion of Φ-derivable theories along with concrete examples for choices of approximate Φ in the setting of mean-field theories, in [28].
Note, however, that the arbitrariness in the choice of an approximation for the LWf leads to an infinite amount of conserving theories [5]. This undercuts the argument for consistency already; in Sec. 4.5, we will present another argument for the inconsistencies that can arise from a purely *Phi*-derivability-based approach.

Conservation of Particle Number

Theories constructed via the LWf, i.e. Φ-derivable theories, conserve the number of particles. This follows by construction and also demonstrates the equivalence of the LWf to the free energy. We try to illustrate this by computing the electron density from Φ, following [194]. The traditional way of obtaining the electron density is:

$$n = \mathrm{Tr}\,[G] = \sum_{\nu\mathbf{k}} G^{\nu}_{\sigma,\mathbf{k}} e^{-i\nu_n(-\eta)} = \frac{1}{\beta}\frac{\partial \ln Z}{\partial\mu} = -\frac{\partial\Omega}{\partial\mu} \tag{4.19}$$

First, we note that Eq. (4.19) and Eq. (4.18) with a change of variables gives the following identity:

$$\frac{\partial\Phi[G]}{\partial\mu} = \mathrm{Tr}\left[\frac{\delta\Phi[G]}{\delta G}\frac{\partial G}{\partial\mu}\right] = \mathrm{Tr}\left[\Sigma\frac{\partial G}{\partial\mu}\right] \tag{4.20}$$

We then use Eq. (4.11) to demonstrate how to obtain the electron density by functional derivation of the LWf:

$$\begin{aligned}
n &= -\frac{\partial}{\partial\mu}\left[\Phi[G] + \mathrm{Tr}[\ln G] - \mathrm{Tr}[\Sigma G]\right] \\
&= -\frac{\partial\Phi[G]}{\partial\mu} - \mathrm{Tr}\left[G^{-1}\frac{\partial G}{\partial\mu} - \frac{\partial\Sigma}{\partial\mu}G - \Sigma\frac{\partial G}{\partial\mu}\right] \\
&= -\frac{\partial\Phi[G]}{\partial\mu} - \mathrm{Tr}\left[\left(-\frac{\partial G^{-1}}{\partial\mu} - \frac{\partial\Sigma}{\partial\mu}\right)G - \Sigma\frac{\partial G}{\partial\mu}\right] \\
&= -\frac{\partial\Phi[G]}{\partial\mu} + \mathrm{Tr}\left[\frac{\partial G_0^{-1}}{\partial\mu}G\right] + \mathrm{Tr}\left[\Sigma\frac{\partial G}{\partial\mu}\right] \\
&= \mathrm{Tr}\,[G] = n
\end{aligned} \tag{4.21}$$

Where we used integration by parts in the third line, the Dyson equation in the 4th line and finally the definition of the free Green's function $G_0^{-1} = \nu - \epsilon_{\mathbf{k}} + \mu$ for the 5th line. A very thorough discussion of the LWf and Φ-derivability is given in [28], specifically section 5.

More examples and a textbook introduction to conserving theories, specifically the RPA and Fluctuation Exchange (FLEX) approximations [30, 29, 228] are given in [227].
We will now switch to the complementary point of view for consistencies through Ward identities obtained through the operator formalism. These are needed to provide a full understanding of how consistencies are only restored on an effective level in lDΓA.

4.4 Ward Identities for the Hubbard Model

The following section is based on lecture notes and private notes by Georg Rohringer. Most derivations follow these notes verbatim. These have also been derived in a more general setting. A particularly comprehensive derivation was given by F. Krien, including the symmetry broken phase and an arbitrary non-interacting part of the Hamiltonian [143, Chapter C.1], [147], earlier works include [280, 200, 48, 265, 112, 166, 91]. A textbook introduction is also given in [61, Sec. 2.3.4]
Our goal here is to derive Ward identities and the f-sum rule in the Hubbard model used for the consistency conditions of lDΓA in detail.

Continuity Equation for the Hubbard Model

We start by obtaining the discrete continuity equation on the Hubbard lattice $\partial_\tau = \partial_\tau \hat{n}_{l\sigma}(\tau) = \left[\hat{n}_{l\sigma}, \hat{H}\right]$ [2]
Evaluation of the time evolution for the density operator $\hat{n}_{l\sigma}$ reads as follows:

$$\begin{aligned}
\partial_\tau \hat{n}_{l\sigma}(\tau) = \left[\hat{H}, \hat{n}_{l\sigma}\right] &= \sum_{ij,\sigma'} t_{ij}\left[\hat{c}_{\,i\sigma'}\hat{c}^\dagger_{j\sigma'}, \hat{c}_{\,l\sigma}\hat{c}^\dagger_{l\sigma}\right] + U\sum_i \underbrace{\left[\hat{n}_{i,\uparrow}\hat{n}_{i,\downarrow}, \hat{n}_{l,\sigma}\right]}_{=0} \\
&\overset{(2.18)}{=} \sum_{ij,\sigma'} t_{ij}\left(\hat{c}_{\,i\sigma'}\left[\hat{c}^\dagger_{j\sigma'}, \hat{c}_{\,l\sigma}\hat{c}^\dagger_{l\sigma}\right] + \left[\hat{c}_{\,i\sigma'}, \hat{c}_{\,l\sigma}\hat{c}^\dagger_{l\sigma}\right]\hat{c}^\dagger_{j\sigma'}\right) \\
&\overset{(2.20)}{=} \sum_{ij,\sigma'} t_{ij}\left(-\hat{c}_{\,i\sigma'}\hat{c}_{\,l\sigma}\left\{\hat{c}^\dagger_{j\sigma'}, \hat{c}^\dagger_{l\sigma}\right\} + \hat{c}_{\,i\sigma'}\left\{\hat{c}^\dagger_{j\sigma'}, \hat{c}_{\,l\sigma}\right\}\hat{c}^\dagger_{l\sigma} - \hat{c}_{\,l\sigma}\left\{\hat{c}_{\,i\sigma'}, \hat{c}^\dagger_{l\sigma}\right\}\hat{c}^\dagger_{j\sigma'} + \left\{\hat{c}_{\,i\sigma'}, \hat{c}_{\,l\sigma}\right\}\hat{c}^\dagger_{j\sigma}\hat{c}^\dagger_{l\sigma}\right) \\
&\overset{(2.21)}{=} \sum_i \left(t_{il}\hat{c}_{\,i\sigma}\hat{c}^\dagger_{l\sigma} - t_{li}\hat{c}_{\,l\sigma}\hat{c}^\dagger_{i\sigma}\right) \qquad (4.22)
\end{aligned}$$

This is a continuity equation on the discrete Hubbard lattice.
Analog, but more tedious computation yields for the creation operator of the general Hubbard Hamiltonian $\hat{H} = -\sum_{ij} t_{ij}\hat{c}^\dagger_i\hat{c}_{\,j} + \sum_{ijkl} U_{ijkl}\hat{c}^\dagger_i\hat{c}^\dagger_j\hat{c}_{\,k}\hat{c}_{\,l} - \mu\sum_i \hat{n}_i$, the equation of motion:

$$\partial_\tau \hat{c}^\dagger_l(\tau) = -\sum_i (t_{il} + \delta_{il}\mu)\hat{c}^\dagger_i + \sum_{ijk}(U_{ijkl} - U_{ijlk})\hat{c}^\dagger_i\hat{c}^\dagger_j\hat{c}_{\,k} \qquad (4.23)$$

Note the formal similarity to the functional form in Eq. (2.239), which underscores how we could have obtained the SDE through the operator formalism as well.

4.4.1 Two-Particle Continuity Equation

To obtain the Ward identities for the Hubbard model, we first derive the continuity equation of the two-particle Green's function by application of Eq. (4.23).

The notation here is shortened by writing $\Theta_{ij} := \Theta(\tau_i - \tau_j)$ and $\delta_{ij} := \delta(\tau_i - \tau_j)$

Important 4.4.1.1 (Continuity Equation in Imaginary Time)
The imaginary time derivative of the two-particle Green's function of the Hubbard model is given by:

$$\begin{aligned}
\partial_{\tau_1} G^{iijl}_{\sigma\sigma'}(\tau_1,\tau_1,\tau_2,\tau_3) = &\sum_m \left(t_{mi}G^{mijl}_{2,\sigma\sigma'}(\tau_1,\tau_1,\tau_2,\tau_3) - t_{im}G^{imjl}_{2,\sigma\sigma'}(\tau_1,\tau_1,\tau_2,\tau_3)\right) \\
&+\delta_{12}\delta_{ij}\delta_{\sigma\sigma'}G^{il}(\tau_1,\tau_3) - \delta_{13}\delta_{il}\delta_{\sigma\sigma'}G^{ji}(\tau_2,\tau_1) \qquad (4.24)
\end{aligned}$$

For the derivation of the symmetry-broken case, we refer to [143, Section C.1].

We will now prove this identity, starting from the definition of the two-particle correlator and Def. 2.1.2.3.

$$\begin{aligned}
G^{iijl}_{\sigma\sigma'}(\tau_1,\tau_1,\tau_2,\tau_3) = &\quad \Theta_{12}\Theta_{23}\langle\hat{n}_{i\sigma}(\tau_1)\hat{c}_{\,j\sigma'}(\tau_2)\hat{c}^\dagger_{l\sigma'}(\tau_3)\rangle \\
&- \Theta_{13}\Theta_{32}\langle\hat{n}_{i\sigma}(\tau_1)\hat{c}^\dagger_{l\sigma'}(\tau_3)\hat{c}_{\,j\sigma'}(\tau_2)\rangle
\end{aligned}$$

[2] This is the Heisenberg equation of motion for the density operator. The non-lattice form of the density operator $\rho = \psi^*\partial_t\psi - \psi\partial_t\psi^*$, recovers the usual continuity equation from electrodynamics $\partial_t\rho + \nabla\cdot\mathbf{j} = 0$, which analogously describes the flux of electrons in the classical and continuum limit.

$$
\begin{aligned}
&+ \Theta_{21}\Theta_{13}\langle \hat{c}_{j\sigma'}(\tau_2)\hat{n}_{i\sigma}(\tau_1)\hat{c}^\dagger_{l\sigma'}(\tau_3)\rangle \\
&- \Theta_{31}\Theta_{12}\langle \hat{c}^\dagger_{l\sigma'}(\tau_3)\hat{n}_{i\sigma}(\tau_1)\hat{c}_{j\sigma'}(\tau_2)\rangle \\
&+ \Theta_{23}\Theta_{31}\langle \hat{c}_{j\sigma'}(\tau_2)\hat{c}^\dagger_{l\sigma'}(\tau_3)\hat{n}_{i\sigma}(\tau_1)\rangle \\
&- \Theta_{32}\Theta_{21}\langle \hat{c}^\dagger_{l\sigma'}(\tau_3)\hat{c}_{j\sigma'}(\tau_2)\hat{n}_{i\sigma}(\tau_1)\rangle
\end{aligned}
$$

Note first, that $\partial_{\tau_j}\hat{c}(\tau_i) = \partial_{\tau_j}\hat{c}^\dagger(\tau_i) = 0$ for $i \neq j$ and only density operators with time argument τ_1 appear. Therefore, we let $\partial_\tau \to \partial_{\tau_1}$.

$$
\begin{aligned}
\partial_{\tau_1} G^{iijl}_{\sigma\sigma'}(\tau_1,\tau_1,\tau_2,\tau_3) = \;& \partial_{\tau_1}\Theta_{12}\Theta_{23}\langle \hat{n}_{i\sigma}(\tau_1)\hat{c}_{j\sigma'}(\tau_2)\hat{c}^\dagger_{l\sigma'}(\tau_3)\rangle \\
&+\Theta_{12}\Theta_{23}\Big\langle \frac{\hat{n}_{i\sigma}}{\partial\tau}(\tau_1)\hat{c}_{j\sigma'}(\tau_2)\hat{c}^\dagger_{l\sigma'}(\tau_3)\Big\rangle + \dots \\
= \;& \delta_{22}\Theta_{23}\langle \hat{n}_{i\sigma}(\tau_1)\hat{c}_{j\sigma'}(\tau_2)\hat{c}^\dagger_{l\sigma'}(\tau_3)\rangle \\
&+\Theta_{12}\Theta_{23}\Big\langle \sum_m \Big(t_{mi}\hat{c}_{m\sigma}\hat{c}^\dagger_{i\sigma} - t_{im}\hat{c}_{i\sigma}\hat{c}^\dagger_{m\sigma}\Big)(\tau_1)\hat{c}_{j\sigma'}(\tau_2)\hat{c}^\dagger_{l\sigma'}(\tau_3)\Big\rangle + \dots
\end{aligned}
$$

We group all derivations of Θ-functions and all those of density operators together. In addition, we note that for the first case, only pairs τ_1,τ_2 and τ_1,τ_3 appear, and $\forall i : \partial\Theta_{i2}/\partial\tau_1 = \partial\Theta_{i1}/\partial\tau_1 = \delta_{1i}$. The second case yields two 2-particle Green's functions.

$$
\begin{aligned}
= \;& \delta_{12}\Big[\quad \Theta_{13}\langle \hat{n}_{i\sigma}(\tau_1)\hat{c}_{j\sigma'}(\tau_1)\hat{c}^\dagger_{l\sigma'}(\tau_3)\rangle - \Theta_{13}\langle \hat{c}_{j\sigma'}(\tau_1)\hat{n}_{i\sigma}(\tau_1)\hat{c}^\dagger_{l\sigma'}(\tau_3)\rangle \\
&\quad -\Theta_{31}\langle \hat{c}^\dagger_{l\sigma'}(\tau_3)\hat{n}_{i\sigma}(\tau_1)\hat{c}_{j\sigma'}(\tau_1)\rangle\Theta_{31}\langle \hat{c}^\dagger_{l\sigma'}(\tau_3)\hat{c}_{j\sigma'}(\tau_1)\hat{n}_{i\sigma}(\tau_1)\rangle\Big] \\
&+\delta_{13}\Big[- \Theta_{12}\langle \hat{n}_{i\sigma}(\tau_1)\hat{c}^\dagger_{l\sigma'}(\tau_1)\hat{c}_{j\sigma'}(\tau_2)\rangle + \Theta_{12}\langle \hat{c}^\dagger_{l\sigma'}(\tau_1)\hat{n}_{i\sigma}(\tau_1)\hat{c}_{j\sigma'}(\tau_2)\rangle \\
&\quad +\Theta_{21}\langle \hat{c}_{j\sigma'}(\tau_2)\hat{n}_{i\sigma}(\tau_1)\hat{c}_{l\sigma'}(\tau_1)\rangle - \Theta_{21}\langle \hat{c}_{j\sigma'}(\tau_2)\hat{c}_{l\sigma'}(\tau_1)\hat{n}_{i\sigma}(\tau_1)\rangle\Big] \\
&+\Theta_{12}\Theta_{23}\sum_m \Big(t_{mi}\langle \hat{c}_{m\sigma}(\tau_1)\hat{c}^\dagger_{i\sigma}(\tau_1)\hat{c}_{j\sigma'}(\tau_2)\hat{c}^\dagger_{l\sigma'}(\tau_3)\rangle \\
&\quad -t_{im}\langle \hat{c}^\dagger_{i\sigma}(\tau_1)\hat{c}_{m\sigma}(\tau_1)\hat{c}_{j\sigma'}(\tau_2)\hat{c}^\dagger_{l\sigma'}(\tau_3)\rangle\Big) \\
&-\Theta_{13}\Theta_{32}\sum_m \Big(t_{mi}\langle \hat{c}_{m\sigma}(\tau_1)\hat{c}^\dagger_{i\sigma}(\tau_1)\hat{c}^\dagger_{l\sigma'}(\tau_3)\hat{c}_{j\sigma'}(\tau_2)\rangle \\
&\quad - t_{im}\langle \hat{c}^\dagger_{i\sigma}(\tau_1)\hat{c}_{m\sigma}(\tau_1)\hat{c}^\dagger_{l\sigma'}(\tau_3)\hat{c}_{j\sigma'}(\tau_2)\rangle\Big) \\
&+ \dots \\
= \;& \delta_{12}\Big[\quad \Theta_{13}\big\langle [\hat{n}_{i\sigma},\hat{c}_{j\sigma'}](\tau_1)\hat{c}^\dagger_{l\sigma'}(\tau_3)\big\rangle - \Theta_{31}\big\langle [\hat{n}_{i\sigma},\hat{c}_{j\sigma'}](\tau_1)\hat{c}^\dagger_{l\sigma'}(\tau_3)\big\rangle \\
&+\delta_{12}\Big[- \Theta_{12}\big\langle [\hat{n}_{i\sigma},\hat{c}^\dagger_{l\sigma'}](\tau_1)\hat{c}_{j\sigma'}(\tau_3)\big\rangle + \Theta_{21}\big\langle \hat{c}_{j\sigma'}(\tau_3)[\hat{n}_{i\sigma},\hat{c}^\dagger_{l\sigma'}](\tau_1)\big\rangle\Big] \\
&+\sum_m t_{mi}G^{mijl}_{\sigma\sigma'} - \sum_m t_{im}G^{imjl}_{\sigma\sigma'} \\
=& \sum_m \Big(t_{mi}G^{mijl}_{\sigma\sigma'} - t_{im}G^{imjl}_{\sigma\sigma'}\Big) \\
&+ \delta_{12}\delta_{ij}\delta_{\sigma\sigma'}G^{il}(\tau_1,\tau_3) - \delta_{13}\delta_{il}\delta_{\sigma\sigma'}G^{ji}(\tau_2,\tau_1)
\end{aligned}
$$

Which proves Eq. 4.24.

4.4.2 Ward Identities

We now move to the momentum representation by Fourier transforming the previous result. This will then enable us to obtain several Ward identities for the Hubbard model, listed in Sec. 4.4.2.1. From time and space translational invariance we can follow:

$$
\mathbf{R}_l = \mathbf{0}, \qquad \wedge \quad \tau_3 = 0 \tag{4.25}
$$

$$
\Leftrightarrow G^{ji}(\tau',\tau) = G^{(j-i)0}(\tau'-\tau,0) =: G^l(\tau) \tag{4.26}
$$

Proceeding with the Fourier transform of Eq. 4.24, we also abbreviate all sums and integrals into one symbol here (e.g. for the 2-particle Green's function: $\sum_{\nu\nu'\omega}\int_{\mathbf{k}}\int_{\mathbf{k}'}\int_{\mathbf{q}} \to \not\int$). We use the usual representation of $\delta_{12} = \frac{1}{2\pi}\int_{-\infty}^{\infty} \mathrm{d}\omega e^{i\omega(\tau_1-\tau_2)}$:

$$
\begin{aligned}
G^{iij0}_{\sigma\sigma'} &= \not\int e^{i(\nu\tau_1 - \mathbf{k}\cdot\mathbf{R}_i)}\cdot e^{-i[(\nu+\omega)\tau_1 - (\mathbf{k}+\mathbf{q})\cdot\mathbf{R}_i]}\cdot e^{i[(\nu'+\omega)\tau_2 - (\mathbf{k}'+\mathbf{q})\cdot\mathbf{R}_j]}\cdot G^{\nu\nu'\omega}_{\sigma\sigma',\mathbf{k}\mathbf{k}'\mathbf{q}} \\
&= \not\int \cdot e^{-i\omega\tau_1 - i\mathbf{q}\mathbf{R}_i}\cdot e^{i[(\nu'+\omega)\tau_2 - (\mathbf{k}'+\mathbf{q})\cdot\mathbf{R}_j]}\cdot G^{\nu\nu'\omega}_{\sigma\sigma',\mathbf{k}\mathbf{k}'\mathbf{q}}
\end{aligned}
$$

$$G^{mij0}_{\sigma\sigma'} = \iint e^{i(\nu\tau_1-\mathbf{k}\cdot\mathbf{R}_m)}\cdot e^{-i[(\nu+\omega)\tau_1-(\mathbf{k}+\mathbf{q})\cdot\mathbf{R}_i]}\cdot e^{i[(\nu'+\omega)\tau_2-(\mathbf{k}'+\mathbf{q})\cdot\mathbf{R}_j]}\cdot G^{\nu\nu'\omega}_{\sigma\sigma',\mathbf{k}\mathbf{k}'\mathbf{q}}$$

$$G^{imj0}_{\sigma\sigma'} = \iint e^{i(\nu\tau_1-\mathbf{k}\cdot\mathbf{R}_i)}\cdot e^{-i[(\nu+\omega)\tau_1-(\mathbf{k}+\mathbf{q})\cdot\mathbf{R}_m]}\cdot e^{i[(\nu'+\omega)\tau_2-(\mathbf{k}'+\mathbf{q})\cdot\mathbf{R}_j]}\cdot G^{\nu\nu'\omega}_{\sigma\sigma',\mathbf{k}\mathbf{k}'\mathbf{q}}$$

$$\delta_{\sigma\sigma'}\delta_{12}\delta_{ij}G^i(\tau_1) = \delta_{\sigma\sigma'}\iint e^{-i[\omega\tau_1-\mathbf{q}\cdot\mathbf{R}_i]}e^{i[(\nu'+\omega)\tau_2-(\mathbf{k}'+\mathbf{q})\cdot\mathbf{R}_j]}G^{\nu'}_{\mathbf{k}'}$$

$$\delta_{\sigma\sigma'}\delta(\tau_1)\delta_{i0}G^{j-i}(\tau_2-\tau_1) = \delta_{\sigma\sigma'}\delta(\tau_1)\delta_{i0}G^j(\tau_2) = \delta_{\sigma\sigma'}\iint e^{-i[\omega\tau_1-\mathbf{q}\cdot\mathbf{R}_i]}e^{i[(\nu'+\omega)\tau_2-(\mathbf{k}+\mathbf{q})\cdot\mathbf{R}_j]}G^{\nu'+\omega}_{\mathbf{k}'+\mathbf{q}}$$

Here, we have explicitly written out all constituents of Eq. 4.24 and use that the hopping is only dependent on the momentum transfer inside the summation, i.e. $t_{mi} = t_{im} = t_{|\mathbf{R}_i-\mathbf{R}_m|} = t_{\mathbf{R}_{m'}}$ and space inversion symmetry of the lattice ($\epsilon_{-\mathbf{k}} = \epsilon_{\mathbf{k}}$):

$$\begin{aligned}
&\Rightarrow \iint (-i\omega)e^{-i[\omega\tau_1-\mathbf{q}\cdot\mathbf{R}_i]}\cdot e^{i[(\nu'+\omega)\tau_2-(\mathbf{k}'+\mathbf{q})\cdot\mathbf{R}_j]}G^{\nu\nu'\omega}_{\sigma\sigma',\mathbf{k}\mathbf{k}'\mathbf{q}}\\
&= \iint e^{-i(\omega\tau_1-\mathbf{q}\cdot\mathbf{R}_i)}\cdot e^{i[(\nu'+\omega)\tau_2]-(\mathbf{k}'+\mathbf{q})\cdot\mathbf{R}_j}\\
&\quad\times\Big[G^{\nu\nu'\omega}_{\sigma\sigma',\mathbf{k}\mathbf{k}'\mathbf{q}}\underbrace{\sum_{m'}t_{m'}\left(e^{-i\mathbf{k}\cdot\mathbf{R}_{m'}}-e^{i(\mathbf{k}+\mathbf{q})\cdot\mathbf{R}_{m'}}\right)}_{\epsilon_{\mathbf{k}}-\epsilon_{\mathbf{k}+\mathbf{q}}}+\delta_{\sigma\sigma'}\left(G^{\nu'+\omega}_{\mathbf{k}'+\mathbf{q}}-G^{\nu'}_{\mathbf{k}'}\right)\Big]\\
\Leftrightarrow 0 &= \iint e^{-i[\omega\tau_1-\mathbf{q}\cdot\mathbf{R}_i]}\cdot e^{i[(\nu'+\omega)\tau_2-(\mathbf{k}'+\mathbf{q})\cdot\mathbf{R}_j}\\
&\quad\times\Big[(i\omega+\epsilon_{\mathbf{k}}-\epsilon_{\mathbf{k}+\mathbf{q}})G^{\nu\nu'\omega}_{\sigma\sigma',\mathbf{k}\mathbf{k}'\mathbf{q}}+\delta_{\sigma\sigma'}\left(G^{\nu'+\omega}_{\mathbf{k}'+\mathbf{q}}-G^{\nu'}_{\mathbf{k}'}\right)\Big]
\end{aligned}\tag{4.27}$$

This Ward identity also holds for the generalized susceptibility, which can be seen by inserting the definition of the generalized susceptibility into Eq. (4.30):

$$\begin{aligned}
\sum_{\omega\mathbf{k}}(i\omega_m+\epsilon_{\mathbf{k}}-\epsilon_{\mathbf{k}+\mathbf{q}})G^{\nu\nu'\omega}_{\sigma\sigma',\mathbf{k}\mathbf{k}'\mathbf{q}} &= \delta_{\sigma\sigma'}\left(G^{\nu'+\omega}_{\mathbf{k}'+\mathbf{q}}-G^{\nu'}_{\mathbf{k}'}\right)\\
\Leftrightarrow\sum_{\omega\mathbf{k}}(i\omega_m+\epsilon_{\mathbf{k}}-\epsilon_{\mathbf{k}+\mathbf{q}})\left(\chi^{\nu\nu'\omega}_{\sigma\sigma',\mathbf{k}\mathbf{k}'\mathbf{q}}-\beta\delta_{\omega0}\delta(\mathbf{q}-\mathbf{0})G^{\nu}_{\mathbf{k}}G^{\nu'}_{\mathbf{k}'}\right) &= \delta_{\sigma\sigma'}\left(G^{\nu'+\omega}_{\mathbf{k}'+\mathbf{q}}-G^{\nu'}_{\mathbf{k}'}\right)
\end{aligned}$$

We can now use, that $i\omega\delta_{\omega0} = 0$ and $\delta(\mathbf{q}-\mathbf{0})(\epsilon_{\mathbf{k}}-\epsilon_{\mathbf{k}+\mathbf{q}}) = 0$

$$\Rightarrow\sum_{\omega\mathbf{k}}(i\omega_m+\epsilon_{\mathbf{k}}-\epsilon_{\mathbf{k}+\mathbf{q}})\,\chi^{\nu\nu'\omega}_{\sigma\sigma',\mathbf{k}\mathbf{k}'\mathbf{q}} = \delta_{\sigma\sigma'}\left(G^{\nu'+\omega}_{\mathbf{k}'+\mathbf{q}}-G^{\nu'}_{\mathbf{k}'}\right)\tag{4.28}$$

Letting $\sigma = \uparrow$ and summing over σ', one obtains expressions for the density and magnetic channel (see Eq. (2.214) and Eq. (2.214)). On the right-hand side, this sum only cancels $\delta_{\sigma\sigma'}$ resulting in the same Ward identity for the generalized susceptibility in Eq. (4.31) and with the definition of the non-interacting Green's function G^{ν}_0, we also obtain the form in Eq. (4.32).
The last important Ward identity for us is the one connecting one- and two-particle irreducible vertices, which can be obtained by inserting the BSE, Eq. (2.257), into Eq. (4.32). This is more conveniently written in the symbolic 4-vector notation with $\nu \coloneqq (\nu,\mathbf{k})$ because we do not need any more explicit Fourier transformations.

$$\begin{aligned}
G^{\omega+\nu}-G^{\nu} &= G^{\nu}G^{\omega+\nu}\Big[\left((G^{\omega+\nu}_0)^{-1}-(G^{\nu}_0)^{-1}\right)\\
&\qquad+\sum_{\nu_1}\Gamma^{\nu\nu_1\omega}\sum_{\nu_2}\left((G^{\omega+\nu_2}_0)^{-1}-(G^{\nu_2}_0)^{-1}\right)\chi^{\nu_1\nu_2\omega}\Big]\\
\Leftrightarrow\frac{G^{\omega+\nu}-G^{\nu}}{G^{\nu}G^{\omega+\nu}}-\left((G^{\omega+\nu}_0)^{-1}-(G^{\nu}_0)^{-1}\right) &= \sum_{\nu_1}\Gamma^{\nu\nu_1\omega}\sum_{\nu_2}\left((G^{\omega+\nu_2}_0)^{-1}-(G^{\nu_2}_0)^{-1}\right)\chi^{\nu_1\nu_2\omega}
\end{aligned}$$

Here, we use the Dyson equation and Eq. (4.32), to obtain

$$\Leftrightarrow\Sigma^{\nu+\omega}+\Sigma^{\nu} = \sum_{\nu_1}\Gamma^{\nu\nu_1\omega}\sum_{\nu_2}\left(G^{\omega+\nu_2}-G^{\nu_2}\right)\tag{4.29}$$

This can be viewed as the integral form of $\delta\Gamma/\delta G$ in Eq. (4.18).
In summary, we have derived the following Ward identities.

Important 4.4.2.1 (Ward Identities)
From Eq. (4.27) *we get a Ward identity formulated in terms of* $G^{(2)}$ *or* $\chi^{\nu\nu'\omega}$. *Because we present paramagnetic calculations in this thesis, the spin indices are suppressed where possible.*

$$\delta_{\sigma\sigma'}\left(G^{\omega+\nu'}-G^{\nu'}\right) = \sum_{\nu}\left[i\omega_m+\epsilon_{\mathbf{k}}-\epsilon_{\mathbf{q}+\mathbf{k}}\right]G^{\nu\nu'\omega}_{\sigma\sigma'}\tag{4.30}$$

$$G^{\omega+\nu}-G^{\nu} = \sum_{\nu'}\left[i\omega_m+\epsilon_{\mathbf{k}}-\epsilon_{\mathbf{q}+\mathbf{k}}\right]\chi^{\nu\nu'\omega}\tag{4.31}$$

$$= \sum_{\nu} \left[(G_0^{\omega+\nu})^{-1} - (G_0^{\nu})^{-1} \right] \chi^{\nu\nu'\omega} \tag{4.32}$$

$$\Sigma^{\omega+\nu} - \Sigma^{\nu} = \sum_{\nu'} \left[G^{\omega+\nu'} - G^{\nu'} \right] \Gamma^{\nu\nu'\omega} \tag{4.33}$$

$$= \sum_{\nu'} \left[(G_0^{\omega+\nu'})^{-1} - (G_0^{\nu'})^{-1} \right] F^{\nu\nu'\omega} G^{\nu} G^{\omega+\nu} \tag{4.34}$$

Connection to Fermi Liquid

The Ward identity Eq. (4.34) allows us to make a connection to Fermi liquid theory (see Sec. 2.5) [61, Sec. 4.4.4] and [147, D.10]. This can be seen by choosing $\omega = \omega_1 = 2\pi/\beta$, $\nu' = \nu_{-1} = -\pi/\beta$ and $\mathbf{q} = \mathbf{0}$. Then $\epsilon_{\mathbf{k}} = \epsilon_{\mathbf{k}+\mathbf{q}}$, and we can write:

$$\Sigma^{\omega_1+\nu_0} - \Sigma^{\nu_{-1}} = \sum_{\nu} \left[G^{\omega_1+\nu} - G^{\nu} \right] \Gamma^{\nu\nu_{-1}\omega_1}$$

$$\Sigma^{\omega_1+\nu_{-1}} - \Sigma^{\nu_{-1}} = -\sum_{\mathbf{k}\nu\sigma'} i\omega_1 F^{\nu\nu_{-1}\omega_1}_{\mathbf{k},\mathbf{k}'\mathbf{0},\sigma\sigma'} G^{\omega_1+\nu}_{\mathbf{0}+\mathbf{k}} G^{\nu}_{\mathbf{k}}$$

With $\Sigma^{\nu_{-1}} = (\Sigma^{\nu_{-1}})^*$ and $2\nu_0 = \omega_1$ it follows that

$$\Leftrightarrow \frac{2 \operatorname{Im} \Sigma^{\nu_0}_{\mathbf{k}}}{\nu_0} = -\sum_{\mathbf{k}\nu\sigma'} F^{\nu\nu_{-1}\omega_1}_{\mathbf{k}\mathbf{k}'\mathbf{0},\sigma\sigma'} G^{\omega_1+\nu}_{\mathbf{k}} G^{\nu}_{\mathbf{k}} \tag{4.35}$$

$$\approx \partial_{\nu} \operatorname{Re} \Sigma^{\mathrm{R},\nu} \tag{4.36}$$

This can be seen as an approximation for the quasi-particle weight $Z_{\mathbf{k}}$ at finite temperatures from Eq. (2.3b), $\partial_{\nu} \operatorname{Re} \Sigma^{\nu}_{\mathbf{k}}\big|_{\nu=0}$, implying a divergence of the full vertex (in each channel) at the *first* bosonic Matsubara frequency when approaching the Mott transition for $T \to 0$[3], demonstrating a direct effect of thermodynamical properties on the two-particle quantities.

Connection Thermodynamics

The lDΓA method presented in Sec. 5.4 does not aim to restore violations of the Ward identities directly but instead renormalizes physical susceptibilities, which are the dominant contributions in the vicinity of second-order phase transitions (where the corresponding susceptibility at the ordering vector diverges). However, these thermodynamic consistencies do not imply fulfillment of the Ward identities in return, leaving properties that rely specifically on these microscopic identities ambiguous. To illustrate the connection, we give an example of how Ward identities relate to the physical susceptibilities: They can be obtained either as a sum over the generalized susceptibilities or directly through the Ward identities that connect these to the self-energy. For example, the spin susceptibility can be calculated via the left-hand side of Eq. (4.34) (see [147, Section D.6] for the derivation):

$$\lim_{h\to 0} \frac{\Sigma^{\nu}_{\overline{\sigma}} - \Sigma^{\nu}_{\sigma}}{h} = -2 \frac{\mathrm{d}\Sigma^{\nu}_{\sigma}}{\mathrm{d}h} \tag{4.37}$$

The static susceptibility can be obtained from the generalized one;

$$\lim_{h\to 0} 2\sigma \sum_{\nu\nu'} \chi^{\nu\nu'\omega=0}_{\mathrm{m}} = \frac{\langle n_{\overline{\sigma}} \rangle - \langle n_{\sigma} \rangle}{h} = -\sigma \frac{\mathrm{d}\langle m \rangle}{\mathrm{d}h}\Big|_{h=0} = -\chi^{\omega=0}_{\mathrm{m},\mathbf{q}=\mathbf{0}} \tag{4.38}$$

Similarly to the magnetic response with the magnetization as observable, the static charge susceptibility corresponds to the compressibility $\kappa^{(1)} = n^{-2} \partial_{\mu} n$ of the system:

$$\chi^{\omega=0}_{\mathrm{d},\mathbf{q}=\mathbf{0}} = \langle n^2 \rangle - \langle n \rangle^2 = \kappa^{(2)} \stackrel{?}{=} \kappa^{(1)} \tag{4.39}$$

The thermodynamic quantities and how to obtain them from one- and two-particle functions are discussed in Sec. 4.5. The last equation indicates the problematic discrepancy between calculations of thermodynamics calculated from the one- and two-particle levels that we will explore in detail in the next sections.

[3] However, the static susceptibility does remain finite [116], as careful consideration of the limit demonstrates [147, D.10].

4.4.3 f-sum Rule and Asymptotic Behavior

One important consequence of the Ward identity in Eq. (4.32) is the f-sum rule. By summing both sides in Eq. (4.32) over the fermionic degrees of freedom $\sum_{\mathbf{k}\mathbf{k}'\nu\nu'}$ at $\mathbf{q} = 0$, we get

$$i\omega_m \chi^{\omega}_{\mathbf{q}=0} = 0 \Leftrightarrow \chi^{\omega\neq 0}_{\mathbf{q}=0} = 0, \tag{4.40}$$

because $\sum_{\mathbf{k}\nu}\left(G^{\omega+\nu}_{\mathbf{q}+\mathbf{k}} - G^{\nu}_{\mathbf{k}}\right) = 0$ and $\sum_{\nu}\left((G^{\omega+\nu}_0)^{-1} - (G^{\nu}_0)^{-1}\right) = i\omega_m$. Eq. (4.40) describes a gapless excitation at $\mathbf{q} = 0$, since $\chi^{\omega}_{\mathrm{d/m},\mathbf{q}=0}$ vanishes for arbitrarily small energies. In the symmetry-broken case, at finite magnetic fields, which can be related to the existence of a Goldstone mode [143, Section D.1].
This identity is of no immediate use for the lDΓA itself but serves as an important numerical check. One can easily verify that the Lindhard function for RPA, see Sec. 5.2.1 fulfills this condition. More importantly, the physical susceptibilities as obtained from DMFT do as well and, by extension, the ones in lDΓA . This is because the tails of $\chi^{\omega}_{r,\mathbf{q}}$ are unchanged by the λ corrections discussed in Sec. 4.5.1. Deviation from the behavior in Eq. (4.40) therefore indicates faulty data or insufficient frequency and $\mathbf{k}$-sampling grids.
By using the definition of the generalized susceptibility and the asymptotic expansion of the bare bubble from Eq. (6.30), one obtains the asymptotic behavior of the generalized susceptibility.

$$\chi^{\nu\nu'\omega}_{\mathbf{k}\mathbf{k}'\mathbf{q}} = N\beta\delta(\mathbf{k}-\mathbf{k}')\delta_{\nu\nu'}\frac{G^{\nu}_{\mathbf{k}} - G^{\omega+\nu}_{\mathbf{q}+\mathbf{k}}}{i\omega_m} + \mathcal{O}(1/\omega^2) \tag{4.41}$$

Where we used the connected part of the susceptibility $G\star G\star F\star G\star G = \mathcal{O}(1/\omega^2)$, we then sum over the fermionic degrees of freedom to obtain the f-sum rule.

Important 4.4.3.1 (f-sum rule)
The f-sum rule connects the susceptibility to the density response:

$$\lim_{|\omega|\to\infty}(i\omega_m)^2\chi^{\omega}_{\mathrm{d/m},\mathbf{q}} = \sum_{\mathbf{k}}\left(2\epsilon_{\mathbf{k}} - \epsilon_{\mathbf{k}+\mathbf{q}} - \epsilon_{\mathbf{k}-\mathbf{q}}\right)n_{\mathbf{k}} \tag{4.42}$$

$$= 2\sum_{\nu\mathbf{k}}\left(2\epsilon_{\mathbf{k}} - \epsilon_{\mathbf{k}+\mathbf{q}} - \epsilon_{\mathbf{k}-\mathbf{q}}\right)G^{\nu}_{\mathbf{k}} \tag{4.43}$$

This is also often expressed differently using the (for this thesis everywhere implicitly defined) convergence factor of $e^{-i\eta\nu}$ in the sums over the bosonic Matsubara frequencies of the Green's function. Doing so for Eq. (4.43) results in the form

$$\sum_{\omega}\left(e^{i\eta\omega} - e^{-i\eta\omega}\right)\chi^{\omega}_{\mathrm{d/m},\mathbf{q}} = \sum_{\mathbf{k}}\left(2\epsilon_{\mathbf{k}} - \epsilon_{\mathbf{k}+\mathbf{q}} - \epsilon_{\mathbf{k}-\mathbf{q}}\right)n_{\mathbf{k}\sigma} \tag{4.44}$$

The most important consequence of the f-sum rule for our context is the relationship to the kinetic energy because it provides a direct connection to a thermodynamic quantity. Furthermore, the f-sum rule defines the high-frequency asymptotic contribution of the physical susceptibilities, that are crucial for the numerical stability of the lDΓA method.

4.5 Two-particle and Thermodynamical Consistency

While Φ-derivable theories based on the LWf functional, as discussed in Sec. 4.3, provide thermodynamically consistent theories, they are not two-particle consistent, a concept we will now explore.
The two-particle Green's function does not enter the LWf directly and must be obtained through the BSE [4], where the irreducible vertex is the input and the two-particle vertex is then obtained, see Eq. (2.256) or Eq. (2.258). The single-particle Green's function obtained through the SDE, Eq. (2.7.4), and the thermodynamical quantities obtained from it will generally not coincide with the thermodynamically consistent ones obtained from the LWf. Concretely, this can be expressed as follows (we omit channel, momentum, and frequency indices here):

$$\begin{aligned}
\Sigma^{(1)} &= \frac{\delta\Phi}{\delta G}, \qquad \Gamma^{(1)} = \frac{\delta^2\Phi}{\delta G\delta G}\\
F^{(1)} &= \Gamma^{(1)} - F^{(1)}\star G\star G\star\Gamma^{(1)}\\
\Sigma^{(2)} &= \Sigma_{\mathrm{H}} + G\star G\star G\star F^{(1)} \neq \Sigma^{(1)}
\end{aligned} \tag{4.45}$$

Here, the self-energies obtained from one and two-particle vertices do not coincide; see also Sec. 5.2.1. This superscript notation for quantities calculated in these two different ways will be used for all otherwise ambiguous quantities in the following.

[4] Extensions to the formalism that incorporate two-particle consistency have been developed [50, 52]. These methods are still being extended, e.g [132], where a renormalized irreducible vertex is defined in this framework. However, methods that make use of this formalism are still rare and come with their own challenges.

While thermodynamic consistency is crucial for an accurate description of transport phenomena, static two-particle consistency is important for phase transitions, and the dynamical two-particle quantities cannot be neglected when quantum mechanical fluctuations start to dominate [115, 107]. For example, it was demonstrated that approximations with static vertices become unstable with respect to spin-flips for temperatures above the Mott transition [113]. Furthermore, the inclusion of local correlations, particularly through the non-perturbative DMFT (Sec. 5.1) seems essential for capturing important phenomena such as high-temperature superconductivity [133]. For example, the fluctuations leading to a divergence of the magnetic susceptibility and consequent onset of antiferromagnetic ordering at the intermediate coupling regime in the three-dimensional Hubbard model are due to dynamical fluctuations of the system contained in the dynamical two-particle vertex [253, 115].
In order to retain Ward identities arising from thermodynamical consistency and capture quantum dynamical criticality at the same time, the divergence of response functions χ^{ω} that correspond to thermodynamically critical behavior must be matched to critical behavior that emerges because of quantum fluctuations, encapsulated on the two-particle level through the use of the SDE [115, 23]. However, it is known that any conserving two-particle vertex that is antisymmetric under the exchange of outgoing particles must contain all possible diagrams [234]; all approximate diagrammatic constructions must therefore fail to be thermodynamically consistent [5]. This means that the discrepancy in the criticality between $\Gamma^{(1)}$ and $\Gamma^{(2)}$ can only be reconciled in the exact solution.
For this thesis, our objective is to motivate an effective method that disambiguates critical behavior between two- and one-particle levels by renormalizing the physical susceptibilities in a way that restores thermodynamical consistent consequences of the Ward identities without requiring a consistent vertex.

4.5.1 Thermodynamic Consistency and λ-corrections

In Sec. 5.4, we will discuss a method that uses the fully non-perturbative but local solution from DMFT and then add non-local corrections through the BSE and SDE. This leads to (i) the problem presented in Eq. (4.45), where a thermodynamical inconsistency is introduced; (ii) the DMFT vertex retains mean-field artifacts such as unphysical phase transitions, violating the Mermin-Wagner theorem and mean-field critical exponents. By introducing effective mass-renormalization parameters λ into the physical susceptibilities, we aim to improve the lDΓA in both aspects [125, 202].
Our core assumption for the following consideration is that non-local fluctuations in the theory are predominantly captured by physical susceptibilities. This is certainly true in the vicinity of second-order phase transitions, where the susceptibilities diverge at the critical temperature T_{C}, ordering vector $\mathbf{q}_{\mathrm{C}}$ and channel r_{C}.

$$\lim_{T\to T_{\mathrm{C}}} \chi^{\omega=0}_{r=r_{\mathrm{C}},\mathbf{q}=\mathbf{q}_{\mathrm{C}}} = \infty \tag{4.46}$$

Our approach will be to correct the susceptibilities obtained through DMFT, which contain all *local* contributions, by a rescaling determined through consistency relations that take non-local effects into account. This scaling is achieved in a way pioneered by T. Moriya for the description of itinerant magnetism [177, 176]. Here, the corrected susceptibilities are defined using a static parameter λ in the following way:

$$\chi^{\lambda_r,\omega}_{r,\mathbf{q}} = \left[\frac{1}{\chi^{\omega}_{r,\mathbf{q}}} + \lambda_r\right]^{-1} \tag{4.47}$$

Our approach relies on the Ornstein-Zernike form of the susceptibility (Eq. (4.48)) that was first designed to incorporate long-range fluctuations into short-ranged ones in classical systems [185], it can, however, also be employed for quantum mechanical systems and is routinely employed in liquid-state methods [92, Chapter 3]. Here, one typically introduces a pair correlation function $h(\mathbf{r}) = \left(\langle\hat{n}(\mathbf{r})\hat{n}\rangle - \langle n\rangle^2\right)/\rho$ with the number density ρ (compare also Eq. (2.96) for our definition of correlation functions). One then introduces a direct correlation function $c(\mathbf{r})$ that is responsible for short-range interactions, with a redefined correlation $h(\mathbf{r}) = c(\mathbf{r}) + \rho\int c(\mathbf{r}-\mathbf{r}')h(\mathbf{r}')\mathrm{d}\mathbf{r}$. In Fourier space, the convolution decouples, due to the convolution theorem Sec. 6.4.2, and one obtains a geometric type structure $h_{\mathbf{k}} = \frac{c_{\mathbf{k}}}{1-\rho c_{\mathbf{k}}} = c_{\mathbf{k}} + \rho c_{\mathbf{k}} \star c_{\mathbf{k}} + \cdots$. Comparing with the definition of the λ correction in Eq. (4.47), we motivate that the role of the short-range correlation is taken up by the local DMFT susceptibility, while the density ρ that is responsible for the coupling of these correlations, is taken on by the λ-parameter. Near a second-order phase transition, the Ornstein-Zernike of the susceptibility (for a discussion, see [49, Eq. 15], [208] and [202, Appendix B]) is:

$$\lim_{\mathbf{q}-\mathbf{q}_{\mathrm{C}}} \lim_{T-T_{\mathrm{C}}} \chi^{\omega=0}_{r,\mathbf{q}} \sim \frac{A}{|\mathbf{q}-\mathbf{q}_{\mathrm{C}}|^2 + \zeta_r^{-2}} \tag{4.48}$$

[5] For an alternative argument see Eq. (4) to Eq. (5) in [115]. Here, the condition for the divergence can also be achieved through the minimum of the span of the convolution operator [115, Eq. 5–6]. More concretely, in the notation of this thesis, the divergencies are linked to the structure of the eigenspace of the generalized susceptibilities $\chi^{\nu\nu'\omega}$ [207, 263].

Where ζ_r is the correlation length for the channel r. In this form we find that the λ parameter in Eq. (4.47) rescales the correlation length:

$$\zeta_{\lambda_r}^{-2} = \zeta_r^{-2} + \lambda_r \tag{4.49}$$

This parameter carries not only information about non-local correlations but can also contain information about mixing between the magnetic and density channel, as explained in detail in Sec. 7.1.
The λ parameters can be employed to fix consistencies between quantities that are defined through one-particle and two-particle (the susceptibilities) operators. In the following, we give an overview of the thermodynamic consistencies we consider and their one- and two-particle representations. These are numerically non-trivial to compute, due to a significant impact of the high-frequency tail behavior on their values, which will be discussed in Sec. 6.2 and Sec. 6.3.

Potential Energy The potential energy is obtained through the self-energy in the one-particle case, and $\chi^{\omega}_{\uparrow\downarrow,\mathbf{q}}$ in the two-particle case:

$$E^{(1)}_{\text{pot}} = \text{Tr}\left[\Sigma G\right] = \sum_{\mathbf{k}\nu} \Sigma^{\nu}_{\mathbf{k}} G^{\nu}_{\mathbf{k}} = U\langle \hat{n}_{\uparrow}\hat{n}_{\downarrow}\rangle \tag{4.50}$$

$$E^{(2)}_{\text{pot}} = U\sum_{\mathbf{q}\omega}\left(\chi^{\omega}_{\text{d},\mathbf{q}} - \chi^{\omega}_{\text{m},\mathbf{q}}\right) + U\frac{n^2}{2} = U\sum_{\mathbf{q}\omega}\chi^{\omega}_{\uparrow\downarrow,\mathbf{q}} + U\frac{n^2}{2} \tag{4.51}$$

We omitted the λ superscript here. Note that also self-energy and non-local Green's functions contain these implicitly because they are computed from λ-corrected susceptibilities. We will discuss how they are obtained in Sec. 5.4.

Consistency of Electron Density The consistency in the electron density, leading to the fulfillment of the Pauli principle, also leads to behavior according to the Mermin-Wagner theorem (see Sec. 4.5.2). We list several consistencies here that will be used in the construction of the thermodynamically consistent variant of the lDΓA method in Sec. 5.4 and therefore make some forward references at this point.
The main equations that fix the λ_{d} parameter are:

$$\text{PP}^{(1)} = \frac{n}{2}\left(1 - \frac{n}{2}\right) \tag{4.52}$$

$$\text{PP}^{(2)} = \sum_{\mathbf{q}\omega}\left(\chi^{\omega}_{\text{d},\mathbf{q}} + \chi^{\omega}_{\text{m},\mathbf{q}}\right) = \sum_{\mathbf{q}\omega}\chi^{\omega}_{\uparrow\uparrow,\mathbf{q}} + \tag{4.53}$$

However, the electron density appears in more places, and inconsistencies between these can lead to problematic effects, most often observed as non-causal self-energies.

$$n \overset{!}{=} \text{Tr}\left[G\right] = \sum_{\mathbf{k}\nu} G^{\nu}_{\mathbf{k}} e^{-i\nu_n 0^+} = \sum_{\nu\mathbf{k}} G^{\lambda_{\text{m}},\lambda_{\text{d}},\nu}_{\mathbf{k}} \tag{4.54}$$

$$\frac{n}{2}\left(1 - \frac{n}{2}\right) \overset{!}{=} \sum_{\omega\mathbf{q}}\left(\chi^{\lambda_{\text{d}},\omega}_{\text{d},\mathbf{q}} + \chi^{\lambda_{\text{m}},\omega}_{\text{m},\mathbf{q}}\right) \tag{4.55}$$

$$U^2\frac{n}{2}\left(1 - \frac{n}{2}\right) \overset{!}{=} \lim_{n\to\infty} \text{Re}\left[i\nu_n\left(\Sigma^{i\nu_n}_{\mathbf{k}} - \frac{Un}{2}\right)\right] \tag{4.56}$$

The first condition, Eq. (4.54), is then satisfied by fixing a chemical potential, implying $\mu_{\text{DMFT}} \neq \mu_{\text{lDΓA}}$ (see Sec. 5.4). Eq. (4.55) and Eq. (4.56) are non-trivial. One fixes the Pauli principle as stated above in Eq. (4.53). However, the electron density appears in the high-frequency tail of the self-energy as well. The structure of this equation (involving a limit) is different from all others considered here. Furthermore, no susceptibility enters this equation explicitly on either side of the equation. One could attempt to employ the λ_{d} parameter to fix the high-frequency tail of the self-energy. However, motivated by the form of the λ correction as the renormalization of response functions close to phase transitions, we choose to emphasize the importance of thermodynamic consistency, which uses one of the λ parameters for the consistency condition of the potential energy. We, therefore, go a different route for the fulfillment of this condition and apply either (i) an ad-hoc fix reminiscent of the self-consistency condition in the dual boson approach [271, Eq. 4] where the fulfillment of this condition leads to an intrinsic consistency between the potential energies; or (ii) by explicitly breaking the symmetry between spin channels. A discussion will be given in Sec. 6.2.4. Note however, that the first introduction of λ parameters for the lDΓA method chose to emphasize the tail condition Eq. (4.56) over thermodynamical ones [125, Sec. V], so our selection of λ-parameter enforced conditions is neither binding nor unique.

Kinetic Energy The kinetic energy stands out against the Pauli principle and the potential energy as only contained in the high-frequency asymptotic of the susceptibility. Specifically as consequence of the f-sum rule Eq. (4.43), we obtain after summation over $\mathbf{q}$:

$$E^{(1)}_{\text{kin}} = \text{Tr}\left[\epsilon_{\mathbf{k}} G\right] = \sum_{\mathbf{k}\nu} \epsilon_{\mathbf{k}} G^{\nu}_{\mathbf{k}} \tag{4.57}$$

$$E_{\text{kin}}^{(2)} = \lim_{|\omega|\to\infty} (i\omega_m)^2 \sum_{\mathbf{q}} \chi^{\omega}_{\text{d/m},\mathbf{q}} \tag{4.58}$$

The kinetic energy may be treated sufficiently on the single-particle level, being defined as the expectation value of a single-particle operator [202, Sec. IV.A]. However, it is, in fact, possible to also keep this quantity consistent by explicitly enforcing the f-sum rule. This will be discussed in Sec. 5.4.3.

4.5.2 Critical Exponents and Mermin-Wagner Theorem

There are many versions of the Mermin-Wagner theorem and a review or introduction is beyond the scope of this thesis and therefore left to the literature [170, 104, 282, 77]. For us, it is sufficient to state that magnetic phase transitions (which specifically exclude infinite-order phase transitions such as the Kosterlitz-Thouless transition) are prohibited in two or fewer dimensions at finite temperatures in a Hubbard-like model.
It can be argued that methods that predict phase transitions in two spatial dimensions should be scrutinized concerning their three-dimensional predictions more carefully as well. We, therefore, want to enforce this property, which is not directly linked to the two-particle consistency discussed before. Instead, it stems from the fact that susceptibilities in approximate theories may have spurious divergent susceptibilities in low dimensions.
Following [277, Section 3] closely, we show that the form of the λ corrected susceptibilities in Eq. (4.47) naturally enforces finite susceptibilities. The fulfillment of the Pauli principle $\langle \hat{n}^2 \rangle = \langle \hat{n} \rangle$ is a sufficient condition for the fulfillment of the Mermin-Wagner theorem:

$$\sum_{\omega\mathbf{q}} \chi^{\lambda_{\text{m}},\omega}_{\text{m},\mathbf{q}} = 2\langle \hat{n}_\uparrow \hat{n}_\uparrow \rangle - \langle \hat{n}_\uparrow \hat{n}_\downarrow \rangle = n - 2\langle \hat{n}_\uparrow \hat{n}_\downarrow \rangle \tag{4.59}$$

$$\sum_{\omega\mathbf{q}} \chi^{\lambda_{\text{d}},\omega}_{\text{d},\mathbf{q}} = 2\langle \hat{n}_\uparrow \hat{n}_\uparrow \rangle + 2\langle \hat{n}_\uparrow \hat{n}_\downarrow \rangle = n + 2\langle \hat{n}_\uparrow \hat{n}_\downarrow \rangle - n^2 \tag{4.60}$$

The sum and difference lead to our definition of the two-particle Pauli-Principle Eq. (4.53) and potential energy Eq. (4.51). The λ_r superscript already indicates that we employ these two free parameters to enforce fulfillment of Eq. (4.53). We can now observe that at a phase transition, leading to a form of the susceptibility given in Eq. (4.48) we prevent a divergence of the susceptibility at all finite values of λ_r, even when the uncorrected correlation length diverges, according to Eq. (4.49). This is necessary, since the non-corrected susceptibility $\chi^{\omega}_{r,\mathbf{q}}$ is obtained from a mean-field theory and will linearly cross the phase boundary at T_{C} (see below).

$$\chi^{\lambda_r,\omega=0}_{r,\mathbf{q}+\mathbf{q}_{\text{C}}} \sim \int \frac{1}{\mathbf{q}^2 + \zeta_{\text{MF}}^{-2} + \lambda_r} \frac{\mathrm{d}^d q}{(2\pi)^d} \overset{!}{=} C \tag{4.61}$$

$$C \coloneqq \frac{n}{2}\left(1 - \frac{n}{2}\right) - \sum_{\mathbf{q}\omega} \chi^{\lambda_{\overline{r}},\omega}_{\overline{r},\mathbf{q}} \tag{4.62}$$

C is finite because the subdominant channel has a finite susceptibility. The integral in Eq. (4.61) can be evaluated and yields a finite value, even at an artificial mean-field phase transition with $\zeta_{\text{MF}} \to \infty$ in 2 spatial dimensions. Setting $d = 2$ the integral in Eq. (4.61) evaluates to

$$\chi^{\lambda_r,\omega=0}_{r,\mathbf{q}+\mathbf{q}_{\text{C}}} \sim \ln(\lambda_r) < \infty \tag{4.63}$$

C has a temperature dependence and has been analyzed in the context of RPA and TPSC [178, 208]. Most importantly here, the existence of a non-zero λ_r parameter prevents a divergence of the susceptibility in Eq. (4.61), which would lead to a spurious phase transition in 2 spatial dimensions.
Near the phase transition, scaling laws with critical exponents obtained from renormalization group techniques take over. Here the susceptibility and correlation length scale as (e.g. [61, Chapter 10])

$$\zeta \sim |T - T_{\text{C}}|^{-\nu}, \quad \chi \sim |T - T_{\text{C}}|^{-\overbrace{\nu(2-\eta)}^{\gamma}}, \quad C_{\text{V}} \sim |T - T_{\text{C}}|^{\alpha} \tag{4.64}$$

For mean-field theories, it is known that

$$\nu = \frac{1}{2}, \quad \eta = 0, \quad \gamma = 1, \quad \alpha = 2 - d/2 \tag{4.65}$$

Mean-field theories become exact in the vicinity of phase transitions above the critical dimension of 4, where fluctuations become less important. Furthermore, mean-field theories may be exact up until a critical region with a size defined through the Ginzburg criterion of size [154]

$$\Delta T_{\text{C}} \sim T_{\text{C}}^2 \tag{4.66}$$

This behavior is indeed observed in our numerical studies for the 3 dimensional cubic lattice, discussed in Sec. 7.1, where the λ-corrected susceptibilities follow mean-field behavior up until a critical region. Here, the critical exponent starts to deviate from the mean-field one. As of the writing of this thesis, the exact

exponent is unknown. For TPSC the Berlin-Kac spherical model universality class was determined [49] which could be assumed to also hold for lDΓA due to its similar rescaling of the correlation function. More importantly for our considerations here, the argument concerning the critical exponents suggests that the rescaling of a DMFT mean-field susceptibility is also valid in regimes above the critical region since the correct behavior is recovered with $\lambda_r(T) \to 0$. Indeed, we find in Sec. 7.1 that at most a static shift in the mean-field critical exponent far above the critical region is observed. Furthermore, we also find a scaling of the critical region with T_C.

5 Methods

In the following, we will discuss several methods for calculating quantities in strongly correlated many-particle systems. Each method will be presented from a pragmatic point of view with a brief summary of the assumptions and an overview of the algorithmic solution. Subsequently, we will discuss the properties with respect to conservation laws and two-particle consistencies, as presented in Sec. 4, building up to the lDΓA *method, whose extensions were developed as the main focus of this thesis. Here we will go into more detail and also thoroughly discuss the numerical details in Sec. 6.*

5.1 Dynamical Mean field Theory

In this section, we present the DMFT method. Due to its immense success of describing strong correlation physics in real materials, for example, by virtue of DFT+DMFT, there are plenty of well-written and pedagogical introductions to this subject matter available [80, 281, 62]. Nevertheless, a very brief derivation will be presented here as well since the construction of approximations to the full many-body problem does play a critical role for this thesis in that the fulfillment of conservation laws can follow from the construction; see also Sec. 4.

5.1.1 Cavity Construction

In the following, we give an abbreviated version of the cavity construction to obtain the DMFT method, originally in [80, Sec. III.A] and later [281]; parts of the derivation are also excerpts from my master's thesis [246].
The central idea for the cavity construction is the same as the mean-field constructions discussed in the limits of the weak coupling and infinite coordination number of the Hubbard model Sec. 3.4.2 and Sec. 3.6.1. Specifically, we will use the correspondence between the Hubbard model and the Anderson impurity model Sec. 3.7. As indicated by our previous considerations in Sec. 3.6, the Feynman diagrams that contribute to the self-energy of the Hubbard model and AIM are identical for an infinite coordination number (see discussion around Eq. (3.98)). We will assume an interacting bath, i.e. full Hubbard model, and then prove that the Anderson impurity model yields the same action in infinite dimensions. This will result in the condition that the self-energy of the bath and the impurity must be equal, making the bath interactions also implicitly dependent on the interaction U, as we have seen during our discussion of the self-energy in the case of strong coupling Sec. 3.3 and weak coupling Sec. 3.4. Algorithmically, this means that self-energy plays the role of the average spin field in the traditional Weiss mean-field theory Sec. 3.6.1, however, the role of the mean-field is indeed taken on by the Weiss Green's function $\mathcal{G}_0$, as discussed below.

Action of the Hubbard Model in $d = \infty$ Details for the following abbreviated calculation can be found in [80, Sec. III.A] and [84, Sec. 2.2.2].
We set $i = 0$ to be the impurity lattice point and write down the action of the full Hubbard model (using the definition of the action in Eq. (2.161), we use $\overline{\phi}$ and ϕ for the Grassmann fields):

$$
\begin{aligned}
S_{\mathrm{Hub}} &= S_{\mathrm{lattice}} + S_{\mathrm{cavity}} + S_{\mathrm{hyb}} \qquad (5.1)\\
S_{\mathrm{lattice}} &= \int \mathrm{d}\tau \sum_{i\neq 0,\sigma} \overline{\phi}_{i\sigma}(\tau)\left[\partial_\tau - \mu\right]\phi_{i\sigma}(\tau) - \sum_{ij\neq 0,\sigma} t_{ij}\overline{\phi}_{i\sigma}(\tau)\phi_{j\sigma}(\tau) + U\sum_{i\neq 0}\overline{\phi}_{i\uparrow}(\tau)\phi_{i\uparrow}(\tau)\overline{\phi}_{i\downarrow}(\tau)\phi_{i\downarrow}(\tau)\\
S_{\mathrm{cavity}} &= \int \mathrm{d}\tau \left(\sum_{\sigma}\overline{\phi}_{0\sigma}(\tau)\left[\partial_\tau - \mu\right]\phi_{0\sigma}(\tau) + U\overline{\phi}_{0\uparrow}(\tau)\phi_{0\uparrow}(\tau)\overline{\phi}_{0\downarrow}(\tau)\phi_{0\downarrow}(\tau)\right)\\
S_{\mathrm{hyb}} &= -\int \mathrm{d}\tau \sum_{i\sigma} t_{i0}\left(\overline{\phi}_{i\sigma}(\tau)\phi_{0\sigma}(\tau) + \overline{\phi}_{0\sigma}(\tau)\phi_{i\sigma}(\tau)\right)
\end{aligned}
$$

For the last line we used $t_{i0} = t_{0i}$. The mapping to an effective single-site problem is obtained by tracing out all sites except $i = 0$. Subsequently, we will argue that for the AIM and Hubbard models, the resulting thermodynamic averages are equivalent under the DMFT approximation (at $z = \infty$). We first perform the integration over the bath and call the remaining action of the lattice site 0 mean-field action.

$$
\begin{aligned}
\frac{1}{Z_{\mathrm{MF}}}e^{-S_{\mathrm{MF}}} &= \frac{1}{Z_{\mathrm{full}}}\int \prod_{i\neq 0,\sigma}\mathcal{D}\left[\overline{\phi}_{i\sigma},\phi_{i\sigma}\right]e^{-S_{\mathrm{Hub}}}\\
&\approx \frac{1}{Z_{\mathrm{full}}}\int \prod_{i\neq 0,\sigma}\mathcal{D}\left[\overline{\phi}_{i\sigma},\phi_{i\sigma}\right]e^{-S_{\mathrm{lattice}}[\overline{\phi}_{i\neq 0\sigma},\phi_{i\neq 0\sigma}]}e^{-S_{\mathrm{hyb}}[\overline{\phi}_{i\sigma},\phi_{i\sigma}]}e^{-S_{\mathrm{cavity}}[\overline{\phi}_{0\sigma},\phi_{0\sigma}]}\\
&= \frac{1}{Z_{\mathrm{full}}}e^{-S_{\mathrm{cavity}}}\int \prod_{i\neq 0,\sigma}\mathcal{D}\left[\overline{\phi}_{i\sigma},\phi_{i\sigma}\right]e^{-S_{\mathrm{hyb}}}e^{-S_{\mathrm{lattice}}} = \frac{Z_{\mathrm{lattice}}}{Z_{\mathrm{full}}}e^{-S_{\mathrm{cavity}}}\left\langle e^{-S_{\mathrm{hyb}}}\right\rangle_{\mathrm{lattice}} \qquad (5.2)\\
\Rightarrow Z_{\mathrm{MF}} &= \frac{Z_{\mathrm{full}}}{Z_{\mathrm{lattice}}} \qquad (5.3)\\
S_{\mathrm{MF}} &= S_{\mathrm{cavity}} - \log\left[\left\langle e^{-S_{\mathrm{hyb}}}\right\rangle_{\mathrm{lattice}}\right] \qquad (5.4)
\end{aligned}
$$

Using this mean-field action, we can write the hybridization under the expectation value of the lattice action. Next, we expand the hybridization action (Eq. (5.2)) and find the leading order of $\frac{1}{\sqrt{z}}$, in order to apply proper scaling.

$$
\begin{aligned}
Z_{\mathrm{MF}} = \int \mathcal{D}\left[\overline{\phi}_{0\sigma}\right]\mathcal{D}\left[\phi_{0\sigma}\right]\\
\times e^{-S_{\mathrm{cavity}}}\left\langle\sum_{n=0}^{\infty}\frac{1}{n!}\prod_{m=1}^{n}\left[\int_0^\beta \mathrm{d}\tau_m \sum_{i,\sigma}\left(t_{i0}\overline{\phi}_{i\sigma}(\tau_m)\phi_{0\sigma}(\tau_m) + t_{0i}\overline{\phi}_{0\sigma}(\tau_m)\phi_{i\sigma}(\tau_m)\right)\right]\right\rangle_{\mathrm{lattice}}
\end{aligned}
$$

$$
\begin{aligned}
= \int \mathcal{D}\left[\overline{\phi}_{0\sigma}\right] \mathcal{D}\left[\phi_{0\sigma}\right] e^{-S_{\text{cavity}}} \Bigg[1 \\
&- \int \mathrm{d}\tau \sum_{\sigma, i\neq 0} \left\langle t_{i0} \overline{\phi}_{i\sigma}(\tau) \phi_{0\sigma}(\tau) + t_{0i} \overline{\phi}_{0\sigma}(\tau') \phi_{i\sigma}(\tau') \right\rangle_{\text{lattice}} \\
&+ \frac{1}{2!} \iint \mathrm{d}\tau \mathrm{d}\tau' \sum_{\sigma, i, j\neq 0} \left\langle t_{i0} t_{j0} \overline{\phi}_{i\sigma}(\tau) \phi_{0\sigma}(\tau) \overline{\phi}_{j\sigma}(\tau') \phi_{0\sigma}(\tau') \right\rangle_{\text{lattice}} \\
&+ \frac{1}{2!} \iint \mathrm{d}\tau \mathrm{d}\tau' \sum_{\sigma, i, j\neq 0} \left\langle t_{0i} t_{j0} \overline{\phi}_{0\sigma}(\tau) \phi_{i\sigma}(\tau) \overline{\phi}_{j\sigma}(\tau') \phi_{0\sigma}(\tau') \right\rangle_{\text{lattice}} \\
&+ \frac{1}{2!} \iint \mathrm{d}\tau \mathrm{d}\tau' \sum_{\sigma, i, j\neq 0} \left\langle t_{i0} t_{0j} \overline{\phi}_{i\sigma}(\tau) \phi_{0\sigma}(\tau) \overline{\phi}_{0\sigma}(\tau') \phi_{j\sigma}(\tau') \right\rangle_{\text{lattice}} \\
&+ \frac{1}{2!} \iint \mathrm{d}\tau \mathrm{d}\tau' \sum_{\sigma, i, j\neq 0} \left\langle t_{0i} t_{0j} \overline{\phi}_{0\sigma}(\tau) \phi_{i\sigma}(\tau) \overline{\phi}_{0\sigma}(\tau') \phi_{j\sigma}(\tau') \right\rangle_{\text{lattice}} \\
&+ \mathcal{O}(t^3) \Bigg]
\end{aligned} \tag{5.5}
$$

Here we apply the knowledge from the infinite coordination number limit of the Hubbard model that a proper rescaling eliminates all terms of order $\Omega(t^3)$, see Eq. (3.93) for a discussion. The first order as well as the first and third term of the second order, are equal to 0, and we arrive at:

$$
Z_{\text{MF}} = \int \mathcal{D}\left[\overline{\phi}_{0\sigma}\right] \mathcal{D}\left[\phi_{0\sigma}\right] e^{-S_{\text{cavity}}} \Big[1 - \iint \mathrm{d}\tau \mathrm{d}\tau' \sum_{\sigma} \Big\langle \overline{\phi}_{0\sigma}(\tau) \sum_{i,j\neq 0} \left(t_{i0} t_{0j} \overline{\phi}_{i\sigma}(\tau) \phi_{j\sigma}(\tau') \right) \phi_{0\sigma}(\tau') \Big] \Big\rangle_{\text{lattice}} \tag{5.6}
$$

With the usual definition of the expectation value $G^{\text{lattice}}_{\cdots}(\cdots) = \langle T\left[\cdots\right] \rangle_{\text{lattice}}$, we can then write:

$$
S_{\text{MF}} = S_{\text{cavity}} - \iint \mathrm{d}\tau \mathrm{d}\tau' \sum_{\sigma i j} \overline{\phi}_{0\sigma}(\tau) t_{i0} t_{0j} G^{\text{lattice}}_{ij}(\tau - \tau') \phi_{0\sigma}(\tau) \tag{5.7}
$$

Here we define the Weiss function $\mathcal{G}_{0\,\sigma}(\tau - \tau')$ with the name in reference to the mean-field approach from Sec. 3.6.1.

$$
\mathcal{G}^{-1}_{0\,\sigma}(\tau - \tau') := -\delta_{ij} \left(\partial_\tau - \mu \right) - \sum_{ij} t_{i0} t_{0j} G^{\text{lattice}}_{ij}(\tau - \tau') \tag{5.8}
$$

Or in frequency notation,

$$
\mathcal{G}^{\nu}_{0,\sigma} = \left[i\nu_n + \mu - \sum_{ij} t_{0i} t_{0j} G^{\text{lattice}}_{ij} \right]^{-1} . \tag{5.9}
$$

Finally, we can now write the mean-field action of the Hubbard model under the $z \to \infty$ approximation (Eq. (5.5)). For comparison, we also restate the full action of the Hubbard model. $G_{ij}(\tau - \tau')$ contains the full Hubbard interaction for each site.

$$
S_{\text{Hub}} = \iint \mathrm{d}\tau \mathrm{d}\tau' \sum_{\sigma} \overline{\phi}_{i\sigma}(\tau) G^{-1}_{ij}(\tau - \tau') \phi_{j\sigma}(\tau) + U \sum_{i} \int \mathrm{d}\tau \overline{\phi}_{i\uparrow}(\tau) \phi_{i\uparrow}(\tau) \overline{\phi}_{i\downarrow}(\tau) \phi_{i\downarrow}(\tau) \tag{5.10}
$$

$$
S_{\text{MF}} = \iint \mathrm{d}\tau \mathrm{d}\tau' \sum_{\sigma} \overline{\phi}_{0\sigma}(\tau) \mathcal{G}^{-1}_{0\,\sigma}(\tau - \tau') \phi_{0\sigma}(\tau) + U \int \mathrm{d}\tau \overline{\phi}_{d\uparrow}(\tau) \phi_{d\uparrow}(\tau) \overline{\phi}_{d\downarrow}(\tau) \phi_{d\downarrow}(\tau) \tag{5.11}
$$

Action of the Anderson Impurity Model We will now derive the equivalence of the mean-field action for the Anderson impurity model. The derivation follows [83].
As before in Sec. 3.7, $\hat{d}_\alpha$ is the annihilation operator of the state α for the impurity and $\hat{c}_\alpha$ the annihilation operator for the bath. The Grassmann fields for impurity and bath are denoted by a c and d subscript, respectively.

$$
\begin{aligned}
Z &= \int \mathcal{D}\left[\overline{\phi}_d, \phi_d, \overline{\phi}_c, \phi_c\right] e^{-S\left[\overline{\phi}_d, \phi_d, \overline{\phi}_c, \phi_c\right]} \\
S_{\text{AIM}}\left[\overline{\phi}_d, \phi_d, \overline{\phi}_c, \phi_c\right] &= \sum_{\alpha} \int \mathrm{d}\tau \left[\overline{\phi}_{c,\alpha}(\tau) \left(\partial_\tau - \mu \right) \phi_{c,\alpha}(\tau) + H_{\text{AIM}}\left[\overline{\phi}_{d,\alpha}(\tau), \phi_{d,\alpha}(\tau), \overline{\phi}_{c,\alpha}(\tau), \phi_{c,\alpha}(\tau) \right] \right] \\
&= \sum_{\sigma} \int \mathrm{d}\tau \Bigg[\overline{\phi}_{d,\sigma}(\tau) \left(\partial_\tau - \mu \right) \phi_{d,\sigma}(\tau) + H_{\text{U}}\left[\overline{\phi}_{d,\sigma}(\tau), \phi_{d,\sigma}(\tau) \right] \\
&\quad + \sum_{ij} \int \mathrm{d}\tau' \Bigg(\overline{\phi}_{c,i\sigma}(\tau) \left(\delta(\tau - \tau') \partial_\tau - \mu + \epsilon_i \right) \phi_{c,j\sigma}(\tau')
\end{aligned}
$$

$$+ \overline{\phi}_{c,i\sigma}(\tau) V^{\star}_{i\sigma} \phi_{d,\sigma}(\tau') + \overline{\phi}_{d,\sigma}(\tau) V_{i\sigma} \phi_{c,i\sigma}(\tau') \Big) \Big]$$

We have again split the action into three contributions. The first line of the equation above is the mean-field action, the second line is the bath action, and the third line is the hybridization.

$$= \sum_{\sigma} \iint \mathrm{d}\tau \mathrm{d}\tau' \Bigg[\overline{\phi}_{d,\sigma}(\tau) G_0^{-1}(\tau - \tau') \phi_{d,\sigma}(\tau)$$
$$- \sum_{ij} \int \Big(-\overline{\phi}_{c,i\sigma}(\tau) M_{ij} \overline{\phi}_{c,j\sigma}(\tau') + \delta_{ij} \overline{\phi}_{c,i\sigma}(\tau)\, J_{i\sigma}(\tau') + \delta_{ij} \overline{J}_{j\sigma}(\tau)\, \phi_{c,j\sigma}(\tau') \Big) \Bigg] + S_U$$

Here, we introduced the following symbols:

$$J_{i\sigma}(\tau) = V_{i\sigma} \phi_{d,\sigma}(\tau), \qquad \overline{J}_{i\sigma}(\tau) = \overline{\phi}_{d,\sigma}(\tau) V^{\star}_{i\sigma}, \qquad M_{ij} = -\left(\partial_\tau + \mu - \epsilon_i\right)$$

This allows us to use Eq. (2.173) in order to integrate out the bath into a constant factor. The constants and pre-factor of $\ln(\det(M))$ is absorbed into Z_{MF}.

$$S_{\mathrm{AIM}} = A - \mathrm{Tr}\left(\ln\left[\delta_{ij}\left(\partial_\tau - e_i + \mu\right)\right]\right) = A - S_0 - \mathrm{Tr}\left(\ln\left(G^{-1}_{0,ij\sigma}(\tau)\right)\right)$$

We denote the bath Green's function with $G_{0,\sigma}(\cdot)$

$$= \sum_{i\sigma} \int \mathrm{d}\tau \left[\overline{\phi}_{d\sigma}(\tau) \left(\partial_\tau - \mu\right) \phi_{d\sigma}(\tau) \right] + \sum_{ij\sigma} \int \mathrm{d}\tau \int \mathrm{d}\tau' J^{\star}_{i\sigma}(\tau) \left[M^{-1}\right]_{ij} J_{j\sigma}(\tau') + S_U$$
$$= \cdots + \sum_{ij\sigma} \int \mathrm{d}\tau \int \mathrm{d}\tau' \overline{\phi}_{i\sigma}(\tau) \underbrace{\left[\Delta_\sigma(\tau - \tau')\right]_{ij}}_{= V^{\star}_{i\sigma} G_{0,\sigma}(i,j,\tau-\tau') V_{j\sigma}} \phi_{j\sigma}(\tau')$$

We can now insert the Hubbard model as the local Hamiltonian:

$$S_{\mathrm{AIM}} = \sum_{ij\sigma} \iint \mathrm{d}\tau \mathrm{d}\tau' \overline{\phi}_{i\sigma}(\tau) \left(\delta(\tau - \tau') \left(\partial_{\tau'} - \mu\right) + \Delta(\tau - \tau') \right) \phi_{j\sigma}(\tau) + U \int \mathrm{d}\tau \overline{\phi}_{d\uparrow}(\tau) \phi_{d\uparrow}(\tau) \overline{\phi}_{d\downarrow}(\tau) \phi_{d\downarrow}(\tau) \tag{5.12}$$

Comments Comparing the action with the mean-field action of the Hubbard model (in Eq. (5.11)) in $z \to \infty$, we conclude that both are identical, with the relationship between the hybridization function and the mean-field Weiss Green's function given below. The action formulation of the AIM allows for sampling of the impurity Green's function through Monte Carlo, by randomly sampling imaginary times τ_i at which the hybridization $\Delta(\tau_i)$ or Weiss Green's function $\mathcal{G}_0(\tau_i)$ acts. A Markov chain can then be constructed by evaluating the transition probability between a state with and without this interaction at τ_i [83, 246]. This setup is called CTQMC and has been used for some of the results presented in this thesis. It allows the unbiased (i.e. when the number of Monte Carlo samples goes to infinity the resulting quantity is exact) computation of the impurity Green's functions for an infinite bath number AIM, compared to the ED approach discussed in Sec. 6.6.

Important 5.1.1.1 (Mean-Field Quantities)
Here we gather important quantities used in the context of DMFT. The hybridization function Δ^{ν}_{σ} and Weiss Green's function $\mathcal{G}^{\nu}_{0,\sigma}$ are defined as follows:

$$\Delta_\sigma(\tau - \tau') = \sum_l |V_{l\sigma}|^2 \left(\Theta(\tau - \tau') - n_{\mathrm{F}}(\epsilon_l)\right) \tag{5.13}$$

$$\Delta^{\nu}_{\sigma} = \sum_l \frac{|V_{l\sigma}|^2}{i\nu_n - \epsilon_l} \tag{5.14}$$

$$\mathcal{G}^{\nu}_{0,\sigma} = \left[i\nu_n + \mu - \Delta^{\nu}_{\sigma}\right]^{-1} = \left[i\nu_n + \mu - \sum_l \frac{|V_{l\sigma}|^2}{i\nu_n - \epsilon_l} \right]^{-1} \tag{5.15}$$

The parametrization through the Anderson parameters $V_{l\sigma}$ and ϵ_l is useful for exact diagonalization impurity solvers, but not required for DMFT.

Despite being only exact in the infinite coordination number limit, DMFT is surprisingly accurate for most lattice types and interaction ranges. We have seen in Sec. 3.3 and Sec. 3.4, that perturbative approaches from the strong- and weak-coupling limits cannot explain the physics of the other case, respectively. The non-perturbative nature of DMFT in the coupling strength is, therefore, a qualitative

improvement that is also capable of fully capturing intermediate regime physics. Only when going to systems with dominant non-local correlations, such as in the vicinity of second-order phase transitions or in two spatial dimensions, one finds significant qualitative deviations from the local solutions. The first case will be investigated in Sec. 7.1, where the discrepancies for the antiferromagnetic ordering in the 3-dimensional simple cubic lattice are discussed. The effects of two spatial dimensions will be investigated in Sec. 7.2. Here, the mean-field nature of DMFT actually predicts an erroneous phase transition, which is prohibited by the Mermin-Wagner theorem Sec. 4.5.2. Furthermore, the **k**-independence of the self-energy implies a Fermi-liquid behavior of the lattice Green's function. This stands in contrast to the Fermi liquid breakdown in the pseudogap regime of the cuprate phase diagram. In the following, we will discuss the concrete algorithmic construction of local solutions, using DMFT. Subsequently, we will discuss a method that introduces non-local corrections diagrammatically.

5.1.2 DMFT Algorithm

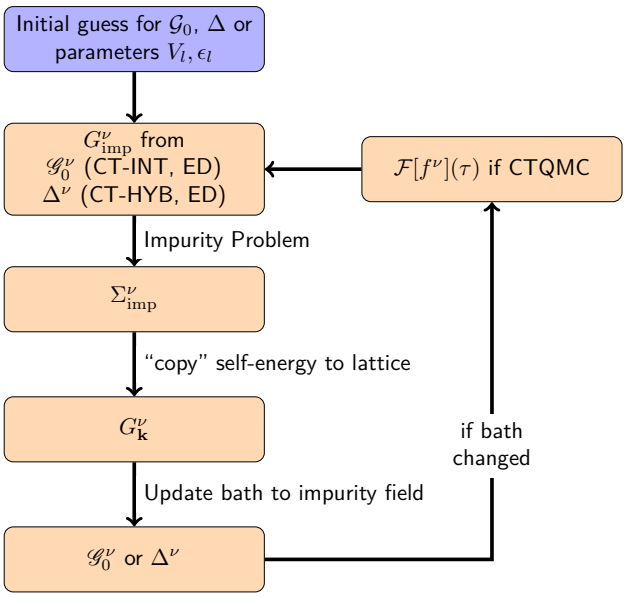

Figure 5.1: Program flow of the DMFT loop

The equivalence of the actions for the Hubbard model in the limit of infinite coordination number and the Anderson impurity model allows for a self-consistent solution method, as usual for mean-field methods.
One begins with an initial guess for the mean-field, here the Weiss Green's function $\mathscr{G}^\nu_{0,\sigma}$ or the hybridization function Δ^ν_σ. This gives rise to an effective single-site equation called *impurity problem*. Solving this, for example, with exact diagonalization Sec. 6.6 yields a (momentum independent) Green's function for the impurity G^ν_{imp}. Following from Eq. (5.9), one obtains a relationship between the impurity and Weiss Green's function given in Eq. (5.16) below [80, Sec. III.C].
One then applies the newly constructed self-energy to the bath (Eq. (5.17)) which gives the bath Green's function $G^\nu_{\mathbf{k}}$. Keeping in mind that the previous Weiss Green's function or hybridization was only an initial guess, we are now looking for a method to obtain the correct ones. Here, we impose the self-consistency condition $G^\nu_{\text{imp}} = \sum_b k G^\nu_b k$ (Eq. (5.18)) and, again, use the relationship between Weiss and impurity Green's function closing the loop to an updated Weiss Green's function (or hybridization). In order to find a solution for this self-consistency, one could try to employ a root finding method, such as Newton's method Sec. 6.5.1, to find correct parameters $V_{l,\sigma}$ and ϵ_l, that fulfill the condition Eq. (5.16). In fact, this is a viable option [255] but is generally not used due to stability issues. Instead, the solution is obtained using a Jacobi iteration by computing a bath Green's function from the impurity self-energy, using Eq. (5.17). This gives rise to a new Weiss Green's function or hybridization that poses a new impurity problem, etc. The Jacobi iteration method is so closely associated with the usual solution method for the DMFT self-consistency equations that it is commonly not even stated as such, but as an integral part of the method itself. This algorithmic way of constructing a solution is shown in Fig. 5.1.
Note that specifically high-precision fixed density calculations using ED as an impurity solver, different root-finding methods may be better suited, since they are able to recover the full spectrum of the solution in the hysteresis region of the Mott insulator transition [255]. However, most of these methods require the calculation of the Jacobi matrix, which can be prohibitively expensive. The introduction of automatic differentiation to most languages due to the increased popularity of machine learning techniques can help solve this issue. We will discuss some aspects in Sec. 6.6.

Important 5.1.2.1 (DMFT Self-Consistency)
The Dynamical Mean Field Theory consists of the following set of equations that must all hold simultaneously. Usually, the left-hand side of the following equations is computed from the right-

hand side. The relationship between impurity and Weiss Green's function:

$$\Sigma^\nu = \left[\mathscr{G}_0^\nu\right]^{-1} - \left[G_{\text{imp}}^\nu\right]^{-1}, \tag{5.16}$$

The lattice Green's function, which incorporates the correlation effects from the impurity by virtue of the local impurity self-energy:

$$\left[G_{\mathbf{k}}^\nu\right]^{-1} = i\nu_n + \mu - \epsilon_{\mathbf{k}} - \Sigma^\nu \tag{5.17}$$

*The DMFT self-consistency equation requires the local (***k** *integrated lattice) Green's function to be equal to the impurity Green's function:*

$$G_{\text{imp}}^\nu = \sum_{\mathbf{k}} G_{\mathbf{k}}^\nu \tag{5.18}$$

Note that Eq. (5.18) implies, for the self-consistency cycle with ED as an impurity solver (discussed below) the following: One defines the Weiss Green's function in terms of the bath parameters that are obtained from some sort of minimizer (in practice `BFSG`) with the condition $\mathscr{G}_0^\nu \stackrel{!}{=} \left[\sum_{\mathbf{k}} \left(i\nu_n + \mu - \epsilon_{\mathbf{k}} - \Sigma^\nu\right)\right]^{-1} + \Sigma^\nu$.

Impurity Solvers

For most implementations, the only non-trivial part of the DMFT algorithm is the impurity problem. The solution to the effective single-particle problem can be obtained given a hybridization or Weiss Green's function. This step is called the "impurity problem" and its solution is typically responsible for almost all computational efforts of the DMFT solution. Since any algorithm that can (approximately) solve simple quantum mechanical problems can solve the impurity problem, there are a large number of different solvers, all with their own advantages and disadvantages [85]. Two well-known ones that have been routinely used during this thesis are CTQMC and ED. A more comprehensive investigation of the former can be found in my master's thesis [246]. A short introduction to ED and an implementation that has been used for this thesis are found in Sec. 6.6.
CTQMC yields, in principle, the exact solution, ED approximates the solution with a finite bath, i.e. the sum over bath sites in Eq. (5.14) is truncated, usually between 4 and 12. However, CTQMC as a Monte Carlo sampler has to be truncated in the number of samples to be drawn. This results in unbiased estimators for each function measured at each Matsubara frequency, but non-zero noise for any finite runtime. This makes the ED algorithm favorable for the development of our diagrammatic extensions, since the reliability of deterministic, exact[1] results is preferable to unbiased but noisy data for the development of a method. We have, however, routinely verified the results with CTQMC and in the case of cuprates the single-particle solution has always been obtained this way (see Sec. 7.2 for a description of the numerical setup).
Note also that it is possible to measure any correlator on the impurity. These quantities belong to a local solution of DMFT and are computed after the root of the system of equations is obtained. We will use the two-particle Green's function and physical susceptibilities obtained in this way for the construction of the dynamical vertex approximation in the next section.

5.1.3 Fulfillment and Violation of Consistencies

Thermodynamic Consistency

DMFT is a Φ derivable method [114], according to our definition in Sec. 4.3. Specifically, the locality implies that the Luttinger-Ward functional consists of diagrams from local propagators.

$$\Phi[G_{ij}] \approx \Phi[G_{ii}] \tag{5.19}$$

However, this constructs a theory that is only exact for the purely local limit - the Anderson impurity model. For the Hubbard model in finite dimensions, the correspondence to the local model becomes approximate. A direct approximation of the LWf in this case is unknown. In practice, one still relies on the cavity construction and the approximate equivalence of the Hubbard and Anderson impurity model. Even for superperturbation theories, like dual fermion [209] and dual boson [210], that expand around a local reference system (AIM) this problem cannot be solved. While it may be possible to construct a dual LWf this functional does not directly imply the Baym-Kadanoff conservation laws [242, Sec. IV][2]. DMFT does not respect momentum conservation due to the local nature of the reference system.

[1] Again, the AIM is solved exactly, the approximation lies in the fact that this model with a finite number of bath sites does not correspond to the infinite bath of the S_{MF} action.
[2] Furthermore, numerical limitations require (i) a truncation of the infinite hierarchy of n-operator vertex functions and (ii) a further truncation of the infinitely many diagrams at each order leading to conservation laws that can in practice only be numerically verified and are not guaranteed under the required approximations [110].

This can be reconciled in a Φ-derivable way by considering the contributing diagrams to the LWf systematically [222] or in the context of the dynamical cluster approximation (DCA) [99] (specifically Appendix D). This class of methods remains thermodynamically consistent but imposes a finite size cluster that can induce spurious long-range correlations (corresponding to the periodicity introduced by the finite cluster) and may suffer numerically from the fermionic sign problem [238, 267]. Especially near second-order phase transitions, where thermodynamical consistency is important, the correlation length diverges and the momentum resolution becomes a limiting problem. There are attempts within the DCA to overcome this problem [237]; our approach, however, will be to use the local solution as a starting point and introduce non-locality through a diagrammatic construction.

Two-Particle Consistency

The discussion of two-particle consistency in DMFT is ambiguous. With respect to impurity quantities, one retains this consistency because an exact solution to the AIM is computed. One can obtain then a fully local 1PI and 2PI vertex according to Eq. (5.19) and Eq. (4.18) from impurity quantities.

$$\frac{\delta\Phi}{\delta G} = \Sigma^{\nu}, \qquad \frac{\delta^2\Phi}{\delta G\delta G} = \Gamma^{\nu\nu'\omega} \tag{5.20}$$

We can now directly plug this into the BSE from Eq. (2.256), solving for the full vertex F. This will yield a 2 particle-consistent method because we solved the AIM exactly. Using the equation of motion (EoM) from Eq. (5.50),

$$\widetilde{\Sigma}^{\nu} = \frac{Un}{2} - U\sum_{\nu'\omega} G^{\nu'} G^{\omega+\nu'} F_{\uparrow\downarrow}^{\nu\nu'\omega} G^{\omega+\nu} = \Sigma^{\nu} \tag{5.21}$$

With Σ^{ν} being the self-energy obtained from the LWf and $\widetilde{\Sigma}^{\nu}$ the one from the BSE and EoM.
However, in the following, we will use exactly the BSE to reintroduce non-locality that arises from the Hubbard model in finite dimensions by replacing G^{ν} with $G^{\nu}_{\mathbf{k}}$ in Eq. (2.256)[3]. This directly leads to non-local self-energy using the SDE, which does not satisfy $\sum_{\mathbf{k}} \Sigma^{\nu}_{\mathbf{k}} \neq \Sigma^{\nu}$. Therefore, quantities such as potential energy (see Sec. 4.5.1) are not the same when computed on the one- and two-particle levels for non-local quantities [253]. Therefore, DMFT is not 2 particle consistent.

Mermin-Wagner Theorem

As a mean-field theory, DMFT neglects precisely the non-local fluctuations that are instrumental to the proof of the non-existence of finite temperature phase transitions in 1 and 2 spatial dimensions in the context of the Mermin-Wagner theorem [170, 104]. Furthermore, as a mean-field theory, DMFT fails to capture the correct critical exponents Sec. 4.5.2.

5.2 Static Vertex Methods

We will outline 4 approaches that employ a static vertex, starting with the RPA. Being a very crude approximation, RPA has many deficiencies, and there are several methods alleviating some of those, which are worth discussing before moving on to dynamical vertices, i.e. $\Gamma \to \Gamma^{\nu\nu'\omega}$. We will give a brief overview of the TPSC [277], which employs the idea of two-particle consistency in some ways similar to lDΓA. A different approach to TPSC, which focuses on the restoration of two-particle consistency through sum rules resulting from the Pauli principle (crossing symmetry of the vertex), is the explicit reintroduction of symmetries to the LWf in a parquet-like manner used by FLEX [30, 29]. Also worth mentioning in this context is the GW approximation, which considers only ring diagrams in the LWf [95]. This results in an effective screening of the bare Coulomb interaction, a route we will not take for the derivation of lDΓA and therefore leave a discussion to the literature [14].
Finally, we briefly mention λ-RPA that has very recently been investigated as a bridging method between RPA and lDΓA. It is worth outlining these attempts here because they address the restoration of 2-particle consistency in different ways: FLEX exploits the parquet-based approach used for DΓA, while TPSC and, to an even greater extent, λ-RPA, employ an effective renormalization scheme. A comprehensive discussion and comparison of these methods is available in [277] and [5].

5.2.1 Random Phase Approximation

We will now make the simplest non-trivial assumption for the construction of a conserving method: taking only the lowest-order, i.e. Hartree-Fock, diagrams for the irreducible vertex in the particle-hole channel (Eq. (5.42)) into account. This will allow us to discuss the two-particle and thermodynamical consistency concretely and introduce effective mass-renormalization parameters to fix the violations on an effective level in Sec. 5.2.5. However, we will also see that neglecting the frequency dependency induced by local correlation effects does not yield qualitatively satisfactory answers. Having built up the machinery, we will then discuss a similar method for the restoration of two-particle self-consistency but incorporating all local diagrams by using an approximation of DΓA, Sec. 5.3.

[3] In fact, we solve the BSE two times, for the local and the non-local path. See Sec. 5.4

The discussion of RPA follows the derivation from [266, Chapter 56]. The simplest form for a guess of the LWf is the Hartree approximation:

$$\Phi[G] \approx \frac{U}{2} \sum_{\sigma} G_{\sigma}(1,\bar{1}) G_{\bar{\sigma}}(\bar{1},1^{+}) \tag{5.22}$$

This leads to a self-energy consisting only of the static Hartree term (compare Eq. (2.205)):

$$\Sigma_{\sigma} = \frac{\delta\Phi[G]}{\delta G_{\sigma}} = \frac{U n_{\bar{\sigma}}}{2} = \Sigma_{\mathrm{H}} \tag{5.23}$$

The irreducible vertex is then obtained similarly. Note again that $\delta\Sigma$ is a shorthand notation for the second derivative of Φ, and one should not use the expression obtained from Eq. (5.23) for explicit calculations.

$$\Gamma_{\sigma\bar{\sigma}}(1,2;3,4) = \frac{\delta\Sigma_{\sigma}(1,2)}{\delta G_{\bar{\sigma}}(3,4)} = \frac{U}{2}\delta(1-2)\delta(1-3)\delta(2-4) \tag{5.24}$$

$$\Gamma_{\sigma\sigma}(1,2;3,4) = \frac{\delta\Sigma_{\sigma}(1,2)}{\delta G_{\sigma}(3,4)} = 0 \tag{5.25}$$

We now use the projected version of the BSE from Eq. (2.259) and the projections from Eq. (2.219) and Eq. (2.220) to write the density and magnetic susceptibilities as:

$$\chi_r = \chi_0 - G_{\sigma} B_r^T \Gamma_{\sigma\sigma'} \frac{1}{2} \left[P_{\mathrm{m}} + P_{\mathrm{d}}\right] (\chi_{\sigma\sigma'} B_r^T) G_{\sigma} \tag{5.26}$$

$$\Rightarrow \chi_{\mathrm{d}} = \chi_0 + G_{\sigma} \left[\frac{\delta\Sigma_{\uparrow}}{\delta G_{\uparrow}} + \frac{\delta\Sigma_{\uparrow}}{\delta G_{\downarrow}}\right] \chi_{\mathrm{d}} G_{\sigma} \tag{5.27}$$

$$\chi_{\mathrm{m}} = \chi_0 - G_{\sigma} \left[\frac{\delta\Sigma_{\uparrow}}{\delta G_{\downarrow}} - \frac{\delta\Sigma_{\uparrow}}{\delta G_{\uparrow}}\right] \chi_{\mathrm{m}} G_{\sigma} \tag{5.28}$$

With the bare susceptibility defined as $\chi_0 = -\beta GG$. The frequency indices from Eq. (2.257) are suppressed here; they are given in full in [277, Sec. III.A-B]. All frequency summations of the susceptibilities entering the BSE (Eq. (2.257)) can be carried out analytically in the case of the frequency-independent irreducible vertex and we obtain, using Eq. (5.24) and Eq. (5.25):

$$\chi^{\omega}_{\mathrm{d/m},\mathbf{q}} = \chi^{\omega}_{0,\mathbf{q}} \left[\mathbb{1} \pm \frac{U}{2} \chi^{\omega}_{\mathrm{d/m},\mathbf{q}}\right] \tag{5.29}$$

$$\Leftrightarrow \chi^{\omega}_{r,\mathbf{q}} = \frac{\chi^{\omega}_{0,\mathbf{q}}}{1 \pm \frac{U}{2}\chi^{\omega}_{0,\mathbf{q}}} \tag{5.30}$$

Where the bare susceptibility $\chi^{\omega}_{0,\mathbf{q}} = -\sum_{\nu\mathbf{k}} \beta G^{\nu}_{0,\mathbf{k}} G^{\omega+\nu}_{0,\mathbf{q}+\mathbf{k}}$ can be written as the Lindhard function

$$\chi^{\omega}_{0,\mathbf{q}} \overset{G\equiv G_0}{=} \sum_{\mathbf{k}} \frac{f(\epsilon_{\mathbf{k}}) - f(\epsilon_{\mathbf{k}+\mathbf{q}})}{i\omega_m - \epsilon_{\mathbf{k}} + \epsilon_{\mathbf{k}+\mathbf{q}}} \tag{5.31}$$

for a non-interacting Green's function.

5.2.2 Fulfillment and Violation of Consistencies in RPA

Since we obtained the self-energy from a diagrammatic approximation of the LWf we can call this theory thermodynamically consistent. In fact, one can easily verify that the f-sum rule from Eq. (4.42) is satisfied due to the properties of the Lindhard function. RPA is not two-particle consistent, as the computation of the self-energy through the SDE demonstrates:

$$\Sigma^{(2),\nu}_{\sigma,\mathbf{k}} = U n_{\bar{\sigma}} + \frac{U}{4} \sum_{\nu\mathbf{q}} \left(U_{\mathrm{m}} \chi^{\omega}_{\mathrm{m},\mathbf{q}} + U_{\mathrm{d}} \chi^{\omega}_{\mathrm{d},\mathbf{q}}\right) G^{\omega+\nu}_{0,\sigma\mathbf{q}+\mathbf{k}} \tag{5.32}$$

Eq. (5.32) is different from the Hartree self-energy we obtained from the LWf in Eq. (5.23), providing us with a concrete example of the two-particle inconsistency described in Eq. (4.45). Furthermore, the Mermin-Wagner theorem is not fulfilled. This can be seen by considering that $\chi_{0,\mathbf{q}}$ is diverging at $T \to 0$ (on a bipartite lattice); therefore, the expression for the spin susceptibility in Eq. (5.30) can become negative for sufficiently large U at the nesting vector $\mathbf{q}_{\mathrm{N}}$, regardless of the dimension.
The Pauli principle is also not fulfilled either, because the crossing symmetry $\Gamma(12;1'2') = -\Gamma(1,2;2',1')$ is not fulfilled from Eq. (5.24). We can verify this by computing Eq. (4.53) explicitly and comparing it with Eq. (4.52).

$$\frac{n}{2}\left(1 - \frac{n}{2}\right) = \sum_{\omega\mathbf{q}} \chi^{\omega}_{\uparrow\uparrow,\mathbf{q}} \overset{\text{Eq. (5.30)}}{=} \frac{1}{2} \sum_{\omega\mathbf{q}} \left(\frac{\chi^{\omega}_{0,\mathbf{q}}}{1 + \frac{U}{2}\chi^{\omega}_{0,\mathbf{q}}} + \frac{\chi^{\omega}_{0,\mathbf{q}}}{1 + \frac{U}{2}\chi^{\omega}_{0,\mathbf{q}}}\right)$$

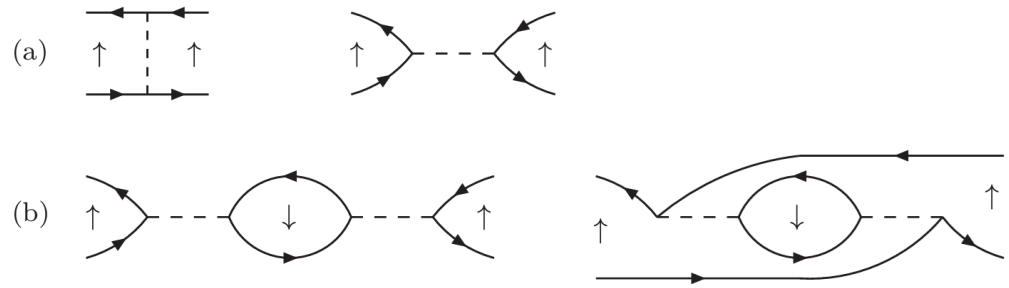

Figure 5.2: (a) Two diagrams that should cancel due to opposite sign because of crossing symmetry/Pauli principle (in our model setup these diagrams do not contribute, because of the ↑↑ interaction). (b) Two diagrams: the first is included in RPA, and the second is not, demonstrating the violation of the Pauli principle in RPA. Figure from [61, Fig. 6.11].

$$= \sum_{\omega\mathbf{q}} \left(\chi^{\omega}_{0,\mathbf{q}} + \frac{U^2}{4} \left(\chi^{\omega}_{0,\mathbf{q}} \right)^3 + \mathcal{O}(U^3) \right) \tag{5.33}$$

Since $\sum_{\omega\mathbf{q}} \chi^{\omega}_{0,\mathbf{q}} = \frac{n}{2}\left(1 - \frac{n}{2}\right)$ and $\chi^{\omega}_{0,\mathbf{q}} \geq 0$ the last line demonstrates that the Pauli principle is not satisfied. This can also be argued from the violation of the crossing symmetry, demonstrated in Fig. 5.2.
Note that the conserving nature of RPA does not hold when the bare Green's function is replaced by a dressed propagator. For example, the f-sum rule is violated in that case [277, Appendix A]. Because this is usually also called RPA, one often refers to RPA as being not conserving.

5.2.3 Two Particle Self-Consistent Method

The two-particle self-consistent method aims to improve upon RPA by explicitly enforcing consistency while extending the (approximate) fulfillment of the f-sum rule[4]. The LWf is thereby approximated as (compare Eq. (5.22)) [277, Eq. 32]

$$\Phi[G] \approx \frac{1}{2} \sum_{\sigma} G_{\sigma}(\overline{1}, \overline{1}^{+}) \Gamma_{\sigma\overline{\sigma}} G_{\overline{\sigma}}(\overline{1}, \overline{1}^{+}) + \frac{1}{2} \sum_{\sigma} G_{\sigma}(\overline{1}, \overline{1}^{+}) \Gamma_{\sigma\sigma} G_{\sigma}(\overline{1}, \overline{1}^{+}) \tag{5.34}$$

With a yet-to-be-determined, static irreducible vertex Γ. The susceptibilities are defined as in RPA but with the static vertex:

$$\chi^{\omega}_{\mathrm{d/m},\mathbf{q}} = \frac{\chi^{\omega}_{0,\mathbf{q}}}{1 \pm \Gamma_{\mathrm{d/m}} \chi^{\omega}_{0,\mathbf{q}}} \tag{5.35}$$

One then considers the two local sum rules for the magnetic and charge susceptibilities, which, however, still contain the double occupancy.

$$\sum_{\omega\mathbf{q}} \chi^{\omega}_{\mathrm{m},\mathbf{q}} = n - n^2 + 2\langle \hat{n}_{\uparrow} \hat{n}_{\downarrow} \rangle \tag{5.36}$$

$$\sum_{\omega\mathbf{q}} \chi^{\omega}_{\mathrm{d},\mathbf{q}} = n - 2\langle \hat{n}_{\uparrow} \hat{n}_{\downarrow} \rangle \tag{5.37}$$

A third equation is then supplied by an ansatz, motivated by the local field approximation [109, 278, 298]:

$$\Gamma_{\mathrm{m}} = U \frac{\langle n_{\uparrow} n_{\downarrow} \rangle}{\langle n_{\uparrow} \rangle \langle n_{\downarrow} \rangle} \tag{5.38}$$

This set of equations can be solved, even though some additional considerations are necessary to stabilize convergence [298, Sec. 5.3]. The two-particle self-energy is computed as

$$\Sigma^{(2),\nu}_{\mathbf{k},\sigma} = U n_{\overline{\sigma}} + \frac{U}{4} \sum_{\omega\mathbf{q}} \left(\Gamma_{\mathrm{m}} \chi^{\omega}_{\mathrm{m},\mathbf{q}} + \Gamma_{\mathrm{d}} \chi^{\omega}_{\mathrm{d},\mathbf{q}} \right) G^{(1),\omega+\nu}_{0,\mathbf{q}+\mathbf{k}} \tag{5.39}$$

Violation of Consistencies Note that we have Green's functions and self-energies obtained from the two-particle level ($G^{(2)} = \left[G_0^{-1} - \Sigma^{(2)} \right]^{-1}$) in TPSC. Updating the right-hand side in the equation of motion, Eq. (5.39), as in FLEX, thereby moving towards a thermodynamically conserving theory, is *not* desirable. This is discussed in detail below equation (46), in [277], many important features, such as

[4] This still involves the non-interacting Green's function. An extension called TPSC+ that extends this notion to interacting Green's functions has recently been proposed [76]

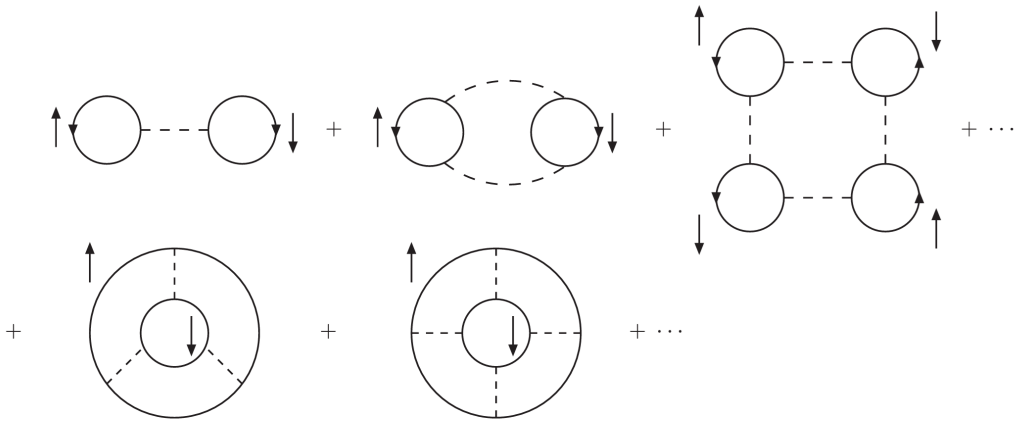

Figure 5.3: Diagrams in the LWf for FLEX, from [61, Fig. 9.5].

Mott physics and pseudogap behavior, would not be captured by this approach. One, therefore, chooses to forgo the consistency of propagators between two and one-particle levels while fixing thermodynamical consistency between these levels. In the context of lDΓA , investigations of fixing this violation are discussed in the context of the partially self-consistent lDΓA method in Sec. 5.4.3. Furthermore, the high-frequency tail of $\Sigma^{(2)}$ is not correct, another property we will discuss in the following chapter for the self-energy obtained from lDΓA .
TPSC directly fixes the potential energy consistency Eq. (4.50) and Eq. (4.51), contrary to FLEX, the Pauli principle and can be shown to fulfill the Mermin-Wagner theorem using the argument in Sec. 4.5.2, given in [277].

5.2.4 FLuctuation EXchange Approximation

The FLEX enforces thermodynamical consistency by the construction of an approximate LWf (see Fig. 5.3) and enforcement of the Pauli principle through the explicit restoration of the crossing symmetry [30, 29]. We leave a detailed derivation and discussion of this method to the literature [227, Chapter 6] and summarize the most important features of this method for our context. The construction of the parquet equations, Sec. 2.8.3, with a static vertex function $\Gamma_r^{\nu\nu'\omega} \equiv \Gamma_r$ leads to the following equation of motion:

$$\Sigma^{(2),\nu}_{\mathbf{k}} = \frac{Un}{2} + \frac{U}{2}\left[(3\chi^{\omega}_{\mathrm{m},\mathbf{q}} - 2U\chi^{\omega}_{0,\mathbf{q}}) + \chi^{\omega}_{\mathrm{d},\mathbf{q}}\right] G^{\omega+\nu}_{\mathbf{q}+\mathbf{k}} \tag{5.40}$$

With $\chi^{\omega}_{r,\mathbf{q}}$ as in the RPA case Eq. (5.30). However, the Green's functions are self-consistently updated, using the EoM Eq. (5.40) and the Dyson equation. However, the susceptibilities that fulfill Ward identities are not the ones appearing in the equation of motion. This inconsistent treatment of vertex corrections in the equation of motion leads to numerous deficiencies in the predictive power of FLEX [277, Appendix B]. While FLEX manages to achieve thermodynamical consistency, it suffers from inconsistencies between one and two-particle levels. Most importantly, the potential energies (double occupancies) can become negative [12, 277] and FLEX does not seem to respect the Mermin-Wagner theorem [53]. It is also known that many important features of strongly correlated electron systems, such as Hubbard bands, are not captured within this approximation (see discussion for TPSC). These problems of the traditional FLEX approach are important to mention here, because the `EoM` high-frequency tail correction scheme for the self-energy in lDΓA seems to inherit some of these (particularly a deficiency in describing pseudogap behavior), due to a similar structure of the EoM.

5.2.5 λ RPA

A different approach to the restoration of the consistencies enforced by TPSC is the effective rescaling of the susceptibilities by a Moriya-like parameter, as discussed in Sec. 4.5.1. This leaves the two-particle vertex at the static Coulomb interaction, just as in RPA, but attempts to restore the same consistencies through the fit of λ parameters. This method, therefore, can be argued to possess the same properties as TPSC while giving more freedom in the choice of which consistencies to enforce or give up. Several sub-methods enforcing different consistencies are shown in Fig. 5.4, which have been defined in Sec. 4.5.1. The partial self-consistency explicitly replaces $G^{(1)}$ on the right-hand side in Eq. (5.41) by $G^{(2)} = \left[G_0^{-1} - \Sigma^{(2)}\right]^{-1}$ in a self-consistency loop, also discussed in Sec. 5.4.3. The equation of motion is:

$$\Sigma^{(2),\nu}_{\mathbf{k},\sigma} = Un_{\overline{\sigma}} + \frac{U}{2}\sum_{\omega\mathbf{q}}\left(3\gamma_{\mathrm{m}}\chi^{\omega+\nu}_{\mathrm{m},\mathbf{q}+\mathbf{k}} + \gamma_{\mathrm{d}}\chi^{\omega+\nu}_{\mathrm{d},\mathbf{q}+\mathbf{k}} + U\right) G^{(1),\omega+\nu}_{\mathbf{q}+\mathbf{k}} \tag{5.41}$$

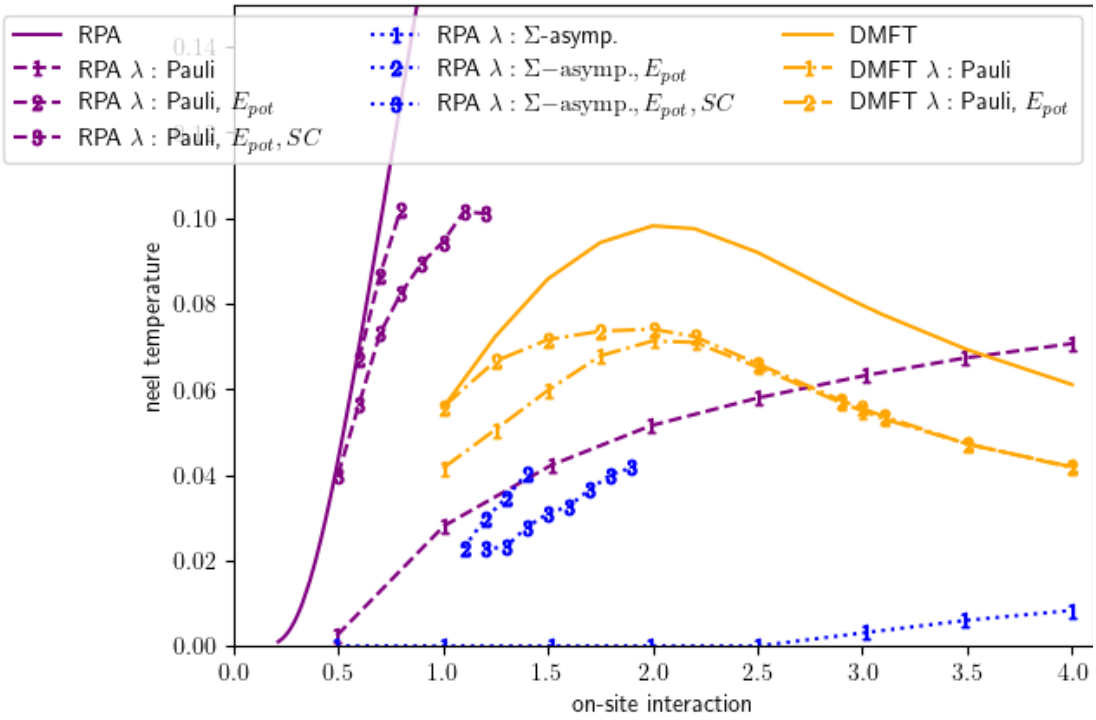

Figure 5.4: Néel temperature for λRPA and lDΓA in the three dimensional Hubbard model at half-filling, compare also Sec. 7.1. Figure from [288]. The orange lines are the data points discussed in Sec. 7.1. The purple lines correspond to the λ-correction schemes discussed in Sec. 4.5.1. The blue lines use the magnetic λ-correction value to fix the self-energy asymptotic instead of the Pauli-principle, as discussed in Sec. 6.3.4.

One of the advantages of this approach is the ability to investigate the influence of particular consistencies in the case of a static vertex on an individual basis. TPSC requires the full set of consistencies to be enforced simultaneously due to the coupled consistency equations. In λ-RPA, it is possible to selectively enforce these in different channels. Furthermore, it gives a clear pathway towards the investigation of these types of consistencies when frequency dependence is introduced because, contrary to TPSC, the vertex is not changed in order to restore these symmetries and may, therefore, be replaced with a frequency dependent one. For example, if we replace $\Gamma_r = \pm U$ (the λ-RPA case) with the one obtained from DMFT, we recover the lDΓA method.
In Fig. 5.4, a comparison between the various sub/schemes of lDΓA and λRPA is shown. Here, we observe that the dynamical nature of the vertex is crucial to obtain quantitatively good results. However, even at the RPA level, effective restoration of two-particle consistency leads to a greatly improved qualitative description, extending the applicability to interaction strengths into the intermediate coupling regime.
Details for this method can be found in [288].

5.3 Dynamical Vertex Approximation

5.3.1 Introduction

The foundation for the diagrammatic approach that the dynamical vertex approximation is built upon was first introduced by Dominicis and Martin [50, 51, 52] and further developed into a computationally applicable method for the Hubbard model [30, 29].
Motivated by the success of DMFT, where the only approximation was made in the locality of the single-particle irreducible one-particle vertex, the self-energy, one can envision a hierarchy of higher-order irreducible vertices that are approximated to be local, with lower orders computed in a non-local setting from them. This allows for significant further improvement, as the irreducible vertex is now obtainable from a non-perturbative setting. Approaches like this are called diagrammatic extensions of DMFT. In one of them, DΓA, the core idea of which is to compute the 2PI vertex Λ from DMFT [264]. In the context of older diagrammatic constructions such as FLEX, this introduces a dynamical vertex in place of a static one (typically the bare interaction U).
We will discuss the core concept here, which employs the relationship between irreducible and full two-particle Green's functions illustrated in Sec. 2.8.1, together with the SDE, Sec. 2.7.4, to push the locality assumption of the irreducible vertex back to the two-particle level, gaining a nonlocal single-particle solution in the process. Algorithmically, one first determines a solution according to the DMFT

method, Sec. 5.1. From this solution, for example, Anderson parameters in ED, Sec. 6.6, one can then obtain the 2PI vertex. The first diagrams of a perturbative expansion of this vertex are (compared to Eq. (2.249)):

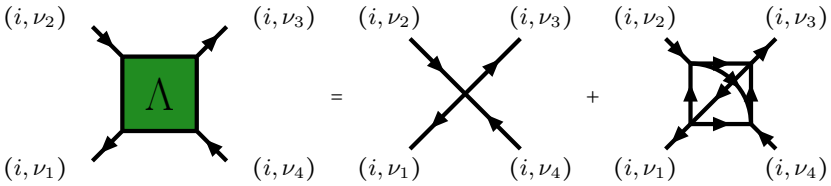

(5.42)

Together with the 4 parquet equations (see Sec. 2.8.1) we have a complete set of equations that can now be solved (see Fig. 5.5). These calculations involve objects with 3 frequency indices and (apart from Λ) 3 momentum indices. The only input (and purely local) quantity in this approach is the fully irreducible vertex Λ. Numerical studies indicate that this quantity is more local than the self-energy or the full vertex [164, 97]. This suggests obtaining it from DMFT (thereby neglecting the momentum dependence) as the only externally determined quantity is a reasonable approximation one could make at the two-particle level. After having obtained the two-particle solution, one can either map back to a new local impurity system, solve the local model, and start the process again with a new Λ until convergence, or converge the set of self-consistency equations with Λ as a fully external parameter. This process is depicted in Fig. 5.5.
In principle, this algorithm defines a systematic approximation in the sense that higher-order local Green's functions introduce more non-locality to all through the hierarchy in the equations of motion. In practice, even the full parquet DΓA on the two-particle level remains extremely challenging for modern supercomputers, and one has to resort to approximations of the approximation, as we do with our method in Sec. 5.4. Fig. 5.5 demonstrates two ways of closing the self-consistency in DΓA: (i)

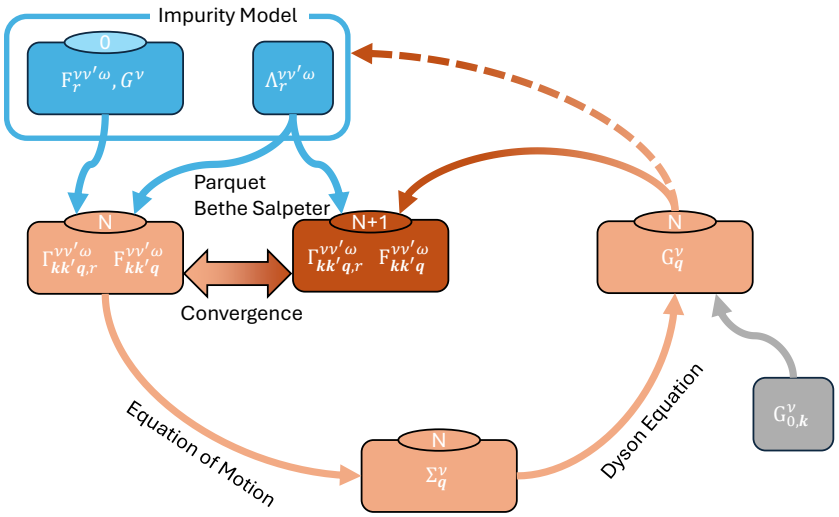

Figure 5.5: Dynamical Vertex Approximation scheme. DMFT provides the local input Λ. The Bethe-Salpeter and parquet equations from Sec. 2.8 provide irreducible vertices for each channel Γ_r and the full 2-particle vertex F. The Dyson equation provides, together with the lattice Green's function $G^\nu_{0,\mathbf{k}}$, the non-local 1-particle Green's function. This is the Green's function that enters the equations in Sec. 2.8 (i.e. all full lines are the N iteration non-local Green's function). Convergence is achieved when the Vertex is no longer changing with each iteration. Blue marks the DMFT input, orange the self-consistently determined quantities, and gray the external parameters.

purely on the two-particle level, by following the solid lines; (ii) via an update of the local reference system by following the dashed arrow. The first version adds non-local correlation effects on top of the DMFT solution and is the framework we will use in the following. Option (ii) achieves full consistency between one and two-particle levels (but no consistency between local lattice two-particle quantities and the two-particle quantities on the local reference model) but does not correspond to any DMFT solution. In practice, the self-consistency in Fig. 5.5 is solved by Jacobi iteration, as with DMFT. The fixed point is a consistent set of $F^{\nu\nu'\omega}_{\mathbf{kk'q}}$, $\Gamma^{\nu\nu'\omega}_{\mathbf{kk'q},r}$ and $\Sigma^\nu_{\mathbf{k}}$ that fulfill the parquet and Bethe-Salpeter equations.

5.3.2 Fulfillment and Violation of Consistencies

The DΓA method is by design two-particle consistent, as shown in Fig. 5.5. All consistency relations argued in Sec. 4.5 are therefore fulfilled. While parquet-based methods are known to fulfill the Pauli principle (due to the explicit construction of the crossing symmetry) they violate Ward identities to some extent since only the exact vertex can be both conserving and antisymmetric [234]. Many approximations of DΓA violate in addition the crossing symmetry and, equivalently, the Pauli principle [42, 114, 150, Sec. IV], as will be discussed in the next section.

5.4 Ladder Dynamical Vertex Approximation

We will now discuss the ladder variant of the dynamical vertex approximation, so-called for the types of diagrams considered. It was first developed without the inclusion of a correlation length renormalization [151, 264], then improved by the introduction of a Moriya-like susceptibility rescaling in the (for the investigated system) dominant magnetic channel [125]. Subsequently, the introduction of thermodynamic consistencies improved the predictive power of this approach [202] and [253]. A thorough review has been given before [204]. Further explorations in improvements to the methods since this publication have been the inclusion of a self-consistency [128], application to the attractive Hubbard model [54], the ordered magnetic phase [56] and the inclusion of consistency in potential energies [253] as well as partial self-consistency to be discussed below and in Sec. 7.2. Recently, the predictive power for addressing the phase diagram of high-temperature superconductors that can be reasonably well approximated with a single band Hubbard model, such as nickelates and cuprates, has been demonstrated [134, 135]. We will discuss this method in this section; details regarding thermodynamic and two-particle consistencies are given in Sec. 4.5, numerical details in Sec. 6.5 and applications to the repulsive Hubbard model in 3 and 2 dimensions in Sec. 7.1 and Sec. 7.2.
The ladder approximation can be understood as a one-shot approximation of the parquet DΓA method discussed before, with the self-consistency cycle outlined in Fig. 5.5. By disregarding feedback between channels through the parquet equations, Eq. (2.260) and Eq. (2.244) one is left with non-local ladder diagrams constructed from local (DMFT) vertices, and by subsequent evaluation of the SDE, the consistency between one and two-particle levels is broken. The diagrammatic contributions are similar to FLEX but with fully frequency-dependent vertices instead of the bare Hubbard interaction. Neglecting mutual screening between channels, which is introduced through the mixing in Eq. (2.260) and Eq. (2.244), is then reintroduced on an effective level, conceptually similar to TPSC, by fixing consistency relations between one- and two-particle levels. Not only do we fix thermodynamical consistencies this way, where TPSC focuses on the correlator equivalence in Eq. (5.36) and Eq. (5.37), lDΓA fixes the consistency of the Pauli principle and the potential energies between one and two-particle levels. This means the equivalence, this is done in a self-consistent way, i.e., both quantities on the single and two-particle levels are computed from lDΓA . The overall scheme of this method is given in Fig. 5.6

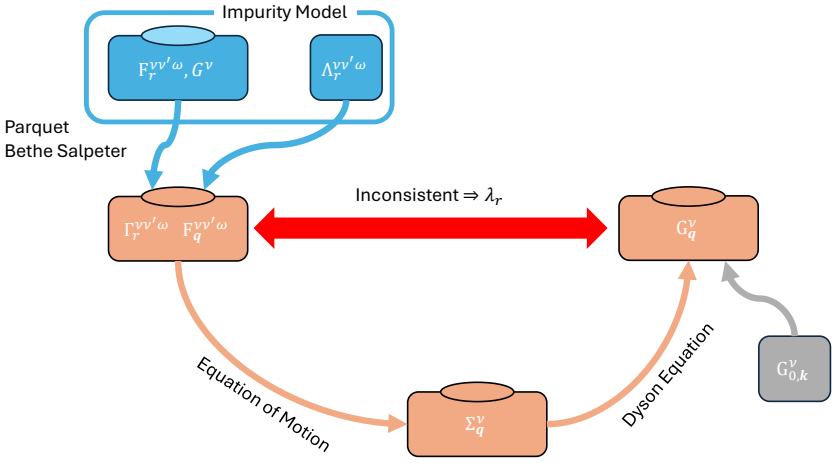

Figure 5.6: Ladder Dynamical Vertex Approximation scheme. This is a one-shot approximation of Fig. 5.6

contrasting the full parquet flow in Fig. 5.5. Here, the initial two-particle inconsistency between the local DMFT self-energy and the lDΓA self-energy becomes apparent[5] and is marked with a red arrow indicating the setup for which we use the λ corrections. The framework for fixing this inconsistency on an effective level was already obtained in Sec. 4.5.1.

[5] Because after the evaluation of the SDE, the newly obtained self-energy is not consistent with the full vertex F, which is (contrary to parquet DΓA) not updated.

5.4.1 Method Details

(0) DMFT

The input of this method are the following quantities obtained from DMFT: (i) one-particle Green's function, (ii) self-energy, (iii) irreducible vertices for magnetic and density channel $\Gamma_{\mathrm{m/d}}$ and (iv) local generalized susceptibilities or full vertices $\chi^{\nu\nu'\omega}_{\mathrm{m/d}}$ or $F^{\nu\nu'\omega}_{\mathrm{m/d}}$ from (i) and (iii). input (iii) requires the inversion of the BSE for the local two-particle Green's function Sec. 6.8.7.

(1a) Bare Susceptibility

The first quantity to be constructed is the tight binding lattice (i.e. helper quantities, symmetry reduction mappings, and so on Sec. 6.8.4) and the non-local bare susceptibility, obtained from the DMFT Green's function:

$$\chi^{\nu\omega}_{0,\mathbf{q}} = -\beta \sum_{\mathbf{k}} G^{\nu}_{\mathbf{k}} G^{\omega+\nu}_{\mathbf{q}+\mathbf{k}} \tag{5.43}$$

This is done using the convolution theorem and a symmetry-reduced lattice Sec. 6.4. For all quantities (including the local ones), the asymptotic information discussed in Sec. 6.2 and Sec. 6.3 is computed and stored as well.

(1b) Bethe-Salpeter Equation

Next, the non-local BSE is inverted for each $\tilde{\omega}$ and $\tilde{\mathbf{q}}$ (here explicitly fixed to indicate the matrix inversion in the fermionic frequencies) but immediately separated into the susceptibility and triangular vertex parts:

$$\chi^{\nu\nu'\omega=\tilde{\omega}}_{r,\mathbf{q}=\tilde{\mathbf{q}}} = \left[\Gamma_r^{\nu\nu'\omega=\tilde{\omega}} + \mathbb{1}\left(\chi^{\nu\omega=\tilde{\omega}}_{0,\mathbf{q}=\tilde{\mathbf{q}}}\right)^{-1}\right]^{-1} \tag{5.44}$$

$$\chi^{\omega}_{r,\mathbf{q}} = \sum_{\nu\nu'} \chi^{\nu\nu'\omega}_{r,\mathbf{q}} \tag{5.45}$$

$$\gamma^{\nu\omega}_{\mathrm{d/m},\mathbf{q}} = \lambda^{\nu\omega}_{r,\mathbf{q}} \cdot \left[\chi^{\nu\omega}_{0,\mathbf{q}}(1 \mp U\chi^{\omega}_{r,\mathbf{q}})\right]^{-1} \tag{5.46}$$

$$\lambda^{\nu\omega}_{r,\mathbf{q}} = \sum_{\nu'} \chi^{\nu\nu'\omega}_{r,\mathbf{q}} \tag{5.47}$$

This decomposition into the triangular vertex $\gamma^{\nu\omega}_{r,\mathbf{q}}$ and the physical susceptibility $\chi^{\omega}_{r,\mathbf{q}}$ does not only reduce system memory demand by a factor of N_ν (typically around 300) but is also essential for the λ corrections. $\gamma^{\nu\omega}_{r,\mathbf{q}}$ does not contain any physical susceptibilities and can therefore be assumed to be treated sufficiently well on the DMFT level [125]. This can also be explicitly understood by considering the U_r-irreducible generalized susceptibility from [205, Eq. 4.125]:

$$\chi^{*,\nu\nu'\omega=\tilde{\omega}}_{\mathrm{d/m},\mathbf{q}=\tilde{\mathbf{q}}} = \left[\Gamma_r^{\nu\nu'\omega=\tilde{\omega}} \mp U + \mathbb{1}\left(\chi^{\nu\omega=\tilde{\omega}}_{0,\mathbf{q}=\tilde{\mathbf{q}}}\right)^{-1}\right]^{-1} \tag{5.48}$$

$$\gamma^{\nu\omega}_{\mathrm{d/m},\mathbf{q}} = (\chi^{\nu\omega}_{0,\mathbf{q}})^{-1} \sum \chi^{\star,\nu\nu'\omega}_{\mathrm{d/m},\mathbf{q}} \pm 1 \tag{5.49}$$

(2) λ Corrections

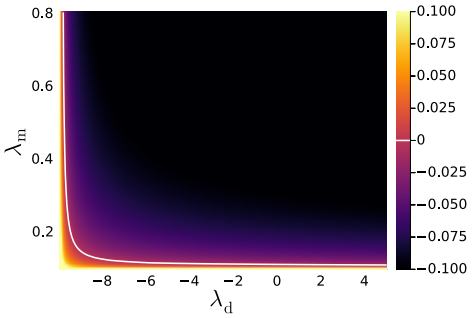

(a) Rebalancing of weights between density and magnetic channel. The plot shows, color-coded, the difference between the Pauli principle values on one and two-particle levels as a function of the λ parameters. All solutions, regardless of the condition for λ_{d}, must live on the white line in order to fulfill the Pauli principle. While the values change with the Hubbard and lattice parameters, the general shape has been observed to be universal for all lattice types, interactions, and hopping strengths that we have investigated.

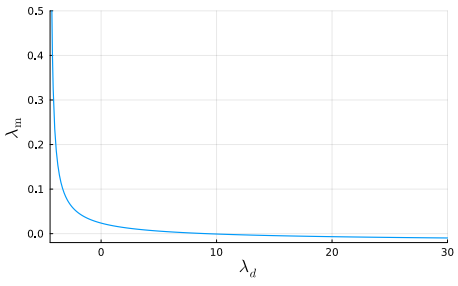

(b) Rebalancing of weights between density and magnetic channel. The plot shows a solution for λ_{m} as function of λ_{d}. The plot shows the solution line at which the Pauli principle values on the two- and one-particle levels match.

Having obtained the physical susceptibilities, one can now determine appropriate λ_r values, according to Sec. 4.5.1.
As discussed in Sec. 7.1 and Sec. 4.5.1, the λ corrections provide a way for effective mutual renormalization between channels. This is illustrated in Fig. 5.7b, where we give an example of the permissible solutions of the $(\lambda_\mathrm{m}, \lambda_\mathrm{d})$ tuple. The specific solution $(\lambda_\mathrm{m}^*, \lambda_\mathrm{d}^*)$ that fulfills the thermodynamic consistency relations from Sec. 4.5.1 then determines the amount of shift between both channels. Note also that the partially self-consistent variant does not change this behavior. The specific value for the potential energy will change, changing the curve of permissible solutions, but the shape, including monotonicity, remains; see also Sec. 5.4.3. We distinguish the following sub-methods:

lDΓA$_\mathbf{m}$: Here, only the Pauli principle in Eq. (4.52) and Eq. (4.53) is enforced. The λ_m value is used as a free parameter since this method works well in models with strong non-local magnetic fluctuations where the density renormalizations are negligible [202]. We also discuss a scheme below where, instead of fixing the Pauli-principle value, the high-frequency asymptotic behavior of the self-energy is fixed with this condition. This, however, is not addressed in this thesis and will be explicitly pointed out.

lDΓA$_\mathbf{dm}$: Here, also Eq. (4.50) and Eq. (4.51) are enforced. This introduces an indirect re-balancing between channels (see, for example, Fig. 5.7b) that significantly improves the predictive power Sec. 7.1.

lDΓA$_{r,\mathbf{sc}}$: This method introduces a partial self-consistency by exchanging the DMFT propagators in the equation of motion with non-local ones, as explained in Sec. 5.4.3. Specifically, the bare susceptibility in Eq. (5.56) This reduces some overestimation of non-local effects and improves spectral property predictions for models far away from the DMFT limiting case. It does, however, only have a minor impact on the thermodynamical quantities, see Sec. 7.2. The λ-correction can be either one of the previous two cases.

lDΓA$_{r,\mathbf{tsc}}$: The added t in the subscript indicates tail-self-consistency of the physical susceptibility. This is achieved by enforcing the f-sum rule Eq. (4.42) explicitly, see also Sec. 5.4.3. Currently, we do not have a clear picture of the advantages and disadvantages of this method and present it as an outlook for future investigation. We have, however, been able to investigate this method on several lattice types in 3 and 2 spatial dimensions and have found similar results to the method without enforcement of the f-sum rule.

Determination of Free Parameters The three free parameters λ_m, λ_d, and μ must be obtained in a hierarchical form, as explained in more detail in Sec. 6.5.1. Fig. 5.8 shows a schematic of the possible program flows, depending on the λ correction type. The quantities marked with a star in equations

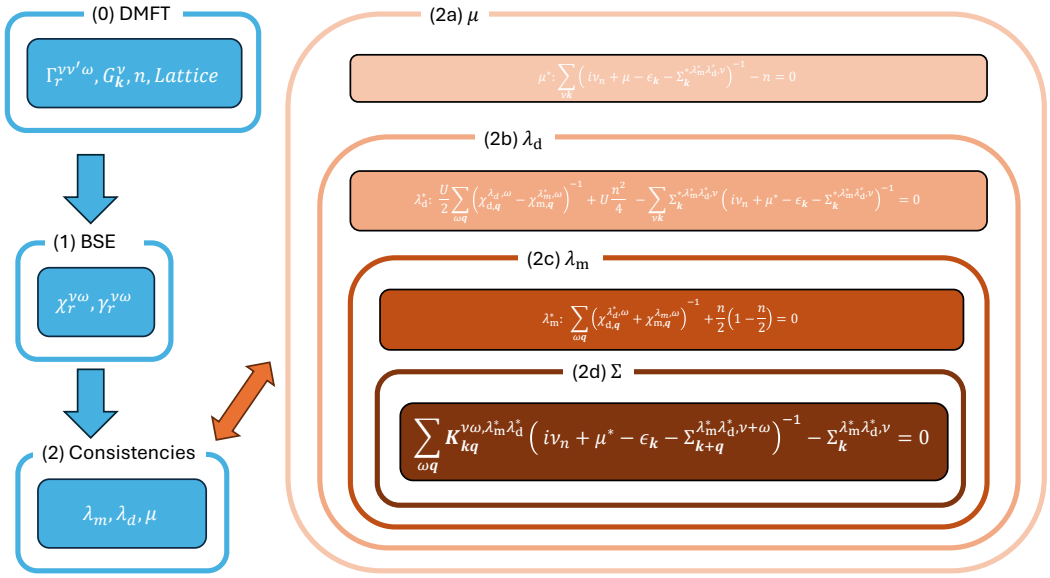

Figure 5.8: Program flow of the lDΓA methods including consistencies for the various sub-methods. $K_\mathbf{q}^{\nu\omega}$ is the sum over the $\lambda^{\nu\omega}$ vertices, defined in Eq. (5.56). Box 2d refers to the self-consistent determination of the self-energy with a non-local internal propagator as discussed in Sec. 5.4.3. Boxes (2d) and (2b) are optional, and one can leave the internal propagator at the DMFT level or omit the potential energy consistency. Especially (2d) seems to only

$2a$ to $2d$ are fixed external parameters; for example, λ_m enters the root finding algorithm for the calculation of λ_d in Eq. ($2b$) of Fig. 5.8 externally. More details are discussed in Sec. 6.5.1.

(3) Self-Energy

Computing the self-energy stands out from the remaining quantities here because this needs to be re-calculated many times (typically on the order of $\sim 10^4$ for the lDΓA$_\mathrm{dm}$ method and $\sim 10^6$ for lDΓA$_\mathrm{dm,sc}$, because it is needed to compute the potential energy. Moreover, because of the focus on the enforcement of thermodynamic properties, lDΓA tends to give less reliable results for spectral properties. Details will be discussed in Sec. 6.2.
The general form of the SDE connecting the two-particle Green's function with the single-particle one has already been sketched in Sec. 2.7.4. The diagrammatic version reads:

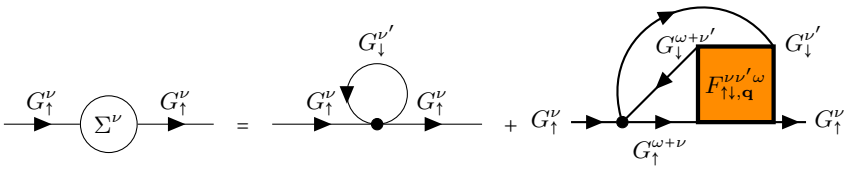

(5.50)

The momentum indices for the Green's functions have been absorbed into the frequency indices (i.e. $\nu \to (i\nu_n, \mathbf{k})$, $\omega \to (i\omega_m, \mathbf{q})$). Note, however, that the specific type of these propagators is important. As mentioned above, the lDΓA$_{r,\mathrm{sc}}$ variants of this method replace the internal propagators here in a self-consistent way by Green's functions obtained from $\Sigma^\nu_\mathbf{k}$.
The EoM from Eq. (5.50) reads:

$$\Sigma^\nu_\mathbf{k} = U\frac{n}{2} - U\sum_{\nu'\omega\mathbf{k}'\mathbf{q}} F^{\nu\nu'\omega}_{\mathbf{k}\mathbf{k}'\mathbf{q}} G^{\nu'+\omega}_{\mathbf{k}'+\mathbf{q}} G^{\nu'}_{\mathbf{k}'} G^{\nu+\omega}_{\mathbf{k}+\mathbf{q}} \tag{5.51}$$

This simplifies in the ladder case, where the two-particle irreducible vertex remains on the local level and the non-local corrections to particle-particle interactions are neglected (see Fig. 1 in [264]):

$$\Sigma^\nu_{\mathbf{k},\mathrm{lD\Gamma A}} = U\frac{n}{2} - U\sum_{\nu'\omega\mathbf{k}'\mathbf{q}} \widetilde{F}^{\nu\nu'\omega}_{\mathbf{q},\mathrm{lD\Gamma A}} G^{\nu'+\omega}_{\mathbf{k}'+\mathbf{q}} G^{\nu'}_{\mathbf{k}'} G^{\nu+\omega}_{\mathbf{k}+\mathbf{q}} \tag{5.52}$$

$$\widetilde{F}^{\nu\nu'\omega}_{\mathbf{q},\mathrm{lD\Gamma A}} = \frac{1}{2}\left(F^{\nu\nu'\omega}_{\mathbf{q},\mathrm{d}} - F^{\nu\nu'\omega}_{\mathbf{q},\mathrm{m}}\right) + F^{\nu,\nu+\omega,\nu'-\nu}_{\mathbf{k}'-\mathbf{k},\mathrm{m}} - \frac{1}{2}\left(F^{\nu\nu'\omega}_\mathrm{d} - F^{\nu\nu'\omega}_\mathrm{m}\right) \tag{5.53}$$

As noted in the derivation in (Sec. B [264]), the last term in Eq. 5.53 subtracts the double-counting of the local contributions. Following [125], we can now shift the frequency and momentum summations and rewrite the lDΓA vertex in order to isolate magnetic and density fluctuations from bare electronic ones [125, 205]:

$$\Sigma^\nu_{\mathbf{k},\mathrm{lD\Gamma A}} = U\frac{n}{2} - U\sum_{\nu'\omega\mathbf{k}'\mathbf{q}} F^{\nu\nu'\omega}_{\mathbf{q},\mathrm{lD\Gamma A}} \chi^{\nu\nu'\omega}_{\mathbf{q},0} G^{\nu+\omega}_{\mathbf{k}+\mathbf{q}} \tag{5.54}$$

$$F^{\nu\nu'\omega}_{\mathbf{q},\mathrm{lD\Gamma A}} = \frac{1}{2}\left(3F^{\nu\nu'\omega}_{\mathbf{q},\mathrm{m}} - F^{\nu\nu'\omega}_{\mathbf{q},\mathrm{d}}\right) - \frac{1}{2}\left(F^{\nu\nu'\omega}_\mathrm{m} - F^{\nu\nu'\omega}_\mathrm{d}\right) \tag{5.55}$$

$$K^{\nu\omega}_\mathbf{q} \coloneqq \sum_{\nu'} F^{\nu\nu'\omega}_{\mathbf{q},\mathrm{lD\Gamma A}} \chi^{\nu\nu'\omega}_{\mathbf{q},0} = \frac{1}{2}\left(3\lambda^{\nu\omega}_{\mathbf{q},\mathrm{m}} - \lambda^{\nu\omega}_{\mathbf{q},\mathrm{d}} - \lambda^{\nu\omega}_{0,\mathbf{q}}\right) \tag{5.56}$$

$$= \frac{1}{2}\left(3\gamma^{\nu\omega}_{\mathbf{q},\mathrm{m}}(1 + U\chi^\omega_{\mathbf{q},\mathrm{m}}) - \gamma^{\nu\omega}_{\mathbf{q},\mathrm{d}}(1 - U\chi^\omega_{\mathbf{q},\mathrm{d}}) - 2 - \lambda^{\nu\omega}_{0,\mathbf{q}}\right) \tag{5.57}$$

This form of the EoM is needed in order to introduce λ corrections and also provides considerable

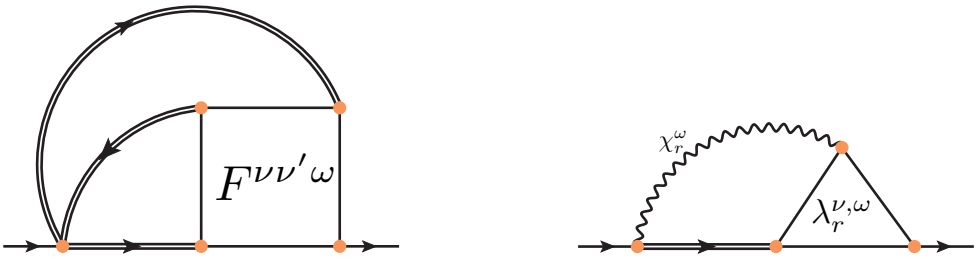

Figure 5.9: Illustration of the transformation for the equation of motion from Eq. (5.50). This demonstrates that the EoM can be understood as a scattering process between electrons and (para-) magnons. This decomposition is also needed in order to introduce λ corrections.

numerical advantages. $K^{\nu\omega}_\mathbf{q}$ is a shorthand notation for the sum over the $\lambda^{\nu\omega}_\mathbf{q}$ vertices which we

sometimes refer to. Fig. 5.9 shows the diagrammatic version of Eq. (5.57). Here we see that the bosonic propagator χ_r^ω couples electrons to the triangular (for this specific role, also called electron paramagnon vertex) vertex [125]. The calculation of the self-energy, including the necessary steps for obtaining the free parameters μ, λ_m and λ_d are shown in Fig. 5.8. Here, also the (optional) partial self-consistency discussed below is included.

5.4.2 Limitations of the λ-corrections approach

There are two limitations to the λ parameter correction approach that are worth mentioning. (i) The dominant ordering vector does not change from that of DMFT in the λ-corrected DΓA approach. (ii) The effective restoration of consistencies is *not fully* reflected in the λ-corrected full vertex $F_{r,\mathbf{q}}^{\lambda_r,\nu\nu'\omega}$.
The first limitation can be immediately obtained by considering (wlog) two vectors Letting $A \coloneqq \chi^{\omega_0}_{r,\mathrm{DMFT},\mathbf{q}_i}$ and $B \coloneqq \chi^{\omega_0}_{r,\mathrm{DMFT},\mathbf{q}_j}$ we consider the three possible signs and use, that at a phase transition the susceptibility approaches infinity, jumps from $+\infty$ to $-\infty$ and then tends towards -0. We therefore have three possible cases in which $\mathbf{q}_i$ is the dominant ordering vector, compared to $\mathbf{q}_j$:

$$\begin{cases} A > B \\ A < B \\ A > B \end{cases} = \begin{cases} \frac{1}{A} < \frac{1}{B} \\ \frac{1}{A} < \frac{1}{B} \\ \frac{1}{A} < \frac{1}{B} \end{cases} = \begin{cases} \frac{1}{A} + \lambda_r < \frac{1}{B} + \lambda_r \\ \frac{1}{A} + \lambda_r < \frac{1}{B} + \lambda_r \\ \frac{1}{A} + \lambda_r < \frac{1}{B} + \lambda_r \end{cases} \tag{5.58}$$

Because the λ_r parameters are defined such that the susceptibilities become strictly positive, the terms in all three cases above are now positive on both sides.

$$= \begin{cases} \left(\frac{1}{A} + \lambda_r\right)^{-1} > \left(\frac{1}{B} + \lambda_r\right)^{-1} & \text{if } A > 0 \wedge B > 0 \\ \left(\frac{1}{A} + \lambda_r\right)^{-1} > \left(\frac{1}{B} + \lambda_r\right)^{-1} & \text{if } A > 0 \wedge B < 0 \\ \left(\frac{1}{A} + \lambda_r\right)^{-1} > \left(\frac{1}{B} + \lambda_r\right)^{-1} & \text{if } A < 0 \wedge B < 0 \end{cases} \tag{5.59}$$

This means the largest susceptibility (for some ordering vector $\mathbf{q}_i$) remains the largest (case 1) or the first divergent susceptibility (case 2 and 3) becomes the largest. Both cases do not change the sequence of most dominant $\mathbf{q}$ vectors and lDΓA ; therefore, it retains mean-field character in the determination of the ordering symmetry.
Case (ii) has already been discussed in Sec. 4.5.1. We do not aim to construct consistent full vertices, but instead obtain consistent effective renormalizations of the susceptibilities. The effects of this are directly visible in the λ-corrected full vertex in Eq. (I8.40). Here we observe by direct comparison with Eq. (6.37) and Eq. (6.38) that the ν, ν' dependence of the asymptotic behavior in the full vertex is not changed from DMFT. These contributions arise exactly from the susceptibilities, that are in all other places renormalized in the lDΓA schemes. Specifically for strongly renormalized susceptibilities in the vicinity of spurious mean-field second-order phase transitions, the full lDΓA vertex $F_{r,\mathbf{q}}^{\lambda_r,\nu\nu'\omega}$ has to be treated carefully and should not be used for calculations, similar to $G^{(2)}$ in TPSC. A potential extension, that treats the asymptotic contributions in the full vertex explicitly is discussed in Sec. 5.5.

5.4.3 Partial Self-Consistent Extension

This extension of the lDΓA method introduces non-local correlation effects into the propagators in the EoM in Eq. (5.56). Note however, that we do *not* update the bare susceptibility $\chi_{0,\mathbf{q}}^{\nu\omega}$. As discussed in [128], this method can be employed to extend the lDΓA formalism to multi-orbital systems by avoiding λ corrections. Because of the additional complications introduced by this method, such as the stability of the self-consistency, uniqueness of the fixed point, potential double-counting, and thermodynamical consistency, we proceed with the form in Eq. (5.57) and only update the single Green's function entering the EoM directly without further comparison with this method.
This is done by evaluating the SDE to obtain a non-local self-energy $\Sigma_\mathbf{k}^\nu$. Using the Dyson equation, we calculate an updated interacting Green's function $G_\mathbf{k}^\nu$, that is *not* used for an updated bare susceptibility. Instead, just the new λ_r parameters are determined, and subsequently, a new self-energy is calculated. This is repeated until convergence. Fig. 5.10 shows the λ corrected charge susceptibilities for partially self-consistent and non-self-consistent methods with two different Σ tail correction schemes. We observe almost no difference between both methods in the thermodynamic properties over a wide range of parameters in 2 and 3 spatial dimensions and tail correction schemes, as demonstrated here on an example that is particularly far away from the DMFT approximation[6]. Most importantly, the sign of the non-local correction of the charge channel remains the same, demonstrating that the predicted enhancement of charge fluctuations due to non-local correlations in the charge order regime for cuprates (as discussed in Sec. 7.2 does not depend on this choice.
The spectral properties, however, are influenced more substantially by the choice of method and tail corrections scheme. This is demonstrated in Fig. 5.11. Both panels show the estimated Fermi surface as a black line. In the left panel in Fig. 5.11, we show the linear extrapolation of the real and imaginary parts of the self-energy $\lim_{\nu\to 0} \Sigma_\mathbf{k}^\nu$ over the first Brillouin zone for the 2 dimensional cubic lattice with

[6] In these cases, lDΓA recovers the correct solution, since the consistencies are already fulfilled, by finding $\lambda_r = 0$.

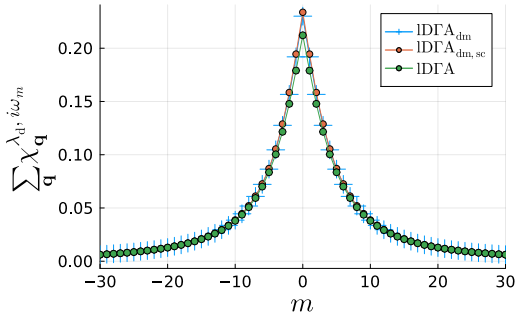

(a) $n \approx 0.83$, Σ correction: Full

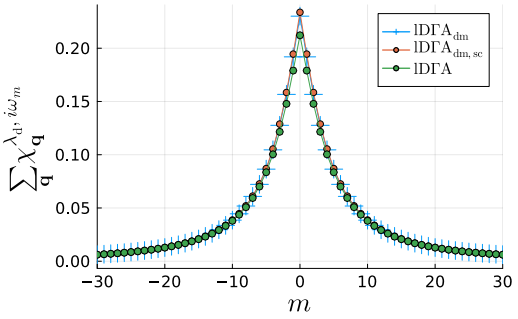

(b) $n \approx 1$, Σ correction: Full

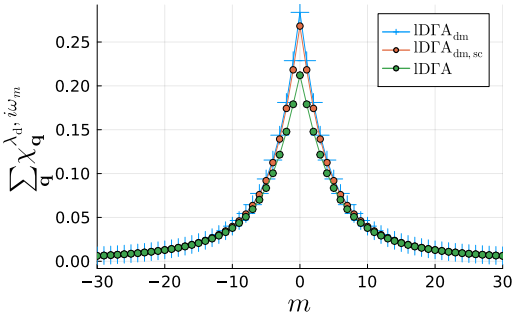

(c) $n \approx 0.83$, Σ correction: EoM

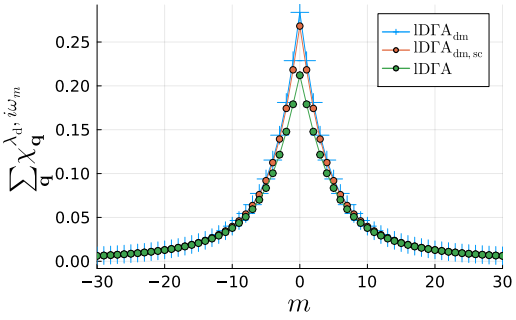

(d) $n \approx 1$, Σ correction: EoM

Figure 5.10: λ corrected charge susceptibilities for 2D simple cubic, $U = 2$, $\beta = 20$ (see Sec. 7.2) at two different fillings. The upper and lower panels are obtained using different Σ tail correction schemes, discussed in Sec. 6.3.4. The `ExpStep` variant is not shown here since it also yields results within 20% deviation from the others.

hopping parameters $t = 0.25, t' = 0.05, t'' = 0.025$ at $n \approx 0.83, \beta = 20$ and $U = 2$. One can observe a more pronounced momentum differentiation in the self-consistent method, as expected when replacing the DMFT Green's function with the lDΓA one, which contains non-local corrections. In the right panel in Fig. 5.11 we show an approximation for the quasi-particle weight $Z_{\mathbf{k}} \approx \left(1 - \mathrm{Re}\left(\Sigma^{\nu_1} - \Sigma^{\nu_0}\right)\frac{\beta}{\pi}\right)^{-1}$ (see Sec. 2.5). Here, we also demonstrate the dependence of this method on the self-energy tail correction scheme by showing data for the modified EoM and full-tail replacement variant, discussed in Sec. 6.3.4. Two of the methods seem to show slightly non-causal behavior in the vicinity of $\mathbf{k} \approx \mathbf{0}$. While this may be an artifact of the linear extrapolation and noisy input data[7], the modified equation of motion correction stays clear of this issue. This does, however, come at the cost of breaking the degeneracy in the spin channel and treating two of them on a local level, potentially also leading to defects such as a failure to fully capture pseudogap behavior in cuprates Sec. 7.2. The right panel in Fig. 5.11 demonstrates substantially modified behavior; specifically, for the direct (i.e. not partially self-consistent) method, the momentum differentiation is much closer to the local DMFT input. The momentum-integrated quantities do not exhibit this issue, as demonstrated above in Fig. 5.10.
As a final remark, we want to point out that the partially self-consistent method introduces numerical instability that can be observed predominantly around half-filling and low $\mathbf{k}$ resolutions. We, therefore, often employ the method without partial self-consistency, specifically when only thermodynamical properties like phase transitions are of interest.

5.4.4 Kinetic Energy Consistency

One can make use of the f-sum rule Eq. (4.43) and directly replace the $\mathbf{q}$-dependent $1/\omega^2$ tail:

$$\lim_{|\omega|\to\infty} (i\omega_m)^2 \chi^{\omega}_{\mathrm{d/m},\mathbf{q}} = 2\sum_{\mathbf{k}\sigma} \left(2\epsilon_{\mathbf{k}} - \epsilon_{\mathbf{k}+\mathbf{q}} - \epsilon_{\mathbf{k}-\mathbf{q}}\right) G^{\nu}_{\mathbf{k}} =: 2\sum_{\mathbf{k}\sigma} t_{\mathbf{k},\mathbf{q}} G^{\nu}_{\mathbf{k}} \tag{5.60}$$

$$\Rightarrow \lim_{|\omega|\to\infty} (i\omega_m)^2 \chi^{\lambda_{\mathrm{d/m}},\omega}_{\mathrm{d/m},\mathbf{q}} \overset{!}{=} 2\sum_{\mathbf{k}\sigma} t_{\mathbf{k},\mathbf{q}} G^{\lambda,\nu}_{\mathbf{k}} \tag{5.61}$$

The λ-corrections leave the $1/\omega^2$ tail unchanged, as can be seen via Taylor expansion of the definition in Eq. (4.47). This extension was already proposed as a future improvement in [202]. While some versions of the code do support an approximate scheme for this method, we did not find sufficient evidence of large violations of the kinetic energy consistency between one- and two-particle levels in any models we

[7] While we do use ED, which does not exhibit statistical noise such as CTQMC, the truncation of Lehmann summands and finite bath-sites effects (in our case 4) required to obtain results often introduces nonphysical or non-convergent behavior in the lDΓA algorithm.

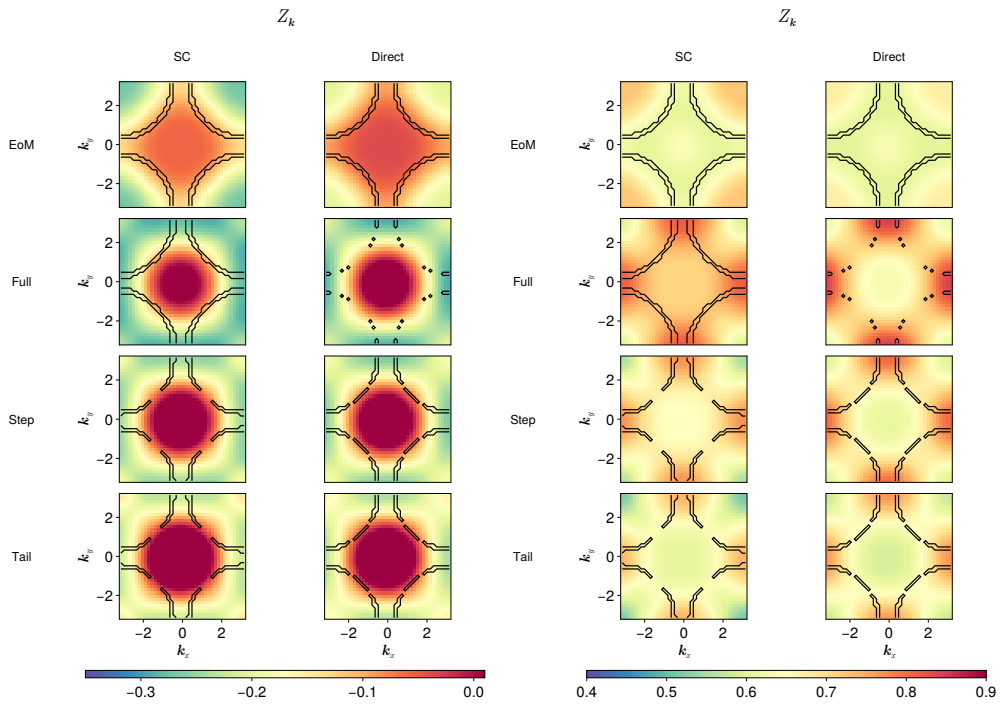

Figure 5.11: Left panel: Linear extrapolation of $\mathrm{Im}\,\Sigma^{\nu}_{\mathbf{k}}$ to $\nu = 0$, including estimated Fermi surface in black for different tail correction schemes, with and without partial self-consistency. Right panel: Linear extrapolation estimate of quasi-particle weight $Z_{\mathbf{k}}$, including estimated Fermi surface in black for different tail correction schemes, with and without partial self-consistency. Data is shown for the 2 dimensional cubic lattice with hopping parameters $t = 0.25, t' = 0.05, t'' = 0.025$ at $n \approx 0.83$, $\beta = 20$ and $U = 2$.

investigated. These are typically well below 5% for the full tail correction of the self-energy and below 3% for the EoM tail correction scheme. Consequently, the additional numerical challenges introduced by this method due to inherently noisy data from the $1/\omega^2$ high-frequency tail as well as the ambiguous choice of the correction schemes (because λ corrections do not affect the $1/\omega^2$ tail of the susceptibilities), we do not present a further discussion here. However, it is worth keeping in mind that without this correction, the kinetic energy on the two-particle level remains on the DMFT level, and the discrepancy to the two-particle value should be observed as an internal consistency check for all other λ correction schemes.

5.4.5 Fulfillment and Violation of Consistencies in lDΓA

By design, the λ corrected lDΓA method fulfills the Mermin-Wagner theorem Sec. 4.5.2 and at least some two-particle consistency by enforcing potential energy between and Pauli-principle values between one- and two-particle levels to match .
We stress that this is only enforced on an effective level and one has to make concessions in approximate methods. The possibly best example is the electron density n, which appears explicitly in the following equations (also discussed in Sec. 4.5):

$$n \overset{!}{=} \sum_{\nu\mathbf{k}} G^{\lambda_\mathrm{m}\lambda_\mathrm{d},\nu}_{\mathbf{k}} \tag{5.62}$$

$$\frac{n}{2}\left(1 - \frac{n}{2}\right) \overset{!}{=} \sum_{\omega\mathbf{q}} \left(\chi^{\lambda_\mathrm{d},\omega}_{\mathrm{d},\mathbf{q}} + \chi^{\lambda_\mathrm{m},\omega}_{\mathrm{m},\mathbf{q}}\right) \tag{5.63}$$

$$U^2 \frac{n}{2}\left(1 - \frac{n}{2}\right) \overset{!}{=} \lim_{\nu\to\infty} \mathrm{Re}\left[i\nu_n \left(\Sigma^{\lambda_\mathrm{m}\lambda_\mathrm{d},i\nu_n}_{\mathbf{k}} - \frac{Un}{2}\right)\right] \tag{5.64}$$

$$\lim_{|\omega|\to\infty} (i\omega_m)^2 \chi^{\omega}_{\mathrm{d/m},\mathbf{q}} = \sum_{\mathbf{k}} \left(2\epsilon_{\mathbf{k}} - \epsilon_{\mathbf{k}+\mathbf{q}} - \epsilon_{\mathbf{k}-\mathbf{q}}\right) n_{\mathbf{k}} \tag{5.65}$$

Having access to 3 free parameters (λ_m, λ_d, μ) we are only able to fix 3 of the 4 conditions, through these parameters, at most. Furthermore, the structure of Eq. (5.65) and Eq. (5.64), which involves limits, makes a systematic correction on finite grid sizes ambiguous. In addition, one also has to consider the feedback of the other correction parameters on the Green's function in Eq. (5.65), when computing $n_{\mathbf{k}} = \sum_{\nu\mathbf{k}} G^{\lambda_\mathrm{m}\lambda_\mathrm{d},\nu}_{\mathbf{k}}$. The various sub-methods discussed above give some freedom for the choice of which consistencies to preserve and which to use as an internal consistency check. In Fig. 5.10 and Fig. 5.11 we argued that the remaining inconsistencies predominantly influence the spectral properties

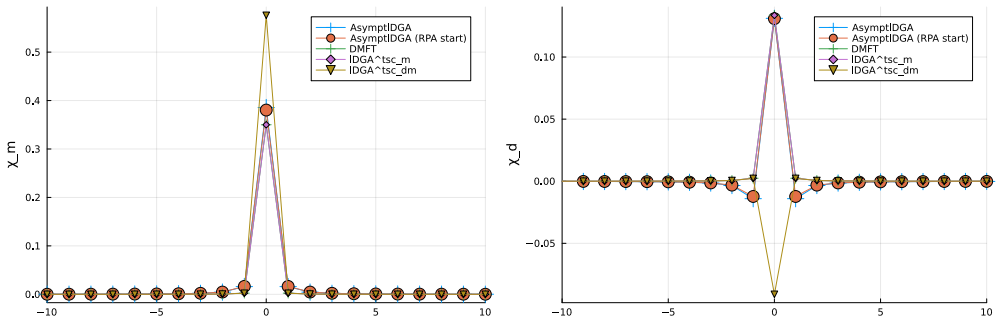

Figure 5.12: Comparison of magnetic and charge susceptibilities for the simple cubic lattice in 3 dimensions at $U = 2$ and $\beta = 1$. the blue and orange lines show the asymptotic method with different starting points $\Gamma_r = \pm U$ is labeled "RPA start".

of the system and are certainly a valuable concern for future extension of the method. However, for the systems we investigated in Sec. 7.1 and Sec. 7.2 we did find only minor improvements with added consistencies beyond the lDΓA$_{\mathrm{dm}}$ method, so specific models in which, for example, the inconsistency of the f-sum rule Eq. (5.65) contributes significantly to the driving physics of the system.

5.5 Asymptotic Ladder Approximation

This section describes an attempt to incorporate the asymptotic contributions discussed in Sec. 6.2 directly into the method. As of the writing of this thesis, there are still many open questions and the results presented here are preliminary. This is especially true for the aspects of this method that introduce effects beyond the ladder approximation by introducing a channel mixing in the irreducible two-particle vertex. Nonetheless, I want to give a short introduction here, because initial benchmarks show very promising results for many parameter regimes of models that are notoriously difficult to access by the previously described methods. However, the code as discussed in Sec. 6.8.5 and Sec. 6.8.6 already supports this method partially for the particle-hole symmetric case where $\chi_{\mathrm{d}} = \chi_{\mathrm{pp}}$.
The idea is to replace the irreducible vertices Γ_r for each channel by their asymptotic contributions, derived in [256]. These consist of physical susceptibilities that can be obtained from the BSE after an initial guess of RPA ($\Gamma_r^{\nu\nu'\omega} \equiv \pm U$) or DMFT (see also Fig. 5.12). Iterative computation of physical susceptibilities, replacement of $\Gamma_r^{\nu\nu'\omega}$, etc. did indeed lead to convergence in our tests at half-filling.
While more rudimentary in the structure of the vertex in the core regions, this method includes feedback beyond the capability of the ladder approximation. Specifically, the diagonal contributions of $F_{r,\mathbf{q}}^{\nu\nu'\omega}$ from Eq. (6.37) and Eq. (6.38) (derivation and discussion from [256]) which are the local physical susceptibilities, stay local, while only the background changes, as can be verified from the construction in Eq. (I8.40).

$$F_{\mathrm{d/m,asympt}}^{\nu\nu'\omega} \sim \pm U - U^2 \chi^{\omega} \to \pm U - U^2 \chi_{\mathbf{q}}^{\lambda,\omega} \tag{5.66}$$

By replacing the asymptotic contributions explicitly, we not only eliminate the remaining local contributions but also introduce full parquet-like feedback between scattering channels. Moreover, extensions of this method could be considered, in which a core region is an irreducible vertex Γ that is still taken from DMFT to retain local non-perturbative contributions.

Scaling to lDΓA

The method can be extrapolated towards the lDΓA variants by the introduction of a cutoff parameter N_ν^{cut} of an inner region for the irreducible two-particle vertices Γ_r. One then inserts the DMFT vertex instead of the asymptotic contributions in this region. Clearly $N_\nu^{\mathrm{cut}} \to N_\nu^{\mathrm{max}}$ recovers lDΓA. An intriguing open question that could be investigated through this method would be how the non-local update in the full vertex $F^{\nu\nu\omega}$ (which remains on DMFT level in lDΓA) affects the predictive power of this class of methods.

Open Questions

While the stabilization of the self-consistency seems to be possible for the three-dimensional cubic lattice at half-filling and moderate interaction strength (up to $U = 2$ and $\beta = 20$), the validity away from half-filling and in two dimensions needs to be established. In addition, this approach seems to be a viable path for the investigation of further inter-channel renormalization effects beyond the effective renormalization that we introduced with the λ corrected lDΓA method. This could be of interest by comparison with the λ RPA method since the irreducible vertex of RPA (which is $\Gamma_r \pm U$) can be systematically extended, by including the physical susceptibilities. This comparison is certainly also

interesting from the point of violation of consistencies between one and two-particle levels, which could as well be reintroduced by λ corrections in the asymptotic case.

6 Numerical Details

In this chapter, we will discuss numerical methods that were either necessary to stabilize the lDΓA method or were developed for related projects. Readers who are developing methods involving Feynman diagrammatic techniques will hopefully find useful discussions here. For a general understanding of the capabilities of these approaches and the understanding of the phenomena they describe, this chapter may be skipped.

6.1 Improved Summations (Series Acceleration)

This section is somewhat isolated from the rest of the chapter, as none of it is applicable to the programs developed during the thesis. The methods discussed here were tested in a first attempt to improve the summation of functions over Matsubara frequencies. However, after thorough testing, it turned out that sums over multiple indices (such as needed in the equation of motion) can suffer from considerable stability issues. We will give an overview here nonetheless, because the general resummation formulas are very general, whereas the method discussed in Sec. 6.3 serves as a reference for more specialized summation methods or can be used when no other methods are available. Furthermore, the general idea of improved summations, (i.e. obtaining a limit from a finite number of summands of an infinite series that is closer to the true limit than plain summation) without introducing additional physics-related information will serve as a preparatory step. Lastly, the concept of improved summation has a surprising connection to the analytical continuation problem that we encounter whenever moving from the Matsubara formalism back to retarded Green's functions. In fact, a direct generalization of this concept can, for example, be used to obtain critical exponents in the 3 dimensional XY model [212] or assign a limit to divergent perturbation series [213]. The code implementing some of these ideas is publicly available [248] (see also Sec. 6.8.1).

6.1.1 Introduction

Our task will be to improve the estimation of infinite series from a finite number of summands. The reason is, of course, that Matsubara sums run over infinitely many frequencies, but one has to define an energy cutoff for numerical computations. Here, we discuss several ways to deal with this inconsistency and improve the estimation of the true value of the sum above plain summation over just some subset of indices. We therefore introduce the index set $I_N = \{a, ..., b\}$ with $N = b - a + 1$.

$$\sum_{n \in I_\infty} F_n \to \sum_{n \in I_N} F_n \tag{6.1}$$

Note that the approximation may depend heavily on the index set. This is especially important since we often have very well-behaved, symmetrical tails for both $N \to \pm\infty$, and unique features appear only in a limited region. Centering the summation around that point can yield greatly improved results.

6.1.2 Series Limits

In the following, we derive formulas for the improved numerical summation over functions of Matsubara frequencies. We will, for now, not assume any knowledge of the convergence to infinity and present some well-known general summation formulas before presenting techniques that incorporate the coefficients of a Taylor expansion around ∞. These coefficients can be obtained from diagrammatic considerations and allow us to sum up contributions analytically, leaving only higher-order sums for numerical evaluation, thus reducing finite-size errors.
In both cases, we split the summation of a function F_n with $n \in \Omega$ into two. Typically $\Omega \equiv \mathbb{Z}$ or $\Omega \equiv \mathbb{Z}^2$. However, we leave the definition for the index set intentionally general for now since these sets can have slightly more complicated definitions. Specifically, for two indices, one may depend on the other, see Sec. 6.4. Let T_n be some analytically known function with $T_n \sim F_n$, i.e. $\lim_{n\to\infty} T_n/F_n = 1$ [40, Chapter 3].

$$\begin{aligned}
\sum_{n\in\Omega} F_n &= \sum_{n\in\Omega} (F_n - T_n + T_n) \\
&= \sum_{n\in\Omega_{\text{core}}} (F_n - T_n) + \sum_{n\in\Omega_{\text{shell}}} (F_n - T_n) + \sum_{n\in\Omega} T_n \\
&\sim \sum_{n\in\Omega_{\text{core}}} (F_n - T_n) + \sum_{n\in\Omega} T_n
\end{aligned} \tag{6.2}$$

In the last line, we made the necessary approximation only to include numerical data in a finite interval. However, by choosing a good approximation T_n of the function F_n, we can hope to improve the numerical accuracy since some contributions are included up to infinity. This may also be motivated as follows: Taylor expansion of F_n around ∞ gives rise to some series $\sum_l \frac{c_l}{x^l}$. By choosing T_n as the first few terms, we only have to numerically sum terms that tend to 0 quickly. For later reference, we first rewrite partial sums over Matsubara frequencies in terms of a closed expression, using the definition of special functions. This helps readability and implementation performance (because there are fast implementations available, for example, using the Euler-Maclaurin summation formula or tabulation of the Bernoulli polynomials).

6.1.3 Useful Identities

We first collect a number of definitions and identities that are used for the derivation of the improved sum formulas or their evaluation. This is mainly used for the numerical evaluation of the sums;

the references to the codes are given below. The Hurwitz ζ and polygamma functions are defined, respectively, as

$$\zeta(a,b) = \sum_{n=0}^{\infty} \frac{1}{(n+b)^a} \tag{6.3}$$

$$\psi^{(a)}(b) = \frac{\mathrm{d}^{a+1}}{\mathrm{d}z^{a+1}} \ln\Gamma(z) \tag{6.4}$$

For our purposes (finite temperature Green's functions), we will only need integer arguments of these functions. Here, the series representation of the polygamma function $\psi^{(m)}(z)$ can be used:

$$\zeta(a+1,b) = (-1)^a \frac{\psi^{(a)}(b)}{a!} = \sum_{n=0}^{\infty} \frac{1}{(n+b)^{(a+1)}} + \delta_{a0}\left(\sum_{n=1}^{\infty} \frac{1}{n} - \gamma\right) \tag{6.5}$$

Note also that an index shift leads to a formula for finite and linearly transformed sums:

$$\sum_{n=0}^{N} \frac{1}{(n+b)^a} = \zeta(a,b) - \sum_{n=N+1}^{\infty} \frac{1}{(n+b)^a} = \zeta(a,b) - \zeta(a,N+1+b) \tag{6.6}$$

$$\sum_{n=0}^{\infty} \frac{1}{(c\cdot n + d\cdot b)^a} = \frac{1}{c^a}\zeta\left(a, \frac{d\cdot b}{c}\right) \tag{6.7}$$

We will use these identities to express sums over Matsubara frequencies. For autocorrelation tails, we will use:

$$\frac{1}{(i\omega_m + i\nu_n)^k} = \frac{1}{\left(i\frac{(2m)\pi}{\beta} + i\frac{(2n+1)\pi}{\beta}\right)^k} = \left(\frac{\beta}{\pi i}\right)^k \frac{1}{(2m+n+1)^k} \tag{6.8}$$

Furthermore we can rewrite Matsubara sums for fermionic ($i\nu_n$) and bosonic ($i\omega_m$) frequencies as follows:

$$\begin{aligned}
\Rightarrow \sum_{n=N}^{\infty} \left(\frac{1}{i\nu_n}\right)^l &= \left(\frac{\beta}{2\pi i}\right)^l \sum_{n=N}^{\infty} \frac{1}{\left(n+\frac{1}{2}\right)^l} = \left(\frac{\beta}{2\pi i}\right)^l \sum_{n=N}^{\infty} \frac{1}{\left(n+\frac{1}{2}\right)^l} \\
&= \left(\frac{\beta}{2\pi i}\right)^l \sum_{n=0}^{\infty} \frac{1}{(n+N+\frac{1}{2})^l} = \left(\frac{\beta}{2\pi i}\right)^l \zeta\left(l, N+\frac{1}{2}\right)
\end{aligned} \tag{6.9}$$

$$\sum_{m=M}^{\infty} \left(\frac{1}{i\omega_m}\right)^l = \left(\frac{\beta}{2\pi i}\right)^l \zeta(l,M) \tag{6.10}$$

$$\Rightarrow \sum_{n=0}^{N} \left(\frac{1}{i\nu_n}\right)^l = \left(\frac{\beta}{2\pi i}\right)^l \left(\zeta\left(l,\frac{1}{2}\right) - \zeta\left(l,N+\frac{3}{2}\right)\right) \tag{6.11}$$

$$\sum_{m=1}^{M} \left(\frac{1}{i\omega_m}\right)^l = \left(\frac{\beta}{2\pi i}\right)^l \left(\zeta(l) - \zeta\left(l,M+1\right)\right) \tag{6.12}$$

Note that sums over Matsubara frequencies pick up an additional normalization factor of $\frac{1}{\beta}$ that is omitted here. The first (approximate) values, which are used in our calculations, are given in table 6.1 for reference.

n	factor	$\zeta(n)$
1	$\frac{\beta}{2\pi i}$	∞
2	$-\left(\frac{\beta}{2\pi}\right)^2$	$\frac{\pi^2}{6}$
3	$i\left(\frac{\beta}{2\pi}\right)^3$	1.2021
4	$\left(\frac{\beta}{2\pi}\right)^4$	$\frac{\pi^4}{90}$
5	$-i\left(\frac{\beta}{2\pi}\right)^5$	1.0369
6	$-\left(\frac{\beta}{2\pi}\right)^6$	$\frac{\pi^6}{945}$
7	$i\left(\frac{\beta}{2\pi}\right)^7$	1.0083
8	$\left(\frac{\beta}{2\pi}\right)^8$	$\frac{\pi^8}{9450}$

Table 6.1: Zeta function values

6.1.4 Aitken's Δ^2-Process and Shanks Transformation

The arguably simplest series acceleration method can be obtained by assuming that the residual term of the partial sum ($S_N = \sum_{n\in I_N} F_n$) follows a power law:

$$S_n - S = \alpha q^n \tag{6.13}$$

Where the exact limit is S, and the error decays with some $q < 1$. The 3 parameters α, q and S can then be obtained by evaluating Eq. (6.13) at three different partial sums [40, Sec.8.1]:

$$S = S_n - \alpha q^n + \mathcal{O}(q^n), \quad S = S_{n+1} - \alpha q^{n+1} + \mathcal{O}(q^n), \quad S = S_{n+2} - \alpha q^{n+2} + \mathcal{O}(q^n) \tag{6.14}$$

This can be solved, yielding the Aitken Δ^2 process [3]:

$$(a_n) \coloneqq \frac{S_{n+1}S_{n-1} - S_n^2}{S_{n+1} + S_{n-1} - 2S_n} + \mathcal{O}(q^{n-1}) \tag{6.15}$$

$$= S_n - \frac{(\Delta S_n)^2}{\Delta^2 S_n} \tag{6.16}$$

Where we defined the forward difference operator of the k-th derivative:

$$\Delta^k a_0 = \sum_{n=0}^{k} (-1)^n \binom{k}{n} a_{k-n} \tag{6.17}$$

Eq. (6.16) is numerically more stable compared to Eq. (6.15). In fact, the denominator can be used to check for underflow in the iterated Aitken's Δ^2-process.
(a_n) is a sequence constructed by this process that often converges faster toward S than S_n.
Around 1980 it was independently discovered by Berzenski and Håvie, that the error term in Eq. (6.13) can be treated more generally [94, 37]:

$$S_n = S + \sum_{j=0}^{k-1} c_j f_j(n) \tag{6.18}$$

Where $f_j(n)$ are known, but arbitrary (even divergent) functions. The extrapolation of the series limit then follows analogously to the Δ^2-process, but for k equations [289]. Using Cramer's rule, the extrapolated value is obtained via

$$e_k(S_n) = \begin{vmatrix} S_n & \cdots & S_{n+k} \\ f_0(n) & \cdots & f_0(n+k) \\ \vdots & \ddots & \vdots \\ f_{k-1}(n) & \cdots & f_{k-1}(n+k) \end{vmatrix} \Bigg/ \begin{vmatrix} 1 & \cdots & 1 \\ f_0(n) & \cdots & f_0(n+k) \\ \vdots & \ddots & \vdots \\ f_{k-1}(n) & \cdots & f_{k-1}(n+k) \end{vmatrix} \tag{6.19}$$

$e_k(S_n)$ stands for the transformation operation and has the value of the improved sum. Eq. (6.19) can be solved via a recursive algorithm instead of (the numerically unfeasible) ratio of determinants. However, the very general form is in practice often less useful than specific choices for the sequence of functions f_j [289]. Let us briefly mention the two most prominent cases. The Levin-Weniger transformation, where $f_j(n) = (n+\beta)^{-j}$ was first used by H. Levine and J. Schwinger to compute diffraction of scalar planar plane wave [160].
The Shanks transformation, with $f_j(n) = \Delta^{n+j}$ can be thought of as fitting the sequence of derivatives of the partial sum sequence [223, 230]:

$$S_n = c_0 + c_1\Delta^m S_n + c_2\Delta^{2m} S_n + \ldots c_k\Delta^{km} S_n \tag{6.20}$$

Again, there exist specialized algorithms circumventing the calculation of the expression from Eq. (6.19). Specifically Wynn's ϵ-algorithm [292]. Because this approach turned out to be unsuccessful for the purpose of this thesis, we leave the discussion to the literature [289]. The implementation used for initial versions of the lDΓA method with improved asymptotic treatment is available as a `Julia` package [248] (see Sec. 6.8.1). The close relationship to Padé approximants[1] makes this technique seem especially intriguing for Green's functions[2]. If the Shanks transformation is applied to a function of the type $f(z) = \sum_{l=0}^{\infty} \alpha_l z^l$, the result is a Padé approximant (that can be obtained by Wynn's ϵ-algorithm)

$$e_k f_n(z) = \left[\frac{n+k}{k}\right]_f (z) \tag{6.21}$$

A very approachable derivation and discussion of features and disadvantages of the methods above and respective algorithms including source code are given E. J. Weniger in [289]. Extensions to resummation techniques of divergent series are discussed in [40, Chapter 8].

6.1.5 Richardson

One of the oldest schemes for accelerated summation of series is the Richardson extrapolation. It was first formally introduced by L.F. Richardson in 1911 [201] but was already used by Huygens for the calculation of π in 1654 [285, 38]. This method specifically excels at slowly convergent series of the

[1] Wynn
[2] Here, these are often used to analytically continue Matsubara Green's functions to the real axis. There has also been work on choosing a Shanks-like transformation specifically for Green's functions [47].

form

$$S_n = \sum_{k \epsilon I_e} \frac{a_k}{n^k} \tag{6.22}$$

With $I_e \subset \mathbb{N}_0$ being a set of exponents, which must include 0. We can immediately notice that for $\lim_{n\to\infty} S_n = a_0 = \sum_{n\epsilon I_\infty} f(i\omega_n)$ will yield the limit. It is possible to obtain a_0 from closed form expressions, [40, Eq. 8.1.16]:

$$a_0 = \sum_{k=0}^{N} \frac{S_{n+k}(n+k)^N(-1)^{k+N}}{k!(N-k)!} \tag{6.23}$$

Specifically for the case of Matsubara summations over symmetric domains around 0, one can also obtain a version that does not require the computation of factorials but instead extrapolates via a matrix-vector multiplication [202, G. 9]:

$$a_0 = \sum_{n=N_{\min}}^{N_{\max}} w_{0n} S_n \tag{6.24}$$

with

$$w_{in} = M_{il}^{-1} n^{-l}, \qquad M_{il} = \sum_{n=N_{\min}}^{N_{\max}} n^{-l} n^{-i} \tag{6.25}$$

Here, M can be precomputed for the desired domain. Both methods have been implemented and tested for one- and two-particle Green's functions in [248]. However, for two-particle Green's functions, this method proved to be extremely unstable and was not further developed. Instead, the significantly more stable approach using the known diagrammatic contributions for the high-frequency tail (discussed in the following) was implemented in [244].

6.2 Asymptotics

In this section, we will discuss the asymptotic behavior of all quantities used for the lDΓA method. These asymptotic contributions will then be used to improve the sum of the respective quantities in Sec. 6.3. For the following sections, we occasionally deviate from our usual notation of **k**-space integration as a sum. Instead, we use an integral symbol to indicate that this **k**-space integration is independent of the sampling chosen for the BSE, that implies the sampling for all other lDΓA related quantities (for the numerical setup in this thesis) as a consequence of the convolution algorithm Sec. 6.4.2.
The derivations of the asymptotic contributions and improved sum formulas are based on unpublished notes by Georg Rohringer and [256].

Spectral Moments of Green's functions

We start with the best-known high-frequency expansion, that of the single-particle Green's function. The so-called spectral moments $c_{l,\mathbf{k}}$ can be obtained via integration by parts from the imaginary time Green's function:

$$\begin{aligned}
G^\nu_{\mathbf{k}} &= \int_0^\beta \mathrm{d}\tau G_{\mathbf{k}}(\tau) e^{i\nu_n\tau} \\
&= \left[G_{\mathbf{k}}(\tau) \frac{1}{i\nu_n} e^{i(2n+1)\frac{\pi}{\beta}\tau} \right]_0^\beta - \frac{1}{i\nu_n} \int_0^\beta \mathrm{d}\tau \left(\frac{\mathrm{d}}{\mathrm{d}\tau} G_{\mathbf{k}}(\tau) \right) e^{i\nu_n\tau} \\
&= \frac{1}{i\nu_n} \left[\lim_{\tau\to\beta^-} G_{\mathbf{k}}(\tau) e^{i(2n+1))\frac{\pi}{\beta}\tau} - \lim_{\tau\to 0^+} G_{\mathbf{k}}(\tau) e^{i(2n+1)\frac{\pi}{\beta}\tau} \right] - \frac{1}{i\nu_n} \int_0^\beta \mathrm{d}\tau \left(\frac{\mathrm{d}}{\mathrm{d}\tau} G_{\mathbf{k}}(\tau) \right) e^{i\nu_n\tau} \\
&= \frac{1}{i\nu_n} \left[-G_{\mathbf{k}}(\beta^-) - G_{\mathbf{k}}(0^+) \right] - \frac{1}{i\nu_n} \int_0^\beta \mathrm{d}\tau \left(\frac{\mathrm{d}}{\mathrm{d}\tau} G_{\mathbf{k}}(\tau) \right) e^{i\nu_n\tau} \\
&= \frac{1}{i\nu_n} \left[G_{\mathbf{k}}(0^+) - G_{\mathbf{k}}(0^-) \right] - \frac{1}{i\nu_n} \int_0^\beta \mathrm{d}\tau \left(\frac{\mathrm{d}}{\mathrm{d}\tau} G_{\mathbf{k}}(\tau) \right) e^{i\nu_n\tau}
\end{aligned}$$

Where we used the β periodicity of the imaginary time Green's function, also discussed in Sec. 2.2. Note also that $\lim_{\tau\to\beta^-}$ and $\lim_{\tau\to 0^+}$ have to be treated carefully and partial integration is only allowed because $\lim_{\tau\to 0} G(\tau) e^{i\nu_n\tau}$ exists.
Iteration of the integration-by-parts formula yields a series expansion of the Green's function,

$$G^\nu_{\mathbf{k}} = \sum_{l=1}^{\infty} \frac{c_{l,\mathbf{k}}}{(i\nu_n)^l} \tag{6.26}$$

with spectral moments, defined by the time derivatives of the imaginary time Green's function

$$c_{l,\mathbf{k}} = (-1)^l \left(\lim_{\tau\to 0^+} \frac{\mathrm{d}^{(l-1)}}{\mathrm{d}\tau^{(l-1)}} G_{\mathbf{k}}(\tau) - \lim_{\tau\to 0^-} \frac{\mathrm{d}^{(l-1)}}{\mathrm{d}\tau^{(l-1)}} G_{\mathbf{k}}(\tau) \right) \tag{6.27}$$

We can evaluate this explicitly for the first terms of the Green's function of the Hubbard model:

Important 6.2.0.1 (Spectral Moments of the Hubbard Model Green's Function)
Evaluation of Eq. (6.27) *using the Heisenberg equation of motion* Eq. (2.16) *with the definition of the AIM* Eq. (3.99) *(local) or Hubbard Hamiltonian* Eq. (3.12) *(non-local) yields the following spectral moments for the one-particle Green's function:*

$$c_1 = 1 \tag{6.28a}$$

$$c_{2,\mathbf{k}} = \frac{Un}{2} - \mu + \begin{cases} 0 & \text{local} \\ \epsilon_{\mathbf{k}} & \text{non-local} \end{cases} \tag{6.28b}$$

$$c_{3,\mathbf{k}} = \left(\frac{Un}{2} - \mu\right)^2 + f^{\nu}_{\mathbf{k}} = \left(\frac{Un}{2} - \mu\right)^2 + U^2 \frac{n}{2}\left(1 - \frac{n}{2}\right) + \begin{cases} \sum_l V_l^2 & \text{local} \\ \epsilon_{\mathbf{k}}^2 + 2\epsilon_{\mathbf{k}}\left(\frac{Un}{2} - \mu\right) & \text{non-local} \end{cases} \tag{6.28c}$$

Fig. 6.1 and Fig. 6.2 show the asymptotic behavior of impurity and local Green's function respectively for the first 400 Matsubara frequencies. The Green's functions were obtained using ED with 4 bath sites on a square lattice with parameters $U = 2$, $\mu = 1.4$ and $n \approx 0.2395$ at $\beta = 20$. These example plots here are meant to give an idea of how we typically investigate the convergence of quantities to their asymptotic behavior.

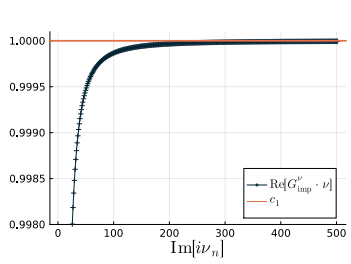

(a) c_1 coefficient for impurity Green's function, and $G^{\nu}_{\text{imp}} \cdot \nu$.

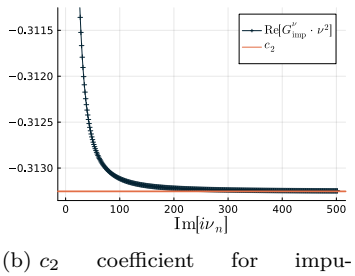

(b) c_2 coefficient for impurity Green's function, and $(G^{\nu}_{\text{imp}} - \frac{c_1}{\nu}) \cdot \nu^2$

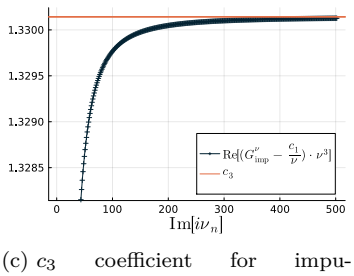

(c) c_3 coefficient for impurity Green's function, and $(G^{\nu}_{\text{imp}} - \frac{c_1}{\nu} - \frac{c_2}{\nu^2}) \cdot \nu^3$

Figure 6.1: Tail coefficients for impurity Green's function, obtained from ED with 4 bath sites, with $U = 2$, $\mu = 1.4$, $n \approx 1.087$. Convergence of the Green's function multiplied with the tail, demonstrates the correct asymptotic behavior.

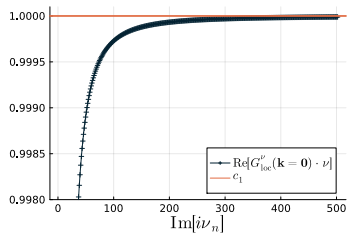

(a) $c_{1,\mathbf{k}}$ coefficient for local Green's function, and $G^{\nu}_{\mathbf{k}=\mathbf{0}} \cdot \nu$.

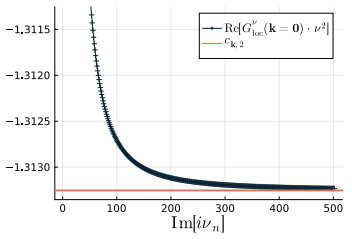

(b) $c_{2,\mathbf{k}}$ coefficient for local Green's function, and $(G^{\nu}_{\mathbf{k}=\mathbf{0}} - \frac{c_{1,\mathbf{k}}}{\nu}) \cdot \nu^2$.

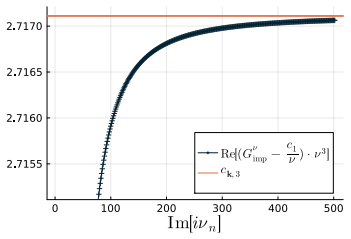

(c) $c_{3,\mathbf{k}}$ coefficient for local Green's function, and $(G^{\nu}_{\mathbf{k}=\mathbf{0}} - \frac{c_{1,\mathbf{k}}}{\nu} - \frac{c_{2,\mathbf{k}}}{\nu^2}) \cdot \nu^3$

Figure 6.2: Tail coefficients for local Green's function on a square lattice, obtained from ED with 4 bath sites, with $U = 2$, $\mu = 1.4$, $n \approx 1.087$.

6.2.1 Bare Susceptibility

The bare susceptibility is defined as the autocorrelation (particle-hole channel) or convolution (particle-particle channel) of the DMFT Green's function. We can therefore obtain the asymptotic behavior by investigating the contributions from the Green's functions for both arguments to the $\chi^{\omega}_{0,\mathbf{q}}$ and sort the coefficients by powers of $i\nu_n + i\omega_m$ using partial fraction decomposition to decouple fermionic and bosonic sums.

$$\chi^{\omega}_{0,\mathbf{q}} = -\beta \sum_{\nu\mathbf{k}} G^{\nu+\omega}_{\mathbf{k}+\mathbf{q}} G^{\nu}_{\mathbf{k}} = -\beta \sum_{\mathbf{k}} \sum_{n\in\mathbb{N}} \sum_{r\in\mathbb{N}_{>0}} \frac{c_{r,\mathbf{k}}}{(i\nu_n)^r} \sum_{s\in\mathbb{N}_{>0}} \frac{c_{s,\mathbf{k}+\mathbf{q}}}{(i\nu_n + i\omega_m)^s}$$

This is a more specific form of the general expansion, that does not assume further knowledge about spectral moments:

$$G^{\nu}_{\mathbf{k}} G^{\omega+\nu}_{\mathbf{q}+\mathbf{k}} = \frac{G^{\nu}_{\mathbf{k}} - G^{\omega+\nu}_{\mathbf{q}+\mathbf{k}}}{(G^{\omega+\nu}_{\mathbf{q}+\mathbf{k}})^{-1} - (G^{\nu}_{\mathbf{k}})^{-1}} \tag{6.29}$$

$$= \frac{1}{\omega} \frac{G^{\nu}_{\mathbf{k}} - G^{\omega+\nu}_{\mathbf{q}+\mathbf{k}}}{1 + (\epsilon_{\mathbf{k}} + \Sigma_{\mathbf{k}} - \epsilon_{\mathbf{q}+\mathbf{k}} - \Sigma_{\mathbf{q}+\mathbf{k}})/\omega} \frac{1}{\omega} = \frac{1}{\omega} \left(G^{\nu}_{\mathbf{k}} - G^{\omega+\nu}_{\mathbf{q}+\mathbf{k}} \right) + \mathcal{O}(1/\omega^2) \tag{6.30}$$

The first few terms of the moment expansion are given in the following table. Note that the expansion only holds for $\omega \neq 0$, since the $\frac{1}{\omega}$ factor is not well defined otherwise. However, in this case, the left-hand side is readily evaluated instead. Each line corresponds to a pair of coefficients, where all contributions with coefficients $c_{j,\mathbf{k}}$ with $j \leq 3$ are listed.

$$\begin{array}{lllllll}
(1)\ c_{1,\mathbf{k}} c_{1,\mathbf{k}+\mathbf{q}}: & \frac{1}{\nu^1}\frac{1}{(\nu+\omega)^1} & = \frac{1}{\omega}\cdot\left(\frac{1}{\nu} - \frac{1}{\nu+\omega}\right) & & & \\
(2)\ c_{1,\mathbf{k}} c_{2,\mathbf{k}+\mathbf{q}}: & \frac{1}{\nu}\frac{1}{(\nu+\omega)^2} & = \frac{1}{\omega}\cdot\left(-\frac{1}{(\nu+\omega)^2}\right) & +\frac{1}{\omega^2}\cdot\left(\frac{1}{\nu} - \frac{1}{\nu+\omega}\right) & & \\
(3)\ c_{1,\mathbf{k}+\mathbf{q}} c_{2,\mathbf{k}}: & \frac{1}{\nu^2}\frac{1}{(\nu+\omega)^1} & = \frac{1}{\omega}\cdot\left(\frac{1}{\nu^2}\right) & +\frac{1}{\omega^2}\cdot\left(-\frac{1}{\nu} + \frac{1}{\nu+\omega}\right) & & \\
(4)\ c_{1,\mathbf{k}} c_{3,\mathbf{k}+\mathbf{q}}: & \frac{1}{\nu}\frac{1}{(\nu+\omega)^3} & = \frac{1}{\omega}\cdot\left(-\frac{1}{(\nu+\omega)^3}\right) & +\frac{1}{\omega^2}\cdot\left(-\frac{1}{(\nu+\omega)^2}\right) & +\frac{1}{\omega^3}\cdot\left(\frac{1}{\nu} - \frac{1}{\nu+\omega}\right) & \\
(5)\ c_{2,\mathbf{k}} c_{2,\mathbf{k}+\mathbf{q}}: & \frac{1}{\nu^2}\frac{1}{(\nu+\omega)^2} & = \frac{1}{\omega}\cdot 0 & +\frac{1}{\omega^2}\cdot\left(\frac{1}{\nu^2} + \frac{1}{(\nu+\omega)^2}\right) & +\frac{1}{\omega^3}\cdot\left(-\frac{2}{\nu} + \frac{2}{\nu+\omega}\right) & \\
(6)\ c_{1,\mathbf{k}+\mathbf{q}} c_{3,\mathbf{k}}: & \frac{1}{\nu^3}\frac{1}{(\nu+\omega)^1} & = \frac{1}{\omega}\cdot\left(\frac{1}{\nu^3}\right) & +\frac{1}{\omega^2}\cdot\left(-\frac{1}{\nu^2}\right) & +\frac{1}{\omega^3}\cdot\left(\frac{1}{\nu} - \frac{1}{\nu+\omega}\right) & \\
(7)\ c_{2,\mathbf{k}} c_{3,\mathbf{k}+\mathbf{q}}: & \frac{1}{\nu^2}\frac{1}{(\nu+\omega)^3} & = \frac{1}{\omega}\cdot 0 & +\frac{1}{\omega^2}\cdot\left(\frac{1}{(\nu+\omega)^3}\right) & +\frac{1}{\omega^3}\cdot\left(\frac{1}{\nu^2} + \frac{2}{(\nu+\omega)^2}\right) & +\frac{1}{\omega^4}\cdot\left(-\frac{3}{\nu} + \frac{3}{\nu+\omega}\right) \\
(8)\ c_{2,\mathbf{k}+\mathbf{q}} c_{3,\mathbf{k}}: & \frac{1}{\nu^3}\frac{1}{(\nu+\omega)^2} & = \frac{1}{\omega}\cdot 0 & +\frac{1}{\omega^2}\cdot\left(\frac{1}{\nu^3}\right) & +\frac{1}{\omega^3}\cdot\left(-\frac{2}{\nu^2} - \frac{1}{(\nu+\omega)^2}\right) & +\frac{1}{\omega^4}\cdot\left(\frac{3}{\nu} - \frac{3}{\nu+\omega}\right)
\end{array} \tag{6.31}$$

Here, many terms vanish, since $\forall l > 1 : \sum_{\nu} \frac{1}{\nu^l} = \sum_{\nu} \frac{1}{(\nu+\omega)^l}$ and terms with odd l do not contribute, according to Eq. (6.81). For the analytical sums without the coefficients over the 8 terms above one, therefore, arrives at:

$$\begin{aligned}
(1): &\ -\delta_{\omega,0}\frac{\beta}{4} \\
(2): &\ +\frac{1-\delta_{\omega,0}}{\omega}\frac{\beta}{4} \\
(3): &\ -\frac{1-\delta_{\omega,0}}{\omega}\frac{\beta}{4} \\
(4),(6): &\ \delta_{\omega,0}\frac{\beta^3}{48} + \frac{1-\delta_{\omega,0}}{\omega^2}\frac{\beta}{4} \\
(5): &\ \delta_{\omega,0}\frac{\beta^3}{48} - 2\frac{1-\delta_{\omega,0}}{\omega^2}\frac{\beta}{4} \\
(7): &\ +2\frac{1-\delta_{\omega,0}}{\omega^3}\frac{\beta}{4} \\
(8): &\ -2\frac{1-\delta_{\omega,0}}{\omega^3}\frac{\beta}{4}
\end{aligned}$$

Next, we sort by orders of $1/\omega^l$ and evaluate all coefficient combinations for the local and non-local

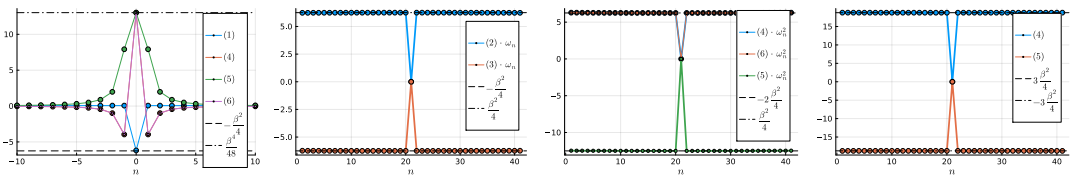

Figure 6.3: Tails for χ^{ω}_0 coefficients as a function of the bosonic Matsubara index, according to table 6.31 at $\beta = 5$. The sums are carried out numerically without the use of the improved sum technique and are shown to converge against the limits computed in this section.

cases. This will result in the corresponding coefficients for the expansion in $1/\omega$ of the bare susceptibility. We also simplify using $c_{1,\mathbf{k}} \to 1$ and $\forall f_{\mathbf{k}} : \int f_{\mathbf{k}+\mathbf{q}} \mathrm{d}\mathbf{k} = \int f_{\mathbf{k}} \mathrm{d}\mathbf{k}$.

$$\begin{aligned}
\chi^{\omega}_{0,\mathbf{q}} = & -\beta\left[\delta_{\omega,0}\left(-\frac{\beta}{4}\int_{\mathbf{k}\in\mathrm{BZ}} 1 + \frac{\beta^3}{48}\int_{\mathbf{k}\in\mathrm{BZ}} (c_{3,\mathbf{k}+\mathbf{q}} + c_{3,\mathbf{k}} + c_{2,\mathbf{k}} c_{2,\mathbf{k}+\mathbf{q}})\right)\right. \\
& \left. + \frac{1}{i\omega_m}\frac{\beta}{4}\left(\int_{\mathbf{k}\in\mathrm{BZ}} (c_{2,\mathbf{k}+\mathbf{q}} - c_{2,\mathbf{k}})\right)\right]
\end{aligned} \tag{6.32}$$

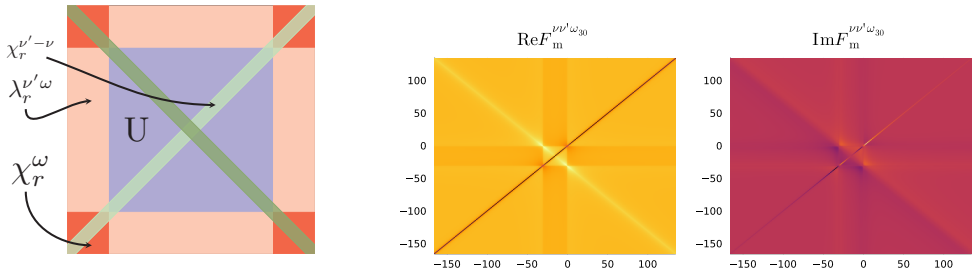

(a) Asymptotic contributions to the full vertex $F_r^{\nu\nu'\omega}$. The physical susceptibility χ_r^{ω} counteracts the double counting from both $\lambda_r^{\nu\omega}$ and $\lambda_r^{\nu'\omega}$. The illustration shows a schematic view $F_r^{\nu\nu'\omega}$ of for a fixed ω_m as a function of ν and ν'. The blue region is the constant (in ω_m) background consisting of $\pm U \pm U^2\chi_r$.

(b) Example of full vertex $F_{\mathrm{m}}^{\nu\nu'\omega}$ at ω_{30} with a shifted (by −15) fermionic grid. The axis labels show the indices. The size of the central features is dependent on the temperature. Here, $\beta = 20$ on a 2D simple cubic lattice around half-filling was used to generate the full vertex.

Figure 6.4: Asymptotic Structure of the full vertex

$$
\begin{aligned}
&+\frac{1}{(i\omega_m)^2}\frac{\beta}{4}\left(\int_{\mathbf{k}\epsilon\mathrm{BZ}}\left(c_{3,\mathbf{k}+\mathbf{q}}+c_{3,\mathbf{k}}-2c_{2,\mathbf{k}}c_{2,\mathbf{k}+\mathbf{q}}\right)\right)\\
&+\frac{1}{(i\omega_m)^3}\frac{\beta}{2}\left(\int_{\mathbf{k}\epsilon\mathrm{BZ}}\left(c_{2,\mathbf{k}}c_{3,\mathbf{k}+\mathbf{q}}-c_{2,\mathbf{k}+\mathbf{q}}c_{3,\mathbf{k}}\right)\right)+\mathcal{O}\left(\frac{1}{\omega^4}\right)\Bigg]\\
&= \quad \delta_{\omega,0}\left(\frac{\beta^2}{4}-\frac{\beta^4}{48}\int_{\mathbf{k}\epsilon\mathrm{BZ}}\left(2c_{3,\mathbf{k}}+c_{2,\mathbf{k}}c_{2,\mathbf{k}+\mathbf{q}}\right)\right)\\
&-\frac{\beta^2}{2(i\omega_m)^2}\left(\int_{\mathbf{k}\epsilon\mathrm{BZ}}\left(c_{3,\mathbf{k}}-c_{2,\mathbf{k}}c_{2,\mathbf{k}+\mathbf{q}}\right)\right)+\mathcal{O}\left(\frac{1}{\omega^4}\right)\\
&= \quad \delta_{\omega,0}\left(\frac{\beta^2}{4}-\frac{\beta^4}{48}(2\tilde{c}_3+\tilde{c}_{2,\mathbf{q}})\right)-\frac{\beta^2}{2(i\omega_m)^2}\left(\tilde{c}_3-\tilde{c}_{2,\mathbf{q}}\right)+\mathcal{O}\left(\frac{1}{\omega^4}\right)
\end{aligned}
\tag{6.33}
$$

Where we have defined the tail coefficients for $\chi^{\omega}_{0,\mathbf{q}}$ (in terms of the coefficients of the Green's function):

$$
\tilde{c}_1 = \int_{\mathbf{k}\epsilon\mathrm{BZ}} c_{2,\mathbf{k}} = \begin{cases}\left(\frac{Un}{2}-\mu\right) & \text{local}\\ \int\left(\frac{Un}{2}-\mu+\epsilon_{\mathbf{k}}\right)\mathrm{d}\mathbf{k} & \text{non-local}\end{cases} \tag{6.34}
$$

$$
\tilde{c}_{2,\mathbf{q}} = \int_{\mathbf{k}\epsilon\mathrm{BZ}} c_{2,\mathbf{k}}c_{2,\mathbf{k}+\mathbf{q}} = \begin{cases}\left(\frac{Un}{2}-\mu\right)^2 & \text{local}\\ \int\left(\epsilon_{\mathbf{k}}-\mu+\frac{Un}{2}\right)\left(\epsilon_{\mathbf{k}+\mathbf{q}}-\mu+\frac{Un}{2}\right)\mathrm{d}\mathbf{k} & \text{non-local}\end{cases} \tag{6.35}
$$

$$
\tilde{c}_3 = \int_{\mathbf{k}\epsilon\mathrm{BZ}} c_{3,\mathbf{k}} = \begin{cases}\left(\frac{Un}{2}-\mu\right)^2+U^2\frac{n}{2}\left(1-\frac{n}{2}\right)+\sum_l V_l^2 & \text{local}\\ \int\left(\epsilon_{\mathbf{k}}-\mu+\frac{Un}{2}\right)^2+U^2\frac{n}{2}\left(1-\frac{n}{2}\right)\mathrm{d}\mathbf{k} & \text{non-local}\end{cases} \tag{6.36}
$$

The derivation here was presented for the particle-hole channel. For the particle-particle channel, the formulas are obtained by a formal substitution of $\nu+\omega \to \omega-\nu$ and $\mathbf{q}+\mathbf{k} \to \mathbf{q}-\mathbf{k}$.

6.2.2 Full Vertex

For the remaining quantities, we will use the known asymptotic contributions to the local full vertex $F^{\nu\nu'\omega}$ [256]. We restrict the discussion to the particle-hole channel for this section. The full vertex asymptotic behavior is given by

$$
F^{\nu\nu'\omega}_{\mathrm{d,asym}} = U+\frac{U^2}{2}\chi_{\mathrm{d}}^{\nu'-\nu}+\frac{3U^2}{2}\chi_{\mathrm{m}}^{\nu'-\nu}-U^2\chi_{\mathrm{pp}}^{\nu+\nu'+\omega}+U\lambda_{\mathrm{d}}^{\nu\omega}+U\lambda_{\mathrm{d}}^{\nu'\omega}+U^2\chi_{\mathrm{d}}^{\omega} \tag{6.37}
$$

$$
F^{\nu\nu'\omega}_{\mathrm{m,asym}} = -U+\frac{U^2}{2}\chi_{\mathrm{d}}^{\nu'-\nu}-\frac{U^2}{2}\chi_{\mathrm{m}}^{\nu'-\nu}+U^2\chi_{\mathrm{pp}}^{\nu+\nu'+\omega}+U\lambda_{\mathrm{m}}^{\nu\omega}+U\lambda_{\mathrm{m}}^{\nu'\omega}+U^2\chi_{\mathrm{m}}^{\omega} \tag{6.38}
$$

Fig. 6.4a gives a schematic overview of the asymptotic contributions to the local full vertex $F_r^{\nu\nu'\omega}$. Here, the green regions correspond to the physical susceptibilities ($\chi^{\omega}_{\mathrm{d/m/pp}}$), the orange areas to the $\lambda_r^{\nu\omega}$ and the dark orange regions are the overlap of $\lambda_r^{\nu\omega}$ and $\lambda_r^{\nu'\omega}$. Algebraically, $\lambda_r^{\nu\omega}$ and $\lambda_r^{\nu'\omega}$ both contain ν/ν' independent contributions from the susceptibilities χ_r^{ω}, that are double counted and must be subtracted accordingly. The blue region is the constant $\pm U$ and $U^2\chi^{\omega}$ background. A vertex

obtained from DMFT will have a significant low-energy frequency dependence, which is not captured by the asymptotic contributions.
The contributions for the irreducible vertex $\Gamma^{\nu\nu'\omega}$ are given by:

$$\Gamma^{\nu\nu'\omega}_{\mathrm{d,asym}} = U + \frac{U^2}{2}\chi_{\mathrm{d}}^{\nu'-\nu} + \frac{3U^2}{2}\chi_{\mathrm{m}}^{\nu'-\nu} - U^2\chi_{\mathrm{pp}}^{\nu+\nu'+\omega} \tag{6.39}$$

$$\Gamma^{\nu\nu'\omega}_{\mathrm{m,asym}} = -U + \frac{U^2}{2}\chi_{\mathrm{d}}^{\nu'-\nu} - \frac{U^2}{2}\chi_{\mathrm{m}}^{\nu'-\nu} + U^2\chi_{\mathrm{pp}}^{\nu+\nu'+\omega} \tag{6.40}$$

The derivation of the asymptotic behavior is left to the literature [207, 131, 290, 256]. However, we will make use of the location of the intersection of the susceptibilities, given by the green bars in the illustration Fig. 6.4a. For this, we consider the possible scattering processes at a bare vertex U, which are given by where the susceptibilities (which decay as $1/\omega^2$) intersect when $\nu = \nu'$ and $\nu + \nu' + \omega = 0$. This is the case at $\nu = -\omega/2$ (see also [256] for a discussion of this shift). We, therefore, employ a sampling scheme that centers around this feature. In Sec. 6.4, we discuss details in conjunction with symmetry reductions.

6.2.3 Triangular Vertices

Here, we derive the asymptotic behavior of the triangular vertices. The calculations for the improved sums of the lDΓA quantities are a verbatim copy of unpublished notes from Georg Rohringer.
We will discuss two different derivations of the asymptotic behavior: (i) an algebraic version, using Ward identities and the decay of diagram classes, (ii) a Feynman diagrammatic derivation.

Algebraic Derivation: We start with the local (DMFT) case, at the Ward identity:

$$\sum_{\nu'}\left(i\omega_m + \Delta^{\nu'} - \Delta^{\omega+\nu'}\right)\chi^{\nu\nu'\omega}_{\mathrm{d/m}} = G^{\omega+\nu} - G^{\nu} \tag{6.41}$$

$$\overset{\text{Eq. (I8.34)}}{\Leftrightarrow} -i\omega_m - \Delta^{\nu} + \Delta^{\omega+\nu} - i\omega_m\sum_{\nu'}G^{\nu'}G^{\omega+\nu'}F^{\nu\nu'\omega}_{\mathrm{d/m}} - \sum_{\nu'}\left(\Delta^{\nu'} - \Delta^{\omega+\nu'}\right)G^{\omega+\nu'}F^{\nu\nu'\omega}_{\mathrm{d/m}} = \left(G^{\omega+\nu} - G^{\nu}\right)\left(\chi_0^{\nu\omega}\right)^{-1} \tag{6.42}$$

$$\overset{\text{Eq. (I8.21)}}{\Leftrightarrow} -i\omega_m - \Delta^{\nu} + \Delta^{\omega+\nu} \mp i\omega_m\lambda^{\nu\omega}_{\mathrm{d/m}} - \sum_{\nu'}\left(\Delta^{\nu'} - \Delta^{\omega+\nu'}\right)G^{\omega+\nu'}F^{\nu\nu'\omega}_{\mathrm{d/m}} = i\nu_n + \mu - \Delta^{\nu} - \Sigma^{\nu} - i\nu_n - i\omega_m - \mu + \epsilon + \Sigma^{\omega+\nu}$$

$$\Leftrightarrow \mp i\omega_m\lambda^{\nu\omega}_{\mathrm{d/m},\mathbf{kq}} - \underbrace{\sum_{\nu'\mathbf{k}'}\left(\Delta^{\nu'} - \Delta^{\omega+\nu'}\right)G^{\omega+\nu'}F^{\nu\nu'\omega}_{\mathrm{d/m}}}_{\mathcal{O}(1/\omega)} = -\Sigma^{\nu} + \underbrace{\Sigma^{\omega+\nu}}_{\mathcal{O}(1/\omega)} \tag{6.43}$$

$$\Leftrightarrow \lambda^{\nu\omega}_{\mathrm{d/m}} = \pm\frac{\Sigma^{\nu} - \Sigma_{\mathrm{H}}}{i\omega_m} + \mathcal{O}\left(\frac{1}{i\omega_m}\right) \tag{6.44}$$

For the non-local case, we start with the local version of the Ward identity in Sec. 4.4.2.1.

$$\sum_{\nu'\mathbf{k}'}\left(i\omega_m + \epsilon_{\mathbf{k}} - \epsilon_{\mathbf{k}+\mathbf{q}}\right)\chi^{\nu\nu'\omega}_{\mathrm{d/m},\mathbf{kk'q}} = G^{\omega+\nu}_{\mathbf{q}+\mathbf{k}} - G^{\nu}_{\mathbf{k}} \tag{6.45}$$

$$\sum_{\nu'\mathbf{k}'}\left(i\omega_m + \epsilon_{\mathbf{k}} - \epsilon_{\mathbf{k}+\mathbf{q}}\right)\chi^{\nu\nu'\omega}_{\mathrm{d/m},\mathbf{kk'q}} = G^{\omega+\nu}_{\mathbf{q}+\mathbf{k}} - G^{\nu}_{\mathbf{k}} \tag{6.46}$$

$$\overset{\text{Eq. (I8.34)}}{\Leftrightarrow} -i\omega_m - \epsilon_{\mathbf{k}} + \epsilon_{\mathbf{k}+\mathbf{q}} - i\omega_m\sum_{\nu'\mathbf{k}'}G^{\nu'}_{\mathbf{k}'}G^{\omega+\nu'}_{\mathbf{q}+\mathbf{k}'}F^{\nu\nu'\omega}_{\mathrm{d/m},\mathbf{kk'q}} - \sum_{\nu'\mathbf{k}'}\left(\epsilon_{\mathbf{k}'} - \epsilon_{\mathbf{q}+\mathbf{k}'}\right)G^{\omega+\nu'}_{\mathbf{q}+\mathbf{k}'}F^{\nu\nu'\omega}_{\mathrm{d/m},\mathbf{kk'q}} = \left(G^{\omega+\nu}_{\mathbf{q}+\mathbf{k}} - G^{\nu}_{\mathbf{k}}\right)\left(\chi^{\nu\omega}_{0,\mathbf{q}}\right)^{-1} \tag{6.47}$$

$$\overset{\text{Eq. (I8.21)}}{\Leftrightarrow} -i\omega_m - \epsilon_{\mathbf{k}} + \epsilon_{\mathbf{k}+\mathbf{q}} \mp i\omega_m\lambda^{\nu\omega}_{\mathrm{d/m},\mathbf{kq}} - \sum_{\nu'\mathbf{k}'}\left(\epsilon_{\mathbf{k}'} - \epsilon_{\mathbf{q}+\mathbf{k}'}\right)G^{\omega+\nu'}_{\mathbf{q}+\mathbf{k}'}F^{\nu\nu'\omega}_{\mathrm{d/m},\mathbf{kk'q}} = i\nu_n + \mu - \epsilon_{\mathbf{k}} - \Sigma^{\nu}_{\mathbf{k}} - i\nu_n - i\omega_m - \mu + \epsilon_{\mathbf{q}+\mathbf{k}} + \Sigma^{\omega+\nu}_{\mathbf{q}+\mathbf{k}}$$

$$\Leftrightarrow \mp i\omega_m\lambda^{\nu\omega}_{\mathrm{d/m},\mathbf{kq}} - \underbrace{\sum_{\nu'\mathbf{k}'}\left(\epsilon_{\mathbf{k}'} - \epsilon_{\mathbf{q}+\mathbf{k}'}\right)G^{\omega+\nu'}_{\mathbf{q}+\mathbf{k}'}F^{\nu\nu'\omega}_{\mathrm{d/m},\mathbf{kk'q}}}_{\mathcal{O}(1/\omega)} = -\Sigma^{\nu}_{\mathbf{k}} + \underbrace{\Sigma^{\omega+\nu}_{\mathbf{q}+\mathbf{k}}}_{\Sigma_{\mathrm{H}}+\mathcal{O}(1/\omega)} \tag{6.48}$$

$$\Leftrightarrow \lambda^{\nu\omega}_{\mathrm{d/m},\mathbf{kq}} = \pm\frac{\Sigma^{\nu}_{\mathbf{k}} - \Sigma_{\mathrm{H}}}{i\omega_m} + \mathcal{O}\left(\frac{1}{\omega^2}\right) \tag{6.49}$$

With the Hartree part of the self-energy as usual $\Sigma_{\mathrm{H}} = \frac{Un}{2}$.
Notably, the bosonic frequency tail of the triangular vertex is independent of the bosonic momentum $\mathbf{q}$.

Alternative Derivation and $\boldsymbol{\lambda_0}$: The correction term in the lDΓA equation of motion $\lambda^{\nu\omega}_{0,\mathbf{q}}$ exhibits the same asymptotic behavior. Here, an alternative derivation is presented, relying on the fact that only the irreducible diagrams of the full vertex F do not decay in $1/\omega$:

$$F_r^{\nu\nu'\omega} = \Gamma_r^{\nu\nu'\omega} + \Phi_r^{\nu\nu'\omega} = \Gamma_r^{\nu\nu'\omega} + \mathcal{O}\left(\frac{1}{\omega}\right) \tag{6.50}$$

We furthermore use the partial fraction decomposition strategy from Sec. 6.2.1 to rewrite the bubble term

$$G^{\nu}_{\mathbf{k}} G^{\omega+\nu}_{\mathbf{q}+\mathbf{k}} = \frac{1}{i\omega_m}\left(G^{\nu}_{\mathbf{k}} - G^{\omega+\nu}_{\mathbf{q}+\mathbf{k}}\right) + \mathcal{O}\left(\frac{1}{\omega^2}\right) \tag{6.51}$$

This leads to the same result as before:

$$\lambda^{\nu\omega}_{\mathrm{d/m},\mathbf{kq}} = \pm \sum_{\nu'\mathbf{k}'} G^{\nu}_{\mathbf{k}} G^{\omega+\nu}_{\mathbf{q}+\mathbf{k}} F^{\nu\nu'\omega}_{\mathrm{d/m}} \tag{6.52}$$

$$\overset{\text{Eq. (6.51)}}{=} \frac{1}{i\omega_m}\left(G^{\nu}_{\mathbf{k}} - G^{\omega+\nu}_{\mathbf{q}+\mathbf{k}}\right) F^{\nu\nu'\omega}_{\mathrm{d/m}} + \mathcal{O}\left(\frac{1}{\omega^2}\right) \tag{6.53}$$

$$\overset{\text{Eq. (6.50)}}{=} \frac{1}{i\omega_m}\left(G^{\nu}_{\mathbf{k}} - G^{\omega+\nu}_{\mathbf{q}+\mathbf{k}}\right) \Gamma^{\nu\nu'\omega}_{\mathrm{d/m}} + \mathcal{O}\left(\frac{1}{\omega^2}\right) \tag{6.54}$$

$$\overset{\text{Eq. (4.33)}}{=} \pm\left(\Sigma^{\nu}_{\mathbf{k}} - \Sigma^{\omega+\nu}_{\mathbf{q}+\mathbf{k}}\right) + \mathcal{O}\left(\frac{1}{\omega^2}\right) \tag{6.55}$$

$$= \pm\frac{\Sigma^{\nu}_{\mathbf{k}} - \Sigma_{\mathrm{H}}}{i\omega_m} + \mathcal{O}\left(\frac{1}{\omega^2}\right) \tag{6.56}$$

The high-frequency tail of the local correction term for the lDΓA equation of motion $\lambda^{\nu\omega}_{0,\uparrow\downarrow,\mathbf{q}}$ can be obtained directly from the definition in Eq. (I8.22).

Summary The λ asymptotic in $1/\omega^n$ is not explicitly used in the improved summation formulas of lDΓA but is nevertheless important for the understanding of the asymptotic behavior in this method. Specifically for the understanding of the self-energy tail from the restoration of the Pauli principle, we require the $\gamma^{\nu\omega}_{r,\mathbf{q}}$ asymptotics.

Important 6.2.3.1 ($\boldsymbol{\lambda}$ and $\boldsymbol{\gamma}$ High Frequency Tail)

$$\lambda^{\nu\omega}_{\mathrm{d/m}} = \pm\frac{\Sigma^{\nu} - \Sigma_H}{i\omega_m} + \mathcal{O}\left(\frac{1}{\omega^2}\right) \tag{6.57}$$

$$\lambda^{\nu\omega}_{\mathrm{d/m},\mathbf{kq}} = \pm\frac{\Sigma^{\nu}_{\mathbf{k}} - \Sigma_H}{i\omega_m} + \mathcal{O}\left(\frac{1}{\omega^2}\right) \tag{6.58}$$

$$\lambda^{\nu\omega}_{0,\uparrow\downarrow,\mathbf{q}} = \mathcal{O}\left(\frac{1}{\omega^2}\right) \tag{6.59}$$

For the triangular vertex without susceptibility contributions, we have the static limit of 1*:*

$$\forall \mathbf{q}, \omega : \lim_{\nu\to\pm\infty} \gamma^{\nu\omega}_{r,\mathbf{q}} = 1 \tag{6.60}$$

$$\forall \mathbf{q}, \nu : \lim_{\omega\to\pm\infty} \gamma^{\nu\omega}_{r,\mathbf{q}} = 1 \tag{6.61}$$

6.2.4 Self-Energy

Single Particle Case

The high-frequency tail of the self-energy can be immediately obtained from the tail of the Green's function.

$$G^{\nu}_{\mathbf{k}} = \left[\nu + \mu + f^{\nu}_{\mathbf{k}}\right]^{-1} = \frac{1}{\nu}\frac{1}{1 + \frac{\mu - f^{\nu}_{\mathbf{k}}}{\nu}} \tag{6.62}$$

Where we have defined $f^{\nu}_{\mathbf{k}}$ as before, absorbing the difference between local and non-local versions. Δ^{ν} is the hybridization function, here expressed in terms of l bath parameters,

$$f^{\nu}_{\mathbf{k}} = \Sigma^{\nu}_{\mathbf{k}} + \Delta^{\nu} \tag{6.63}$$

$$= \mathcal{O}\left(\frac{1}{\nu^2}\right) + \Sigma_{\mathrm{H}} + \frac{1}{\nu}U^2\frac{n}{2}\left(1-\frac{n}{2}\right) + \begin{cases} \frac{1}{\nu}\sum_l V_l^2 & \text{local} \\ -\epsilon_{\mathbf{k}} & \text{non-local} \end{cases}$$

From this, we follow for the self-energy tail:

$$\Sigma^{\nu}_{\mathbf{k}} = \Sigma_{\mathrm{H}} + \frac{1}{\nu}U^2\frac{n}{2}\left(1-\frac{n}{2}\right) + \mathcal{O}\left(\frac{1}{\nu^2}\right) \tag{6.64}$$

Two-Particle Case

We can also obtain the (non-local) self-energy from lDΓA through the SDE. Here, we obtain the asymptotic behavior by considering the full vertex F.

$$\Sigma^{\nu}_{\mathbf{k}} = \Sigma_{\mathrm{H}} - U\sum_{\nu'\omega\mathbf{k}'\mathbf{q}} G^{\nu'}_{\mathbf{k}'}G^{\nu'+\omega}_{\mathbf{k}'+\mathbf{q}}F^{\nu\nu'\omega}_{\uparrow\downarrow,\mathbf{k}\mathbf{k}'\mathbf{q}}G^{\nu+\omega}_{\mathbf{k}+\mathbf{q}} \tag{6.65}$$

We start with the following observations: (i) $G^{\nu+\omega}_{\mathbf{k}+\mathbf{q}} = \frac{1}{i\nu_n} + \mathcal{O}\left(\frac{1}{\nu^2}\right)$, following the proof for Eq. (6.81). (ii) We only need to consider constant (ν-independent) contributions of the full vertex for the leading orders of the high-frequency expansion of the self-energy because the Green's functions suppress all contributions by at least $\mathcal{O}\left(\frac{1}{\nu}\right)$.
In order to obtain the constant contributions for (ii), we need to consider the Bethe-Salpeter equation in the ↑↓ channel, which implies the substitution of $F^{\nu\nu'\omega}_{\uparrow\uparrow}$ with a full vertex of different spin and frequency arguments (the BSE mixes these, see Eq. (2.256) or [205, Figure B.1]). The lowest order contribution is:

$F^{\nu\nu'\omega}_{\uparrow\downarrow} =$ 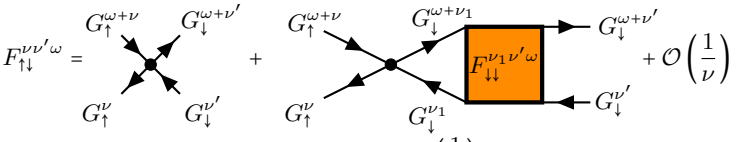 $+ \mathcal{O}\left(\frac{1}{\nu}\right)$ (6.66)

$$= U + U\sum_{\nu_1} G^{\nu_1}_{\mathbf{k}_1}G^{\omega+\nu_1}_{\mathbf{q}+\mathbf{k}_1}F^{\nu_1\nu'\omega}_{\uparrow\uparrow,\mathbf{k}_1\mathbf{k}'\mathbf{q}} + \mathcal{O}\left(\frac{1}{\nu}\right) \tag{6.67}$$

We used the SU(2) symmetry and set $F^{\nu_1\nu'\omega}_{\downarrow\downarrow} = F^{\nu_1\nu'\omega}_{\uparrow\uparrow}$ in the above equation. With the first-order contribution in hand, we find the asymptotic behavior of the self-energy:

$$\Sigma^{\nu}_{\mathbf{k}} = \Sigma_{\mathrm{H}} - U\sum_{\nu'\omega\mathbf{k}'\mathbf{q}} G^{\nu'}_{\mathbf{k}'}G^{\omega+\nu'}_{\mathbf{q}+\mathbf{k}'}\frac{1}{i\nu_n}\left(U + U\sum_{\nu_1\mathbf{k}_1} G^{\nu_1}_{\mathbf{k}_1}G^{\omega+\nu_1}_{\mathbf{q}+\mathbf{k}_1}F^{\nu_1\nu'\omega}_{\uparrow\uparrow,\mathbf{k}_1\mathbf{k}'\mathbf{q}}\right) + \mathcal{O}\left(\frac{1}{\nu^2}\right) \tag{6.68}$$

$$\overset{\text{Eq. (2.233)}}{=} \Sigma_{\mathrm{H}} + \frac{U^2}{i\nu_n}\sum_{\nu_1\nu'\omega\mathbf{k}_1\mathbf{k}'\mathbf{q}} \chi^{\nu_1\nu'\omega}_{\uparrow\uparrow,\mathbf{k}_1\mathbf{k}'\mathbf{q}} + \mathcal{O}\left(\frac{1}{\nu^2}\right) \tag{6.69}$$

$$\overset{\text{Eq. (4.53)}}{=} \Sigma_{\mathrm{H}} + \frac{U^2}{i\nu_n}\frac{n}{2}\left(1-\frac{n}{2}\right) + \mathcal{O}\left(\frac{1}{\nu^2}\right) \tag{6.70}$$

This proves the correct asymptotic behavior of the self-energy when obtained from the SDE for the general non-local self-energy. However, lDΓA leads to an approximate full vertex F that depends only on a single momentum index $\mathbf{q}$. The term $F^{\nu(\nu+\omega)(\nu'-\nu)}$ which leads to the factor of 3 in front of the magnetic full vertex in Eq. (5.56) introduces an imbalance between the local and non-local ↑↓ vertices that in turn leads to a violation of the asymptotic behavior of the self-energy. Moreover, we typically do not compute the full vertex, only the susceptibilities and triangular vertices. On the level of these quantities, we can construct an explicit expression for the condition required to fulfill the correct tail asymptotic.

$$\Sigma^{\nu}_{\mathbf{k}} = \Sigma_{\mathrm{H}} - \frac{U}{2}\sum_{\omega\mathbf{q}}\left(-3\gamma^{\nu\omega}_{\mathrm{m},\mathbf{q}}(1+U\chi^{\lambda_{\mathrm{m}},\omega}_{\mathrm{m},\mathbf{q}}) + 2 + \gamma^{\nu\omega}_{\mathrm{d},\mathbf{q}}(1-U\chi^{\lambda_{\mathrm{d}},\omega}_{\mathrm{d},\mathbf{q}}) - \sum_{\nu'}\chi^{\nu'\omega}_{0,\mathbf{q}}F^{\nu\nu'\omega}_{\uparrow\downarrow,\mathrm{DMFT}}\right)G^{\omega+\nu}_{\mathbf{q}+\mathbf{k}} \tag{6.71}$$

$$\overset{\nu\to\infty}{\sim} \Sigma_{\mathrm{H}} - \frac{U}{2}\sum_{\omega\mathbf{q}}\Big(\left(-3\gamma^{\nu\omega}_{\mathrm{m},\mathbf{q}} + 2 + \gamma^{\nu\omega}_{\mathrm{d},\mathbf{q}}\right)G^{\omega+\nu}_{\mathbf{q}+\mathbf{k}}$$
$$-\left(2U\chi^{\lambda_{\mathrm{m}},\omega}_{\mathrm{m},\mathbf{q}} + U\chi^{\lambda_{\mathrm{m}},\omega}_{\mathrm{m},\mathbf{q}} + U\chi^{\lambda_{\mathrm{d}},\omega}_{\mathrm{d},\mathbf{q}} + Un\left(1-\frac{n}{2}\right)\right)\frac{1}{i\nu_n}\Big) + \mathcal{O}\left(\frac{1}{\nu^2}\right) \tag{6.72}$$

$$\overset{\nu\to\infty}{\sim} \Sigma_{\mathrm{H}} - \frac{U}{2}\left(2U\sum_{\omega\mathbf{q}}\left(\delta_{\mathbf{q}0}\chi^{\omega}_{\mathrm{m,loc}} - \chi^{\lambda_{\mathrm{m}},\omega}_{\mathrm{m},\mathbf{q}}\right) - Un\left(1-\frac{n}{2}\right)\right)\frac{1}{i\nu_n} + \mathcal{O}\left(\frac{1}{\nu^2}\right) \tag{6.73}$$

The last line follows from the fact, that the DMFT equation of motion exhibits the correct $\frac{1}{\nu}$ behavior and therefore

$$\lim_{n\to\infty} i\nu_n\sum_{\omega\mathbf{q}}\left(2 - 3\gamma^{\nu\omega}_{\mathrm{m},\mathbf{q}} + \gamma^{\nu\omega}_{\mathrm{d},\mathbf{q}}\right)G^{\omega+\nu}_{\mathbf{q}+\mathbf{k}} = \frac{Un}{2}\left(1-\frac{n}{2}\right) - 2U\sum_{\omega}\chi^{\omega}_{\mathrm{m,loc}} \tag{6.74}$$

This leaves the following error term to be considered for the correct tail behavior:

$$\tilde{\Sigma}^{\nu}_{\mathrm{tc}} = -\frac{U^2}{i\nu_n}\left(\sum_{\omega\mathbf{q}} \chi^{\lambda_\mathrm{m},\omega}_{\mathrm{m},\mathbf{q}} - \sum_{\omega} \chi^{\omega}_{\mathrm{m,loc}}\right) \tag{6.75}$$

Instead of using the exact limits, we typically use the difference between local and non-local summed susceptibilities instead, to also incorporate error compensations (because both susceptibilities have been obtained over the same truncated Matsubara frequency space):

$$\Sigma^{\nu}_{\mathrm{tc}} = -\frac{U^2}{i\nu_n}\left[\sum_{\omega\mathbf{q}} \chi^{\lambda_\mathrm{m},\omega}_{\mathrm{m},\mathbf{q}} - \sum_{\omega} \chi^{\omega}_{\mathrm{m,loc}} + \frac{1}{3}\sum_{\omega\mathbf{q}} \chi^{\lambda_\mathrm{d},\omega}_{\mathrm{d},\mathbf{q}} - \frac{1}{3}\sum_{\omega} \chi^{\omega}_{\mathrm{d,loc}}\right] \tag{6.76}$$

The second term is derived by assuming the same decomposition into χ^{ω}_{r} and $\gamma^{\nu\omega}_{r}$ in the local correction term as in the non-local Another approach of forcing correct high-frequency behavior is to modify the SDE directly. Here, we argue that $\lambda^{\nu\omega}_{\mathrm{m},\mathbf{q}}$ still contains the local, not λ-corrected magnetic susceptibility $\chi^{\omega}_{\mathrm{m}}$ in the $1/(\nu+\omega)$ tail. This can be fixed by introducing the correct asymptotic behavior as follows:

$$\Rightarrow \tilde{\gamma}^{\nu\omega}_{\mathrm{m},\mathbf{q}} = \gamma^{\nu\omega}_{\mathrm{m},\mathbf{q}} \frac{1 + U\chi^{\omega}_{\mathrm{m,loc}}}{1 + U\chi^{\lambda_\mathrm{m},\omega}_{\mathrm{m},\mathbf{q}}} \tag{6.77}$$

For the equation of motion, we then use:

$$\Sigma^{\lambda,\nu}_{\mathbf{k}} - \Sigma_{\mathrm{H}} = -U\sum_{\omega\mathbf{q}}\left(2\lambda^{\lambda,\nu\omega}_{\uparrow\downarrow,\mathbf{q}} - \lambda^{\nu\omega}_{\uparrow\downarrow,\mathbf{q}}\right) G^{\omega+\nu}_{\mathbf{q}+\mathbf{k}} \tag{6.78}$$

$$= -U\sum_{\omega\mathbf{q}}\left(\frac{1}{2}\left(\lambda^{\lambda,\nu\omega}_{\mathrm{d},\mathbf{q}} + \lambda^{\lambda,\nu\omega}_{\mathrm{m},\mathbf{q}}\right) + \lambda^{\lambda,\nu\omega}_{\mathrm{m},\mathbf{q}} - \lambda^{\nu\omega}_{\uparrow\downarrow,\mathbf{q}}\right) G^{\omega+\nu}_{\mathbf{q}+\mathbf{k}} \tag{6.79}$$

$$= -U\sum_{\omega\mathbf{q}}\Big(\frac{1}{2}\gamma^{\nu\omega}_{\mathrm{d},\mathbf{q}}\left(1 - U\chi^{\lambda_\mathrm{d},\omega}_{\mathrm{d},\mathbf{q}}\right) - \frac{1}{2}\gamma^{\nu\omega}_{\mathrm{m},\mathbf{q}}\left(1 + U\chi^{\lambda_\mathrm{m},\omega}_{\mathrm{m},\mathbf{q}}\right)$$
$$- \tilde{\gamma}^{\nu\omega}_{\mathrm{m},\mathbf{q}}\left(1 + U\chi^{\lambda_\mathrm{m},\omega}_{\mathrm{m},\mathbf{q}}\right)\Big) G^{\omega+\nu}_{\mathbf{q}+\mathbf{k}} + U\sum_{\omega\mathbf{q}} \lambda^{\nu\omega}_{\uparrow\downarrow,\mathbf{q}} \tag{6.80}$$

In Sec. 6.3.4, we discuss the tail correction schemes for improved summation and the correct asymptotic behavior in more detail, including an analysis of the validity of this approach, where the transverse spin fluctuations remain local. Fig. 6.5 shows the tail behavior of the individual parts of the non-local self-energy. The square brackets indicate which summand of the equation of motion is used, e.g. $\Sigma[\chi_\mathrm{m}] = \frac{U}{2}\sum_{\omega\mathbf{q}}\left(-3\gamma^{\nu\omega}_{\mathrm{m}}\chi^{\lambda_\mathrm{m},\omega}_{\mathrm{m},\mathbf{q}}\right) G^{\omega+\nu}_{\mathbf{q}+\mathbf{k}}$ and $\Sigma[\gamma_\mathrm{d}] = \frac{U}{2}\sum_{\omega\mathbf{q}}\left(\gamma^{\nu\omega}_{\mathrm{d}}\right) G^{\omega+\nu}_{\mathbf{q}+\mathbf{k}}$.

Consistency Checks We occasionally replace the local $F_{\uparrow\downarrow}$ vertex with F_m for the local counter term in the equation of motion. This can be done since $F_{\uparrow\uparrow}$ does not contribute to the asymptotic, as demonstrated in the following. This heuristically tends to improve numerical calculations due to

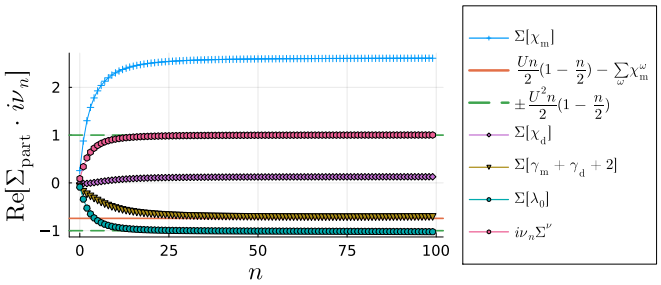

Figure 6.5: Example for the asymptotic behavior of different parts of the non-local self-energy.

better-conditioned summations.
The following calculations further verify that we did consider all contributing diagrams by checking that the sum rule for the two-particle Green's function is fulfilled.

6.3 Improved Matsubara Sums

In this section, we will derive improved summation formulas for all quantities in the DΓA variants. We will use the asymptotic behavior of the quantities derived in Sec. 6.2 to improve the numerical value of computed limits. The central idea was already discussed in the introduction of Sec. 6.1 but is now extended to summations over two indices, and explicit formulas will be computed. Many of the examples here, including further documentation, can be found in 4 Jupyter notebooks. `Sigma_Tail` and `Thermodynamics` of the `LadderDGA.jl` project; `BSE_Asym_Demo` and `Bubble_Test` of the `BSE_Asym`

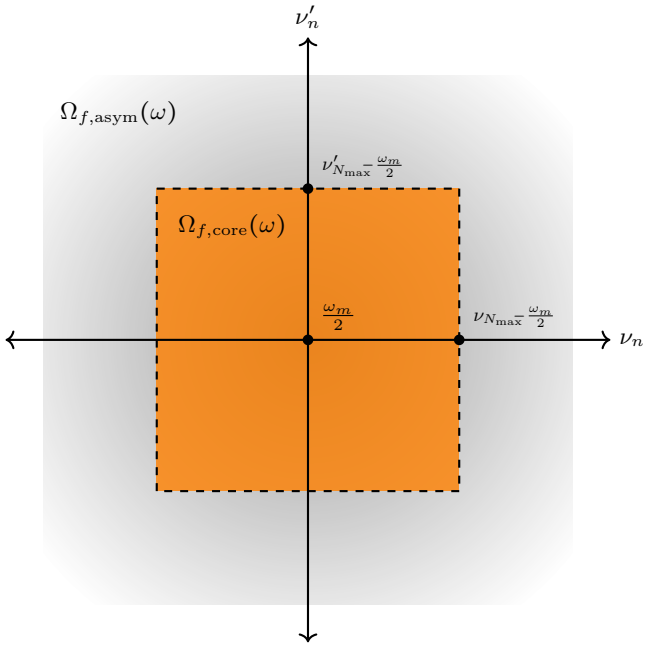

Figure 6.6: Illustration for core and asymptotic regions. The orange region has full numerical data available. The gray region is known from asymptotic contributions, but no further data is available. Note that the center of this region may not be at 0, depending on the quantity and chosen sampling of the Matsubara space.

project (see also Sec. 6.8.5 and Sec. 6.8.6).

Fig. 6.6 illustrates how summation regions are set up, in this case for a 3 frequency object like the full vertex (which has asymptotic contributions shown in Fig. 6.4a). Numerical data is available in the orange core region, while leading-order asymptotic contributions are assumed to be sufficient for the gray region.
The following calculations involve quantities with 4 different superscripts:

core: f^{core} denotes a quantity that is obtained by plain summation over the numerically available points in a region; The frequency indices in this region are also written with this subscript. Furthermore, we give an f or b, indicating fermionic or bosonic summations, e.g. $\Omega_{f,\mathrm{core}}(\omega)$ for fermionic summation over a core region, which may be shifted (Sec. 6.4.1).

asym: f^{asympt} is the analytically obtained asymptotic contribution. Summations of asymptotic contributions will sometimes be split into f^{shell} asymptotic contributions outside the core region) and f^{rem} for **rem**aining asymptotic contributions from inside the core region.

impr: f^{impr} indicates the improved expression that contains numerical and analytic tail information.

We again indicate terms that can be obtained with higher accuracy in **k**-space (since they do not depend on the **k**-space sampling of the BSE and related convolutions, see Sec. 6.4.2), by using the integral symbol.

6.3.1 Bare Susceptibility

We start with the improved summation formula for the bubble term, using the asymptotic contributions obtained in Sec. 6.2.1. Here, we use general sum formula of the form

$$\begin{aligned}
\sum_\nu \left(F^{\nu+\omega}_{\mathbf{k}} - \sum_{n=-\infty}^{\infty} \frac{c_{1,\mathbf{k}}}{(i\nu_n + i\omega_m)} \right) &= \frac{1}{\beta} \sum_{n=-\infty}^{\infty} \sum_{l=2}^{\infty} \frac{c_{l,\mathbf{k}}}{(i\nu_n + i\omega_m)^l} \\
&= \frac{1}{\beta} \sum_{l=2}^{\infty} c_{l,\mathbf{k}} \sum_{n=-\infty}^{\infty} \left(i\frac{(2n+1)\pi}{\beta} + i\frac{(2m)\pi}{\beta} \right)^{-l} \\
&= \frac{1}{\beta} \sum_{l=2}^{\infty} c_{l,\mathbf{k}} \left(\frac{i\pi}{\beta} \right)^{-l} \sum_{n=-\infty}^{\infty} \left(\frac{1}{2n+1+2m} \right)^{l} \\
&= \frac{\pi^2}{4} \frac{-\beta^2}{\pi^2 \beta} c_{2,\mathbf{k}} \sin^{-2}(x_m) \\
&\quad + \frac{\pi^3}{8} \frac{-i\beta^3}{\pi^3 \beta} c_{3,\mathbf{k}} \cdot \frac{\cos(x_m)}{\sin^3(x_m)}
\end{aligned}$$

$$+\frac{\pi^4}{48}\frac{\beta^4}{\pi^4\beta}c_{4,\mathbf{k}}\cdot\left(\sin^{-4}(x_m)+\frac{\cos^2(x_m)}{\sin^4(x_m)}\right)$$
$$+\dots$$

with $x_m=\frac{\pi(2m+1)}{2}$. This can further be simplified, using $\forall m\in\mathbb{Z}:\sin(x_m)=1\wedge\cos(x_m)=0$

$$=-\frac{\beta}{4}c_{2,\mathbf{k}}+\frac{\beta^3}{48}c_{4,\mathbf{k}}-\frac{\beta^5}{480}c_{6,\mathbf{k}}+\dots \tag{6.81}$$

Note, that the limit does not depend on $i\omega_m$.
The coefficients for the local (χ_0^ω) and non-local ($\chi_{0,\mathbf{q}}^\omega$) bare bubble improved sum terms are readily obtained from the asymptotic behavior derived above in Sec. 6.2.1. This leads to the following improved sum:

$$\chi_{0,\mathbf{q}}^{\mathrm{impr},\omega}=-\int_{\mathbf{k}\in\mathrm{BZ}}\sum_\nu G_{\mathbf{k}}^\nu G_{\mathbf{q}+\mathbf{k}}^{\omega+\nu}=-\int_{\mathbf{k}\in\mathrm{BZ}}\left(\sum_{\nu\in\Omega_{\mathrm{f,core}}(m)}G_{\mathbf{k}}^\nu G_{\mathbf{q}+\mathbf{k}}^{\omega+\nu}+\sum_{\nu\in\Omega_{\mathrm{f,asym}}(m)}G_{\mathbf{k}}^\nu G_{\mathbf{q}+\mathbf{k}}^{\omega+\nu}\right) \tag{6.82}$$

$$=\chi_{0,\mathbf{q}}^{\mathrm{core},\omega}-\left(\int_{\mathbf{k}\in\mathrm{BZ}}\sum_{j,l=1}^{3}\sum_\nu\frac{c_{j,\mathbf{k}}c_{l,\mathbf{k}+\mathbf{q}}}{\nu^j(\nu+\omega)^l}-\int_{\mathbf{k}\in\mathrm{BZ}}\sum_{j,l=1}^{3}\sum_{\nu\in\Omega_{\mathrm{f,core}}(\omega)}\frac{c_{j,\mathbf{k}}c_{l,\mathbf{k}+\mathbf{q}}}{\nu^j(\nu+\omega)^l}\right)+\mathcal{O}\left(|\omega+\nu|^{-5}\right) \tag{6.83}$$

$$=\chi_{0,\mathbf{q}}^{\mathrm{core},\omega}+\chi_{0,\mathbf{q}}^{\mathrm{asym},\omega}-\chi_{0,\mathbf{q}}^{\mathrm{rem},\omega}+\mathcal{O}\left(|\omega+\nu|^{-5}\right) \tag{6.84}$$

with

$$\chi_{0,\mathbf{q}}^{\mathrm{asym},\omega}\overset{\text{Eq. (6.33)}}{=}-\delta_{\omega0}\left(\frac{-\beta}{4}+\tilde{c}_{2,\mathbf{q}}\frac{\beta^3}{48}+\tilde{c}_3\frac{\beta^3}{24}\right)-\beta\frac{1-\delta_{\omega0}}{2\omega^2}\left(\tilde{c}_3-\tilde{c}_{2,\mathbf{q}}\right) \tag{6.85}$$

$$\chi_{0,\mathbf{q}}^{\mathrm{core},\omega}=-\sum_{\nu\in\Omega_{\mathrm{f,core}}(\omega)}\sum_{\mathbf{k}}G_{\mathbf{k}}^\nu G_{\mathbf{q}+\mathbf{k}}^{\omega+\nu} \tag{6.86}$$

$$\chi_{0,\mathbf{q}}^{\mathrm{rem},\omega}=-\sum_{\nu\in\Omega_{\mathrm{f,core}}(\omega)}\sum_{j,l=1}^{3}\int_{\mathbf{k}\in\mathrm{BZ}}\frac{c_{j,\mathbf{k}}c_{l,\mathbf{k}+\mathbf{q}}}{\nu^j(\nu+\omega)^l} \tag{6.87}$$

$$\chi_{0,\mathbf{q}}^{\mathrm{shell},\omega}=\chi_{0,\mathbf{q}}^{\mathrm{asym},\omega}-\chi_{0,\mathbf{q}}^{\mathrm{rem},\omega} \tag{6.88}$$

The improved summation formula in Eq. (6.84) leads for the bare susceptibility to a correct tail up to 5th order. The necessary tail coefficients have been derived in Eq. (6.34) to Eq. (6.36). We again indicate **k**-space integrations that are independent of the sampling for the lDΓA quantities with an integral sign.
The implementation of this can be found in the $\chi_{0,\mathbf{q}}^\omega$ `constructor` of the lDΓA code (see Sec. 6.8.6) and also demonstrated in the example notebook for the asymptotic improvement code (see Sec. 6.8.6).

6.3.2 Triangular Vertex

Next, we derive the improved summation formula for the electron-boson vertex $\lambda_{\mathbf{q}}^{\nu\omega}$. The lDΓA method uses the Hedin vertex $\gamma_{\mathbf{q}}^{\nu\omega}$ instead, because it does not contain any susceptibilities and can therefore be treated on a DMFT level. However, it is sufficient to formulate improved summations for $\lambda_{\mathbf{q}}^{\nu\omega}$ and $\chi_{\mathbf{q}}^\omega$ and then use Eq. (I8.25) to obtain $\gamma_{\mathbf{q}}^{\nu\omega}$. For the following calculation, the upper sign corresponds to the charge, the lower to the magnetic channel.

$$\begin{aligned}
\lambda_{r,\mathbf{q}}^{\nu\omega}&=\pm\frac{\sum_{\nu'}\chi_{r,\mathbf{q}}^{\nu\nu'\omega}}{\chi_{0,\mathbf{q}}^{\nu\omega}}\mp1=\pm\frac{\sum_{\nu'}\left(\chi_{0,\mathbf{q}}^{\nu\nu'\omega}-\sum_{\nu_1\nu_2}\chi_{0,\mathbf{q}}^{\nu\nu_1\omega}F_r^{\nu_1\nu_2\omega}\chi_{0,\mathbf{q}}^{\nu_2\nu'\omega}\right)}{\chi_{0,\mathbf{q}}^{\nu\omega}}\mp1\\
&=\mp\frac{\sum_{\nu'}\left(\sum_{\nu_1\nu_2}\chi_{0,\mathbf{q}}^{\nu\nu_1\omega}F_r^{\nu_1\nu_2\omega}\chi_{0,\mathbf{q}}^{\nu_2\nu'\omega}\right)}{\chi_{0,\mathbf{q}}^{\nu\omega}}\\
&=\pm\frac{\sum_{\nu'}\left(\sum_{\nu_1\nu_2\mathbf{k}_1\mathbf{k}_2}\left(\delta_{\nu\nu_1}\beta G_{\mathbf{k}_1}^\nu G_{\mathbf{q}+\mathbf{k}_1}^{\omega+\nu_1}\right)F_r^{\nu_1\nu_2\omega}\left(\delta_{\nu'\nu_2}\beta G_{\mathbf{k}_2}^{\nu_2}G_{\mathbf{q}+\mathbf{k}_2}^{\omega+\nu_2}\right)\right)}{G_{\mathbf{k}}^\nu G_{\mathbf{q}+\mathbf{k}}^{\omega+\nu}}\\
&=\pm\frac{\sum_{\nu'}\left(G_{\mathbf{k}}^\nu G_{\mathbf{q}+\mathbf{k}}^{\omega+\nu}F_r^{\nu\nu'\omega}G_{\mathbf{k}'}^{\nu'}G_{\mathbf{q}+\mathbf{k}'}^{\omega+\nu'}\right)}{G_{\mathbf{k}}^\nu G_{\mathbf{q}+\mathbf{k}}^{\omega+\nu}}=\pm\sum_{\nu'}\left(F_r^{\nu\nu'\omega}G_{\mathbf{k}'}^{\nu'}G_{\mathbf{q}+\mathbf{k}'}^{\omega+\nu'}\right)\\
&=\pm\sum_{\nu'\in\Omega_{\mathrm{core}}(\omega)}\left(F_r^{\nu\nu'\omega}G_{\mathbf{k}'}^{\nu'}G_{\mathbf{q}+\mathbf{k}'}^{\omega+\nu'}\right)\pm\sum_{\nu'\in\Omega_{\mathrm{shell}}(\omega)}\left(F_r^{\nu\nu'\omega}G_{\mathbf{k}'}^{\nu'}G_{\mathbf{q}+\mathbf{k}'}^{\omega+\nu'}\right)\\
&\approx\pm\sum_{\nu'\in\Omega_{\mathrm{core}}(\omega)}\left(F_r^{\nu\nu'\omega}G_{\mathbf{k}'}^{\nu'}G_{\mathbf{q}+\mathbf{k}'}^{\omega+\nu'}\right)\pm\sum_{\nu'\in\Omega_{\mathrm{shell}}(\omega)}\left(F_{r,\mathrm{asym}}^{\nu\nu'\omega}G_{\mathbf{k}'}^{\nu'}G_{\mathbf{q}+\mathbf{k}'}^{\omega+\nu'}\right)
\end{aligned}$$

$$= \pm\lambda_{r,\mathbf{q}}^{\nu\omega} \pm \sum_{\substack{\nu'\epsilon \\ \Omega_{\text{shell}}(\omega)}} \left(F_{\text{asym},r}^{\nu\nu'\omega} + U\lambda_{r,\mathbf{q}}^{\nu\omega} \pm U \right) G_{\mathbf{k}'}^{\nu'} G_{\mathbf{q}+\mathbf{k}'}^{\omega+\nu'} \tag{6.89}$$

$$\Leftrightarrow \lambda_{r,\mathbf{q}}^{\text{impr},\nu\omega} = \pm \left(1 \mp U \sum_{\substack{\nu'\epsilon \\ \Omega_{\text{shell}}(\omega)}} G_{\mathbf{k}'}^{\nu'} G_{\mathbf{q}+\mathbf{k}'}^{\omega+\nu'} \right)^{-1} \cdot \left(\lambda_{r,\mathbf{q}}^{\text{core},\nu\omega} + \lambda_{r,\mathbf{q}}^{\text{asym},\nu\omega} \right)$$

$$\approx \pm \left(1 \pm U\chi_{0,\mathbf{q}}^{\text{shell},\omega} \right)^{-1} \cdot \left(\lambda_{r,\mathbf{q}}^{\text{core},\nu\omega} + \lambda_{r,\mathbf{q}}^{\text{asym},\nu\omega} \right) \tag{6.90}$$

Eq. (6.89) is obtained by considering Eq. (6.38) and Eq. (6.37) as well as the asymptotic regions of $F_r^{\nu\nu'\omega}$ depicted in Fig. 6.4a. We have also defined:

$$F_{\text{asym,m}}^{\nu\nu'\omega} = \frac{U^2}{2}\chi_{\text{d}}^{\nu-\nu'} - \frac{U^2}{2}\chi_{\text{m}}^{\nu-\nu'} + \chi_{\text{pp},\uparrow\downarrow}^{\nu+\nu'+\omega} \tag{6.91}$$

$$F_{\text{asym,d}}^{\nu\nu'\omega} = \frac{U^2}{2}\chi_{\text{d}}^{\nu-\nu'} + \frac{3U^2}{2}\chi_{\text{m}}^{\nu-\nu'} - \chi_{\text{pp},\uparrow\downarrow}^{\nu+\nu'+\omega} \tag{6.92}$$

$$\lambda_{r,\mathbf{q}}^{\text{asym},\nu\omega} = \sum_{\substack{\nu'\epsilon \\ \Omega_{\text{shell}}(\omega)}} F_{\text{asym},r}^{\nu\nu'\omega} G_{\mathbf{k}'}^{\nu'} G_{\mathbf{q}+\mathbf{k}'}^{\omega+\nu'} \pm U\chi_{0,\mathbf{q}}^{\text{shell},\omega} \tag{6.93}$$

Note, that the $\lambda_r^{\nu'\omega}$ term does not appear in $F_{\text{asym},r}^{\nu\nu'\omega}$. This is due to the fact, that the $\lambda_r^{\nu'\omega} G_{\mathbf{k}'}^{\nu'} G_{\mathbf{q}+\mathbf{k}'}^{\omega+\nu'}$ term is (i) unknown in the asymptotic region (ii) decays as $\mathcal{O}(1/\nu^3)$.
The susceptibilities appearing in Eq. (6.91) and Eq. (6.92) are local and can be directly obtained from the DMFT impurity solver, see for example Sec. 6.8.3. This is a feature of the ladder approximation that arises from the fact that the vertex is not self-consistently updated through parquet equations, as discussed in Sec. 5.3. Here a numerical parameter determines the size of the asymptotic region over which to approximate the limit of this sum and in which the asymptotic object $F_{\text{asym},r}^{\nu\nu'\omega}$ is constructed according to Fig. 6.4a. From our experience, values of additional 10 to 30 frequencies lead to a convergence of the improved sum for $\lambda_{r,\mathbf{q}}^{\nu\omega}$ in terms of double precision accuracy.
Additional approximations can be made to $F_{\text{asym},r}^{\nu\nu'\omega}$ in order to increase the numerical performance for the evaluation of the asymptotic contributions further. Details are discussed in Sec. 6.8.6 and example plots are presented in the supplemental notebook `BSE_SC_test.ipynb` of that project.

6.3.3 Physical susceptibilities

The physical susceptibility can be obtained in a similar fashion. However, the additional summation requires some attention to avoid double counting the dark orange regions in Fig. 6.4a.

$$\begin{aligned}
\chi_{r,\mathbf{q}}^{\omega} &= \sum_{\nu\nu'} \chi_{r,\mathbf{q}}^{\nu\nu'\omega} = \sum_{\nu\nu'} \left(\chi_{0,\mathbf{q}}^{\nu\nu'\omega} - \sum_{\nu_1\nu_2} \chi_{0,\mathbf{q}}^{\nu\nu_1\omega} F_r^{\nu_1\nu_2\omega} \chi_{0,\mathbf{q}}^{\nu_2\nu'\omega} \right) \\
&= \sum_{\nu\nu'} \chi_{0,\mathbf{q}}^{\nu\nu'\omega} - \sum_{\nu\nu'} G_{\mathbf{k}}^{\nu} G_{\mathbf{q}+\mathbf{k}}^{\omega+\nu} F_r^{\nu\nu'\omega} G_{\mathbf{k}'}^{\nu'} G_{\mathbf{q}+\mathbf{k}'}^{\omega+\nu'} \\
&= \chi_{r,\mathbf{q}}^{\text{core},\omega} + \sum_{\substack{\nu\nu'\epsilon \\ \Omega_{\text{asym}}(\omega)}} \chi_{0,\mathbf{q}}^{\nu\nu'\omega} - \sum_{\substack{\nu\nu'\epsilon \\ \Omega_{\text{asym}}(\omega)}} G_{\mathbf{k}}^{\nu} G_{\mathbf{q}+\mathbf{k}}^{\omega+\nu} F_r^{\nu\nu'\omega} G_{\mathbf{k}'}^{\nu'} G_{\mathbf{q}+\mathbf{k}'}^{\omega+\nu'} \\
&\approx \chi_{r,\mathbf{q}}^{\text{core},\omega} + \sum_{\substack{\nu\nu'\epsilon \\ \Omega_{\text{asym}}(\omega)}} \chi_{0,\mathbf{q}}^{\nu\nu'\omega} - \sum_{\substack{\nu\nu'\epsilon \\ \Omega_{\text{asym}}(\omega)}} G_{\mathbf{k}}^{\nu} G_{\mathbf{q}+\mathbf{k}}^{\omega+\nu} \left(F_{\text{asym},r}^{\nu\nu'\omega} + U(\mp 1 + U\chi_{r,\text{loc}}^{\omega}) \right) G_{\mathbf{k}'}^{\nu'} G_{\mathbf{q}+\mathbf{k}'}^{\omega+\nu'} \\
&\qquad - U\chi_{0,\mathbf{q}}^{\text{shell},\omega} \sum_{\substack{\nu\epsilon \\ \Omega_{\text{shell}}(\omega)}} (\pm 1 + \lambda_r^{\nu\omega})\, G_{\mathbf{k}}^{\nu} G_{\mathbf{q}+\mathbf{k}}^{\omega+\nu} - U\chi_{0,\mathbf{q}}^{\text{shell},\omega} \sum_{\substack{\nu'\epsilon \\ \Omega_{\text{shell}}(\omega)}} \left(\pm 1 + \lambda_{r,\text{loc}}^{\nu'\omega} \right) G_{\mathbf{k}'}^{\nu'} G_{\mathbf{q}+\mathbf{k}'}^{\omega+\nu'} \qquad (6.94) \\
&= \chi_{r,\mathbf{q}}^{\text{core},\omega} + \chi_{0,\mathbf{q}}^{\text{shell},\omega} + \chi_{r,\mathbf{q}}^{\text{asym}_1,\omega} + U(\mp 1 + U\chi_{r,\mathbf{q}}^{\omega}) \left(\chi_{0,\mathbf{q}}^{\text{shell},\omega} \right)^2 \\
&\qquad - 2U\chi_{0,\mathbf{q}}^{\text{shell},\omega} \sum_{\substack{\nu\epsilon \\ \Omega_{\text{shell}}(\omega)}} \left(\pm 1 + \lambda_{r,\mathbf{q}}^{\nu\omega} \right) G_{\mathbf{k}}^{\nu} G_{\mathbf{q}+\mathbf{k}}^{\omega+\nu} \qquad (6.95) \\
&= \chi_{r,\mathbf{q}}^{\text{core},\omega} + U(\mp 1 + U\chi_{r,\mathbf{q}}^{\omega}) \left(\chi_{0,\mathbf{q}}^{\text{shell},\omega} \right)^2 + \chi_{r,\mathbf{q}}^{\text{asym},\omega} \qquad (6.96) \\
\Leftrightarrow \chi_{r,\mathbf{q}}^{\text{impr},\omega} &= \left(1 - \left(U\chi_{0,\mathbf{q}}^{\text{shell},\omega} \right)^2 \right)^{-1} \left(\chi_{r,\mathbf{q}}^{\text{core},\omega} + \chi_{r,\mathbf{q}}^{\text{asym},\omega} \right) \qquad (6.97)
\end{aligned}$$

Eq. (6.94) again uses Fig. 6.4a to collect all asymptotic contributions. Here, the $\lambda_r^{\nu\omega}$ and $\lambda_r^{\nu'\omega}$ terms correspond to the left/right and top/bottom regions for any given ω. The $U(\mp 1 + U\chi_{r,\mathbf{q}}^{\omega})$ is the double counting subtraction from the overlap of the horizontal and vertical $\lambda_{r,\mathbf{q}}^{\nu\omega}$ regions. Note, this is the non-local susceptibility; the local contributions are contained in the $F_{\text{asym},r}^{\nu\nu'\omega}$ term, as before. The $\pm U$ term subtracts the double-counted background contribution in the shell region, which is already taken into account by $\chi_{r,\mathbf{q}}^{\omega}$. The factor 2 in front of the ν sum in Eq. (6.96) comes from the fact that

$\sum_\nu \lambda_r^{\nu\omega} = \sum_{\nu'} \lambda_r^{\nu'\omega}$. The contribution of $\lambda^{\nu\omega}$ in the asymptotic region with ν and ν', both outside of

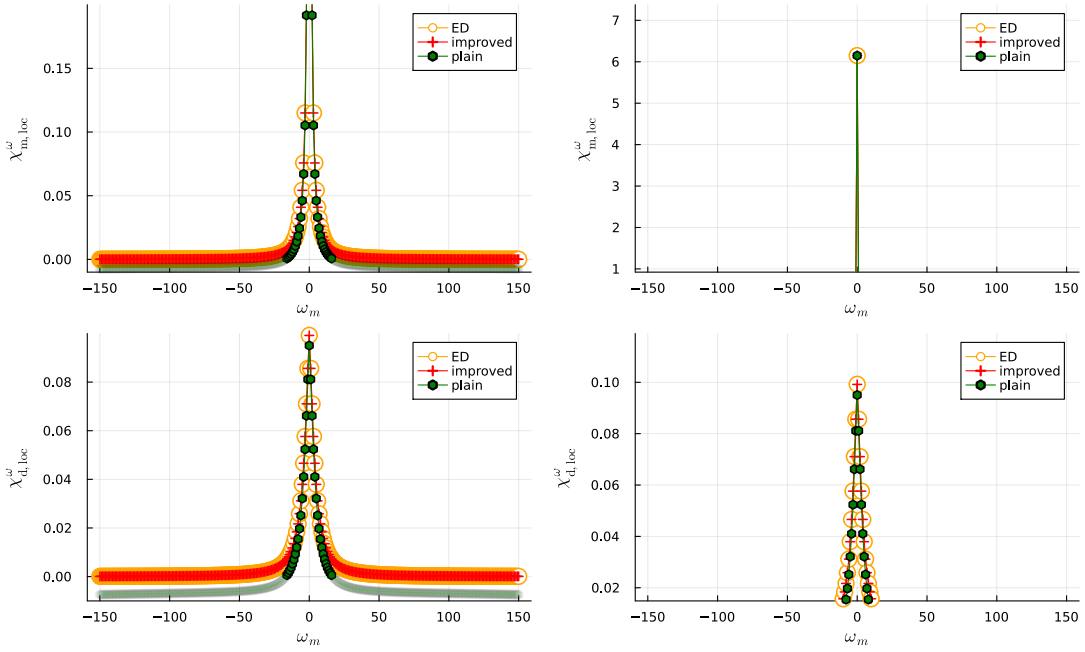

Figure 6.7: Demonstration of improved summation for physical susceptibility. Orange circles show χ_r^ω directly sampled from the impurity, red crosses the improved summation with $\chi_r^{\mathrm{impr},\omega} = \sum_{\nu\nu'} \chi_r^{\nu\nu'\omega}$ and green for the plain summation. The range with nonphysical (negative) susceptibilities is shaded.

the core region, has to be neglected (this is allowed because it decays as $1/\nu$, as discussed before) since we cannot obtain $\lambda_{r,\mathbf{q}}^{\nu\omega}$ in that region, as already mentioned in the previous section.
We have also defined:

$$\chi_{r,\mathbf{q}}^{\mathrm{asym}_1,\omega} = \mp U \left(\chi_{0,\mathbf{q}}^{\mathrm{shell},\omega}\right)^2 - \sum_{\substack{\nu\nu'\epsilon \\ \Omega_{\mathrm{asym}}(\omega)}} G_{\mathbf{k}}^{\nu} G_{\mathbf{q}+\mathbf{k}}^{\omega+\nu} F_{\chi,r,\mathrm{asym}}^{\nu\nu'\omega} G_{\mathbf{k}'}^{\nu'} G_{\mathbf{q}+\mathbf{k}'}^{\omega+\nu'} \tag{6.98}$$

$$\chi_{r,\mathbf{q}}^{\mathrm{asym},\omega} = \chi_{0,\mathbf{q}}^{\mathrm{shell},\omega} + \chi_{r,\mathbf{q}}^{\mathrm{asym}_1,\omega} - 2U\chi_{0,\mathbf{q}}^{\mathrm{shell},\omega} \sum_{\substack{\nu\epsilon \\ \Omega_{\mathrm{shell}}(\omega)}} \left(\pm 1 + \lambda_{r,\mathbf{q}}^{\nu\omega}\right) G_{\mathbf{k}}^{\nu} G_{\mathbf{q}+\mathbf{k}}^{\omega+\nu} \tag{6.99}$$

Details for the numerical evaluation are, again, discussed in Sec. 6.8.6.
Fig. 6.7 shows the local (i.e. DMFT, the BSE is used with $\chi_{0,\mathbf{q}}^{\nu\omega}$ obtained from the impurity Green's function) physical susceptibility χ_r^ω obtained from the generalized susceptibility $\chi_r^{\nu\nu'\omega}$ in the magnetic and density channel. In this case, the physical susceptibility can also be directly sampled (see Sec. 6.6.1 and Sec. 2). This is shown with orange circles. Fig. 6.8 shows the same for the non-local case, (i.e. $\chi_{r,\mathbf{q}}^{\nu\nu'\omega}$ is obtained through the BSE from the $\mathbf{k}$ depended local Green's function) as discussed for the lDΓA method in Sec. 5.4.1. The local susceptibility is also shown here but serves only as a reference for the change of fluctuations due to non-local correlations.

Kinetic Energy

From the f-sum rule in Eq. (4.42), we know that the kinetic energy can be obtained as

$$E_{\mathrm{kin}}^{(2)} = \lim_{m\to\infty} (i\omega_m)^2 \sum_{\mathbf{q}} \chi_{r,\mathbf{q}}^{\omega} \tag{6.100}$$

This energy remains on the DMFT level unless we employ the partial self-consistent method from Sec. 5.4.3 to explicitly replace it with the lDΓA value. We can therefore explicitly use this tail for summations over $\mathbf{q}$-summed susceptibilities, according to table 6.1:

$$\chi_r^{\mathrm{impr}} = \sum_\omega \left(\sum_{\mathbf{q}} \chi_{r,\mathbf{q}}^{\omega} \right) - \frac{E_{\mathrm{kin}}^{(2)}}{(i\omega_m)^2} - \frac{\beta}{12} \tag{6.101}$$

Importantly, the λ-correction (see for example Sec. 5.4.1) does not change the tail as Taylor expansion of $\left(c_2 x^2 + c_4 x^4 + \cdots + \lambda\right)^{-1}$ demonstrates (all susceptibilities are real in the context of this thesis and we therefore only consider even powers). This improved summation is used, for example, in the computation of the Pauli-Principle value for the λ-correction of the magnetic channel.

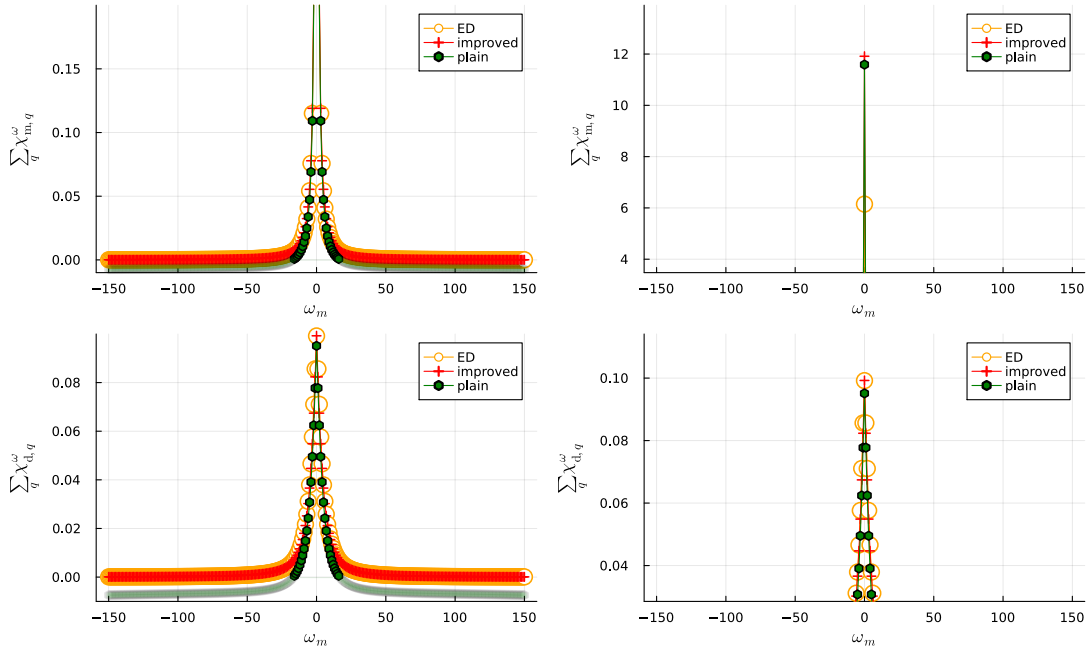

Figure 6.8: Demonstration of improved summation for non-local physical susceptibility. Red crosses the improved summation with $\chi_r^{\mathrm{impr},\omega} = \sum_{\nu\nu'\mathbf{q}} \chi_{r,\mathbf{q}}^{\nu\nu'\omega}$ and green for the plain summation. The range with nonphysical (negative) susceptibilities is shaded. Orange circles show χ_r^ω directly sampled from the impurity; for the non-local case, this purely serves as a reference to the change due to non-local correlations.

6.3.4 Self-energy

There are three components to the correction of the self-energy term: (i) the ω-sum, (ii) the local correction term, and (iii) the asymptotic correction. Out of all improved summation formulas, the improved summation of the self-energy (i) has the smallest impact on the numerical calculations in our experience. In fact, the change between plain and improved summation is typically only barely resolvable with double precision. However, the correction term (ii) significantly depends on the summation type. The tail correction term (iii) has already been discussed leading up to Eq. (6.108). Here, we also discuss potential numerical fixes to avoid a substantial change of $\lim_{\nu\to 0} \Sigma_{\mathbf{k}}^\nu$ with that term.

Sum Correction

We start with the equation of motion for the self-energy from Sec. 6.2.4:

$$\begin{aligned}
\Sigma_{\mathbf{k}}^\nu - \Sigma_{\mathrm{H}} &= U \sum_{\omega\mathbf{q}} \sum_{\nu'\mathbf{k}'} G_{\mathbf{k}'}^{\nu'} G_{\mathbf{q}+\mathbf{k}'}^{\omega+\nu'} F_{\uparrow\downarrow}^{\nu\nu'\omega} G_{\mathbf{q}+\mathbf{k}}^{\omega+\nu} = U \sum_{\omega\mathbf{q}} \lambda_{\uparrow\downarrow}^{\nu\omega} G_{\mathbf{q}+\mathbf{k}}^{\omega+\nu} \\
&= -U \sum_{\omega\mathbf{q}} \sum_{\nu'\mathbf{k}'} G_{\mathbf{k}'}^{\nu'} G_{\mathbf{q}+\mathbf{k}'}^{\omega+\nu'} F_{\mathrm{d}}^{\nu\nu'\omega} G_{\mathbf{q}+\mathbf{k}}^{\omega+\nu} = -U \sum_{\omega\mathbf{q}} \lambda_{\mathrm{d}}^{\nu\omega} G_{\mathbf{q}+\mathbf{k}}^{\omega+\nu} \\
&= \sum_{\omega\mathbf{q}} \sum_{\nu'\mathbf{k}'} G_{\mathbf{k}'}^{\nu'} G_{\mathbf{q}+\mathbf{k}'}^{\omega+\nu'} F_{\mathrm{m}}^{\nu\nu'\omega} G_{\mathbf{q}+\mathbf{k}}^{\omega+\nu} = U \sum_{\omega\mathbf{q}} \lambda_{\mathrm{m}}^{\nu\omega} G_{\mathbf{q}+\mathbf{k}}^{\omega+\nu} \\
&=: U \sum_{\omega\mathbf{q}} \Sigma_{\mathbf{kq}}^{\nu\omega} G_{\mathbf{q}+\mathbf{k}}^{\omega+\nu} - \Sigma_{\mathrm{H}}
\end{aligned}$$

We can use Eq. (6.49) to obtain the improved summation formula:

$$\Sigma_{\mathbf{k}}^\nu - \Sigma_{\mathrm{H}} = \sum_{\omega\mathbf{q}} \Sigma_{\mathbf{kq}}^{\nu\omega} = U \sum_{\substack{\omega\in\\ \Omega_{\mathrm{core}}(\nu)}} \sum_{\mathbf{q}} \Sigma_{\mathbf{kq}}^{\nu\omega} + U \sum_{\substack{\omega\in\\ \Omega_{\mathrm{asym}}(\nu)}} \frac{\pm(\Sigma_{\mathbf{k}}^\nu - \Sigma_{\mathrm{H}})}{(i\omega_m)^2} + \mathcal{O}\left(\frac{1}{\omega^2}\right) \tag{6.102}$$

$$\Leftrightarrow \Sigma_{\mathbf{k}}^{\mathrm{impr},\nu} = \left(1 \mp U \sum_{\substack{\omega\in\\ \Omega_{\mathrm{asym}}(\nu)}} \frac{1}{(i\omega_m)^2}\right)^{-1} U \sum_{\substack{\omega\in\\ \Omega_{\mathrm{core}}(\nu)}} \sum_{\mathbf{q}} \Sigma_{\mathbf{kq}}^{\nu\omega} + \Sigma_{\mathrm{H}} + \mathcal{O}\left(\frac{1}{\omega^2}\right) \tag{6.103}$$

This formula carries over when rewriting $\Sigma_{\mathbf{kq}}^{\nu\omega}$ in the usual lDΓA from:

$$\Sigma_{\mathbf{k}}^{\mathrm{impr},\nu} = \Sigma_{\mathrm{H}} - \frac{U}{2} \sum_{\omega\mathbf{q}} \left(-3\gamma_{\mathrm{m},\mathbf{q}}^{\nu\omega}(1 + U\chi_{\mathrm{m},\mathbf{q}}^{\lambda_{\mathrm{m}},\omega}) + 2 + \gamma_{\mathrm{d},\mathbf{q}}^{\nu\omega}(1 - U\chi_{\mathrm{d},\mathbf{q}}^{\lambda_{\mathrm{d}},\omega}) - \lambda_{0,\mathbf{q}}^{\nu\omega}\right) G_{\mathbf{q}+\mathbf{k}}^{\omega+\nu} + U \sum_{\substack{\omega\in\\ \Omega_{\mathrm{asym}}(\nu)}} \frac{\Sigma_{\mathbf{k}}^\nu - \Sigma_{\mathrm{H}}}{(i\omega_m)^2} \tag{6.104}$$

λ_0 Correction

The DMFT correction term $\lambda_{0,\mathbf{q}}^{\nu\omega}$ can be obtained again by considering the asymptotic contributions of $F_r^{\nu\nu'\omega}$ in Fig. 6.4a, given in Eq. (6.37) and Eq. (6.37). We obtain:

$$\lambda_{0,\mathbf{q}}^{\nu\omega} = \sum_{\nu'\mathbf{k}'} G_{\mathbf{k}'}^{\nu'} G_{\mathbf{q}+\mathbf{k}'}^{\omega+\nu'} F_{\uparrow\downarrow}^{\nu\nu'\omega} \tag{6.105}$$

$$= \sum_{\substack{\nu'\in \\ \Omega_{\mathrm{core}}(\omega)}} \sum_{\mathbf{k}'} G_{\mathbf{k}'}^{\nu'} G_{\mathbf{q}+\mathbf{k}'}^{\omega+\nu'} F_{\uparrow\downarrow}^{\nu\nu'\omega} + \sum_{\substack{\nu'\in \\ \Omega_{\mathrm{shell}}(\omega)}} \sum_{\mathbf{k}'} G_{\mathbf{k}'}^{\nu'} G_{\mathbf{q}+\mathbf{k}'}^{\omega+\nu'} \left(U(1+\lambda_{\uparrow\downarrow}^{\nu\omega}) + U^2 \chi_{\mathrm{m}}^{\nu'-\nu} - U^2 \chi_{\mathrm{pp}}^{\nu'-\nu} \right) \tag{6.106}$$

$$= \lambda_{0,\uparrow\downarrow}^{\mathrm{core},\nu\omega} + U\chi_{0,\mathbf{q}}^{\mathrm{shell},\nu\omega}(1+\lambda_{\uparrow\downarrow}^{\nu\omega}) + U^2 \chi_{0,\mathbf{q}}^{\mathrm{shell},\nu\omega} \left(\sum_{\substack{\nu'\in \\ \Omega_{\mathrm{shell}}(\omega)}} \chi_{\mathrm{m}}^{\nu'-\nu} - \chi_{\mathrm{pp}}^{\nu'-\nu} \right) \tag{6.107}$$

The calculation of the $\lambda_{0,\mathbf{q}}^{\nu\omega}$ term is done in the `calc_λ0_impr` function of the code discussed in Sec. 6.8.6. In practice, the diagonal term involving the local susceptibilities was often omitted because its contribution was negligible, while it has the largest performance impact for large $\mathbf{q}$ grids.

Self-Energy Tail Correction

Obtaining the correct tail for the self-energy is not just limited to the improved summation technique, but also requires a correct counter term, as discussed in the previous section. At the same time, the correct asymptotic behavior is crucial in order for the partial self-consistency method (see Sec. 5.4.3). It furthermore contains the filling, which we aim to keep consistent in all other places. Therefore, considerable effort was put into fixing this issue.

Ad-Hoc Fixes This section discusses the method of fixing the self-energy tail via an ad-hoc fix. To this end, we use the known deviation in the lDΓA self-energy and add the difference in the $1/\nu$ tail back in:

$$\Sigma_{\mathrm{tc,Full}}^{\nu} = -\frac{U^2}{i\nu_n} \left(\sum_{\omega\mathbf{q}} \chi_{\mathrm{m},\mathbf{q}}^{\lambda_{\mathrm{m}},\omega} - \sum_{\omega} \chi_{\mathrm{m,loc}}^{\omega} \right) \tag{6.108}$$

$$\Sigma_{\mathrm{plain}} = \Sigma_{\mathrm{H}} - \frac{U}{2} \sum_{\omega\mathbf{q}} \left(-3\gamma_{\mathrm{m},\mathbf{q}}^{\nu\omega}(1+U\chi_{\mathrm{m},\mathbf{q}}^{\lambda_{\mathrm{m}},\omega}) + 2 + \gamma_{\mathrm{d},\mathbf{q}}^{\nu\omega}(1-U\chi_{\mathrm{d},\mathbf{q}}^{\lambda_{\mathrm{d}},\omega}) - \lambda_{0,\mathbf{q}}^{\nu\omega} \right) G_{\mathbf{q}+\mathbf{k}}^{\omega+\nu} \tag{6.109}$$

$$\Sigma_{\mathbf{k}}^{\nu} = \Sigma_{\mathbf{k},\mathrm{plain}}^{\nu} + \Sigma_{\mathrm{tc,Full}}^{\nu} \tag{6.110}$$

This method is referred to as `ΣTail_Full` in the codes. It can be expected that this method considerably over-corrects low frequencies, and it does, in fact, sometimes lead to a positive imaginary part of the self-energies at some $\mathbf{k}$-points (we never observed this at the Fermi surface), as demonstrated in Fig. 6.11 where it is shown in green. If we assume that the lowest frequencies are captured correctly by the non-tail corrected formula, we can employ a fade-in of the tail correction. In the codes, this is referred to as `ΣTail_ExpStep{`δ`}`. Here, we introduce a numerical parameter δ that governs the transition speed of a step function. As a measure of the proximity to the asymptotic behavior, we use the difference between the high-frequency limit of the tail and the impurity self-energy:

$$\Delta_{\Sigma}^{\nu} \coloneqq \mathrm{Re}[\Sigma_{\mathrm{loc}}^{\nu} \cdot i\nu_n] + \frac{U^2 n}{2} \left(1 - \frac{n}{2} \right) \tag{6.111}$$

$$\Sigma_{\mathrm{tc,ExpStep}}^{\nu} \coloneqq \exp\left(-\frac{(\Delta^{\nu})_{\Sigma}^2}{\delta} \right) \Sigma_{\mathrm{tc,Full}}^{\nu} \tag{6.112}$$

$$\Sigma_{\mathbf{k}}^{\nu} = \Sigma_{\mathbf{k},\mathrm{plain}}^{\nu} + \Sigma_{\mathrm{tc,ExpStep}}^{\nu} \tag{6.113}$$

This method is shown for different values of δ for two different fillings n in Fig. 6.9. The δ parameter interpolates between the full ($\delta \to \infty$) and plain ($\delta = 0$) corrections and governs how fast the tail correction is switched on, proportional to the distance between the impurity self-energy and the asymptotic tail. While the imaginary part of the self-energy is negative, contrary to the example shown for the full correction method, we can now observe problematic behavior in the intermediate regime. Here, the self-energy exhibits an unusual behavior when the slope changes. While this may seem certainly more acceptable than the previous attempt, we now have a numerical parameter that can have a substantial influence on the potential energy. The potential can depend on the choice of δ, and the difference in potential energies on the one and two-particle levels may lead to different solutions for the λ_{d} parameter (even be accompanied by a sign change in λ_{d}). This is demonstrated in Fig. 6.16. Note that the solution range is not arbitrary because any root for the potential energy condition must fall between that of the `ΣTail_Full` and the `ΣTail_Plain` method. We furthermore stress that the role of the λ_{d} parameter is that of renormalization for the susceptibilities. For a detailed analysis of the influence of the tail correction schemes, see Sec. 7.2.
While the potentially non-causal self-energies and parameter-dependent λ_{d} solutions are problematic,

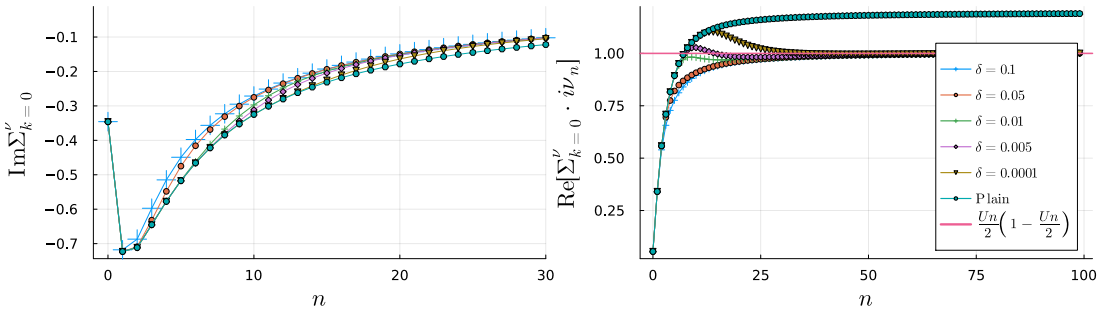

(a) $n = 1$.

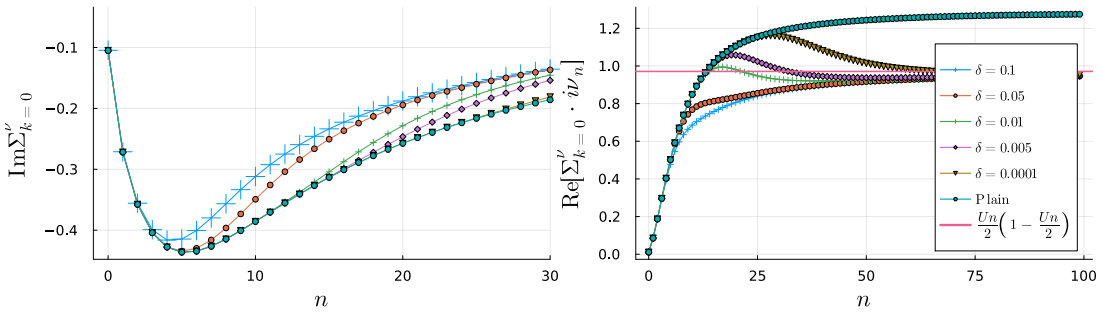

(b) $n \approx 0.83$.

Figure 6.9: Comparison between different exponential step parameters δ for self-energies at two different fillings. Data is shown for the first tail coefficient $1/\nu$ at $\mathbf{k} = (0, 0)$, for the 2 dimensional cubic lattice (see Sec. 7.2) at $\beta = 20$, $U = 2$.

the parameter range in which they can occur is exotic. Specifically, very large corrections to the density channel due to non-local correlations and substantial doping are required to observe this behavior combined with insufficient **k**-space sampling. The roots for the fade-in method are also typically unique since the left side of curves, such as the green one shown in Fig. 6.16, can be excluded for different reasons as will be discussed in the root-finding section Sec. 6.5.1. This can be done by iteratively searching for condition curves with increasing δ, such as shown in Fig. 6.16 until a unique solution is obtained. As demonstrated in the right panel of that figure, even in numerically unstable cases such as these, the solution does not change qualitatively.

Giving up on the Pauli Principle Instead of using the λ_m value to restore two-particle consistency for the density and thereby fixing the Pauli principle, one can also use the λ_m parameter to fix the tail explicitly, as done in the first publication of the λ corrected lDΓA method [125].
Using the knowledge of the EoM tail, we can achieve the corrected tail in a closed form by requiring, similar to the dual boson self-consistency condition [270], which is fixed by computing the appropriate λ_m:

$$\Sigma - \Sigma_\mathrm{H} = -\frac{U}{2}\sum_{\omega\mathbf{q}}\left(-3\gamma^{\nu\omega}_{\mathrm{m},\mathbf{q}}(1 + U\chi^{\lambda_\mathrm{m},\omega}_{\mathrm{m},\mathbf{q}}) + 2 + \gamma^{\nu\omega}_{\mathrm{d},\mathbf{q}}(1 - U\chi^{\lambda_\mathrm{d},\omega}_{\mathrm{d},\mathbf{q}}) - \lambda^{\nu\omega}_{0,\mathbf{q}}\right) G^{\omega+\nu}_{\mathbf{q}+\mathbf{k}} \tag{6.114}$$

$$\overset{\nu\to\infty}{\sim} -\frac{U}{2}\sum_{\omega\mathbf{q}}\left(-U\chi^{\lambda_\mathrm{m},\omega}_{\mathrm{m},\mathbf{q}} - U\chi^{\lambda_\mathrm{d},\omega}_{\mathrm{d},\mathbf{q}}\right) - U^2\frac{n}{2}\left(1 - \frac{n}{2}\right) \tag{6.115}$$

$$\Rightarrow \sum_{\omega\mathbf{q}}\chi^{\lambda_\mathrm{m},\omega}_{\mathrm{m},\mathbf{q}} \overset{!}{=} \frac{1}{3}\left(n\left(1 - \frac{n}{2}\right) - \sum_{\omega\mathbf{q}}\chi^{\lambda^*_\mathrm{d},\omega}_{\mathrm{d},\mathbf{q}}\right) \tag{6.116}$$

Where λ^*_d is an external parameter, as usual, and we used the asymptotic behavior of lambda and that $\sum_{\omega\mathbf{q}}\lambda^{\nu\omega}_{0,\mathbf{q}}G^{\omega+\nu}_{\mathbf{q}+\mathbf{k}} \sim U^2\frac{n}{2}(1 - \frac{n}{2})$. Here, we call this tail correction scheme `ΣTail_`λ_m (or just tail, e.g. in Fig. 5.11). Eq. (6.116) is the condition used to determine λ_m.
This method has not been used in practice for three reasons: (i) The central idea of this thesis to restore thermodynamical consistency stands opposed to the emphasis on microscopic features (such as the high-frequency tail) of this tail correction scheme; (ii) The results tend to produce unacceptable levels of causality violation of the self-energy or otherwise nonphysical solutions such as extreme suppression or enhancement of the susceptibilities, see Fig. 5.11, thereby not even improving spectral properties; (iii) The λ values and consequently the thermodynamical properties obtained from this method tend to follow the equation of motion scheme (discussed below) closely.

Modified EoM The modified version of the equation of motion has already been discussed in Eq. (6.80). Here, we want to discuss some numerical properties. Fig. 6.11 and Fig. 6.10 show self-energies and the

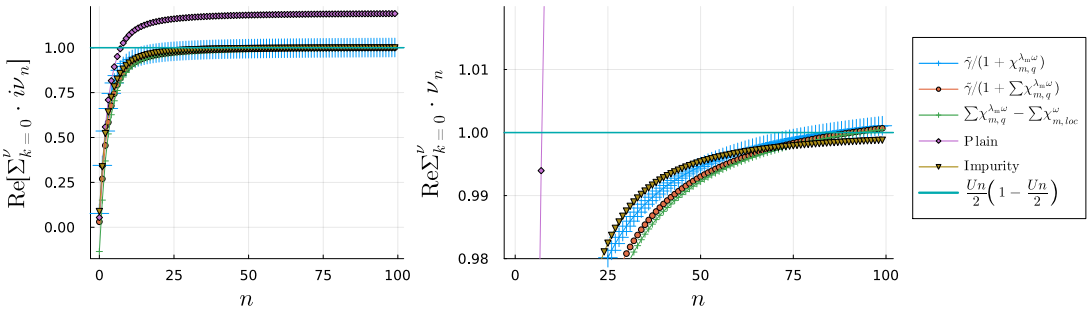

(a) $n = 1$.

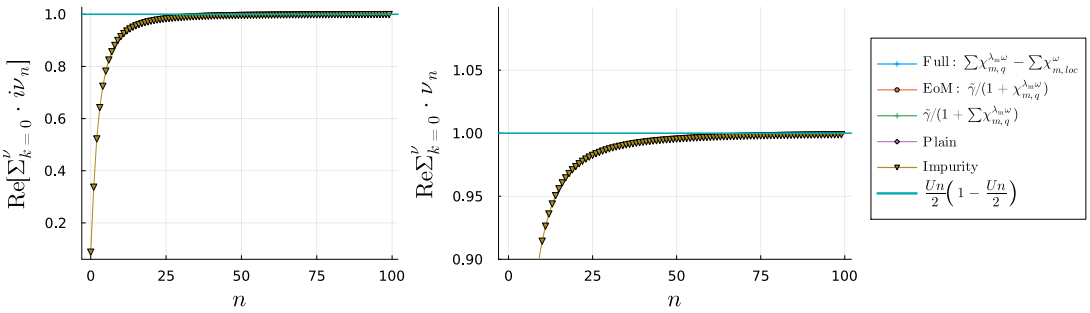

(b) $n \approx 0.83$.

Figure 6.10: Comparison between different tail correction schemes for the self-energy. Data is shown for the first tail coefficient $1/\nu$ at $\mathbf{k} = (0,0)$, for the 2 dimensional cubic lattice (see Sec. 7.2) at $\beta = 20$, $U = 2$. $\lambda_\mathrm{d} = 150$ has been chosen deliberately large to demonstrate the differences in schemes. The value fulfilling the potential energy condition is on the order of $\lambda_\mathrm{d} \sim -1$ and would show almost no visual difference between the schemes.

first tail coefficient for this modified equation of motion in blue, using the removal of the λ-corrected susceptibility from a portion of the magnetic channel:

$$\tilde{\gamma}^{\nu\omega}_{\mathrm{m},\mathbf{q}} = \gamma^{\nu\omega}_{\mathrm{m},\mathbf{q}} \frac{1 + U\chi^{\omega}_{\mathrm{m,loc}}}{1 + U\chi^{\lambda_\mathrm{m},\omega}_{\mathrm{m},\mathbf{q}}} = \lambda^{\nu\omega}_{\mathrm{m,DMFT},\mathbf{q}} \tag{6.117}$$

The orange line shows a slightly modified version, where instead $\tilde{\gamma}^{\nu\omega}_{r,\mathbf{q}}$ is calculated by using the $\mathbf{q}$-integrated non-local susceptibility instead.

$$\tilde{\gamma}^{\nu\omega}_{\mathrm{m},\mathbf{q}} = \gamma^{\nu\omega}_{\mathrm{m},\mathbf{q}} \frac{1 + U\chi^{\omega}_{\mathrm{m,loc}}}{1 + U\sum_{\mathbf{q}}\chi^{\lambda_\mathrm{m},\omega}_{\mathrm{m},\mathbf{q}}} \tag{6.118}$$

In Fig. 6.11, we observe that this scheme is the only one that tends to move the solution closer to the local one (shown with dark yellow triangles). This does not necessarily translate to the predicted values of the λ-parameters, as demonstrated in Fig. 6.16, where the λ_d is greater in magnitude than for the other correction schemes. This version of tail corrections has been observed to be the most

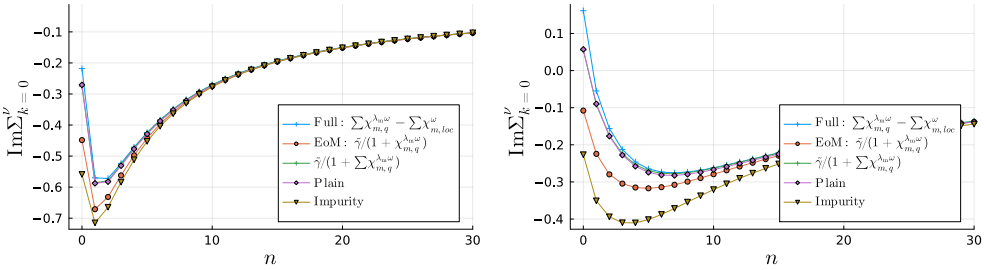

(a) Electron density $n = 1$. x-axis is over the fermionic Matsubara index n

(b) Electron density $n \approx 0.83$. x-axis is over the fermionic Matsubara index n

Figure 6.11: Comparison between different tail correction schemes for the self-energy. Data is shown at $\mathbf{k} = (0,0)$, for the 2 dimensional cubic lattice (see Sec. 7.2) at $\beta = 20$, $U = 2$. $\lambda_\mathrm{d} = -1$ was set externally since the potential energy conditions do not agree between tail correction methods. In fact, the plain and full tail correction produce non-causal self-energies for $n \approx 0.83$. See also Fig. 6.12.

stable, with no positive imaginary parts of the self-energy or unstable solutions for the potential energy condition in any lattice type. Fig. 6.12 demonstrates that the equation of motion correction keeps a causal self-energy over large ranges of λ_d. We can often restrict the range of admissible λ_d to cases with causal self-energies, as will be discussed in Sec. 6.5.2.

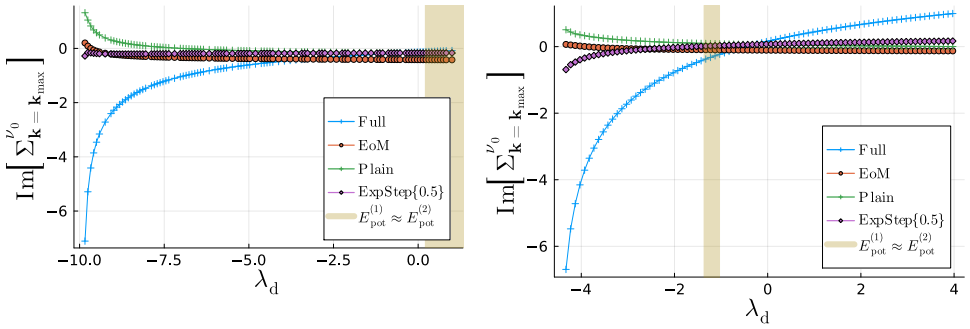

(a) $n = 1$ (b) $n \approx 0.83$

Figure 6.12: $\mathrm{Im}\,\Sigma^{\lambda,i\nu_0}_{\mathbf{k}=\mathbf{k}_{\max}}$ with $\mathbf{k}_{\max}$ being the $\mathbf{k}$ vector that maximizes the imaginary part of the self-energy. Data is shown for different tail-correction methods, for the 2D simple cubic, $U = 2$, $\beta = 20$ (see Sec. 7.2). The magnetic λ-correction for each λ_d value has been done before obtaining a self-energy.

The full self-energy in this modified equation of motion approach reads:

$$\Sigma_{\mathrm{EoM}} - \Sigma_{\mathrm{H}} = \frac{U}{2} \sum_{\omega\mathbf{q}} \left(-\gamma^{\nu\omega}_{\mathrm{m},\mathbf{q}} (1 + U\chi^{\lambda_\mathrm{m},\omega}_{\mathrm{m},\mathbf{q}}) - 2\gamma^{\nu\omega}_{\mathrm{m},\mathbf{q}} (1 + U\chi^{\omega}_{\mathrm{m,loc}}) + 2 + \gamma^{\nu\omega}_{\mathrm{d},\mathbf{q}} (1 - U\chi^{\lambda_\mathrm{d},\omega}_{\mathrm{d},\mathbf{q}}) - \lambda^{\nu\omega}_{0,\mathbf{q}} \right) G^{\omega+\nu}_{\mathbf{q}+\mathbf{k}} \tag{6.119}$$

Validity of the EoM approach and alternatives

By breaking the symmetry between the magnetic channels, we violate not only this symmetry but also a core assumption that the spin fluctuations must be renormalized close to phase transitions because their non-local components are not treated within DMFT. However, even in two dimensions at relatively low temperatures and away from half-filling, where DMFT as a mean-field theory will certainly produce inaccurate results, including spurious phase transitions that violate the Mermin-Wagner theorem Sec. 4.5.2, the thermodynamic properties do not change qualitatively between the different tail-correction approaches, except the modified EoM approach. We demonstrate this, for example, in Fig. 6.16. This again shows that two-particle consistencies (such as the fulfillment of local sum rules for the density in the self-energy tail, discussed in Sec. 4.4) and thermodynamic consistencies (as discussed in Sec. 4.3) are, in large parts, independent of each other in this approximate theory. One has to decide which questions a (necessarily approximate many-body) theory one wants to answer in order to make a decision on which consistencies to violate or preserve.
We focus on thermodynamic consistencies and thereby expect quantities derived from these to be more precisely captured in the lDΓA theory. However, if one wants to obtain spectral properties, such as the retarded self-energy via analytic continuation, one has to give up on some properties that may stabilize thermodynamical calculations. This is clearly illustrated by the problem of choosing a suitable tail-correction scheme. Here, one could also choose to give up on the Pauli principle and instead obtain λ parameters that explicitly retain the correct tail behavior, as done in the first publication of the lDΓA method [264]. As argued in Sec. 4.3.1, the conservation of the particle number is closely connected to thermodynamic consistencies, and therefore we find this approach to be less desirable. Moreover, in the case of our investigations in Sec. 7.1, the differences in the tail-correction schemes are so minor that we neglected them altogether (in the three-dimensional case they all roughly coincide). There is another significant downside to the applicability of this tail-correction scheme discussed in Sec. 7.2, as it may not be able to fully capture the momentum differentiation in cuprates. This demonstrates that for any investigation involving spectral properties, one must carefully argue which form of the self-energy is deemed appropriate and for what reason.

6.3.5 Energies

The potential and kinetic energies obtained from the one-particle level can also be computed using improved summation formulas. The two-particle summations use the high-frequency tail of the susceptibilities discussed in the last section.

Potential Energy

The 1-particle potential energy is obtained via the Galitskii-Migdal formula.

$$E_{\text{pot}}^{(1)} = \int_{\mathbf{k}\epsilon\text{BZ}} \sum_{\nu} G_{\mathbf{k}}^{\nu} \Sigma_{\mathbf{k}}^{\nu} \tag{6.120}$$

The corrections terms rely on the high-frequency expansion of the Green's function (Eq. 6.28) and self-energy (Eq. 6.64). We also disregard the $1/\nu^3$ term, as it is asymmetric over a symmetric interval and therefore 0. Furthermore, we use $\sum_\nu \frac{1}{\nu} = \frac{1}{2}$.

$$\begin{aligned} E_{\text{pot}}^{(1),\text{asympt}} &= \left[\frac{1}{\nu} + \frac{\frac{Un}{2} - \mu + \epsilon_{\mathbf{k}}}{\nu^2} + \frac{\left(\frac{Un}{2} - \mu\right)^2 + U^2 \frac{n}{2}\left(1 - \frac{n}{2}\right) + \epsilon_{\mathbf{k}}^2 + 2\epsilon_{\mathbf{k}}\left(\frac{Un}{2} - \mu\right)}{\nu^4} \right] \\ &\qquad \cdot \left[\frac{Un}{2} + \frac{U^2 \frac{n}{2}\left(1 - \frac{n}{2}\right)}{\nu} \right] + \mathcal{O}\left(\frac{1}{\nu^4}\right) \\ &= \left[\frac{c_1^{\text{p}}}{\nu} + \frac{c_{2,\mathbf{k}}^{\text{p}}}{\nu^2} + \frac{c_{4,\mathbf{k}}^{\text{p}}}{\nu^4} \right] + \mathcal{O}\left(\frac{1}{\nu^4}\right) \end{aligned}$$

with

$$\begin{aligned} c_1^{\text{p}} &= \frac{Un}{2} \\ c_2^{\text{p}} &= U^2 \frac{n}{2}\left(1 - \frac{n}{2}\right) + \frac{Un}{2}\left(\frac{Un}{2} + \epsilon_{\mathbf{k}} - \mu\right) \end{aligned} \tag{6.121}$$

Carrying out the sums over the asymptotic contributions analytically, analogously to Sec. 6.2, we obtain the following coefficients. Because the third tail coefficient of the potential energy is unknown, the coefficient $\tilde{c}_4$ is incomplete and we only use c_0 and c_2.

$$\sum_{\nu\mathbf{k}} \left[\frac{c_1^{\text{p}}}{\nu} + \frac{c_{2,\mathbf{k}}^{\text{p}}}{\nu^2} + \frac{c_{4,\mathbf{k}}^{\text{p}}}{\nu^4} \right] = \tilde{c}_1^{\text{p}} \frac{1}{2} + \tilde{c}_2^{\text{p}} \frac{-\beta}{4} + \tilde{c}_4^{\text{p}} \frac{\beta^3}{48} \tag{6.122}$$

$$\begin{aligned} \tilde{c}_1^{\text{p}} &= \frac{Un}{2} \\ \tilde{c}_2^{\text{p}} &= U^2 \frac{n}{2}\left(1 - \frac{n}{2}\right) + \frac{Un}{2}\left(\frac{Un}{2} + \int_{\mathbf{k}\epsilon\text{BZ}} \epsilon_{\mathbf{k}} - \mu\right) \\ \tilde{c}_4^{\text{p}} &= \left[\left(\frac{Un}{2} - \mu\right)^2 + U^2 \frac{n}{2}\left(1 - \frac{n}{2}\right) + \int_{\mathbf{k}\epsilon\text{BZ}} \epsilon_{\mathbf{k}}^2 + 2\left(\frac{Un}{2} - \mu\right) \int_{\mathbf{k}\epsilon\text{BZ}} \epsilon_{\mathbf{k}} \right] \cdot \left[U^2 \frac{n}{2}\left(1 - \frac{n}{2}\right) \right] \end{aligned}$$

The resulting improved summation formula is then

$$E_{\text{pot}}^{(1),\text{impr}} = \sum_{\substack{\nu\epsilon \\ \Omega_{\text{core}}(\omega)}} \sum_{\mathbf{k}} \left(G_{\mathbf{k}}^{\nu} \Sigma_{\mathbf{k}}^{\nu} - \frac{c_{2,\mathbf{k}}}{(i\nu_n)^2} \right) + \tilde{c}_0^{\text{p}} \frac{1}{2} - \tilde{c}_2^{\text{p}} \frac{\beta}{4} \tag{6.123}$$

Kinetic Energy

The 1-particle kinetic energy is given by the usual improved summation formula for the single-particle Green's function with the coefficients given in Sec. 6.2.0.1. Note that, as for the potential energy above, $\sum_n \left(\frac{1}{i(2n+1)}\right)^3 = 0$ and we therefore only need to take the first two coefficients into account.

$$E_{\text{kin}}^{(1),\text{impr}} = \sum_{\substack{\nu\epsilon \\ \Omega_{\text{core}}(\omega)}} \sum_{\mathbf{k}} \left(\epsilon_{\mathbf{k}} G_{\mathbf{k}}^{\nu} - \frac{1}{(i\nu_n)^1} - \frac{c_{2,\mathbf{k}}}{(i\nu_n)^2} \right) + \frac{1}{2} + \tilde{c}_2 \frac{\beta}{4} \tag{6.124}$$

6.3.6 Filling

We use the Hurwitz ζ function, as in Eq. (6.12):

$$\frac{2}{\beta} \sum_{n=N}^{N-1} \frac{1}{(i\nu_n)^2} = \frac{2}{\beta} \left(\frac{\beta}{2\pi i}\right)^2 \zeta(2, N - \frac{1}{2}) = -\frac{\beta}{2\pi^2} \zeta(2, N - \frac{1}{2}) \tag{6.125}$$

Again, we only need to consider the two first tail coefficients, because the third tail coefficient does not contribute because of the symmetric sum over an antisymmetric function):

$$\frac{n}{2} = \sum_{\mathbf{k},\nu} G_{\mathbf{k}}^{\nu} = \sum_{\mathbf{k},\Omega_{\text{core}}} G_{\mathbf{k}}^{\nu} + \sum_{\mathbf{k},\Omega_{\text{asym}}} G_{\mathbf{k}}^{\nu}$$

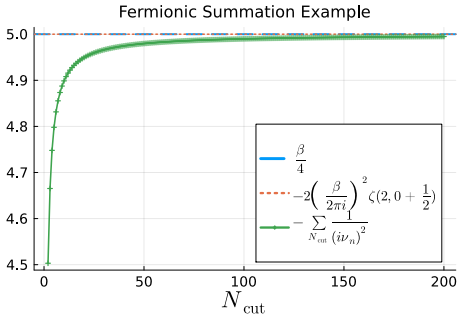

(a) Convergence of plain summation of the second power of the fermionic Matsubara frequencies for increasing cutoff. Compared to exact solutions $\beta/4$ and the closed form solution in terms of the Hurwitz zeta function.

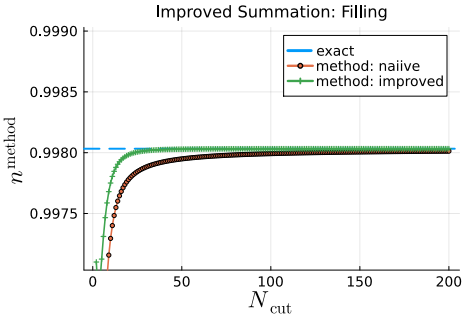

(b) Convergence of plain summation of the second power of the fermionic Matsubara frequencies for increasing cutoff. Compared to exact solutions $\beta/4$ and the closed form solution in terms of the Hurwitz zeta function.

$$= \sum_{\mathbf{k},\Omega_{\text{core}}} G^{\nu}_{\mathbf{k}} + \sum_{\mathbf{k},\Omega_{\text{asym}}} \left(\frac{1}{i\nu_n} + \frac{\frac{Un}{2} + \epsilon_{\mathbf{k}} - \mu}{(i\nu_n)^2} \right) + \mathcal{O}\left(\frac{1}{(i\nu_n)^4}\right) \tag{6.126}$$

$$= \sum_{\mathbf{k},\Omega_{\text{core}}} G^{\nu}_{\mathbf{k}} - \underbrace{\sum_{\Omega_{\text{core}}} \frac{1}{i\nu_n}}_{0} + \underbrace{\sum_{\nu} \frac{1}{i\nu_n}}_{\frac{1}{2}} + \sum_{\mathbf{k}} (\epsilon_{\mathbf{k}} - \mu) \sum_{\Omega_{\text{asym}}} \frac{1}{(i\nu_n)^2} + \frac{Un}{2} \sum_{\Omega_{\text{asym}}} \frac{1}{(i\nu_n)^2} + \mathcal{O}\left(\frac{1}{\nu^4}\right) \tag{6.127}$$

$$= \sum_{\mathbf{k},\Omega_{\text{core}}} G^{\nu}_{\mathbf{k}} + \frac{1}{2} + \sum_{\mathbf{k}} (\epsilon_{\mathbf{k}} - \mu) \left(-\frac{\beta}{2\pi^2} \zeta(2, N + \frac{1}{2}) \right) + \frac{Un}{2} \left(-\frac{\beta}{2\pi^2} \zeta(2, N + \frac{1}{2}) \right) + \mathcal{O}\left(\frac{1}{\nu^4}\right) \tag{6.128}$$

$$\Leftrightarrow \left(1 - \frac{U\beta}{2\pi^2} \zeta(2, N + \frac{1}{2})\right) n^{\text{impr}} = 2 \sum_{\mathbf{k},\Omega_{\text{core}}} G^{\nu}_{\mathbf{k}} + \frac{1}{2} + \frac{\sum_{\mathbf{k}} (\epsilon_{\mathbf{k}} - \mu)\beta}{2\pi^2} \zeta(2, N + \frac{1}{2}) + \mathcal{O}\left(\frac{1}{\nu^4}\right) \tag{6.129}$$

$$\Leftrightarrow n^{\text{impr}} = 2 \frac{\sum_{\mathbf{k},\Omega_{\text{core}}} G^{\nu}_{\mathbf{k}} + \frac{1}{2} + \frac{\sum_{\mathbf{k}} (\epsilon_{\mathbf{k}} - \mu)\beta}{2\pi^2} \zeta(2, N + \frac{1}{2})}{1 - \frac{U\beta}{2\pi^2} \zeta(2, N + \frac{1}{2})} + \mathcal{O}\left(\frac{1}{\nu^4}\right) \tag{6.130}$$

Fig. 6.13a demonstrates the convergence behavior of the plain summation over Matsubara frequencies against the analytically computed one. In Fig. 6.13b the convergence of plain (green) and improved (orange) summation for the electron density is plotted against the number of summands (N_{cut}). This is done for the impurity Green's function for which the exact result can be obtained directly.

6.4 Symmetry Reductions and Convolutions

We have already discussed symmetries of two-particle Green's functions in Chapter 2, which were also derived in detail for the full vertex $F_r^{\nu\nu'\omega}$ and the generalized susceptibilities $\chi_r^{\nu\nu'\omega}$ in [205]. Fig. 6.4 demonstrates some of these visually. In addition, there are also the well-known lattice symmetries that are present in the non-local quantities. In this section, we will discuss how these can be exploited in order to reduce the system memory demands and runtime of the lDΓA algorithms. We will discuss the general setup; some additional details can be found in the description or the `SymmetryClasses` and `TightBinding` codes in Sec. 6.8 and their documentation. By symmetries in the context of this section, we also include relationships that are trivial to compute, such as $f(x) = -f^*(-x)$.

6.4.1 Algorithm for Minimal Sampling

The following algorithm is implemented in the `EquivalenceClassesConstructor.jl` Julia package (see also Sec. 6.8.2) and is used for Matsubara grids and **k**-space sampling.
It requires a sampling space (e.g., a list of 3-tuples with Matsubara indices or a list of **k**-vectors) and a list of relationships, for example, $\texttt{f(x)} = [-\texttt{f}(-\texttt{x}), \texttt{f}^*(\texttt{x}+\texttt{3})]$. Furthermore, a list of operation identifiers can be given, for example, here $[\texttt{1}, \texttt{2}]$ [3]. The algorithm then constructs a forest of trees with all sampling points being nodes, connected by labeled edges for each relationship. This is done by setting up two parent arrays (the code uses hash maps to avoid constructing an additional list that maps between the node index and content, requiring the user to specify the vertices in a compressed format for very large inputs; see Sec. 6.8.2). The `parent` array contains at the index `i`, the child index of the node with index `i`. The `parent_edge` hash map does the same for the operation that leads from the child to the parent. Furthermore, a hash map of `open` (not checked) vertices and a stack of next-to-check vertices are defined. The parent arrays are initialized with each vertex being its own parent (i.e. the

[3] There is a version of the code available that operates on a set of predicates and constructs an adjacency matrix. This version is not used for the lDΓA method and will not be discussed here.

graph initially consists of a forest of a forest with trees of size 1).

Then, each node in the sampling space is checked in an outer loop if it is marked `open` (with the corresponding index in the `open` list set to `false`). The node is first pushed to the `search` stack. Then the current `search` stack is iteratively treated as follows: One element `el` is removed. If it is marked `open`, then all neighbors `ne` are obtained from $f(x)$. If the neighbor is contained in the sample space and marked `open`, it is pushed to the current search stack, and the parent arrays are marked with `parent[el]=ne`. The parent arrays are then returned. Fig. 6.14 shows a representation of the graph for our example from before. This representation is not unique, as it depends on the ordering of the lists of nodes.
This graph can now be used to determine the minimal set required and the mapping from the minimal set back to the full sampling set. This is done by iterating through the parent array and picking out all root nodes as class representatives. In our example above we obtain `-5` and `-3`. The reconstruction of the full grid is then later possible by iterating through all nodes of the sampling space and following the parent array values up the tree (tracking the operations here is crucial) until a computed value is found. This must be the case at least for the root node; the unknown elements along the path are then obtained recursively; see also Sec. 6.8.7.

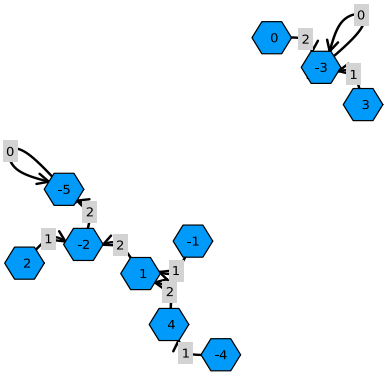

Figure 6.14: Example for symmetry classes graph.

Matsubara Grids and Lattice Symmetries The algorithm above is used in two places for the lDΓA results: Generation of (i) Matsubara frequency grids (ii) $\mathbf{k}/\mathbf{q}$ sampling for the first Brillouin zone. Case (i) is completely detached from the actual runtime but only required as a postprocessing for the DMFT solution. We exclusively used ED for the two-particle Green's function since the noisy CTQMC data is less suitable for method development and requires significantly more compute time. This means a self-consistent impurity Green's function is obtained (possibly with a different impurity solver such as CTQMC) from which the Anderson bath parameters ϵ_l and V_l are fitted (see Sec. 6.6.2). These can then be used to obtain a two-particle Green's function from the Lehmann representation with a set of frequency triples. Because these terms are independent between frequencies (see, for example, in the one-particle case in Eq. (6.160)), it is sufficient to pre-generate a minimal frequency grid according to the symmetries in [205, Table. 2.2], perform the summation of all energy eigenstates and then restore the full vertex. There is no performance benefit in using the reduced frequency grid in the lDΓA method. This method is dominated by the impact of the $\mathbf{k}$-space sampling, and repeated reduction and expansion in the frequency space does not yield a performance benefit. This is particularly important close to a phase transition, where the $\mathbf{k}$-space resolution becomes the limiting factor.
The reduction of the $\mathbf{k}$-sampling is done in the tight-binding module (see Sec. 6.8.4). Some lattice types have hard-coded reduction and expansion algorithms, but the option to implement new ones rapidly is aided by this module. Here, the reduction and expansion are crucial for the performance of the lDΓA method. Specifically, the convolutions and cross-correlations, which have been implemented using the Fast Fourier Transform (FFT), require the expansion to the full sample space, as we will discuss next.

6.4.2 Convolutions

There are two places in the lDΓA algorithm where we encounter sums of the following type:

$$h^{\nu\omega}_{\mathrm{ph/pp},\mathbf{k}} = \sum_{\mathbf{q}} K_{\mathbf{q}} G^{\omega+\nu}_{\mathbf{q}\pm\mathbf{k}} \tag{6.131}$$

$$\chi^{\nu\omega}_{0,\mathbf{q}}: \; K_{\mathbf{q}} = G^{\nu}_{\mathbf{q}}, \tag{6.132}$$

$$\Sigma^{\nu}_{\mathbf{k}}: \; K_{\mathbf{q}} = \sum_{r\in\{\mathrm{d},\mathrm{m}\}} c_r \lambda^{\nu\omega}_{r,\mathbf{q}} - \lambda^{\nu\omega}_{0,\mathbf{q}} \tag{6.133}$$

Where K refers to the $\mathbf{q}$-sampled quantity at some externally fixed frequency indices. The two occurrences are the calculations of the bare susceptibility $\chi^{\nu\omega}_{0,\mathbf{q}}$ and the non-local self-energy $\Sigma^{\nu}_{\mathbf{k}}$. Especially the second quantity requires a fast algorithm since it typically has to be computed many times to obtain a solution for the λ_{d} parameter. Here, every step of the Newton algorithm requires at least 3 evaluations (one for the value of the function, two for an estimator of the derivative) of the self-energy. The self-energy requires $N_\omega \times N_\nu$ convolutions of $\mathbf{k}$-sampled quantities. This number is typically around $100,000$. If the partial self-consistent method is used, this is further multiplied by the number of self-consistent iterations.
The bare susceptibility is only calculated once for the setup discussed in this thesis, but the code does allow for a fully self-consistent lDΓA cycle as described for a much more generic setting in [128]. Here,

the fast computation of this quantity is crucially important. For these reasons, we employ the convolution theorem to reduce the runtime for the computation of Eq. (6.131) for $N_{\mathbf{k}}$ $\mathbf{k}$-points, from $\mathcal{O}(N_{\mathbf{k}}^2)$ to $\mathcal{O}(N_{\mathbf{k}} \log(N_{\mathbf{k}}))$.
We define the operations for convolution and cross-correlation as follows:

$$\mathrm{Conv}\left[K, G\right]_i = \sum_j K_j G_{i-j} \tag{6.134}$$

$$\mathrm{CrossC}\left[K, G\right]_i = \sum_j K_j G_{i+j} \tag{6.135}$$

The convolution theorem then allows us to rewrite these as the element-wise multiplication of the Fourier transform of f and g and subsequent inverse Fourier transformation $\mathcal{F}^-$.

$$\mathrm{Conv}\left[K, G\right] = \mathcal{F}^{-1}\left(\mathcal{F}\left[K\right] \cdot \mathcal{F}\left[G\right]\right) \tag{6.136}$$

We can map the cross-correlation to the convolution within $\mathcal{O}(N_{\mathbf{k}})$ by including 2 reverse operations, denoted with a R superscript below. This reverses the N dimensional array along each dimension, i.e. $G^{\mathrm{R}}(\mathbf{k}_x, \mathbf{k}_y, \dots)$ to $g(-\mathbf{k}_x, -\mathbf{k}_y, \dots)$.

$$\mathrm{CrossC}\left[K, G\right]_{\mathbf{q}} = \sum_{\mathbf{k}} K_{\mathbf{k}} G_{\mathbf{q}+\mathbf{k}} = \left(\sum_{\mathbf{k}} K_{\mathbf{k}} G_{-\mathbf{q}+\mathbf{k}}\right)^{\mathrm{R}} = \left(\sum_{\mathbf{k}} K_{\mathbf{k}}\, G^{\mathrm{R}}_{\mathbf{q}-\mathbf{k}}\right)^{\mathrm{R}} \tag{6.137}$$

$$= \left(\mathrm{Conv}\left[K, G^{\mathrm{R}}\right]_{\mathbf{q}}\right)^{\mathrm{R}} \tag{6.138}$$

Even though we are in principle dealing with a continuous function over $\mathbf{k}$-space, the application of the fast Fourier algorithm requires a discrete and evenly spaced (see discussion regarding sampling below) sampling. This is, as usual, emphasized by using sums over $\mathbf{k}$-space. The discrete Fourier operation is then defined as follows in our context (N_l is the number of $\mathbf{k}$-points in each dimension):

$$\mathcal{F}[x_{\mathbf{k}}] = \sum_{\mathbf{k}_1}^{N_l-1} e^{-\frac{2\pi i}{N_l}} \sum_{\mathbf{k}_2}^{N_l-2} e^{-\frac{2\pi i}{N_l}} \cdots x_{\mathbf{k}} \tag{6.139}$$

For the computation of convolutions, we employ FFT provided by the `FFTW3` package[4]. The algorithm design and properties are very thoroughly explained in the publication of the lead developers [72]. We will therefore skip an explanation here, but instead comment on some points that are important to the implementation within the lDΓA method.

Expansion to Full Grid and Sampling As discussed in the beginning of this section, the symmetries of the lattice can be used to reduce memory and computational costs. All quantities in $\mathbf{q}$ space only need to be computed and stored over the minimal set. The FFT implementation requires the data fully expanded and pre/post-processed. This is accomplished by the tight-binding module described further in Sec. 6.8.4. The important concepts here are (i) buffers for the repeated `expansion`, `reverse`, and multiplication operations[5] and (ii) index maps for reduction and expansion. The buffers are essential because millions of convolutions are computed in a single lDΓA run, while the index maps provide fast copying between reduced and expanded forms of the data.
Specifically, at low temperatures and close to phase transitions, one would prefer a $\mathbf{k}$-sampling with an adaptive mesh that centers around the dominant $\mathbf{q}$-vector at which the susceptibility becomes spiked. However, while there are non-equidistant FFT algorithms available, they do typically require approximations and are far less straightforward to use. Consider, for example, the sum over $G_{\mathbf{k}+\mathbf{q}}$ in Eq. (6.137). In case of an arbitrary (or even just different) sampling of $\mathbf{k}$ and $\mathbf{q}$, the sum or difference between both would certainly fall on values that have not been calculated. This would require interpolations for these values, and we, therefore, use equal spacing in all $\mathbf{k}$-grids.

6.5 lDΓA Details

This section describes necessary algorithms that are specific to the lDΓA method. The general structure and characteristics of the code used to produce the results for this thesis are outlined in Sec. 6.8.5. Here, we discuss the most important numerical algorithms of the method.

6.5.1 Root finding

The λ parameters and their role have been extensively discussed in this thesis. Their algorithmic determination using a root-finding algorithm, such as Newton's method, will be substantiated here.

[4] specifically the Julia frontend, `FFTW.jl`.
[5] In addition, the result from FFT requires a `circshift` operation to recenter the data, in our case, so the $\mathbf{q} = 0$ vector is at the expected index. This reordering of the output is a somewhat sparsely documented but very prevalent property of many implementations of FFT algorithms.

The lDΓA method requires some considerations with regard to these algorithms due to (i) divergences and physically admissible solution ranges, (ii) uniqueness of the solution, and (iii) variation in the numerical cost of a function call. These have to be considered in detail because the correction in the density channel is either impossible numerically (when the divergences and non-uniqueness are not treated properly) or dominates the total runtime by an order of magnitude when obtained without choosing a suitable algorithm. The second issue then excludes the partial self-consistency from being numerically feasible.
The λ parameters in the lDΓA method are obtained by finding roots to the corresponding two equations for the Pauli principle and the potential energy. There are 3 functions for which we need to determine a root for λ_m, λ_d and μ:

$$f_\mathrm{m}^{\lambda_\mathrm{d},\mu}(\lambda_\mathrm{m}) = \frac{1}{2}\sum_{\omega\mathbf{q}}\left(\chi_{\mathrm{d},\mathbf{q}}^{\lambda_\mathrm{d},\omega} + \chi_{\mathrm{m},\mathbf{q}}^{\lambda_\mathrm{m},\omega}\right) - \frac{n}{2}\left(1-\frac{n}{2}\right) \tag{6.140}$$

$$f_\mathrm{d}^{\lambda_\mathrm{m},\mu}(\lambda_\mathrm{d}) = \frac{1}{2}\sum_{\omega\mathbf{q}}\left(\chi_{\mathrm{d},\mathbf{q}}^{\lambda_\mathrm{d},\omega} - \chi_{\mathrm{m},\mathbf{q}}^{\lambda_\mathrm{m},\omega}\right) - U\frac{n^2}{4} - \frac{1}{U}\sum_{\nu\mathbf{k}} G_\mathbf{k}^{\lambda,\nu}\Sigma_\mathbf{k}^{\lambda,\nu} \tag{6.141}$$

$$f_\mu^{\lambda_\mathrm{m},\lambda_\mathrm{d}}(\mu) = n^\mathrm{impr}\left(\Sigma_\mathbf{k}^{\lambda,\nu}\right) - n \approx \sum_{\nu\mathbf{k}}\left(i\nu_n + \mu - \epsilon_\mathbf{k} - \Sigma_\mathbf{k}^{\lambda,\nu}\right)^{-1} - n \tag{6.142}$$

These must be solved in the following hierarchical structure:

1. λ_m fixes the Pauli principle and must be determined first to obtain a well-defined potential energy and filling.

2. μ determines the filling and needs to be adjusted when computing the Green's function.

3. λ_d, just as λ_m, requires specific attention with regard to the smallest value $\lambda_{\mathrm{d,min}}$, since there are divergencies for smaller values. The admissible interval may depend on the value of μ, as discussed in the next section. Note that we used the previously discussed improved summation for the electron density, making the last equation in Eq. (6.142) approximate

A simultaneous determination including λ_m is impossible because the algorithm would pick pairs (or triples) of values that do not lead to physical self-energies and routinely lead to infinities, causing the algorithm to crash. μ and λ_d could be determined simultaneously, but our tests have shown that the performance gain from this change is negligible in exchange for significantly deteriorated stability. The reason is vastly different requirements for the root-finding algorithm for both cases, which we will discuss next.
Eq. (6.142) is well-behaved, without divergencies, and the derivative is accessible analytically and through automatic differentiation[6]. A call to this function is numerically as expensive as Eq. (6.140) (see discussion below). It is also strictly monotonic in a reasonable range around the initial guess and changes little from the chemical potential of DMFT, further increasing performance. We will discuss suitable algorithms below in Sec. 6.5.3 after investigating the properties of Eq. (6.140) and Eq. (6.141).

6.5.2 Divergencies and Minimal Values

Next, we discuss the admissible range of λ parameters and our choice of algorithm to guarantee a solution in that interval. As also discussed in Sec. 4.5.1 only the largest root of Eq. (6.140) and

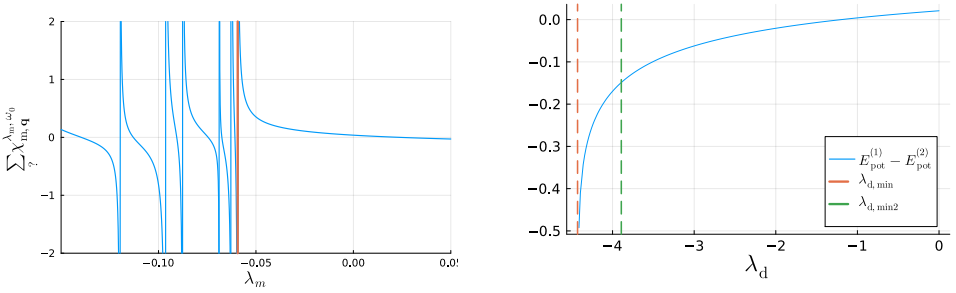

(a) Divergencies of $\sum_\mathbf{q} \chi_{\mathrm{m},\mathbf{q}}^{\lambda_\mathrm{m},\omega_0}$. The largest (in λ_m) divergency, $\lambda_{\mathrm{m,min}}$, is marked with an orange vertical line.

(b) Comparison of λ_min (Eq. (6.143)) and $\lambda_{\mathrm{d,min},E_\mathrm{pot}}$ (see Eq. (6.144)).

Figure 6.15: Conditions for minimal λ values.

Eq. (6.141) guarantees positivity of the susceptibilities according to Eq. (4.47).

[6] Automatic differentiation replaces the argument, in this case μ with a `dual-type`, that traces `f(x)` as well as `f'(x)` through the full function, thereby almost completely eliminating the computational overhead of computing the derivative while also yielding exact results.

Both Eq. (6.140) and Eq. (6.141) have divergences at $\frac{1}{\lambda_\mathrm{d}} = -\chi^{\lambda_\mathrm{d},\omega}_{\mathrm{d},\mathbf{q}}$ and $\frac{1}{\lambda_\mathrm{m}} = -\chi^{\lambda_\mathrm{m},\omega}_{\mathrm{m},\mathbf{q}}$ according to this definition. The largest divergence (in λ_r) can be determined in the following way. We want to renormalize the susceptibility at the classical frequency $\omega = 0$, at which the susceptibility will diverge towards the phase transition and become negative below it, then approaching 0 from below[7]; therefore, we only need to consider the $\mathbf{q}$ index. The $N_\mathbf{q}$ divergences in Eq. (4.47) are at the points $\lambda_\mathbf{q} = -\frac{1}{\chi^{\omega_0}_{r,\mathbf{q}}}$, the largest of which (called $\lambda_{r,\mathrm{min}}$) guarantees the positivity of $\chi^{\lambda_r,\omega}_{r,\mathbf{q}}$:

$$\lambda_{r,\mathrm{min}} = -\min_\mathbf{q}\left[\frac{1}{\chi^{\omega_0}_{r,\mathbf{q}}}\right] \tag{6.143}$$

As is also discussed in more detail in [219, Chapter 2.4], differentiation of Eq. (4.47) with respect to λ demonstrates that $f_\mathrm{m}(\lambda)$ is strictly monotonically decreasing and therefore has exactly one root in the admissible region. Note that the form of Eq. (6.143) needs to renormalize the largest positive, but crucially, also all negative susceptibilities. Those are present when the DMFT phase transition has already been crossed. It is clear that this form guarantees exactly the desired behavior.
Fig. 6.15a shows the divergences of $\sum_\mathbf{q} \chi^{\lambda_\mathrm{m},\omega_0}_{\mathrm{m},\mathbf{q}}$. This range marks the lower bound of both Eq. (6.140). There is another constraint we typically want to enforce: the causality of the self-energy. As demonstrated in Fig. 6.12, for some datasets and tail-correction schemes, it is necessary to restrict further the value $\lambda_{\mathrm{d,min}}$. This is done by also imposing a causality constraint on the self-energy. The comparison for the two different schemes of determining $\lambda_{r,\mathrm{min}}$ is demonstrated in Fig. 6.15b. Especially in the

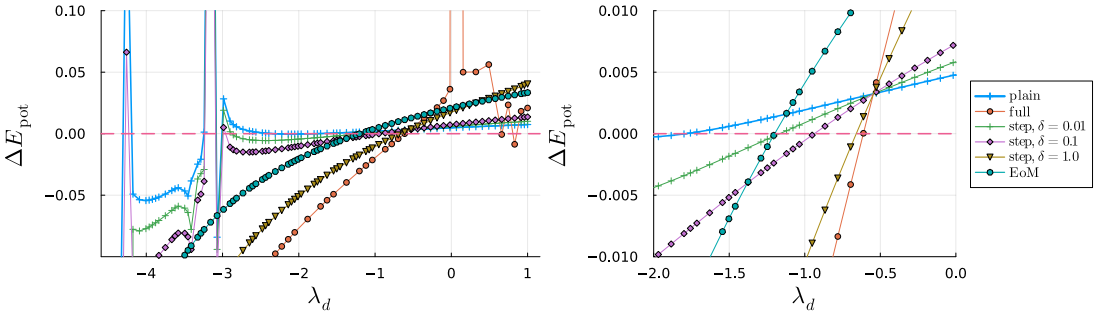

Figure 6.16: $E^{(1)}_\mathrm{pot} - E^{(2)}_\mathrm{pot}$ for different tail-correction methods. Data for 2D simple cubic, $U = 2$, $\beta = 20$, $n \approx 0.83$ (see Sec. 7.2).

left panel of Fig. 6.16, for the plain correction scheme, we see that a typical dataset can produce a very noisy condition curve. Details are discussed in the next paragraph. We observe that the EoM tail correction scheme almost always succeeds in doing so, even in otherwise numerically unstable cases. In Sec. 5.4, we have demonstrated that this does not impact thermodynamical properties severely. Refined (typically extremely numerically costly) computations for the input can, therefore, often be avoided.

Potential Energy Term Eq. (6.141) exhibits the same divergencies as Eq. (6.140), but the right-hand side (for λ_m it is $n(1-n/2)$) is no longer constant, but self-consistently dependent on the left-hand side. Monotonicity and even divergencies from the previous consideration can be different, depending on the choice of tail correction for the self-energy. This is demonstrated in Fig. 6.16 for a particularly badly behaved parameter set. Here, the DMFT vertex was obtained with very aggressive numerical cutoff parameters in the energy differences of the Lehmann representation, and a small number of $\mathbf{k}$ and $\mathbf{q}$ points was chosen to illustrate potential problems with this condition. For many temperatures, it is not feasible to calculate the vertex or Brillouin zone sampling any better, but one can still find suitable algorithms to stabilize a solution.
We employ two different schemes: For the full and EoM tail correction (see Sec. 6.3.4), $\lambda_{r,\mathrm{min}}$ can be obtained as for Eq. (6.140). Here, the stability of the causality condition for the self-energy (see Fig. 6.12 and discussion) leads to a stable single-particle potential energy over a wide (or even full) spectrum of the λ_d parameter. The `ExpStep` method, however, can show singularities of the right-hand side ($G^\lambda \Sigma^\lambda$) in extreme parameter ranges. Specifically, this happens when the self-energy violates the causality condition and the calculation of the lDΓA Green's function from Dyson's equation diverges:

$$\begin{aligned} E^{(1)}_\mathrm{pot} &= \sum_{\nu\mathbf{k}}\left[i\nu_n + \mu - \epsilon_\mathbf{k} - \Sigma^{\lambda,\nu}_\mathbf{k}\right]^{-1}\Sigma^{\lambda,\nu}_\mathbf{k} \\ \Rightarrow \lambda_{\mathrm{d,min},E_\mathrm{pot}} &> \lambda_{\mathrm{d,min}} \exists_n : i\nu_n + \mu - \epsilon_\mathbf{k} \approx \Sigma^{\lambda,\nu}_\mathbf{k} \end{aligned} \tag{6.144}$$

This clearly depends on the self-energy at the lowest Matsubara frequency $\Sigma^{\lambda,i\nu_0}_\mathbf{k}$, which is the first to become positive. We can therefore check this condition to obtain a larger $\lambda_{\mathrm{d,min}}$ and avoid divergencies in the search range.

[7] $1/\chi^{\omega_0}_{\mathbf{q}_\mathrm{C}}(T) \sim T - T_\mathrm{C}$ around the phase transition for mean-field theories such as DMFT.

Of course, one should instead try to obtain a vertex with less numerical instability on a larger frequency grid to avoid unphysical (i.e., non-causal) self-energies. However, for many questions, we are not interested in the spectral properties but in thermodynamic ones. These do not involve self-energy directly but instead are derived quantities governed by normalized susceptibilities. Even for this deliberately problematic input vertex, we observe little change in the difference between the obtained renormalization parameters λ_r, which determine the thermodynamical observables.

Time per Call The last point that separates the three condition equations is the time per function call and the availability of a derivative. This plays a crucial role in the selection of a good algorithm, as one typically has to trade off the order of the method (higher order means faster convergence) against the number of calls to the function. Eq. (6.140) is just a sum over an array and the derivative can be determined analytically. The runtime for the function is negligible, and therefore, high-order methods are a natural choice. We will discuss this below.
Eq. (6.142) still possesses an analytic derivative in μ and has no significant runtime. Here, however, two circumstances make those methods less appealing: (i) memory allocations for the computation of the Green's function from the self-energy (and potentially also the derivative), (ii) a very precise initial guess is available. The chemical potential does not change much from DMFT to lDΓA or between self-consistency cycles of the partially self-consistent lDΓA method. Therefore, even the lowest-order derivative-free methods converge very quickly.
Condition Eq. (6.141) is different from the last two in that a function call can take many core hours (in the case of the partially self-consistent method). To complicate matters, we do not have access to the derivative of the function[8] which excludes many algorithms. Together with the problematic behavior in many parts, due to divergencies or nonmonotonicity, this condition requires the most attention. We will next discuss which algorithms have been tested, are available in the code, and have proven successful for all three conditions.

6.5.3 Root finding Algorithms

The very different requirements for the equations above require us to pick an algorithm based on very specific details. However, at least the *asymptotic efficiency* is one generic measure that is often employed and useful in our context. As a definition of asymptotic efficiency, we follow [296] where it is defined through the order of convergence q and the number of required function calls r:

$$\text{eff} = q^{1/r} \tag{6.145}$$

With r being the number of function calls and the order of convergence q, which is defined for a sequence $(x_n)_{n\in\mathbb{N}}$ with limit x^* and rate of convergence μ as:

$$\lim_{n\to\infty} \frac{\left|x^{(n+1)} - x^*\right|}{\left|x^{(n)} - x^*\right|^q} = \mu \tag{6.146}$$

Newtons Method

Probably the best-known method for determining the root of a nonlinear equation is Newton's method. It constructs the solution by iteratively moving closer to the root from an initial guess x_0 with steps that are obtained from the value of the function at that point divided by the slope.

$$x_{n+1} = x_{n+1} - \frac{f_r(x_{n+1})}{f_r'(x_{n+1})} \tag{6.147}$$

One can see that direction and step length scale as desired by considering all 4 possible cases ($f \gtrless 0$ and $f' \gtrless 0$). More generally, the class of Householder methods of order p [105, Chapter 4.2] is given by:

$$x_{n+1} = x_{n+1} - (p+1)\frac{(1/f)_r^{(p)}(x_n)}{(1/f)_r^{(p-1)}(x_n)} \tag{6.148}$$

This recovers Newton's and Halley's method for $p = 1$ and $p = 2$ and has an order of convergence of $p + 1$, from which we follow an asymptotic efficiency of $p^{1/p}$ [105, Chapter 4.2]. Increasing orders p improve the asymptotic efficiency but also require higher-order derivatives, which, even if these are available, can also decrease numerical stability and lead to more function calls (note the chain rule in Eq. (6.148), which generates the additional terms). The efficiencies for Newton and Halley's method are then $\text{eff}_{\text{Newton}} = 2^{1/2} \approx 1.41$ and $3^{1/3} = 1.44$.
This class of methods is well suited with high order for Eq. (6.142) where little numerical instability is expected and lower orders for Eq. (6.142) which may exhibit some instability. For the latter, we

[8] Automatic differentiation is tough to impossible to implement because one cannot easily build automatic differentiation on top of the existing FFT implementation, which is required for the evaluation of the equation of motion with each λ_d step. This means that each evaluation of a derivative requires at least 2 function evaluations to obtain an approximation of the derivative.

have already arrived at our choice of algorithm. However, the previously discussed divergencies of Eq. (6.141) require a modification to avoid jumping to a solution with $\lambda_\mathrm{m} < \lambda_{\mathrm{m,min}}$.

Bisection and Regula Falsi

Following Eq. (6.143), we want to restrict our search to the open interval of the largest root $(\lambda_\mathrm{min}, \infty)$. This can be achieved directly by the so-called bracketing algorithms. These typically have a lower order of convergence but have a guaranteed search interval. Moreover, some of them require only a single function call per iteration, making them especially well-suited for condition Eq. (6.141).
We first set up an interval $[\lambda_{r,\mathrm{min}}, \lambda_{r,\mathrm{max}}]$, choosing some arbitrary $\lambda_{r,\mathrm{max}}$. In case the interval is non-bracketing, i.e. $f(\lambda_{r,\mathrm{min}})$ and $f(\lambda_{r,\mathrm{max}})$ have the same sign, the $\lambda_{r,\mathrm{max}}$ is increased.
The most straightforward bracketing method is the `bisection` method. Here, one divides the initial interval in half, evaluates the function at that point, and then continues recursively with the interval that fulfills the bracketing condition. With an order of $q = 1$ and a number of function calls $r = 1$ we have $\mathrm{eff} = 1$ for this method.
The bracketing method that turned out to be the best suited for our purpose is the regula falsi or false position method. It is with certainty the oldest method for finding roots to non-linear equations, predating the formalization of algebra, as it has been described in problem 26 on the Rhind Papyrus 1550 BC [127, p. 15]. For a bracket $[a, b]$, the estimation of the root is given by

$$x = \frac{a \cdot f(b) - b \cdot f(a)}{f(b) - f(a)} \tag{6.149}$$

which can then be improved by bisection. The order of this method is $q = \sqrt{2}$ improving the asymptotic efficiency over the bisection method to $\mathrm{eff}_\mathrm{RF} = \sqrt{2}^{1/1} = \sqrt{2}$. The real-world performance can further be improved using different weights for the function calls [74, Table 1]. We found that the Anderson-Björck algorithm [8] works particularly well for our problem, with typically fewer than 15 function calls. This makes the regular falsi the optimal candidate for Eq. (6.141), especially for the partially self-consistent case.

Variable Transform and Reset

Instead of bracketing algorithms, there are also two modifications to Newton's method that enforce the correct root of Eq. (6.140). These are advantageous for Eq. (6.140), where the function call is relatively cheap and the derivative is available. The one we typically refer to as `NewtonTransform` is based on a transformation that has been studied for secular equations [168, 169], where the variable is transformed so that convergence to the correct root is guaranteed, often with increased performance. In order to achieve that, we introduce a transformation function g with the following properties (this is according to [168], where also the rate of convergence, admissible transformations, and their effect have been discussed):

$$\lim_{x\to-\infty} g(x) = \lambda_\mathrm{min}, \qquad \lim_{x\to\infty} g(x) = \infty \tag{6.150}$$

$$\forall x : g'(x) \neq 0 \tag{6.151}$$

$$\forall x : g''(x) \leq 0 \tag{6.152}$$

A natural choice is

$$g(x) = \lambda_\mathrm{min} + \sqrt{x}, \qquad g'(x) = \frac{1}{2\sqrt{x}}, \qquad g''(x) = -\frac{1}{2x^{3/2}} \tag{6.153}$$

Since the root can become complex in cases of numerical unstable solutions, we also often employ $g(x) = \lambda_\mathrm{min} + \frac{1}{x^2}$. Newton's method can still be applied directly on $f(g(x))$, keeping the chain rule in mind:

$$x_{n+1} = x_n - \frac{f(g(x))}{f'(g(x)) \cdot g'(x)} \tag{6.154}$$

Note that the root of f is then given as $g(x^*)$ with x^* determined as a fixed point of the Newton iteration of Eq. (6.154).
This has by far the fastest rate of convergence in our performance testing but does require additional function calls. Therefore, it is typically used for Eq. (6.140). Table 6.2 shows that there is little difference between some bracketing methods and the transformation method. However, empirically, it performs better over a wide range of datasets.
Another method that has been developed for a previous variant of the lDΓA implementation, we will call `NewtonReset` [206]. Here, in each Newton iteration, one checks if $\lambda_r < \lambda_{r,\mathrm{min}}$ and, if so, instead reverts to a bracketing method. This has a slower convergence rate than `NewtonTransform` but typically requires fewer function calls. Table 6.3 gives a comparison for slow function calls, such as Eq. (6.141). Here, we can immediately notice that the total runtime is completely dominated by the number of function calls. The Newton methods could outperform bracketing methods but require at least two additional function calls for each step because the derivative is not available analytically or through

Method	Time (ms)	Function Calls
A42	151	12
NewtonReset	103	24
Bisection	101	32
AlefeldPotraShi	36.5	11
ITP	34.2	19
Ridders	32.0	14
Brent	31.3	9
FalsePosition	27.2	7
Chandrapatla	25.0	12
NewtonTransform	24.0	10

Table 6.2: Comparison of methods by execution time and number of function calls for an intermediate size dataset. Methods implemented in [254] and [275]. Data for λ_m correction. Compared to the λ_d correction we observe that higher order methods with more function calls can outperform lower order methods. The time is given to provide an intuition on the performance impact of the root finding step.

Method	Time (s)	Function Calls
Bisection	4.09	33
AlefeldPotraShi	2.53	20
Ridders	2.25	18
NewtonTransform	2.17	18
Brent	2.15	17
Chandrapatla	2.14	17
A42	2.12	17
NewtonReset	1.89	15
ITP	1.88	15
FalsePosition	1.16	9

Table 6.3: Comparison of methods by execution time and number of function calls for an intermediate size dataset. Data for λ_d correction. Methods implemented in [254] and [275]. The time serves (i) as a reference for the order magnitude for the λ_d-correction with a $\mathbf{k}$-sampling of 400 points on a 300^3 Matsubara frequency grid and (ii) as a relative comparison between methods.

automatic differentiation, as discussed before.
Future extensions of the method may want to adopt more sophisticated bracketing methods for the Halley and Newton methods, presented in [4]. The algorithms presented here are sufficient to make the λ corrections (including the partially self-consistent version) negligible in computational costs compared to the inversions involved in the solution for the BSE.

6.5.4 Implementation Details and Usable Ranges

We will present some auxiliary considerations that are necessary for the lDΓA method to work properly; more details can be found in the documentation for the code [254].

Handling of Improved Summations

All data shown in this thesis is computed for shifted and reduced Matsubara grids. How these can be obtained is discussed in Sec. 6.4, Sec. 6.8.2, and the appendix of Sec. 7.1. After reading the input, a helper `struct` is initialized by the code described in Sec. 6.8.6. This deals with all quantities involved in improved summation formulas and keeps asymptotic quantities and caches (used, for example, in the improvement of $\lambda^{\nu\omega}_{0,\mathbf{q}}$) allocated. The summations of $\mathbf{k}$ and frequency axis are then carried out using specialized functions that take the high-frequency expansion into account automatically.

Usable Ranges

In order to exclude data from insufficiently sized fermionic Matsubara grids and allow computations without improved summations, we also compute usable intervals of $i\omega_m$ frequencies for physical susceptibilities. This interval is defined in such a way that $\sum_\mathbf{q} \chi^\omega_{r,\mathbf{q}}$ is positive and monotonically decreasing from $i\omega_0$ (see also Fig. 6.8). The frequency range is then adjusted internally to a suitable range to avoid unphysical cancellations in the equation of motion. Note that this algorithm must take the divergence (and subsequently negative) susceptibility at second-order phase transitions at ω_0 into account and not treat these negative values as the end of the usable ω_m range.
The computation of the SDE presents another pitfall regarding the frequency ranges. The previously discussed shift in the fermionic Matsubara frequencies leads to a ν dependence of the ω range. Specifically for $\nu > \nu_\mathrm{max}/2$ we have less ω frequencies available than below. This has a noticeable effect on the tail behavior, which then starts to deviate from the asymptotic behavior. We solve this issue by defining a cutoff ν-frequency that is set to $\omega_m/2$ for shifted grids. Starting from that point, we use the local tail of the impurity self-energy. The partially self-consistent lDΓA method requires repeated evaluation of the equation of motion and would otherwise reduce the length of the usable ν range to 0.

Sanity checks

Because the two-particle Green's function is very costly to obtain, approximations are often made. Most prominently, there is a cutoff for small energy differences in the Lehmann representation when using

ED and small frequency grids. This can lead to problems that are sometimes hard to detect. To help identify problematic input data or program settings, a number of "sanity checks" are employed. The local full vertex $F_r^{\nu\nu'\omega}$ and irreducible vertex $\Gamma_r^{\nu\nu'\omega}$ can be checked manually for the correct asymptotic behavior according to [256]. This often has to be done by hand as there is no clear threshold to which contributions have to be converged, how large the "inner region" is, and how many deviations affect the lDΓA calculations. The code responsible for asymptotic summations, Sec. 6.8.6, provides a notebook with a summary of all values that can be checked. However, most of the time, the derived quantities are sufficient to exclude bad data.
Because the impurity solver constructs an exact solution of the AIM, we know that the equation of motion must be fulfilled for the input data. We can, therefore, give the discrepancy between the impurity self-energy and the self-energy obtained from the two-particle Green's function as a measure for the error in the full vertex:

$$\Delta\Sigma_{\text{imp}} = \left| \sum_{\nu} \left[\Sigma_{\text{H}} - U \sum_{\nu\nu'} F_{\uparrow\downarrow}^{\nu\nu'\omega} G_{\text{imp}}^{\nu'} G_{\text{imp}}^{\omega+\nu'} G_{\text{imp}}^{\omega+\nu} \right] - \Sigma_{\text{imp}}^{\nu} \right| \tag{6.155}$$

However, this does not reflect possible cut-off effects that are amplified through the inversion of the local and non-local BSE, which is used to obtain the irreducible vertices $\Gamma_r^{\nu\nu'\omega}$. This effect can usually only be observed from the physical susceptibility (obtained from Eq. (2.257)) by checking the magnitude of the violation of Eq. (4.40).

$$\Delta\chi_r = \left| \sum_{\omega\neq 0} \chi_{r,\mathbf{q}=\mathbf{0}}^{\omega} \right| \tag{6.156}$$

6.6 Exact Diagonalization

The exact diagonalization method has many shortcomings compared to tailored approaches for certain physical limits or more accurate Monte Carlo methods, but it does excel in terms of simplicity and numerical stability. This is the reason why it is still of great use when numerically stable observables in settings with small enough Hilbert spaces are required. This was, for example, the case for the Green's function inputs of lDΓA in this Thesis. Although somewhat well known[9] and easy to derive, the following contains a very brief derivation of the formulas for the 1 and 2-particle Green's function.

6.6.1 Lehmann Representation of 1 and 2-particle Green's function

1 particle Green's function

We have already derived the Lehmann representation of the single-particle Green's function in Sec. 2.

$$G_{\sigma\mathbf{k}}^{\text{R/A}}(t) = -\frac{i}{Z}\Theta(\pm t) \sum_{nm} \left(e^{-\beta E_n} + e^{-\beta E_m} \right) e^{i(E_n - E_m)t} |\langle n| \hat{c}_{\sigma\mathbf{k}} |m\rangle|^2 \tag{6.157}$$

$$G_{\sigma\mathbf{k}}(\tau) = \frac{1}{Z} \sum_{nm} \left(e^{-\beta E_n} + e^{-\beta E_m} \right) e^{(E_n - E_m)\tau} |\langle n| \hat{c}_{\sigma\mathbf{k}} |m\rangle|^2 \tag{6.158}$$

$$G_{\sigma\mathbf{k}}^{\text{R/A},\nu} = \frac{1}{Z} \left(e^{-\beta E_n} + e^{-\beta E_m} \right) \frac{|\langle n| \hat{c}_{\sigma\mathbf{k}} |m\rangle|^2}{\nu \pm i\eta + E_n - E_m} \tag{6.159}$$

$$G_{\sigma\mathbf{k}}^{\nu} = \frac{1}{Z} \left(e^{-\beta E_n} + e^{-\beta E_m} \right) \frac{|\langle n| \hat{c}_{\sigma\mathbf{k}} |m\rangle|^2}{i\nu_n + E_n - E_m} \tag{6.160}$$

Note that the Wick-rotated version of this derivation (i.e. finite temperature) also has a factor of i missing in the exponent, according to Eq. (2.57) and that the energy levels are shifted by $-\mu n$, as before. This expression is algorithmically evaluated in 3 steps: (1) definition of a Fock basis and corresponding basis states in terms of actual vectors, (2) diagonalization of the Hamiltonian in this basis, (3) computation of the overlaps. I will give a very brief overview of how the `jED.jl` code accomplishes these steps as an example of how to obtain a solution concretely.

Step (1) For the N-site Anderson impurity model a Boolean vector of length $2N$ is defined, the first N entries store `True` if a $\sigma =\uparrow$ electron is present at that site; the second half of the vector does the same for $\sigma =\downarrow$ (compare file `States.jl`). The `basis` contains a set of all possible combinations (i.e. 4^N vectors).

Step (2) The eigenspace is constructed by explicitly iterating through all possible transitions $H_{ij} = \langle j| \hat{H} |i\rangle$ with $|i\rangle, |j\rangle \in$ `basis`. Typically, one segments the basis into blocks of good quantum numbers first. For example, if the Hamiltonian is particle number conserving, only blocks of equal particle numbers need to be considered (and those can decompose again). After constructing the (blocks of the) Hamiltonian as an explicit matrix H_{ij} in this way, a diagonalization routine is called to obtain eigenvectors and eigenvalues (compare file `Eigenspace.jl`).

[9] At least in the case of the 2-particle Green's function, the Lehmann representation is still subject of current research [90, 232].

Step (3) The list of overlaps is constructed similarly to step (2), although this is now done in the eigenspace (compare `_overlap_cdagger_ev!`) and finally, one iterates over the eigen energies and desired number of frequencies.

2 particle Green's function

The procedure above is similar for arbitrary combinations of creation and annihilation operators. However, the number of possible time-ordering combinations that we were able to circumvent in the single-particle case grows faster than exponentially. We will go through the derivation of one term as an example and then give the full expression for example, derived in the documentation of this code [241]. We first note that of the 4 spin indices only 2 survive (see Sec. 2.7.2) and then start with Sec. 2.1.2.3 written in a more compact form of $\Theta_{1>2>3} \coloneqq \Theta(\tau_1-\tau_2)\Theta(\tau_2-\tau_3)$ furthermore, we used $E_{n,m} \coloneqq E_n - E_m$ and $l_{mnop}(1,2,3) \coloneqq e^{-\beta E_m} e^{\tau_1 E_{m,n}} e^{\tau_2 E_{n,o}} e^{\tau_3 E_{o,p}}$ (compare Eq. (2.7.1.1)).

$$f^{\nu\nu'\omega}_{\mathrm{ph},\alpha_1\dots\alpha_4} = \int \mathrm{d}\tau_1\tau_2\tau_3 e^{i(\omega+\nu)\tau_1} e^{i\nu'0} e^{-i\nu\tau_1'} e^{-i(\omega+\nu')\tau_2'} f_{\mathrm{ph},\alpha_1\dots\alpha_2'}(\tau_1,0;\tau_1',\tau_2')$$

We now insert a full basis, as before in the one-particle case:

$$\begin{aligned}
G_{\uparrow\downarrow}(\tau_1,0;\tau_2,\tau_3) = \sum_{mnop} e^{-\beta E_{n_1}} \Big[& \\
& \Theta_{1>2>3} l_{mnop} \langle m|\hat{c}^\dagger_\sigma(\tau_1)|n\rangle\langle n|\hat{c}_{\overline{\sigma}}(\tau_2)|o\rangle\langle o|\hat{c}_{\overline{\sigma}}(\tau_3)|p\rangle\langle p|\hat{c}^\dagger_\sigma(0)|m\rangle \\
& + \Theta_{1>3>2} l_{mnop} \langle m|\hat{c}^\dagger_\sigma(\tau_1)|n\rangle\langle n|\hat{c}_{\overline{\sigma}}(\tau_3)|o\rangle\langle o|\hat{c}_{\overline{\sigma}}(\tau_2)|p\rangle\langle p|\hat{c}^\dagger_\sigma(0)|m\rangle \\
& - \Theta_{2>1>3} l_{mnop} \langle m|\hat{c}_{\overline{\sigma}}(\tau_2)|n\rangle\langle n|\hat{c}^\dagger_\sigma(\tau_1)|o\rangle\langle o|\hat{c}_{\overline{\sigma}}(\tau_3)|p\rangle\langle p|\hat{c}^\dagger_\sigma(0)|m\rangle \\
& + \Theta_{2>3>1} l_{mnop} \langle m|\hat{c}_{\overline{\sigma}}(\tau_2)|n\rangle\langle n|\hat{c}_{\overline{\sigma}}(\tau_3)|o\rangle\langle o|\hat{c}^\dagger_\sigma(\tau_1)|p\rangle\langle p|\hat{c}^\dagger_\sigma(0)|m\rangle \\
& - \Theta_{3>1>2} l_{mnop} \langle m|\hat{c}_{\overline{\sigma}}(\tau_3)|n\rangle\langle n|\hat{c}^\dagger_\sigma(\tau_1)|o\rangle\langle o|\hat{c}_{\overline{\sigma}}(\tau_2)|p\rangle\langle p|\hat{c}^\dagger_\sigma(0)|m\rangle \\
& + \Theta_{3>2>1} l_{mnop} \langle m|\hat{c}_{\overline{\sigma}}(\tau_3)|n\rangle\langle n|\hat{c}_{\overline{\sigma}}(\tau_2)|o\rangle\langle o|\hat{c}^\dagger_\sigma(\tau_1)|p\rangle\langle p|\hat{c}^\dagger_\sigma(0)|m\rangle \Big]
\end{aligned}$$

We obtain the Matsubara frequency representation by Fourier transform. The frequency arguments f_1, f_2, f_3 are arbitrary and a matter of convention, see Sec. 2.7.2.1 and Sec. 2.7.2. Straight forward calculation yields [241]:

$$\begin{aligned}
\tilde{l}_{mnop}(f_1,f_2,f_3) &\coloneqq \int \mathrm{d}\tau_3 e^{if_1\tau_3} \int \mathrm{d}\tau_2 e^{if_2\tau_2} \int \mathrm{d}\tau_1 e^{if_1\tau_1} \Theta_{1>2>3} l_{mnop}(1,2,3) \\
&= \frac{-1}{f_1+E_{m,n}} \Big[\frac{1}{f_2+E_{n,o}} \Big(\frac{e^{-\beta E_o}+e^{-\beta E_p}}{f_3+E_{o,p}} + \frac{e^{-\beta E_n}-e^{-\beta E_p}}{f_2+f_3+E_{n,p}} \Big) \\
&\quad - \frac{1}{f_1+f_2+E_{m,o}} \Big(\frac{e^{-\beta E_o}+e^{-\beta E_p}}{f_3+E_{o,p}} - \frac{e^{-\beta E_m}+e^{-\beta E_p}}{f_1+f_2+f_3+E_{m,p}} \Big) \Big]
\end{aligned} \tag{6.161}$$

The exchange of the frequency arguments then leads to the following representation.

$$\begin{aligned}
G^{\nu\nu'\omega}_{\uparrow\downarrow} = \sum_{mnop} \Big[& \\
& \tilde{l}_{mnop}(\omega+\nu,-\nu,\omega+\nu') \langle m|\hat{c}^\dagger_\sigma(\tau_1)|n\rangle\langle n|\hat{c}_{\overline{\sigma}}(\tau_2)|o\rangle\langle o|\hat{c}_{\overline{\sigma}}(\tau_3)|p\rangle\langle p|\hat{c}^\dagger_\sigma(0)|m\rangle && (6.162) \\
& + \tilde{l}_{mnop}(\omega+\nu,\omega+\nu',-\nu) \langle m|\hat{c}^\dagger_\sigma(\tau_1)|n\rangle\langle n|\hat{c}_{\overline{\sigma}}(\tau_3)|o\rangle\langle o|\hat{c}_{\overline{\sigma}}(\tau_2)|p\rangle\langle p|\hat{c}^\dagger_\sigma(0)|m\rangle && (6.163) \\
& - \tilde{l}_{mnop}(-\nu,\omega+\nu,\omega+\nu') \langle m|\hat{c}_{\overline{\sigma}}(\tau_2)|n\rangle\langle n|\hat{c}^\dagger_\sigma(\tau_1)|o\rangle\langle o|\hat{c}_{\overline{\sigma}}(\tau_3)|p\rangle\langle p|\hat{c}^\dagger_\sigma(0)|m\rangle && (6.164) \\
& + \tilde{l}_{mnop}(-\nu,\omega+\nu',\omega+\nu) \langle m|\hat{c}_{\overline{\sigma}}(\tau_2)|n\rangle\langle n|\hat{c}_{\overline{\sigma}}(\tau_3)|o\rangle\langle o|\hat{c}^\dagger_\sigma(\tau_1)|p\rangle\langle p|\hat{c}^\dagger_\sigma(0)|m\rangle && (6.165) \\
& - \tilde{l}_{mnop}(\omega+\nu',\omega+\nu,-\nu) \langle m|\hat{c}_{\overline{\sigma}}(\tau_3)|n\rangle\langle n|\hat{c}^\dagger_\sigma(\tau_1)|o\rangle\langle o|\hat{c}_{\overline{\sigma}}(\tau_2)|p\rangle\langle p|\hat{c}^\dagger_\sigma(0)|m\rangle && (6.166) \\
& + \tilde{l}_{mnop}(\omega+\nu',-\nu,\omega+\nu) \langle m|\hat{c}_{\overline{\sigma}}(\tau_3)|n\rangle\langle n|\hat{c}_{\overline{\sigma}}(\tau_2)|o\rangle\langle o|\hat{c}^\dagger_\sigma(\tau_1)|p\rangle\langle p|\hat{c}^\dagger_\sigma(0)|m\rangle \Big] && (6.167)
\end{aligned}$$

The frequency arguments can be obtained from our definition in Eq. (2.7.1.1), i.e. $f_1 = \nu_n + \omega_m$, $f_2 = -\nu_n$ and $f_3 = -\omega_m + \nu'_n$. Further considerations in equilibrium let us use symmetry to avoid computation of some terms [241]; moreover, we can avoid the computation of some $\tilde{l}_{mnop}(1,2,3)$ by introducing cutoff parameters for the exponents, disregarding summands. Nonetheless, the number of summands grows very quickly, and one is limited to 4 bath sites for reasonable $\sim 300^3$ frequency grids and 5 bath sites for smaller 50^3 grids. We found these parameters to be sufficiently close to CTQMC calculations in all investigated models and parameter ranges.

6.6.2 Parameter Fitting Details

The choice of algorithm and cost function for the fitting of bath parameters has an immense influence on the quality of the 2-particle Green's functions. I will, therefore, give a brief overview of the setup that ended up producing reliable vertices.

Even though CTQMC has become the state-of-the-art algorithm for solving the impurity problem in DMFT because it is able to produce an unbiased solution for the infinite bath-site AIM, there are advantages of using ED, especially in method development. Importantly for our case, it produces exact (in the sense of a solution for the finite bath site AIM) values without Monte Carlo noise. Additionally, vertices over large frequency grids can be obtained in a very reasonable time by trading off accuracy through a lower number of bath sites or cutoffs in the Lehmann representation (see last section). However, the greatly improved performance is brought about by several free numerical parameters that need to be adjusted correctly.

Fits

Our fit method for the l bath parameters uses the local Green's function (for CTQMC, the hybridization function is often preferable in order to suppress noise).

$$\mathscr{G}_0^\nu \stackrel{!}{=} \left[\sum_{\mathbf{k}} \left(i\nu_n + \mu - \epsilon_{\mathbf{k}} - \Sigma^\nu\right)\right]^{-1} + \Sigma^\nu \tag{6.168}$$

$$\mathscr{G}_0^\nu = \frac{1}{i\nu_n + \mu - \sum_l \frac{V_l^2}{i\nu_n - \epsilon_l}} \tag{6.169}$$

We found that the Broyden-Fletcher-Goldfarb-Shanno (BFGS) yielded the best results [71]. As a gradient-based method, one has to take care to use a reasonable initial guess, often based on the atomic limit Sec. 3.3.1. Direct methods such as least squares fit have been outperformed by this method in our tests over a large range of lattice types, temperatures, and interaction strengths.
Another numerical degree of freedom is the choice of the distance function. Finding one for the specific application is crucial, and the ED code written for this thesis contains a benchmark script comparing different ones. After thorough testing and advice from H. Kitatani, we found that the following distance and transformation functions yielded the best results at low temperatures:

$$\left|f(G_0^\nu, i\nu_n) - f(\mathscr{G}_0^\nu, i\nu_n)\right|^2 \stackrel{!}{=} 0 \tag{6.170}$$

$$f(G^\nu, \nu) = \frac{1}{G^\nu \cdot \sqrt{\nu}} \tag{6.171}$$

For more details, see also Sec. 6.8.3 and the examples in the referred code.

Consistency Tests

We employ multiple checks for the validity of data, 4 of which are done on the single particle level and 3 on the two-particle level. On the single particle level, we check that all bath sites contribute, and the correct high-frequency tail is obtained by checking the following values.

$$\sum_l V_l^2 \stackrel{!}{=} \frac{1}{4} \tag{6.172}$$

$$\min V_l \stackrel{!}{>} \epsilon_{\text{cut}} \tag{6.173}$$

$$\min |\epsilon_l - \epsilon_{l'}| \stackrel{!}{>} \epsilon_{\text{cut}} \tag{6.174}$$

With $\epsilon_{\text{cut}} \sim 0.01$.
These tests give a good indication if the DMFT and fitting routine have been successful and can, of course, also be employed when calculating a solution with CTQMC and then fitting an ED bath to obtain the 2 particle Green's function and physical susceptibilities[10] there.
Checks on the 2 particle level are:

- Calculation of the local equation of motion
- Direct asymptotics checks
- Violation of the f-sum rule.

Since DMFT yields the exact solution of the (finite bath site) AIM, the local equation of motion must hold.

$$G^{\nu'} G^{\omega+\nu'} G^{\omega+\nu} F_{\uparrow\downarrow}^{\nu\nu'\omega} = \Sigma_{\text{imp}}^\nu \tag{6.175}$$

For valid solutions this holds to around $0.1\% to 5\%$ accuracy at the lowest frequencies.
The check of asymptotics is done using the known high-frequency behavior of $\Gamma_r^{\nu\nu'\omega}$ and $F_r^{\nu\nu'\omega}$, see Sec. 6.2 and [256].
The violation of the f-sum rule can be checked by comparing the following condition [277]

$$\sum_{\omega \neq 0} \left|\chi_{r,\mathbf{q}=\mathbf{0}}^\omega\right| < \epsilon_{\text{cut}} \tag{6.176}$$

[10] Physical susceptibilities are needed for our improved summation formulas in Sec. 6.3. Equal time operators are notoriously difficult to obtain from Monte Carlo samplers.

The last condition is also dependent on the choice of the **k**-sampling, and a strong violation may still lead to valid results, but it is an indication of problematic parameter settings or corrupt input data.

6.7 Compressed Representation of Single-Particle Green's Functions

In this sub-project, we trained a neural network to learn some structure of the LWf, discussed in Sec. 4.3. While not fully successful as of the writing of this thesis, two unrelated but very promising partial results were obtained from this project. Some of the code for this project was developed with help from Daniel Springer and Marco Knipfer.

6.7.1 Neural Networks

Machine learning, in general, and neural networks especially, have become very popular in almost all fields of research in the past years. This field is by far too vast and too far out of the scope of this thesis that we can hope to give an appropriate introduction here [32, 82]. Therefore, we focus on two of the simplest network types and investigate their applicability to the Green's function methods discussed in this thesis. Specifically, we will use feedforward neural networks and autoencoders. Feedforward networks, while algorithmically just a sequence of linear algebra operations, can be thought of as layers of neurons v_i that are activated with a (non-linear) activation function f, via weighted edges e_{ij} from other neurons $f(e_{ij})$. This is implemented as repeated matrix-vector multiplications with each resulting vector modified by the activation function f (typically some Fermi-function-like step function, e.g. tanh) [32, Sec. 6.3]:

$$v^{(l+1)} = f^{(l)}(M^{(l)}v^{(l)} + b^{(l)}) \tag{6.177}$$

The index l enumerates the layers of the network, and $b^{(l)}$ is a vector of bias weights in each layer. The entries of the matrix $M^{(l)}$ and the bias vector $b^{(l)}$ are called parameters of the model and need to be learned from training data. This is done by supplying known input-output pairs $(\mathbf{x}, \mathbf{y})$. Training with such labeled data is called supervised learning. The prediction of a network with L layers, $\hat{\mathbf{y}} \coloneqq v^{(L)}$, is then compared to the known label, yielding an error under a distance function (called the loss function) d:

$$E(\mathbf{x}) = \mathrm{dist}(\hat{\mathbf{y}}, \mathbf{y}) \tag{6.178}$$

Note that we distinguish predicted values from labeled (i.e. given during training) data with a hat. The parameters of the network can be learned using backpropagation [32, Chapter 8], which uses the gradient of the error to tune all parameters of the network.
Besides the parameters, there are several undefined quantities, such as the choice of loss function, non-linear activation function, and so on. These are called hyperparameters and are also subject to tuning for a given use case. These, however, are typically set explicitly by the programmer after performing experiments with the datasets. We will also employ autoencoders, which work exactly as feedforward networks, by having size-restricted layers, i.e. $M^{(l)} \in \mathbb{R}^{n\times m}$ with $n < m$ for the first few layers and $n > m$ after that. The innermost layer with the fewest nodes encodes data of the so-called latent space. Here, the essential information of the data is contained in a compressed representation. In order to train autoencoders, one sets the labels equal to the input $(\mathbf{x}, \mathbf{y}) \to (\mathbf{x}, \mathbf{x})$, where the difference between predicted output $E = \mathrm{dist}(\mathbf{x}, \hat{\mathbf{y}})$ and input data is called reconstruction error.

6.7.2 Connection to the Luttinger Ward Functional

The aim of this project is to learn the structure of the LWf by obtaining data from an exactly solvable model, the AIM and use the identity Eq. (4.18), $\frac{\delta\Phi[G]}{\delta G(1;1')} = \Sigma(1';1)$. Two open questions need to be answered before this project can be concluded: (i) By providing pairs of G and Σ, some relationship between both is learned. However, at the time of writing, it needs to be clarified how the functional derivative should be formulated and built into the machine learning apparatus; (ii) We currently employ an equilibrium ED solver. This means $1 \equiv 1'$, which clearly makes it impossible to learn a structure that would be able to generate the two-particle irreducible vertex $\Gamma^{\nu\nu'\omega}$ (even though $\Gamma^{\nu\nu'\omega_0}$ could be learned).
Nonetheless, approaching a model that is able to learn some relationship between the Green's function and self-energy of a system with some residual universality from the LWf would certainly be valuable. Moreover, we were able to achieve two important results, purely on the level of Green's functions as a partial success of this project, which will be discussed below.

6.7.3 Setup and Hyperparameters

Because the rest of this thesis is focused on physics, we give a brief introduction to common terminology and our algorithmic setup that is typically omitted in publications. For the current training runs, we chose a 2 bath site AIM as training data with variable hybridization and onsite energies V_l and ϵ_l and a range of chemical potentials μ. The interaction strength U has been fixed since it is also an external parameter to the LWf; the temperature has been fixed in order to avoid different spacings of the Matsubara frequencies ν_n. Furthermore, the dataset has been pruned not to include extreme electron dopings, with $n \notin [0.1, 0.9]$. These restrictions may seem severe, but many of them, especially the number of bath sites and the temperature, have been relaxed in tests without problems for the model, but hugely increased computational and memory demands. In order to validate the applicability

of this model, these tests need to be systematically investigated.
The current neural network architectures employ automatic differentiation for the backpropagation algorithm that updates the weights. These algorithms typically are not implemented for complex numbers, and we therefore prepare the input data as follows:

$$\mathtt{x} = [n, \beta, \mathrm{Re}G^{\nu}, \mathrm{Im}G^{\nu}] \tag{6.179}$$

6.7.4 Hyperparameters

We investigated a number of commonly used hyperparameters for different network setups. The following gives a short introduction to their generally expected effect on networks and their specific impact on our models.

Test and Validation Data, Epochs For supervised learning, the full dataset is split into three parts: training, test, and validation sets. The training set is used to train the network. After all training data has been seen, the performance of the model is tested on the validation set. Here, the optimizer can use the loss on this unseen data to tune hyperparameters like the learning rate. One such cycle is called an epoch. The test set is withheld from training and used to judge the final performance of the model. It is important not to mix any information from the test set into the training process to detect potential overfitting and measure the ability of the model to generalize to unseen data. One can also decide to segment certain classes of inputs (for example, Green's functions belonging to insulators) in this set.

Optimizer The optimizer governs the minimization of the loss function. They find a (local) optimum (or even just a saddle point), similar to the fitting procedures discussed in the previous sections for the bath parameter fit in ED; however, in much higher-dimensional space. Because of the high-dimensional space, many traditional optimization methods are ineffective. We employ a version of gradient descent that uses an adaptive learning rate. In the first algorithm of this class we are using, `AdaGrad` [59], the weights $w_i^{(\tau)}$ at epoch τ are updated using a learning rate η (an important hyperparameter for the training) and a stability parameter δ [32, p. 7.3.3]:

$$r_i^{(\tau)} = r_i^{(\tau-1)} + \left(\partial_{w_i} E(\mathbf{w})\right)^2 \tag{6.180}$$

$$w_i^{(\tau)} = w_i^{(\tau-1)} - \frac{\eta}{\sqrt{r_i^{(\tau)}} + \delta} \left(\partial_{w_i} E(\mathbf{w})\right) \tag{6.181}$$

A further development was `RMSProp` (Root-Mean-Square propagation) [100] and `Adam` (adaptive moments) [130]. We tested `Adam` and a plain version of `SGD` (Stochastic Gradient Descent). Adam is known to converge much faster but seems to prefer steep minima, sometimes leading to worse generalization performance [299]. `SGD`, however, requires much more fine-tuning and practical experience with the training of models. Since we did not manage to find hyperparameters for `SGD` rivaling the performance of `Adam`, all training runs, except these tests, were performed with the latter.

Dropout Dropouts (statistically ignoring individual neurons) lead to fewer co-adaptations[11] between neighboring neurons, resulting in networks that generalize better and are, therefore, used to regularize overfitting. Our experiments with dropout layers in hidden layers yielded smoother functions in prediction. This was especially noticeable in the test runs for the denoising network. The range of dropout percentages we found to work the best in our case was between 10% and 40%.
However, dropouts in the input layer result in substantially worse models (not even the general shape of the self-energy is captured). These results, for now, do not fall in line with the common wisdom that dropouts in the input layers of autoencoders lead to a denoising behavior. Consequently, dropouts will have to be revisited in future extensions of this work. We would expect that the optimizer would push the network in a direction where co-adaptations responsible for high-frequency behavior (manifesting as noise in the self-energy) are eliminated.

Activation Function Not many tests have been done using this hyperparameter with different choices. Initial scans over the typically used ones did not make any significant difference. We therefore stuck with `ReLU`:

$$\mathrm{ReLU}(x) = \max(0, x) \tag{6.182}$$

One has to keep in mind that this activation function is not self-normalizing, so normalization layers should be tested, especially in deeper networks. It is known that increasingly deep neural networks run into the problem that some weights grow disproportional to others, leading to diminishing returns when more layers are added. This can be partially counteracted by normalization layers or self-normalizing activation functions [137].

[11] Co-adaptations are highly correlated weights, i.e. there is less information stored in the set of co-adapted neurons than in independent ones.

Batch Size Grouping multiple instances of training data results in much faster training and can smooth out the gradient while learning. However, with increasing batch size, the network parameters are updated less frequently, and the training time typically increases. Especially for our training setup with an AIM with only 2 bath sites, we are working with (relatively) small datasets and networks. We did, however, perform several experiments with different batch sizes between 4 and 4028 and observed that training performance improved when larger batch sizes were chosen for the initial epochs of the training process, where smoother gradients are especially useful and then gradually reduced. The batch size obviously depends on the dataset size and type of data. In our case, 32 to 128 seemed to give the best results for `Set1` results. Fewer instances result in extremely long training due to the under-utilization of GPU and difficulty determining the learning rate of the optimizer gradient. The batch size parameter needs to be adjusted for each new training set and GPU memory.

Normalization Normalization layers can improve performance by rescaling data between layers' outputs along different ranks of the tensors: $\tilde{x} = \frac{x-\mu_x}{\sigma_x}$. This form is only practicable for input data. Within the network, the normalization is typically done over a batch or layer. Accordingly, these are called `BatchNorm`, `InstanceNorm` or `LayerNorm`) [32, p. 7.4.1]. In our experiments, we found that for very few layers ($N_L < 10$), normalization does not make any difference. With more layers, the loss can diverge without batch normalization layers. However, for the small models discussed here, we were able to obtain results avoiding this additional dimension in the hyperparameter space.

Loss Function As a choice for the loss function, we investigated the commonly used mean squared error $\texttt{MSE} = \frac{1}{n}\sum_n (y-\hat{y})^2$ and a scaled version that attempts to bring the real and imaginary parts to a similar scale:

$$\mathbf{s}_{\mathrm{re}} = \frac{\max(\mathbf{y}_{\mathrm{re}})}{\max(\mathbf{y}_{\mathrm{re}}) - \min(\mathbf{y}_{\mathrm{re}})} \tag{6.183}$$

$$\mathbf{s}_{\mathrm{im}} = \frac{\max(\mathbf{y}_{\mathrm{im}})}{\max(\mathbf{y}_{\mathrm{im}}) - \min(\mathbf{y}_{\mathrm{im}})} \tag{6.184}$$

$$\texttt{scaledMSE}(\hat{\mathbf{y}}, \mathbf{y}) = \mathrm{mean}(\mathbf{s}_{\mathrm{re}}(\hat{\mathbf{y}}_{\mathrm{re}} - \mathbf{y}_{\mathrm{re}})^2) + \mathrm{mean}(\mathbf{s}_{\mathrm{im}}(\hat{\mathbf{y}}_{\mathrm{im}} - \mathbf{y}_{\mathrm{im}})^2) \tag{6.185}$$

The `scaledMSE` did improve the predictive power in some test cases but did not yield as consistently good results as `MSE`. Especially for the autoencoder setups, the scaled loss did not perform well and was therefore not used. However, one has to keep in mind that datasets over a wider range of physical parameters (temperature β and interaction strength U) will lead to more variation in the input, and the `scaledMSE` could be more stable in these cases.
We have been able to converge all networks presented here to a degree where further improvements in the loss function seem unnecessary. However, for future extensions, one should also keep in mind that the lowest frequencies of the self-energy are the most important ones for the determination of physical properties on the real axis. One should, therefore, keep the distance functions discussed in Sec. 6.6.2 as an option for the loss function in mind.

6.7.5 Training Data and Setup

The following datasets have been used in training. For all training, a 80/20 split between the training and validation set has been performed. The order of the training set was randomized before storage, but not the split, in order to prevent leakage of information with repeated training. A further dataset (`Set0`) has been generated exclusively for testing, with little to no overlap with the other datasets.

`Set1`: Set 1 is a 2 bath site Anderson model, i.e., the Weiss Green's function is defined as:

$$\mathcal{G}_0^{\nu} = \left(\nu + \mu - \sum_l \frac{V_l^2}{\nu - \epsilon_l}\right)^{-1} \tag{6.186}$$

With the following parameter range: U: fixed at 1.0; β: fixed at 30; μ: 20 samples, linearly spaced between $-U$ and $2U$, V_l: 30 samples, linearly spaced between 0 and 1; ϵ_l: 30 samples, linearly spaced between $-2U$ and $2U$. Samples with an electron density smaller than 0.1 or larger than 1.9 have been removed from the dataset. This leads to 2.7 million data points for 2 bath sites. This set has been generated for 3 and 4 bath sites, with the latter having fewer sampling points for the Anderson parameters.

`Set2`: After the initial training on 2 bath sites, an extension to 3 is the next step in order to verify that the model extends to more realistic physics. While the test with predictions of models exclusively trained on 2 for 3 and 4 bath sites test data (Fig. 6.18a and Fig. 6.18b) already indicates that the sparse encoding remains in good agreement, we also prepared a dataset with 210 million data points. Here, 35 samples for each bath level ϵ_l and hopping V_l and 20 samples for μ were taken for 3 bath levels. Again, the density was pruned to $n \in [0.1, 0.9]$ (by removing all samples that have fillings outside this range after the dataset has been generated).

Set3: This dataset was generated for testing and has not yet been used in training. It consists of approximately $N_\mathrm{S} \approx 10.000.000$ sample points ($\sim$ 30GB) in the range of `Set1` with $s = \left\lfloor N_\mathrm{S}^{\frac{1}{2N_\mathrm{B}+1}} \right\rfloor$ samples for each bath level ϵ_l, hopping V_l and μ. All sample points are smeared out by a Gaussian distribution with $x_i = x_i + \mathcal{N}(x_i, \sigma_p^2)$, where we chose σ_p to be the mean distance between samples of the non-noisy parameter (ϵ_l, V_l, μ). Extreme densities are pruned, as before. This dataset has a significantly improved coverage of the space of possible Green's functions for this model. However, due to its significantly larger size and lack of reproducibility, we did not use this dataset in training.

6.7.6 Outline of Models

In order to facilitate more consistent learning of the properties of the LWf, the overall architecture of this project is as follows: Two autoencoders are trained. One for the Green's function and one for the self-energy. These pre-trained networks are then used in conjunction with a third network, connecting the latent spaces of both, an illustration is given in Fig. 6.21. This setup is meant to ensure that the mapping between Green's function and self-energy is learned just from the relevant data, possibly using different network architectures. This approach is compared to a baseline mapping achieved by a dense feedforward network directly mapping the Green's function to the self-energy. We will, therefore, now discuss three different architectures: (i) autoencoders and their capabilities to encode Green's functions and self-energies; (ii) fully connected networks mapping Green's functions to self-energies; (iii) a combined architecture that maps Green's functions to self-energies using a compressed representation.

6.7.7 Autoencoders

The autoencoders we investigated consist of 1 to 30 layers with dimensions linearly interpolated between the input dimension of 200 and the latent dimension of 4 to 50. This means, according to Eq. (6.179), that we took the first 100 positive values of the Green's function (the electron density is not given to the autoencoder network). After initial tests, we found diminishing returns for more than 3 layers, independent of the latent dimension, and will therefore only show results for 3 or less.

Training Setup

For the training of the AE, we used `Adam` as the optimizer algorithm with a dynamically determined learning rate. The maximum number of epochs was 250. For this small network with less than 100k free parameters and, accordingly, small training sets, the batch size had the largest impact on the training speed of the model. Furthermore, the probability of convergence to a better optimum seems greatly enhanced when starting with a very large batch size and gradually decreasing it. This could also be achieved with careful tuning of the learning rate (including a scheduler).

Latent Dimension Scaling

Fig. 6.17a shows the validation loss as a function of the latent dimension for shallow autoencoders. We observe an exponential decrease in the validation loss as a function of the latent dimension up until 10 to 16, depending on the number of layers. After that point, an improvement in accuracy is negligible on

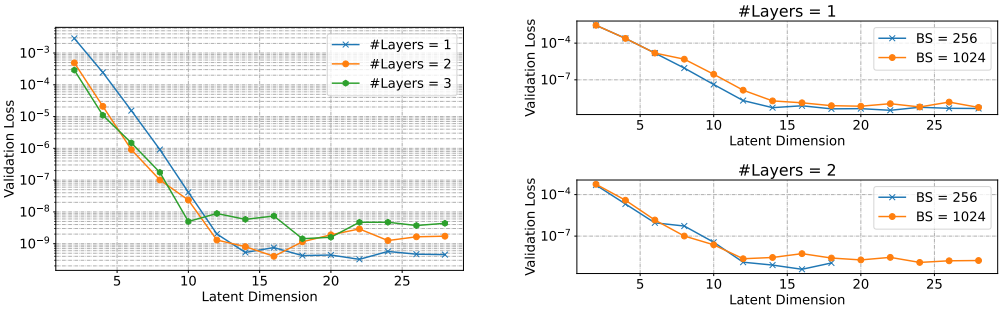

(a) Validation loss as a function of latent dimension for $1, 2$ and 3 layers. The latent dimension encodes the real and imaginary part of the Green's function. The encoders were trained on (complex-valued) Green's functions cut off after 100 frequencies.

(b) Validation loss of autoencoder for the Green's functions for two different training batch sizes as a function of the latent dimension. Dataset 1 was used 6.7.5.

Figure 6.17: Scaling of autoencoder for batch-size and latent dimensions.

the scale of the variance. This means 10 to 14 real values are enough to reconstruct a complex-valued Green's function over 100 data points up to machine precision. Note that the single-layer autoencoder

without activation function is just a linear transformation $Ax+b$ with a closed-form solution [240]. This falls in line with the concept of sparse modeling via a singular value decomposition [186, 283].
We observe in Fig. 6.17a that the 3 layer network seems to be outperformed by the 1 and 2 layer ones. This, however, is the case due to a more stable convergence with a wider range of hyperparameters in smaller networks. Hyperparameter tuning and tests on the larger input set Sec. 6.7.5 indicated that the larger networks indeed outperform the smaller ones when trained more carefully. Since we already achieved a reconstruction error close to machine precision, the final hyperparameter search to attain optimal performance has been postponed until the full setup, specifically the prediction of the latent representation of the self-energy from one of Green's functions, is completed. Furthermore, large datasets require an increase in model size as well in order to prevent overfitting. The larger dataset was, therefore, also not suitable for most initial model exploration tests.
Fig. 6.17b demonstrates convergence to a slightly better minimum by choosing a smaller batch size. This serves as an example of how hyperparameters can influence the performance of the model. Note that the relationship between hyperparameters, such as the batch size and network performance, is seldom linear and can change during training. For example, choosing a small batch size at the start of the training will typically lead to inferior performance. In the end, using gradient accumulation of 512 to 1 times the batch size, decreasing over the first 80 epochs, turned out to be the most stable approach. We investigated the previously mentioned hyperparameters in a wide range but found that dropouts and normalization layers degraded the reconstruction error.

Scaling in Bath Sites

Fig. 6.18a shows the reconstruction loss of various AEs when applied to Green's functions generated from 3 bath sites after being trained exclusively on 2 bath site Green's functions. We observe some

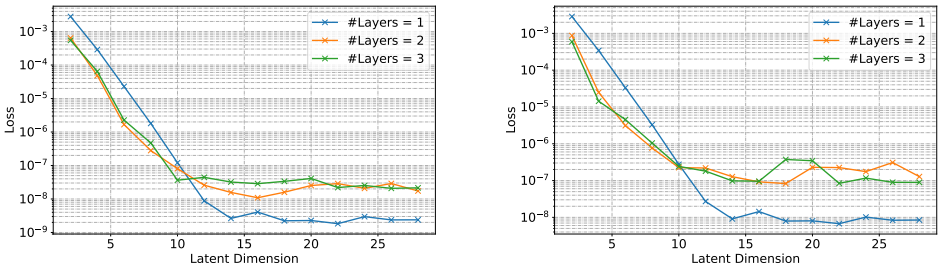

(a) Loss of AE for Green's functions generated from 3 bath sites. The model has been trained exclusively on 2 bath sites.

(b) Loss of AE for Green's functions generated from 4 bath sites. The model has been trained exclusively on 2 bath sites.

Figure 6.18: Test loss on input with different number of bath sites, than seen during training.

decrease in performance, but the loss changes by less than an order of magnitude. This indicates clearly that generalization in the number of parameters is possible even without giving examples of different bath site data points.

Green's Function Compression and Denoising

As a side effect of this approach, we obtain a network that is able to compress one-particle Green's functions, even outperforming others, at the moment, more general setups using basis functions [231, 283, 175]. It is known that shallow, linear (without activation functions) autoencoders are equivalent to principal component analysis (PCA) [193], i.e. yield the same results as singular value decompositions (SVD) [240]. For this reason, we expect similar results for our autoencoder setup in this edge case, as previously obtained from SVDs [283].
Even without convolutional layers and training on noisy data, the autoencoder architecture turns out to be very capable of predicting denoised Green's functions. This was achieved without the use of dropout layers, indicating that the sparse representation is sufficient when the network is trained on data without noise. Fig. 6.19 shows the prediction of a 2 layer AE that has been trained on noise-free data (set 1 6.7.5). The orange lines show the imaginary (left panels) and real (right panels) parts of the Green's function data points as calculated with ED. The green lines show the same data but with added Gaussian noise ($\sigma = 0.01$). Blue and red lines show the compressed and then decompressed data for the non-noisy and noisy data, respectively. We observe a negligible decrease in the validation loss from non-noisy to noisy data of less than a factor of 5.

6.7.8 Fully Connected Network

We now switch the discussion from just encoding of either the Green's function or self-energy to a prediction of Σ^ν from G^ν. We will first investigate a simple, fully connected network and then discuss

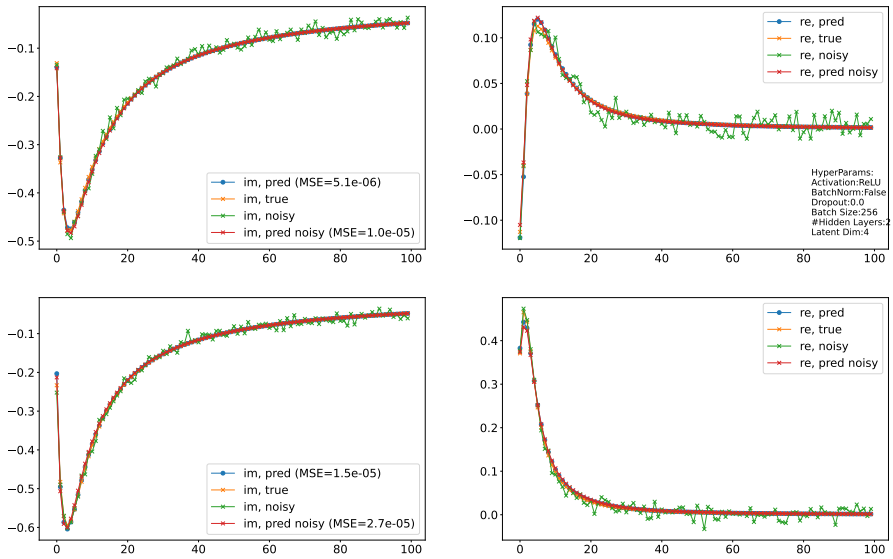

Figure 6.19: Predictions of 2 Layer AE with a latent dimension of 4 with added Gaussian noise (σ = 0.01). The input data is shown in yellow, and the data with added noise is in green. The predictions of the autoencoder from the data without (with) noise are shown in blue (red).

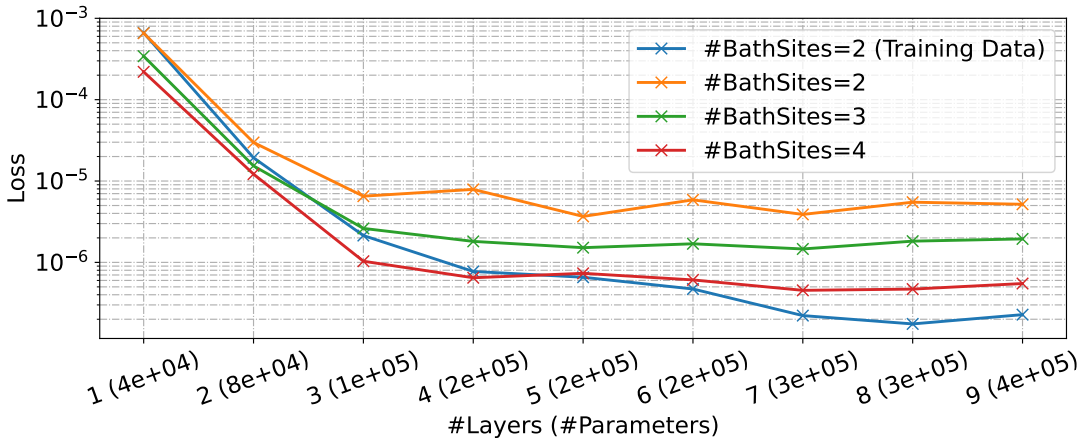

Figure 6.20: Loss of fully connected network, trained on 2 bath sites (`Set1`), loss computed on tests sets generated from 2, 3 and 4 bath sites for `Set3`.

a more sophisticated setup.
Tests for a fully connected network with 202 inputs, according to Eq. (6.179) with G^{ν_0} to $G^{\nu_{99}}$, N_d dense hidden layers with width $W_{\mathrm{d},i} \equiv 200$, 1 output layer of width 200 (real part Σ^ν, imaginary part Σ^ν). The number of dense layers is a hyperparameter that we tuned by training networks with $N_\mathrm{d} \in \{1, ..., 16\}$. Fig. 6.20 shows the loss as a function of the number of layers (number of trainable parameters). The blue line shows the loss on the training set `Set1`. The other three lines show the loss on `Set3` generated for 2, 3, and 4 bath sites. It appears that the model performs better on 3 and 4 bath sites than on the original set. As of now, it is unclear why the datasets with more bath sites perform better. One potential explanation is that a substantial percentage of the Green's function/self-energy pairs generated by very few bath sites are not representative of the vast majority of these data points for more bath sites. This would mean that data points for a larger number of bath sites have a higher probability of being "easy" to predict. An example of a rare data point is the particle-hole symmetric case, for which the bath levels are paired up with opposite signs and equal hoppings. A further investigation with even more bath sites would be beneficial to substantiate this point. However, generating a sufficiently large dataset that is consistent with the definition of `Set3` becomes impossible because of the low number of samples for each bath site, while other methods risk sampling an effective dimensional space by keeping one bath site fixed.
The performance of this model, again, indicates an exponential decrease in loss with an increase in layers and a saturation at around 4 layers (163618 parameters), which could also be attributed to the rather small training dataset `Set1` and lack of normalization or dropout layers for this reference model. Further improvements can certainly be made to this approach in the future.

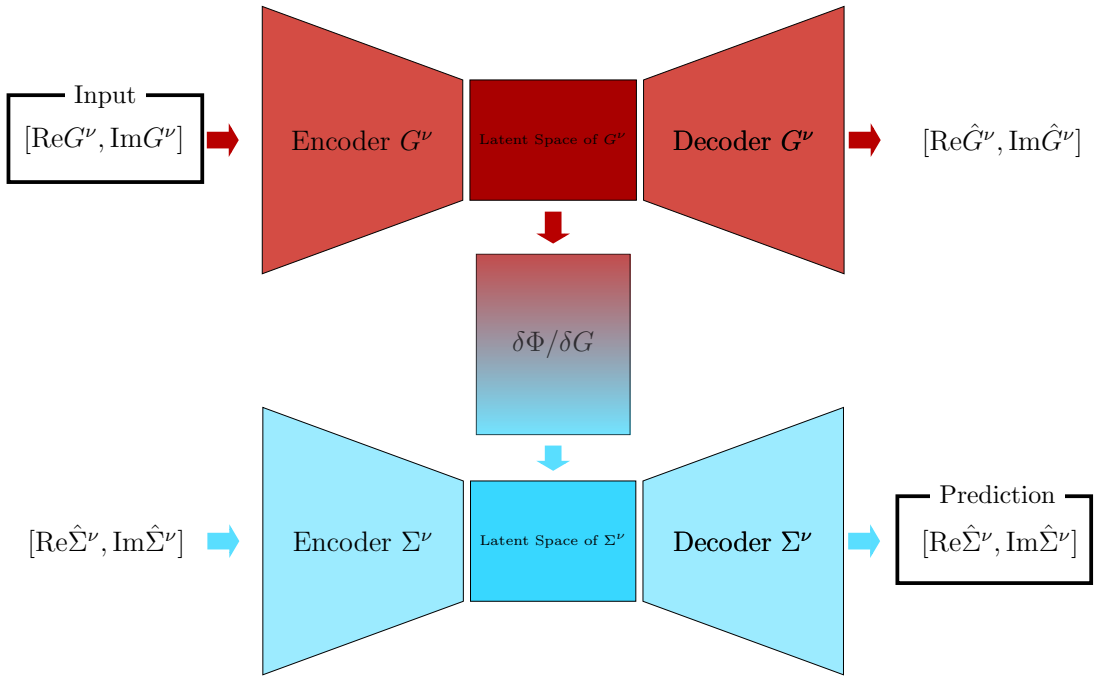

Figure 6.21: Illustration of the latent mapping. Two autoencoders are pre-trained to encode a sparse representation of G^ν and Σ^ν. Then a network is trained that maps the latent space representation of G^ν to that of Σ^ν.

6.7.9 Latent Space Mapping

For this architecture (below referred to as `AE_FC`), we combine the pre-trained autoencoders with (for this first attempt) a fully connected network in latent space; the network setup is illustrated in Fig. 6.21. Here, the encoder part of the pre-trained Green's function autoencoder network and the decoder part of the self-energy autoencoder are connected by a fully connected network. The combined network is then given the same training data as the fully connected network. Note that in this setup, we are very unlikely to exceed the loss of the autoencoder that is responsible for the latent space representation. To allow the network to find a better encoding for the transfer part, we investigated a setup with and without freezing the parameters of the autoencoders. Frozen parameters are not allowed to change during the training process, so in this case, the previously learned latent space representation of Green's function and self-energy is enforced.
After identifying 14 `AE` latent dimensions as sufficient for the sparse representation of Green's function and self-energy, we keep the latent dimension fixed at that value. However, the dimension of the fully connected network may be larger. This means the restriction layer of width 14 still exists, but the network may use wider layers after that, before again restricting to 14 layers before the self-energy decoder part. Fig. 6.22b shows the logarithm of the `MSE` on `Set0` for different numbers of fully connected

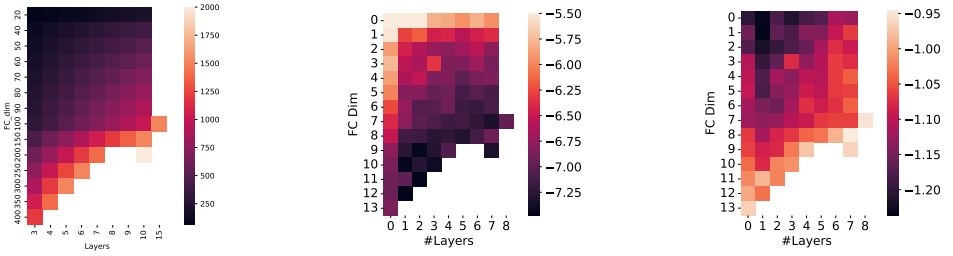

(a) Overview of the number of parameters for different numbers of layers and dimensions for the fully connected network between the latent dimensions of the autoencoders. The latent dimension was fixed at 14. The loss is the `MSE`.

(b) Comparison of the logarithm of the test loss for different numbers of layers and dimensions for the fully connected network between the latent dimensions of the autoencoders. The latent dimension was fixed at 14. The loss is the `MSE`.

(c) Comparison of the logarithm of the test loss, divided by the logarithm of the number of parameters of the model. Shown for different numbers of layers and dimensions for the fully connected network between the latent dimensions of the autoencoders. The latent dimension was fixed at 14. The loss is the `MSE`.

Figure 6.22: Comparison of fully connected networks with different dimensions and number of layers.

layers and dimensions of these layers. Fig. 6.22a shows the number of parameters for the corresponding models, and Fig. 6.22c shows the log loss divided by the logarithm of the number of parameters. It is worth noting that the hyperparameter search for this model has not been completed as of the writing of this thesis. Therefore, models with a large number of parameters, especially, have a significant error bar attached to their performance (test loss). It can be expected that this performance could be significantly improved by carefully fine-tuning the parameters of the optimizer. The same is true for the bath site scaling as in the fully connected case, even though the encoding is worse, according to the AE section above. However, we observe a clear trend that the test loss does not seem to improve significantly after a network size of 1000 parameters is reached. In terms of modern neural network architectures, this is incredibly small and indicates that the inclusion of more bath sites would certainly be possible. Fig. 6.24 and Fig. 6.25 show examples for predictions of the `FC` and `AE_FC` network, respectively. The left panels are for 2, and the right panels are for 3 bath sites; the networks have been trained on 2 bath sites. These are not the best-converged networks but just general examples of an average network of this type.
In Fig. 6.23 we also show the log(MSE) for predictions of the networks from Fig. 6.22 with test data from `Set 3` for 2, 3 and 4 bath sites. As before, the network has been trained on `Set 1` with 2 bath sites. We, again, observe better performance for an increase in the number of bath sites, but the performance is below that of the validation loss by about 0.5 to 2 orders of magnitude.

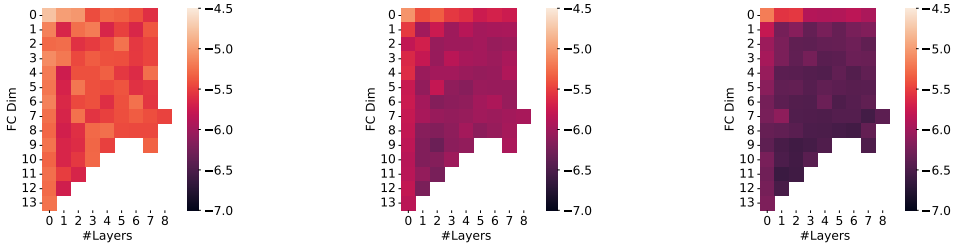

(a) Test log-loss for 2 bath sites. (b) Test log-loss for 3 bath sites. (c) Test log-loss for 3 bath sites.

Figure 6.23: Comparison of test loss for a network trained on two bath sites with `Dataset 1` and tested on data from `Set 3` for 2, 3 and 4 bath sites.

6.7.10 Open Questions

The generalization of these models must be explored in more detail. Here, it would be desirable to find more parameters that divide the input space in a meaningful way. Examples would be insulating or metallic behavior or Green's function within or outside the Kondo regime.
The convergence of the models has not yet been explored in detail. From observing the convergence of loss rates over many experiments, it seems that a systematic exploration of the hyperparameter space, specifically employing different learning rate schedulers, optimizers, and training set sizes (for example, more noisy sampling), could improve the performance of larger models by at least one order of magnitude.
Scaling of performance in both bath sites and temperature would add more information to learn for the networks, specifically by learning different representations because the temperature induces a changed spacing of the samples on the Matsubara axis.

6.7.11 Appendix

Here we demonstrate selected predictions from the `FC` and `AE_FC` networks.

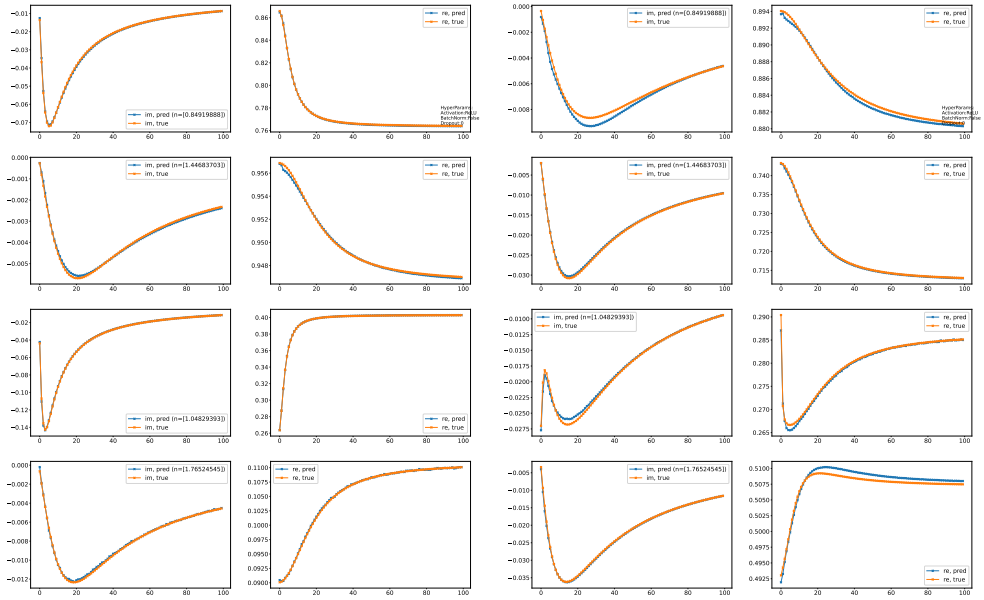

(a) Prediction on 2 bath site Green's functions. (b) Prediction on 4 bath site Green's functions.

Figure 6.24: Predictions by the `FC` model with 9 fully connected layers of width 80, trained on 2 bath sites. Examples have been selected from the set with a loss below the average.

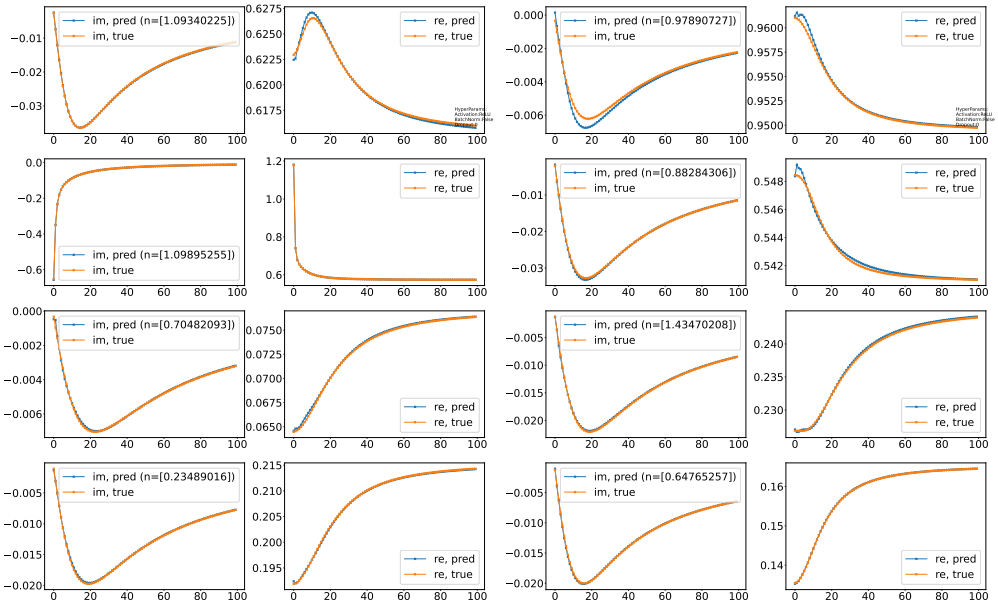

(a) Prediction on 2 bath site Green's functions. (b) Prediction on 3 bath site Green's functions.

Figure 6.25: Example predictions of the `AE_FC` model trained on 2 bath sites, predictions by the `AE_FC` model with 9 fully connected layers of width 80. Examples have been selected from the set with a loss below the average.

6.8 List of Codes

In the following, I will give a short introduction to the codes developed during this thesis. Most of them come with their own documentation and examples in the form of scripts and `Jupyter` notebooks. However, extensions or improvements of the lDΓA method will necessarily solve similar problems and hopefully benefit from some of this work. For this reason, the following sections contain a brief introduction to the core ideas and algorithms needed for each of the sub-problems.

6.8.1 Sum Extrapolations

The improved summation code was written for the first (failed) attempt to obtain better numerical results for Matsubara summations before the method discussed in Sec. 6.3 was developed [248]. However, the very general setup makes this technique an interesting black-box approach for many applications. The code has been published as an official `Julia` package and is capable of calculating improved sums through the Richardson method using two different algorithms. Some capability for the Shanks method is also implemented. Since this method was not successful in obtaining an improved Matsubara sum, it has not been further developed beyond these initial tests.

6.8.2 Symmetry Classes

Two-particle Green's functions have many symmetry relations as derived and further discussed in detail in [205]. These are not necessarily direct symmetries but also relationships of the form $f(x) = -f(x+p)$. Another example of symmetries is the $\mathbf{k}$ grids required for the calculation of non-local quantities.
The code developed [245] for this is very general with the core idea explained above in Sec. 6.4. For the two use cases above, scripts are given that compute (i) lists of frequencies that the ED solver for the two-particle Green's function can read (see also Sec. 6.6.1) (ii) functions that facilitate the generation of reduced $\mathbf{k}$-grids. Specifically, the second capability is crucial for the tight binding module (see Sec. 6.8.4), which is responsible for the reduction and expansion of all $\mathbf{k}/\mathbf{q}$ indexed quantities in the lDΓA code Sec. 6.8.5. Without this reduction (the expansion is required for `FFT` base convolutions, see Sec. 6.4.2), the lDΓA method would be at least one order of magnitude slower. The mappings between reduced and expanded lattice are computed from the list of well-known lattice symmetries and returned by the corresponding function. All further capabilities are delegated to higher-order libraries.
The algorithm for the computation of these mappings is not well optimized for very large sample spaces, as also mentioned in Sec. 6.4. Specifically, the script for the frequency representation circumvents this issue by mapping symmetries and their operations to representation with as few bits as possible. Since the construction of a mapping to a reduced representation is very general, there are approaches discussed in the literature, and future development of this code or replacement by a different one should take more optimized algorithms into account.

6.8.3 Exact Diagonalization

The `jED.jl` [121] code is one of the core algorithms developed for this thesis. While there are many well-developed ED and CTQMC codes available, having very tight control over this simple algorithm[12] proved necessary to construct usable input for the lDΓA method. The code has, therefore, also been written with a priority on readability, which should allow students to extend it where needed. Furthermore, the very specialized nature of this implementation allowed for very rapid computation of Green's functions, employed in the machine learning project Sec. 6.7
There is a large number of examples available that may be instructive for students learning DMFT and investigating different numerical obstacles DMFT faces.
This code relies on the tight-binding module from Sec. 6.8.4 for the construction of the local Green's function.

6.8.4 TightBinding

This module [252] serves as a library for all codes using any type of $\mathbf{k}$ grid. It can generate tight-binding dispersions and export a `struct` from a `string` definition of the lattice. This struct can then be passed to any exported function that operates on arbitrary data sampled over this lattice. Specifically, the $\mathbf{k}$-space integration, reduction, and expansion from and to reduced representation, convolutions, and autocorrelations (see Sec. 6.4.2) can be done over arbitrary data, supplying this `struct` in addition to the data itself. There are internal caches to avoid repeated memory allocations for convolutions that require mapping from reduced samplings to full ones and back.

6.8.5 LadderDGA

`LadderDGA.jl` implements all functionality assiciated to the lDΓA and related methods [254]. Besides lDΓA , the code also provides helpers for the asymptotic lDΓA method discussed in Sec. 5.5, and λ-RPA

[12] One just needs to construct a basis in Fockspace, diagonalized the Hamiltonian in this basis and can obtain the Green's functions from the Lehmann representation.

from Sec. 5.2.5 [13]. The original version of this code was very close to a previous implementation by Georg Rohringer [206] but has evolved a lot throughout this thesis. Nevertheless, the core structure remains compatible, and there are dedicated I/O functions to move data between both programs.
This code aims to provide a set of functions and data types that are often needed for lDΓA and then typically used in script-like Julia codes to obtain specific results. There exist `examples`, `scripts`, and `notebook` directories with a large number of use cases for which the code has been employed. Some of them are outdated by now due to changes in the API but should nonetheless be easily adaptable.
A typical lDΓA calculation consists of the calculation of the bare susceptibility $\chi_{0,\mathbf{q}}^{\nu,\omega}$, the non-local physical susceptibilities $\chi_{r,\mathbf{q}}^{\omega}$ and the triangular vertices $\gamma_{r,\mathbf{q}}^{\nu\omega}$. The code provides functions that calculate these quantities (see `example00.jl`). From that point on, the program flow depends on the project, and the code does not attempt to impose a predetermined flow. There are numerous functions available to handle typical operations such as calculating λ values, $\mathbf{k}/\mathbf{q}$ integrations, frequency summations, calculating the non-local self-energy, calculating the non-local Green's function and fitting a chemical potential, calculating the potential and kinetic energy, calculating the leading eigenvalue for the linearized Eliashberg equation (on a sub-sampled lattice).
The code has been written with readability and extensibility in mind, forgoing many performance considerations, including parallelization[14]. As such, the code is meant as a baseline for others to understand the method, test extensions, or be used as a reference for more performant implementations.
This code also provides a helper `struct` (of type `RunHelper`, sub-typed for either regular lDΓA , asymptotic DΓA or λ-RPA calculations) that provides a context for functions of this package (i.e. all auxiliary variables for a run).

LambdaCorrections

This is a submodule of the `LadderDGA.jl` code, responsible for the calculation of the λ correction values [254]. It exports the main variants of corrections presented in this thesis as functions. These are both types of $\mathrm{lD\Gamma A_m}$, $\mathrm{lD\Gamma A_{dm}}$, $\mathrm{lD\Gamma A_{dm,sc}}$, and $\mathrm{lD\Gamma A_{m,sc}}$, see also Sec. 5.4. All calculations are returned in the form of a `struct` that contains additional information, such as validation for consistencies and the λ-corrected non-local self-energy (specifically important for the partially self-consistent method).
The different custom Newton methods and wrappers for the bracketing methods (which were discussed earlier in this chapter) are also implemented here.

6.8.6 BSE Asympt

This library [244] is responsible for the improved Matsubara sum from Sec. 6.3. While it can be used separately, for example, in order to construct a self-consistently improved full vertex [256], it is mainly used as a library for the `LadderDGA.jl` code Sec. 6.8.5. In order to facilitate fast summations, one first obtains a helper `struct` by supplying the asymptotic values that are required for the improved summations Sec. 6.3. This `struct` also contains caches and auxiliary information required by functions that implement these summations. One can also specify some approximations; for example, one can choose to disregard the diagonal part of the asymptotic expansion of the $\lambda_{0,\uparrow\downarrow}$ because it rarely has any influence but is responsible for more than 90% of the computation time.

6.8.7 Vertex Postprocessing

The calculation of lDΓA input data from the local two-particle Green's function requires inversion of the local BSE and some other linear algebra operations. While rather simple, these routines are also very general and have therefore been exported to a standalone code [249]. Noteworthy is the capability of dealing with shifted grids (i.e. Matsubara grids centered around $-\omega_m/2$), expanding vertices from the reduced representation (through the use of Sec. 6.8.2) and the combination of two vertices (useful for high precision calculations in the core region and lower precision outside of it). This code also calculates the particle-particle vertex from the particle-hole notation, in case that vertex is not provided, using the frequency mapping from Sec. 2.7.1.

6.8.8 PythonWrapper

The lDΓA method relies on a number of other codes (as also demonstrated by this list) in order to work properly. This glue-code [251] is responsible for managing these multi-stage calculations of

(0) Setup of dependency queue; preallocation of space; editing, copying and compiling of all codes; writing of input files and startup scripts

(i) The core DMFT loop in either ED or CTQMC.

(ii) Fitting of bath parameters and consistency checks, early stopping if necessary.

[13] The λ-RPA portion has entirely been developed by Frederik Weißler[288].
[14] There are some less maintained parallel versions of performance-critical functions, such as the inversion of the BSE available.

(iiia) Calculation of physical susceptibility and triangular vertex from the bath parameters (ED).

(iiib) Calculation of the two-particle Green's function

(iv) Vertex post processing Sec. 6.8.7, including preparation of particle-particle vertex

(v) lDΓA calculations

(vi) Data post processing and cleanup

This code manages these steps: can submit jobs, check for failed jobs, and restart them if necessary, saving many potentially bug-introducing manual steps. While probably the most useful piece of code for this thesis, it may also be the only one without any relevance for future work on this method.

6.8.9 Machine Learning Code

This `PyTorch` based neural network [250] has been used for the attempt to learn details about the LWf from the Green's function self-energy pairs generated from the AIM.

7 Ladder DΓA Results for the Hubbard Model

The following two sections present results of the lDΓA *with two-particle consistent improvements for the repulsive Hubbard model in three and two spatial dimensions. The first section is a verbatim copy of previously published results [253], while the latter is still in preparation as of the writing of this thesis.*
Here we want to demonstrate the improved predictive power of the lDΓA *method under restoration of an effective two-particle consistency.*

7.1 Results on the Hubbard Model in three dimensions

7.1.1 Introduction

The description and understanding of interacting many-particle systems represents one of the fundamental challenges in contemporary physics. It arises in various research areas which include nuclear and atomic physics [98], solid state theory [96] or soft matter systems [67]. In the latter two cases we are typically concerned with a very large (Avogadro) number of interacting particles which facilitates a statistical treatment of the problem. Of particular interest are the one- and two-particle correlation functions of the system such as the (position dependent) pair correlation function in classical statistical mechanics or the position and time dependent one- and two-particle Green's functions in many-body quantum systems which describe one- and two-particle excitations. Apart from being interesting on their own, they provide access to thermodynamic observable such as pressure, entropy or free as well as kinetic and potential energies. The calculation of these correlation functions is, however, difficult in the presence of interactions between the particles. For weakly interacting systems, an effective independent particle description is possible which is exploited in static mean field [211] or density functional theories [44, 120] where the interaction between the particles is replaced by a selfconsistent field. At stronger coupling this procedure yields increasingly unreliable results since the interaction between the particles must be taken into account explicitly. As there is no exact solution to this problem for more than two particles one has to consider approximations. For classical systems, the Ornstein-Zernicke equation [185] together with specific closure relations [117] can be exploited while quantum mechanical Green's functions can be calculated by Feynman diagrammatic perturbation theory [1]. Unfortunately, the correlation functions obtained in this way lead to thermodynamic inconsistencies. In classical systems thermodynamic observables such as pressure or free energy can be obtained from the pair correlation functions in different ways. For the exact solution all results of course coincide, however, an approximate pair correlation function typically provides different results depending on the route which is exploited for the determination of thermodynamic variables [268]. Such thermodynamic inconsistencies can be also observed in the quantum case where potential and kinetic energies differ [271, 147] when they are calculated from one- and two-particle Green's functions respectively. It is obvious that these discrepancies limit the predictive power of theoretical calculations.

A good example for such thermodynamics inconsistencies is the dynamical mean field theory (DMFT) [172, 80]. For a (finite dimensional) lattice model with purely local interactions between electrons at the same lattice site, such as the Hubbard Hamiltonian, DMFT approximates the irreducible part of the one- and two-particle Green's function (i.e. the electronic self-energy Σ and the vertex Γ_r irreducible in the scattering channel r) by summing up all purely local Feynman diagrams for these correlation functions. In this way all purely local correlation effects in the system are captured exactly while nonlocal correlations are described on a mean field level. Since DMFT is a conserving theory it satisfies all conservation laws of the system (except for momentum conservation [99]) which guarantees consistent results for the kinetic energy at the one- and the two-particle level. However, the potential energy obtained via the one-particle self-energy Σ differs from the one calculated by the two-particle vertex Γ_r.

A similar situation is often observed for the diagrammatic extensions of DMFT [204, 264, 209, 210, 205, 261, 20, 18, 19] that include non-local correlations beyond the local ones of DMFT by a Feynman diagrammatic expansion around the DMFT starting point. Which of the sum rules and conservation laws are violated in this case depends of course on the actual choice of Feynman diagrams. For example, the dynamical vertex approximation (DΓA) [264, 269, 63, 146, 144, 16] and the QUADRILEX [18] approach are based on the parquet formalism [58, 28, 294, 259, 17] using the fully irreducible vertex of DMFT [203, 263]. The parquet equations lead to a fulfillment of the Pauli principle and all sum rules depending on the EoM, specifically guaranteeing consistency of the potential energy between one- and two-particle levels. However, for all approximate choices of the fully irreducible vertex, it has been demonstrated [234, 42] that the parquet formalism violates conservation laws and the related f-sum rule. This implies different results for the kinetic energy when obtained from one- and two-particle correlation functions.

Another limitation of the parquet formalism is its very high numerical complexity even for single-orbital models, making its extension to realistic multi-orbital systems unrealistic in the foreseeable future. Hence, other routes have been pursued to achieve consistent results for the potential energies. Within the dual boson (DB) method [242, 192] a purely local reference system (analogous to DMFT) with an effective frequency-dependent interaction is introduced. The latter is determined by the condition that the local parts of the lattice charge and spin susceptibilities are equal to the corresponding ones of the local reference system. While this approach certainly improves the consistency between the one- and the two-particle level, it has recently been shown that an additional term in the calculation of the potential energy from one-particle correlation function emerges due to the frequency dependence of the interaction [147], which again destroys the consistency. Moreover, the DB approach requires the repeated solution of an effective Anderson impurity model (AIM) with a frequency-dependent interaction making it numerically challenging.

In this work, we will consider the consistency of the potential energy within another diagrammatic extension of DMFT, the ladder version of the dynamical vertex approximation [125, 203, 216, 217, 218]. Within this approach, the sum rule for the up-up susceptibility (which corresponds to the Pauli principle) has been already restored by means of a so-called λ-correction parameter in the spin channel. More specifically, the correlation length of the DΓA spin susceptibility is renormalized with a constant parameter λ_{m} determined by the above-mentioned sum rule. Here we will extend this idea [202] by also correcting the charge susceptibility

by a second parameter λ_{d}. Both parameters are then simultaneously fixed by the sum rule for the up-up susceptibility and the requirement that the potential energies at the one- and the two-particle level should be equivalent. This idea shares some similarities with the two-particle self-consistent approach (TPSC) [278, 277] where the fulfillment of two-particle consistency is achieved by considering (different) effective Hubbard interaction parameters in the charge and spin channel. However, the latter approach is restricted to the weak coupling regime, while the DMFT input in our improved version of ladder DΓA makes the method applicable to the entire range of the coupling parameter. With this method, we achieve an improved description of the phase diagram in the weak-to-intermediate coupling regime and consistent results for the potential energy in the entire parameter space. Finally, we also restore the correct hierarchy of the kinetic energy between DΓA and DMFT in the weak-to-intermediate coupling regime.

The paper is organized as follows: In Sec. 7.1.2 we discuss the general formalism of the ladder DΓA approach and introduce our new method. In Sec. 7.1.3 we present our results for the three-dimensional half-filled Hubbard model on a simple cubic lattice and discuss the impact of the extended λ correction scheme on charge and spin susceptibilities, phase diagram, electronic self-energies as well as on the potential and kinetic energies. In Sec. 7.1.4 we conclude our work.

7.1.2 Method

In this study we will consider the single band Hubbard model,

$$\hat{\mathcal{H}} = -t \sum_{\langle ij\rangle\sigma} \hat{c}^{\dagger}_{i\sigma}\hat{c}_{j\sigma} + U\sum_{i}\hat{n}_{i\uparrow}\hat{n}_{i\downarrow} \tag{7.1}$$

with hopping amplitude t between nearest neighbors and effective Hubbard interaction U between particles at the same lattice site. We will restrict ourselves to the half filled ($n = 1$) 3 dimensional simple cubic lattice with nearest neighbor hopping. The energy scale will be fixed to $D = 2\sqrt{6}t$ which corresponds to twice the standard deviation of the noninteracting density of states. Furthermore, we will use $\nu = (2n+1)\frac{\pi}{\beta}$ to indicate fermionic and $\omega = 2m\frac{\pi}{\beta}$ for bosonic Matsubara frequencies. $\beta = 1/T$ denotes the inverse temperature of the system. Lastly, the factor of $\frac{1}{\beta}$ for Matsubara sums is omitted, i.e. $\sum_{\nu} \coloneqq \frac{1}{\beta}\sum_{n=-\infty}^{\infty}$ and integrals over the momentum vectors $\mathbf{k}$ or $\mathbf{q}$ over the Brillouin zone (BZ) are written as sums $\sum_{\mathbf{k}} \coloneqq \frac{1}{V_{\mathrm{BZ}}}\int_{\mathrm{BZ}}\mathrm{d}\mathbf{k}$.

ladder DΓA formalism

The method employed in this work is based on DΓA [264] in its ladder approximation [125, 202]. DΓA is a natural generalization of DMFT in the following sense: DMFT assumes the one-particle irreducible vertex (1PI), the electronic self-energy Σ^{ν}, to be purely local, i.e. $\mathbf{k}$ independent. DΓA raises this concept to the two-particle level and assumes the 2PI vertex $\Lambda^{\nu\nu'\omega}_{\sigma\sigma'}$ to be local. This is a controlled approximation in the sense that the theory becomes exact in the limit of $n \to \infty$ for local nPI vertices. $\Lambda^{\nu\nu'\omega}_{\sigma\sigma'}$ introduces nonlocal correlation effects on top of the local ones of DMFT via a momentum dependent self-energy $\Sigma^{\nu}_{\mathbf{k}}$ which is obtained from the equation of motion

$$\Sigma^{\nu}_{\mathbf{k}} = \frac{Un}{2} - U\sum_{\nu'\omega\mathbf{k'q}} F^{\nu\nu'\omega}_{\uparrow\downarrow,\mathbf{kk'q}} G^{\nu'}_{\mathbf{k'}} G^{\nu'+\omega}_{\mathbf{k'+q}} G^{\nu+\omega}_{\mathbf{k+q}} \tag{7.2}$$

The full vertex $F^{\nu\nu'\omega}_{\uparrow\downarrow,\mathbf{kk'q}}$ is calculated from $\Lambda^{\nu\nu'\omega}_{\sigma\sigma'}$ through the Bethe-Salpeter and parquet equations [58, 259]. The former connect $\Lambda^{\nu\nu'\omega}_{\sigma\sigma'}$ with $F^{\nu\nu'\omega}_{\uparrow\downarrow,\mathbf{kk'q}}$ in three different ways, corresponding to fluctuations in the charge, spin and particle-particle channels. The latter takes into account the mutual renormalization effects between these three different channels. However, this approach is not only numerically very expensive but the inherent self consistency loops are also not guaranteed to converge due to intrinsic singularities [215] in $\Lambda^{\nu\nu'\omega}_{\sigma\sigma'}$. The ladder approximation therefore omits the self consistency and calculates the full vertex only once via a one-shot Bethe-Salpeter equation in the relevant scattering channels. For the repulsive particle-hole symmetric Hubbard model these are the charge (density, $r = \mathrm{d}$) and the spin (magnetic, $r = \mathrm{m}$) channel while particle-particle fluctuation are typically strongly suppressed and sufficiently well captured by DMFT. Moreover, also the Green's functions appearing in Eq. (7.2) remain on the DMFT level, contrary to self consistent methods like parquet. Unfortunately, the ladder approximation violates the two-particle self-consistency. This leads to (i) a spurious $1/i\nu$ asymptotic behavior of the self-energy [202] and (ii) ambiguous results for the potential energy. To overcome these problems it is necessary to rewrite Eq. (7.2) in terms of physical susceptibilities. To this end we introduce the bare, generalized and physical susceptibilities as well as the triangular vertex which are defined as follows (the upper sign corresponds to the spin, the lower to the charge channel):

$$\chi^{\nu\nu'\omega}_{0,\mathbf{q}} = -\beta\delta_{\nu\nu'}\sum_{\mathbf{k}} G^{\nu}_{\mathbf{k}} G^{\nu+\omega}_{\mathbf{k+q}} \tag{7.3}$$

$$\chi^{\nu\nu'\omega}_{r,\mathbf{q}} = \chi^{\nu\nu'\omega}_{0,\mathbf{q}} - \chi^{\nu\nu'\omega}_{0,\mathbf{q}}\sum_{\nu_1}\Gamma^{\nu\nu_1\omega}_{r}\chi^{\nu_1\nu'\omega}_{r,\mathbf{q}} \tag{7.4}$$

$$\chi^{\omega}_{r,\mathbf{q}} = \sum_{\nu\nu'}\chi^{\nu\nu'\omega}_{r,\mathbf{q}} \tag{7.5}$$

$$\gamma^{\nu\omega}_{r,\mathbf{q}} = \sum_{\nu'} \left(\chi^{\nu\nu'\omega}_{0,\mathbf{q}} (1 \pm U\chi^{\omega}_{r,\mathbf{q}}) \right)^{-1} \chi^{\nu\nu'\omega}_{r,\mathbf{q}}. \tag{7.6}$$

$G^{\nu}_{\mathbf{k}} = [i\nu + \mu - \varepsilon_{\mathbf{k}} - \Sigma^{\nu}]^{-1}$ is the DMFT lattice Green's function and Σ^{ν} the local DMFT self-energy. $\Gamma^{\nu\nu'\omega}_{r}$ denotes the local vertex which is irreducible in channel r. These quantities allow us to reformulate the equation of motion: [203, 125, 202]

$$\begin{aligned}\Sigma^{\nu}_{\mathbf{k}} = \frac{Un}{2} - U \sum_{\nu'\omega\mathbf{q}} \Big[1 + \frac{1}{2}\gamma^{\nu\omega}_{\mathrm{d},\mathbf{q}}(1 - U\chi^{\omega}_{\mathrm{d},\mathbf{q}}) - \\ \frac{3}{2}\gamma^{\nu\omega}_{\mathrm{m},\mathbf{q}}(1 + U\chi^{\omega}_{\mathrm{m},\mathbf{q}}) - \chi^{\nu'\omega}_{0,\mathbf{q}} F^{\nu\nu'\omega}_{\mathrm{m}} \Big] G^{\nu+\omega}_{\mathbf{k}+\mathbf{q}},\end{aligned} \tag{7.7}$$

where $F^{\nu\nu'\omega}_{\mathrm{m}}$ is the local full vertex of DMFT.

With these definition we can formulate above problems (i), which corresponds to a violation of the consistency relation for the ↑↑ (i.e., the sum of charge and spin) susceptibility (equivalent to the Pauli principle), and (ii) the ambiguity in the potential energy, as

$$\frac{1}{2}\sum_{\omega\mathbf{q}} \left(\chi^{\lambda_{\mathrm{d}},\omega}_{\mathrm{d},\mathbf{q}} + \chi^{\lambda_{\mathrm{m}},\omega}_{\mathrm{m},\mathbf{q}} \right) \overset{!}{=} \frac{n}{2}\left(1 - \frac{n}{2}\right) \tag{7.8a}$$

$$\underbrace{\frac{U}{2}\sum_{\omega\mathbf{q}} \left(\chi^{\lambda_{\mathrm{d}},\omega}_{\mathrm{d},\mathbf{q}} - \chi^{\lambda_{\mathrm{m}},\omega}_{\mathrm{m},\mathbf{q}} \right) + U\frac{n^2}{4}}_{E^{(2)}_{\mathrm{pot}}} \overset{!}{=} \underbrace{\sum_{\nu,\mathbf{k}} G^{\boldsymbol{\lambda},\nu}_{\mathbf{k}} \Sigma^{\boldsymbol{\lambda},\nu}_{\mathbf{k}}}_{E^{(1)}_{\mathrm{pot}}}, \tag{7.8b}$$

where we introduced the free parameters λ_{d} and λ_{m} to fulfill these consistency relations. The λ's enter into the formalism via a renormalization of the physical susceptibilities in the spirit of the Moriya theory of itinerant magnetism [176] as follows[202]

$$\chi^{\lambda_r}_{r} = \left(\frac{1}{\chi_r} + \lambda_r \right)^{-1} \tag{7.9a}$$

A previous version of ladder DΓA[125] has already exploited a simpler version of this idea where the sum rule in Eq. (7.8a) has been enforced by considering a λ correction *only* in the spin channel (i.e. $\lambda_{\mathrm{d}} = 0$). In our new approach we achieve a higher degree of consistency by overcoming the ambiguity in the determination of the potential energy with a corresponding renormalization in the charge channel.

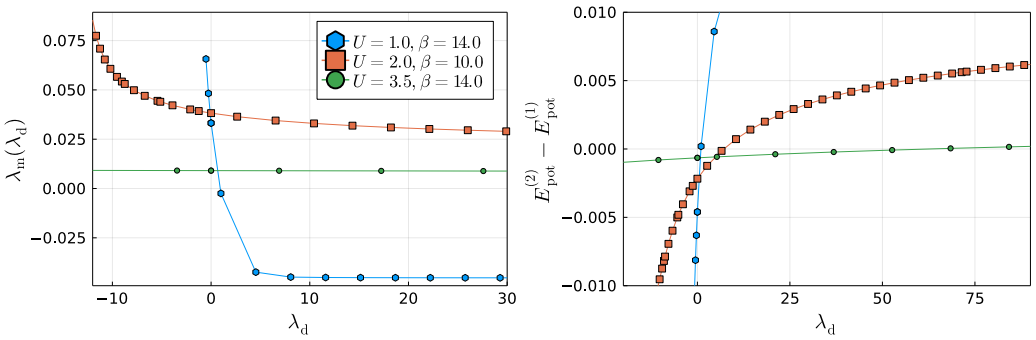

(a) λ_{m} as function of λ_{d} for three different values of U at $\beta = 10$ and $\beta = 14$. The divergence of $\lambda_{\mathrm{m}}(\lambda_{\mathrm{d}})$ indicates the largest pole of $\chi^{\lambda_{\mathrm{d}},\omega}_{\mathrm{d},\mathbf{q}}$ as a function of λ_{d} [see Eq. (7.9a)] after which this susceptibility would become negative making all solutions with smaller λ_{d} unphysical.

(b) Difference between the potential energies obtained from one- and two-particle correlation functions as on the right and left hand sides of Eq. (7.8b) respectively as a function of λ_{d} where λ_{m} is obtained (for a given λ_{d}) from Eq. (7.8a). Results at three different values of U at $\beta = 10$ and $\beta = 14$ are shown, corresponding to weak, intermediate and strong coupling. The crossing of the lines with the x-axis indicates a solution for the set of consistency Eqs. (7.8).

Figure 7.1: Conditions for λ corrections.

7.1.3 Results

In the following we present results for the charge (density) and spin (magnetic) susceptibilities and the related magnetic phase diagram, the self-energies as well as the potential and kinetic energies, which are obtained by our method. We focus particularly on the mutual renormalization effects between charge and spin fluctuations which are introduced by the consistency relations in Eqs. (7.8). Moreover, we compare our findings with previous ladder DΓA calculations [125, 203, 202, 217], where only the spin channel has been

renormalized, as well as to other diagrammatic and numerical techniques.

In order to more concisely distinguish the different methods, we use the following notation: The previous version of DΓA will be denoted with $\mathrm{lDF\Gamma A_m}$. The index "m" indicates that only the magnetic susceptibility is renormalized by a parameter $\lambda_\mathrm{m} \neq 0$ while $\lambda_\mathrm{d} = 0$. $\mathrm{lDF\Gamma A_{dm}}$ refers to our new approach where both the charge and spin susceptibility are corrected by renormalization constants $\lambda_\mathrm{d}, \lambda_\mathrm{m} \neq 0$.

The local DMFT self-energy Σ^ν and vertex functions $\Gamma_r^{\nu\nu'\omega}$ have been obtained from an exact diagonalization (ED) impurity solver using four bath sites. While the applicability of ED is certainly limited by the necessity of fitting the hybridization function to a finite bath, it does not suffer from any statistical noise which typically arises in quantum Monte Carlo calculations. The latter particularly affects the two-particle vertex $\Gamma_r^{\nu\nu'\omega}$ which is obtained from a matrix inversion in the space of the fermionic Matsubara frequencies ν and ν'. For the development of the new method we deemed statistical fluctuations of the input data as problematic, since the effect of specific features in the approach and the statistical error on the results cannot easily be disentangled. Such problems are indeed absent in ED which is in any case expected to provide reliable results at the rather high temperatures above the T_N of DΓA. We have nevertheless checked our numerical findings for a broad range of points in the U vs. T phase diagram with continuous time quantum Monte Carlo (CTQMC) calculations in the hybridization expansion implementation using the w2dynamics package [284].

Physical interpretation and determination of λ_d and λ_m

Considering an Ornstein-Zernike form for the physical charge and spin susceptibilities

$$\chi^\omega_{r,\mathbf{q}} \sim \frac{1}{\mathbf{q}^2 - \xi_r^{-2}}, \tag{7.10}$$

it is obvious that the λ-corrections introduced in Eqs. (7.9) corresponds to a renormalization of the correlation length $(\xi_r)^{-2} \to (\xi_r^{\lambda_r})^{-2} = \xi_r^{-2} + \lambda_r$ or, after rewriting, $\xi_r \to \xi_r^{\lambda_r} = \frac{\xi_r}{\sqrt{1+\lambda_r \xi_r}}$. Let us remark that, from field theoretical perspective, ξ_r^{-2} corresponds to the mass of the propagator of the corresponding charge and spin fluctuations and, hence, λ_r can be also interpreted as a mass renormalization. The actual values of the parameters λ_d and λ_m are determined be the consistency relations Eq. (7.8a) for the Pauli principle and Eq. (7.8b) for the potential energy, respectively. A numerically efficient algorithm to determine λ_d and λ_m from these equations is discussed in appendix 7.1.7. Here, instead, we present a solution method which better highlights the physical content of our approach. This method consists in two steps:

First, we use only sum rule Eq. (7.8a), corresponding to the Pauli principle, to calculate λ_m for given values of λ_d. In this way we obtain a function $\lambda_\mathrm{m}(\lambda_\mathrm{d})$ which is depicted in Fig. 7.1a for three different values of U at $\beta = 10$ and $\beta = 14$. The values for the temperature are chosen such that the distance to the phase transition is similar (c.f. Sec. 7.1.3). The allowed range of values for λ_d and λ_m is determined by the condition that both the density and the magnetic susceptibilities $\chi^\omega_{\mathrm{d},\mathbf{q}}$ and $\chi^\omega_{\mathrm{m},\mathbf{q}}$ must be real and positive for all frequencies ω and momenta $\mathbf{q}$ (see also appendix 7.1.7 for a discussion of the physically relevant interval). We observe that λ_m is monotonously decreasing with increasing λ_d. This behavior can be directly understood from Eq. (7.8a): A larger value of λ_d corresponds to a smaller $\chi^\omega_{\mathrm{d},\mathbf{q}}$. Hence, in order to fulfill this sum rule the decrease of $\chi^\omega_{\mathrm{d},\mathbf{q}}$ must be compensated by a corresponding increase of $\chi^\omega_{\mathrm{m},\mathbf{q}}$ which is achieved by lowering the value of λ_m. Therefore, Eq. (7.8a) provides in a simplified way the *mutual* renormalization of the charge and spin susceptibilities as it is usually achieved only by a full parquet treatment [227, 269, 146] of the problem. To determine the value of λ_d we have to consider Eq. (7.8b) which corresponds to the consistency of the potential energies between the one- and the two-particle level. In Fig. 7.1b we show the difference between the left and the right hand side of this equation as a function of λ_d for three different values of U at $\beta = 14$. The value of λ_d at which the curve crosses zero corresponds to a solution of the consistency equation for the potential energy Eq. (7.8b). For each of the considered values of U we find such a crossing for positive values of λ_d. Moreover, we observe that the slope of the lines decreases with increasing interaction strength. This behavior can be attributed to the overall magnitude of charge fluctuations in the respective parameter regime. At weak coupling ($U = 1$), $\chi^\omega_{\mathrm{d},\mathbf{q}}$ is still comparatively large and, hence, its inverse is small. Correcting a small value by λ_d and inverting again [see Eqs. (7.9)] results in a substantial modification of $\chi^\omega_{\mathrm{d},\mathbf{q}}$ and all quantities depending on it. On the contrary, at larger values of U ($U = 2$ and $U = 3.5$) close to or beyond the Mott metal-to-insulator transition charge fluctuations are strongly suppressed and $\chi^\omega_{\mathrm{d},\mathbf{q}}$ becomes very small. Consequently its inverse gets very large and is only weakly affected by the addition of the parameter λ_d in Eq. (7.9) explaining the overall weaker dependence of observables on λ_d at strong coupling. This observation has also implications for the numerical determination of λ_d: In fact, the calculation of λ_d becomes gradually more difficult upon increasing U as the correction of the already strongly suppressed charge susceptibility requires an increasingly higher numerical precision. This also implies that the solution starts to depend stronger on small changes in the DMFT input in this parameter regime which requires a particularly precise evaluation of the DMFT correlation functions Σ^ν and $\Gamma_r^{\nu\nu'\omega}$.

Let us briefly address the signs of the (real) renormalization parameters λ_d and λ_m. On general grounds we expect that DMFT overestimates nonlocal fluctuations described by $\chi^\omega_{r,\mathbf{q}}$ as it is a mean field theory with respect to spatial degrees of freedom. Hence, the λ corrections should *suppress* these DMFT fluctuations by assuming positive values $\lambda_r > 0$. This assertion is indeed true in in the entire parameter regime as can

be seen in Figs. 7.1b-7.4a. In Fig. 7.1b the curve corresponding to the consistency relation for the potential energy crosses zero at positive values of λ_d for all U which is confirmed by the heatmap of λ_d as a function of U and T in Fig. 7.4a. In the latter, we indeed observe $\lambda_\mathrm{d} > 0$ for all values of U and β which is also true for $\lambda_\mathrm{m} = \lambda_\mathrm{m}(\lambda_\mathrm{d})$.

Density and magnetic susceptibilities

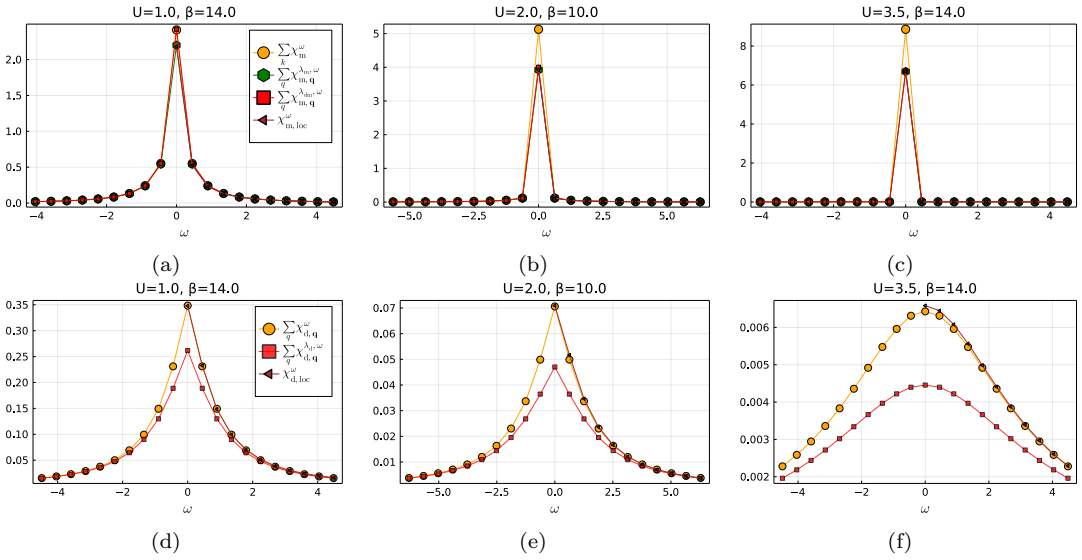

Figure 7.2: Momentum integrated susceptibilities in spin (top row) and charge (bottom row) channel for $\mathrm{lD\Gamma A_{dm}}$ (red squares) vs. DMFT (i.e. $\lambda_\mathrm{d} = \lambda_\mathrm{m} = 0$, orange circles) and $\mathrm{lD\Gamma A_m}$ (green hexagons). Data is presented in the weak ($U = 1$), intermediate ($U = 2$) and strong ($U = 3.5$) coupling regime above the critical temperature of DMFT. Note that for $\mathrm{lD\Gamma A_m}$ no charge renormalization is performed making it equivalent to the DMFT solution in the lower panel. The local impurity susceptibilities of DMFT (brown triangles) are shown for comparison.

In this section we discuss the lattice susceptibilities $\chi^\omega_{r,\mathbf{q}}$ in the charge ($r = \mathrm{d}$) and spin ($r = \mathrm{m}$) channels. These observables are interesting on their own as they are subject to the renormalization procedure discussed in the previous section. Moreover, they determine the antiferromagnetic phase transition and transfer the effects of charge and spin renormalization to the electronic self-energy as well as to the potential (and kinetic) energies via Eqs. (7.7) and (7.8b).

Figure 7.2 shows the frequency dependence of the momentum-integrated charge and spin susceptibilities obtained by three different methods. The red squares indicate the $\mathrm{lD\Gamma A_{dm}}$ results where both the charge and the spin susceptibilities have been renormalized by a λ correction. They are compared to the corresponding DMFT results where $\lambda_\mathrm{d} = \lambda_\mathrm{m} = 0$ (orange circles) and the $\mathrm{lD\Gamma A_m}$ where only the spin susceptibility is corrected using Eq. (7.8a) (green hexagons). For further comparison, we also present the local impurity susceptibilities $\chi^\omega_{r,\mathrm{loc}}$ (brown triangles) which have been obtained directly from the DMFT impurity solver. We present our data for three different values of U in the weak ($U = 1$), intermediate ($U = 2$) and strong ($U = 3.5$) coupling regimes at temperatures slightly above the DMFT phase transition.

We observe that the introduction of λ-corrections leads to an overall suppression of the charge and spin susceptibilities with respect to DMFT in the entire parameter regime. For the spin susceptibility in the upper panels, this reduction becomes more pronounced upon increasing U. This observation can be attributed to the overall increase of spin fluctuations by the gradual emergence of a local moment for larger interaction values. In fact, the absence of two-particle self-consistency in DMFT leads to a substantially larger violation of the sum rule Eq. (7.8a) when local spin fluctuations enhance the nonlocal spin susceptibility [55]. Let us remark that the renormalization of the spin susceptibility becomes also stronger when the temperature is decreased. This can be readily understood by the substantial growth of this correlation function upon approaching T_N of DMFT (where it actually diverges) leading to a stronger violation of Eq. (7.8a).

Let us now address the difference in the spin renormalization between the $\mathrm{lD\Gamma A_m}$ and $\mathrm{lD\Gamma A_{dm}}$ methods. The reduction is larger for $\mathrm{lD\Gamma A_m}$ where *only* the spin fluctuations are renormalized by means of Eq. (7.8a) (green hexagons) compared to $\mathrm{lD\Gamma A_{dm}}$ where we consider a λ-correction in both the spin *and* the charge channel (red squares). As discussed in the previous Sec. 7.1.3, this behavior can be understood from Eq. (7.8a) where a suppression of $\chi^\omega_{\mathrm{d},\mathbf{q}}$ through $\lambda_\mathrm{d} > 0$ must be compensated by a smaller value of λ_m and, hence, a larger $\chi^\omega_{\mathrm{m},\mathbf{q}}$ compared to $\mathrm{lD\Gamma A_m}$ where $\lambda_\mathrm{d} = 0$, to match the constant on the right hand side of this equation. This effect is more pronounced at weak coupling ($U = 1$, upper left panel) and gradually decreases upon increasing U. In fact, while at intermediate coupling ($U = 2$, upper middle panel) the difference between $\mathrm{lD\Gamma A_m}$ and $\mathrm{lD\Gamma A_{dm}}$ is still visible (albeit very small) both methods provide virtually the same result at strong coupling ($U = 3.5$, upper right panel).

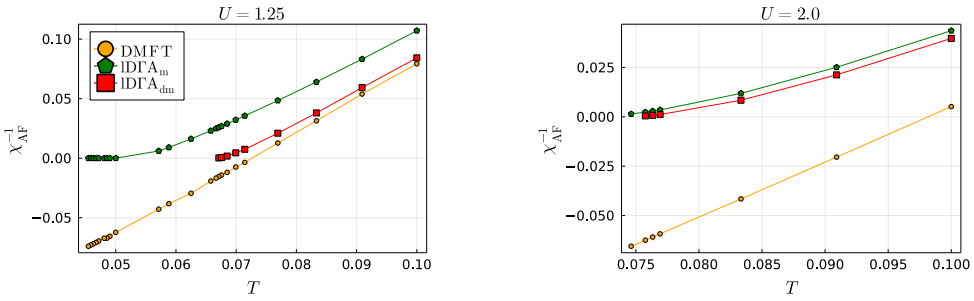

Figure 7.3: Inverse of the antiferromagnetic susceptibility $\chi_{\mathrm{AF}}(T) = \chi_{\mathrm{m}}(\omega = 0, \mathbf{q} = \mathbf{\Pi})$ as a function of the temperature $T = \frac{1}{\beta}$ for $U = 1.25$ (left panel) and $U = 2$ (right panel) obtained by DMFT (orange circles), lDΓA$_\mathrm{m}$ (green hexagons) and lDΓA$_\mathrm{dm}$ (red squares).

On the contrary, the (relative) change of the charge susceptibility due to the introduction of λ_d is rather constant (about 30%) in the entire parameter regime (see difference between red squares and orange circles in the lower panels of Fig. 7.2). However, the effect of this renormalization on other physical quantities strongly depends on the coupling strength. At weak coupling ($U = 1$, lower left panel), charge fluctuations are still significant (compared to the value of the spin fluctuations) and their correction by means of λ_d is indeed highly relevant for the fulfillment of sum rule (7.8a). In fact, at $U = 1$ the charge renormalization is almost solely responsible for the enforcement of this consistency relation as the spin susceptibility is more or less equivalent to DMFT (cf. red squares and orange circles in the left upper panel of Fig. 7.2). Upon increase of the interaction strength to $U = 2$ and $U = 3.5$ the overall size of the charge susceptibility decreases by one to two-orders of magnitude. Hence, the effect of the charge correction on the spin renormalization becomes gradually smaller and almost vanishes in the strong coupling regime where only the spin susceptibility contributes significantly to Eq. (7.8a).

It is also instructive to consider the deviations of the momentum-summed lattice susceptibilities of DMFT (orange circles) from the local ones of the AIM related to the DMFT solution of the Hubbard model (brown triangles in Fig. 7.2). Since DMFT is not a two-particle self-consistent theory considerable differences between these quantities are to be expected. This is indeed true for the spin channel (upper panels), while no significant (relative) difference can be observed in the charge channel. Introducing a λ correction solely in the spin channel (green hexagons) we observe that the consistency between the momentum summed lattice susceptibility and the local one of the AIM is implicitly restored. While at a first glance this effect from the lDΓA$_\mathrm{m}$ method appears to be preferable, we argue that in fact the opposite is the case. The local impurity model of DMFT contains no nonlocal correlation effects. Hence, its local correlation functions are expected to deviate from the local part of the corresponding DΓA lattice correlation functions which indeed contain such nonlocal contributions. These nonlocal contributions can be included in an impurity model only by introducing an effective frequency dependent interaction $U(\omega)$ as done in the dual boson approach [210]. In this method, a consistency between local lattice quantities and the corresponding impurity quantities is indeed meaningful because nonlocal correlation effects are partially encoded in the frequency dependence of the effective U. Since we do not consider such a modification of the impurity model within the ladder DΓA, a consistency between momentum summed and impurity correlation function at the two-particle level is not to be expected. On the contrary, an additional λ-correction in the charge channel leads to physically reasonable deviations from the correlation function of the AIM (red squares).

Phase diagram

In three dimensions, the half-filled Hubbard model on a bipartite simple cubic lattice features an antiferromagnetically ordered phase at low temperatures for all values of the interaction parameter U. The second-order phase transition to this antiferromagnetic state is indicated by the divergence of the antiferromagnetic susceptibility $\chi_{\mathrm{AF}}(T) = \chi_{\mathrm{m}}(\omega = 0, \mathbf{q} = \mathbf{\Pi})$. In Fig. 7.3 we present the results for the *inverse* of this observable as a function of the temperature for two different values of U. A divergence of $\chi_{\mathrm{AF}}(T)$, i.e., vanishing of $\chi^{-1}_{\mathrm{AF}}(T)$ marks the onset of antiferromagnetic order. We observe the same hierarchy of curves as in the previous section: The DMFT antiferromagnetic susceptibility (orange circles), which corresponds to $\lambda_\mathrm{d} = \lambda_\mathrm{m} = 0$, is larger than the DΓA susceptibilities (green hexagons and red squares) where λ-corrections have been applied. Consistent with the discussion above, the lDΓA$_\mathrm{m}$ results where $\lambda_\mathrm{d} = 0$ (green hexagons) are smaller than the ones obtained by lDΓA$_\mathrm{dm}$ where both the charge and the spin channels are renormalized (red squares). As has been detailed in Sec. 7.1.3 this is explained by the consistency relation (7.8a) where the suppression of charge fluctuations by $\lambda_\mathrm{d} > 0$ requires a larger spin susceptibility compared to the case where $\lambda_\mathrm{d} = 0$. The difference between the two approaches is particularly pronounced at weak and intermediate coupling while it gradually decreases for increasing U when charge fluctuations are strongly suppressed and, hence, have lesser effect on the overall physical picture.

Close to the transition temperature T_N, $\chi_{\mathrm{AF}}(T)$ takes the form of a universal scaling function [31]

$$\chi_{\mathrm{AF}}(T) \sim a|T - T_\mathrm{N}|^{-\gamma} \tag{7.11}$$

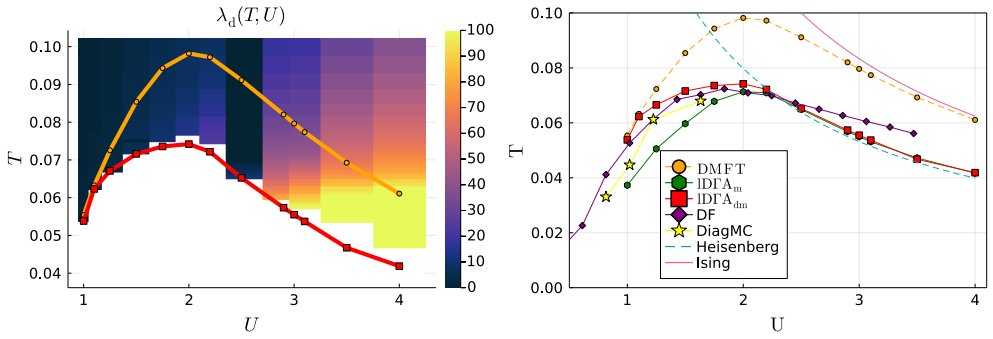

(a) Heat map of λ_d as a function of U and T from weak to strong coupling. The orange line indicates the Néel temperature of DMFT while the red line corresponds to the T_N of lDΓA$_{dm}$.

(b) Phase diagram of the $3d$ half-filled Hubbard model on a simple cubic lattice with nearest neighbor hopping. The curves correspond to the transition temperature to the antiferromagnetically ordered state obtained by the different methods indicated in the legend of the figure.

Figure 7.4

where γ is the critical exponent associated with the susceptibility. The mean field (MF) value $\gamma = \gamma_{MF} = 1$ is consistent with the linear temperature dependence of the DMFT $\chi^{-1}_{AF}(T)$ in Fig. 7.3 (orange circles). The renormalization of this DMFT susceptibility by a λ parameter leads to a modification of the mean field behavior and provides a $\gamma > 1$ which is clearly visible for the green hexagons and red squares in Fig. 7.3. The deviation from the linear mean field behavior can be only observed in the critical temperature region $\Delta T_{crit} \propto T_N^2$ according to the Ginzburg criterion[154]. This explains why the bending of $\chi^{-1}_{AF}(T)$ is more pronounced in a wider temperature range for $U = 2$ where T_N is substantially larger than for $U = 1.25$ (for lower values of U the critical regime is hardly visible at all on our scales). In Ref. [54] it has been discussed, that the ladder DΓA provides critical exponents consistent with the spherical symmetric Kac model[239] where $\gamma = 2$, similar as in TPSC [49]. However, fitting the exponent of a scaling function such as Eq. (7.11) is intrinsically difficult and $\gamma = 2$ can be only achieved by including subleading terms in the fit as has been shown in Refs. [226, 54].

In any case, the determination of T_N from numerical data is stable, and its value depends only very weakly on changes in γ [54]. We have, hence, fitted the results for $\chi_{AF}(T)$ to the scaling function in Eq. (7.11) in order to obtain the transition temperature T_N for different interaction values U. The transition curves $T_N(U)$ for DMFT (orange circles), the lDΓA$_m$ (green hexagons), and lDΓA$_{dm}$ (red squares) are depicted in Fig. 7.4b where also results obtained with other methods are shown for comparison. Overall, a reduction of T_N obtained by both versions of DΓA with respect to the DMFT curve can be observed. This is indeed the expected behavior as mean field theories (such as DMFT) typically overestimate the transition temperature to an ordered state. This can be attributed to the fact that nonlocal correlations, which are included in DΓA in an effective way by the λ corrections but not in DMFT, destroy the order in an intermediate temperature regime and predict a reduced T_N. Remarkably, in the weak to intermediate coupling region ($U \sim 1$ to $U \sim 2$) this reduction is much more pronounced when only the renormalization of the spin susceptibility through Eq. 7.8a is taken into account (green hexagons). This is a direct consequence of the mechanism which has been discussed in Sec. 7.1.3 for the susceptibilities: The positive λ_d leads to a decrease of the charge susceptibility $\chi^{\omega}_{d,\mathbf{q}}$ in Eq. (7.8a) requiring a larger spin susceptibility $\chi^{\omega}_{m,\mathbf{q}}$ (corresponding to a smaller value of λ_m with respect to the case where only the spin channel is corrected). Consequently, the related antiferromagnetic spin susceptibility $\chi_{AF}(T)$ will diverge at a higher temperature T in lDΓA$_{dm}$ giving rise to a higher transition temperature T_N with respect to lDΓA$_m$.

For $U \lesssim 1$ our numerical data for T_N coincide with the corresponding DMFT results. This means nonlocal correlations do not reduce the transition temperature in this parameter regime, which is indeed the expected behavior and has been predicted by analytical considerations and numerical simulations [257, 221, 55]. In fact, it was demonstrated that T_N is affected mainly by local particle-particle fluctuations (which are of course already included in DMFT) in the weak coupling region. In the intermediate coupling regime ($U \sim 1$ to $U \sim 2$) we observe a reduction of T_N with lDΓA$_{dm}$ with respect to DMFT which is in good agreement with dual fermion (DF) [102] and diagrammatic Monte Carlo [142] results. This is consistent with the fact that within the DF treatment of the problem both the spin and the charge fluctuations are renormalized within a self-consistent update of the generalized susceptibilities in the dual space [204] (although a consistency of the potential energy has not been demonstrated in this framework). Diagrammatic Monte Carlo calculations provide (in principle) the exact solution of the problem. In the intermediate coupling region, they also predict a T_N in good agreement with lDΓA$_{dm}$ which can therefore be considered a more reliable method than lDΓA$_m$ for the estimation of the transition temperature in this parameter regime.

Finally, in the strong coupling region $U \gtrsim 2$ the results of both DΓA schemes coincide and match excellently the data from the Heisenberg model onto which the Hubbard model can be mapped at large interaction strength. This is consistent with the fact, that in this parameter region the charge degrees of freedom are

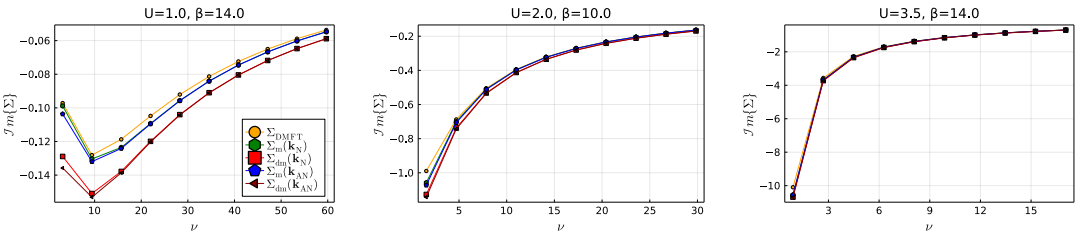

(a) (b) (c)

Figure 7.5: Imaginary part of the electronic self-energy at the nodal [$\mathbf{k}_{\mathrm{N}} = (\frac{\pi}{2}, \frac{\pi}{2}, \frac{\pi}{2})$] and antinodal [$\mathbf{k}_{\mathrm{AN}} = (\pi, \frac{\pi}{2}, 0)$] points on the Fermi surface for three different coupling strengths at $\beta = 10$ and $\beta = 14$ as a function of the fermionic Matsubara frequency ν. We present data for DMFT (orange circles), lDΓA$_{\mathrm{m}}$ (green hexagons and blue pentagons) and lDΓA$_{\mathrm{dm}}$ (red squares and brown triangles).

almost frozen and, hence, the renormalization in the charge channel has no effect on T_{N}.

Self-energies

In this section we discuss the momentum dependent imaginary part of the electronic self-energies obtained by lDΓA$_{\mathrm{dm}}$ as a function of the Matsubara frequency ν at the nodal $\mathbf{k}_{\mathrm{N}} = (\pi/2, \pi/2, \pi/2)$ and antinodal $\mathbf{k}_{\mathrm{AN}} = (\pi, \pi/2, 0)$ momentum on the Fermi surface. In Fig. 7.5 we compare our findings (red squares and brown triangles) to the corresponding local self-energy Σ^{ν} of DMFT (orange circles) and and to lDΓA$_{\mathrm{m}}$ results (green hexagons and blue pentagons) for three different values of U at $\beta = 10$ and $\beta = 14$, slightly above T_{N} of DMFT for the respective U values. In general, the absolute values of the momentum dependent self-energies in both DΓA schemes are larger than the corresponding DMFT correlation function. This is the expected behavior [202] as nonlocal correlations typically suppress the spectral weight at the Fermi level (in addition to the suppression due to local correlations which are already captured by DMFT). As has been discussed in several previous papers [202, 204], the enhancement of $\Sigma^{\nu}_{\mathbf{k}}$ is stronger at the antinodal point $\mathbf{k}_{\mathrm{AN}}$ than at the nodal point $\mathbf{k}_{\mathrm{N}}$ which is confirmed by our data (for both variants of DΓA). We observe that the lDΓA$_{\mathrm{dm}}$ method yields larger (in absolute value) self-energies than the ones obtained by the lDΓA$_{\mathrm{m}}$ method over the entire U range. This can easily be understood from the different magnitudes of the spin and charge susceptibilities in both approaches and the way how they enter in the EoM (7.7). To this end we split Eq. (7.7) into a magnetic contribution, a density contribution and a remainder which accounts for the remaining terms on the right hand side of this equation:

$$\Sigma^{\nu}_{\mathrm{d},\mathbf{k}} = \frac{U^2}{2} \sum_{\omega\mathbf{q}} \gamma^{\nu\omega}_{d,\mathbf{q}} \chi^{\omega}_{\mathrm{d},\mathbf{q}} G^{\nu+\omega}_{\mathbf{k}+\mathbf{q}}, \tag{7.12a}$$

$$\Sigma^{\nu}_{\mathrm{m},\mathbf{k}} = \frac{3U^2}{2} \sum_{\omega\mathbf{q}} \gamma^{\nu\omega}_{\mathrm{m},\mathbf{q}} \chi^{\omega}_{\mathrm{m},\mathbf{q}} G^{\nu+\omega}_{\mathbf{k}+\mathbf{q}}, \tag{7.12b}$$

$$\Sigma^{\nu}_{\mathrm{rem},\mathbf{k}} = \Sigma^{\nu}_{\mathbf{k}} - \Sigma^{\nu}_{\mathrm{d},\mathbf{k}} - \Sigma^{\nu}_{\mathrm{m},\mathbf{k}} \tag{7.12c}$$

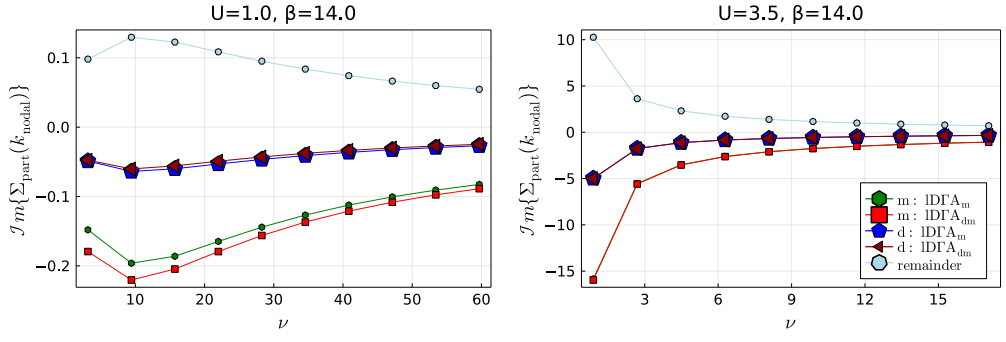

(a) (b)

Figure 7.6: Left: Imaginary part of the self-energy $\Sigma^{\nu}_{\mathbf{k}_{\mathrm{N}}}$ split into contributions from the charge susceptibility (blue pentagons and brown triangles), the spin susceptibility (green hexagons and red squares) and an remainder (blue heptagons) according to Eqs. (7.12) at $\beta = 14$, $U = 1$. Results are presented for lDΓA$_{\mathrm{dm}}$ (red squares and brown triangles) and lDΓA$_{\mathrm{m}}$ (green hexagons and blue pentagons). Note that the correction term is equivalent for both methods as it does not depend on any λ parameter.
Right: Same as in Fig. 7.6a but for $U = 3.5$.

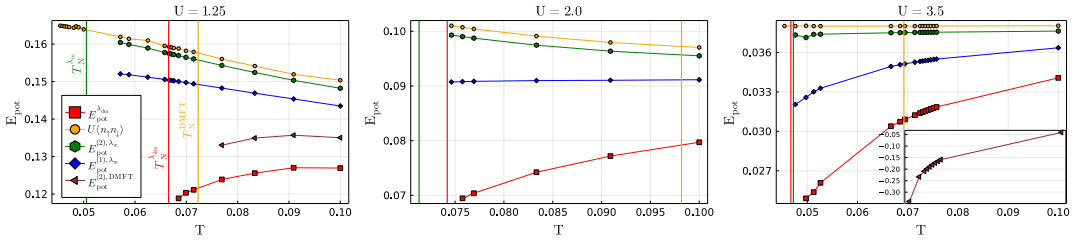

Figure 7.7: Potential energy as a function of temperature for three different values of U as obtained by the DMFT (orange circles and brown triangles), $\mathrm{lD\Gamma A_m}$ (blue diamonds and green hexagons), and $\mathrm{lD\Gamma A_{dm}}$ (red squares). Note that for DMFT and $\mathrm{lD\Gamma A_m}$ the results for E_{pot} calculated from the one- and the two-particle level [corresponding to the right and left hand side of Eq. (7.8b), respectively] differ. Vertical lines indicate the transition temperature T_{N} of the respective method. Due to the unphysical large scale of the two-particle potential energy of DMFT at $U = 3.5$, the data is shown as inset.

Note that the remainder term does not contain $\chi^{\omega}_{\mathrm{d},\mathbf{q}}$ or $\chi^{\omega}_{\mathrm{m},\mathbf{q}}$ and therefore does not depend on any λ parameter. It is for this reason equivalent in the $\mathrm{lD\Gamma A_m}$ and $\mathrm{lD\Gamma A_{dm}}$ method. As discussed in Sec. 7.1.3 $\chi^{\omega}_{\mathrm{m},\mathbf{q}}$ is larger for $\mathrm{lD\Gamma A_{dm}}$ than for $\mathrm{lD\Gamma A_m}$. This property is directly transferred to $\Sigma^{\nu}_{\mathrm{m},\mathbf{k}}$ in Eq. (7.12b) where at weak coupling ($U = 1$) we indeed observe a larger contribution of spin fluctuations to the self-energy for $\mathrm{lD\Gamma A_{dm}}$ (red squares) compared to $\mathrm{lD\Gamma A_m}$ as shown in Fig. 7.6a. The opposite behavior is observed for the charge susceptibility. It is smaller for $\mathrm{lD\Gamma A_{dm}}$ with respect to $\mathrm{lD\Gamma A_m}$ and the same behavior is observed for the corresponding contribution to the self-energy $\Sigma^{\nu}_{\mathrm{d},\mathbf{k}}$. However, since the charge fluctuations are substantially smaller than the spin fluctuations, the former are less relevant in the equations of motion which leads to an overall larger self-energy for $\lambda_{\mathrm{d}} > 0$. The same should in principle hold in the strong coupling regime. However, as discussed in the previous sections, due to the extremely small values of charge fluctuation also the differences in the self-energies and their various contributions are strongly suppressed and almost no differences in the results for $\mathrm{lD\Gamma A_{dm}}$ and $\mathrm{lD\Gamma A_m}$ can be observed as it is shown in Fig. 7.6b.

Potential and kinetic energies

Figure 7.7 shows the potential energies obtained from DMFT (orange circles and brown triangles), $\mathrm{lD\Gamma A_m}$ (blue diamonds and green hexagons) and $\mathrm{lD\Gamma A_{dm}}$ (red squares). Let us stress that for the first two cases (DMFT and $\mathrm{lD\Gamma A_m}$) the potential energies obtained at the one particle level ($E^{(1)}_{\mathrm{pot}}$, orange circles and blue diamonds) deviate from the corresponding results at the two-particle level ($E^{(2)}_{\mathrm{pot}}$, brown triangles and green hexagons) as these approaches are not two-particle self-consistent [c.f., Eq. (7.8b)]. The vertical lines indicate T_{N} for the respective methods.

We observe the same hierarchy of curves for all values of U. The largest potential energy is $E^{(1)}_{\mathrm{pot}}$ of DMFT (orange circles) which is obtained via the right hand side of Eq. (7.8b) with the local DMFT self-energy and the (lattice) Green's function of DMFT. Considering the DMFT self-consistency relation we obtain

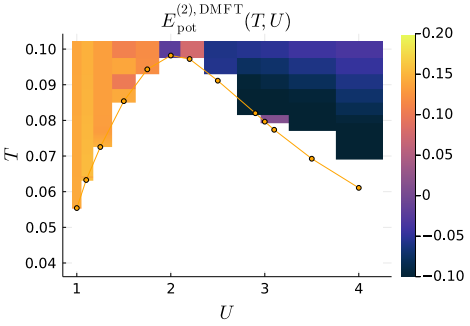

Figure 7.8: DMFT two particle potential energy $E^{(2)}_{\mathrm{pot}}$ as function of T and U.

$$E^{(1)}_{\mathrm{pot,DMFT}} = \sum_{\nu} \underbrace{\sum_{\mathbf{k}} G^{\nu}_{\mathbf{k}}}_{G^{\nu}} \Sigma^{\nu} = \sum_{\nu} G^{\nu}\Sigma^{\nu}$$
$$= \frac{U}{2} \sum_{\omega} \chi^{\omega}_{\mathrm{d}} - \chi^{\omega}_{\mathrm{m}} = U\langle n_{\uparrow} n_{\downarrow}\rangle, \tag{7.13}$$

where $G^{\nu}_{\mathbf{k}}$ is the DMFT lattice Green's function and G^{ν} denotes the local impurity Green's function which is equivalent to the local (i.e., momentum summed) DMFT lattice Green's function due to the DMFT self-consistency condition. $\chi^{\omega}_{\mathrm{d/m}}$ are the local impurity charge and spin susceptibilities and $\langle n_{\uparrow} n_{\downarrow}\rangle$ corresponds to the impurity double occupancy. Note that the AIM is solved exactly and, hence, all consistency relations, in particular the local version of Eq. (7.8b), are fulfilled as also indicated in Eq. (7.13). This implies that $E^{(1)}_{\mathrm{pot}}$ of DMFT is equivalent to U times the double occupancy of the auxiliary AIM which is obtained directly from the impurity solver. Alternatively, the same results can be calculated by summing the local susceptibility $\chi^{\omega}_{\uparrow\downarrow} = \frac{1}{2}[\chi^{\omega}_{\mathrm{d}} - \chi^{\omega}_{\mathrm{m}}]$ over all bosonic Matsubara frequencies ω. In Sec. 7.1.3 we have demonstrated that the momentum summed spin and charge lattice susceptibilities in $\mathrm{lD\Gamma A_m}$ (green hexagons in the upper and orange circles in the lower panels of Fig. 7.2)[1] are almost equivalent to the corresponding correlation

[1] Note that the momentum summed lattice susceptibility of $\mathrm{lD\Gamma A_m}$ in the charge channel is equivalent to the corre-

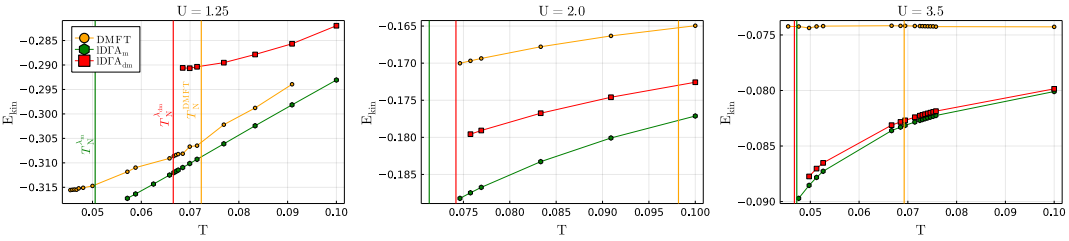

Figure 7.9: Kinetic energy as a function of temperature for three different values of U as obtained by the DMFT (orange circles), $\mathrm{lD\Gamma A_m}$ (green hexagons), and $\mathrm{lD\Gamma A_{dm}}$ (red squares). Vertical lines indicate the transition temperature T_N of the respective method.

function of the AIM (brown triangles in Fig. 7.2). This explains why $E_\mathrm{pot}^{(2)}$ of $\mathrm{lD\Gamma A_m}$ (green hexagons) is almost the same (or only very slightly smaller) than the DMFT potential energy $E_\mathrm{pot}^{(1)}$ (orange circles) in Fig. 7.7.

The DΓA values for $E_\mathrm{pot}^{(1)}$ (blue diamonds) on the other hand, are considerably smaller than the corresponding DMFT results which has been also reported in Ref. [202]. In latter reference it has been discussed, that this is indeed the expected behavior at weak coupling where the antiferromagnetic ground state is of Slater type. Within such a weak coupling Slater mechanism, the antiferromagnetic phase is stabilized by a decrease in the potential. Our results indicate that this mechanism is reflected in the corresponding antiferromagnetic fluctuations above T_N where the inclusion of nonlocal correlations leads to a suppression of E_pot with respect to DMFT. We observe the same behavior at strong coupling where, in principle, a reversed order of the hierarchy in magnitude of potential energies could have been expected due to the antiferromagnetic phase being of Heisenberg type and a stabilization through a gain of kinetic energy [202]. This is, however, not observed as DΓA *always* leads to a reduction of the potential energy with respect to DMFT, indicating that this change in the nature of the antiferromagnetic order from weak to strong coupling is not fully captured by the corresponding fluctuations above T_N (see also the discussion of the kinetic energy below). Whether this behavior is an artifact of the ladder DΓA method or the correct result requires further investigation.

The $\mathrm{lD\Gamma A_{dm}}$ approach (red squares), where by construction $E_\mathrm{pot}^{(1)} = E_\mathrm{pot}^{(2)}$, predicts much smaller potential energies than $E_\mathrm{pot}^{(1)}$ and $E_\mathrm{pot}^{(2)}$ of $\mathrm{lD\Gamma A_m}$ (blue diamonds and green hexagons) and $E_\mathrm{pot}^{(1)}$ of DMFT (orange circles). For $E_\mathrm{pot}^{(2)}$) this difference can be easily explained by the different magnitudes of the lattice charge and spin susceptibilities which have been analyzed in Sec. 7.1.3. In fact, $\chi^\omega_{\mathrm{d},\mathbf{q}}$ is smaller for $\mathrm{lD\Gamma A_{dm}}$ than for $\mathrm{lD\Gamma A_m}$ while the opposite behavior is observed for $\chi^\omega_{\mathrm{m},\mathbf{q}}$ which is larger for $\mathrm{lD\Gamma A_{dm}}$ compared to $\mathrm{lD\Gamma A_m}$. Equation (7.8b) for $E_\mathrm{pot}^{(2)}$ then implies that the corresponding potential energy for $\mathrm{lD\Gamma A_{dm}}$ is larger compared to the one obtained with $\mathrm{lD\Gamma A_m}$.

The fact, that the potential energy of $\mathrm{lD\Gamma A_{dm}}$ is smaller than $E_\mathrm{pot}^{(1)}$ of $\mathrm{lD\Gamma A_m}$ can be easily understood by the difference in the size of the self-energies in both approaches. In fact, considering Eq. (7.8b) for the calculation of $E_\mathrm{pot}^{(1)}$ we find that

$$\begin{aligned} E_\mathrm{pot}^{(1)} &= \sum_{\nu\mathbf{k}} \Sigma^\nu_\mathbf{k} G^\nu_\mathbf{k} = \sum_{\nu\mathbf{k}} \frac{i\nu + \mu - \varepsilon_\mathbf{k}}{i\nu - \varepsilon_\mathbf{k} - i\mathfrak{Im}\Sigma^\nu_\mathbf{k}} - 1 \\ &= \frac{U}{4} + \sum_{\nu\mathbf{k}} \frac{i\nu - \varepsilon_\mathbf{k}}{i[\nu - \mathfrak{Im}\Sigma^\nu_\mathbf{k}] - \varepsilon_\mathbf{k}} - 1 \end{aligned} \tag{7.14}$$

In the second line we have used that $\mu = \frac{U}{2} = \mathfrak{Re}\Sigma^\nu_\mathbf{k}$ for half filling ($n = 1$). Considering that $\mathfrak{Im}\Sigma^\nu_\mathbf{k} < 0$ for $\nu > 0$ (at least for the most relevant momenta $\mathbf{k}_\mathrm{F}$ at the Fermi level as well as in the asymptotic high-frequency regime), it is obvious that a larger self-energy will lead to a smaller potential energy $E_\mathrm{pot}^{(1)}$ (and vice versa). As we have discussed in Sec. 7.1.3, the self-energies for $\mathrm{lD\Gamma A_{dm}}$ are indeed larger than the corresponding self-energies for $\mathrm{lD\Gamma A_m}$ in the entire parameter regime which explains the corresponding differences in the potential energies.

Let us also briefly comment on the DMFT potential energy $E_\mathrm{pot}^{(2)}$ (brown triangles in Fig. 7.7) which is obtained from the charge and spin susceptibilities $\chi^\omega_{\mathrm{d},\mathbf{q}}$ and $\chi^\omega_{\mathrm{m},\mathbf{q}}$ without any λ correction via the left hand side of Eq. (7.8b). In the first and third panel of Fig. 7.7 we observe that $E_\mathrm{pot}^{(2)}$ of DMFT is smaller than the corresponding $E_\mathrm{pot}^{(2)}$ for the $\mathrm{lD\Gamma A_m}$ approach. This can be understood by the fact that $\chi^\omega_{\mathrm{m},\mathbf{q}}$ is larger for DMFT compared to $\mathrm{lD\Gamma A_m}$ (c.f., orange circles and green hexagons in the upper panels in Fig. 7.2) and enters into Eq. (7.8b) for $E_\mathrm{pot}^{(2)}$ with a negative sign.

The situation is more complicated for $\mathrm{lD\Gamma A_{dm}}$ where an additional renormalization via $\lambda_\mathrm{d} > 0$ is applied to $\chi^\omega_{\mathrm{d},\mathbf{q}}$. Such a correction has the opposite effect compared to the λ correction in the spin channel because the charge correlation function enters in $E_\mathrm{pot}^{(2)}$ with a positive sign. Hence, the introduction of λ_d tends to suppress the corresponding potential energy with respect to DMFT while λ_m typically increases it. At weak coupling ($U = 1$, left panel in Fig. 7.7) we can see that the renormalization of the charge susceptibility has

sponding DMFT results as no λ correction is applied to charge fluctuations (i.e., $\lambda_\mathrm{d} = 0$) within $\mathrm{lD\Gamma A_m}$.

indeed a more pronounced effect and the $E_{\text{pot}}^{(2)}$ of DMFT (brown triangles) is larger than the corresponding results for $\text{lD}\Gamma\text{A}_{\text{dm}}$ (red squares). On the contrary, at strong coupling ($U = 3.5$, right panel in Fig. 7.7) the reduction of the potential energy due to the spin susceptibility dominates and $E_{\text{pot}}^{(2)}$ of DMFT is located below the corresponding $\text{lD}\Gamma\text{A}_{\text{dm}}$ result. In fact, at these large values of U, $E_{\text{pot}}^{(2)}$ of DMFT becomes even negative due to the large value of the unrenormalized spin susceptibility. This unphysical behavior at strong coupling has already been reported for the two dimensional Hubbard model in Ref. [271]. In the heat map for $E_{\text{pot}}^{(2)}$ of DMFT in Fig. 7.8 it can be clearly seen that such unphysical negative values emerge beyond $U \approx 2.5$. Note also, that below T_{N} of DMFT $E_{\text{pot}}^{(2)}$ becomes numerically ill defined, since the divergence of the magnetic susceptibility around the antiferromagnetic ordering vector introduces $\mathbf{k}$-sampling dependent noise.

Let us finally comment on the temperature dependence of E_{pot} for the different methods. At weak coupling ($U = 1$, left panel in Fig. 7.7) we observe an increase of $E_{\text{pot}}^{(1)}$ for DMFT (orange circles) and $E_{\text{pot}}^{(1)}$ as well as $E_{\text{pot}}^{(2)}$ for $\text{lD}\Gamma\text{A}_{\text{m}}$ (green hexagons and blue diamonds) upon decreasing temperature. For DMFT this is indeed the expected behavior as the system becomes more metallic at low temperatures[2]. For the $\text{lD}\Gamma\text{A}_{\text{m}}$ results, on the other hand, this increase with decreasing temperature is indeed unphysical as the double occupancy is expected to become smaller when approaching the antiferromagnetic order at T_{N}. The latter (physical) behavior is indeed observed when we consider $\lambda_{\text{d}} > 0$ in the $\text{lD}\Gamma\text{A}_{\text{dm}}$ approach (red squares) which further demonstrates the improved consistency of our new approach with respect to the $\text{lD}\Gamma\text{A}_{\text{m}}$ method. At intermediate and strong coupling (middle and right panels) both versions of DΓA feature the physically correct decrease of $E_{\text{pot}}^{(1)}$ with decreasing temperature.

Let us close this section by briefly discussing the kinetic energy of the system as depicted in Fig. 7.9. It is calculated via the equation

$$E_{\text{kin}} = \sum_{\nu\mathbf{k}} \varepsilon_{\mathbf{k}} G_{\mathbf{k}}^{\nu} \tag{7.15}$$

At weak coupling, the antiferromagnetic state is of coupling Slater type. As it has been discussed extensively in Ref. [202], this implies that the symmetry broken phase is stabilized by a reduction of the potential energy while the kinetic energy is larger in the symmetry broken than in the normal state. It has been demonstrated in the latter publication, that at the very small value of $U = 0.75$ this also holds for the corresponding fluctuations above T_{N} and is reflected in the kinetic energy of $\text{lD}\Gamma\text{A}_{\text{m}}$.

At a slightly larger value of the coupling on the other hand (i.e., $U = 1.25$, left panel of Fig. 7.9) E_{kin} for $\text{lD}\Gamma\text{A}_{\text{m}}$ (green hexagons) is located beyond the corresponding DMFT result (orange circles). This implies that within the $\text{lD}\Gamma\text{A}_{\text{m}}$ method the system is already in an intermediate coupling region. On the contrary, our new result for $\text{lD}\Gamma\text{A}_{\text{dm}}$ (red squares) predicts a kinetic energy above the one of DMFT indicating that the system is still in the weak coupling regime. This is indeed consistent with the predicted T_{N} which is very close to the DMFT result at this value of U. Overall one can see that the $\text{lD}\Gamma\text{A}_{\text{dm}}$ approach extends the range where a Slater type antiferromagnetism is observed with respect to the $\text{lD}\Gamma\text{A}_{\text{m}}$ method.

At intermediate and strong coupling, both DΓA approaches predict a kinetic energy below the one of DMFT which is the correct behavior in this parameter regime. Interestingly, E_{kin} for $\text{lD}\Gamma\text{A}_{\text{dm}}$ is always larger (smaller in absolute value) than the one obtained via $\text{lD}\Gamma\text{A}_{\text{m}}$. This is again a consequence of the larger self-energy in the $\text{lD}\Gamma\text{A}_{\text{dm}}$ approach and can be explicitly demonstrated by rewriting Eq. (7.15) for E_{kin} into a similar form as the equation for $E_{\text{pot}}^{(1)}$ in Eq. (7.14). The difference between E_{kin} of the two versions of ladder DΓA decreases upon increasing U as the charge renormalization becomes gradually less important and eventually almost vanishes at the strongest coupling $U = 3.5$ (see also the corresponding discussions in the previous sections).

7.1.4 Conclusions and Outlook

In this paper, we have presented a method which takes into account nonlocal correlations beyond the local ones of DMFT and fulfills specific exact sum rules which connect one- and two-particle correlation functions. Our new approach is based on the ladder dynamical vertex approximation where nonlocal corrections to the purely local DMFT self-energy are obtained via a diagrammatic expansion around DMFT. More specifically, within this method a momentum dependent self-energy is constructed from the DMFT Green's function and the DMFT charge and spin lattice susceptibilities. Since we do not perform a fully self-consistent treatment of the problem the results initially violate certain sum rules for these susceptibilities which control the total density and the potential energy of the system. To overcome this problem, we have introduced a mass renormalization of the charge and spin susceptibilities by means of (constant) parameters λ_{d} and λ_{m} which are determined by the requirement that the above mentioned sum rules are fulfilled. A simpler version of this idea, where a correction is applied only to the spin channel, has been already successfully exploited in previous research works [125, 202].

We have applied our new approach to the three dimensional half-filled Hubbard model on a simple cubic lattice with nearest neighbor hopping which features an antiferromagnetically ordered phase at low temperatures for all values of the interaction strength. The introduction of the correction parameters λ_{d} and λ_{m} leads to a mutual renormalization of charge and spin fluctuations which can be usually only achieved

[2] Note that the one-particle as well as the impurity quantities of DMFT are not affected by nonlocal antiferromagnetic fluctuations in the proximity of the antiferromagnetic phase transition

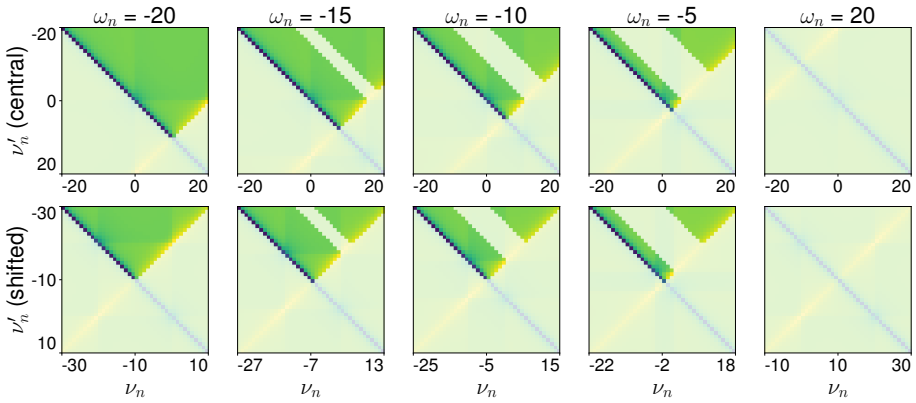

Figure 7.10: Full vertex $F_{\mathrm{m}}^{\nu\nu'\omega}$ as function of ν, ν' at 5 different ω. Labels indicate the (integer) index of the Matsubara frequency. Shaded colors indicate points connected to others by symmetries. Upper panel: unshifted grids, lower panel: ν, ν' shifted by $-\omega/2$

in far more complicated theories such as the parquet approach. The latter is, however, restricted to simple one-band models due to its numerical complexity while our method is, in principal, applicable for multi-band systems or systems with a nonlocal interaction.

We have demonstrated that our method, which takes into account the renormalization of both the charge and spin susceptibility, improves several results compared to the above mentioned previous version of DΓA where only the spin susceptibility has been renormalized. In particular, at weak-to-intermediate coupling it predicts a higher transition temperature T_{N} to the antiferromagnetically ordered state with respect to the old approach which is in good agreement with dual fermion and diagrammatic Monte Carlo calculations. At strong coupling it gradually becomes similar to the old technique as charge fluctuations are strongly suppressed and their renormalization has (almost) no effect on the physical results.

We have also analyzed the potential energy which is obtained by our new method. In contrast to DMFT and the previous version of DΓA, it is uniquely defined and lower than the corresponding ones obtained by the latter approaches. Moreover, at weak coupling it always decreases upon decreasing temperatures approaching the antiferromagnetic phase transition which is indeed the expected behavior for a Slater type antiferromagnet where the ordered phase is stabilized by the potential energy. The kinetic energy is located above the one of DMFT at weak coupling which is also consistent with Slater type antiferromagnetism while the previous non-selfconsistent version of DΓA predicts a lower kinetic energy with respect to DMFT. Overall, our new approach describes the weak and intermediate coupling regime, where charge fluctuations still play an important role, substantially better than the previous approach where a renormalization of charge fluctuations is absent.

Let us finally state, that our new method is not yet fully two-particle consistent as it violates sum rules which originate from conservation laws in the system. The inclusion of such consistency relations in the DΓA formalism (and also other diagrammatic extension of DMFT) is an interesting future research perspective. Moreover, the extension of the presented approach to more realistic multi-orbital systems can potentially lead to an improved theoretical description of nonlocal correlation effects in real materials.

Acknowledgements We thank K. Held, A. Katanin, Th. Schäfer and A. Toschi for useful discussions. We acknowledge financial support from the Deutsche Forschungsgemeinschaft (DFG) through Projects No. 407372336 and No. 449872909. The work was supported by the North-German Supercomputing Alliance (HLRN).

7.1.5 Use of symmetries

The irreducible vertex $\Gamma_r^{\nu\nu'\omega}$, which is required for the calculation of the lattice generalized susceptibility $\chi_{r,\mathbf{q}}^{\nu\nu'\omega}$ in Eq. (7.4), is calculated from the local generalized susceptibility $\chi_r^{\nu\nu'\omega}$ via a local version of Eq. (7.4). The latter is obtained directly from the ED impurity solver which represents the numerically most expensive part of the entire method. To reduce the number of frequencies for which $\chi_r^{\nu\nu'\omega}$ has to be evaluated explicitly we have considered two algorithmic improvements:

(i) We have shifted the fermionic Matsubara frequencies (ν, ν') by $-\frac{\omega}{2}$. This improves our calculations since the main nonperturbative structures of $\chi_r^{\nu\nu'\omega}$ are centered around $(-\frac{\omega}{2}, -\frac{\omega}{2})$ (see Refs. [207, 205]). This can be seen in the upper panels of Fig. 7.10 where we present the full vertex $F_{\mathrm{m}}^{\nu\nu'\omega}$, which is obtained

from $\chi_{\mathrm{m}}^{\nu\nu'\omega}$ by amputating the four outer Green function lines[207], as a function of ν, ν' at different ω slices. The main structures, indicated by the crossing of the yellow and blue diagonal contributions, indeed move to the center if the frequency grid is shifted by $-\frac{\omega}{2}$.

(ii) We have considered all physical symmetries of $\chi_r^{\nu\nu'\omega}$ which allows us to reduce the actual calculation to a subset of Matsubara frequencies in the selected frequency grid. In fact, the generalized susceptibility $\chi_r^{\nu\nu'\omega}$ is equivalent for all frequency triples $(\nu, \nu'\omega)$ which are related to each other via a specific physical symmetry. Consequently, it is sufficient to determine this correlation function for only *one* of this related triples. In Fig. 7.10, the frequencies which are related to another one by a symmetry are shaded. Overall this leads to a reduction in the number of triples (ν, ν', ω) by more than a factor of 10.

For the determination of equivalent arguments for the Green's function we have proceeded in the following way:

1. Define the grid of size $N_{\mathrm{tot}} = N_\nu^2 \times N_\omega$, possibly with shifted ν, ν' values.

2. Define the symmetry mapping, i.e. $f(p)$ = "*list of points p maps to*". This includes only direct symmetries, so for 5 symmetries in the system, the list will have the length 5.

3. Construct an undirected graph with N_{tot} vertices, each representing a point on the grid while edges for each vertex v are given by $f(v)$. It suffices to loop over all vertices and call f on its value, disregarding double edges. In case the equivalent points are related by some operation other than the identity, for example complex conjugation, one has to track the operation connecting two vertices as edge "weight", for example in a parent array.

4. Determine all connected components, for example using depth first search [68], and choose a (random) node as representative. The construction of the mapping from the reduced to the full grid, including the "weights", can be done with a modified depth first search as well.

5. Hand off the reduced grid and mapping to the full grid to the impurity solver and DΓA code.

7.1.6 Improved asymptotics

For the $\mathrm{lDF\Gamma A_{dm}}$ method it is necessary to solve the two coupled equations in Eq. (7.8a) and Eq. (7.8b) for λ_{m} and λ_{d} simultaneously. This requires a precise evaluation of the corresponding frequency sums in these relations as well as in Eqs. (7.5) and (7.6). For a numerical evaluation, these sums over an infinite number of Matsubara frequencies obviously have to be restricted to a finite frequency grid. A plane summation in such a finite frequency domain is typically not sufficient to determine λ_{d} and λ_{m}, but the consideration of the high-frequency asymptotic behavior of all involved correlation functions provides accurate and stable enough results, even if small frequency grids or noisy Monte Carlo input data is used. This section gives an overview of the improved Matsubara summation method used to perform the Matsubara frequency sums for the determination of the λ parameters. The central idea for this summation technique is to divide functions of Matsubara frequencies f^ω, where ω is now a generic variable which can represent a (set of) fermionic and/or bosonic Matsubara frequencies, into a core and asymptotic region. The summation is then performed separately for both. In the core region (indicated by a subscript "c"), a sum over the exact numerical data for f^ω is carried out while in the asymptotic high-frequency regime f^ω (or shell region, indicated by a subscript "s") is replaced by leading order diagrams T^ω which do not decay as a function of frequency. The frequency sum over the latter can be performed semi-analytically. Formally, this idea can be represented as follows:

$$\begin{aligned}\sum_\omega f^\omega &= \sum_{\substack{\omega\in \\ \Omega_{\mathrm{core}}(\nu)}} (f^\omega - T^\omega + T^\omega) + \sum_{\substack{\omega\in \\ \Omega_{\mathrm{asym}}(\nu)}} (f^\omega - T^\omega + T^\omega) \\ &\approx \sum_{\substack{\omega\in \\ \Omega_{\mathrm{core}}(\nu)}} (f^\omega - T^\omega) + \sum_\omega T^\omega,\end{aligned}$$

where in the second line of this equation we have neglected the term $f^\omega - T^\omega$ in the high-frequency shell region as it rapidly decays with increasing frequency ω. As discussed in appendix 7.1.5, the core region $\Omega_{\mathrm{c}} = \Omega_{\mathrm{c}}^\nu$ for the bosonic or fermionic frequency ω can depend on a (fermionic or bosonic) Matsubara frequency ν which is not involved in the summation when shifted grids are considered for the calculation. If two indices are used for a core or shell summation, the notation implies that the *tuple* lies either within the core or the shell region. In the following we will denote quantities summed over the core and shell region by corresponding superscripts. Furthermore, we use a tilde to distinguish quantities obtained through improved summation from ones obtained through plain summation. For the bare susceptibility ("bubble" term) this reads as follows:

$$\begin{aligned}\chi_{0,\mathbf{q}}^{\nu\omega} &= -\beta \sum_{\mathbf{k}} G_{\mathbf{k}}^\nu G_{\mathbf{k}+\mathbf{q}}^{\nu+\omega} \\ \chi_{0,\mathbf{q}}^{\omega} &= \sum_{\substack{\nu\in \\ \Omega_{\mathrm{core}}(\omega)}} \chi_{0,\mathbf{q}}^{\nu\omega} + \sum_{\substack{\nu\in \\ \Omega_{\mathrm{shell}}(\omega)}} \chi_{0,\mathbf{q}}^{\nu\omega} = \chi_{0,\mathbf{q}}^{\mathrm{core},\omega} + \chi_{0,\mathbf{q}}^{\mathrm{shell},\omega}.\end{aligned}$$

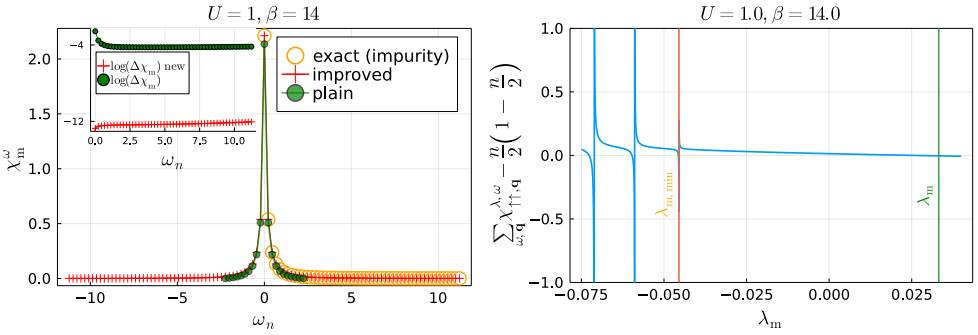

(a) Local physical susceptibility spin χ^ω_m as a function of ω for $U = 1$ and $\beta = 14$ as obtained by summing the generalized physical susceptibility $\chi^{\nu\nu'\omega}_m$ over the fermionic frequencies ν and ν' using the improved frequency sums (red crosses) vs. a plain frequency sum on a finite grid (green filled circles) and the exact results obtained directly from the impurity solver (empty orange circles). The inset shows the log of the difference between normal summation and improved summation to the exact values. The plain Matsubara summation is cut of at values of ω where it becomes negative (i.e. unphysical).

(b) $\sum_{\omega\mathbf{q}} \chi^{\lambda,\omega}_{\uparrow\uparrow,\mathbf{q}} - \frac{n}{2}(1 - \frac{n}{2}) = \frac{1}{2}\sum_{\omega\mathbf{q}} \left(\chi^{\lambda_d,\omega}_{d,\mathbf{q}} + \chi^{\lambda_m,\omega}_{m,\mathbf{q}}\right) - \frac{n}{2}(1 - \frac{n}{2})$ for $\lambda_d = 0$ showing the root for the equation (which determines λ_m) and poles for $\lambda_m < \lambda_{m,min}$.

Figure 7.11: Improved sums and minimal λ values.

The asymptotic contribution to the bare susceptibility $\chi^{\omega,\text{shell}}_{0,\mathbf{q}}$ can be obtained directly from the high frequency tails of the DMFT Green's functions. Following the derivation of the high frequency behavior of the vertex functions $F^{\nu\nu'\omega}_{r,\mathbf{q}}$ and $\Gamma^{\nu\nu'\omega}_r$ as discussed in Refs. [207, 256, 290], we obtain for the improved frequency sums for the calculation of $\chi^\omega_{r,\mathbf{q}}$ and $\gamma^{\nu\omega}_{r,\mathbf{q}}$ in Eqs. (7.5) and (7.6) the following expressions:

$$\tilde{\lambda}^{\nu\omega}_{r,\mathbf{q}} = \left(1 \mp U\chi^{\text{shell},\omega}_{0,\mathbf{q}}\right)^{-1} \cdot \left(\lambda^{\text{core},\nu\omega}_{r,\mathbf{q}} + \lambda^{\text{shell},\nu\omega}_{r,\mathbf{q}}\right) \tag{7.16}$$

$$\tilde{\chi}^\omega_{r,\mathbf{q}} = \left(1 - \left(U\chi^{\text{shell},\omega}_{0,\mathbf{q}}\right)^2\right)^{-1} \cdot \left(\chi^{\text{core},\omega}_{r,\mathbf{q}} + \chi^{\text{shell},\omega}_{r,\mathbf{q}}\right) \tag{7.17}$$

$$\tilde{\gamma}^{\nu\omega}_{r,\mathbf{q}} = \frac{1 \mp \tilde{\lambda}^{\nu\omega}_{r,\mathbf{q}}}{1 \pm U\tilde{\chi}^\omega_{r,\mathbf{q}}}. \tag{7.18}$$

We have introduced the following abbreviations:

$$F^{\nu\nu'\omega}_{m,\text{diag}} = \frac{1}{2}\chi^{\nu-\nu'}_d - \frac{1}{2}\chi^{\nu-\nu'}_m + \chi^{\nu+\nu'+\omega}_{pp,\uparrow\downarrow}$$

$$F^{\nu\nu'\omega}_{d,\text{diag}} = \frac{1}{2}\chi^{\nu-\nu'}_d + \frac{3}{2}\chi^{\nu-\nu'}_m - \chi^{\nu+\nu'+\omega}_{pp,\uparrow\downarrow}$$

$$\lambda^{\text{core},\nu\omega}_{r,\mathbf{q}} = \pm\beta \sum_{\substack{\nu' \in \\ \Omega_{\text{core}}(\omega)}} \left(\delta_{\nu\nu'} - \frac{\chi^{\nu\nu'\omega}_{\mathbf{q}}}{\chi^{\nu\omega}_{0,\mathbf{q}}}\right)$$

$$\lambda^{\text{shell},\nu\omega}_{r,\mathbf{q}} = U\chi^{\text{shell},\omega}_{0,\mathbf{q}} \mp U^2 \sum_{\substack{\nu' \in \\ \Omega_{\text{shell}}(\omega)}} F^{\nu\nu'\omega}_{r,\text{diag}}\chi^{\nu'\omega}_{0,\mathbf{q}}$$

$$\chi^{\text{core},\omega}_{r,\mathbf{q}} = \sum_{\substack{\nu\nu' \in \\ \Omega_{\text{core}}(\omega)}} \chi^{\nu\nu'\omega}_{r,\mathbf{q}}$$

$$\chi^{\text{shell},\omega}_{r,\mathbf{q}} = \pm U\left(\chi^{\text{shell},\omega}_{0,\mathbf{q}}\right)^2 - U^2 \sum_{\substack{\nu\nu' \in \\ \Omega_{\text{asym}}(\omega)}} \chi^{\nu\omega}_{0,\mathbf{q}} F^{\nu\nu'\omega}_{r,\text{diag}} \chi^{\nu'\omega}_{0,\mathbf{q}}$$

$$- \sum_{\substack{\nu' \in \\ \Omega_{\text{shell}}(\omega)}} \chi^{\nu'\omega}_{0,\mathbf{q}} \left(1 + 2U \sum_{\substack{\nu \in \\ \Omega_{\text{core}}(\omega)}} (\tilde{\lambda}^{\nu\omega}_{r,\mathbf{q}} \mp 1)\chi^{\nu\omega}_{0,\mathbf{q}}\right).$$

The local physical susceptibilities χ^ω_r for the diagonal term $F^{\nu\nu'\omega}_{r,\text{diag}}$ of the full vertex are local and can be obtained directly from the DMFT impurity solver. The contributions from $F^{\nu\nu'\omega}_{r,\text{diag}}$ are typically negligible, when the physical susceptibilities in the three channels fall off sufficiently fast with increasing frequency. Fig. 7.11a shows a benchmark for our improved summation method for the summation of the purely local generalized susceptibility $\chi^{\nu\nu'\omega}_m$ (in the spin channel) over the fermionic Matsubara frequencies ν and ν'

yielding the physical susceptibility $\chi^{\omega}_{\mathrm{m}}$. The $\chi^{\omega}_{\mathrm{m}}$ obtained via our improved summation technique (red crosses) agrees excellently with the exact results (orange empty circles) obtained directly from the impurity solver. The $\chi^{\omega}_{\mathrm{m}}$ obtained through a plain sum on a finite frequency grid (green filled circles), on the other hand, shows substantially larger deviations from the exact results (see inset in Fig. 7.11a) and eventually features unphysical negative values at larger frequencies ω which is not observed for the improved frequency sum.

7.1.7 Root finding procedure

Finding the roots λ_{d} and λ_{m} for Eqs. (7.8a) and (7.8b) can be done with any root finding algorithm, but requires two considerations in order to yield reasonable results: (i) the physical tails must be free of finite size effects and (ii) the unphysical, $\mathbf{q}$ dependent poles of Eq. (7.9a) must be avoided in the calculation (i.e. the resulting λ corrected physical susceptibility must non-negative).

The first difficulty can be overcome by using the procedure for treating the high-frequency asymptotic tails of all correlation functions as explained in appendix 7.1.6. The second requirement has been avoided by the procedure described in Sec. 7.1.3. However, this method is not applicable for large simulations, due to the numerical cost of the many evaluations of the equation of motion, required to obtain the curves in Figs. 7.1a and 7.1b over a large range of λ values. Instead, a more elaborate root finding algorithm, such as the Newton method, is preferable requiring substantially fewer evaluations of the EOM. To avoid unphysical solutions, let us consider that the λ corrected physical susceptibilities are continuous and monotonically decreasing (as a function of λ) for all λ values larger than the largest pole, i.e. $\lambda_r > \lambda_{r,\mathrm{min}}$ [219]. The location of the largest pole is:

$$\lambda_{r,\mathrm{min}} = \min_{\mathbf{q}} \frac{1}{\chi^{\omega_0}_{r,\mathbf{q}}}$$

The monotonously decreasing behavior follows directly from the derivative of $\chi^{\lambda_r,\omega}_{r,\mathbf{q}}$ with respect to λ_r:

$$\frac{\mathrm{d}}{\mathrm{d}\lambda_r} \sum_{\omega\mathbf{q}} \chi^{\lambda_r,\omega}_{r,\mathbf{q}} = -\sum_{\omega\mathbf{q}} \left(\chi^{\lambda_r,\omega}_{r,\mathbf{q}}\right)^2 \leq 0$$

In Fig. 7.11b the difference between right and left hand side of Eq. (7.8a) is shown for $U = 1$ and $\beta = 14$ as a function of λ_{m}. Here we see the $\mathbf{q}$-sampling dependent divergences for $\lambda_{\mathrm{m}} < \lambda_{\mathrm{m,min}}$. Since both λ corrected physical susceptibilities exhibit the same behavior, the $\lambda_{r,\mathrm{min}}$ values can be determined independently. This pole structure leads to an interval $[\lambda_{r,\mathrm{min}}, \infty)$ in which a single root for Eq. (7.8a) is located. Eq. (7.8b) could in principle exhibit non-monotonous behavior, since the right hand side is a function of both λ corrected physical susceptibilities. However, as discussed in Sec. 7.1.3 (see Figs. 7.1a and 7.1b), this does not happen for our calculations. Therefore, by means of the following transforming one can obtain a result, guaranteed to yield exactly one, physically correct, root.

$$\tilde{\lambda}_r = \frac{\lambda_{r,\mathrm{min}} - \lambda_{r,\mathrm{max}}}{2} \left(\tanh\left(\lambda_r\right) + 1\right) + \lambda_{r,\mathrm{min}} \tag{7.19}$$

$\lambda_{r,\mathrm{max}}$ can in principle be arbitrarily large, but a reasonable value can be chosen from the known fluctuations strength of the system. This transformation is then applied to the function, before it is handed over to the solver and the resulting root is transformed in the same way.

For our purposes, we use the multivariate Newton method, which is a reasonable choice over more modern methods such as BFGS, due to the low dimensionality of our problem and the smoothness of the search space [see Sec. 7.1.3]. The Jacobian was determined by finite differences since Eq. (7.8b) involves a convolution over numerical data, making automatic and analytic differentiation challenging. Note, that the transformation in Eq. (7.19) concentrates sampling points at the borders of the search interval. For very high precision, especially at strong coupling where the Jacobian becomes small (see also Fig. 7.1a), one can first run a low precision pass with the transformation and then use the obtained result as a starting point for a high precision search.

7.2 Results on the Hubbard Model in two dimensions

7.2.1 Introduction

The well-known family of high-temperature superconductors with quasi-two-dimensional layers of copper oxide, cuprates, has been of immense interest since their discovery in 1986 [24]. Among their many interesting and unique properties, the prevalence of strong electronic correlations and interplay with magnetic ordering stands out, for example, manifested in the pseudogap (PG) phase, one of the most interesting phenomena in condensed matter physics. Here, a momentum-dependent partial suppression of weight around the Fermi surface (see Fig. 7.12) and anomalous (linear in T) resistivity are observed. The importance of strong electronic correlations was realized early on by P. Anderson with the proposal of the superexchange mechanism [11]. However, many details of the phase diagram still remain the subject of ongoing research. The current consensus for the hole-doped region is shown in Fig. 7.12 (Fig. 4 from [108]). As a function of hole doping, one finds several distinct phases. Close to the Mott insulating phase at half-filling, antiferromagnetic fluctuations prevail but are subsequently replaced by a pseudogap phase. Inelastic neutron scattering experiments suggest that this phase is associated with a collective magnetic mode [161] that hides a quantum critical point at $T = 0$ [272]. Interestingly, the ground state of the PG phase has a restored Fermi surface, contrasting the characteristic non-Fermi liquid behavior at finite temperature [197]. In fact, antiferromagnetic fluctuations start to appear already above the critical temperature for the superconducting phase T_C and seem to be influencing the Fermi surface reconstruction in this region as well [243]. It has also been experimentally confirmed that the remnants of Mott physics for finite hole dopings and the ensuing transition to the multitude of phases like spin and charge stripes and spin glasses [225, 73, 279], are a generic feature of these electronic structures and not unique to the traditional cuprates [21]. Here, we investigate the impact of non-local electronic correlations in the finite temperature regime as a function of doping. We use the two-dimensional Hubbard model, where full antiferromagnetic ordering is prevented by the Mermin-Wagner theorem. Nonetheless, the particulars regarding the breakdown are intricate with numerous proposed scenarios [279, 73] and measurements of the magnetic susceptibility demonstrate a strong dependence not only on doping but also on impurities [196, 295]. It has been demonstrated that a qualitative description of the physics can be achieved by solely considering electronic correlations [158]. Here, we will employ a method that is able to mix different electronic scattering channels, similar to a previous work [17]. However, the effective nature allows for much finer $\mathbf{k}$-space resolution. In addition, this method has been demonstrated in the 3 dimensional cubic lattice at half-filling to capture antiferromagnetic fluctuations very well on a quantitative level [253].

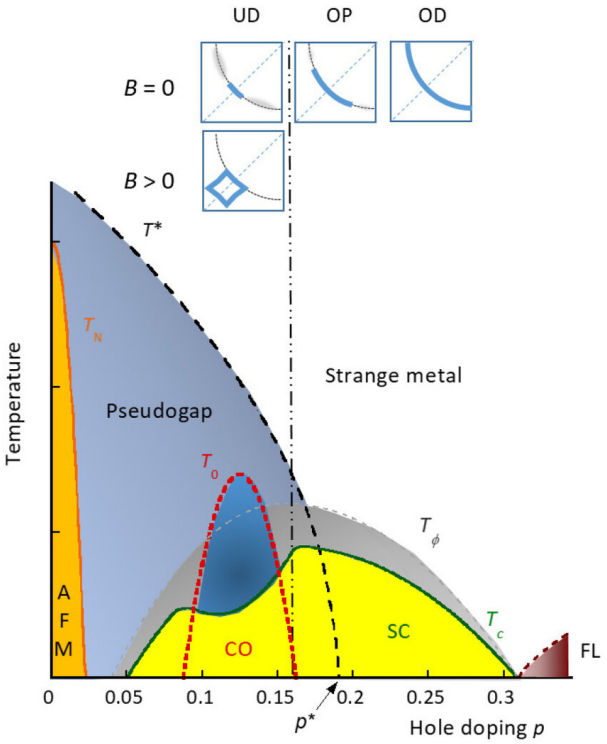

Figure 7.12: Fig. 4 from [108]. Schematic representation of the hole-doped phase diagram, including the pseudogap (PG), charge-ordered (CO), and superconducting (SC) regions. Inset shows the evolution of the Fermi surface from under-doped (UD) over optimally doped (OP) to over-doped (OD). T_ϕ marks the region of superconducting fluctuations, see [108, Sec. 5] for the in-depth discussion.

7.2.2 Model

Here, we consider the single-band Hubbard model

$$\hat{\mathcal{H}} = \sum_{\mathbf{k}} (\epsilon_{\mathbf{k}} - \mu) \hat{c}^\dagger_{\mathbf{k}\sigma} \hat{c}_{\mathbf{k}\sigma} + U \sum_i \hat{n}_{i\uparrow} \hat{n}_{i\downarrow} \tag{7.20}$$

on the two-dimensional square lattice with the well-established hoppings for cuprates [7, 187], specifically for BSSCO $\epsilon_{\mathbf{k}} = -2t\,(\cos(\mathbf{k}_x) + \cos(\mathbf{k}_y)) + 4t' \cos(\mathbf{k}_x)\cos(\mathbf{k}_y) - 2t''\,(\cos(2\mathbf{k}_x) + \cos(2\mathbf{k}_y))$ with $t = 0.25$, $t' = 0.05$,$t'' = 0.025$, in order to facilitate comparison with [182, 17]. It has long been established that van Hove singularities are linked to the transition from non-Fermi liquid to Fermi liquid

behavior at the quantum critical point [46]. Specifically, the next-nearest neighbor hopping t' in the non-interacting tight-binding model is vital for the description of the pseudogap phase [291].
The single band Hubbard model does have certain deficiencies in the quantitative description of cuprates, especially in the electron-doped regime. It has however been demonstrated that a good quantitative agreement in the hole-doped regime can be expected [163]. Furthermore, electron-phonon coupling is known to enhance T_C in the underdoped regime due to a suppression of antiferromagnetic fluctuations [129]. These effects have been neglected in our approach as well.

7.2.3 Method

We employ the ladder DΓA method in a modified version that enforces two-particle consistency in the potential energy [264, 125, 202, 253]. For details of the definition of the lDΓA method with two-particle consistent potential energy, we refer to [253, Sec. II.A] and Sec. 5.4. Compared to the previous iteration of this method, we introduce three changes: (i) partial self-consistency in the Schwinger-Dyson equation of motion; (ii) introduction of a lDΓA chemical potential for calculations out of half-filling; (iii) high-frequency tail correction schemes for the self-energy.
The partial self-consistency in the Schwinger-Dyson equation of motion is achieved by replacing the DMFT propagator in the equation with the lDΓA Green's function:

$$\Sigma^{\lambda,\nu}_{\mathbf{k}} = \frac{Un}{2} - U\sum_{\omega\mathbf{q}}\Big[1 + \frac{1}{2}\gamma^{\nu\omega}_{\mathrm{d},\mathbf{q}}(1 - U\chi^{\lambda_\mathrm{d},\omega}_{\mathrm{d},\mathbf{q}}) - \frac{3}{2}\gamma^{\nu\omega}_{\mathrm{m},\mathbf{q}}(1 + U\chi^{\lambda_\mathrm{m},\omega}_{\mathbf{q}}) + \sum_{\nu'}\frac{1}{2}\chi^{\nu'\omega}_{0,\mathbf{q}}F^{\nu\nu'\omega}_{\uparrow\downarrow}\Big]G^{\lambda,\nu+\omega}_{\mathbf{k}+\mathbf{q}} - \Sigma^{\mathrm{corr},\nu}_{\mathbf{k}} \tag{7.21}$$

Where $G^{\lambda,\nu+\omega}_{\mathbf{k}+\mathbf{q}}$ is determined from $\Sigma^{\lambda,\nu}_{\mathbf{k}}$ via the Dyson equation. Here, the chemical potential is fitted in order to keep the electron density consistent with the DMFT calculation. Lastly, we introduce a correction term $\Sigma^{\mathrm{corr},\nu}_{\mathbf{k}}$ that restores the otherwise violated high-frequency asymptotic behavior of $\lim_{\nu\to\infty}\Sigma^{\nu} = U^2\frac{n}{2}\left(1 - \frac{n}{2}\right)$.
The numerical setup has been discussed in detail in Sec. 5.4 and Sec. 6.5. Here, we employ the lDΓA method with and without partial self-consistency in the equation of motion. The Matsubara summations are carried out using the improved tails, derived in Sec. 6.2 and Sec. 6.3. Let us briefly reiterate the necessary steps here that are required for this version of the lDΓA method.
In preparation for the calculations, we generate a frequency grid and tight-binding solution using the codes presented in Sec. 6.8.2 and Sec. 6.8.4. The frequency and $\mathbf{k}$ grid for the two-particle Green's function is generated using known symmetry relations, as discussed in Sec. 6.4.
We then obtain a DMFT solution using either CTQMC or ED as an impurity solver, depending on the temperatures (above $\beta \approx 50$, the solutions between both impurity solvers match within numerical accuracy, and the stability and low computational cost of the ED solutions with 8 bath sites, are preferable). As ED code, we use Sec. 6.8.3. Subsequently, a 4 bath site AIM is fitted to the DMFT solution, using `BFGS` as a solver, $\left[G^{\nu}\cdot\sqrt{\nu}\right]^{-1}$ as transformation and $|v|^2$ as a distance function (see Sec. 6.6.2).
We then obtain a two-particle Green's function from the local reference model and generate the local irreducible vertices in the particle-hole and particle-particle channel using the code from Sec. 6.8.7.
Subsequently, the lDΓA code presented in Sec. 6.8.5 is used to compute the bare susceptibility $\chi^{\nu\omega}_{0,\mathbf{q}}$. Finally, the physical susceptibilities $\chi^{\omega}_{r,\mathbf{q}}$ and triangular $\gamma^{\nu\omega}_{r,\mathbf{q}}$ vertices in the density and magnetic channels are computed from the local irreducible vertex using the Bethe-Salpeter equation. Depending on the specific sub-method, we now obtain λ_m, λ_d and μ values according to Fig. 5.8. In the case of the partially self-consistent method, this yields a new self-energy $\Sigma^{\lambda_\mathrm{m},\lambda_\mathrm{d},\nu}_{\mathbf{k}}$ as well[3]. As a last step, we perform a sub-sampling of the $\mathbf{k}$ grid, compute the full lDΓA vertex $F^{\nu\nu'\omega}_{\mathrm{pp},\mathbf{q}}$, as described in Sec. 4. Depending on the size of the subsampling, either a matrix-free or direct diagonalization method is employed to obtain the leading eigenvalue of $\Gamma^{\nu\nu'\omega=0}_{\mathrm{pp},\mathbf{k}\mathbf{k}'0}$, using the code from Sec. 6.8.5.

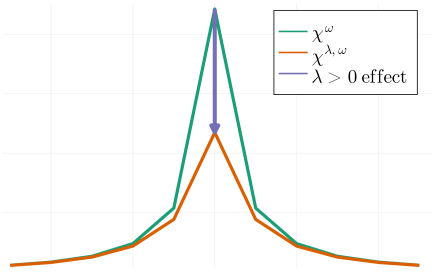

Figure 7.13: Illustration of λ parameter effect.

7.2.4 Susceptibilities and Renormalization Parameters

We first present the values of the λ correction parameters. Their role as renormalization of the correlation length due to non-local correlations (see Sec. 4.5.1) serves as a qualitative indicator for the fluctuations due to electronic correlations that are not captured in the (local) DMFT approach. The values of λ_r strongly depend on numerical parameters such as $\mathbf{k}$ space resolution and frequency grid. This has been considered by calculating all values for a sweep at one temperature at fixed parameters.

[3] The λ_r values and the self-energies are usually obtained for all tail-correction schemes described in Sec. 6.2.4.

λ parameters Fig. 7.14 and Fig. 7.15 show the λ_r values for 4 different inverse temperatures β and the self-energy correction schemes presented in Sec. 6.3.4. Using the λ_m value to fix the tail instead of the Pauli principle does not yield roots and is therefore not shown. Around half-filling, the solutions for the λ values become numerically difficult to stabilize (due to small charge fluctuations, high numerical precision is needed) and have, therefore, not been computed for all temperatures. Note that the `ExpStep` method interpolates between `Plain` and `Full`, depending on the δ parameter and can, therefore, be used to obtain a stable solution if either one of both converges. The data here is shown for $\delta = 0.8$. Both limiting cases, therefore, also provide insight into the range of potential solutions obtainable through different values of this numerical parameter. The lDΓA$_\mathrm{m}$ method does not depend on the choice of the self-energy tail correction scheme because this quantity only appears as an exogenous quantity, similar to TPSC.
In addition to the values, we also show a color-coded background in the lower panels (to keep the plots less busy the upper panels are shown without the background) indicating the DMFT ordering vector. As discussed in Sec. 5.4.2, the lDΓA method does not reorder the $\mathbf{q}$ vectors. The colors are pink for $\mathbf{q}_\mathrm{max} = (\pi, 0)$, blue for $\mathbf{q}_\mathrm{max} = (0, 0)$, orange for $\mathbf{q}_\mathrm{max} = (\pi, \pi)$ and green for incommensurate ordering.
For high temperatures ($\beta = 12$), the $\lambda_\mathrm{m}(n)$ curve[4] Fig. 7.12 is mostly featureless, with a peak at around half filling and a minimum in the hole-doped region at around 20% for the lDΓA$_\mathrm{dm}$ and lDΓA$_\mathrm{dm,sc}$ methods, while lDΓA$_\mathrm{m}$ is monotonically decreasing. The `Plain` tail correction scheme already begins to show the onset of a maximum at around 25% hole doping (only observed at lower temperatures for the other tail-correction schemes).
We observe a slight asymmetry between the electron-doped and hole-doped regimes. This suppression of magnetic fluctuations compared to DMFT is specifically pronounced in the vicinity of half-filling, where antiferromagnetic fluctuations play an important role. For inverse temperatures of $\beta = 30$ and above, the $\lambda_\mathrm{m}(n)$ functions show a local minimum at around 15% and a local maximum at around 30% hole doping. These doping values coincide with the end of the charge-ordered phase and the end of the super-conducting dome fillings (compare Fig. 7.12). The beginning of the Fermi liquid phase at 30% hole doping shows an inflection point in the λ_m parameter. We note that these features are not present in the lDΓA$_\mathrm{m}$ method, while both methods that incorporate re-balancing between channels see an increased suppression of magnetic fluctuations due to non-local correlations. The lDΓA$_\mathrm{m}$ scheme predicts larger spin fluctuation (the λ_m parameter is small) in the region of optimal doping than the other methods, which is interpreted as a deficiency of this method due to a lack of this re-balancing. This is supported by the established notion in the literature that the interplay between spin order in the form of anti-ferromagnetic fluctuations and charge ordering plays a vital role in the emergence of the superconducting dome.
The magnetic fluctuations are monotonically decreasing as a function of both electron- and hole doping. Comparison between the lDΓA$_\mathrm{dm}$ and lDΓA$_\mathrm{dm,sc}$ schemes shows little difference in the magnetic channel corrections. As a function of temperature, we observe that the antiferromagnetic fluctuations are being pushed towards half-filling with a lowering of the temperature.
The λ_d parameter in Fig. 7.15 also experiences a slight asymmetry in the doping around half-filling. Opposite to the magnetic channel, the larger correction due to non-local effects is in the hole-doped region. Next to the minimum at around half-filling (where, due to frozen charge fluctuation, neither local nor non-local contributions play a role), we observe two peaks at around 5% electron-doping and hole-doping.
Most importantly, we observe a sign change at around 15% hole-doping, coinciding roughly with the transition from uniform to stripe ordering in the charge channel (on the DMFT level, note also that the magnetic fluctuations are orders of magnitude larger.). This enhancement of charge fluctuation due to non-local correlation effects (compare Fig. 7.13) persists throughout the full superconducting dome but decreases towards the Fermi-liquid regime. Here, we observe decreasing non-local corrections, indicating that the charge fluctuations are fully captured within the local DMFT approach. These effects can only be captured by the lDΓA$_\mathrm{dm}$ and lDΓA$_\mathrm{dm,sc}$ methods, due to a neglected charge fluctuation renormalization in lDΓA$_\mathrm{m}$. In the charge susceptibilities, we observe no significant quantitative difference between the values predicted from the lDΓA$_\mathrm{dm}$ and lDΓA$_\mathrm{dm,sc}$ approaches. In all self-energy tail correction schemes, the lDΓA$_\mathrm{dm}$ seems to overestimate the non-local corrections. Similar to the magnetic channel, the `Plain` tail correction scheme seems to predict the largest effect and is the most numerically unstable scheme, while the inverse is true for the `EoM` scheme.
In the Fermi-liquid regime, ferromagnetic fluctuations dominate. We stress that our approach is not capable of capturing all details of the interaction between charge density and spin waves due to the neglected phonon interactions, reduction to a single-band model, and mean-field ordering vectors. Nevertheless, the ferromagnetic ordering (seen by the blue coloring in the λ_m figures) at very high hole-doping levels has also been observed in experiments [141, 235, 214] and FLEX calculations [262]. The persistence of enhancement in the charge response beyond the CDW region also has some support in experiments [174].

[4] Note that we use the electron density n on the x-axis and the hole-doping p has to be read off from $n = 1$ to the left.

Susceptibilities Fig. 7.16 and Fig. 7.17 show the λ corrected susceptibilities in the magnetic and charge channels. In the magnetic channel, the agreement between self-energy tail correction schemes is much closer, especially qualitatively as a function of the electron density n. The agreement between tail-correction schemes remains quantitatively on the same level as for the correction parameters. We also note that the spurious divergence of the magnetic susceptibility due to the mean-field character of DMFT is renormalized, but sizable antiferromagnetic fluctuations remain. Note that the λ-correction does not change the ordering vector, as by design of the λ-correction method, discussed in Sec. 4.5.1. The charge fluctuations are suppressed around half-filling and enhanced in the doping regime of the superconducting dome. The $\chi^{\lambda_\mathrm{d},\omega_0}_{\mathrm{d},\mathbf{q}_\mathrm{max}}$ curve is mostly featureless at high temperatures and the `Full` tail-correction scheme. However, at sufficiently low temperatures, an enhancement in charge fluctuations between 15 and 30% hole doping can be seen.

Energies and compressibility Fig. 7.18 and Fig. 7.19 show the potential and kinetic energy using the same setup as before. Here, we observe a strong asymmetry in the potential energy (due to an increase of double occupancies in the electron-doped regime) around half-filling that is not fully reflected in the kinetic energy. Interestingly, the tail-correction scheme has a much more pronounced impact on the energies than the susceptibilities. The `Full` schemes do not see a local maximum in the potential energy as a function of hole doping in the superconducting regime, while the `EoM` and `Plain` do have a moderate and strong local maximum at 25% hole doping. We attribute this to an over-correction of the lowest Matsubara frequencies because the `ExpStep`, which retains the `Plain` solution for low and the `Full` solution at high frequencies, also predicts a maximum of the potential energy at around optimal doping. This maximum is also accompanied by a local minimum at 10% that is much less pronounced in the modified EoM approach and only appears at lower temperatures. We do not see this reduction in potential energy reflected by an increase in the kinetic energy. The accompanying feature in the one-particle compressibility $\kappa^{(1)}$ suggests that this feature is driven by the non-local charge corrections. The kinetic energy shows a sudden and strong decrease at 15% hole doping for the `Plain` tail-correction scheme, after which it slowly increases towards the overdoped regime. This behavior is washed out in the $\mathrm{lD\Gamma A}_{\mathrm{dm,sc}}$ approach and less pronounced in the remaining tail-correction schemes, but visible in all of them at low temperatures and not captured with DMFT.
We also note that the `Plain` correction scheme can result in negative potential energies between 5% and 15% hole doping, serving as a further indicator that no tail correction can lead to unphysical results.
Importantly, we note an indication that the partially self-consistent method sees a slight increase (local maximum) of the kinetic energy at low temperatures ($\beta = 30$ and $\beta = 50$) around $10 - 15\%$ hole doping. This coincides with the (CO) phase and is not captured fully by the other approaches. This feature is also reflected in a suppression of the compressibility. However, because only very few data points contribute to this feature, further investigation should exclude potential numerical problems in this doping range.
Lastly, we note that around 20% hole doping, at which the PG phase ends, the kinetic (potential) energy has a local minimum (maximum).

Fig. 7.20 and Fig. 7.21 show the compressibility obtained on the one-particle ∂_n/∂_μ and two-particle $2\chi^{\lambda_\mathrm{d},\omega_0}_{\mathrm{d},\mathbf{q}=0}$ levels. These are not consistent through the λ correction scheme but match qualitatively somewhat closely. In general, the one-particle exhibits not only significantly more numerical noise (due to the derivative) but is also only indirectly renormalized through the λ_d parameter. Here, we generally observe inverse behavior to the kinetic energy, as expected, suggesting the validity of both quantities, that are not explicitly made consistent in this method.

7.3 Self-Energies

In Fig. 7.22 we show the difference of the imaginary part of the self-energy at the lowest Matsubara frequency between nodal $\mathbf{k}_\mathrm{N} = (\pi/2, \pi/2)$ and anti-nodal $\mathbf{k}_\mathrm{AN} = (\pi, 0)$ points for several temperatures. For obvious reasons, the momentum differentiation in self-energy is the most pronounced difference between tail-correction schemes, but the partial self-consistency also substantially modifies the result. For one, we note that the `EoM` does not capture any consistent momentum differentiation in the pseudogap regime. This failure of the FLEX type equation of motion has been observed before [277] and seems to be a clear deficiency of this tail-correction scheme. The `Full` and `Plain` schemes both show a significant momentum differentiation in the $\mathrm{lD\Gamma A}_\mathrm{dm}$ method with a maximum at 9% hole doping that increases with lower temperatures. For lower temperatures, we also observe an inversion of the nodal and anti-nodal point with a significantly less pronounced momentum differentiation at 5% electron-doping.
The partial self-consistent method shows no inversion of nodal and anti-nodal points in the electron-doped region but instead a spurious inversion for low temperatures at around 15% hole-doping for the `Full` tail-correction scheme. At the moment, it is unclear if this is a numerical issue, a problem with this particular tail-correction scheme, or a failure of the partially self-consistent method. At least for the `ExpStep` and `Plain` schemes, it seems to yield reasonable results up until $\beta = 30$.

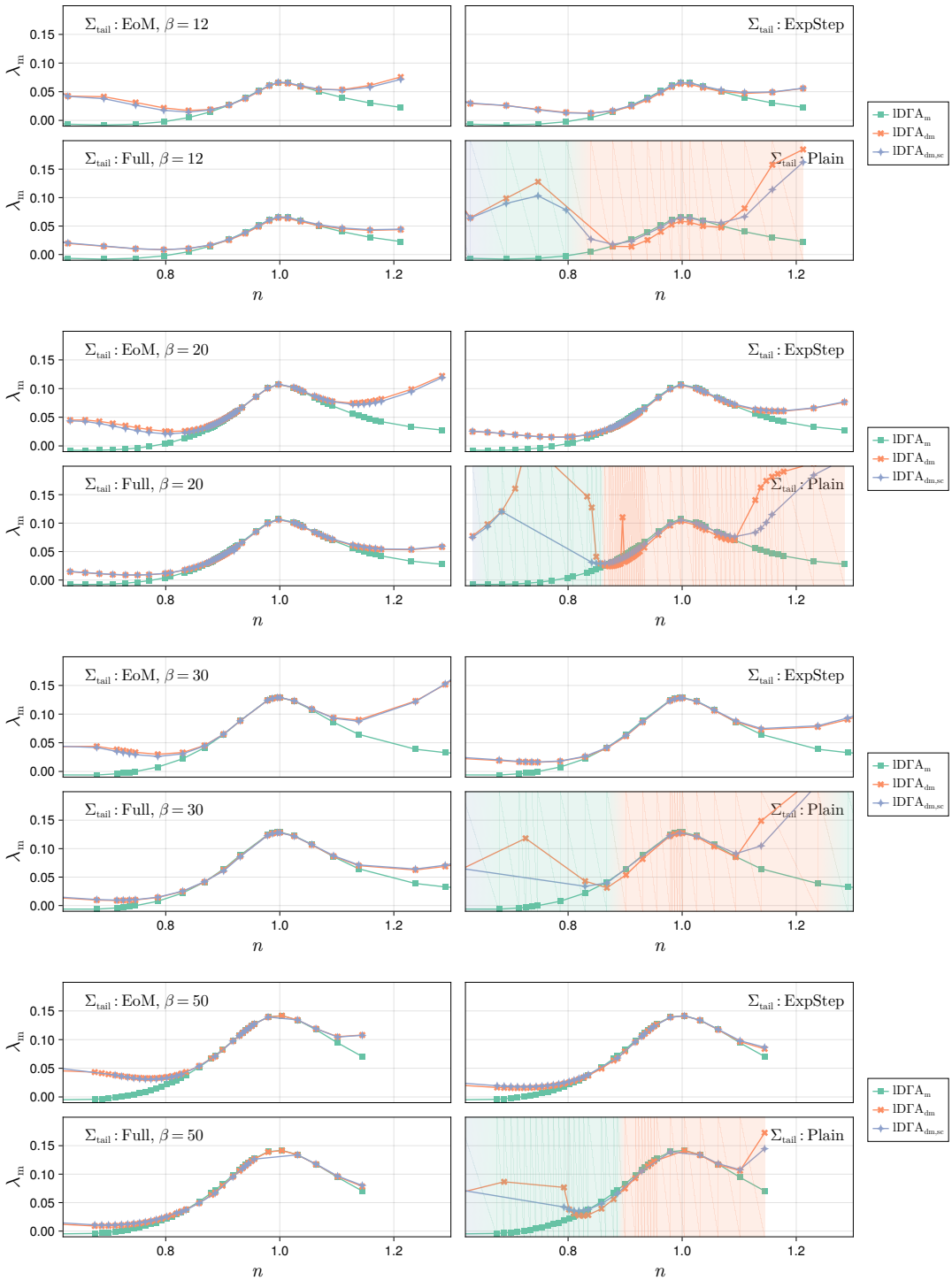

Figure 7.14: λ_m values for inverse temperatures β between 12 and 50. All self-energy correction schemes are shown. Data obtained from $N_{\mathbf{k}}$ = 200, DMFT solutions have been obtained from CTQMC, the 2 particle vertex was calculated using 4 bath site ED over 300^3 Matsubara frequencies with shifted grids.

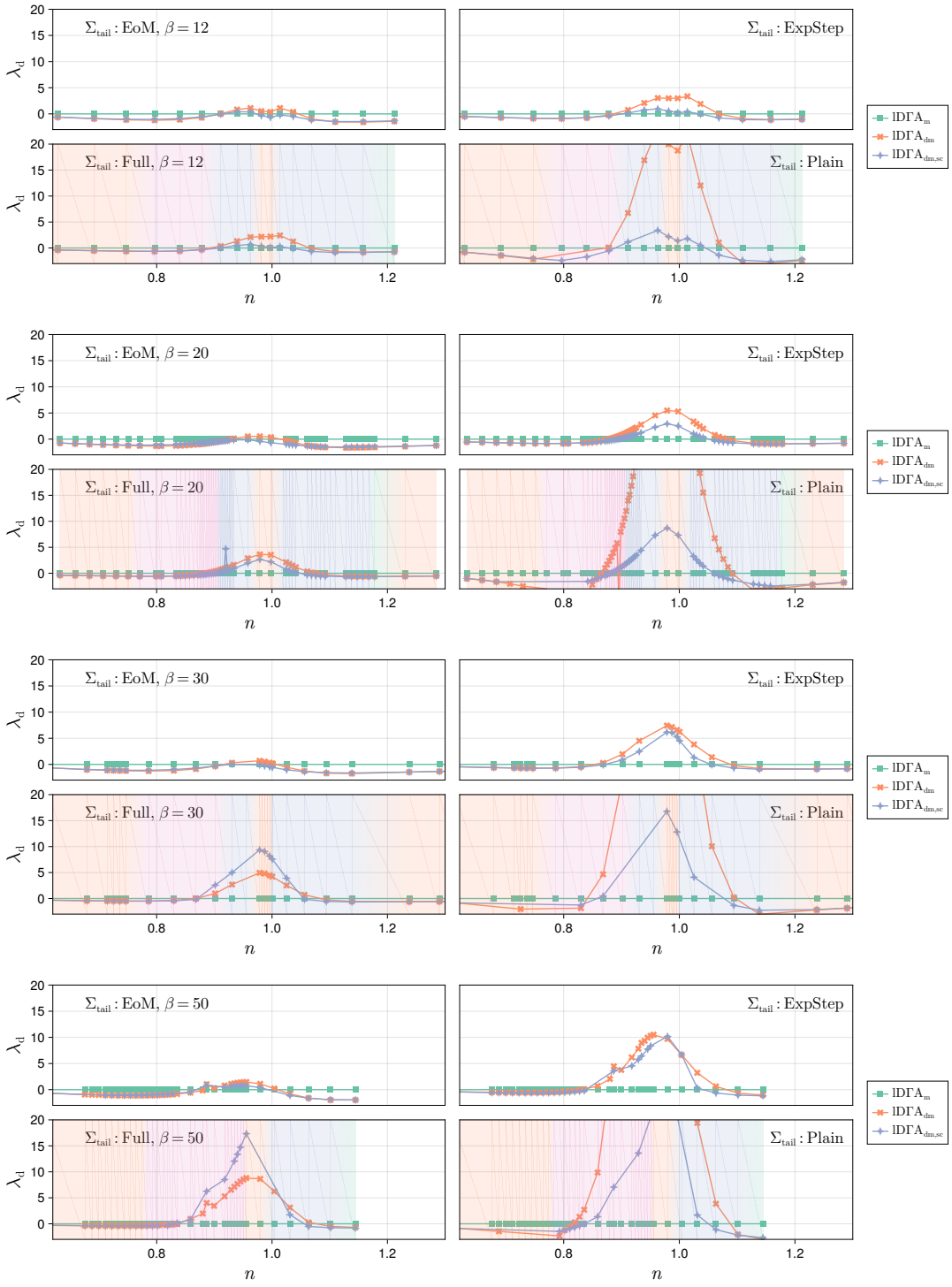

Figure 7.15: λ_d values for inverse temperatures β between 12 and 50. All self-energy correction schemes are shown. Data obtained from $N_{\mathbf{k}} = 100$, DMFT solutions have been obtained from CTQMC, the 2 particle vertex was calculated using 4 bath site ED over 300^3 Matsubara frequencies with shifted grids.

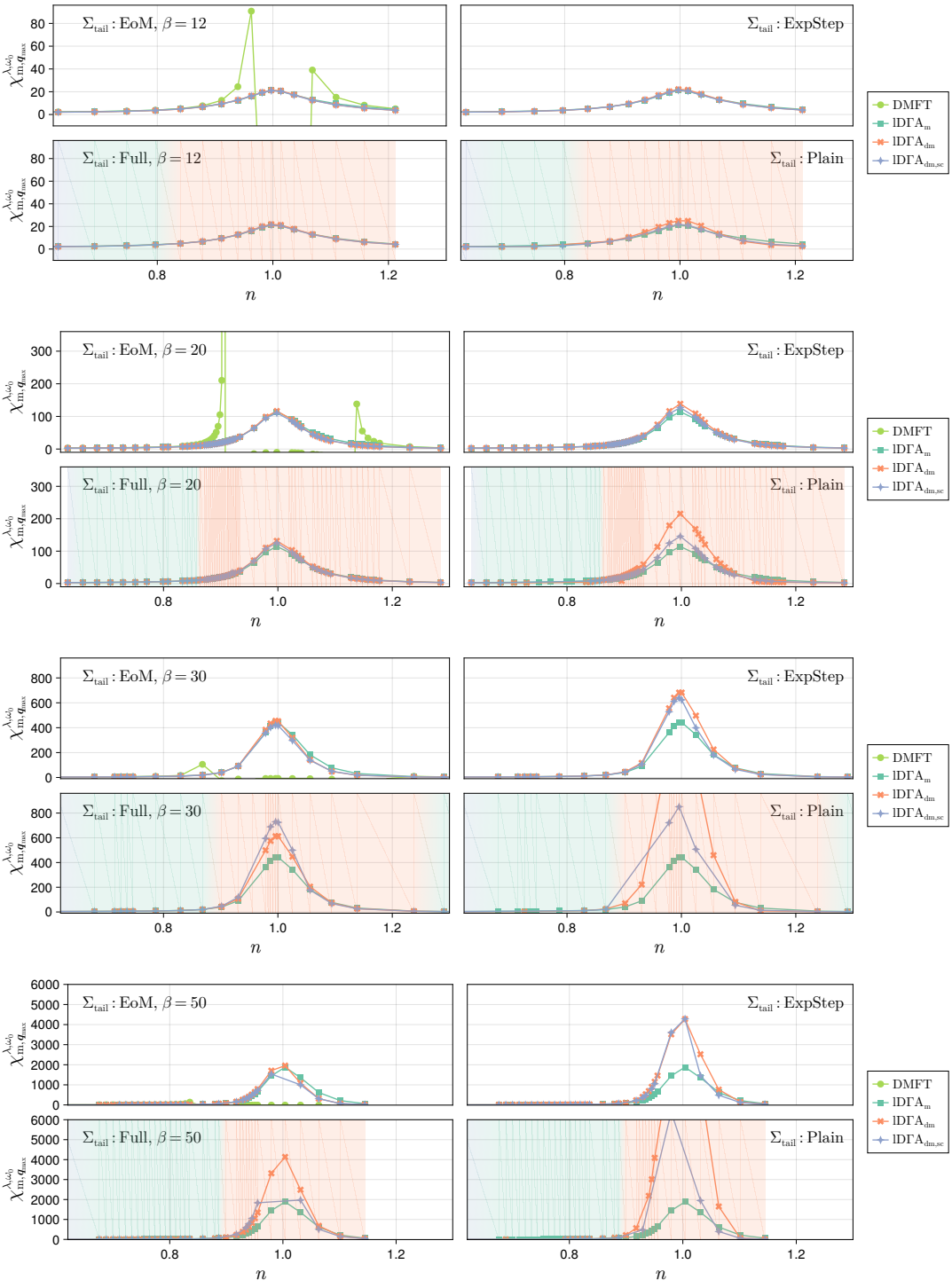

Figure 7.16: $\chi^{\lambda_{\mathrm{m}},\omega=0}_{\mathrm{m},\mathbf{q}=\mathbf{q}_{\mathrm{max}}}$ ($\mathbf{q}_{\mathrm{max}}$ is color coded, see main text) values for inverse temperatures β between 12 and 50. All self-energy correction schemes are shown. Data obtained from $N_{\mathbf{k}}$ = 100, DMFT solutions have been obtained from CTQMC, the 2 particle vertex was calculated using 4 bath site ED over 300^3 Matsubara frequencies with shifted grids.

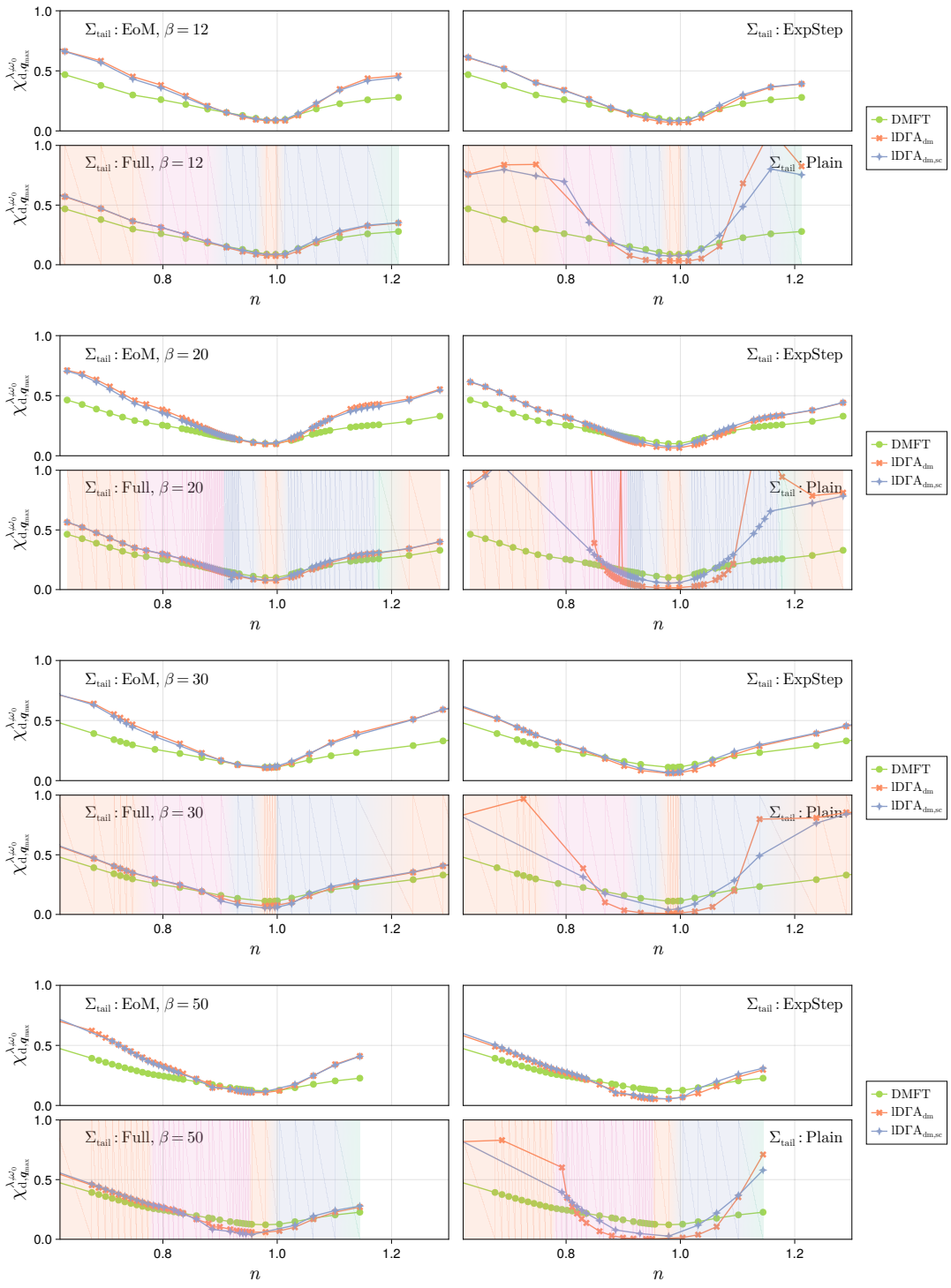

Figure 7.17: $\chi^{\lambda_d,\omega=0}_{d,\mathbf{q}=\mathbf{q}_{max}}$ ($\mathbf{q}_{max}$ is color coded, see main text) values for inverse temperatures β between 12 and 50. All self-energy correction schemes are shown. Data obtained from $N_{\mathbf{k}}$ = 100, DMFT solutions have been obtained from CTQMC, the 2 particle vertex was calculated using 4 bath site ED over 300^3 Matsubara frequencies with shifted grids.

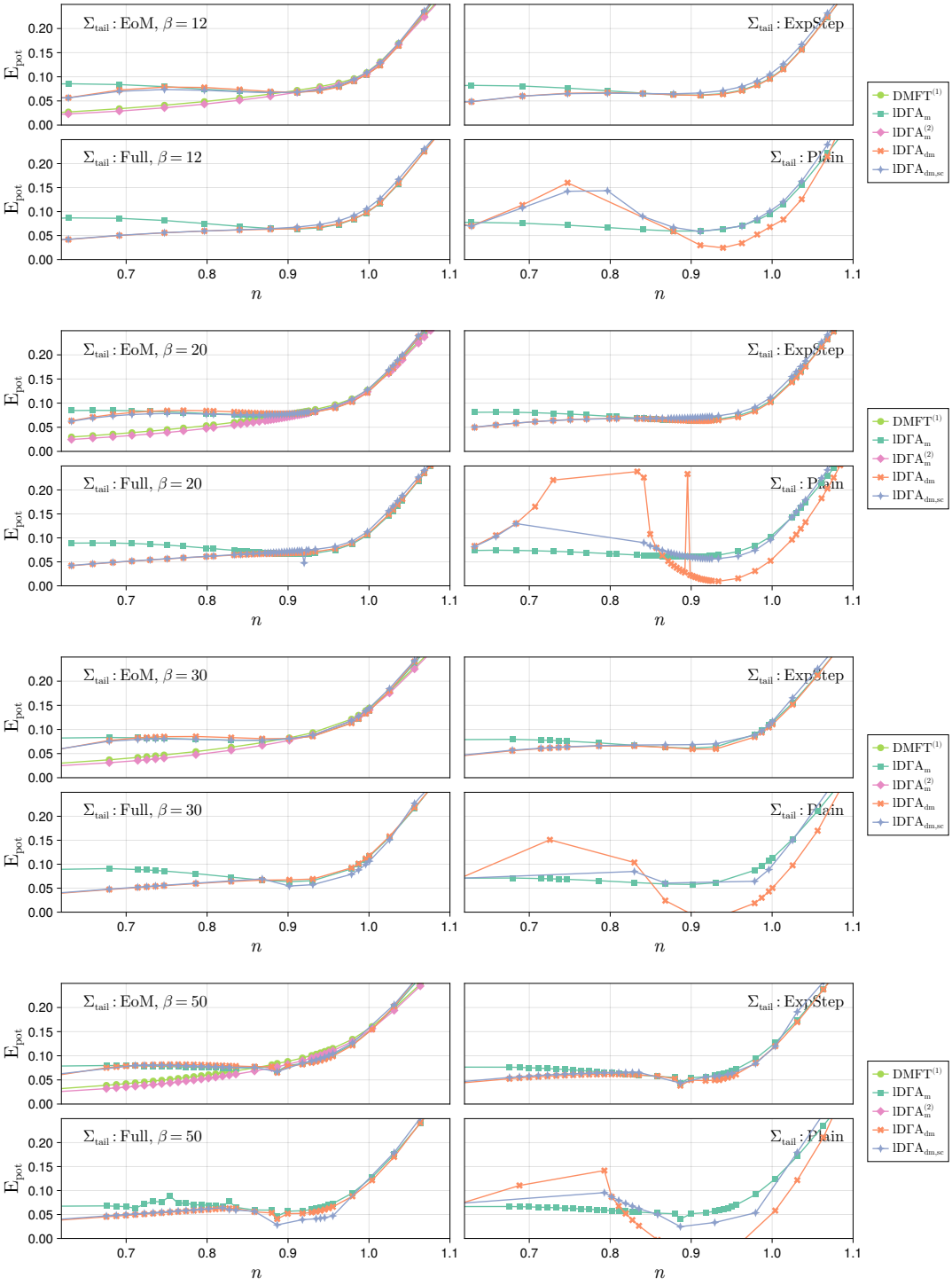

Figure 7.18: Potential energy (if not two-particle consistent, single particle $\mathrm{Tr}\, G^{\nu}_{\mathbf{k}}\Sigma^{\nu}_{\mathbf{k}}$) values for inverse temperatures β between 12 and 50. All self-energy correction schemes are shown. Data obtained from $N_{\mathbf{k}} = 100$, DMFT solutions have been obtained from CTQMC, the 2 particle vertex was calculated using 4 bath site ED over 300^3 Matsubara frequencies with shifted grids.

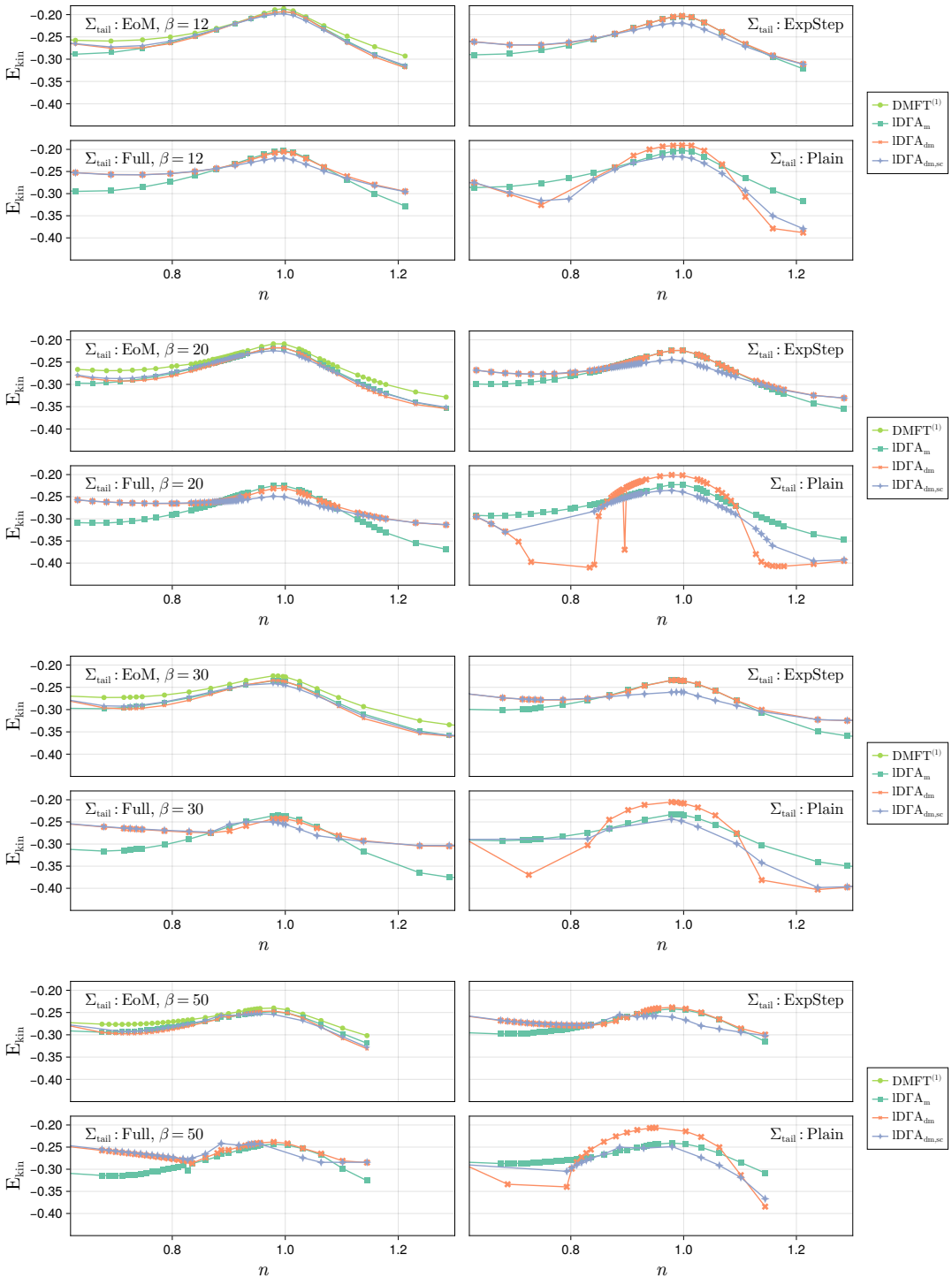

Figure 7.19: Single particle kinetic energy ($\mathrm{Tr}[\epsilon_{\mathbf{k}} G^{\nu}_{\mathbf{k}}]$) values for inverse temperatures β between 12 and 50. All self-energy correction schemes are shown. Data obtained from $N_{\mathbf{k}}$ = 100, DMFT solutions have been obtained from CTQMC, the 2 particle vertex was calculated using 4 bath site ED over 300^3 Matsubara frequencies with shifted grids.

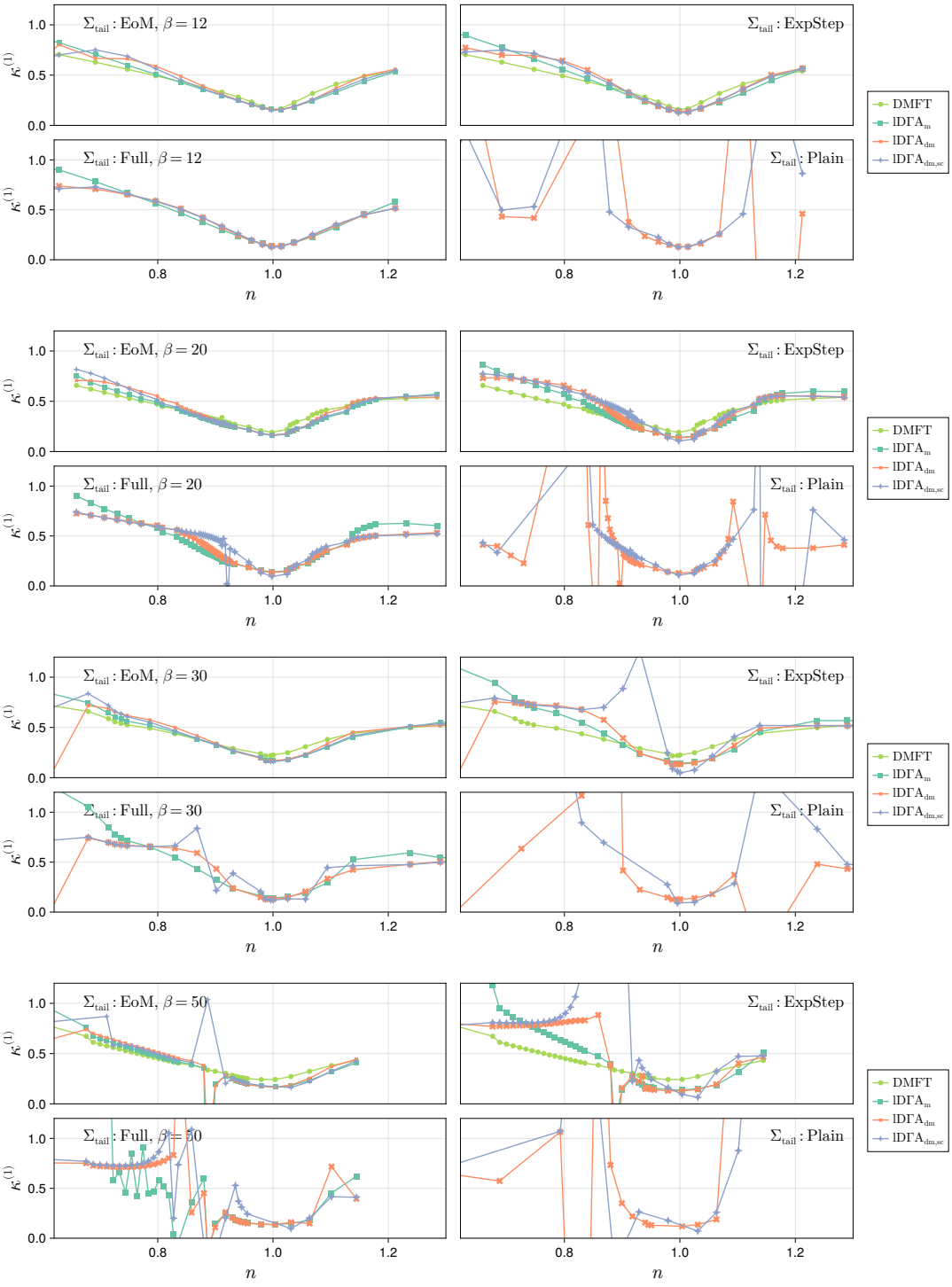

Figure 7.20: Compressibility on the one particle level $\kappa^{(1)} = \partial_n/\partial_\mu$ values for inverse temperatures β between 12 and 50. All self-energy correction schemes are shown. Data obtained from $N_{\mathbf{k}} = 100$, DMFT solutions have been obtained from CTQMC, the 2 particle vertex was calculated using 4 bath site ED over 300^3 Matsubara frequencies with shifted grids.

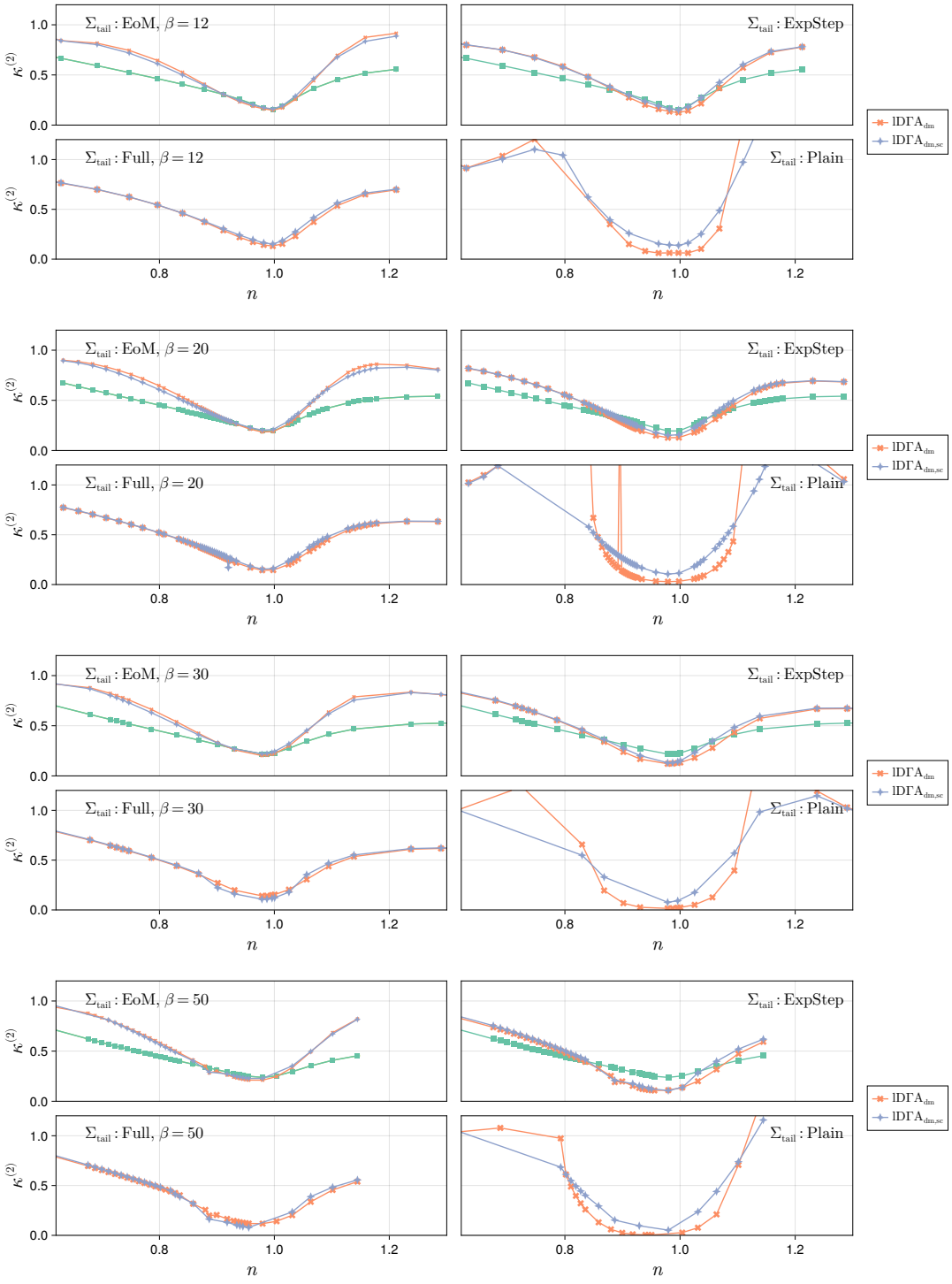

Figure 7.21: Compressibility on the one particle level $\kappa^{(2)} = 2\chi^{\omega_0}_{\mathrm{d},\mathbf{q}=0}$ values for inverse temperatures β between 12 and 50. All self-energy correction schemes are shown. Data obtained from $N_{\mathbf{k}} = 100$, DMFT solutions have been obtained from CTQMC, the 2 particle vertex was calculated using 4 bath site ED over 300^3 Matsubara frequencies with shifted grids.

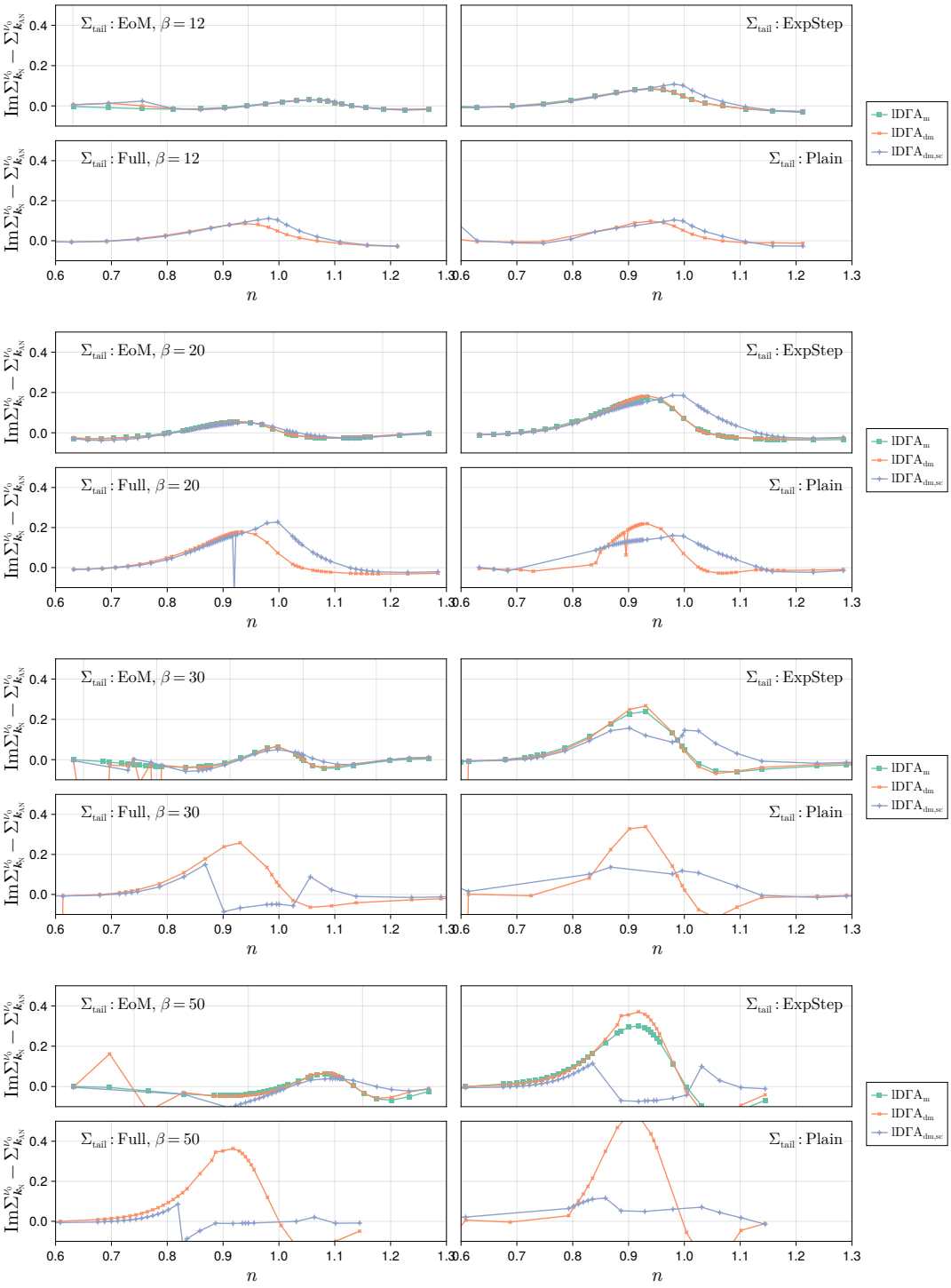

Figure 7.22: Difference of the imaginary part of the self-energy at the lowest Matsubara frequency between nodal $\mathbf{k}_{\text{N}} = (\pi/2, \pi/2)$ and anti nodal points $\mathbf{k}_{\text{AN}} = (\pi, 0)$, for inverse temperatures β between 12 and 50. All self-energy correction schemes are shown. Data obtained from $N_{\mathbf{k}} = 100$, DMFT solutions have been obtained from CTQMC, the 2 particle vertex was calculated using 4 bath site ED over 300^3 Matsubara frequencies with shifted grids. Note, that the `Full` correction scheme for the self-energy runs into numerical difficulties at low temperatures, that have not yet been resolved.

8 Conclusion and Outlook

In this thesis, we presented a new extension to the existing lDΓA method, which restores two-particle consistency on an effective level. We provided verification for the improved predictive power of this extension for the antiferromagnetic ordering in the Hubbard model on the three-dimensional cubic lattice at half-filling and the two-dimensional lattice with parameters relevant for high T_C superconductors. As for the first, we demonstrated that the two-particle consistency improved the predicted Néel temperature and restored the correct stabilization mechanisms of the ordered state, characterized by the relative magnitude of potential and kinetic energies. This improved description can be attributed to the introduction of renormalization effects between the channels. For the cuprate parameters, we found that non-local correlations lead to an enhancement of charge fluctuations in the pseudogap region. Here, we also found that momentum differentiation in the non-local self-energy is enhanced by the introduction of a partial self-consistency in the Schwinger-Dyson equation of motion. We concluded with an in-depth discussion of the numerical challenges this method faces and the solutions employed for this thesis. Specifically, the numerical discussion may prove useful for future work in the direction of this method and is not limited to only the lDΓA method.
Besides providing these results, this thesis is written with many references to textbooks and well-established knowledge in the hope that it provides a good starting point for students in the process of learning DΓA and related methods.
There are several open questions and possible improvements which were pointed out throughout this thesis. The most prominent ones are: (i) The restoration of the kinetic energy consistency via the f-sum rule has to systemically be investigated on a suitable system. (ii) The ambiguity of the restoration for the correct self-energy high-frequency tail and its influence on the thermodynamical properties (through the feedback in the potential energy consistency) is still not fully understood. (iii) The relationship to the recently introduced λ-RPA method has not yet been fully explored. (iv) The proposed asymptotic lDΓA method has not been shown to converge and yield reasonable results but has not been explored in any detail. (v) Multi-band systems cannot be solved using the lDΓA method yet; however, the necessary consistency equations have been derived for the TPSC case [298]. (vi) Electron-phonon coupling, for example by extending lDΓA to the Hubbard-Holstein model, cannot be treated yet.
Besides these methodological improvements, the very promising partial results of the machine learning approach for the learning structure of the Luttinger-Ward functional have not been brought to a conclusion yet, due to time constraints.

Acknowledgments

First and foremost, I want to express my gratitude to my supervisor, Georg Rohringer, for his kindness, support, and patience throughout my time in Hamburg. Without the countless hours he dedicated to sharing his knowledge of Feynman diagrammatic techniques, as well as the moral support he provided outside the realm of physics, this thesis would not have been possible.
I would like to express my gratitude to Michael Potthoff, as well as my colleagues, for the many uplifting coffee breaks.
I thank my friends and family for their support and understanding. In particular, I thank my parents for their moral support, Marco Knipfer and Eduard Kisner for their help with proofreading, and Irakli Titvinidze for many relaxing bouldering sessions.
Finally, I also want to thank Alexander Lichtenstein for accepting me as a student.

Appendix

1 Properties of single-particle Green's functions

Following are proofs for some identities of single-particle Green's functions that are used throughout this thesis. They have been taken from my Master's thesis [246]. The identities can be extended to higher-order Green's functions, since the trace properties can be applied analogously[1].
From the real-time definition in Def. 2.2.2.1 we get:

Property (1): Periodicity of the finite temperature Green's function

$$\begin{aligned}
G_{\alpha_1\alpha_2}(t_1;t_1') &= -i\frac{1}{Z}\operatorname{Tr}\left[e^{-\beta\hat{H}}\hat{c}^\dagger_{\alpha_1}(t_1)\hat{c}_{\ \alpha_2}(t_1')\right] \\
&= -i\frac{1}{Z}\operatorname{Tr}\left[e^{-\beta\hat{H}}e^{i\hat{H}t_1}\hat{c}^\dagger\alpha_1(0)e^{-i\hat{H}t_1}e^{\beta\hat{H}}e^{-\beta\hat{H}}\hat{c}_{\ \alpha_2}(t_1')\right] \\
&= -i\frac{1}{Z}\operatorname{Tr}\left[e^{i\hat{H}(t_1-i\beta)}\hat{c}^\dagger\alpha_1(0)e^{-i\hat{H}(t_1-i\beta)}e^{-\beta\hat{H}}\hat{c}_{\ \alpha_2}(t_1')\right] \\
&= -i\frac{1}{Z}\operatorname{Tr}\left[e^{-\beta\hat{H}}\hat{c}_{\ \alpha_2}(t_1')\hat{c}^\dagger\alpha_1(t_1-i\beta)\right] \\
&= G_{\alpha_1\alpha_2}(t_1-i\beta;t_1')
\end{aligned}$$

Property (2): A time-independent Hamiltonian implies time translational invariance For time-independent Hamiltonians, the Green's function only depends on the difference in times. Let $\tau > \tau$

$$\begin{aligned}
G_{\alpha\alpha'}(\tau,\tau') &= \frac{1}{Z}\operatorname{Tr}\Big[e^{-\beta\hat{H}}\hat{c}_{\ \alpha}(\tau)\hat{c}^\dagger_\alpha(\tau')\Big] = \frac{1}{Z}\operatorname{Tr}\Big[e^{-\beta\hat{H}}e^{\tau H}\hat{c}_{\ \alpha}(0)e^{-\tau\hat{H}}e^{\tau'\hat{H}}\hat{c}^\dagger_\alpha(0)e^{-\tau'\hat{H}}\Big] \\
&= \frac{1}{Z}\operatorname{Tr}\Big[e^{-\beta\hat{H}}e^{(\tau-\tau')\hat{H}}\hat{c}\,\alpha(0)e^{-(\tau-\tau')\hat{H}}\hat{c}^\dagger_\alpha(0)\Big] \\
&= G_{\alpha\alpha'}(\tau-\tau',0) =: G_{\alpha\alpha'}(\tau-\tau')
\end{aligned} \tag{I8.1}$$

Property (3): A lattice with translational symmetry implies translational invariance For a system on a discrete lattice, such as the Hubbard model, the same argument applies for spatial invariance under translation of some lattice vector $\mathbf{R}$.

$$\begin{aligned}
G_{\mathbf{r},\mathbf{r}'}(\tau,\tau') &= \frac{1}{Z}\operatorname{Tr}\Big[e^{-\beta\hat{H}}T_{-\mathbf{r}'}T_{\mathbf{r}'}\hat{c}\,\mathbf{r}(\tau)T_{-\mathbf{r}'}T_{\mathbf{r}'}\hat{c}^\dagger_{\mathbf{r}'}(\tau')\Big] = \frac{1}{Z}\operatorname{Tr}\Big[T_{-\mathbf{r}'}e^{-\beta\hat{H}}\hat{c}\,\mathbf{r}-\mathbf{r}'(\tau)T_{\mathbf{r}'}\hat{c}^\dagger_{\mathbf{r}'}(\tau')\Big] \\
&= \frac{1}{Z}\operatorname{Tr}\Big[e^{-\beta\hat{H}}\hat{c}\,\mathbf{r}-\mathbf{r}'(\tau)T_{\mathbf{r}'}\hat{c}^\dagger_{\mathbf{r}'}(\tau')T_{-\mathbf{r}'}\Big] \\
&= G_{\mathbf{r}-\mathbf{r}',\mathbf{0}}(\tau,\tau')
\end{aligned} \tag{I8.2}$$

Property (4): Complex conjugation Complex conjugation of a Green's function is equivalent to the swapping of state arguments.

$$\begin{aligned}
[G_{\alpha\alpha'}(\tau)]^* &= \frac{1}{Z}\operatorname{Tr}\Big\{\Big(e^{-\beta\hat{H}}e^{\tau\hat{H}}\hat{c}^\dagger_\alpha(0)e^{-\tau\hat{H}}\hat{c}\,\alpha'(0)\Big)\Big\}^* \\
&= \frac{1}{Z}\operatorname{Tr}\Big(\hat{c}^\dagger_{\alpha'}(0)e^{-\tau\hat{H}}\hat{c}\,\alpha(0)e^{\tau\hat{H}}e^{-\beta\hat{H}}\Big) \\
&= \frac{1}{Z}\operatorname{Tr}\Big(e^{-\beta\hat{H}}e^{\tau\hat{H}}\hat{c}^\dagger_{\alpha'}(0)e^{-\tau\hat{H}}\hat{c}\,\alpha(0)\Big) \\
&= G_{\alpha'\alpha}(\tau)
\end{aligned} \tag{I8.3}$$

The same is true for the frequency representation (see next section):

$$[G_{\alpha\alpha'}(i\nu_n)]^\dagger = \int_0^\beta e^{-i\nu_n\tau}[G_{\alpha\alpha'}(\tau)]^\dagger d\tau \overset{\text{Eq. (I8.3)}}{=} \int_0^\beta d\tau e^{-i\nu_n\tau}G_{\alpha'\alpha}(\tau) = G_{\alpha'\alpha}(i\nu_n) \tag{I8.4}$$

Property (5): β (anti-) periodicity in imaginary time This extremely important property is the reason for the inherintly discrete representation of imaginary time Green's functions in frequency space – the Matsubara formalism.

$$G_{\alpha\alpha'}(\tau-\beta) = \frac{1}{Z}\operatorname{Tr}\Big(e^{-\beta\hat{H}}T_\zeta\Big[\hat{a}_{\ \alpha}(\tau)\hat{a}^\dagger_{\alpha'}(\beta)\Big]\Big) = \zeta\frac{1}{Z}\operatorname{Tr}\Big(e^{-\beta\hat{H}}T_\zeta\Big[\hat{a}^\dagger_{\alpha'}(\beta)\hat{a}_{\ \alpha}(\tau)\Big]\Big)$$

[1] Generalizations of properties (4) and (5) is somewhat lengthy to proof. They are given following Eq. 2.33 and Eq. 2.116 [205].

$$= \zeta \frac{1}{Z} \operatorname{Tr}\left(e^{-\beta\hat{H}} e^{\beta\hat{H}} \hat{a}^\dagger_{\alpha'}(0) e^{-\beta\hat{H}} \hat{a}_{\ \alpha}(\tau)\right) = \zeta \frac{1}{Z} \operatorname{Tr}\left(e^{-\beta\hat{H}} \hat{a}_{\ \alpha}(\tau) \hat{a}^\dagger_{\alpha'}(0)\right)$$
$$= \zeta G_{\alpha\alpha'}(\tau), \qquad 0 < \tau < \beta \tag{I8.5}$$

2 Lehmann Representation for physical Susceptibility

The physical susceptibilities must be obtained from the impurity model, in addition to the one and two-particle Green's functions, in order for the improved summation formulas to work. These equal-time correlators are notoriously difficult to obtain through traditional CTQMC methods. Therefore, we sample them from ED. For this reason, we need the Lehman representations, which are then directly evaluated by ED using a finite number of basis states.

Charge Susceptibility

$$\begin{aligned}
\chi^{\mathrm{C}}_{\mathrm{ph,d}}(\tau) &= \langle \hat{n}(\tau)\hat{n} \rangle \\
&\overset{\text{Eq. (2.61)}}{=} \frac{1}{Z} \sum_{nm} e^{(\tau-\beta)E_n - \tau E_m} \langle n| \hat{c}^\dagger_\uparrow \hat{c}_{\ \downarrow} |m\rangle \langle m| \hat{c}^\dagger_\uparrow \hat{c}_{\ \downarrow} |n\rangle \\
&= \frac{1}{Z} \sum_{n\in\{\uparrow,\uparrow\downarrow\}} \sum_{m\in\{\downarrow,\uparrow\downarrow\}} e^{(\tau-\beta)E_n - \tau E_m} \langle n| \hat{c}^\dagger_\uparrow \hat{c}_{\ \downarrow} |m\rangle \langle m| \hat{c}^\dagger_\uparrow \hat{c}_{\ \downarrow} |n\rangle \\
&= \frac{1}{Z}\left[e^{(\tau-\beta)(-\mu)-\tau(-\mu)} + e^{(\tau-\beta)(-\mu)-\tau(U-2\mu)} + e^{(\tau-\beta)(U-2\mu)-\tau(-\mu)} + e^{(\tau-\beta)(U-2\mu)-\tau(U-2\mu))}\right] \\
&= \frac{1}{Z}\left[e^{\beta\mu} + e^{\tau(\mu-U)+\beta\mu} + e^{\tau(U-\mu)-\beta(U-2\mu)} + e^{-\beta(U-2\mu)}\right]
\end{aligned}$$

Magnetic Susceptibility

$$\chi^{\mathrm{C}}_{\mathrm{m}}(\tau) = \chi^{\mathrm{C}}_{\hat{S}_x} = \left\langle \left(\hat{c}^\dagger_\uparrow \hat{c}_{\ \downarrow} + \hat{c}^\dagger_\downarrow \hat{c}_{\ \uparrow}\right)(\tau) \left(\hat{c}^\dagger_\uparrow \hat{c}_{\ \downarrow} + \hat{c}^\dagger_\downarrow \hat{c}_{\ \uparrow}\right) \right\rangle \tag{I8.6}$$

$$\begin{aligned}
&= \frac{1}{Z} \sum_{nm} e^{(\tau-\beta)E_n - \tau E_m} \Big(\langle n| \hat{c}^\dagger_\uparrow \hat{c}_{\ \downarrow} |m\rangle \langle m| \hat{c}^\dagger_\uparrow \hat{c}_{\ \downarrow} |n\rangle + \langle n| \hat{c}^\dagger_\uparrow \hat{c}_{\ \downarrow} |m\rangle \langle m| \hat{c}^\dagger_\downarrow \hat{c}_{\ \uparrow} |n\rangle \\
&\qquad + \langle n| \hat{c}^\dagger_\downarrow \hat{c}_{\ \uparrow} |m\rangle \langle m| \hat{c}^\dagger_\uparrow \hat{c}_{\ \downarrow} |n\rangle + \langle n| \hat{c}^\dagger_\downarrow \hat{c}_{\ \uparrow} |m\rangle \langle m| \hat{c}^\dagger_\downarrow \hat{c}_{\ \uparrow} |n\rangle \Big)
\end{aligned} \tag{I8.7}$$

$$= \frac{1}{Z} \sum_{nm} e^{(\tau-\beta)E_n - \tau E_m} \left(\delta_{n,\uparrow}\delta_{m,\downarrow}\delta_{m,\uparrow}\delta_{n,\downarrow} + \delta_{n,\uparrow}\delta_{m,\downarrow}\delta_{m,\downarrow}\delta_{n,\uparrow} + \delta_{n,\downarrow}\delta_{m,\uparrow}\delta_{m,\uparrow}\delta_{n,\downarrow} + \delta_{n,\downarrow}\delta_{m,\uparrow}\delta_{m,\downarrow}\delta_{n,\uparrow}\right) \tag{I8.8}$$

$$= \frac{2\cdot 0 + 2\cdot e^{(\tau-\beta)(-\mu))-\tau(-\mu)}}{Z} = \frac{2\cdot e^{\beta\mu}}{Z} \tag{I8.9}$$

$$\chi^0_{\mathrm{m}}(0) = \frac{1}{Z} \sum_n e^{-\beta n} \langle n| \left(\hat{c}^\dagger_\uparrow \hat{c}_{\ \downarrow} + \hat{c}^\dagger_\downarrow \hat{c}_{\ \uparrow}\right) |n\rangle \tag{I8.10}$$

$$= 0 \tag{I8.11}$$

$$\chi^\omega_{\mathrm{m}} = \chi^{\mathrm{C},\omega}_{\mathrm{m}} - \chi^{0,\omega}_{\mathrm{m}} = \int_0^\beta \mathrm{d}\tau e^{i\omega_m \tau} \chi^{\mathrm{C}}_{\mathrm{m}}(\tau) - 0 \tag{I8.12}$$

$$= \delta_{\omega,0} \frac{2e^{\mu\beta}}{1 + 2e^{+\beta\mu} + e^{-\beta(U-2\mu)}} \tag{I8.13}$$

$$\mu = \frac{U}{2} \Rightarrow \chi^\omega_{\mathrm{m}} = \delta_{\omega,0} \frac{1}{e^{-\beta U/2} + 1} \tag{I8.14}$$

3 Common Quantities

The following gives an overview over commonly used quantities in the lDΓA context.

$$\chi^\omega_r = \frac{1}{\beta^2} \sum_{\nu\nu'} \chi_{\mathrm{r}}^{\nu\nu'\omega} \tag{I8.15}$$

λ and γ terms for spin and charge channel

$$\chi^{\nu\nu'\omega}_{0,\mathrm{ph},\mathbf{q}} = -\beta\delta_{\nu\nu'} \sum_{\mathbf{k}} G^\nu_{\mathbf{k}} G^{\omega+\nu}_{\mathbf{q}+\mathbf{k}} \tag{I8.16}$$

$$\chi^{\nu\nu'\omega}_{0,\mathrm{pp},\mathbf{q}} = -\frac{\beta}{2}\delta_{\nu\nu'} \sum_{\mathbf{k}} G^\nu_{\mathbf{k}} G^{\omega-\nu}_{\mathbf{q}-\mathbf{k}} \tag{I8.17}$$

$$\chi^{\nu\omega}_{0,\mathrm{ph},\mathbf{q}} = \sum_{\nu'} \chi^{\nu\nu'\omega}_{0,\mathrm{ph},\mathbf{q}} = -G^{\nu}_{\mathbf{k}} G^{\omega+\nu}_{\mathbf{q}+\mathbf{k}} \tag{I8.18}$$

$$\chi^{\nu\omega}_{0,\mathrm{pp},\mathbf{q}} = \sum_{\nu'} \chi^{\nu\nu'\omega}_{0,\mathrm{pp},\mathbf{q}} = -\frac{\beta}{2} G^{\nu}_{\mathbf{k}} G^{\omega-\nu}_{\mathbf{q}-\mathbf{k}} \tag{I8.19}$$

$$\lambda^{\nu\omega}_{\mathrm{d/m}} = \pm \frac{1}{\beta} \frac{\sum_{\nu'} \chi^{\nu\nu'\omega}_{\mathrm{d/m}}}{\chi^{\nu\omega}_{0}} \mp 1 \tag{I8.20}$$

$$= \sum_{\nu'} \chi^{\nu'\omega}_{0,\mathbf{q}} F^{\nu\nu'\omega}_{\mathrm{d/m}} \tag{I8.21}$$

$$\lambda^{\nu\nu'\omega}_{\uparrow\downarrow} = \frac{1}{2}\left(\lambda^{\nu\nu'\omega}_{\mathrm{d}} + \lambda^{\nu\nu'\omega}_{\mathrm{m}}\right) \tag{I8.22}$$

$$\gamma^{\nu\nu'\omega}_{\mathrm{d/m}} = \frac{1}{\beta} \frac{\sum_{\nu'} \chi^{\nu\nu'\omega}_{\mathrm{d/m}}}{(1 \pm U\chi^{\omega}_{\mathrm{d/m}})\chi^{\nu\nu'\omega}_{0}} \tag{I8.23}$$

$$\Rightarrow \lambda^{\nu\nu'\omega}_{\mathrm{d/m}} = \pm \gamma^{\nu\nu'\omega}_{\mathrm{d/m}}\left(1 \mp U\chi^{\omega}_{\mathrm{d/m}}\right) \mp 1 \tag{I8.24}$$

$$\gamma^{\nu\nu'\omega}_{\mathrm{d/m}} = \frac{1 \pm \lambda^{\nu\nu'\omega}_{\mathrm{d/m}}}{1 \mp U\chi^{\omega}_{\mathrm{d/m}}} \tag{I8.25}$$

$$\lambda^{\nu\omega}_{0,\mathbf{q}} = \sum_{\nu'} \chi^{\nu'\omega}_{0,\mathbf{q}} F^{\nu\nu'\omega}_{\uparrow\downarrow,\mathrm{DMFT}} \tag{I8.26}$$

4 Linearized Eliashberg Equations

We have obtained the second-order phase transition for the Néel temperature by fitting the critical behavior of the lDΓA λ-corrected susceptibility (Sec. 4.5.2 and Sec. 7.1). For the investigation of d-wave conductivity, we need to incorporate nonlocal spin-fluctuations and, therefore, go beyond the one-shot approach of lDΓA . Instead, we obtain the signal of a phase transition from the eigenvalue of the irreducible vertex and do so from the renormalized physical susceptibility [136]. We, therefore, write down the BSE (Eq. (2.258)) in the particle-particle ((s)inglet and (t)riplet) channel.

$$\chi^{\nu\nu'\omega}_{\mathrm{s},\mathbf{q}} = -\chi^{\nu\nu'\omega}_{0,\mathrm{pp},\mathbf{k}\mathbf{k}'\mathbf{q}} - \frac{1}{2}\sum_{\nu_1\nu_2}\left(\chi^{\nu\nu_1\omega}_{0,\mathrm{pp},\mathbf{k}\mathbf{k}'\mathbf{q}} - \chi^{\nu\nu_1\omega}_{\mathrm{s},\mathbf{q}}\right)\Gamma^{\mathrm{s},\nu_1\nu_2\omega_0}_{\mathrm{s},\mathbf{k}\mathbf{k}'\mathbf{q}}\chi^{\nu_2\nu'\omega}_{0,\mathrm{pp},\mathbf{k}\mathbf{k}'\mathbf{q}}, \tag{I8.27}$$

The susceptibility diverges when the largest eigenvalue of $\Gamma^{\nu\nu'\omega_0}_{\mathbf{k}\mathbf{k}'\mathbf{q}=0} G^{\nu'}_{\mathbf{k}'} G^{-\nu'}_{-\mathbf{k}'}$ approaches 1:

$$\lambda\Delta^{\nu}_{\mathbf{k}} = \sum_{\nu\mathbf{k}} \Gamma^{\nu\nu'\omega_0}_{\mathbf{k}\mathbf{k}'\mathbf{q}=0} G^{\nu'}_{\mathbf{k}'} G^{-\nu'}_{-\mathbf{k}'} \Delta^{\nu'}_{\mathbf{k}'} \tag{I8.28}$$

This approach of determining the largest eigenvalue of the linearized Eliashberg equations (the frequency-dependent generalization of the BCS gap equation) is discussed in the literature as well [26, Chapter 3]. However, we need to reconstruct $\Gamma_{\mathrm{s/t}}$ from the particle-hole channel. Furthermore, the $\mathbf{k}$ and $\mathbf{k}'$ dependence of this object makes it necessary to employ some additional numerical tricks to obtain results. Specifically, the $\mathbf{k}$ resolution required for the stabilization of the λ correction is too large to store the full vertex or obtain eigenvalues.

In order to obtain the particle-particle vertex $\Gamma^{\nu\nu'\omega}_{\mathrm{pp}\uparrow\downarrow,\mathbf{k}\mathbf{k}'\mathbf{q},\mathrm{lD\Gamma A}}$ we make use of the frequency mapping from the particle-hole to the particle-particle channel discussed in Sec. 2.7.2. Here one can select from one of the two options, depending on the available data in the particle-hole channel.

In order to construct the λ corrected version of the lDΓA full vertex, we make use of the U irreducible formalism from Eq. (5.49), for a derivation see the original definition in [205, Eq. 4.125]. F is then expressed as follows:

$$\begin{aligned} F^{\nu\nu'\omega}_{r,\mathbf{q}} &= \beta^2(\chi^{\nu\nu'\omega}_{0,\mathbf{q}})^{-1} - \beta^2(\chi^{\nu\omega}_{0})^{-1}\chi^{*,\nu\nu'\omega}_{r,\mathbf{q}}(\chi^{\nu'\omega}_{0})^{-1} \\ &\quad + U_r(1 - U_r\chi^{\omega}_{r})(\chi^{\nu\omega}_{0,\mathbf{q}})^{-1}\sum_{\nu_1\nu_2}\chi^{*,\nu\nu_1\omega}_{r,\mathbf{q}}\chi^{*,\nu_2\nu'\omega}_{r,\mathbf{q}}(\chi^{\nu'\omega}_{0,\mathbf{q}})^{-1} \qquad \text{(I8.29)} \\ &= \beta^2(\chi^{\nu\nu'\omega}_{0,\mathbf{q}})^{-1} - \beta^2(\chi^{\nu\omega}_{0,\mathbf{q}})^{-1}\chi^{*,\nu\nu'\omega}_{r,\mathbf{q}}(\chi^{\nu'\omega}_{0,\mathbf{q}})^{-1} \\ &\quad + U_r(1 - U_r\chi^{\omega}_{r})(\gamma^{\nu\omega}_{r} \mp 1)(\gamma^{\nu'\omega}_{r} \mp 1) \qquad \text{(I8.30)} \\ &= \beta^2\left(\chi^{\nu\nu'\omega}_{0,\mathbf{q}}\right)^{-1} + \beta^2\left(\chi^{\nu\omega}_{0,\mathbf{q}}\right)^{-1}\chi^{\nu\nu'\omega}_{r,\mathbf{q}}\left(\chi^{\nu'\omega}_{0,\mathbf{q}}\right)^{-1} \qquad \text{(I8.31)} \end{aligned}$$

In this formalism, we can replace the physical susceptibilities, with the λ corrected ones in Eq. (I8.30). Using the BSE, we can also find the expression for the generalized susceptibility:

$$\begin{aligned} \chi^{\nu\nu'\omega}_{r,\mathbf{q}} &= \chi^{\nu\nu'\omega}_{0,\mathbf{q}} - \sum_{\nu_1\nu_2}\chi^{\nu\nu_1\omega}_{0,\mathbf{q}}\Gamma^{\nu_1\nu_2\omega}_{r}\chi^{\nu_2\nu'\omega}_{r,\mathbf{q}} \qquad \text{(I8.32)} \\ &= \chi^{\nu\nu'\omega}_{0,\mathbf{q}} - \chi^{\nu\omega}_{0,\mathbf{q}}\sum_{\nu_2}\Gamma^{\nu\nu_2\omega}_{r}\chi^{\nu_2\nu'\omega}_{r,\mathbf{q}} \qquad \text{(I8.33)} \end{aligned}$$

$$= \chi_{0,\mathbf{q}}^{\nu\nu'\omega} - \chi_{0,\mathbf{q}}^{\nu\nu_1\omega} F_{r,\mathbf{q}}^{\nu_1\nu_2\omega} \chi_{0,\mathbf{q}}^{\nu'\nu_2\omega} \tag{I8.34}$$

$$= \left[(\chi_{0,\mathbf{q}}^{\nu\nu'\omega})^{-1} + \frac{1}{\beta^2} \Gamma_{r,\mathrm{loc}}^{\nu\nu'\omega} \right]^{-1} \tag{I8.35}$$

$$= \chi_{r,\mathbf{q}}^{\star,\nu\nu'\omega} - U_r (1 - U_r \chi_{r,\mathbf{q}}^{\omega}) \sum_{\nu_1\nu_2} \chi_{r,\mathbf{q}}^{\star,\nu\nu_1\omega} \chi_{r,\mathbf{q}}^{\star,\nu_2\nu'\omega} \tag{I8.36}$$

$$= \chi_{r,\mathbf{q}}^{\star,\nu\nu'\omega} - U_r (1 - U_r \chi_{r,\mathbf{q}}^{\omega}) \gamma_{r,\mathbf{q}}^{\nu\omega} \gamma_{r,\mathbf{q}}^{\nu'\omega} \tag{I8.37}$$

We then obtain for the λ corrected full vertex F:

$$F_{r,\mathbf{q}}^{\lambda_r,\nu\nu'\omega} = \beta^2 \left(\chi_{0,\mathbf{q}}^{\nu\nu'\omega} \right)^{-1} - \left(\chi_{0,\mathbf{q}}^{\nu\omega} \right)^{-1} \chi_{r,\mathbf{q}}^{\lambda_r,\nu\nu'\omega} \left(\chi_{0,\mathbf{q}}^{\nu'\omega} \right)^{-1} \tag{I8.38}$$

$$= \chi_{r,\mathbf{q}}^{\star,\nu\nu'\omega} - U_r (1 - U_r \chi_{r,\mathbf{q}}^{\lambda_r,\omega}) \sum_{\nu_1\nu_2} \chi_{r,\mathbf{q}}^{\star,\nu\nu_1\omega} \chi_{r,\mathbf{q}}^{\star,\nu_2\nu'\omega} \tag{I8.39}$$

$$= \beta^2 \left(\chi_{0,\mathbf{q}}^{\nu\nu'\omega} \right)^{-1} - (\chi_{0,\mathbf{q}}^{\nu\omega})^{-1} \chi_{r,\mathbf{q}}^{\star,\nu\nu'\omega} (\chi_{0,\mathbf{q}}^{\nu'\omega})^{-1} + U_r (1 - U_r \chi_{r,\mathbf{q}}^{\lambda_r,\omega}) \gamma_{r,\mathbf{q}}^{\nu\omega} \gamma_{r,\mathbf{q}}^{\nu'\omega} \tag{I8.40}$$

Using this reformulation, $\Phi_{\uparrow\downarrow} = \frac{1}{2}(\Phi_\mathrm{s} + \Phi_\mathrm{t})$ and the index shift for the mapping, we obtain the following expression for the irreducible vertex in the singlet channel:

$$F_{\mathrm{lD\Gamma A},\mathbf{kk'q}}^{\lambda,\nu\nu'\omega} = \frac{1}{2} \left(F_{\mathrm{d},\mathbf{q}}^{\lambda_\mathrm{m},\nu\nu'\omega} - F_{\mathrm{m},\mathbf{q}}^{\lambda_\mathrm{d},\nu\nu'\omega} \right) - F_{\mathrm{m},\mathbf{k'-k}}^{\nu(\nu+\omega)(\nu'-\nu)} - \frac{1}{2} \left(F_{\mathrm{loc,d}}^{\nu\nu'\omega} - F_{\mathrm{loc,m}}^{\nu\nu'\omega} \right) \tag{I8.41}$$

$$\Gamma_{\mathrm{s},\mathbf{kk'q}}^{\lambda,\nu\nu'\omega} = F_{\mathrm{ladder},\mathbf{k'(-k)(k-k')}}^{\lambda,\nu'(-\nu)(\nu-\nu')} - \Phi_{\mathrm{loc,s},\mathbf{kk'q}}^{\nu\nu'\omega} \tag{I8.42}$$

Omitting the λ superscript for better readability, one then obtaines for the singlet and triplet channel:

$$\Rightarrow \Gamma_{\mathrm{s},\mathbf{kk'q}=0}^{\nu\nu'\omega_0} = \frac{1}{2} \left(F_{\mathrm{d},\mathbf{k-k'}}^{\lambda,\nu'(-\nu)(\nu-\nu')} - F_{\mathrm{m},\mathbf{k-k'}}^{\lambda,\nu'(-\nu)(\nu-\nu')} \right) - F_{\mathrm{m},\mathbf{k'-k}}^{\lambda,\nu'\nu(-\nu'-\nu)} - F_{\mathrm{loc},\uparrow\downarrow}^{\nu'(-\nu)(\nu-\nu')} - \Phi_{\mathrm{loc,s}}^{\nu\nu'\omega_0} \tag{I8.43}$$

$$= \frac{1}{2} F_{\mathrm{d},\mathbf{k-k'}}^{\lambda,\nu'(-\nu)(\nu-\nu')} - \frac{3}{2} F_{\mathrm{m},\mathbf{k-k'}}^{\lambda,\nu'(-\nu)(\nu-\nu')} - F_{\mathrm{loc},\uparrow\downarrow}^{\nu'(-\nu)(\nu-\nu')} - \Phi_{\mathrm{loc,s}}^{\nu\nu'\omega=0} \tag{I8.44}$$

$$\Gamma_{\mathrm{t},\mathbf{kk'q}=0}^{\nu\nu'\omega_0} = \frac{1}{2} F_{\mathrm{d},\mathbf{k-k'}}^{\lambda,\nu'(-\nu)(\nu-\nu')} - \frac{1}{2} F_{\mathrm{m},\mathbf{k-k'}}^{\lambda,\nu'(-\nu)(\nu-\nu')} - F_{\mathrm{loc},\uparrow\downarrow}^{\nu'(-\nu)(\nu-\nu')} - \Phi_{\mathrm{loc,pp}}^{\nu\nu'\omega_0} \tag{I8.45}$$

We can then insert this into the linearized Eliashberg equation at the dominant frequency ω_0 and obtain the leading eigenvalue, which approaches 1 for $T \to T_\mathrm{C}$.

$$\lambda \Delta_k^\nu = -\frac{1}{\beta N_k} \sum_{\nu' k'} \Gamma_{kk'q=0}^{\nu\nu'\omega=0} \chi_{0,\mathrm{s},k'}^{\nu'\omega_0} \Delta_{k'}^{\nu'} \tag{I8.46}$$

Bibliography

[1] A. A. Abrikosov et al. *Methods of quantum field theory in statistical physics*. eng. Rev. English ed. Dover books on physics and chemistry. New York: Dover, 1975. ISBN: 978-0-486-63228-5.

[2] Swagata Acharya, Mikhail I. Katsnelson, and Mark Van Schilfgaarde. "Vertex dominated superconductivity in intercalated FeSe". en. In: *npj Quantum Materials* 8.1 (May 2023), p. 24. ISSN: 2397-4648. DOI: 10.1038/s41535-023-00556-9. URL: https://www.nature.com/articles/s41535-023-00556-9 (visited on 05/02/2024).

[3] A. C. Aitken. "XXV.—On Bernoulli's Numerical Solution of Algebraic Equations". en. In: *Proceedings of the Royal Society of Edinburgh* 46 (1927), pp. 289–305. ISSN: 0370-1646. DOI: 10.1017/S0370164600022070. URL: https://www.cambridge.org/core/product/identifier/S0370164600022070/type/journal_article (visited on 12/25/2024).

[4] G. Alefeld, F. A. Potra, and Yixun Shi. "On enclosing simple roots of nonlinear equations". en. In: *Mathematics of Computation* 61.204 (1993), pp. 733–744. ISSN: 0025-5718, 1088-6842. DOI: 10.1090/S0025-5718-1993-1192965-2. URL: https://www.ams.org/mcom/1993-61-204/S0025-5718-1993-1192965-2/ (visited on 11/10/2024).

[5] S. Allen, A.-M. S. Tremblay, and Y. M. Vilk. *Conserving approximations vs Two-Particle Self-Consistent Approach*. arXiv:cond-mat/0110130. Oct. 2003. URL: http://arxiv.org/abs/cond-mat/0110130 (visited on 11/20/2024).

[6] B. Ammon, M. Troyer, and Hirokazu Tsunetsugu. "Effect of the three-site hopping term on the t - J model". en. In: *Physical Review B* 52.1 (July 1995), pp. 629–636. ISSN: 0163-1829, 1095-3795. DOI: 10.1103/PhysRevB.52.629. URL: https://link.aps.org/doi/10.1103/PhysRevB.52.629 (visited on 05/04/2024).

[7] O.K. Andersen et al. "LDA energy bands, low-energy hamiltonians, t , t , t (k), and J ". en. In: *Journal of Physics and Chemistry of Solids* 56.12 (Dec. 1995), pp. 1573–1591. ISSN: 00223697. DOI: 10.1016/0022-3697(95)00269-3. URL: https://linkinghub.elsevier.com/retrieve/pii/0022369795002693 (visited on 12/18/2024).

[8] Ned Anderson and Åke Björck. "A new high order method of regula falsi type for computing a root of an equation". en. In: *BIT* 13.3 (Sept. 1973), pp. 253–264. ISSN: 0006-3835, 1572-9125. DOI: 10.1007/BF01951936. URL: http://link.springer.com/10.1007/BF01951936 (visited on 11/09/2024).

[9] P. W. Anderson. "Localized Magnetic States in Metals". en. In: *Physical Review* 124.1 (Oct. 1961), pp. 41–53. ISSN: 0031-899X. DOI: 10.1103/PhysRev.124.41. URL: https://link.aps.org/doi/10.1103/PhysRev.124.41 (visited on 12/10/2024).

[10] P. W. Anderson. "More Is Different: Broken symmetry and the nature of the hierarchical structure of science." en. In: *Science* 177.4047 (Aug. 1972), pp. 393–396. ISSN: 0036-8075, 1095-9203. DOI: 10.1126/science.177.4047.393. URL: https://www.science.org/doi/10.1126/science.177.4047.393 (visited on 05/02/2024).

[11] P. W. Anderson. "The Resonating Valence Bond State in La $_2$ CuO $_4$ and Superconductivity". en. In: *Science* 235.4793 (Mar. 1987), pp. 1196–1198. ISSN: 0036-8075, 1095-9203. DOI: 10.1126/science.235.4793.1196. URL: https://www.science.org/doi/10.1126/science.235.4793.1196 (visited on 05/05/2024).

[12] Ryotaro Arita et al. "Magnetic Properties of the Hubbard Model on Three-Dimensional Lattices: Fluctuation-Exchange and Two-Particle Self-Consistent Studies". en. In: *Journal of the Physical Society of Japan* 69.3 (Mar. 2000), pp. 785–795. ISSN: 0031-9015, 1347-4073. DOI: 10.1143/JPSJ.69.785. URL: http://journals.jps.jp/doi/10.1143/JPSJ.69.785 (visited on 12/10/2024).

[13] Daniel P. Arovas et al. "The Hubbard Model". In: *Annual Review of Condensed Matter Physics* 13.1 (Mar. 2022). arXiv:2103.12097 [cond-mat], pp. 239–274. ISSN: 1947-5454, 1947-5462. DOI: 10.1146/annurev-conmatphys-031620-102024. URL: http://arxiv.org/abs/2103.12097 (visited on 05/05/2024).

[14] F Aryasetiawan and O Gunnarsson. "The $\boldsymbol{GW}$ method". In: *Reports on Progress in Physics* 61.3 (Mar. 1998), pp. 237–312. ISSN: 0034-4885, 1361-6633. DOI: 10.1088/0034-4885/61/3/002. URL: https://iopscience.iop.org/article/10.1088/0034-4885/61/3/002 (visited on 12/10/2024).

[15] Ferdi Aryasetiawan and Fredrik Nilsson. *Down-folding methods in many-electron theory*. First. Melville: AIP Publishing, 2022. ISBN: 978-0-7354-2246-9.

[16] K. Astleithner et al. “Parquet dual fermion approach for the Falicov-Kimball model”. en. In: *Physical Review B* 101.16 (Apr. 2020), p. 165101. ISSN: 2469-9950, 2469-9969. DOI: 10.1103/PhysRevB.101.165101. URL: https://link.aps.org/doi/10.1103/PhysRevB.101.165101 (visited on 01/12/2025).

[17] Grigory V. Astretsov, Georg Rohringer, and Alexey N. Rubtsov. “Dual parquet scheme for the two-dimensional Hubbard model: Modeling low-energy physics of high- T c cuprates with high momentum resolution”. en. In: *Physical Review B* 101.7 (Feb. 2020), p. 075109. ISSN: 2469-9950, 2469-9969. DOI: 10.1103/PhysRevB.101.075109. URL: https://link.aps.org/doi/10.1103/PhysRevB.101.075109 (visited on 12/20/2024).

[18] Thomas Ayral and Olivier Parcollet. “Mott physics and collective modes: An atomic approximation of the four-particle irreducible functional”. en. In: *Physical Review B* 94.7 (Aug. 2016), p. 075159. ISSN: 2469-9950, 2469-9969. DOI: 10.1103/PhysRevB.94.075159. URL: https://link.aps.org/doi/10.1103/PhysRevB.94.075159 (visited on 01/12/2025).

[19] Thomas Ayral and Olivier Parcollet. “Mott physics and spin fluctuations: A functional viewpoint”. en. In: *Physical Review B* 93.23 (June 2016), p. 235124. ISSN: 2469-9950, 2469-9969. DOI: 10.1103/PhysRevB.93.235124. URL: https://link.aps.org/doi/10.1103/PhysRevB.93.235124 (visited on 01/12/2025).

[20] Thomas Ayral and Olivier Parcollet. “Mott physics and spin fluctuations: A unified framework”. en. In: *Physical Review B* 92.11 (Sept. 2015), p. 115109. ISSN: 1098-0121, 1550-235X. DOI: 10.1103/PhysRevB.92.115109. URL: https://link.aps.org/doi/10.1103/PhysRevB.92.115109 (visited on 01/12/2025).

[21] I. Battisti et al. “Universality of pseudogap and emergent order in lightly doped Mott insulators”. en. In: *Nature Physics* 13.1 (Jan. 2017), pp. 21–25. ISSN: 1745-2473, 1745-2481. DOI: 10.1038/nphys3894. URL: https://www.nature.com/articles/nphys3894 (visited on 12/27/2024).

[22] Gordon Baym. “Self-Consistent Approximations in Many-Body Systems”. en. In: *Physical Review* 127.4 (Aug. 1962), pp. 1391–1401. ISSN: 0031-899X. DOI: 10.1103/PhysRev.127.1391. URL: https://link.aps.org/doi/10.1103/PhysRev.127.1391 (visited on 07/04/2024).

[23] Gordon Baym and Leo P. Kadanoff. “Conservation Laws and Correlation Functions”. en. In: *Physical Review* 124.2 (Oct. 1961), pp. 287–299. ISSN: 0031-899X. DOI: 10.1103/PhysRev.124.287. URL: https://link.aps.org/doi/10.1103/PhysRev.124.287 (visited on 07/04/2024).

[24] J. G. Bednorz and K. A. M ller. “Possible highT c superconductivity in the Ba?La?Cu?O system”. en. In: *Zeitschrift f r Physik B Condensed Matter* 64.2 (June 1986), pp. 189–193. ISSN: 0722-3277, 1434-6036. DOI: 10.1007/BF01303701. URL: http://link.springer.com/10.1007/BF01303701 (visited on 12/18/2024).

[25] G. Benfatto, A. Giuliani, and V. Mastropietro. “Fermi Liquid Behavior in the 2D Hubbard Model at Low Temperatures”. en. In: *Annales Henri Poincaré* 7.5 (Aug. 2006), pp. 809–898. ISSN: 1424-0637, 1424-0661. DOI: 10.1007/s00023-006-0270-z. URL: https://link.springer.com/10.1007/s00023-006-0270-z (visited on 05/04/2024).

[26] K. H. Bennemann and John B. Ketterson, eds. *Superconductivity*. en. Berlin, Heidelberg: Springer Berlin Heidelberg, 2008. ISBN: 978-3-540-73252-5. DOI: 10.1007/978-3-540-73253-2. URL: http://link.springer.com/10.1007/978-3-540-73253-2 (visited on 11/28/2024).

[27] Marco Bianucci and Mauro Bologna. “About the foundation of the Kubo generalized cumulants theory: a revisited and corrected approach”. In: *Journal of Statistical Mechanics: Theory and Experiment* 2020.4 (Apr. 2020), p. 043405. ISSN: 1742-5468. DOI: 10.1088/1742-5468/ab7755. URL: https://iopscience.iop.org/article/10.1088/1742-5468/ab7755 (visited on 04/29/2024).

[28] N. E. Bickers. “Self-Consistent Many-Body Theory for Condensed Matter Systems”. en. In: *Theoretical Methods for Strongly Correlated Electrons*. Ed. by David Sénéchal, André-Marie Tremblay, and Claude Bourbonnais. Series Title: CRM Series in Mathematical Physics. New York: Springer-Verlag, 2004, pp. 237–296. ISBN: 978-0-387-00895-0. DOI: 10.1007/0-387-21717-7_6. URL: http://link.springer.com/10.1007/0-387-21717-7_6 (visited on 11/12/2024).

[29] N. E. Bickers and S. R. White. “Conserving approximations for strongly fluctuating electron systems. II. Numerical results and parquet extension”. en. In: *Physical Review B* 43.10 (Apr. 1991), pp. 8044–8064. ISSN: 0163-1829, 1095-3795. DOI: 10.1103/PhysRevB.43.8044. URL: https://link.aps.org/doi/10.1103/PhysRevB.43.8044 (visited on 07/23/2024).

[30] N.E Bickers and D.J Scalapino. “Conserving approximations for strongly fluctuating electron systems. I. Formalism and calculational approach”. en. In: *Annals of Physics* 193.1 (July 1989), pp. 206–251. ISSN: 00034916. DOI: 10.1016/0003-4916(89)90359-X. URL: https://linkinghub.elsevier.com/retrieve/pii/000349168990359X (visited on 07/15/2024).

[31] James Binney, ed. *The Theory of critical phenomena: an introduction to the renormalization group*. Oxford science publications. Oxford : Oxford ; New York: Clarendon Press ; Oxford University Press, 1992. ISBN: 978-0-19-851394-0.

[32] Christopher M. Bishop and Hugh Bishop. *Deep Learning*. eng. Springer, 2024. ISBN: 978-3-031-45468-4.

[33] Philippe Blanchard and Erwin Brüning. "Mathematical Methods in Physics". In: *Progress in Mathematical Physics* (2015). ISBN: 9783319140445, p. 419. ISSN: 1544-9998. URL: https://www.academia.edu/32715176/Mathematical_Methods_in_Physics_Distributions_Hilbert_Space_Operators_and_Variational_Methods (visited on 01/30/2024).

[34] Tim Bode. "The two-particle irreducible effective action for classical stochastic processes". In: *Journal of Physics A: Mathematical and Theoretical* 55.26 (July 2022), p. 265401. ISSN: 1751-8113, 1751-8121. DOI: 10.1088/1751-8121/ac73c6. URL: https://iopscience.iop.org/article/10.1088/1751-8121/ac73c6 (visited on 04/29/2024).

[35] M. Born and R. Oppenheimer. "Zur Quantentheorie der Molekeln". en. In: *Annalen der Physik* 389.20 (Jan. 1927), pp. 457–484. ISSN: 0003-3804, 1521-3889. DOI: 10.1002/andp.19273892002. URL: https://onlinelibrary.wiley.com/doi/10.1002/andp.19273892002 (visited on 05/02/2024).

[36] H. J. Brascamp. "The Fredholm theory of integral equations for special types of compact operators on a separable Hilbert space". en. In: *Compositio Mathematica* 21.1 (1969). Publisher: Wolters-Noordhoff Publishing, pp. 59–80. URL: http://www.numdam.org/item/CM_1969__21_1_59_0/.

[37] C. Brezinski. "A general extrapolation algorithm". en. In: *Numerische Mathematik* 35.2 (June 1980), pp. 175–187. ISSN: 0029-599X, 0945-3245. DOI: 10.1007/BF01396314. URL: http://link.springer.com/10.1007/BF01396314 (visited on 12/25/2024).

[38] Claude Brezinski. "Some pioneers of extrapolation methods". en. In: *The Birth of Numerical Analysis*. ISBN: 978-981-283-626-7. WORLD SCIENTIFIC, Nov. 2009, pp. 1–22. ISBN: 978-981-283-625-0. DOI: 10.1142/9789812836267_0001. URL: http://www.worldscientific.com/doi/abs/10.1142/9789812836267_0001 (visited on 12/25/2024).

[39] Henrik Bruus and Karsten Flensberg. *Many–Body Quantum Theory in Condensed Matter Physics: An Introduction*. en. ISBN: 978-0-19-856633-5. Oxford University PressOxford, Sept. 2004. ISBN: 978-1-383-02959-8. DOI: 10.1093/oso/9780198566335.001.0001. URL: https://academic.oup.com/book/54902 (visited on 05/11/2024).

[40] Carl M. Bender and Steven A. Orszag. *Advanced Mathematical Methods for Scientists and Engineers I*. New York: Springer, Mar. 1999. ISBN: 978-1-4757-3069-2.

[41] Michele Casula, Alexey Rubtsov, and Silke Biermann. "Dynamical screening effects in correlated materials: plasmon satellites and spectral weight transfers from a Green's function ansatz to extended dynamical mean field theory". In: *Physical Review B* 85.3 (Jan. 2012). arXiv:1107.3123 [cond-mat], p. 035115. ISSN: 1098-0121, 1550-235X. DOI: 10.1103/PhysRevB.85.035115. URL: http://arxiv.org/abs/1107.3123 (visited on 04/29/2024).

[42] Patrick Chalupa-Gantner et al. "Fulfillment of sum rules and Ward identities in the multiloop functional renormalization group solution of the Anderson impurity model". en. In: *Physical Review Research* 4.2 (Apr. 2022), p. 023050. ISSN: 2643-1564. DOI: 10.1103/PhysRevResearch.4.023050. URL: https://link.aps.org/doi/10.1103/PhysRevResearch.4.023050 (visited on 07/08/2024).

[43] K A Chao, J Spalek, and A M Oles. "Kinetic exchange interaction in a narrow S-band". In: *Journal of Physics C: Solid State Physics* 10.10 (May 1977), pp. L271–L276. ISSN: 0022-3719. DOI: 10.1088/0022-3719/10/10/002. URL: https://iopscience.iop.org/article/10.1088/0022-3719/10/10/002 (visited on 05/04/2024).

[44] J. T. Chayes, L. Chayes, and Mary Beth Ruskai. "Density functional approach to quantum lattice systems". en. In: *Journal of Statistical Physics* 38.3-4 (Feb. 1985), pp. 497–518. ISSN: 0022-4715, 1572-9613. DOI: 10.1007/BF01010474. URL: http://link.springer.com/10.1007/BF01010474 (visited on 01/12/2025).

[45] Hanghui Chen et al. "Dynamical Mean Field Studies of Infinite Layer Nickelates: Physics Results and Methodological Implications". In: *Frontiers in Physics* 10 (Feb. 2022), p. 835942. ISSN: 2296-424X. DOI: 10.3389/fphy.2022.835942. URL: https://www.frontiersin.org/articles/10.3389/fphy.2022.835942/full (visited on 05/02/2024).

[46] K.-S. Chen et al. "Role of the van Hove singularity in the quantum criticality of the Hubbard model". en. In: *Physical Review B* 84.24 (Dec. 2011), p. 245107. ISSN: 1098-0121, 1550-235X. DOI: 10.1103/PhysRevB.84.245107. URL: https://link.aps.org/doi/10.1103/PhysRevB.84.245107 (visited on 06/14/2024).

[47] C. Craeye and F. Capolino. "Accelerated Computation of the Free Space Green's Function of Semi-Infinite Phased Arrays of Dipoles". en. In: *IEEE Transactions on Antennas and Propagation* 54.3 (Mar. 2006), pp. 1037–1040. ISSN: 0018-926X. DOI: 10.1109/TAP.2006.869945. URL: http://ieeexplore.ieee.org/document/1603830/ (visited on 12/25/2024).

[48] Anne-Marie Daré, Liang Chen, and A.-M. S. Tremblay. "Comparisons between Monte Carlo simulations and a simple crossing-symmetric approach to the Hubbard model at low density". en. In: *Physical Review B* 49.6 (Feb. 1994), pp. 4106–4118. ISSN: 0163-1829, 1095-3795. DOI: 10.1103/PhysRevB.49.4106. URL: https://link.aps.org/doi/10.1103/PhysRevB.49.4106 (visited on 11/14/2024).

[49] Anne-Marie Daré, Y. M. Vilk, and A. -M. S. Tremblay. "Crossover from two- to three-dimensional critical behavior for nearly antiferromagnetic itinerant electrons". en. In: *Physical Review B* 53.21 (June 1996), pp. 14236–14251. ISSN: 0163-1829, 1095-3795. DOI: 10.1103/PhysRevB.53.14236. URL: https://link.aps.org/doi/10.1103/PhysRevB.53.14236 (visited on 11/21/2024).

[50] C. De Dominicis. "Variational Statistical Mechanics in Terms of "Observables" for Normal and Superfluid Systems". en. In: *Journal of Mathematical Physics* 4.2 (Feb. 1963), pp. 255–265. ISSN: 0022-2488, 1089-7658. DOI: 10.1063/1.1703949. URL: https://pubs.aip.org/jmp/article/4/2/255/230131/Variational-Statistical-Mechanics-in-Terms-of (visited on 02/12/2024).

[51] Cyrano De Dominicis and Paul C. Martin. "Stationary Entropy Principle and Renormalization in Normal and Superfluid Systems. I. Algebraic Formulation". en. In: *Journal of Mathematical Physics* 5.1 (Jan. 1964), pp. 14–30. ISSN: 0022-2488, 1089-7658. DOI: 10.1063/1.1704062. URL: https://pubs.aip.org/jmp/article/5/1/14/719419/Stationary-Entropy-Principle-and-Renormalization (visited on 07/20/2024).

[52] Cyrano De Dominicis and Paul C. Martin. "Stationary Entropy Principle and Renormalization in Normal and Superfluid Systems. II. Diagrammatic Formulation". en. In: *Journal of Mathematical Physics* 5.1 (Jan. 1964), pp. 31–59. ISSN: 0022-2488, 1089-7658. DOI: 10.1063/1.1704064. URL: https://pubs.aip.org/jmp/article/5/1/31/719402/Stationary-Entropy-Principle-and-Renormalization (visited on 02/12/2024).

[53] J. J. Deisz, D. W. Hess, and J. W. Serene. "Incipient Antiferromagnetism and Low-Energy Excitations in the Half-Filled Two-Dimensional Hubbard Model". en. In: *Physical Review Letters* 76.8 (Feb. 1996), pp. 1312–1315. ISSN: 0031-9007, 1079-7114. DOI: 10.1103/PhysRevLett.76.1312. URL: https://link.aps.org/doi/10.1103/PhysRevLett.76.1312 (visited on 11/24/2024).

[54] Lorenzo Del Re, Massimo Capone, and Alessandro Toschi. "Dynamical vertex approximation for the attractive Hubbard model". en. In: *Physical Review B* 99.4 (Jan. 2019), p. 045137. ISSN: 2469-9950, 2469-9969. DOI: 10.1103/PhysRevB.99.045137. URL: https://link.aps.org/doi/10.1103/PhysRevB.99.045137 (visited on 11/25/2024).

[55] Lorenzo Del Re and Georg Rohringer. "Fluctuations analysis of spin susceptibility: Néel ordering revisited in dynamical mean field theory". en. In: *Physical Review B* 104.23 (Dec. 2021), p. 235128. ISSN: 2469-9950, 2469-9969. DOI: 10.1103/PhysRevB.104.235128. URL: https://link.aps.org/doi/10.1103/PhysRevB.104.235128 (visited on 01/12/2025).

[56] Lorenzo Del Re and Alessandro Toschi. "Dynamical vertex approximation for many-electron systems with spontaneously broken SU(2) symmetry". en. In: *Physical Review B* 104.8 (Aug. 2021), p. 085120. ISSN: 2469-9950, 2469-9969. DOI: 10.1103/PhysRevB.104.085120. URL: https://link.aps.org/doi/10.1103/PhysRevB.104.085120 (visited on 11/25/2024).

[57] Thomas P. Devereaux and Rudi Hackl. "Inelastic light scattering from correlated electrons". en. In: *Reviews of Modern Physics* 79.1 (Jan. 2007), pp. 175–233. ISSN: 0034-6861, 1539-0756. DOI: 10.1103/RevModPhys.79.175. URL: https://link.aps.org/doi/10.1103/RevModPhys.79.175 (visited on 12/08/2024).

[58] I. T. Diatlov, V. V. Sudakov, and K. A. Ter-Martirosian. "ASYMPTOTIC MESON-MESON SCATTERING THEORY". English. In: *Soviet Phys. JETP* Vol: 5 (Nov. 1957). Institution: Originating Research Org. not identified. URL: https://www.osti.gov/biblio/4338008 (visited on 01/12/2025).

[59] John Duchi, Elad Hazan, and Yoram Singer. "Adaptive Subgradient Methods for Online Learning and Stochastic Optimization". en. In: (2011).

[60] Ian Duck, Wolfgang Pauli, and E. C. G. Sudarshan. *Pauli and the spin-statistics theorem*. Singapore ; River Edge, NJ: World Scientific, 1997. ISBN: 978-981-02-3114-9.

[61] Nicolas Dupuis. *Field theory of condensed matter and ultracold gases. Volume 1*. eng. OCLC: 1396698162. London, England: World Scientific Publishing Europe Ltd., 2023. ISBN: 978-1-80061-391-1.

[62] *Dynamical mean-field theory of correlated electrons lecture notes of the Autumn School on Correlated Electrons 2022*. eng. OCLC: 1394993265. Jülich: Forschungszentrum Jülich GmbH, Institute for Advanced Simulation, 2022. ISBN: 978-3-95806-619-9.

[63] Christian J. Eckhardt et al. "Truncated unity parquet solver". en. In: *Physical Review B* 101.15 (Apr. 2020), p. 155104. ISSN: 2469-9950, 2469-9969. DOI: 10.1103/PhysRevB.101.155104. URL: https://link.aps.org/doi/10.1103/PhysRevB.101.155104 (visited on 01/12/2025).

[64] V. J. Emery, ed. *Correlated electron systems: Jerusalem, Israel, 30 Dec. 91-8 Jan. 92*. Meeting Name: Jerusalem Winter School for Theoretical Physics ISBN: 978-981-02-1269-8. Singapore ; River Edge, NJ: World Scientific, 1993. ISBN: 978-981-02-1232-2.

[65] D. M. Esterling and H. C. Dubin. "Moment-Generated Solution to the Hubbard Narrow-Energy-Band Model". en. In: *Physical Review B* 6.11 (Dec. 1972), pp. 4276–4283. ISSN: 0556-2805. DOI: 10.1103/PhysRevB.6.4276. URL: https://link.aps.org/doi/10.1103/PhysRevB.6.4276 (visited on 05/31/2024).

[66] Donald M. Esterling and Robert V. Lange. "Hubbard Model. I. Degeneracy in the Atomic Light". en. In: *Physical Review B* 1.5 (Mar. 1970), pp. 2231–2237. ISSN: 0556-2805. DOI: 10.1103/PhysRevB.1.2231. URL: https://link.aps.org/doi/10.1103/PhysRevB.1.2231 (visited on 05/06/2024).

[67] Robert Evans, Daan Frenkel, and Marjolein Dijkstra. "From simple liquids to colloids and soft matter". en. In: *Physics Today* 72.2 (Feb. 2019), pp. 38–39. ISSN: 0031-9228, 1945-0699. DOI: 10.1063/PT.3.4135. URL: https://pubs.aip.org/physicstoday/article/72/2/38/825244/From-simple-liquids-to-colloids-and-soft (visited on 01/12/2025).

[68] Shimon Even and Guy Even. *Graph algorithms*. 2nd ed. Cambridge, NY: Cambridge University Press, 2012. ISBN: 978-0-521-51718-8.

[69] Lukong Cornelius Fai. *Feynman path integrals in quantum mechanics and statistical physics*. Boca Raton: CRC Press, 2021. ISBN: 978-0-367-69785-3.

[70] A.L. Fetter and J.D. Walecka. *Quantum Theory of Many-particle Systems*. Dover Books on Physics. Dover Publications, 2003. ISBN: 978-0-486-42827-7. URL: https://books.google.de/books?id=0wekf1s83b0C.

[71] R. Fletcher. *Practical methods of optimization*. eng. Online-Ausg. ISBN: 978-1-118-72321-0, 978-0-471-49463-8. Chichester, West Sussex, U.K: Wiley, 2008. ISBN: 978-0-471-91547-8.

[72] M. Frigo and S.G. Johnson. "The Design and Implementation of FFTW3". en. In: *Proceedings of the IEEE* 93.2 (Feb. 2005), pp. 216–231. ISSN: 0018-9219. DOI: 10.1109/JPROC.2004.840301. URL: http://ieeexplore.ieee.org/document/1386650/ (visited on 11/03/2024).

[73] Masaki Fujita et al. "Progress in Neutron Scattering Studies of Spin Excitations in High- T_c Cuprates". en. In: *Journal of the Physical Society of Japan* 81.1 (Jan. 2012), p. 011007. ISSN: 0031-9015, 1347-4073. DOI: 10.1143/JPSJ.81.011007. URL: http://journals.jps.jp/doi/10.1143/JPSJ.81.011007 (visited on 12/20/2024).

[74] Sergio Mario Lins Galdino. "A family of regula falsi root-finding methods". In: 2011. URL: https://api.semanticscholar.org/CorpusID:15854811.

[75] V M Galitskii and A B Migdal. "APPLICATION OF QUANTUM FIELD THEORY METHODS TO THE MANY BODY PROBLEM". en. In: *Moscow Engineering-Physics Institute* 34 (1958). URL: https://www.osti.gov/biblio/4348538.

[76] C. Gauvin-Ndiaye et al. "Improved two-particle self-consistent approach for the single-band Hubbard model in two dimensions". en. In: *Physical Review B* 108.7 (Aug. 2023), p. 075144. ISSN: 2469-9950, 2469-9969. DOI: 10.1103/PhysRevB.108.075144. URL: https://link.aps.org/doi/10.1103/PhysRevB.108.075144 (visited on 01/19/2025).

[77] Axel Gelfert and Wolfgang Nolting. "The absence of finite-temperature phase transitions in low-dimensional many-body models: a survey and new results". In: *Journal of Physics: Condensed Matter* 13.27 (July 2001), R505–R524. ISSN: 0953-8984, 1361-648X. DOI: 10.1088/0953-8984/13/27/201. URL: https://iopscience.iop.org/article/10.1088/0953-8984/13/27/201 (visited on 07/17/2024).

[78] Murray Gell-Mann and Francis Low. "Bound States in Quantum Field Theory". In: *Phys. Rev.* 84.2 (Oct. 1951). Publisher: American Physical Society, pp. 350–354. DOI: 10.1103/PhysRev.84.350. URL: https://link.aps.org/doi/10.1103/PhysRev.84.350.

[79] Antoine Georges, Luca De' Medici, and Jernej Mravlje. "Strong Correlations from Hund's Coupling". en. In: *Annual Review of Condensed Matter Physics* 4.1 (Apr. 2013), pp. 137–178. ISSN: 1947-5454, 1947-5462. DOI: 10.1146/annurev-conmatphys-020911-125045. URL: https://www.annualreviews.org/doi/10.1146/annurev-conmatphys-020911-125045 (visited on 05/02/2024).

[80] Antoine Georges et al. "Dynamical mean-field theory of strongly correlated fermion systems and the limit of infinite dimensions". en. In: *Reviews of Modern Physics* 68.1 (Jan. 1996), pp. 13–125. ISSN: 0034-6861, 1539-0756. DOI: 10.1103/RevModPhys.68.13. URL: https://link.aps.org/doi/10.1103/RevModPhys.68.13 (visited on 06/17/2024).

[81] James Glimm and Arthur Jaffe. *Quantum Physics*. en. New York, NY: Springer, 1987. ISBN: 978-1-4612-4728-9. DOI: 10.1007/978-1-4612-4728-9. URL: http://link.springer.com/10.1007/978-1-4612-4728-9 (visited on 02/13/2024).

[82] Ian Goodfellow, Yoshua Bengio, and Aaron Courville. *Deep learning*. Adaptive computation and machine learning. Cambridge, Massachusetts: The MIT Press, 2016. ISBN: 978-0-262-03561-3.

[83] J. E. Gubernatis, N. Kawashima, and P. Werner. *Quantum Monte Carlo methods: algorithms for lattice models*. Cambridge: Cambridge University Press, 2016. ISBN: 978-1-107-00642-3.

[84] Emanuel Gull. "Continuous-Time Quantum Monte Carlo Algorithms for Fermions". en. Artwork Size: 161 S. Medium: application/pdf Pages: 161 S. PhD thesis. ETH Zurich, 2008. DOI: 10.3929/ETHZ-A-005722583. URL: http://hdl.handle.net/20.500.11850/104013 (visited on 06/18/2024).

[85] Emanuel Gull et al. "Continuous-time Monte Carlo methods for quantum impurity models". en. In: *Reviews of Modern Physics* 83.2 (May 2011), pp. 349–404. ISSN: 0034-6861, 1539-0756. DOI: 10.1103/RevModPhys.83.349. URL: https://link.aps.org/doi/10.1103/RevModPhys.83.349 (visited on 06/19/2024).

[86] O Gunnarsson and O Rösch. "Interplay between electron–phonon and Coulomb interactions in cuprates". In: *Journal of Physics: Condensed Matter* 20.4 (Jan. 2008), p. 043201. ISSN: 0953-8984, 1361-648X. DOI: 10.1088/0953-8984/20/04/043201. URL: https://iopscience.iop.org/article/10.1088/0953-8984/20/04/043201 (visited on 05/02/2024).

[87] O. Gunnarsson and K. Schönhammer. "Density-Functional Treatment of an Exactly Solvable Semiconductor Model". en. In: *Physical Review Letters* 56.18 (May 1986), pp. 1968–1971. ISSN: 0031-9007. DOI: 10.1103/PhysRevLett.56.1968. URL: https://link.aps.org/doi/10.1103/PhysRevLett.56.1968 (visited on 01/20/2025).

[88] O. Gunnarsson et al. "Breakdown of Traditional Many-Body Theories for Correlated Electrons". en. In: *Physical Review Letters* 119.5 (Aug. 2017), p. 056402. ISSN: 0031-9007, 1079-7114. DOI: 10.1103/PhysRevLett.119.056402. URL: http://link.aps.org/doi/10.1103/PhysRevLett.119.056402 (visited on 07/09/2024).

[89] O. Gunnarsson et al. "Parquet decomposition calculations of the electronic self-energy". en. In: *Physical Review B* 93.24 (June 2016), p. 245102. ISSN: 2469-9950, 2469-9969. DOI: 10.1103/PhysRevB.93.245102. URL: https://link.aps.org/doi/10.1103/PhysRevB.93.245102 (visited on 11/12/2024).

[90] H. Hafermann et al. "Superperturbation solver for quantum impurity models". In: *EPL (Europhysics Letters)* 85.2 (Jan. 2009), p. 27007. ISSN: 0295-5075, 1286-4854. DOI: 10.1209/0295-5075/85/27007. URL: https://iopscience.iop.org/article/10.1209/0295-5075/85/27007 (visited on 06/06/2024).

[91] Hartmut Hafermann et al. "Collective charge excitations of strongly correlated electrons, vertex corrections, and gauge invariance". en. In: *Physical Review B* 90.23 (Dec. 2014), p. 235105. ISSN: 1098-0121, 1550-235X. DOI: 10.1103/PhysRevB.90.235105. URL: https://link.aps.org/doi/10.1103/PhysRevB.90.235105 (visited on 11/14/2024).

[92] Jean-Pierre Hansen. *Theory of Simple Liquids*. eng. 3rd ed. London: Elsevier Science & Technology, 2006. ISBN: 978-0-08-045507-5.

[93] P Hansmann et al. "Importance of $d - p$ Coulomb interaction for high T_C cuprates and other oxides". In: *New Journal of Physics* 16.3 (Mar. 2014), p. 033009. ISSN: 1367-2630. DOI: 10.1088/1367-2630/16/3/033009. URL: https://iopscience.iop.org/article/10.1088/1367-2630/16/3/033009 (visited on 07/10/2024).

[94] T. Håvie. "Generalized neville type extrapolation schemes". en. In: *BIT* 19.2 (June 1979), pp. 204–213. ISSN: 0006-3835, 1572-9125. DOI: 10.1007/BF01930850. URL: http://link.springer.com/10.1007/BF01930850 (visited on 12/25/2024).

[95] Lars Hedin. "New Method for Calculating the One-Particle Green's Function with Application to the Electron-Gas Problem". en. In: *Physical Review* 139.3A (Aug. 1965), A796–A823. ISSN: 0031-899X. DOI: 10.1103/PhysRev.139.A796. URL: https://link.aps.org/doi/10.1103/PhysRev.139.A796 (visited on 12/10/2024).

[96] K. Held. "Electronic structure calculations using dynamical mean field theory". en. In: *Advances in Physics* 56.6 (Nov. 2007), pp. 829–926. ISSN: 0001-8732, 1460-6976. DOI: 10.1080/00018730701619647. URL: http://www.tandfonline.com/doi/abs/10.1080/00018730701619647 (visited on 01/12/2025).

[97] Karsten Held. *Dynamical Vertex Approximation*. arXiv:1411.5191 [cond-mat]. Nov. 2014. URL: http://arxiv.org/abs/1411.5191 (visited on 06/27/2024).

[98] Or Hen et al. "Nucleon-nucleon correlations, short-lived excitations, and the quarks within". en. In: *Reviews of Modern Physics* 89.4 (Nov. 2017), p. 045002. ISSN: 0034-6861, 1539-0756. DOI: 10.1103/RevModPhys.89.045002. URL: https://link.aps.org/doi/10.1103/RevModPhys.89.045002 (visited on 01/12/2025).

[99] M. H. Hettler et al. "Dynamical cluster approximation: Nonlocal dynamics of correlated electron systems". en. In: *Physical Review B* 61.19 (May 2000), pp. 12739–12756. ISSN: 0163-1829, 1095-3795. DOI: 10.1103/PhysRevB.61.12739. URL: https://link.aps.org/doi/10.1103/PhysRevB.61.12739 (visited on 07/08/2024).

[100] Geoffrey Hinton. "Neural Networks for Machine Learning". en. In: (2012).

[101] J. E. Hirsch. "Attractive Interaction and Pairing in Fermion Systems with Strong On-Site Repulsion". en. In: *Physical Review Letters* 54.12 (Mar. 1985), pp. 1317–1320. ISSN: 0031-9007. DOI: 10.1103/PhysRevLett.54.1317. URL: https://link.aps.org/doi/10.1103/PhysRevLett.54.1317 (visited on 05/04/2024).

[102] Daniel Hirschmeier et al. "Mechanisms of finite-temperature magnetism in the three-dimensional Hubbard model". en. In: *Physical Review B* 92.14 (Oct. 2015), p. 144409. ISSN: 1098-0121, 1550-235X. DOI: 10.1103/PhysRevB.92.144409. URL: https://link.aps.org/doi/10.1103/PhysRevB.92.144409 (visited on 01/12/2025).

[103] P. Hohenberg and W. Kohn. "Inhomogeneous Electron Gas". en. In: *Physical Review* 136.3B (Nov. 1964), B864–B871. ISSN: 0031-899X. DOI: 10.1103/PhysRev.136.B864. URL: https://link.aps.org/doi/10.1103/PhysRev.136.B864 (visited on 01/20/2025).

[104] P. C. Hohenberg. "Existence of Long-Range Order in One and Two Dimensions". en. In: *Physical Review* 158.2 (June 1967), pp. 383–386. ISSN: 0031-899X. DOI: 10.1103/PhysRev.158.383. URL: https://link.aps.org/doi/10.1103/PhysRev.158.383 (visited on 07/17/2024).

[105] A. S. Householder. *The numerical treatment of a single nonlinear equation*. eng. OCLC: 476702168. London: McGraw-Hill, 1970. ISBN: 978-0-07-030465-9.

[106] Cheng Hu et al. "Momentum-resolved visualization of electronic evolution in doping a Mott insulator". en. In: *Nature Communications* 12.1 (Mar. 2021), p. 1356. ISSN: 2041-1723. DOI: 10.1038/s41467-021-21605-6. URL: https://www.nature.com/articles/s41467-021-21605-6 (visited on 05/31/2024).

[107] C. Husemann, K.-U. Giering, and M. Salmhofer. "Frequency-dependent vertex functions of the (t , t) Hubbard model at weak coupling". en. In: *Physical Review B* 85.7 (Feb. 2012), p. 075121. ISSN: 1098-0121, 1550-235X. DOI: 10.1103/PhysRevB.85.075121. URL: https://link.aps.org/doi/10.1103/PhysRevB.85.075121 (visited on 11/19/2024).

[108] N E Hussey, J Buhot, and S Licciardello. "A tale of two metals: contrasting criticalities in the pnictides and hole-doped cuprates". In: *Reports on Progress in Physics* 81.5 (May 2018), p. 052501. ISSN: 0034-4885, 1361-6633. DOI: 10.1088/1361-6633/aaa97c. URL: https://iopscience.iop.org/article/10.1088/1361-6633/aaa97c (visited on 12/18/2024).

[109] Setsuo Ichimaru. "Strongly coupled plasmas: high-density classical plasmas and degenerate electron liquids". en. In: *Reviews of Modern Physics* 54.4 (Oct. 1982), pp. 1017–1059. ISSN: 0034-6861. DOI: 10.1103/RevModPhys.54.1017. URL: https://link.aps.org/doi/10.1103/RevModPhys.54.1017 (visited on 12/10/2024).

[110] Sergei Iskakov, Andrey E. Antipov, and Emanuel Gull. "Diagrammatic Monte Carlo for dual fermions". en. In: *Physical Review B* 94.3 (July 2016), p. 035102. ISSN: 2469-9950, 2469-9969. DOI: 10.1103/PhysRevB.94.035102. URL: https://link.aps.org/doi/10.1103/PhysRevB.94.035102 (visited on 07/09/2024).

[111] J.W. Negele and H.O. Orland. *Quantum Many-Particle Systems*. Perseus Books, 1998. ISBN: 0-7382-0052-2. (Visited on 09/21/2017).

[112] V. Janiš. "Parquet approach to nonlocal vertex functions and electrical conductivity of disordered electrons". en. In: *Physical Review B* 64.11 (Aug. 2001), p. 115115. ISSN: 0163-1829, 1095-3795. DOI: 10.1103/PhysRevB.64.115115. URL: https://link.aps.org/doi/10.1103/PhysRevB.64.115115 (visited on 11/14/2024).

[113] V. Janiš. "Stability of self-consistent solutions for the Hubbard model at intermediate and strong coupling". en. In: *Physical Review B* 60.16 (Oct. 1999), pp. 11345–11360. ISSN: 0163-1829, 1095-3795. DOI: 10.1103/PhysRevB.60.11345. URL: https://link.aps.org/doi/10.1103/PhysRevB.60.11345 (visited on 07/07/2024).

[114] V. Janiš and D. Vollhardt. "COMPREHENSIVE MEAN FIELD THEORY FOR THE HUBBARD MODEL". en. In: *International Journal of Modern Physics B* 06.05n06 (Mar. 1992), pp. 731–747. ISSN: 0217-9792, 1793-6578. DOI: 10.1142/S0217979292000438. URL: https://www.worldscientific.com/doi/abs/10.1142/S0217979292000438 (visited on 07/07/2024).

[115] Václav Janiš, Vladislav Pokorný, and Šimon Kos. *Failure of the Baym-Kadanoff construction to match consistently quantum dynamics with thermodynamic critical behavior*. arXiv:2309.07699 [cond-mat]. Jan. 2024. URL: http://arxiv.org/abs/2309.07699 (visited on 02/12/2024).

[116] M. Jarrell and Th. Pruschke. "Anomalous properties of the Hubbard model in infinite dimensions". en. In: *Physical Review B* 49.2 (Jan. 1994), pp. 1458–1461. ISSN: 0163-1829, 1095-3795. DOI: 10.1103/PhysRevB.49.1458. URL: https://link.aps.org/doi/10.1103/PhysRevB.49.1458 (visited on 11/17/2024).

[117] Jean-Pierre Hanse and Ian R. McDonald. "Theory of Simple Liquids". en. In: *Theory of Simple Liquids*. Elsevier, 2013, p. i. ISBN: 978-0-12-387032-2. DOI: 10.1016/B978-0-12-387032-2.00013-1. URL: https://linkinghub.elsevier.com/retrieve/pii/B9780123870322000131 (visited on 01/12/2025).

[118] Ro Jefferson. *Cumulants, correlators, and connectivity*. Apr. 2019. URL: https://rojefferson.blog/2019/08/04/cumulants-correlators-and-connectivity/.

[119] John Hubbard. "Electron correlations in narrow energy bands". en. In: *Proceedings of the Royal Society of London. Series A. Mathematical and Physical Sciences* 276.1365 (Nov. 1963), pp. 238–257. ISSN: 0080-4630, 2053-9169. DOI: 10.1098/rspa.1963.0204. URL: https://royalsocietypublishing.org/doi/10.1098/rspa.1963.0204 (visited on 05/02/2024).

[120] R. O. Jones and O. Gunnarsson. "The density functional formalism, its applications and prospects". en. In: *Reviews of Modern Physics* 61.3 (July 1989), pp. 689–746. ISSN: 0034-6861. DOI: 10.1103/RevModPhys.61.689. URL: https://link.aps.org/doi/10.1103/RevModPhys.61.689 (visited on 01/12/2025).

[121] Julian Stobbe. *jED.jl*. Hamburg, Nov. 2024. URL: https://github.com/atomtomate/jED.jl/.

[122] Henrik Kajueter and Gabriel Kotliar. "New Iterative Perturbation Scheme for Lattice Models with Arbitrary Filling". en. In: *Physical Review Letters* 77.1 (July 1996), pp. 131–134. ISSN: 0031-9007, 1079-7114. DOI: 10.1103/PhysRevLett.77.131. URL: https://link.aps.org/doi/10.1103/PhysRevLett.77.131 (visited on 05/06/2024).

[123] Junjiro Kanamori. "Electron Correlation and Ferromagnetism of Transition Metals". en. In: *Progress of Theoretical Physics* 30.3 (Sept. 1963), pp. 275–289. ISSN: 0033-068X. DOI: 10.1143/PTP.30.275. URL: https://academic.oup.com/ptp/article-lookup/doi/10.1143/PTP.30.275 (visited on 05/02/2024).

[124] Byungkyun Kang et al. "Impact of f-d Kondo cloud on superconductivity of nickelates". en. In: *Cell Reports Physical Science* 4.3 (Mar. 2023), p. 101325. ISSN: 26663864. DOI: 10.1016/j.xcrp.2023.101325. URL: https://linkinghub.elsevier.com/retrieve/pii/S2666386423000905 (visited on 05/02/2024).

[125] A. A. Katanin, A. Toschi, and K. Held. "Comparing pertinent effects of antiferromagnetic fluctuations in the two- and three-dimensional Hubbard model". en. In: *Physical Review B* 80.7 (Aug. 2009), p. 075104. ISSN: 1098-0121, 1550-235X. DOI: 10.1103/PhysRevB.80.075104. URL: https://link.aps.org/doi/10.1103/PhysRevB.80.075104 (visited on 07/08/2024).

[126] Tosio Kato. *Perturbation Theory for Linear Operators*. Vol. 132. Classics in Mathematics. Berlin, Heidelberg: Springer, 1995. ISBN: 978-3-540-58661-6. DOI: 10.1007/978-3-642-66282-9. URL: http://link.springer.com/10.1007/978-3-642-66282-9 (visited on 02/06/2024).

[127] Victor J. Katz. *A history of mathematics: an introduction*. 2nd ed. Reading, Mass: Addison-Wesley, 1998. ISBN: 978-0-321-01618-8.

[128] Josef Kaufmann et al. "Self-consistent ladder dynamical vertex approximation". en. In: *Physical Review B* 103.3 (Jan. 2021), p. 035120. ISSN: 2469-9950, 2469-9969. DOI: 10.1103/PhysRevB.103.035120. URL: https://link.aps.org/doi/10.1103/PhysRevB.103.035120 (visited on 11/03/2024).

[129] E. Khatami, A. Macridin, and M. Jarrell. "Effect of long-range hopping on T c in a two-dimensional Hubbard-Holstein model of the cuprates". en. In: *Physical Review B* 78.6 (Aug. 2008), p. 060502. ISSN: 1098-0121, 1550-235X. DOI: 10.1103/PhysRevB.78.060502. URL: https://link.aps.org/doi/10.1103/PhysRevB.78.060502 (visited on 12/31/2024).

[130] Diederik P. Kingma and Jimmy Ba. *Adam: A Method for Stochastic Optimization*. arXiv:1412.6980 [cs]. Jan. 2017. DOI: 10.48550/arXiv.1412.6980. URL: http://arxiv.org/abs/1412.6980 (visited on 12/06/2024).

[131] Michael Kinza and Carsten Honerkamp. "Two-particle correlations in a functional renormalization group scheme using a dynamical mean-field theory approach". en. In: *Physical Review B* 88.19 (Nov. 2013), p. 195136. ISSN: 1098-0121, 1550-235X. DOI: 10.1103/PhysRevB.88.195136. URL: https://link.aps.org/doi/10.1103/PhysRevB.88.195136 (visited on 11/02/2024).

[132] Takafumi Kita. "Legendre Transformation of the Luttinger-Ward Functional from the Bare Interaction Vertex to the Renormalized One". In: (2022). Publisher: arXiv Version Number: 1. DOI: 10.48550/ARXIV.2210.08660. URL: https://arxiv.org/abs/2210.08660 (visited on 11/20/2024).

[133] Motoharu Kitatani, Naoto Tsuji, and Hideo Aoki. "FLEX+DMFT approach to the d -wave superconducting phase diagram of the two-dimensional Hubbard model". en. In: *Physical Review B* 92.8 (Aug. 2015), p. 085104. ISSN: 1098-0121, 1550-235X. DOI: 10.1103/PhysRevB.92.085104. URL: https://link.aps.org/doi/10.1103/PhysRevB.92.085104 (visited on 11/19/2024).

[134] Motoharu Kitatani et al. "Nickelate superconductors—a renaissance of the one-band Hubbard model". en. In: *npj Quantum Materials* 5.1 (Aug. 2020), p. 59. ISSN: 2397-4648. DOI: 10.1038/s41535-020-00260-y. URL: https://www.nature.com/articles/s41535-020-00260-y (visited on 05/02/2024).

[135] Motoharu Kitatani et al. "Optimizing Superconductivity: From Cuprates via Nickelates to Palladates". en. In: *Physical Review Letters* 130.16 (Apr. 2023), p. 166002. ISSN: 0031-9007, 1079-7114. DOI: 10.1103/PhysRevLett.130.166002. URL: https://link.aps.org/doi/10.1103/PhysRevLett.130.166002 (visited on 11/25/2024).

[136] Motoharu Kitatani et al. "Why the critical temperature of high- T c cuprate superconductors is so low: The importance of the dynamical vertex structure". en. In: *Physical Review B* 99.4 (Jan. 2019), p. 041115. ISSN: 2469-9950, 2469-9969. DOI: 10.1103/PhysRevB.99.041115. URL: https://link.aps.org/doi/10.1103/PhysRevB.99.041115 (visited on 12/01/2024).

[137] Günter Klambauer et al. "Self-Normalizing Neural Networks". In: (2017). Publisher: arXiv Version Number: 5. DOI: 10.48550/ARXIV.1706.02515. URL: https://arxiv.org/abs/1706.02515 (visited on 01/21/2025).

[138] Hagen Kleinert. *Path Integrals in Quantum Mechanics, Statistics, Polymer Physics, and Financial Markets*. en. 5th ed. WORLD SCIENTIFIC, May 2009. ISBN: 978-981-4273-55-8. DOI: 10.1142/7305. URL: https://www.worldscientific.com/worldscibooks/10.1142/7305 (visited on 02/06/2024).

[139] W. Kohn. "Analytic Properties of Bloch Waves and Wannier Functions". en. In: *Physical Review* 115.4 (Aug. 1959), pp. 809–821. ISSN: 0031-899X. DOI: 10.1103/PhysRev.115.809. URL: https://link.aps.org/doi/10.1103/PhysRev.115.809 (visited on 05/02/2024).

[140] W. Kohn and L. J. Sham. "Self-Consistent Equations Including Exchange and Correlation Effects". en. In: *Physical Review* 140.4A (Nov. 1965), A1133–A1138. ISSN: 0031-899X. DOI: 10.1103/PhysRev.140.A1133. URL: https://link.aps.org/doi/10.1103/PhysRev.140.A1133 (visited on 05/02/2024).

[141] Angela Kopp, Amit Ghosal, and Sudip Chakravarty. "Competing ferromagnetism in high-temperature copper oxide superconductors". en. In: *Proceedings of the National Academy of Sciences* 104.15 (Apr. 2007), pp. 6123–6127. ISSN: 0027-8424, 1091-6490. DOI: 10.1073/pnas.0701265104. URL: https://pnas.org/doi/full/10.1073/pnas.0701265104 (visited on 01/02/2025).

[142] E. Kozik et al. "Néel temperature and thermodynamics of the half-filled three-dimensional Hubbard model by diagrammatic determinant Monte Carlo". en. In: *Physical Review B* 87.20 (May 2013), p. 205102. ISSN: 1098-0121, 1550-235X. DOI: 10.1103/PhysRevB.87.205102. URL: https://link.aps.org/doi/10.1103/PhysRevB.87.205102 (visited on 01/12/2025).

[143] Friedrich Krien. "Conserving dynamical mean- eld approaches to strongly correlated systems". Dissertation. Hamburg: University Hamburg, Apr. 2018. URL: https://ediss.sub.uni-hamburg.de/handle/ediss/7726.

[144] Friedrich Krien, Alexander I. Lichtenstein, and Georg Rohringer. "Fluctuation diagnostic of the nodal/antinodal dichotomy in the Hubbard model at weak coupling: A parquet dual fermion approach". en. In: *Physical Review B* 102.23 (Dec. 2020), p. 235133. ISSN: 2469-9950, 2469-9969. DOI: 10.1103/PhysRevB.102.235133. URL: https://link.aps.org/doi/10.1103/PhysRevB.102.235133 (visited on 01/12/2025).

[145] Friedrich Krien, Angelo Valli, and Massimo Capone. "Single-boson exchange decomposition of the vertex function". en. In: *Physical Review B* 100.15 (Oct. 2019), p. 155149. ISSN: 2469-9950, 2469-9969. DOI: 10.1103/PhysRevB.100.155149. URL: https://link.aps.org/doi/10.1103/PhysRevB.100.155149 (visited on 01/09/2025).

[146] Friedrich Krien et al. "Boson-exchange parquet solver for dual fermions". en. In: *Physical Review B* 102.19 (Nov. 2020), p. 195131. ISSN: 2469-9950, 2469-9969. DOI: 10.1103/PhysRevB.102.195131. URL: https://link.aps.org/doi/10.1103/PhysRevB.102.195131 (visited on 01/12/2025).

[147] Friedrich Krien et al. "Conservation in two-particle self-consistent extensions of dynamical mean-field theory". en. In: *Physical Review B* 96.7 (Aug. 2017), p. 075155. ISSN: 2469-9950, 2469-9969. DOI: 10.1103/PhysRevB.96.075155. URL: https://link.aps.org/doi/10.1103/PhysRevB.96.075155 (visited on 07/09/2024).

[148] Ryogo Kubo. "Generalized Cumulant Expansion Method". en. In: *Journal of the Physical Society of Japan* 17.7 (July 1962), pp. 1100–1120. ISSN: 0031-9015, 1347-4073. DOI: 10.1143/JPSJ.17.1100. URL: https://journals.jps.jp/doi/10.1143/JPSJ.17.1100 (visited on 04/29/2024).

[149] Ryogo Kubo. "Statistical-Mechanical Theory of Irreversible Processes. I. General Theory and Simple Applications to Magnetic and Conduction Problems". en. In: *Journal of the Physical Society of Japan* 12.6 (June 1957), pp. 570–586. ISSN: 0031-9015, 1347-4073. DOI: 10.1143/JPSJ.12.570. URL: https://journals.jps.jp/doi/10.1143/JPSJ.12.570 (visited on 06/08/2024).

[150] Fabian B. Kugler and Jan von Delft. "Derivation of exact flow equations from the self-consistent parquet relations". In: (2018). Publisher: arXiv Version Number: 3. DOI: 10.48550/ARXIV.1807.02898. URL: https://arxiv.org/abs/1807.02898 (visited on 11/24/2024).

[151] Hiroaki Kusunose. "Influence of Spatial Correlations in Strongly Correlated Electron Systems: Extension to Dynamical Mean Field Approximation". en. In: *Journal of the Physical Society of Japan* 75.5 (May 2006), p. 054713. ISSN: 0031-9015, 1347-4073. DOI: 10.1143/JPSJ.75.054713. URL: http://journals.jps.jp/doi/10.1143/JPSJ.75.054713 (visited on 11/25/2024).

[152] C. Lanczos. "An iteration method for the solution of the eigenvalue problem of linear differential and integral operators". en. In: *Journal of Research of the National Bureau of Standards* 45.4 (Oct. 1950), p. 255. ISSN: 0091-0635. DOI: 10.6028/jres.045.026. URL: https://nvlpubs.nist.gov/nistpubs/jres/045/jresv45n4p255_A1b.pdf (visited on 07/11/2024).

[153] L. D. Landau. "The Theory of a Fermi Liquid". In: *Zh. Eksp. Teor. Fiz.* 30.6 (1956), p. 1058.

[154] L. D. LANDAU and E. M. LIFSHITZ. "CHAPTER XIV - PHASE TRANSITIONS OF THE SECOND KIND AND CRITICAL PHENOMENA". In: *Statistical Physics (Third Edition)*. Ed. by L. D. LANDAU and E. M. LIFSHITZ. Third Edition. Oxford: Butterworth-Heinemann, 1980, pp. 446–516. ISBN: 978-0-08-057046-4. DOI: https://doi.org/10.1016/B978-0-08-057046-4.50021-X. URL: https://www.sciencedirect.com/science/article/pii/B978008057046450021X.

[155] Lev Davidovich Landau. "On the Theory of the Fermi Liquid". In: *J. Exp. Theor. Phys.* 35 (1958). Ed. by D. ter Haar. DOI: 10.1016/b978-0-08-010586-4.50100-0.

[156] Lev Davidovich Landau. "Oscillations in a Fermi Liquid". In: *Zh. Eksp. Teor. Fiz.* 32 (1957). Ed. by D. ter Haar. DOI: 10.1016/b978-0-08-010586-4.50096-1.

[157] Kyungmin Lee et al. "Triangular lattice Hubbard model physics at intermediate temperatures". en. In: *Physical Review B* 107.23 (June 2023), p. 235105. ISSN: 2469-9950, 2469-9969. DOI: 10.1103/PhysRevB.107.235105. URL: https://link.aps.org/doi/10.1103/PhysRevB.107.235105 (visited on 05/04/2024).

[158] Patrick A. Lee, Naoto Nagaosa, and Xiao-Gang Wen. "Doping a Mott insulator: Physics of high-temperature superconductivity". en. In: *Reviews of Modern Physics* 78.1 (Jan. 2006), pp. 17–85. ISSN: 0034-6861, 1539-0756. DOI: 10.1103/RevModPhys.78.17. URL: https://link.aps.org/doi/10.1103/RevModPhys.78.17 (visited on 07/15/2024).

[159] Seung-Sup B. Lee, Jan Von Delft, and Andreas Weichselbaum. "Generalized Schrieffer-Wolff transformation of multiflavor Hubbard models". en. In: *Physical Review B* 96.24 (Dec. 2017), p. 245106. ISSN: 2469-9950, 2469-9969. DOI: 10.1103/PhysRevB.96.245106. URL: https://link.aps.org/doi/10.1103/PhysRevB.96.245106 (visited on 05/04/2024).

[160] Harold Levine and Julian Schwinger. "On the Theory of Diffraction by an Aperture in an Infinite Plane Screen. I". en. In: *Physical Review* 74.8 (Oct. 1948), pp. 958–974. ISSN: 0031-899X. DOI: 10.1103/PhysRev.74.958. URL: https://link.aps.org/doi/10.1103/PhysRev.74.958 (visited on 12/25/2024).

[161] Yuan Li et al. "Hidden magnetic excitation in the pseudogap phase of a high-Tc superconductor". en. In: *Nature* 468.7321 (Nov. 2010), pp. 283–285. ISSN: 0028-0836, 1476-4687. DOI: 10.1038/nature09477. URL: https://www.nature.com/articles/nature09477 (visited on 12/18/2024).

[162] J. M. Luttinger and J. C. Ward. "Ground-State Energy of a Many-Fermion System. II". In: *Phys. Rev.* 118.5 (June 1960). Publisher: American Physical Society, pp. 1417–1427. DOI: 10.1103/PhysRev.118.1417. URL: https://link.aps.org/doi/10.1103/PhysRev.118.1417.

[163] A. Macridin et al. "Physics of cuprates with the two-band Hubbard model: The validity of the one-band Hubbard model". en. In: *Physical Review B* 71.13 (Apr. 2005), p. 134527. ISSN: 1098-0121, 1550-235X. DOI: 10.1103/PhysRevB.71.134527. URL: https://link.aps.org/doi/10.1103/PhysRevB.71.134527 (visited on 12/31/2024).

[164] T. A. Maier, M. S. Jarrell, and D. J. Scalapino. "Structure of the Pairing Interaction in the Two-Dimensional Hubbard Model". en. In: *Physical Review Letters* 96.4 (Feb. 2006), p. 047005. ISSN: 0031-9007, 1079-7114. DOI: 10.1103/PhysRevLett.96.047005. URL: https://link.aps.org/doi/10.1103/PhysRevLett.96.047005 (visited on 07/17/2024).

[165] Nicola Marzari et al. "Maximally localized Wannier functions: Theory and applications". en. In: *Reviews of Modern Physics* 84.4 (Oct. 2012), pp. 1419–1475. ISSN: 0034-6861, 1539-0756. DOI: 10.1103/RevModPhys.84.1419. URL: https://link.aps.org/doi/10.1103/RevModPhys.84.1419 (visited on 05/02/2024).

[166] Atsushi Masumizu and Kiyoshi Sogo. "Ward-Takahashi relations for SO(4) symmetry in the Hubbard model". en. In: *Physical Review B* 72.11 (Sept. 2005), p. 115107. ISSN: 1098-0121, 1550-235X. DOI: 10.1103/PhysRevB.72.115107. URL: https://link.aps.org/doi/10.1103/PhysRevB.72.115107 (visited on 11/14/2024).

[167] M. B. J. Meinders, H. Eskes, and G. A. Sawatzky. "Spectral-weight transfer: Breakdown of low-energy-scale sum rules in correlated systems". en. In: *Physical Review B* 48.6 (Aug. 1993), pp. 3916–3926. ISSN: 0163-1829, 1095-3795. DOI: 10.1103/PhysRevB.48.3916. URL: https://link.aps.org/doi/10.1103/PhysRevB.48.3916 (visited on 05/05/2024).

[168] A. Melman. "Numerical solution of a secular equation". In: *Numerische Mathematik* 69.4 (Feb. 1995), pp. 483–493. ISSN: 0029-599X, 0945-3245. DOI: 10.1007/s002110050104. URL: http://link.springer.com/10.1007/s002110050104 (visited on 08/10/2024).

[169] Aaron Melman. "Root Finding Techniques That Work". en. In: *THE TEACHING OF MATHEMATICS* XXV.1 (2022), pp. 38–52.

[170] N. D. Mermin and H. Wagner. "Absence of Ferromagnetism or Antiferromagnetism in One- or Two-Dimensional Isotropic Heisenberg Models". en. In: *Physical Review Letters* 17.22 (Nov. 1966), pp. 1133–1136. ISSN: 0031-9007. DOI: 10.1103/PhysRevLett.17.1133. URL: https://link.aps.org/doi/10.1103/PhysRevLett.17.1133 (visited on 07/17/2024).

[171] Walter Metzner and Dieter Vollhardt. "Analytic calculation of ground-state properties of correlated fermions with the Gutzwiller wave function". en. In: *Physical Review B* 37.13 (May 1988), pp. 7382–7399. ISSN: 0163-1829. DOI: 10.1103/PhysRevB.37.7382. URL: https://link.aps.org/doi/10.1103/PhysRevB.37.7382 (visited on 06/15/2024).

[172] Walter Metzner and Dieter Vollhardt. "Correlated Lattice Fermions in d = ∞ Dimensions". en. In: *Physical Review Letters* 62.3 (Jan. 1989), pp. 324–327. ISSN: 0031-9007. DOI: 10.1103/PhysRevLett.62.324. URL: https://link.aps.org/doi/10.1103/PhysRevLett.62.324 (visited on 06/14/2024).

[173] Walter Metzner and Dieter Vollhardt. "Ground-state properties of correlated fermions: Exact analytic results for the Gutzwiller wave function". en. In: *Physical Review Letters* 59.1 (July 1987), pp. 121–124. ISSN: 0031-9007. DOI: 10.1103/PhysRevLett.59.121. URL: https://link.aps.org/doi/10.1103/PhysRevLett.59.121 (visited on 06/15/2024).

[174] H. Miao et al. "Charge density waves in cuprate superconductors beyond the critical doping". en. In: *npj Quantum Materials* 6.1 (Mar. 2021), p. 31. ISSN: 2397-4648. DOI: 10.1038/s41535-021-00327-4. URL: https://www.nature.com/articles/s41535-021-00327-4 (visited on 01/03/2025).

[175] Emin Moghadas et al. "Compressing the two-particle Green's function using wavelets: Theory and application to the Hubbard atom". In: *The European Physical Journal Plus* 139.8 (Aug. 2024). arXiv:2402.13030 [cond-mat], p. 700. ISSN: 2190-5444. DOI: 10.1140/epjp/s13360-024-05403-9. URL: http://arxiv.org/abs/2402.13030 (visited on 12/04/2024).

[176] Tôru Moriya. "Self-Consistent Renormalization (SCR) Theory of Spin Fluctuations". In: *Spin Fluctuations in Itinerant Electron Magnetism*. Ed. by Peter Fulde, Manuel Cardona, and Hans-Joachim Queisser. Vol. 56. Series Title: Springer Series in Solid-State Sciences. Berlin, Heidelberg: Springer Berlin Heidelberg, 1985, pp. 44–81. ISBN: 978-3-642-82501-9. DOI: 10.1007/978-3-642-82499-9_4. URL: http://link.springer.com/10.1007/978-3-642-82499-9_4 (visited on 11/20/2024).

[177] Tôru Moriya. "Theory of Spin Fluctuations in Itinerant Electron Ferromagnets –Persistence of Spin Waves Above T_C". en. In: *Journal of the Physical Society of Japan* 40.4 (Apr. 1976), pp. 933–946. ISSN: 0031-9015, 1347-4073. DOI: 10.1143/JPSJ.40.933. URL: https://journals.jps.jp/doi/10.1143/JPSJ.40.933 (visited on 11/20/2024).

[178] Tôru Moriya, Yoshinori Takahashi, and Kazuo Ueda. "Antiferromagnetic Spin Fluctuations and Superconductivity in Two-Dimensional Metals -A Possible Model for High T_c Oxides". en. In: *Journal of the Physical Society of Japan* 59.8 (Aug. 1990), pp. 2905–2915. ISSN: 0031-9015, 1347-4073. DOI: 10.1143/JPSJ.59.2905. URL: http://journals.jps.jp/doi/10.1143/JPSJ.59.2905 (visited on 11/21/2024).

[179] N F Mott. "The Basis of the Electron Theory of Metals, with Special Reference to the Transition Metals". In: *Proceedings of the Physical Society. Section A* 62.7 (July 1949), pp. 416–422. ISSN: 0370-1298. DOI: 10.1088/0370-1298/62/7/303. URL: https://iopscience.iop.org/article/10.1088/0370-1298/62/7/303 (visited on 05/04/2024).

[180] Julian Mußhoff. "Susceptibility calculations for strongly correlated materials". de. PhD thesis. Aachen: RWTH Aachen, 2021. URL: https://publications.rwth-aachen.de/record/816888/?ln=de.

[181] E. M ller-Hartmann. "Correlated fermions on a lattice in high dimensions". en. In: *Zeitschrift f r Physik B Condensed Matter* 74.4 (Dec. 1989), pp. 507–512. ISSN: 0722-3277, 1434-6036. DOI: 10.1007/BF01311397. URL: http://link.springer.com/10.1007/BF01311397 (visited on 06/15/2024).

[182] D. Nicoletti et al. "High-Temperature Optical Spectral Weight and Fermi-liquid Renormalization in Bi-Based Cuprate Superconductors". en. In: *Physical Review Letters* 105.7 (Aug. 2010), p. 077002. ISSN: 0031-9007, 1079-7114. DOI: 10.1103/PhysRevLett.105.077002. URL: https://link.aps.org/doi/10.1103/PhysRevLett.105.077002 (visited on 12/21/2024).

[183] E. Noether. "Invariante Variationsprobleme". ger. In: *Nachrichten von der Gesellschaft der Wissenschaften zu Göttingen, Mathematisch-Physikalische Klasse* 1918 (1918), pp. 235–257. URL: http://eudml.org/doc/59024.

[184] Mariana M Odashima, Beatriz G Prado, and E Vernek. "Pedagogical introduction to equilibrium Green's functions: condensed-matter examples with numerical implementations". In: *Revista Brasileira de Ensino de Física* 39.1 (Apr. 2017). arXiv: 1604.02499. ISSN: 1806-1117. DOI: 10.1590/1806-9126-RBEF-2016-0087.

[185] L. S. Ornstein and F. Zernike. "Integral equation in liquid state theory". In: *Proc. K. Ned. Akad. Wet.* 17 (1914), p. 793. URL: https://dwc.knaw.nl/DL/publications/PU00012727.pdf.

[186] Junya Otsuki et al. "Sparse modeling approach to analytical continuation of imaginary-time quantum Monte Carlo data". en. In: *Physical Review E* 95.6 (June 2017), p. 061302. ISSN: 2470-0045, 2470-0053. DOI: 10.1103/PhysRevE.95.061302. URL: https://link.aps.org/doi/10.1103/PhysRevE.95.061302 (visited on 12/24/2024).

[187] E. Pavarini et al. "Band-Structure Trend in Hole-Doped Cuprates and Correlation with T c max". en. In: *Physical Review Letters* 87.4 (July 2001), p. 047003. ISSN: 0031-9007, 1079-7114. DOI: 10.1103/PhysRevLett.87.047003. URL: https://link.aps.org/doi/10.1103/PhysRevLett.87.047003 (visited on 12/18/2024).

[188] Eva Pavarini et al., eds. *Correlated electrons: from models to materials: lecture notes of the Autumn School Correlated Electrons 2012: at Forschungszentrum Jülich, 3-7 September 2012*. eng. Schriften des Forschungszentrums Jülich. Reihe Modeling and Simulation Band 2. Meeting Name: Autumn School Correlated Electrons. Jülich: Forschungszentrum Jülich, Zentralbibliothek, Verl, 2012. ISBN: 978-3-89336-796-2.

[189] Eva Pavarini et al., eds. *DMFT: From Infinite Dimensions to Real Materials: lecture notes of the Autumn School on Correlated Electrons 2018: at Forschungszentrum Jülich, 17-21 September 2018*. eng. Schriften des Forschungszentrums Jülich. Reihe Modeling and Simulation Band 8. Meeting Name: Autumn School on Correlated Electrons. Jülich: Forschungszentrum, Zentralbibliothek, 2018. ISBN: 978-3-95806-313-6.

[190] Eva Pavarini et al., eds. *Quantum materials: experiments and theory: lecture notes of the Autumn School on Correlated Electrons 2016: at Forschungszentrum Jülich, 12-16 September 2016*. en. Schriften des Forschungszentrums Jülich. Reihe Modeling and Simulation Band 6. Meeting Name: Autumn School on Correlated Electrons. Jülich: Forschungszentrum, Zentralbibliothek, 2016. ISBN: 978-3-95806-159-0.

[191] John P. Perdew et al. "Density-Functional Theory for Fractional Particle Number: Derivative Discontinuities of the Energy". en. In: *Physical Review Letters* 49.23 (Dec. 1982), pp. 1691–1694. ISSN: 0031-9007. DOI: 10.1103/PhysRevLett.49.1691. URL: https://link.aps.org/doi/10.1103/PhysRevLett.49.1691 (visited on 01/20/2025).

[192] L. Peters et al. "Dual boson approach with instantaneous interaction". en. In: *Physical Review B* 100.16 (Oct. 2019), p. 165128. ISSN: 2469-9950, 2469-9969. DOI: 10.1103/PhysRevB.100.165128. URL: https://link.aps.org/doi/10.1103/PhysRevB.100.165128 (visited on 01/12/2025).

[193] Elad Plaut. *From Principal Subspaces to Principal Components with Linear Autoencoders*. Version Number: 3. 2018. DOI: 10.48550/ARXIV.1804.10253. URL: https://arxiv.org/abs/1804.10253 (visited on 12/24/2024).

[194] Potthoff. "Non-perturbative construction of the Luttinger-Ward functional". en. In: *Condensed Matter Physics* 9.3 (2006), p. 557. ISSN: 1607324X. DOI: 10.5488/CMP.9.3.557. URL: http://www.icmp.lviv.ua/journal/zbirnyk.47/011/abstract.html (visited on 07/04/2024).

[195] M. Potthoff, T. Wegner, and W. Nolting. "Interpolating self-energy of the infinite-dimensional Hubbard model: Modifying the iterative perturbation theory". en. In: *Physical Review B* 55.24 (June 1997). arXiv:cond-mat/9704005, pp. 16132–16142. ISSN: 0163-1829, 1095-3795. DOI: 10.1103/PhysRevB.55.16132. URL: http://arxiv.org/abs/cond-mat/9704005 (visited on 12/06/2023).

[196] D. J. Pringle, G. V. M. Williams, and J. L. Tallon. "Effect of doping and impurities on the oxygen isotope effect in high-temperature superconducting cuprates". en. In: *Physical Review B* 62.18 (Nov. 2000), pp. 12527–12533. ISSN: 0163-1829, 1095-3795. DOI: 10.1103/PhysRevB.62.12527. URL: https://link.aps.org/doi/10.1103/PhysRevB.62.12527 (visited on 12/20/2024).

[197] Cyril Proust and Louis Taillefer. "The Remarkable Underlying Ground States of Cuprate Superconductors". en. In: *Annual Review of Condensed Matter Physics* 10.1 (Mar. 2019), pp. 409–429. ISSN: 1947-5454, 1947-5462. DOI: 10.1146/annurev-conmatphys-031218-013210. URL: https://www.annualreviews.org/doi/10.1146/annurev-conmatphys-031218-013210 (visited on 12/18/2024).

[198] Mingpu Qin et al. "The Hubbard Model: A Computational Perspective". en. In: *Annual Review of Condensed Matter Physics* 13.1 (Mar. 2022), pp. 275–302. ISSN: 1947-5454, 1947-5462. DOI: 10.1146/annurev-conmatphys-090921-033948. URL: https://www.annualreviews.org/doi/10.1146/annurev-conmatphys-090921-033948 (visited on 05/04/2024).

[199] John J. Quinn and Richard A. Ferrell. "Electron Self-Energy Approach to Correlation in a Degenerate Electron Gas". en. In: *Physical Review* 112.3 (Nov. 1958), pp. 812–827. ISSN: 0031-899X. DOI: 10.1103/PhysRev.112.812. URL: https://link.aps.org/doi/10.1103/PhysRev.112.812 (visited on 05/12/2024).

[200] M. Revzen et al. "Baym-Kadanoff criteria and the Ward-Takahashi relations in many-body theory". en. In: *Physical Review B* 40.1 (July 1989), pp. 769–771. ISSN: 0163-1829. DOI: 10.1103/PhysRevB.40.769. URL: https://link.aps.org/doi/10.1103/PhysRevB.40.769 (visited on 11/14/2024).

[201] Lewis Fry Richardson. "IX. The approximate arithmetical solution by finite differences of physical problems involving differential equations, with an application to the stresses in a masonry dam". en. In: *Philosophical Transactions of the Royal Society of London. Series A, Containing Papers of a Mathematical or Physical Character* 210.459-470 (Jan. 1911), pp. 307–357. ISSN: 0264-3952, 2053-9258. DOI: 10.1098/rsta.1911.0009. URL: https://royalsocietypublishing.org/doi/10.1098/rsta.1911.0009 (visited on 12/25/2024).

[202] G. Rohringer and A. Toschi. "Impact of nonlocal correlations over different energy scales: A dynamical vertex approximation study". en. In: *Physical Review B* 94.12 (Sept. 2016), p. 125144. ISSN: 2469-9950, 2469-9969. DOI: 10.1103/PhysRevB.94.125144. URL: https://link.aps.org/doi/10.1103/PhysRevB.94.125144 (visited on 07/08/2024).

[203] G. Rohringer et al. "Critical Properties of the Half-Filled Hubbard Model in Three Dimensions". en. In: *Physical Review Letters* 107.25 (Dec. 2011), p. 256402. ISSN: 0031-9007, 1079-7114. DOI: 10.1103/PhysRevLett.107.256402. URL: https://link.aps.org/doi/10.1103/PhysRevLett.107.256402 (visited on 01/12/2025).

[204] G. Rohringer et al. "Diagrammatic routes to nonlocal correlations beyond dynamical mean field theory". en. In: *Reviews of Modern Physics* 90.2 (May 2018), p. 025003. ISSN: 0034-6861, 1539-0756. DOI: 10.1103/RevModPhys.90.025003. URL: https://link.aps.org/doi/10.1103/RevModPhys.90.025003 (visited on 11/12/2024).

[205] Georg Rohringer. "New routes towards a theoretical treatment of nonlocal electronic correlations". en. PhD thesis. TU Wien, 2013. DOI: 10.34726/HSS.2013.21498. URL: https://repositum.tuwien.at/handle/20.500.12708/6957 (visited on 12/13/2023).

[206] Georg Rohringer and Thomas Schaefer. *LadderDGA*. June 2017. URL: https://github.com/ladderDGA/ladderDGA.

[207] Georg Rohringer, Angelo Valli, and Alessandro Toschi. "Local Electronic Correlation at the Two-Particle Level". In: *Physical Review B* 86.12 (Sept. 2012). arXiv:1202.2796 [cond-mat], p. 125114. ISSN: 1098-0121, 1550-235X. DOI: 10.1103/PhysRevB.86.125114. URL: http://arxiv.org/abs/1202.2796 (visited on 06/27/2024).

[208] S. Roy and A.-M. S. Tremblay. "Scaling and commensurate-incommensurate crossover for the d=2, z=2 quantum critical point of itinerant antiferromagnets". In: *EPL (Europhysics Letters)* 84.3 (Nov. 2008), p. 37013. ISSN: 0295-5075, 1286-4854. DOI: 10.1209/0295-5075/84/37013. URL: https://iopscience.iop.org/article/10.1209/0295-5075/84/37013 (visited on 11/21/2024).

[209] A. N. Rubtsov, M. I. Katsnelson, and A. I. Lichtenstein. "Dual fermion approach to nonlocal correlations in the Hubbard model". en. In: *Physical Review B* 77.3 (Jan. 2008), p. 033101. ISSN: 1098-0121, 1550-235X. DOI: 10.1103/PhysRevB.77.033101. URL: https://link.aps.org/doi/10.1103/PhysRevB.77.033101 (visited on 07/07/2024).

[210] A.N. Rubtsov, M.I. Katsnelson, and A.I. Lichtenstein. "Dual boson approach to collective excitations in correlated fermionic systems". en. In: *Annals of Physics* 327.5 (May 2012), pp. 1320–1335. ISSN: 00034916. DOI: 10.1016/j.aop.2012.01.002. URL: https://linkinghub.elsevier.com/retrieve/pii/S0003491612000164 (visited on 07/09/2024).

[211] Dalton A R Sakthivadivel. "Magnetisation and Mean Field Theory in the Ising Model". In: *SciPost Physics Lecture Notes* (Jan. 2022), p. 35. ISSN: 2590-1990. DOI: 10.21468/SciPostPhysLectNotes.35. URL: https://scipost.org/10.21468/SciPostPhysLectNotes.35 (visited on 01/12/2025).

[212] Sören Sanders and Martin Holthaus. "Hypergeometric continuation of divergent perturbation series. I. Critical exponents of the Bose-Hubbard model". In: *New Journal of Physics* 19.10 (Nov. 2017). arXiv:1803.04876 [cond-mat], p. 103036. ISSN: 1367-2630. DOI: 10.1088/1367-2630/aa9165. URL: http://arxiv.org/abs/1803.04876 (visited on 05/26/2024).

[213] Sören Sanders and Martin Holthaus. "Hypergeometric continuation of divergent perturbation series. II. Comparison with Shanks transformation and Pad\'e approximation". In: *Journal of Physics A: Mathematical and Theoretical* 50.46 (Nov. 2017). arXiv:1803.04882 [cond-mat], p. 465302. ISSN: 1751-8113, 1751-8121. DOI: 10.1088/1751-8121/aa8f01. URL: http://arxiv.org/abs/1803.04882 (visited on 05/26/2024).

[214] Tarapada Sarkar et al. "Ferromagnetic order beyond the superconducting dome in a cuprate superconductor". en. In: *Science* 368.6490 (May 2020), pp. 532–534. ISSN: 0036-8075, 1095-9203. DOI: 10.1126/science.aax1581. URL: https://www.science.org/doi/10.1126/science.aax1581 (visited on 01/02/2025).

[215] T. Schäfer et al. "Divergent Precursors of the Mott-Hubbard Transition at the Two-Particle Level". en. In: *Physical Review Letters* 110.24 (June 2013), p. 246405. ISSN: 0031-9007, 1079-7114. DOI: 10.1103/PhysRevLett.110.246405. URL: https://link.aps.org/doi/10.1103/PhysRevLett.110.246405 (visited on 11/12/2024).

[216] T. Schäfer et al. "Fate of the false Mott-Hubbard transition in two dimensions". en. In: *Physical Review B* 91.12 (Mar. 2015), p. 125109. ISSN: 1098-0121, 1550-235X. DOI: 10.1103/PhysRevB.91.125109. URL: https://link.aps.org/doi/10.1103/PhysRevB.91.125109 (visited on 01/12/2025).

[217] T. Schäfer et al. "Interplay of Correlations and Kohn Anomalies in Three Dimensions: Quantum Criticality with a Twist". en. In: *Physical Review Letters* 119.4 (July 2017), p. 046402. ISSN: 0031-9007, 1079-7114. DOI: 10.1103/PhysRevLett.119.046402. URL: http://link.aps.org/doi/10.1103/PhysRevLett.119.046402 (visited on 01/12/2025).

[218] T. Schäfer et al. "Quantum Criticality in the Two-Dimensional Periodic Anderson Model". en. In: *Physical Review Letters* 122.22 (June 2019), p. 227201. ISSN: 0031-9007, 1079-7114. DOI: 10.1103/PhysRevLett.122.227201. URL: https://link.aps.org/doi/10.1103/PhysRevLett.122.227201 (visited on 01/12/2025).

[219] Thomas Schäfer. "Classical and quantum phase transitions in strongly correlated electron systems". en. Artwork Size: 176 pages Medium: application/pdf Pages: 176 pages. PhD thesis. TU Wien, 2016. DOI: 10.34726/HSS.2016.28659. URL: https://repositum.tuwien.at/handle/20.500.12708/3282 (visited on 11/04/2024).

[220] Thomas Schäfer, Alessandro Toschi, and Karsten Held. "Dynamical vertex approximation for the two-dimensional Hubbard model". en. In: *Journal of Magnetism and Magnetic Materials* 400 (Feb. 2016), pp. 107–111. ISSN: 03048853. DOI: 10.1016/j.jmmm.2015.07.103. URL: https://linkinghub.elsevier.com/retrieve/pii/S030488531530411X (visited on 11/12/2024).

[221] T. Schauerte and P. G. J. Van Dongen. "Symmetry breaking in the Hubbard model at weak coupling". en. In: *Physical Review B* 65.8 (Feb. 2002), p. 081105. ISSN: 0163-1829, 1095-3795. DOI: 10.1103/PhysRevB.65.081105. URL: https://link.aps.org/doi/10.1103/PhysRevB.65.081105 (visited on 01/12/2025).

[222] Avraham Schiller and Kevin Ingersent. "Systematic 1 / d Corrections to the Infinite-Dimensional Limit of Correlated Lattice Electron Models". en. In: *Physical Review Letters* 75.1 (July 1995), pp. 113–116. ISSN: 0031-9007, 1079-7114. DOI: 10.1103/PhysRevLett.75.113. URL: https://link.aps.org/doi/10.1103/PhysRevLett.75.113 (visited on 07/17/2024).

[223] R.J. Schmidt. "XXXII. On the numerical solution of linear simultaneous equations by an iterative method". en. In: *The London, Edinburgh, and Dublin Philosophical Magazine and Journal of Science* 32.214 (Nov. 1941), pp. 369–383. ISSN: 1941-5982, 1941-5990. DOI: 10.1080/14786444108520797. URL: http://www.tandfonline.com/doi/abs/10.1080/14786444108520797 (visited on 12/25/2024).

[224] J. R. Schrieffer and P. A. Wolff. "Relation between the Anderson and Kondo Hamiltonians". en. In: *Physical Review* 149.2 (Sept. 1966), pp. 491–492. ISSN: 0031-899X. DOI: 10.1103/PhysRev.149.491. URL: https://link.aps.org/doi/10.1103/PhysRev.149.491 (visited on 05/04/2024).

[225] G. Seibold et al. "Spin excitations of ferronematic order in underdoped cuprate superconductors". en. In: *Scientific Reports* 4.1 (June 2014), p. 5319. ISSN: 2045-2322. DOI: 10.1038/srep05319. URL: https://www.nature.com/articles/srep05319 (visited on 12/20/2024).

[226] Patrick Sémon and A.-M. S. Tremblay. "Importance of subleading corrections for the Mott critical point". en. In: *Physical Review B* 85.20 (May 2012), p. 201101. ISSN: 1098-0121, 1550-235X. DOI: 10.1103/PhysRevB.85.201101. URL: https://link.aps.org/doi/10.1103/PhysRevB.85.201101 (visited on 01/12/2025).

[227] David Sénéchal, André-Marie Tremblay, and Claude Bourbonnais, eds. *Theoretical methods for strongly correlated electrons*. en. The CRM series in mathematical physics. New York: Springer, 2004. ISBN: 978-0-387-00895-0.

[228] J. W. Serene and D. W. Hess. "Quasiparticle properties of the two-dimensional Hubbard model in a propagator-renormalized fluctuation-exchange approximation". en. In: *Physical Review B* 44.7 (Aug. 1991), pp. 3391–3394. ISSN: 0163-1829, 1095-3795. DOI: 10.1103/PhysRevB.44.3391. URL: https://link.aps.org/doi/10.1103/PhysRevB.44.3391 (visited on 11/19/2024).

[229] L. J. Sham and M. Schlüter. "Density-Functional Theory of the Energy Gap". en. In: *Physical Review Letters* 51.20 (Nov. 1983), pp. 1888–1891. ISSN: 0031-9007. DOI: 10.1103/PhysRevLett.51.1888. URL: https://link.aps.org/doi/10.1103/PhysRevLett.51.1888 (visited on 01/20/2025).

[230] Daniel Shanks. "Non-linear Transformations of Divergent and Slowly Convergent Sequences". en. In: *Journal of Mathematics and Physics* 34.1-4 (Apr. 1955), pp. 1–42. ISSN: 0097-1421. DOI: 10.1002/sapm19553411. URL: https://onlinelibrary.wiley.com/doi/10.1002/sapm19553411 (visited on 12/25/2024).

[231] Hiroshi Shinaoka et al. "Compressing Green's function using intermediate representation between imaginary-time and real-frequency domains". en. In: *Physical Review B* 96.3 (July 2017), p. 035147. ISSN: 2469-9950, 2469-9969. DOI: 10.1103/PhysRevB.96.035147. URL: http://link.aps.org/doi/10.1103/PhysRevB.96.035147 (visited on 12/04/2024).

[232] Hiroshi Shinaoka et al. "Overcomplete compact representation of two-particle Green's functions". en. In: *Physical Review B* 97.20 (May 2018), p. 205111. ISSN: 2469-9950, 2469-9969. DOI: 10.1103/PhysRevB.97.205111. URL: https://link.aps.org/doi/10.1103/PhysRevB.97.205111 (visited on 01/20/2025).

[233] Eric Smith. "Large-deviation principles, stochastic effective actions, path entropies, and the structure and meaning of thermodynamic descriptions". In: *Reports on Progress in Physics* 74.4 (Apr. 2011). arXiv:1102.3938 [cond-mat, physics:math-ph], p. 046601. ISSN: 0034-4885, 1361-6633. DOI: 10.1088/0034-4885/74/4/046601. URL: http://arxiv.org/abs/1102.3938 (visited on 04/29/2024).

[234] Roger Alan Smith. "Planar version of Baym-Kadanoff theory". en. In: *Physical Review A* 46.8 (Oct. 1992), pp. 4586–4597. ISSN: 1050-2947, 1094-1622. DOI: 10.1103/PhysRevA.46.4586. URL: https://link.aps.org/doi/10.1103/PhysRevA.46.4586 (visited on 07/08/2024).

[235] J. E. Sonier et al. "Direct search for a ferromagnetic phase in a heavily overdoped nonsuperconducting copper oxide". en. In: *Proceedings of the National Academy of Sciences* 107.40 (Oct. 2010), pp. 17131–17134. ISSN: 0027-8424, 1091-6490. DOI: 10.1073/pnas.1007079107. URL: https://pnas.org/doi/full/10.1073/pnas.1007079107 (visited on 01/02/2025).

[236] Jozef Spalek. "t-J model then and now: A personal perspective from the pioneering times". In: (2007). Publisher: [object Object] Version Number: 1. DOI: 10.48550/ARXIV.0706.4236. URL: https://arxiv.org/abs/0706.4236 (visited on 05/04/2024).

[237] Peter Staar, Thomas Maier, and Thomas Schulthess. "Two-particle correlations in a dynamic cluster approximation with continuous momentum dependence: Superconductivity in the 2D Hubbard model". In: (2014). Publisher: arXiv Version Number: 1. DOI: 10.48550/ARXIV.1402.4329. URL: https://arxiv.org/abs/1402.4329 (visited on 11/24/2024).

[238] Peter Staar, Thomas Maier, and Thomas C. Schulthess. "Dynamical cluster approximation with continuous lattice self-energy". en. In: *Physical Review B* 88.11 (Sept. 2013), p. 115101. ISSN: 1098-0121, 1550-235X. DOI: 10.1103/PhysRevB.88.115101. URL: https://link.aps.org/doi/10.1103/PhysRevB.88.115101 (visited on 07/17/2024).

[239] H. Eugene Stanley. *Introduction to phase transitions and critical phenomena*. New York: Oxford University Press, 1987. ISBN: 978-0-19-505316-6.

[240] Harald Steck. "Embarrassingly Shallow Autoencoders for Sparse Data". In: *The World Wide Web Conference*. arXiv:1905.03375 [cs]. May 2019, pp. 3251–3257. DOI: 10.1145/3308558.3313710. URL: http://arxiv.org/abs/1905.03375 (visited on 12/04/2024).

[241] Steffen Backes and Julian Stobbe. *sfED*. 2022. URL: https://github.com/steffenbackes/sfED.

[242] E. A. Stepanov et al. "Self-consistent dual boson approach to single-particle and collective excitations in correlated systems". en. In: *Physical Review B* 93.4 (Jan. 2016), p. 045107. ISSN: 2469-9950, 2469-9969. DOI: 10.1103/PhysRevB.93.045107. URL: https://link.aps.org/doi/10.1103/PhysRevB.93.045107 (visited on 07/09/2024).

[243] Evgeny A. Stepanov et al. "Quantum spin fluctuations and evolution of electronic structure in cuprates". en. In: *npj Quantum Materials* 3.1 (Oct. 2018), p. 54. ISSN: 2397-4648. DOI: 10.1038/s41535-018-0128-x. URL: https://www.nature.com/articles/s41535-018-0128-x (visited on 12/20/2024).

[244] Julian Stobbe. *BSE_Asymptotics.jl*. Hamburg, Oct. 2024. URL: https://github.com/Atomtomate/BSE_Asymptotics.jl.

[245] Julian Stobbe. *EquivalenceClassesConstructor.jl*. Hamburg, Nov. 2024. URL: https://github.com/Atomtomate/EquivalenceClassesConstructor.jl.

[246] Julian Stobbe. "Implementation of continuous time quantum Monte Carlo solvers for the infinite dimensional Hubbard model at half filling". MA thesis. Frankfurt: Johann Wolfgang Goethe-Universität, Mar. 2018.

[247] Julian Stobbe. "Risk sensitivities in risk-neutral network valuations". Thesis. Frankfurt am Main: Johann Wolfgang Goethe-Universität, Apr. 2019.

[248] Julian Stobbe. *SeriesAcceleration.jl*. Hamburg, Nov. 2024. URL: https://github.com/Atomtomate/SeriesAcceleration.j.

[249] Julian Stobbe. *VertexPostprocessing.jl*. Hamburg, Nov. 2024. URL: https://github.com/Atomtomate/VertexPostprocessing.jl.

[250] Julian Stobbe, Marco Knipfer, and Daniel Springer. *LW_ML*. Oct. 2024. URL: https://github.com/Atomtomate/PyTorchLightningTemplate.

[251] Julian Stobbe and Marvin Leusch. *lDGAPythonWrapper*. Hamburg, Nov. 2024. URL: https://github.com/Atomtomate/lDGAPythonWrapper.

[252] Julian Stobbe, Marvin Leusch, and Frederik Weissler. *Dispersions.jl*. Hamburg, Nov. 2024. URL: https://github.com/Atomtomate/Dispersions.jl.

[253] Julian Stobbe and Georg Rohringer. "Consistency of potential energy in the dynamical vertex approximation". en. In: *Physical Review B* 106.20 (Nov. 2022), p. 205101. ISSN: 2469-9950, 2469-9969. DOI: 10.1103/PhysRevB.106.205101. URL: https://link.aps.org/doi/10.1103/PhysRevB.106.205101 (visited on 05/04/2024).

[254] Julian Stobbe, Frederik Weissler, and Georg Rohringer. *LadderDGA.jl*. Hamburg, Nov. 2024. URL: https://github.com/Atomtomate/LadderDGA.jl.

[255] Hugo U. R. Strand et al. "The Dynamical Mean Field Theory phase space extension and critical properties of the finite temperature Mott transition". In: *Physical Review B* 83.20 (May 2010). arXiv: 1012.3829 ISBN: 9789162882266, p. 205136. ISSN: 1098-0121. DOI: 10.1103/PhysRevB.83.205136. URL: http://arxiv.org/abs/1012.3829%0Ahttp://dx.doi.org/10.1103/PhysRevB.83.205136 (visited on 03/11/2018).

[256] Agnese Tagliavini et al. "Efficient Bethe-Salpeter equation treatment in dynamical mean-field theory". en. In: *Physical Review B* 97.23 (June 2018), p. 235140. ISSN: 2469-9950, 2469-9969. DOI: 10.1103/PhysRevB.97.235140. URL: https://link.aps.org/doi/10.1103/PhysRevB.97.235140 (visited on 10/16/2024).

[257] A. N. Tahvildar-Zadeh, J. K. Freericks, and M. Jarrell. "Magnetic phase diagram of the Hubbard model in three dimensions:The second-order local approximation". en. In: *Physical Review B* 55.2 (Jan. 1997), pp. 942–946. ISSN: 0163-1829, 1095-3795. DOI: 10.1103/PhysRevB.55.942. URL: https://link.aps.org/doi/10.1103/PhysRevB.55.942 (visited on 01/12/2025).

[258] Y. Takahashi. "On the generalized ward identity". en. In: *Il Nuovo Cimento* 6.2 (Aug. 1957), pp. 371–375. ISSN: 0029-6341, 1827-6121. DOI: 10.1007/BF02832514. URL: http://link.springer.com/10.1007/BF02832514 (visited on 07/06/2024).

[259] Ka-Ming Tam et al. "Solving the parquet equations for the Hubbard model beyond weak coupling". en. In: *Physical Review E* 87.1 (Jan. 2013), p. 013311. ISSN: 1539-3755, 1550-2376. DOI: 10.1103/PhysRevE.87.013311. URL: https://link.aps.org/doi/10.1103/PhysRevE.87.013311 (visited on 01/12/2025).

[260] Kiyohisa Tanaka et al. "Quantitative Comparison between Electronic Raman Scattering and Angle-Resolved Photoemission Spectra in Bi_2 Sr_2 $CaCu_2$ O_{8+} Superconductors: Doping Dependence of Nodal and Antinodal Superconducting Gaps". en. In: *Journal of the Physical Society of Japan* 88.4 (Apr. 2019), p. 044710. ISSN: 0031-9015, 1347-4073. DOI: 10.7566/JPSJ.88.044710. URL: https://journals.jps.jp/doi/10.7566/JPSJ.88.044710 (visited on 12/08/2024).

[261] C. Taranto et al. "From Infinite to Two Dimensions through the Functional Renormalization Group". en. In: *Physical Review Letters* 112.19 (May 2014), p. 196402. ISSN: 0031-9007, 1079-7114. DOI: 10.1103/PhysRevLett.112.196402. URL: https://link.aps.org/doi/10.1103/PhysRevLett.112.196402 (visited on 01/12/2025).

[262] Shingo Teranishi et al. "Effect of On-site Coulomb Repulsion on Ferromagnetic Fluctuations in Heavily Overdoped Cuprates". en. In: *Journal of the Physical Society of Japan* 90.9 (Sept. 2021), p. 094707. ISSN: 0031-9015, 1347-4073. DOI: 10.7566/JPSJ.90.094707. URL: https://journals.jps.jp/doi/10.7566/JPSJ.90.094707 (visited on 01/03/2025).

[263] P. Thunström et al. "Analytical investigation of singularities in two-particle irreducible vertex functions of the Hubbard atom". en. In: *Physical Review B* 98.23 (Dec. 2018), p. 235107. ISSN: 2469-9950, 2469-9969. DOI: 10.1103/PhysRevB.98.235107. URL: https://link.aps.org/doi/10.1103/PhysRevB.98.235107 (visited on 05/29/2024).

[264] A. Toschi, A. A. Katanin, and K. Held. "Dynamical vertex approximation: A step beyond dynamical mean-field theory". en. In: *Physical Review B* 75.4 (Jan. 2007), p. 045118. ISSN: 1098-0121, 1550-235X. DOI: 10.1103/PhysRevB.75.045118. URL: https://link.aps.org/doi/10.1103/PhysRevB.75.045118 (visited on 07/03/2024).

[265] Tadashi Toyoda and Masamichi Okada. "Exact relations for the spin-correlation functions for an interacting electron gas in a nonuniform magnetic field". en. In: *Physical Review B* 58.3 (July 1998), pp. 1210–1217. ISSN: 0163-1829, 1095-3795. DOI: 10.1103/PhysRevB.58.1210. URL: https://link.aps.org/doi/10.1103/PhysRevB.58.1210 (visited on 11/14/2024).

[266] AndrÈ-Marie Tremblay. *PHY-892 Quantum Materials Theory, from perturbation theory to dynamical-mean Field theory (lecture notes)*. en. 2024. URL: https://www.physique.usherbrooke.ca/tremblay/cours/phy-892/N-corps.pdf.

[267] Matthias Troyer and Uwe-Jens Wiese. "Computational Complexity and Fundamental Limitations to Fermionic Quantum Monte Carlo Simulations". en. In: *Physical Review Letters* 94.17 (May 2005), p. 170201. ISSN: 0031-9007, 1079-7114. DOI: 10.1103/PhysRevLett.94.170201. URL: https://link.aps.org/doi/10.1103/PhysRevLett.94.170201 (visited on 07/17/2024).

[268] Tsogbayar Tsednee and Tyler Luchko. "Closure for the Ornstein-Zernike equation with pressure and free energy consistency". en. In: *Physical Review E* 99.3 (Mar. 2019), p. 032130. ISSN: 2470-0045, 2470-0053. DOI: 10.1103/PhysRevE.99.032130. URL: https://link.aps.org/doi/10.1103/PhysRevE.99.032130 (visited on 01/12/2025).

[269] A. Valli et al. "Dynamical vertex approximation in its parquet implementation: Application to Hubbard nanorings". en. In: *Physical Review B* 91.11 (Mar. 2015), p. 115115. ISSN: 1098-0121, 1550-235X. DOI: 10.1103/PhysRevB.91.115115. URL: https://link.aps.org/doi/10.1103/PhysRevB.91.115115 (visited on 01/12/2025).

[270] Erik G. C. P. Van Loon et al. "Beyond extended dynamical mean-field theory: Dual boson approach to the two-dimensional extended Hubbard model". en. In: *Physical Review B* 90.23 (Dec. 2014), p. 235135. ISSN: 1098-0121, 1550-235X. DOI: 10.1103/PhysRevB.90.235135. URL: https://link.aps.org/doi/10.1103/PhysRevB.90.235135 (visited on 12/08/2024).

[271] Erik G. C. P. Van Loon et al. "Double occupancy in dynamical mean-field theory and the dual boson approach". en. In: *Physical Review B* 93.15 (Apr. 2016), p. 155162. ISSN: 2469-9950, 2469-9969. DOI: 10.1103/PhysRevB.93.155162. URL: https://link.aps.org/doi/10.1103/PhysRevB.93.155162 (visited on 07/08/2024).

[272] C. M. Varma. "Non-Fermi-liquid states and pairing instability of a general model of copper oxide metals". en. In: *Physical Review B* 55.21 (June 1997), pp. 14554–14580. ISSN: 0163-1829, 1095-3795. DOI: 10.1103/PhysRevB.55.14554. URL: https://link.aps.org/doi/10.1103/PhysRevB.55.14554 (visited on 12/18/2024).

[273] C. M. Varma. "Pseudogap Phase and the Quantum-Critical Point in Copper-Oxide Metals". In: *Phys. Rev. Lett.* 83.17 (Oct. 1999). Publisher: American Physical Society, pp. 3538–3541. DOI: 10.1103/PhysRevLett.83.3538. URL: https://link.aps.org/doi/10.1103/PhysRevLett.83.3538.

[274] A. N. Vasil'ev and A. K. Kazanskii. "Legendre transforms of the generating functionals in quantum field theory". en. In: *Theoretical and Mathematical Physics* 12.3 (Sept. 1972), pp. 875–887. ISSN: 0040-5779, 1573-9333. DOI: 10.1007/BF01035606. URL: http://link.springer.com/10.1007/BF01035606 (visited on 07/23/2024).

[275] John Verzani and Contributors. *Roots.jl*. URL: https://github.com/JuliaMath/Roots.jl.

[276] Sean Vig et al. "Measurement of the dynamic charge response of materials using low-energy, momentum-resolved electron energy-loss spectroscopy (M-EELS)". In: (2015). Publisher: arXiv Version Number: 5. DOI: 10.48550/ARXIV.1509.04230. URL: https://arxiv.org/abs/1509.04230 (visited on 12/08/2024).

[277] Y. M. Vilk and A.-M.S. Tremblay. "Non-Perturbative Many-Body Approach to the Hubbard Model and Single-Particle Pseudogap". In: *Journal de Physique I* 7.11 (Nov. 1997), pp. 1309–1368. ISSN: 1155-4304, 1286-4862. DOI: 10.1051/jp1:1997135. URL: http://www.edpsciences.org/10.1051/jp1:1997135 (visited on 07/15/2024).

[278] Y.M. Vilk, Liang Chen, and A.-M.S. Tremblay. "Two-particle self-consistent theory for spin and charge fluctuations in the Hubbard model". en. In: *Physica C: Superconductivity* 235-240 (Dec. 1994), pp. 2235–2236. ISSN: 09214534. DOI: 10.1016/0921-4534(94)92339-6. URL: https://linkinghub.elsevier.com/retrieve/pii/0921453494923396 (visited on 12/10/2024).

[279] Matthias Vojta. "Lattice symmetry breaking in cuprate superconductors: stripes, nematics, and superconductivity". en. In: *Advances in Physics* 58.6 (Nov. 2009), pp. 699–820. ISSN: 0001-8732, 1460-6976. DOI: 10.1080/00018730903122242. URL: http://www.tandfonline.com/doi/abs/10.1080/00018730903122242 (visited on 12/20/2024).

[280] D. Vollhardt and P. Wölfle. "Diagrammatic, self-consistent treatment of the Anderson localization problem in d 2 dimensions". en. In: *Physical Review B* 22.10 (Nov. 1980), pp. 4666–4679. ISSN: 0163-1829. DOI: 10.1103/PhysRevB.22.4666. URL: https://link.aps.org/doi/10.1103/PhysRevB.22.4666 (visited on 11/14/2024).

[281] Dieter Vollhardt, Krzysztof Byczuk, and Marcus Kollar. "Dynamical Mean-Field Theory". en. In: *Strongly Correlated Systems*. Ed. by Adolfo Avella and Ferdinando Mancini. Vol. 171. Series Title: Springer Series in Solid-State Sciences ISBN: 978-3-642-21831-6. Berlin, Heidelberg: Springer Berlin Heidelberg, 2012, pp. 203–236. ISBN: 978-3-642-21830-9. DOI: 10.1007/978-3-642-21831-6_7. URL: https://link.springer.com/10.1007/978-3-642-21831-6_7 (visited on 06/17/2024).

[282] M. B. Walker and Th. W. Ruijgrok. "Absence of Magnetic Ordering in One and Two Dimensions in a Many-Band Model for Interacting Electrons in a Metal". en. In: *Physical Review* 171.2 (July 1968), pp. 513–515. ISSN: 0031-899X. DOI: 10.1103/PhysRev.171.513. URL: https://link.aps.org/doi/10.1103/PhysRev.171.513 (visited on 07/17/2024).

[283] Markus Wallerberger et al. "sparse-ir: Optimal compression and sparse sampling of many-body propagators". en. In: *SoftwareX* 21 (Feb. 2023), p. 101266. ISSN: 23527110. DOI: 10.1016/j.softx.2022.101266. URL: https://linkinghub.elsevier.com/retrieve/pii/S2352711022001844 (visited on 12/04/2024).

[284] Markus Wallerberger et al. "w2dynamics: Local one- and two-particle quantities from dynamical mean field theory". en. In: *Computer Physics Communications* 235 (Feb. 2019), pp. 388–399. ISSN: 00104655. DOI: 10.1016/j.cpc.2018.09.007. URL: https://linkinghub.elsevier.com/retrieve/pii/S0010465518303217 (visited on 01/12/2025).

[285] Guido Walz. "The History of Extrapolation Methods in N umerical Analysis". en. In: (Oct. 1991).

[286] J. C. Ward. "An Identity in Quantum Electrodynamics". en. In: *Physical Review* 78.2 (Apr. 1950), pp. 182–182. ISSN: 0031-899X. DOI: 10.1103/PhysRev.78.182. URL: https://link.aps.org/doi/10.1103/PhysRev.78.182 (visited on 07/06/2024).

[287] Pierre Weiss. "L'hypothèse du champ moléculaire et la propriété ferromagnétique". In: *Journal de Physique Théorique et Appliquée* 6.1 (1907), pp. 661–690. ISSN: 0368-3893. DOI: 10.1051/jphystap:019070060066100. URL: http://www.edpsciences.org/10.1051/jphystap:019070060066100 (visited on 06/15/2024).

[288] Frederik Weissler. "Two-particle consistency for correlated electron systems". PhD thesis. Hamburg: Hamburg, 2024.

[289] Ernst Joachim Weniger. *Nonlinear sequence transformations for the acceleration of convergence and the summation of divergent series*. arXiv:math/0306302. June 2003. DOI: 10.48550/arXiv.math/0306302. URL: http://arxiv.org/abs/math/0306302 (visited on 12/25/2024).

[290] Nils Wentzell et al. "High-frequency asymptotics of the vertex function: Diagrammatic parametrization and algorithmic implementation". en. In: *Physical Review B* 102.8 (Aug. 2020), p. 085106. ISSN: 2469-9950, 2469-9969. DOI: 10.1103/PhysRevB.102.085106. URL: https://link.aps.org/doi/10.1103/PhysRevB.102.085106 (visited on 11/02/2024).

[291] Wei Wu et al. "Effect of Van Hove singularities in the onset of pseudogap states in Mott insulators". en. In: *Physical Review Research* 2.3 (July 2020), p. 033067. ISSN: 2643-1564. DOI: 10.1103/PhysRevResearch.2.033067. URL: https://link.aps.org/doi/10.1103/PhysRevResearch.2.033067 (visited on 12/27/2024).

[292] P. Wynn. "On a Device for Computing the e m (S n) Transformation". In: *Mathematical Tables and Other Aids to Computation* 10.54 (Apr. 1956), p. 91. ISSN: 08916837. DOI: 10.2307/2002183. URL: https://www.jstor.org/stable/2002183?origin=crossref (visited on 12/25/2024).

[293] Cenke Xu and Leon Balents. "Topological Superconductivity in Twisted Multilayer Graphene". en. In: *Physical Review Letters* 121.8 (Aug. 2018), p. 087001. ISSN: 0031-9007, 1079-7114. DOI: 10.1103/PhysRevLett.121.087001. URL: https://link.aps.org/doi/10.1103/PhysRevLett.121.087001 (visited on 05/04/2024).

[294] S. X. Yang et al. "Parquet approximation for the 4 × 4 Hubbard cluster". en. In: *Physical Review E* 80.4 (Oct. 2009), p. 046706. ISSN: 1539-3755, 1550-2376. DOI: 10.1103/PhysRevE.80.046706. URL: https://link.aps.org/doi/10.1103/PhysRevE.80.046706 (visited on 01/12/2025).

[295] T. Yoshida et al. "Systematic doping evolution of the underlying Fermi surface of La 2 − x Sr x Cu O 4". en. In: *Physical Review B* 74.22 (Dec. 2006), p. 224510. ISSN: 1098-0121, 1550-235X. DOI: 10.1103/PhysRevB.74.224510. URL: https://link.aps.org/doi/10.1103/PhysRevB.74.224510 (visited on 12/20/2024).

[296] D. M. Young and J. F. Traub. "Iterative Methods for the Solution of Equations." In: *The American Mathematical Monthly* 74.3 (Mar. 1967), p. 346. ISSN: 00029890. DOI: 10.2307/2316079. URL: https://www.jstor.org/stable/2316079?origin=crossref (visited on 11/07/2024).

[297] Tianlun Yu. *Does ARPES truly represent high-Tc superconductivity in cuprates?* Artwork Size: 23046 Pages: 23046. 2020. DOI: 10.7910/DVN/3OFENZ. URL: https://dataverse.harvard.edu/citation?persistentId=doi:10.7910/DVN/3OFENZ (visited on 12/08/2024).

[298] Karim Zantout. "The two-particle self-consistent approach and its application to real materials". de. PhD thesis. Goethe-Universität Frankfurt am Main, 2021. DOI: 10.21248/gups.61114. URL: http://publikationen.ub.uni-frankfurt.de/frontdoor/index/index/docId/61114 (visited on 04/11/2024).

[299] Pan Zhou et al. *Towards Theoretically Understanding Why SGD Generalizes Better Than ADAM in Deep Learning*. arXiv:2010.05627 [cs]. Nov. 2021. DOI: 10.48550/arXiv.2010.05627. URL: http://arxiv.org/abs/2010.05627 (visited on 12/06/2024).

[300] Rok Zitko, Janez Bonca, and Thomas Pruschke. "Van Hove singularities in the paramagnetic phase of the Hubbard model: a DMFT study". In: *Physical Review B* 80.24 (Dec. 2009). arXiv:0908.0887 [cond-mat], p. 245112. ISSN: 1098-0121, 1550-235X. DOI: 10.1103/PhysRevB.80.245112. URL: http://arxiv.org/abs/0908.0887 (visited on 06/14/2024).